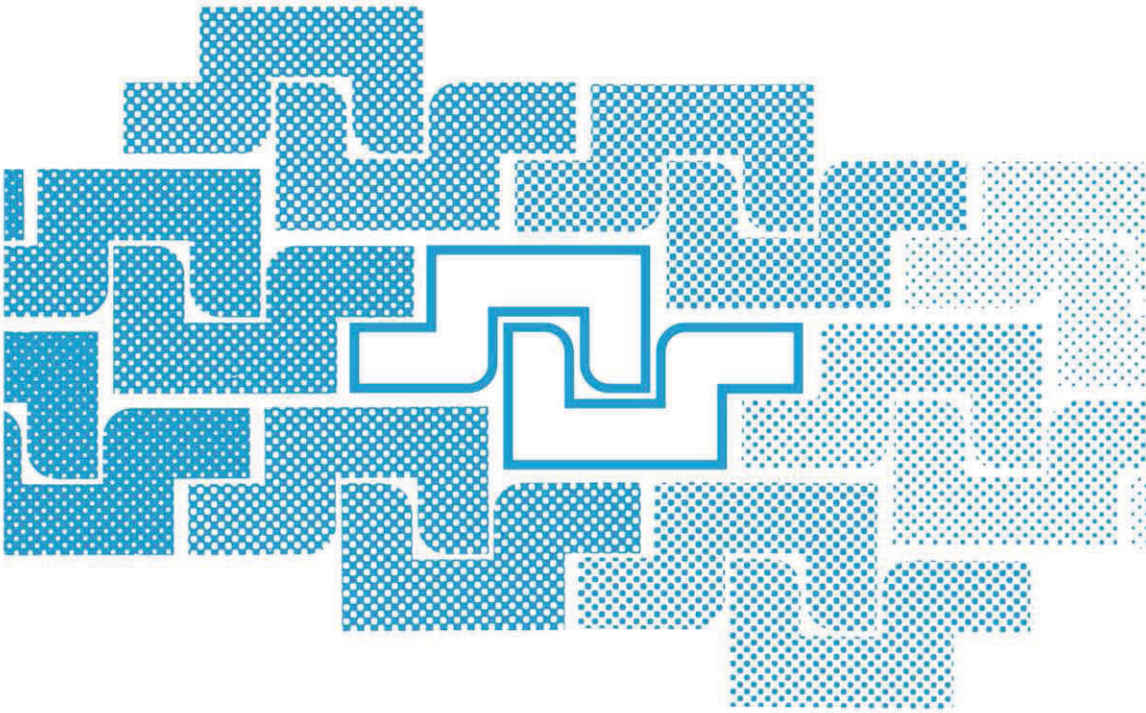

Flow and Transport Processes with Complex Obstructions

Edited by

Yevgeny A. Gayev and Julian C.R. Hunt

NATO Science Series

II. Mathematics, Physics and Chemistry – Vol. 236

Flow and Transport Processes with Complex Obstructions

NATO Science Series

A Series presenting the results of scientific meetings supported under the NATO Science Programme.

The Series is published by IOS Press, Amsterdam, and Springer in conjunction with the NATO Public Diplomacy Division.

Sub-Series

I. Life and Behavioural Sciences	IOS Press
II. Mathematics, Physics and Chemistry	Springer
III. Computer and Systems Science	IOS Press
IV. Earth and Environmental Sciences	Springer

The NATO Science Series continues the series of books published formerly as the NATO ASI Series.

The NATO Science Programme offers support for collaboration in civil science between scientists of countries of the Euro-Atlantic Partnership Council. The types of scientific meeting generally supported are "Advanced Study Institutes" and "Advanced Research Workshops", and the NATO Science Series collects together the results of these meetings. The meetings are co-organized by scientists from NATO countries and scientists from NATO's Partner countries — countries of the CIS and Central and Eastern Europe.

Advanced Study Institutes are high-level tutorial courses offering in-depth study of latest advances in a field.
Advanced Research Workshops are expert meetings aimed at critical assessment of a field, and identification of directions for future action.

As a consequence of the restructuring of the NATO Science Programme in 1999, the NATO Science Series was re-organized to the four sub-series noted above. Please consult the following web sites for information on previous volumes published in the Series.

http://www.nato.int/science
http://www.springer.com
http://www.iospress.nl

Series II: Mathematics, Physics and Chemistry – Vol. 236

Flow and Transport Processes with Complex Obstructions

Applications to Cities, Vegetative Canopies, and Industry

edited by

Yevgeny A. Gayev
Institute of Hydromechanics of
Ukrainian National Academy of Sciences,
Ukraine

and

Julian C.R. Hunt
University College London,
U.K.

Published in cooperation with NATO Public Diplomacy Division

Proceedings of the NATO Advanced Study Institute on
Flow and Transport Processes in Complex Obstructed Geometries: from Cities and Vegetative Canopies to Engineering Problems
Kyiv, Ukraine
4–15 May 2004

A C.I.P. Catalogue record for this book is available from the Library of Congress.

ISBN-10 1-4020-5384-3 (PB)
ISBN-13 978-1-4020-5384-9 (PB)
ISBN-10 1-4020-5383-5 (HB)
ISBN-13 978-1-4020-5383-2 (HB)
ISBN-10 1-4020-5385-1 (e-book)
ISBN-13 978-1-4020-5385-6 (e-book)

Published by Springer,
P.O. Box 17, 3300 AA Dordrecht, The Netherlands.

www.springer.com

Printed on acid-free paper

Contents

Preface **ix**

1 Variety of problems associated with Canopies, or EPRs **1**
1.1 Vegetative canopies in meteorology 2
1.2 Vegetated river beds 9
1.2.1 The problem in a vertical plane 9
1.2.2 The problem in a horizontal plane 12
1.3 Urban canopies 15
1.4 Spraying coolers 16
1.5 Terminology. Other examples of penetrable roughnesses 22
1.6 Laboratory modelling of the canopy flows 24
1.7 Preliminary conclusion. Turbulence 26

2 Discrete and continuum models of flow and dispersion through canopies **29**
2.1 Introduction 29
2.2 Over/through canopies: characteristic regions and flow patterns 31
2.3 Computational models and physical concepts, especially for meteorology and air flow in urban areas 40
2.3.1 Different types of model 40
2.3.2 Boundary layer (or overall scale) 41
2.3.3 Continuum (or neighbourhood) scale 45
2.3.4 Discrete obstacle or the building/street scale 47
2.4 Dispersion in canopies 51
2.4.1 Discrete/obstacle scale 51
2.4.2 Continuum (or neighbourhood) scale dispersion models 72
2.4.3 Dispersion modelling over the outer-scale 77
2.5 Conclusion 79
2.6 Appendix A: dispersion from a steady source between elongated obstacles with cross wind (e.g. street canyon) 80
2.7 Appendix B: notation and abbreviations 85

3 Easily Penetrable Roughnesses of different structures 89
3.1 EPR made up of immobile elements . . . 89
3.1.1 Fully developed pressure driving flow in a duct with EPR . . . 90
3.1.2 Pulsating laminar flow in a duct with EPR . . . 95
3.1.3 EPR in ducts with non-circular cross sections . . . 100
3.1.4 Boundary layer flow over EPRs . . . 101
3.1.5 Viscous flow entrance to a duct with EPRs . . . 108
3.1.6 Flow entrance into a duct with short EPR inserts . . . 114
3.1.7 Heat and mass exchange in immobile EPRs . . . 116
3.2 EPRs made up of mobile elements . . . 122
3.2.1 Mathematical model of a "droplet EPR" . . . 122
3.2.2 Boundary layer formed by a droplet layer . . . 127
3.2.3 Heat and mass exchange between the flow and the droplet layer . . . 131
3.2.4 Joined heat and mass exchange . . . 138
3.2.5 EPR in the form of a dispersed droplet layer . . . 140
3.2.6 EPR in the form of a multispeed droplet layer . . . 145
3.3 Turbulence in EPRs . . . 150
3.3.1 Heat and mass exchange coefficients . . . 150
3.3.2 Laboratory investigation of the mean properties of the EPR turbulence . . . 152
3.3.3 Algebraic turbulence model for EPR . . . 158
3.3.4 Performance of the spraying cooling system as an EPR . . . 165
3.3.5 Fine structure of the turbulence in EPRs . . . 170
3.3.6 Conclusion . . . 177

4 Observation and simulation of flow in vegetation canopies 179
4.1 Introduction . . . 179
4.2 Flow above the canopy . . . 180
4.3 Flow within the canopy . . . 181
4.4 Computational representations of canopy flow . . . 185
4.5 Higher-order closure schemes . . . 186
4.6 Large-eddy simulation . . . 187
4.7 Contribution of canopy elements to small- and large-scale turbulence . . . 188
4.8 Conditional sampling and composite averaging of large-eddy simulations . . . 190
4.9 Empirical orthogonal function (EOF) analysis . . . 194
4.10 Summary . . . 197

5 Turbulent flow in canopies on complex topography and the effects of stable stratification 199
5.1 Introduction . . . 199
5.2 The windfield over a canopy covered hill . . . 204
5.3 The scalar field over a canopy covered hill . . . 210

5.4 Stable stratification . . . 216
5.5 Summary and conclusions . . . 217

6 Transport in aquatic canopies 221
6.1 Introduction: comparison of aquatic and terrestrial canopies . . . 221
6.2 Emergent canopies . . . 224
6.2.1 Turbulence within emergent canopies . . . 229
6.3 Diffusion within emergent vegetation . . . 230
6.3.1 Longitudinal dispersion . . . 233
6.4 Submerged canopies . . . 239
6.4.1 Scale constraints in a vegetated shear-layer . . . 242
6.5 Summary . . . 250

7 Vorticity annihilation and inviscid blocking in multibody flows 251
7.1 Introduction . . . 251
7.2 Vorticity annihilation in multibody flows . . . 252
7.2.1 Flow generated by isolated body . . . 252
7.2.2 Effect of straining on an isolated wake . . . 254
7.2.3 Intermingling wakes . . . 256
7.3 Inviscid blocking effects in multibody flows . . . 259
7.3.1 Potential flow around a rigid body . . . 259
7.3.2 The mean Eulerian velocity . . . 260
7.3.3 The interstitial Eulerian flow . . . 261
7.3.4 Mean potential flows through groups of fixed bodies . . . 262
7.4 Modelling drag forces and inviscid blocking . . . 264
7.5 High Reynolds number bubbly flows . . . 264
7.5.1 Experimental method and diagnostics . . . 265
7.5.2 Conditionally averaged velocity field . . . 266
7.5.3 Interstitial velocity measurement . . . 267
7.6 Concluding remarks . . . 269

8 Fires in porous media: natural and urban canopies 271
8.1 Introduction . . . 271
8.2 Forest and wildland fire statistics . . . 272
8.3 Historic large urban fires . . . 273
8.4 Fire classification . . . 275
8.4.1 Mass fires . . . 275
8.4.2 Nuclear winter . . . 275
8.5 Modeling methodologies . . . 276
8.5.1 Full scale fire tests . . . 276
8.5.2 Zone modeling . . . 277
8.5.3 Field modeling . . . 277
8.5.4 Physical modeling . . . 277
8.6 Forest and urban climate meteorology . . . 278
8.6.1 Agricultural/forest canopy behavior . . . 279
8.6.2 Urban canopy behavior . . . 288

8.7 Fluid mechanics of fires and porous canopies 295
8.7.1 Field scale experiments 296
8.7.2 Laboratory scale experiments 297
8.7.3 Numerical experiments 298
8.8 Fire whirls and fire tornadoes 303
8.8.1 Physical modeling of fire whirls 307
8.9 Numerical modeling fire whirls 308
8.10 Conclusions and recommendations 308

9 Urban air flow researches for air pollution, emergency preparedness and urban weather prediction 311
9.1 Introduction 311
9.2 Applications to urban air quality forecasting and numerical weather predictions 316
9.2.1 Introduction to the problem 316
9.2.2 FUMAPEX methodology for urbanization of city-scale meteorological models 317
9.2.3 Approach based on improved urban roughness and fluxes . . . 324
9.2.4 Building Effect Parameterization (BEP) models for NWP 331
9.2.5 The soil model for sub-meso scales: the urbanised SM2-U model 335
9.2.6 Conclusions and recommendations 340
9.3 Applications to emergency preparedness for urban areas 343
9.3.1 Introduction 343
9.3.2 Possible risk sources 344
9.3.3 Modelling of urban air flows and release dispersion for emergency preparedness 346
9.3.4 Source-receptor problem and inverse modelling 354
9.3.5 Concluding remarks 355

Conclusion 359

Bibliography 361

Index 411

Preface

The NATO Advanced Study Institute "Flow and Transport Processes in Complex Obstructed Geometries: from cities and vegetative canopies to engineering problems" was held in Kyiv, Ukraine in the period of May 4 - 15, 2004. This book based on the papers presented there provides an overview of this new area in fluid mechanics and its applications that have developed over the past three decades. The subject, whose origins lie both in theory and in practice, is now rapidly developing in many directions.

The focus of applied fluid mechanics research has steadily been shifting from engineering to environmental applications. In both fields there has been great interest in the study of flows around obstacles; initially single isolated obstacles, and then groups, together with the effects of nearby resistive surfaces, such as the walls of a pipe, the ground or a free surface in hydraulics.

Simplified theoretical analysis began with studies of axisymmetric and cylindrical free-mounted bodies. However other methods had to be used for quantifying the complete flow fields past arbitrary bluff bodies, either by using experiments or, when powerful computers became available, by direct calculation and solution of the full equations of fluid dynamics. In most practical cases the Reynolds numbers are too large to compute all the small scale eddy motions which therefore have to be described statistically. There are various approaches to deriving these models, all of which are approximate. The models have to account for the way in which the obstacles interact with the spectrum of random eddies in the approach flow and, on the downstream side, how they interact with eddies shed from those obstacles. For some practical applications only the mean flow properties are required, for example mean heat transfer. B.E. Launder and J.L. Lumley have shown (starting with the concepts of A.N. Kolmogorov in 1942) that Reynolds stress closure models can provide 'engineering approximations' in many cases. However, if fluctuating loads on the obstacles or the noise produced by them have to be predicted, for example, it is necessary to calculate the full spectrum and how it is distorted. Useful concepts and estimates have been derived from G.K. Batchelor's rapid distortion theory and from 'flow receptivity', or 'shear sheltering'. With a better understanding of these different methods, it is becoming possible to predict when and where different models are appropriate. General concepts of flow patterns around bodies with complex shapes have been proposed, based on M.J. Lighthill's analysis, using topological ideas; by classifying and locating singular points where the velocity (or certain components) are zero, it is possible to describe complex flows very efficiently.

The first fundamental study of the flow through groups of obstacles (for calculating the performance of aircraft radiators) was conducted by G.I. Taylor in 1944. This was later applied by P.R. Owen to the estimation of the flow between tall cooling towers which collapsed in high winds at Ferrybridge in the UK in 1965. Meteorologists who investigate the energy balance between the whole atmosphere and the Earth's surface require detailed information about the flow within forests and agricultural canopies, where heat, moisture and gases are produced and transported aloft. Researchers from different countries, including early pioneers H. Penman and I. Long, Z. Uchijima, E. Inoue, O. Denmead, J. Wright and E. Lemon, I. Cowan, R. Cionco, A. Thom, L. Allen, M. Budyko, A. Konstantinov G. Thurtell, and researchers of the younger generation J. Finnigan, M. Raupach and R. Shaw, A. Dubov, G. Menzhulin, G. Thurtell, Y. Brunet, D. Baldocchi were among the first who investigated such "obstructed flows" experimentally and theoretically. Wind engineers, such as M. Jensen, J. Cermak, R. Meroney and E. Plate, recognised that similar flow distortion occurs in human settlements and showed how laboratory experiments in wind tunnels, based on well-established scaling laws, could accurately simulate the field measurements, along with contributing to the further development of penetrable roughness theory.

Similar problems emerged in the study of hydraulics of vegetated channels or flood plains, although these were addressed quite independently. Penetrable structures of aquatic vegetation considerably change features of the water flows. Investigations initiated by N. Kouwen, I. Nickitin, K. Kosorin, D. Knight, E. Pasche and S. Petryk, in different countries, are now being continued by H. Nepf, I. Nezu, H. Stefan, T. Tsujimoto, F. Lopez and others. Experiments in water flumes, together with theoretical studies, have highlighted the significant features that are common with the air flow and turbulence determined earlier by meteorologists. However, there is still insufficient collaboration between the experts in meteorology, engineering and hydraulics.

Research on flow through canopies is especially relevant for understanding the general quality of the urban environment, which is under great threat as an increasing proportion of the world's population, above 70%, will be living in these areas by the year 2050. The main environmental hazards are associated with high concentrations of pollutants in the air, water and ground. The contribution of applied fluid mechanics lies in the improved prediction of the dispersion of hazardous materials within complex obstructed geometries. An important special problem is concerned with the sudden release of pollutants from accidents or terrorist action. The European programs TRAPOS, SATURN and FUMAPEX have contributed useful results, as have similar programs in the USA. Some aspects of the research by meteorologists for vegetative canopies have been relevant to these flow problems. Equally, there are other significant features of the urban wind environment that are quite different. These include the large variation in the height and spacing of buildings, and the effects of the heat island that drives the urban flow when the approaching atmospheric boundary layer flow is relatively weak. These issues are being considered in recent research and are addressed in papers presented here.

A flow interacting with a number of obstructions is also important for many engineering applications. For example, the Institute of Hydromechanics of UNAS has adopted this approach to improve the performance of the large spraying cooler at the Zaporizhzhya nuclear power plant. The small droplets produced by the spraying cooler have a sufficiently high concentration that they resist the air flow entering the spray by

a similar mechanism to the flow distortion in a vegetation canopy layer. On a larger scale, engineering designers of wind 'farms' have observed how the mean velocity and higher turbulence downwind of groups of wind turbines can reduce the average power output. To estimate these effects designers are making use of research on flow through resistive layers. The scales of these flows are sufficiently large that mesoscale meteorological phenomena, such as wind jets in coastal areas, have to be considered.

Clearly, there are a number of special but similar features of turbulence and transport processes in various types of obstructed flows whether in air or water, or uniform or non-uniform canopies, whose elements may be rigid or mobile. The basic mean flow characteristic is that the drag decelerates the flow within the canopy, but as it interacts with the free flow outside the obstructed layer, it tends to cause stagnation or/and vortical zones upwind, whilst leading to mean acceleration above the canopy. The turbulence that arises within the canopy from the small scale eddies shed from individual obstructions interacts with the mean velocity profile and with the large distorted eddies above the canopy generated within the approaching boundary layer. These mechanisms significantly change the statistical structure, resulting, for example, in the formation of larger scale coherent vortices in the shear layer. The "mixing-layer analogy", recently suggested by M. Raupach and J. Finnigan [530], provides a powerful model. These concepts are highly relevant to many aspects of the natural or agricultural environments that are affected by flow processes in canopies, both in the atmosphere and in riverine or coastal flows through vegetated beds in natural conduits and also during flood events [172, 347, 350, 492].

Many expert colleagues contributed to this book. Prof. Robert Meroney (Colorado State University), a pioneer of the use of wind tunnels for simulating complex wind engineering phenomena, has, in this volume, reviewed important new research into numerical simulation of the propagation of fires in forests and urban canopies.

Prof. Roger Shaw (University of California, Davis) describes new developments in the analysis of the turbulent velocity fields in vegetative canopies, using proper orthogonal decomposition (a technique for eddy identification first introduced by J. Lumley in 1967). He argues that this technique complements the previous studies based on statistical models and large eddy simulation numerical methods.

Dr. John Finnigan from Australian Commonwealth Scientific and Industrial Research Organization (CSIRO), Australia in his chapter extends his analysis of the eddy structure of canopy winds to include the effects of complex topography. He shows that there are special features of airflow through forests and over hills that significantly affect the weather and the ecology in these very common situations.

Prof. Yevgeny Gayev (Institute of Hydromechanics UNAS, Ukraine) gives a general review that shows how, by taking an engineering approach to canopy flows, both fundamental insights and useful mathematical models are obtained in addition to those derived from environmental considerations. His field measurements in industrial spraying coolers provide a unique experimental database for this phenomenon.

Prof. Julian Hunt (University College London) introduces a classification of the types of turbulent flow through canopies of different kinds of geometry and length scale. He shows how, by integrating recently developed concepts by many authors, a more comprehensive understanding of eddy structure and turbulence statistics is now emerging. In the atmosphere where canopies may extend over tens of kilometres in

urban areas, the combined effects of the earth's rotation and buoyancy forces play a significant role.

Canopy flows are critically dependent on how the wakes of the obstacles interact with each other. Dr. Ian Eames (University College London, UK) analyses how the vorticity is both diffused and annihilated, depending on the spacing and the form of the spatial distribution of the obstacles.

Prof. Heidi Nepf (Massachusetts Institute of Technology, USA) focuses on the similarities between flows through aquatic (deformable) and terrestrial (mainly rigid) canopies. In both cases the flows can be analyzed by assuming the effect of the obstacles, can be approximated by a distributed drag force. However, special features of the aquatic canopies have to be included. Diffusion and dispersion processes within aquatic vegetation are of comparable importance to those in atmospheric and engineering canopy flows.

Dr. Alexander Baklanov (Danish Meteorological Institute, Copenhagen) applies the recent achievements of the theory of canopy flow and diffusion and provides further development and improvement of models for urban meteorology and pollution to emergency preparedness and urban weather prediction.

An extended list of references has been added to this book, for the reader's convenience, along with an index of the most important terms and names and a list of figures.

We hope that this book will be useful to scientists and engineers entering the field of canopy dynamics, architecture, planning, engineering, agriculture and ecology. There has undoubtedly been real progress in research, but we hope this book will stimulate new discoveries and new applications.

The authors are grateful for the financial support of the NATO Science Affairs Division. The Physical and Engineering Science and Technology Programme provided a grant that covered most of the costs of the NATO Advanced Study Institute organization during our excellent 12 day meeting. Special thanks are due to the director of the Institute of Hydromechanics of Ukrainian National Academy of Sciences (UNAS), academician of the UNAS Prof. Victor Grinchenko. From their experience of Ukraine's generous hospitality, all of the NATO ASI participants were very impressed with the achievements of Ukrainian science and culture.

We would like to thank also Dr. Valery Oliynik for designing the Book of Abstracts [300] and Dr. Pavlo Lukianov (both from the Institute of Hydromechamics NASU) for designing this book in LaTeX 2_ε text processor.

Finally, we are grateful to all the co-authors whose names are mentioned at the beginning of each chapter, and whose generous contributions made this book possible.

Prof. **Yevgeny Gayev**,
Institute of Hydromechanics NASU,
National aviation university (Kyiv, Ukraine)

Prof. **Julian Hunt**,
University College London (Department of Earth Sciences),
Lord Hunt of Chesterton

Chapter 1

Variety of problems associated with Canopies, or EPRs

Ye. Gayev[⋆,†1]
[⋆] Institute of Hydromechanics
Ukrainian National Academy of Science,
[†] National Aviation University, Kyiv, Ukraine

Classical fluid mechanics developed during the XVIIIth and XIXth centuries and the first half of the XXth century dealt mainly with flows over smooth or rough surfaces. The idealization of a sand roughness suggested by L. Prandtl and I. Nickuradze was quite sufficient and successful for contemporaneous problems and brought light to many engineering inventions, as well as for the applications of fluid mechanics in hydraulics and meteorology of that time. No real attention was paid to the fluid motion between roughness elements.

By the middle of the XXth century, new flow-related problems arose in the area of environmental science, particularly in the study of "tall" roughnesses, i.e. structures submerged in a flow and interacting with it. These structures can be treated as a kind of roughness, especially for the flow sufficiently far away over them.

Meteorologists investigated the air motion through vegetation canopies. Hydrologists studied water flows in vegetated channels and in ducts with tall artificial structures. Heat exchangers with a developed roughness required to consider the cooling medium motion between roughness elements, whilst the knowledge of air motion, heat and mass transfer inside a droplet layer is required to correctly specify and operate the spraying cooling systems. Studies of wind engineers and urban ecologists include the experimental investigations of the wind motion and its turbulence between buildings within residential or industrial urban areas, see Chapters 2 and 8. Some of these very

[1]E-mail of the author: *ye_gayev@public.icyb.kiev.ua*

Ye.A. Gayev and J.C.R. Hunt (eds.), Flow and Transport Processes with Complex Obstructions, 1–28.

distinct structures in the flow will be shortly overviewed in what follows. The analysis indicates their several common features, so that a universal approach to study them could be suggested.

The logarithmic velocity profile of a flow over structures in the turbulent flow regime demonstrates that they resemble, indeed, a roughness. However, one needs to know the motion within the roughness, i.e. between the structure elements, as well as to know some associated physical phenomena like diffusion, excitation of elements, and so on. Regardless of the physical nature of the submerged obstructions, the intense shedding of vortices takes place so that the level of the flow turbulence is significantly high. This is an explanation of the 'penetrable roughness' (PR) or 'easily penetrable roughness' (EPR) term used by Brutsaert [90] and Gayev [208] and applied here along with the 'canopy' term.

Common physical features may evidently lead to a uniform theoretical representation of the phenomena. Many authors, particularly those presented in this book, introduced a distributed mass force in the momentum equations (or a distributed source term for the diffusion problem) to represent the influence of obstructions on the flow. The question was whether these mathematical models can cover the main flow features. Below, the overview of several such models will be given. We will start from simple one-dimensional models allowing an analytical investigation, generalize the results to two-dimensional problems, and apply them to some practical problems.

The models and their solutions could be useful both in teaching and research. They confirm once more that distinct structures in different disciplines may be similar from the viewpoint of generalized fluid mechanics.

1.1 Vegetative canopies in meteorology

Natural wind in forests is the most evident and historically first example of a flow through an obstructed geometry. The first qualitative deductions were done yet in the XIXth century. The famous Russian naturalist A.I. Voeikov concluded in his book of 1894: "*The question is very important what happens with the air currents when they meet a high and dense forest... The wind still penetrates into the forest, filtrates through it. But passing it slowly, air changes its properties, especially in temperature and in humidity...*". How the wind changes while moving through the forest was considered by the next generation of scientists who were able to apply already quantitative methods to studying the phenomenon.

Ludwig Prandtl, the originator of many of our recent concepts about fluid motion, also noticed a significant change in the "air properties" when it moves through a tall vegetation. Figure 1.1 reproduced from his book of 1939 [510] demonstrated the qualitative ideas about the wind distribution within a vegetated layer at that time. The logarithmic portion of the mean wind profile 1 was expected over the vegetated layer but nothing was known concerning the distorted portion 2. A number of efforts was still required to parametrize the wind distribution within the forest stand. This was stimulated by practical ecology (forest microclimate or crop microclimate and harvest forecast) as well as by the fundamental problems of the soil-vegetation-atmosphere interaction and its influence on the global Earth surface energy balance.

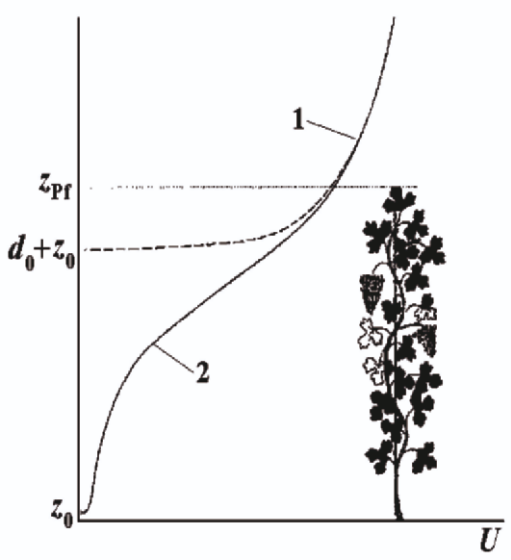

Figure 1.1: Prandtl's [510] qualitative idea of the air flow in vegetative canopies: 1 – logarithmic portion of the wind profile; 2 – distorted profile portion.

Intensive investigations in this field were started in 1950 and 1960 [6, 343, 410, 520]. The first theoretical considerations were suggested in the works of Inoue, Cionco, Lemon, Cowan, and Menzhulin [155, 407, 409, 522]. The recent state of the field has been summarized in the publications of Raupach and Thom, Dubov et al. (1981), Finnigan (2000) [155, 187, 522], as well as in Chapters 4 and 5 of this book. Let us briefly consider the most significant results in this field.

Typical measured vertical wind distributions within two distinct vegetation stands, in a maize crop [366] and in a deciduous forest [520], have been presented in Fig. 1.1 and look similar. The character of the air motion is obviously very different within and over stands. Over the stand, the velocity distributions follow a logarithmic shape. The known logarithmic formula for a rough surface, $U = \frac{U_*}{k} \ln \frac{z}{z_0}$, with the roughness coefficient z_0, or roughness length has been generalized and may be applied in the form

$$U(z) = \frac{U_*}{k} \ln \frac{z - d_0}{z_0} \tag{1.1}$$

where d_0 is an additional fitting parameter called the 'displacement height', $U_* = \sqrt{\frac{\tau_h}{\rho}}$ is the friction velocity, and κ is the von Karman parameter that is equal to 0.40 in the neutrally stratified atmosphere. Several empirical relations for the roughness coefficient and the displacement height have been mentioned in the Chapter 8.

Within the canopy stands, the air motion is significantly decelerated, but nevertheless it is of a considerable value and evidently of vital importance for agrometeorological practice. The internal motion is expected to be less or more depended also on how dense is the vegetated layer. The most popular relation derived theoretically by Inoue

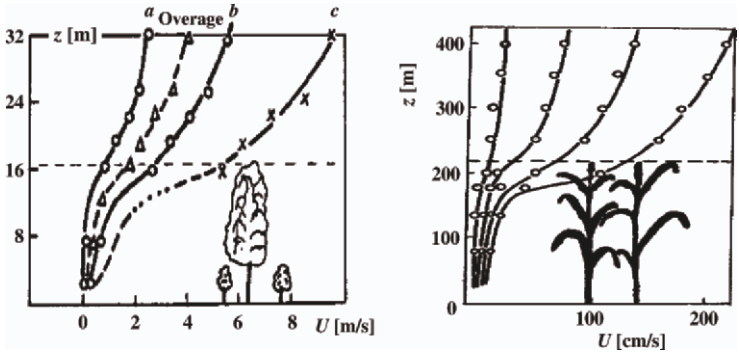

Figure 1.2: Measured mean velocity profiles in (A) maize crop [366] and in (B) deciduous forest [520].

[306] and Cionco [124] takes the form

$$U(z) = U_h e^{\alpha\left(\frac{z}{h}-1\right)} \tag{1.2}$$

where h is the canopy height, and U_h is the velocity at this level. The constant α is dependent on the canopy stiffness (density). We take as an imperfection of this and similar formulas that the velocity does not vanish at the surface, $z = 0$. The Inoue equation [306]

$$U(z) = U_h \frac{\sinh\left(\frac{\alpha z}{h}\right)}{\sinh(\alpha)} \tag{1.3}$$

avoids this flaw. The reason for the flow deceleration within the canopy is evidently the resistance caused by vegetation and its elements. This proves the introduction of forces suggested below.

It is interesting to note that the shapes of many internal wind profiles measured in natural forests reveal a weak 'bulge' on them. R. Shaw [572] paid attention to this remarkable phenomenon called the "secondary maximum" that occurs even in vertically homogeneous canopies, see also Section 5.1 of this book. In the discussion commenced afterwards, few new turbulence closures were suggested to reproduce this bulge in the flows through forest canopies. Particularly, a non-traditional hypothesis of a non-local way of the turbulent exchange was published [599] with a suggestion that the turbulence exchange between separated points A and C may be more pronounced than that with an intermediate point B. However, no wind tunnel simulation having used vertically homogeneous arrays confirmed this phenomenon. Therefore, we keep this question still open.

It is also worth noting that the early measurements in forests or in agricultural stands were done with the use of mechanical cup-anemometers placed on several levels of high masts, as was mentioned in [186]. Because of their inertia, they were adequate for recording the average speeds, but insufficient to reflect the turbulence properties.

Nowadays, one applies mainly sonic anemometers in meteorological measurements, [186].

Turbulence of the flow is greatly increased inside the canopy. Turbulence intensity divided by mean longitudinal velocity has been shown in the Fig. 1.1 for several types of forests, [155]. The high level of the turbulence, up to 40% and 60%, can be attributed to vortices in the flow shed from obstructions like tree branches, trunks, and leaves constituting the forest.

There are several theoretical approaches to the canopy flows considered by meteorologists, [17, 155, 187, 522]. In the simplest one-dimensional mathematical model, the canopy is of an infinite extent along the axis Ox of the flow direction. The following mathematical model with coupled ordinary differential equations is the usual approximation in this case [155]:

$$\begin{aligned} \frac{d}{dz}\left(\nu_T \frac{dU}{dz}\right) &= -kV + f_U(z), \\ \frac{d}{dz}\left(\nu_T \frac{dV}{dz}\right) &= k\left(U - U_g\right) + f_V(z). \end{aligned} \tag{1.4}$$

A two-dimensional model is required for the wind running onto a forest edge or onto a finite-length fetch (green belts or shelterbelts). In this case, the significant two-dimensional transformation of the air flow takes place from the entry towards the downstream region, where the flow adjusts to an equilibrium state (1.4). A suitable mathematical model uses partial differential equations [155]:

$$\begin{aligned} U\frac{\partial U}{\partial x} + W\frac{\partial U}{\partial z} &= \frac{\partial}{\partial z}\left(\nu_T \frac{\partial U}{\partial z}\right) + kV - f_U, \\ U\frac{\partial V}{\partial x} + W\frac{\partial V}{\partial z} &= \frac{\partial}{\partial z}\left(\nu_T \frac{\partial V}{\partial z}\right) - k\left(U - U_g\right) - f_V, \\ \frac{\partial U}{\partial x} + \frac{\partial W}{\partial z} &= 0. \end{aligned} \tag{1.5}$$

Here, U and V are horizontal flow velocity components of the geostrophic wind U_g directed, respectively, along Ox and Oy axes, and W is its vertical Oz-component. Nothing is changed in Oy-direction in the two-dimensional case (1.5) and also in Oz-direction in the one-dimensional case (1.4). ν_T is the effective kinematical turbulence viscosity that varies over Oz and Ox in the general case, $\nu_T = \nu_T(x, z)$. The Coriolis force $\vec{f}_g = k\cdot\{V, U_g - U\}$ linearly depends on the local velocity but needs to be accounted for only in tall forest canopies.

The drag force $\vec{f}_* = \{f_U, f_V\}$ on the right-hand side of equations (1.4) or (1.5) parameterizes the influence of the canopy: it equals zero outside it but depends on the local velocity and on the density within the canopy. All the individual obstructions that produce drag forces $\vec{F}_i$ onto the flow in a unit volume Ω, "smeared" into an average

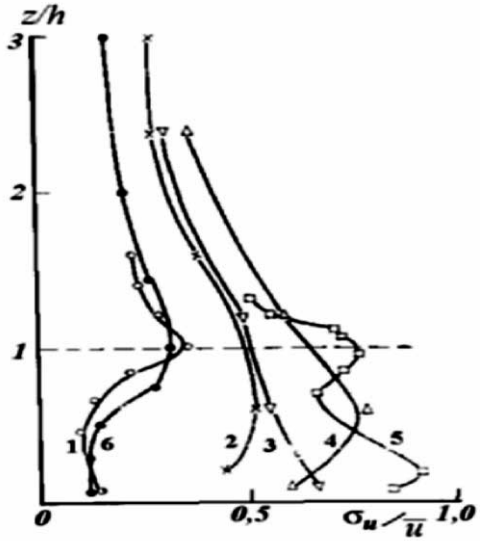

Figure 1.3: Turbulence intensity in various canopies: 1 – spruce and 2 – pine forests [155], 3 – deciduous forest in winter and 4 – in summer [124], 5 – jungle [124], 6 – in a wind tunnel forest model [410]. Cited from [155].

local mass force to the flow by means of the procedure

$$\vec{f} = \{f_U, f_V\} = -\lim_{\Omega \to 0} \frac{\sum_{i=1}^{N} \vec{F}_i}{\rho_1 \Omega}. \tag{1.6}$$

The relations for individual body forces have been well known for a number of body shapes and various circumstances (like turbulence level, body' tandems, etc.) in aerodynamics and in hydraulics [273, 304] and can be explored here. From the general empirical relation for the drag to a body $\vec{F}_i = \frac{1}{2} c_F \rho_1 |\vec{V} - \vec{W}| S$, where S is the cross section area, ρ_1 is the density of the carrying medium (air in this case), $\vec{V} - \vec{W}$ is the relative local velocity of the obstructions with regard to the medium, and $c_F = c_F(\mathrm{Re})$ is the empirical drag coefficient that accounts both for body's form and viscous drag, one obtains the following final parametrization of the mass force *to the medium*:

$$\vec{f}_*(z) = \begin{cases} k_d \left(U\vec{i} + V\vec{j} \right), & z \in [0, h] \\ 0, & z > h \end{cases} \tag{1.7}$$

where h is the canopy height. This force is in the same direction as the local flow velocity $\{U, V\}$, and its magnitude is determined by the drag coefficient k_d. Really, we deem that it is worth to investigate the models discussed below with this coefficient kept constant, i.e. for the linear force law (1.7). However, the force law should be

taken quadratic for most practical calculations, because

$$k_d = 0.5 c_F s \sqrt{U^2 + V^2}, \tag{1.8}$$

where

$$s = \lim \frac{\sum_{i=1}^{N} S_i}{\Omega},$$

$1/m$, represents the specific drag area, thus characterizing the canopy density (stiffness) provided $\Omega \to 0$. More generally, Raupach and Thom [522] declare that the distributed force f within forests may be parameterized in the form $f \propto (U-u)^k$ with the exponent $\frac{3}{2} \le k \le 2$.

Boundary conditions for the one-dimensional (1.4) and two-dimensional (1.5) models are evident. They are the no-slip condition on the surface and a prescribed velocity value (often, the geostrophic wind velocity U_g) sufficiently far away of the surface:

$$z = o \quad U = 0, \quad V = 0, \qquad z \to \infty \quad U = U_g, \quad V = 0. \tag{1.9}$$

The velocity vector $\vec{V}(z) = U\vec{i} + V\vec{j}$ is known from the general meteorology to rotate by an angle with z, the Eckman arc. The main reason for the rotation is still the Coriolis force, but vegetative resistance favours it, [155].

Three-dimensional performances have been realized by some authors for a few practical arrangements, for example for the forests on hilly terrains, or for a few fundamental investigations like the large-eddy simulation of turbulence structures. This chapter is restricted to only $1d$ or $2d$ problems.

Vegetation that constitutes the forest or agricultural canopy reveals living activities that are vitally important for its influence on the environment or for practical needs of the mankind. This activity manifests itself in the thermal and mass exchange with the air flowing through. The last is the carrier and the mediator in this exchange. The typical vertical distributions of the air temperature and its humidity expressed through the water vapour partial pressure are displayed in Fig. 1.1. For mathematical modelling, the corresponding equations for the relevant quantities should be written down. Similarly to the force parameterizations (1.6)–(1.7), the discontinuous source terms for heat and mass should be included in the form

$$i_H = \begin{cases} \alpha_H S_0 (T - t), & z \in [0, h] \\ 0, & z > h \end{cases}$$

and

$$i_E = \begin{cases} \alpha_H S_0 (E - e), & z \in [0, h] \\ 0, & z > h \end{cases}$$

where i_H (in Wt/m^2) and i_E (in $kg/(s \cdot m^2)$) are the rates of heat and mass sources, correspondingly, T (in grad) and E (in kg/m^3) are the temperature and the admixture

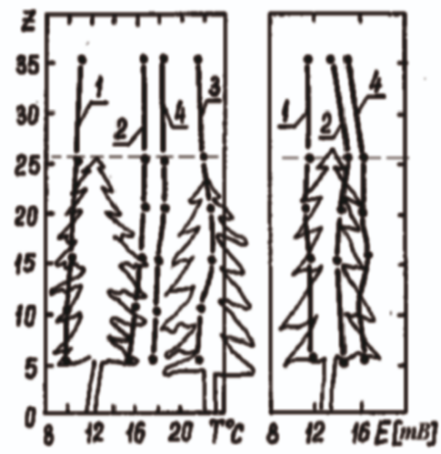

Figure 1.4: Daily course of time-averaged air temperature (A) and aqueous tension (B) within and over a spruce forest for several day moments: 1 – 1 a.m., 2 – 7 a.m. 3 – 1 p.m. and 4 – 7 p.m. [343].

concentration in the flow passing through. The exchange coefficients α_H and α_E should account for the kind of obstructions; biophysics of leaves should be applied in the case of the forest or crop canopies [544, 631].

Most works took the canopy elements rigid and did not consider their motion under the action of a wind. However, when the wind blows over a vegetation stand, the leaves, branches, and stems significantly bend and wave. The motion of agricultural or forest plants and the wind velocity distribution are evidently coupled mutually. A few experiments were carried out however by Finnigan and Raupach, Stacey and Wood e.a. [530, 652]. The early theoretical paper of the Russian scientist Menzhulin [408] introduced the additional equation for tree's stem bending. The resulting mathematical model turned out to be extremely difficult for the investigation. A set of models was suggested by Wood [652], but, again, it hasn't obtained any wide development and application. A much wider attention was given to a closer practically applicable problem of the forests on hills and on the other really complex orography, see chapter 5.

The most important parameter of the models is the turbulent viscosity ν_T that varies over the whole boundary layer, $\nu_T = \nu_T\left(z, \frac{\partial U}{\partial z}, ...\right)$. It should account evidently for the mechanism of mixing processes running in the canopy layer and thus for the regularities of vortices produced there. As in the general turbulence theory, several turbulence models are in use. They vary from relatively simple algebraic closures to the models including several additional differential equations. Some more information will be provided later.

The results obtained by meteorologists for forest canopies are the most advanced. They are widely applied now by other scientists who deal with canopies of other kinds. The theoretical investigations of the forest canopy flows stimulated their laboratory investigations, to which a special paragraph has been devoted.

1.2 Vegetated river beds

Hydraulics and hydrology are another field of study, where we meet structures interacting with a flow. Water flows in natural or artificial conduits with vegetation or with artificial obstructions have obtained a considerable attention of researchers over past 50 years. The main question arisen initially was a reduction in the water discharge associated with vegetation that was estimated to be from 20% to 70%. Prof. V.N. Goncharov stated in his book of 1962 that there were no tools, at that time, to perform such calculations of flows.

Whilst researchers were interested in estimating only the hydraulic discharge capacity of vegetated conduits, the empirical solution of the problem in terms of hydraulic resistance coefficients was quite sufficient in the opinion of Kouwen, Petryk, Knight and Macdonalds and other early authors [338, 350, 492]. During the last 20 years, ecologists require to prohibit the cutting off the vegetation in natural conduits. Its preservation was a new stimulus to understand the problem in more details. From the other side, another practical applications have appeared. For example, the Ukrainian authors Sherenkov and Bennovitsky suggested that water reservoirs vegetated by selected species should be able to absorb biological and chemical impurities in the water stream; the invention was named the "biological plateaus", [55]. For designing this system, one needs to know the mean velocity and the turbulence of flows within vegetation. The investigations of diurnal periodic flows over the aquatic vegetation in coastal regions published in [172] also required to know better of the detailed flow behaviour. The German researchers Rouve, Pasche, Nuding [470, 483, 553] and, later, the Japanese researchers Naot and Nezu [453, 454], Tsujimoto [617, 618, 619] focused on the flows over wetlands and flood plains obstructed by trees, bushes, and buildings during flood events [48, 453, 454, 470, 483, 540, 553, 617]. Some other applications of the fluid dynamics involved the design of passageways that allow fishes to bypass dams. Typically, passageways include artificial obstructions that were penetrable for the flow and fishes, but changed the water stream structure and created the regions with definite levels of the current and the turbidity, that fishes can take advantage of. So, in hydraulics, there are many applications of the studies of the flows in obstructed geometries. The transport of contaminants, nutrients, and sediments will be omitted in this book; a person interested in could be referred to the publication [658].

The fluid mechanics of the water flows through obstructed geometries may be divided into two groups of problems with respect to open surface flows, vertical-plane and horizontal-plane problems.

1.2.1 The problem in a vertical plane

The problem in a vertical plane is formulated for a wide channel, ideally for an infinitely wide one, of a constant depth assuming that the flow pattern is approximately the same in each vertical plane along the flow direction, as it has been depicted in Fig. 1.5. A usual vertical velocity distribution that follows formula (1.1) takes place only above the vegetation submerged in the water flow. This distribution becomes complex and uncommon within the vegetation layer where a significant motion of the water still takes place. A number of experimental data given in [69, 172, 347, 370, 617] confirms

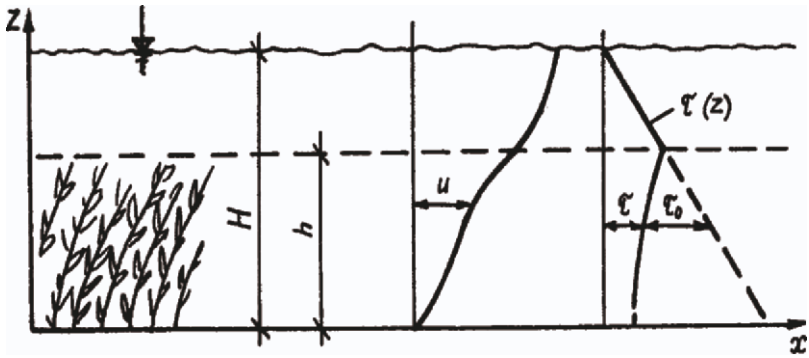

Figure 1.5: Schematic of the vertical-plane hydraulics problem.

this conclusion. Shear stress is distributed linearly (or closely to the linearity) over the vegetating grass, but its profile needs the sophisticated calculations within obstructed layers, as seen from measurements by Lopez and Garcia [377], Fig. 1.6.

Kouwen seemed to be the first among hydraulicians who doubted yet in 1969 the ability of traditional resistance formulas to correctly represent the role of vegetation, its possible features (solidity or flexibility) and characteristics like its height and spacing (density) [86]. In his experimental work, he introduced an empirical "slip velocity" taken proportionally to the velocity gradient outside the "penetrable block". Later, he carried out the experiment with a flexible artificial grass in a laboratory flume [350].

The formulation of the theoretical problem was firstly suggested by Kosorin in 1977 [344]. He suggested that the vertical mean velocity profile should account for a distributed force acting within the vegetated layer. Because of the longitudinal homogeneity, an equilibrium takes place between the shear stress τ and two forces, the pressure gradient because of the hydraulic slope J and a quadratic force representing the vegetation:

$$\frac{1}{\rho}\frac{d\tau}{dz} = KU^2 - gJ \tag{1.10}$$

with the coefficient K which represents the stiffness of the vegetation [344] and vanishes above it, $K = 0$. Similar approaches were used later on by other authors, [147, 462, 463]. The up-to-date calculations involve even three-dimensional versions of the same vertical-plane problem with the $k - \epsilon$ turbulence closures, [581, 658]. One could evidently see numerous similarities in the phenomenology and its theoretical description between the aquatic and terrestrial vegetation. Terrestrial flows are unconfined, but this hasn't been important. The main mechanisms to account for is the retarding influence of obstructions. Initially, hydrologists carried out their experiments and developed theoretical models independently. But later on, they began intensively use the extended experience of meteorologists.

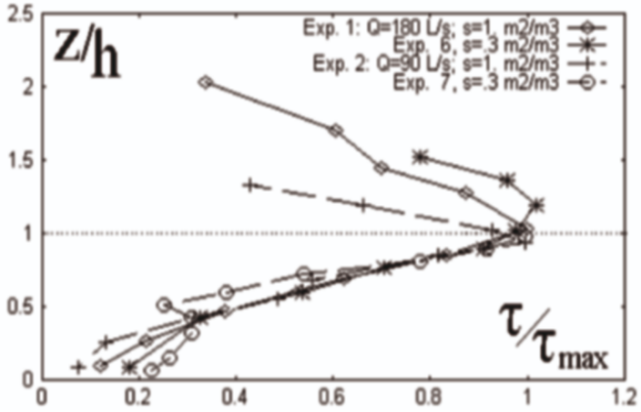

Figure 1.6: Distribution of the shear stress $\rho u'v'$ across the water flow over a tall grass as dense as $s = 1.09\ m^2/m^3$ accordingly to [377, 378].

The significant contribution to the field under study was also done by Rouve, Pasche, Nuding [470, 553], Tsujimoto and Kitamura [581, 617, 618, 619] (both experiment and theory), by Garcia [377] and Ginsberg [231] (mainly experiment).

As for the terrestrial vegetation, the difficulty appeared here concerns to the problem of the estimate of the vegetation stiffness that may be also called *the density* of the obstruction layer (the canopy). In the field measurements of Bennovitsky [53, 54], the natural vegetation (the reed) provided the blockage 7, 40, and 120 plants on m^2. In the measurements of Nepf [463], the blockage of plants was 330 $plants/m^2$. Another measure for the canopy density, the frontal area per unit volume s, $1/m$, has been more universal. Its typical vertical distribution is shown in Fig. 1.7, [463].

This brief overview of the vertical-plane hydraulics problem may be accomplished with references to non-stationary problems. It is important for oceanography problems that the flow evolves in time because of the seagrass-current periodicity. In article [172], the one-dimensional problem (1.10) accounted also for the time- and space-periodicity of the sea water surface, $\zeta(x,t) = A\sin(\omega_x x - \omega_t t)$. The final motion equation was written as

$$\frac{\partial U}{\partial t} - \frac{\partial U}{\partial z}\left(\nu_T \frac{\partial U}{\partial z}\right) = -g\frac{\partial \zeta}{\partial x} - c_f U|U|. \tag{1.11}$$

The problem in a similar formulation will be considered in the section 3.1.1.

Another important feature of aquatic obstructions consists in their significant flexibility. Experiments of many authors show that water plants exhibit a grate range of motion with increase in the flow speed, i.e. erect state, gentle swaying, strong coherent swaying (monami), and almost prone state, [463]. None of models (1.10) or (1.11) accounts for the above feature. Hence, other new elements should be introduced into models. The Russian author Sokolov [585] included the obstruction inclination into the force expression (1.7) and supplemented the model by an additional equation of console static equilibrium. Other work was done also by Kouwen, [350].

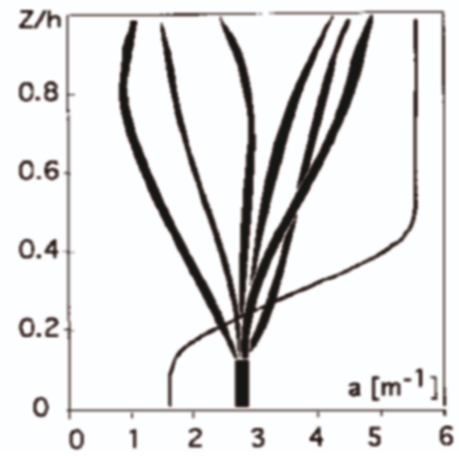

Figure 1.7: Typical vertical canopy density distribution within the aquatic vegetation after Nepf [463].

1.2.2 The problem in a horizontal plane

The problem in a horizontal plane expresses flow parameter distributions across the water conduit width which is vegetated near one or both banks like the situation shown in Fig. 1.8. It was assumed there that the "local mean velocity" was averaged over all the flow depth $0 \le z \le \zeta(x, y)$. In fact, the flow field in such a geometry, even in the simplest configurations, is completely three-dimensional and is varied in the flow direction Ox, across the conduit Oy, and in the vertical direction Oz, i.e., $U = U(x, y, z)$. It is natural, however, to average the velocities over the whole flow depth ζ, [540]:

$$\overline{U}(x,y) = \frac{1}{\zeta}\int_0^{\zeta} U(x,y,z)dz, \qquad \overline{V}(x,y) = \frac{1}{\zeta}\int_0^{\zeta} V(x,y,z)dz. \tag{1.12}$$

Therefore the velocity vector $\{\overline{U}, \overline{V}\}$ is related to every point (x, y) of the flow plan.

The problem under consideration was experimentally investigated by Bennovitsky both in natural streams and on laboratory scale [52]–[56] and compared with the above vertical-plane problem. He reported that the closeness of vegetation varied from $N = 40$ till 500 stems per meter squared in the nature. Usual stem diameters $2r$ were between 0.5 and 1 cm, so that the relative distance between neighboring stems $l/2r$ varied from 4.5 to 30. The flow was decelerated in the area of vegetation and became faster in the free stream. The flow was reproduced in a laboratory modeling, the results of which have been presented in Fig. 1.9. Cylindrical obstructions were "planted" on berms symmetricly, as it has been shown in the insert. The depth-averaged velocity distribution depended on the relative obstructed cross section area ω_{veg}/ω_0. Only symmetric halves for two measurements have been shown. If the vegetated section was relatively narrow, ω_{veg}/ω_0=0.19, the flow in the middle was almost uniform, and the

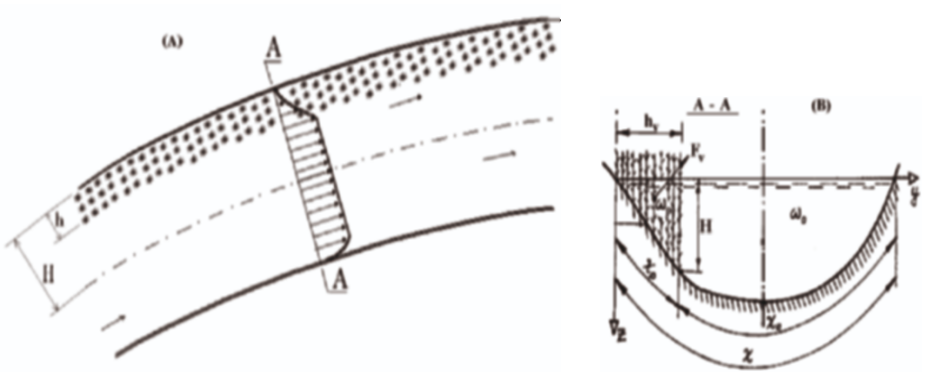

Figure 1.8: Schematic of the horizontal-plane hydraulics problem: (A) plane view of the flow with vegetation near left bank; (B) typical flow cross-section.

latter had a jet-like form in the case of a wider vegetation ω_{veg}/ω_0=0.45. Other data for horizontal plane problem were published by Nuding [470], Tsujimoto, Kitamura e.a. [581, 618, 619] and a few other authors.

Bennovitsky suggested and validated the experimental evidence that velocity profiles followed the logarithmic law just over the vegetation in the free stream [56]. So the approximation (1.1) may be employed in this problem again. Three empirical parameters required were adopted from the theory of atmospheric canopy flows [155]. For instance, the relation $d = 0.65h$ was found [56].

No approaches were known however for the velocity distribution within the vegetated layer. Bennovitsky stated that formulas (1.3) may be approximately applied. So both kinds of hydraulic problems turned out to be similar to the forest canopy problem.

Theoretical approaches to the horizontal-plane hydraulic problem are often based upon momentum equations derived from the Navier—Stokes equations being averaged over the flow depth. This approach was developed by Rodi, Emtsev, Sherenkov, Beffa, and other authors [48, 171, 540]. In the case where the vegetation is present, the resulting two-dimensional shallow-water equations for a time-dependent flow read as follows [540]:

$$\frac{\partial \zeta}{\partial t} + \frac{\partial \left(\zeta \overline{U}\right)}{\partial x} + \frac{\partial \left(\zeta \overline{V}\right)}{\partial x} = 0,$$

$$\begin{aligned} \frac{\partial \overline{U}}{\partial t} + \overline{U}\frac{\partial \overline{U}}{\partial x} + \overline{U}\frac{\partial \overline{V}}{\partial y} &= -g\frac{\partial \zeta}{\partial x} + \frac{1}{\rho\zeta}\frac{\partial}{\partial x}\left(\zeta \overline{\tau}_{xx}\right) + \frac{1}{\rho\zeta}\frac{\partial}{\partial y}\left(\zeta \overline{\tau}_{xy}\right) - \frac{\overline{\tau}_{bx}}{\rho\zeta} - f_{*x}, \\ \frac{\partial \overline{V}}{\partial t} + \overline{U}\frac{\partial \overline{V}}{\partial x} + \overline{V}\frac{\partial \overline{V}}{\partial y} &= -g\frac{\partial \zeta}{\partial y} + \frac{1}{\rho\zeta}\frac{\partial}{\partial x}\left(\zeta \overline{\tau}_{xy}\right) + \frac{1}{\rho\zeta}\frac{\partial}{\partial y}\left(\zeta \overline{\tau}_{yy}\right) - \frac{\overline{\tau}_{by}}{\rho\zeta} - f_{*y}. \end{aligned} \tag{1.13}$$

Here ζ is the actual water depth at the location (x, y). A characteristic feature of the water flows is the presence of the free water surface which varies at different points of the flow plan. It is higher in the zones of flow deceleration and lower in the free

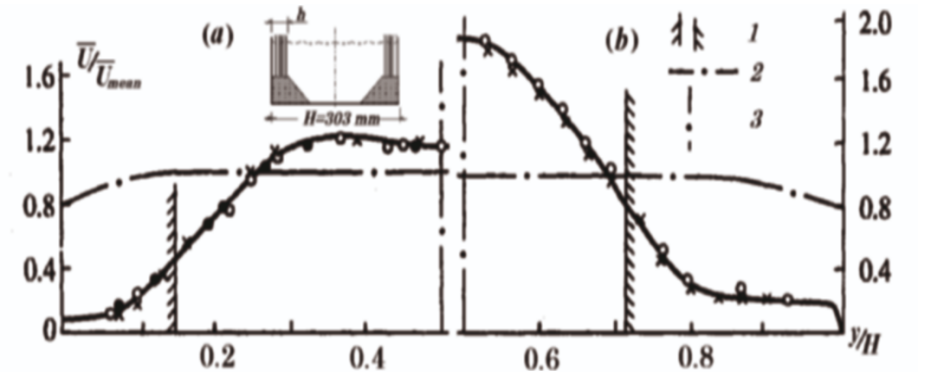

Figure 1.9: Typical velocity distributions measured in the horizontal-plane problem by Bennovitsky [56]: (a) relative obstructed cross section $\omega_{veg}/\omega_0 = 0.19$, and (b) $\omega_{veg}/\omega_0 = 0.45$. Line markings: *1* - border of the vegetated area; *2* - velocity distribution if vegetation is absent; *3* - flume symmetry line.

stream zone. This characteristic may be important in the performance of the flow plan and is thus included as an unknown variable $\zeta(x, y)$ in the equations. $\overline{\tau}_{xx}, \overline{\tau}_{xy}, \overline{\tau}_{yy}$ are the depth-averaged shear stresses being often neglected, and $\{\overline{\tau}_{bx}, \overline{\tau}_{by}\}$ is the shear stress vector usually linked, due to the bottom influence, with a bottom inclination Θ and the local velocity vector $\vec{U} = \{\overline{U}, \overline{V}\}$ as

$$\{\overline{\tau}_{bx}, \overline{\tau}_{by} = (\cos\Theta)^{-1} \rho C_b |\vec{U}| \vec{U}.$$

The force vector $\{f_{*x}, f_{*y}\}$ should represent the discontinuous influence of the vegetation in a form like (1.7). The model closed by boundary conditions and hypotheses as for turbulent viscosity allows the numerical performance of a practical importance, [453, 658].

Natural water vegetation waves very easily under the action of a flow. In turn, the velocity of the flow and the turbulence in it depend upon the waving motion of obstructions. There are few works that investigated the mutual behavior of the flow and the canopy, [305]. Sokolov [585] suggested that the flow-governing equations (1.11) or (1.13) should be supplemented with an additional one to express the shape of a strained thread. An equation was derived for the inclination of a vegetation plant in terms of the angle to the horizontal direction. On the other hand, the force (1.6) or (1.7) should also depend on it. The model becomes more complex as the flowing medium and the medium of bending grass are linked with each other.

It has been few years only since hydraulics began the implementation of methods used by meteorologists for modeling the flows obstructed by vegetation. A more close exchange between both sciences seems to be very useful.

1.3 Urban canopies

The investigation of air flows, turbulence, heat exchange, and pollutant transport within residential urban areas have become important in recent years because of the ecological reasons and the elaboration of measures for a better urban comfort and countermeasures to possible terrorist's attacks. There are several scientific programs running by the USA and European Union towards a better understanding of relevant physical mechanisms and forecasts for the urban climate of some test cities, see Chapters 2 and 9.

On a certain scale, the wind flow well over an urban settlement may by considered as distributed conventionally in the logarithmic form $U = \frac{U_*}{k} \ln \frac{z}{z_0}$ for the neutrally stratified atmospheric boundary layer with a certain roughness coefficient z_0 depending on the particular properties of the underlying urban surface, or in the form (1.1) more close to the rough surface. These assumptions that did not account for the motion within an obstructed layer were accepted in many early studies on urban climatology [356] but turned out insufficient for modern requirements. One of the first systematic instrumental measurements within a real urban surrounding was carried out by Rotach [545]. He confirmed that most time the horizontal wind within the urban structure has been considerably reduced as compared with its above-roof value. Basing on this fact, some authors suggested a scheme of the wind distribution within and over the urban canopy h shown in Figure 1.10, [425]. The canopy height can be usually determined only approximately as the mean height of buildings. The flow beneath the inertial sublayer 1 regularly departs from the above logarithmic law because it is constantly influenced by particular urban obstructions. The most decelerated, distorted, and variable velocity profile takes place in the layer between buildings called *urban canopy*.

The real structure of an urban canopy consists of individual buildings, clusters of buildings, and various city objects such as squares, street intersections, parks, boulevards, etc. The wind causes the shedding of vortices around buildings that are of many scales. The interaction of vortices produces various flow patterns. Therefore, researchers classify them into typical patterns that can be reproduced in wind tunnels or modeled theoretically. For instance, the model of a wind canyon is developed in [71, 425]. A phenomenon of wind channeling causing the wind to move even faster that the external wind over roofs is known for city canyons. Generally, a variety of urban flow features suggested by Britter and Hanna [81] can be divided into four ranges of spatial scales: the regional scale with an extension up to 100 or 200 *km*, city scale extended for an averaged city diameter up to 10 or even 20 *km*, neighborhood scale up to 1 or 2 *km*, and street scale with an extension less than 100 or 200 *m*. The internal motion within an urban canopy is important for the city and neighborhood scale phenomena, and it can be treated in a statistical way. Several mathematical models that interpreted an urban canopy as a penetrable layer exerting a distributed force to the flow were independently suggested by Sorbjan and Uliasz [589], Bykova [96] and Jerram, Belcher and Hunt [319] and led to some practically used results. The theory gave a base for some idealized laboratory simulations where relatively homogeneous urban settlements were modeled with an array of cubes, [386]. The photo of a cubic array and two their possible arrangements are presented in Fig. 1.11. The exponential

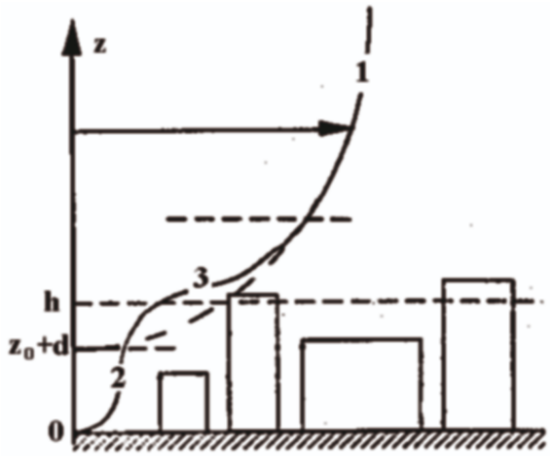

Figure 1.10: Schematic wind distribution over an urban territory after Bottema, 1993 [71] and Fisher et al., 2005 [193]: 1 – logarithmic portion high enough over the city; 2 – decelerated and distorted velocity profile within the urban canopy; 3 – transition layer (roughness sublayer).

formula (1.3) for the internal velocity distribution treated in a statistical way has been experimentally confirmed for the urban canopies, [81].

It is natural that equations like (1.4) and (1.5) can be considered as correct for only forest or riparian structures but only as approximate for urban canopies. The fundamental difference between two canopy types lies in the fact that trees in a forest and grass in a water stream displace a negligibly small amount of air and so the volume of all obstructions $\Omega_{obstructions}$ divided to the whole volume Ω is very small,

$$\varepsilon = \frac{\Omega_{obstructions}}{\Omega} << 1.$$

However, his fraction was estimated approximately as $\varepsilon \approx 0.6$ for the urban canopy [394]. Maruyama suggested to introduce the coefficient G meaning the residuary volume ratio to be equal to 1 outside the urban roughness and to 1-ε within it [394] into governing equations in the form like that in (1.5). It is not our aim to analyze this suggestion which must lead to some conjugation problem on the canopy height level $z = h$. The conclusion we would like to infer sounds that the concept of a penetrable canopy or a penetrable roughness expressed in equations (1.4) and (1.5) can be successfully employed in a number of applications.

1.4 Spraying coolers

Landscapes of our planet become more and more artificial today. Canopies of an artificial kind have replaced forests in some places. One of the examples gives a wind farm consisted of a cluster of wind turbines [168]. Each wind turbine takes out some momentum from the passing wind, thus causing a reduction in the wind speed at the

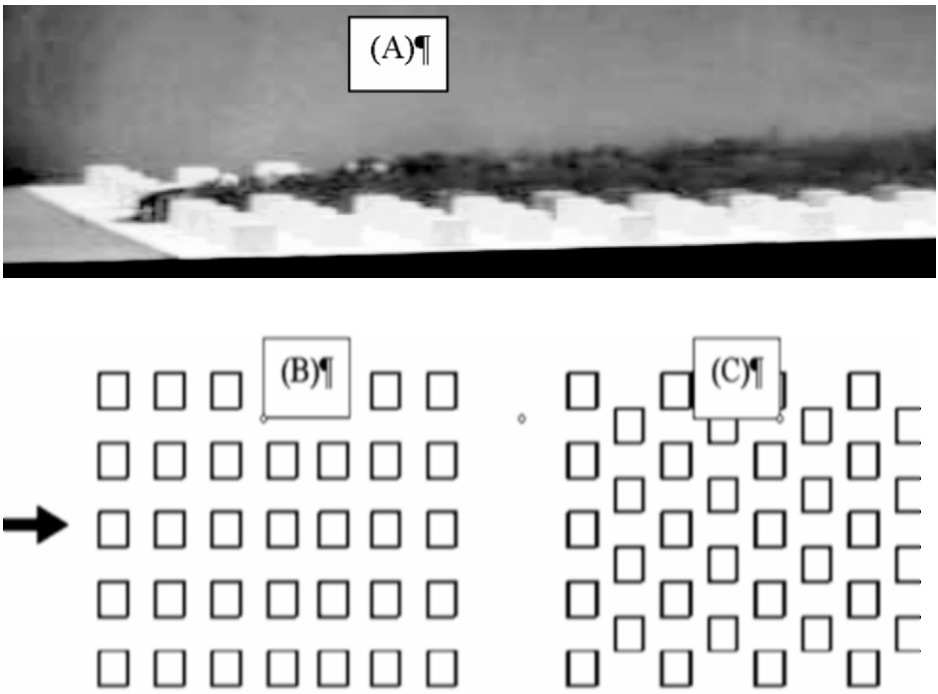

Figure 1.11: Cubic array in a wind tunnel as the simulation of a homogeneous urban settlement (A); two types of experimental setups: aligned (B) and staggered (C) arrays, Macdonald [386].

height of a wind hub. This means also a reduction in the energy production by consequent turbines. Despite the "wind mill forest" is very sparse, its influence on the wind structure is remarkable, and so engineers need to know it exactly, [168].

Another example of an artificial landscape is given by extended spraying cooling systems (SCS) like that displayed in Fig. 1.12 which can be often meet near electric power plants. To know how they interact with the atmosphere is necessary both for the project designers, SCS engineering exploitation, and for preventing their enormous ecological impact. Spraying coolers are very rarely considered as a kind of "canopy." Therefore, a greater attention is given to them in the present work.

To obtain the effective heat dissipation in circular water supply systems, cooling ponds, cooling towers, "dry" cooling towers, and spraying coolers are used in the energy producing industry. It is known, for example, that the power station capacity can be increased by 1% provided the cooling system ensures the cooling by 2^oC deeper. Particularly, spraying coolers have been widely used for a long time on thermal and nuclear power electric plants especially in the USA and in countries of the former Soviet Union. Up-to-date Spraying Cooling Systems give the example of a human-made artificial terrain that is formed by a number of tall fountains. Getting a big output of warm water from a power plant, fountains divide it into a plenty of droplets sized from several microns to $6 - 10$ *mm*, thus ensuring a developed heat and mass exchange surface. In this way, the SCSs ensure the cooling of water $\Delta t = 7 - 10^oC$ under summer

Figure 1.12: Panoramic view of the long scale spaying cooling system (SCS) of the Zaporizhzhya' nuclear power plant (South Ukraine): 1 - nuclear reactors; 2, 3 - two channels that cool the circulating water through fountains; 4 - two cooling towers for the additional water cooling.

conditions provided that the wasted water initial temperature is $30-40^oC$. Although the droplets are small, their concentration n, $1/m^3$ is extremely high within a drop layer $x > 0$, $0 \le z \le h$ and reaches 2 000 - 300 000 drops/m^3 depending on their radii and the elevation of the considered space point over the ground. This is the reason that an extended spray cooler has evidently a sufficient influence on the ambient and should be investigated both for industrial purposes and for the prevention of an unfavorable influence on the adjacent atmosphere.

For instance, Ladyzhyn thermal power plant's SCS (Middle Ukraine; a generating capacity of 1800 MW, came into commission in 1972) is an open channel 1000 m long and 90 m wide with 1300 fountains with the height h=6 m placed over the channel and having the total water output of about 21 m^3/s. Zaporizhzhya nuclear power plant' SCS presented in the photo in Fig. 1.12 (South Ukraine; its construction began in 1985, and now it keeps a capacity of 6000 MW) is arranged as two parallel open channels 1500 m long and 90 m wide containing 21 spraying modules sized 300 $m \times$ 90m with a total water output of 105 m^3/sec. So the problem of the interaction between SCS and the atmosphere is significant and important for the energy production and the impact on the environment.

For the last 30 years, the experience of the operation of extended spraying cooling systems in different meteorological conditions has been accumulated. It is clear now that the functioning of spraying coolers is related to a great number of physical phenomena. It was found that the dependence of SCS operations on meteorological conditions or on design parameters is different from that of a single fountain or even a small spray basin. This can be explained by the deceleration of a wind by droplets and the saturation of air with vapor, while the wind is moving along the fountain system.

Such a mechanism of functioning of a spraying cooling system was not however highlighted in the available literature. American researchers [114, 118] were the first who made attempt to estimate a decrease of the SCS cooling efficiency along the wind. Another attempt to perform an even more detailed SCS study was done in the Institute of Hydromechanics of NASU (Kyiv, Ukraine) by Gayev e.a [209]–[217]. A real

Figure 1.13: Gradient mast within spraying system (A) and the measurement unit of a remote anemometer (left) and a psychrometer (right) on it (B) used in the field investigations within a SCS [209, 217].

Ladyzhyn SCS was taken as a pattern system for new projects, and the *in-situ* field observations and measurements were carried out in summers of 1981 and 1982.

A floating gradient mast was placed inside the spraying cooler being equipped with ten cup-anemometers and ten special aspiration psychrometers assembled at different levels z and with a wind vane at the top of the mast, as shown in Fig. 1.13. Six of the measuring sensor pairs were placed within the droplet layer, and four of them were located over it in the free wind stream. Horizontal roofs shielded the sensors from the direct impacts of sprayed drops. Anemometers and dry or wet temperature-sensitive resistors of the psychrometers were remotely monitored, so that the registration equipment was connected with them by a cable and placed in a floating cabin 20 m downwind. The measuring devices were calibrated in a laboratory before the field work and after it.

The profiles of the time-averaged wind velocity $U(z)$, temperatures on dry T(z) and wet T_w(z) thermometers both inside the drop layer $0 \leq z \leq h$ and over it up to 10 m height were obtained in 12 measurement series. Some results typical for windy weather can be seen in Fig. 1.14. The relative humidity φ was defined from the standard psychometric table. More data can be found in papers [209, 213, 216].

Note that the distributions are cardinally different from those over smooth surfaces like in the previous cases. Again, two parts of the profiles have to be discussed. Over the top SCS's level $z = h = 6$ m, the wind velocity distributions grow monotonically in the case of a strong wind; the temperature diminishes, as a rule. Few cases where the wind velocity diminishes over the SCS are characterized by a weak external wind so that the horizontal forced convection is perhaps comparative with the intense natural convective motion rising up from the heated and wetted air layer within SCS.

Inside the droplet layer, the wind velocity profiles have distortions similar to those observed in plant canopies. The magnitudes of air temperature and humidity, just oppositely, have been greatly increased within the droplet layer. These profiles inside the

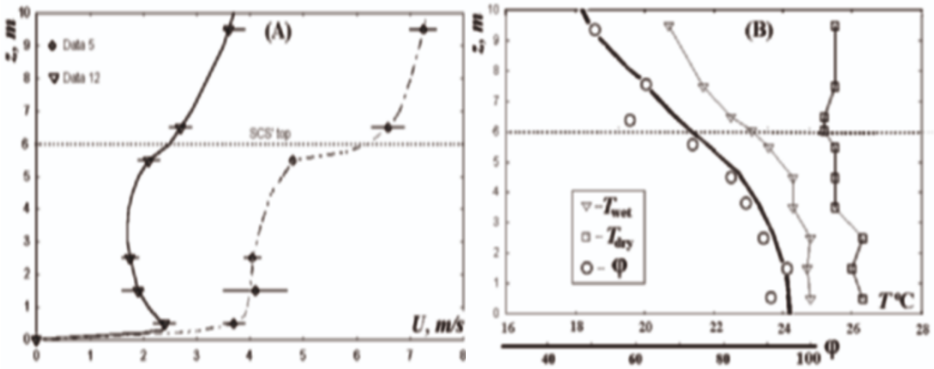

Figure 1.14: Typical distributions of wind velocity (A) and air temperature and humidity (B) within and above the spraying cooling system.

drop layer are likely to reflect the work of droplets as sinks of the kinetic energy and sources of heat and humidity. One can expect that the horizontal air discharge through the layer $0 \le z \le h$ considerably decreases and depends on the droplet concentration $n, 1/m^3$. It is necessary to know this air discharge if one wants to make all required aerodynamic and thermal estimations correctly. The humidity inside SCS is very high and almost reaches its maximum of 100%. Therefore, subsequent fountain torches cool water worse than previous ones.

In several measurements, some velocity profiles were obtained to be non-monotonous in their shape having an extreme on lower levels of a droplet layer that seems surprising. However, they should not be considered as a mistake of the measurement. The theory given below makes it possible to explain this phenomenon. Extremes on a velocity profile are caused by the vertical non-uniformity of the droplet concentration $n(z)$ and the effect of droplet drift along the air flow.

Practical engineers should distinguish the regime of forced convection like in the data given above and the natural convection regime that occurs under windless conditions. The latter regime is known to be the most unfavorable for spraying systems. Fortunately, the windless conditions are seldom, unlikely more than 20% of time. There are no experimental data for this operational case. The theories of both regimes must be significantly different as the dominant transfer direction is horizontal for windy conditions and vertical for natural conditions. Some theoretical models for the natural convection regime can be found in [211, 448]. Here we focus on the forced convection regime.

It is clear from the above argumentation that the model for a "distributed force" (1.4) or (1.5)–(1.8) can be applied to the air flow passing through the droplet layer. However, the "medium of droplets" that interacts with the air medium principally differs from the "medium of forest obstructions" in that the first one is very sensitive to the air gusts and is generally carried by air. Therefore, it is worth to introduce the quantities $\vec{V} = \{u, v\}$ that characterize the velocity field of the droplet medium itself. Each droplet of mass $m(r)$ is governed by the second Newton law with the gravitational

force vector $m\vec{g} = \{0, mg\}$ and the wind drag force

$$\vec{F} = \frac{1}{2} c_F \rho_1 |\vec{V} - \vec{v}| \left(\vec{V} - \vec{v}\right). \tag{1.14}$$

Each droplet draws its own trajectory in space that depends on its radius r. One could easily get a Lagrangian model for the droplet ensemble if the air velocity field would be exactly known. The problem consists however in the fact that the latter field $\vec{V}(x, z)$ itself is dependent on all the moving obstructions and their complex velocity field $\vec{V}(x, y; z)$. Interpreting droplets as a continuous medium, as a "gas of droplets", and substituting the individual derivatives by local ones, one gets the following Eulerian model for it:

$$m\left(u\frac{\partial u}{\partial x} + v\frac{\partial u}{\partial z}\right) = F_x, \tag{1.15}$$

$$m\left(u\frac{\partial v}{\partial x} + v\frac{\partial v}{\partial z}\right) = F_z - mg. \tag{1.16}$$

Note that there are as many droplet media (1.15), (1.16) as many are typical radii $r_1, r_2, ..., r_N$ in the droplet ensemble. It has also been assumed here that (*i*) the flow situation is steady; (*ii*) no droplets change their size as well as there are no breaks up or coalescence for them what is true to some extent for spraying cooling; (*iii*) there are no internal pressure and shear stresses within each continuous droplet medium [468].

All the droplets have their own temperatures $t(x, z; r)$ and the air vapour concentration close to their surfaces $e(x, z; r)$ that are considered as scalar fields along with the fields of the corresponding quantities for the air flow, $T(x, z)$ and $E(x, z)$. The following heat conservation equation for any individual droplet is valid:

$$c_2 m\left(u\frac{\partial t}{\partial x} + v\frac{\partial t}{\partial z}\right) = I_H + \mathcal{L} \cdot I_E. \tag{1.17}$$

Here c_2 is the specific heat of water $J/kg\ ^{\circ}\mathrm{C}$. The heat income arises because of the sensible heat income and the evaporation from a particular droplet, so that

$$I_H = \alpha_H (T - t) S_0 \qquad \text{and} \qquad I_E = \alpha_E \rho_1 (E - e) S_0 \tag{1.18}$$

with $\mathcal{L}$, J/kg being the specific latent heat.

The carrying air flow is coupled with the droplet medium. To represent the averaged effect of the droplet ensemble on the air flow, all the individual forces (1.14) and the heat and mass incomes (1.18) should be "smeared out" accordingly to (1.6) in the unit volume Ω. Bearing in mind the droplet size distribution $n(r)$, formulas (1.7) and (1.10) should be rewritten in the form

$$\vec{f}_*(z) = \begin{cases} -\frac{1}{2} c_F \rho_1 \int_0^\infty (U - u) S(r) n(r) dr, & z \in [0, h], \\ 0, & z > h \end{cases}$$

and

$$i_H = \begin{cases} -\alpha_H \rho_1 \int_0^\infty (T-t)\, S_0(r) n(r) dr, & z \in [0,h], \\ 0, & z > h, \end{cases}$$

$$i_E = \begin{cases} -\alpha_E \int_0^\infty (E-e)\, S_0(r) n(r) dr, & z \in [0,h], \\ 0, & z > h. \end{cases}$$

The symbols $S = \pi r^2$ and $S_0 = 4\pi r^2$ in formulas (1.14) and (1.18), (1.19) denote the frontal area and the whole surface areas of a droplet, correspondingly. Simultaneously, the parameters $s = Sn$ and $s_0 = S_0 n$ characterize the specific surface of droplets of radius r.

The source/sink terms (1.19) should be used in equations (1.4) or (1.5) and also in equations (1.14)–(1.18) to form a "droplet" mathematical model. Along with some further modeling hypotheses, this allows us getting the practically useful results that are presented in section 3.3.3.

Spraying systems can also be met in agriculture as sprinkling devices for watering the agricultural fields. Another their application is the water-spray barriers against extreme heat fluxes or toxic gas releases [92, 424]. Again, one needs to predict the nuances of air penetrating the water spray curtain along with trajectories and temperatures of droplets. In contrast to our model, Buchlin [92] used a model of the Lagrangian type. Calculations were performed as a number of iterations: the initial velocity distribution in air was postulated and the trajectories of droplets and their speeds at different locations were calculated; with this in view, the air flow was recalculated, which required, in turn, the next corrections for the droplet ensemble. The model suggested above holds for both coupled fields.

1.5 Terminology. Other examples of penetrable roughnesses

The term **canopy** was used to characterize the above structures subjected to a flow. The term originated, perhaps, from geographical science but was naturally adopted by the meteorology of the Earth's vegetative cover. This term however has not been so natural for other research fields. In addition, the term does not have any inheritance to the general area of fluid mechanics that investigates these structures now.

Even meteorologists used another terms, a *very rough* or *random surface* at the early history of their recent theories, [522]. The terms *penetrable obstruction* or a *grid* [554] are evidently incorrect for such extensive and lengthy structures. The term *the porous medium* also used by some researchers resembles some features of the object under investigation but has already been employed in filtration theory and thus is associated with theoretical approaches of the latter theory. The term a *layer with distributed force* suggested by Hunt et al. [50, 319] clearly expresses the mathematical idea used but does not reflect the physical phenomenon under focus.

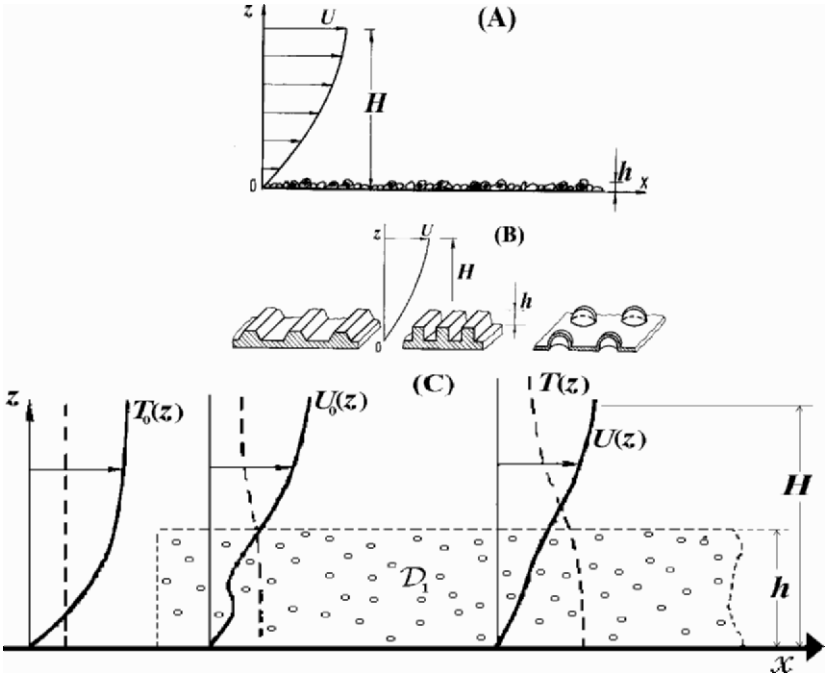

Figure 1.15: Penetrable roughness or the canopy (C) as a generalization of the normal roughness concept: (A) sand roughness; (B) regular technical roughnesses.

Cermak applied the term *high roughness* in his experimental works. Indeed, the idea of a roughness turned out very fruitful after its appearance in hydraulics at the middle of the XIXth century. The introduction of a roughness coefficient, or roughness length, z_0 into the velocity distribution formula allowed fitting the flow calculations to particular properties of the underlying surface. The concept of a uniform sand roughness, Figure 1.15,A, did not account for any motion below the roughness height h. The concept was also successfully adopted to geophysical flows. When the technical needs of the XXth century led to the investigations of riblets on surfaces, or a thread, or rivets, Fig. 1.15,B, the idea of a roughness was used again, because the logarithmic dependence of the mean flow $U \sim \ln \frac{z}{z_0}$ still holds aloft of the surface. Compare also with discussion in Section 8.6.1.

All the structures discussed above are also characterized by the logarithmic law sufficiently far away from the structures, and so all they can be called the roughness. However, their height turns out to be comparable with the flow height. Thus, the forecast of an internal flow in terms of the velocity and temperature distribution is vitally important for the problem considered in contrast to the cases of regular roughnesses. The general schematization of such flows can be presented as in Figure 1.15,C. It follows that this new kind of roughness can be called a *penetrable roughness*, PR. Such a term first suggested by Brutsaert [90] seems to be the most pithy usage that inherits

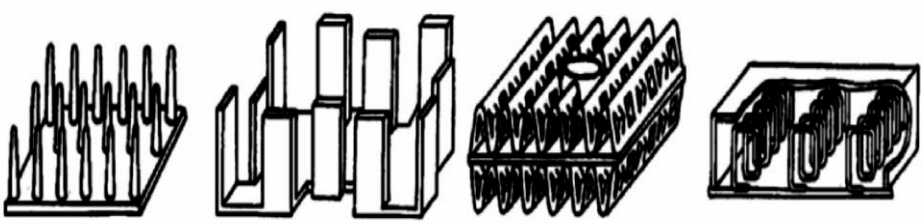

Figure 1.16: Examples of penetrable roughness used for heat exchangers.

the previous concepts of fluid mechanics. It was widely applied by Gayev along with additional requirements that gave base for the usage easily penetrable roughness, EPR [213, 211, 214]. So the canopy and EPR terms will be equally used in this chapter.

The collection of canopies or EPR flows discussed above can be extended by some other examples of such flows to demonstrate the even wider importance of the theme.

"Dusty winds" over deserted territories carry air-born particles that influence the wind profile. A similar situation can be observed over the storming ocean when air-born droplets sized from 0.1 to 1 *mm* are lifted to some elevations thus distorting the wind velocity distribution [655]. Accounting for the wind and droplet motion, and finally for their evaporation, provides an important estimate of the ocean heat flux to the Earth atmosphere [70].

Heat exchangers in engineering often contain elements deeply protruding into the flow like those presented in Fig. 1.16 to provide the effective heat removal. Some interesting examples named *porous matrix* were reported by Pedras and Lemos [485] and some other authors [2, 8, 600]. Penetrable roughnesses are also applied in engineering.

There are two uncommon examples to conclude. In all the situations considered, a gas or a liquid was moved and influenced by a penetrable structure, a PR that could be motionless or set in a motion itself by the medium. The droplet jet like that from a shower provides a situation when 'porous medium' moves and induces a motion of the surrounding air, Fig. 1.17,A. A theoretical approach was suggested by Hunt [230] to consider droplets as a porous medium. A similar situation occurs when a bubble column arises from a source deeply in the sea or ocean, Fig. 1.17,B. Bubbles form a 'porous medium' that induces the motion of the surrounding water. Of course, particular equations should be employed in each case, either for droplets or bubbles. The broadening of the jets can be explained in such models. Another approach to bubbles as to obstructions is suggested in the Chapter 7.

1.6 Laboratory modelling of the canopy flows

Any science resorts to the laboratory simulation of objects under investigation on small scale models to reduce the expenses for getting the data, to get them with regard to wider or particular conditions or regimes, to discover new governing physical laws, and examine a design solution before its practical use.

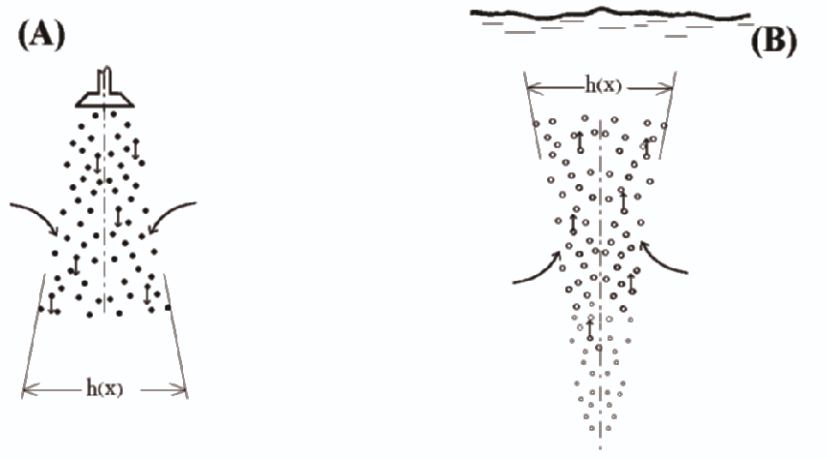

Figure 1.17: Droplet jet from a shower (A) and the bubble column from a source deeply in a sea (B) are the examples of a penetrable roughnesses that induces a motion of the surrounding medium.

The first wind tunnel simulations of vegetative canopies were carried out in the environmental wind engineering laboratory of the Colorado State University, USA, by J. Cermak and R. Meroney and their students [278, 410, 411]. Perhaps, the first modelers did not understand initially the general nature of canopy being simply penetrable roughness, as they tried to reproduce the shape of forest elements literally. The same concerns some later works like [500, 530, 652]. An understanding appeared later that the bulk types of canopy elements in the form of pegs or cylinders [568, 521] can be used, because their particular shapes do not affect the main features of the flow to be reproduced in the experiment. These features are: (*i*) the presence of a decelerated flow that occurs within the permeable structure, (*ii*) the presence of the free flow outside it. The attention of modelers should be attracted by both flow regions, i.e. the retarded and free flows, and (*iii*) the interaction between both on their interface level $z = h$.

Modeling the flows with aquatic vegetation was also widely carried out in laboratory water flumes [377, 453, 454, 462, 470, 483, 617]. These experiments were aimed mainly at solving the particular hydraulics problems without establishing any knowledge of the universal kind. However, the understanding is growing now that the results for canopies in wind tunnels and that in water flumes reveal the essence of a penetrable roughness and are so of mutual interest for both fields.

Modeling on a laboratory scale can be a useful instrument in developing and designing the spraying cooling systems. However, the problem is that fountains with real droplets cannot be scaled without significant distortions of physical processes under focus, and it was thought therefore that spraying cooling systems cannot be modeled at all. The comments aforesaid give, however, a hint that one should not seek for the literal reproduction of the phenomenon but rather for the simulation of its most important features. The latter should be the only flow deceleration and the suppression of

exchange processes within the droplet layer. Using the abstract obstructions could be so the effective work around in simulating the real spraying systems.

A need in modeling criteria appears when one deals with simulations. Such dimensionless criteria may be only derived from the governing equations. In such a way, we arrive at the necessity to learn the mathematical models of particular penetrable roughnesses. Some possible models will be discussed in the chapter 3.1.

We noticed that the flow field features have been entirely common for the EPRs of different nature and include

- decelerated mean flow within the permeable structures,
- the free flow outside it that interacts with the decelerated flow on its level $z = h$ and, may be, with the structure itself, and
- intense vortex shedding within the EPR.

Such an insight gives the base not only for the theoretical modeling, but also for the simulation of any EPR on the laboratory scale. The latter may be realized with water or air as the carrying medium and in hydraulic flumes or in wind tunnels, correspondingly.

1.7 Preliminary conclusion. Turbulence

The collection of various structures in nature or in engineering subjected to a flow of water or air will be extended and discussed in more details in the consequent chapters. The flows associated with them, despite their diversity, can be nevertheless united by the fact that one needs to account both for the internal flow within the permeable structure and for the external free flow over it. Deceleration of the flow within the obstructed but penetrable layer was found to depend significantly upon the "closeness" of the obstructions characterized by the density n, $1/m^3$ or s, m^2/m^3. This fact prompts a uniform mathematical treatment of all the above-discussed different flows. It can be suggested to represent obstructions in mathematical models by individual forces $\vec{F}_i$, whereas their "collective" action on the flow can be described by a "smeared" (distributed) force (1.6)–(1.7) that acts within the layer but equals zero outside it. The force is discontinuous on the interface between the structure and the flow $z = h$, so that the interaction between the internal retarded flow and the free external one takes place.

Many authors have successfully applied the models of a distributed force to a number of problems (see [318, 319] and the consequent chapters; the general investigation of such models is presented in the Section 3.1). The structures thus affecting the flow may be equally called *canopies* or *penetrable roughnesses*. The hypothesis of the additivity of individual forces is applied to almost all canopies except, perhaps, urban canopy. With this idealization in mind, it might be spoken about *easily penetrable roughnesses* (EPR).

The mathematical expression for the force acting on an individual obstruction $\vec{F}_i$ can be taken from various precise results in basic fluid mechanics. It is known to depend upon the first or second power k of the flow speed relative to the obstacle and be directed oppositely to the flow direction. While "smearing" all the forces in a unit

volume, one should integrate over the whole spectrum of obstacle sizes $r = d/2$, which yields

$$\vec{f} = \lim_{V\to 0} \frac{N\vec{F}_i}{V} = \frac{1}{2} c_d \rho_1 \int_0^\infty \left(\vec{U} - \vec{u}\right) |\vec{U} - \vec{u}|^k s(r;z)\, dr \tag{1.19}$$

where $k = 0$ for the linear force law and $k = 1$ for the quadratic one. So, the general mathematical model takes the following form:

$$\rho_1 \left(\vec{U}\vec{\nabla}\right)\vec{U} = -grad\ p + grad\ \tau + \vec{f}_*, \qquad div\vec{U} = 0 \tag{1.20}$$

where the obstructions are characterized by their own motion $\vec{u}(x, z; r)$ while the variables $\vec{U}$, p, and τ are related to the carrying medium of air or water.

In this Eulerian theoretical approach, a number of obstructions is considered as a continuous medium, or even media. They may have their own motion, for example, the waving of leafs in the case of vegetation canopy. In the case of droplets, their motion in the vertical direction and along the wind can be described by the following momentum equation for each size r :

$$m(r)\{u(r)\frac{\partial u}{\partial x} - \mathbf{v}(r)\frac{\partial u}{\partial z}\} = F_{*x} \tag{1.21}$$

(the sign "minus" has been taken here as the droplets move vertically oppositely to the axis Oz).

Figure 1.18: Evidence for the intense vorticity within any canopy layer (permission to publish of Prof. J. Cermak, Colorado University, USA is kindly acknowledged).

The purpose of the Section 3.1 is to analyze the implications for mathematical models, each of a practical value, because of the introduction of this force term. A number of known fluid mechanics models can be generalized in such a way. Their consideration highlights most of the properties of the obstructed flows, allows the verification of this theoretical approach, and is a useful methodological tool for teaching and learning the general problem.

Another vitally important question is how to model the turbulence within the canopy. It is clear by intuition that a number of vortices exists there, each shed from an individual obstruction. Figure 1.18 provides an experimental evidence to this. The known possible approach would be to introduce the effective turbulent viscosity ν_t and to model it as a function of coordinates and flow field quantities. The simplest case of a constant effective viscosity $\nu_t = const$ is known as the quasilaminar flow model. It will precede, in the Chapter 3, to more sophisticated models of turbulence considered in the Chapters 2, 4–8.

Chapter 2

Discrete and continuum models of flow and dispersion through canopies

J.C.R. Hunt[⋆,†] **D.J. Carruthers**[†] **and N.C. Daish**[†]
[⋆] University College London, Torrington Place, London, UK
[†] Cambridge Environmental Research Consultants Ltd, UK

2.1 Introduction

As with other characteristic types of complex fluid flows, turbulent flows over and between different types or flexible obstacles above resistive surfaces have many features in common. This is why such flows can be studied in a similar conceptual framework and with similar techniques of analysis, computation and measurement.

This paper is mainly a general review of turbulent atmospheric flows through canopy flows and the various mathematical and computational modelling approaches that are available. The review which is mostly non-mathematical in its presentations, is particularly relevant to urban areas because of the urgency of developing methods for dealing with accidental releases in urban areas. The dispersion of contaminants flow studies is also included in this review. We focus on dispersion from localised sources released suddenly, or over longer periods.

In reviewing the physical concepts governing the flow and dispersion over and through groups of obstacles, and the computational methods that are used, three spatial ranges are identified; boundary layer scales for the whole canopy, continuum scales extending over many obstacles but less than the boundary layer scales, and discrete scales around individual obstacles. In urban areas these correspond to mesoscale, neighbourhood and building/street scales. At the discrete scale the nature of the airflow and

Ye.A. Gayev and J.C.R. Hunt (eds.), Flow and Transport Processes with Complex Obstructions, 29–87.

dispersion patterns depends considerably on the type of layout of obstacles or buildings and streets. We particularly assess developments of 'fast approximate' modelling used in practice in emergency response mode and for scenario planning. The porous canopy model shows how, as the flow enters and leaves the canopy over a limited length scale, it has a crucial effect in determining flow and mixing in the canopy. The unsteadiness and vorticity dynamics of the shear layer over the obstacles is shown to be a key mechanism controlling interactions between the turbulence within and above the canopy layer.

It is noted that there are two types of dispersion model at the discrete scale, both based on idealised calculations. One type considers how dispersion is affected by individual obstacles and their wakes, while the other concentrates more on dispersion defined by groups of obstacles along and above street canyons. Such models have the capability of being combined and extended. Future work should include the special problems of dispersion in particular building complexes and the use of real time data to assess and predict releases whose occurrence is not detected until consequences have become apparent.

The development of the concepts and the calibration of these models require systematic use of 'fully computational models' with long runs on big computing systems, and laboratory and field experiments. It is noted that FCM's are being speeded up by innovative approximations, in particular by modelling the effect of buildings in terms of a force (or source) so that the representation of their shape is not exact and by ignoring Reynolds stresses in the dynamical equations which are solved inexactly by allowing numerical diffusion (caused by approximate discretisation of the equations) to simulate the physical process of turbulent diffusion.

In Section 2.2 we review the underlying concepts and prediction methods related to the airflow through canopies that are particularly relevant for understanding and modelling dispersion from local sources. We note how spatial and temporal patterns of flow and dispersion in canopies greatly depend on the type of large scale flow in which they are situated (e.g. new larger obstacles, roughness change, etc.), the prevailing approach flow conditions (e.g. level of turbulence, stratification) and on the patterns and forms of canopy obstacles. Research in the related disciplines of mesoscale meteorology, geography and urban planning has led to useful concepts about all these features of urban areas. Similarly research in crop science/forestry produces valuable data on agricultural/forest canopies (e.g. Finnigan, 2000 [187]). These and other canopy studies have suggested that there are three characteristic ranges of length scale, each with their own general features and where different modelling approaches are necessary, depending on the requirements for accuracy and speed of computation. There is the boundary layer (or overall) scale where the whole canopy area is considered, the continuum (or multi-obstacle) scale where average affects of groups of obstacles flow over/between obstacles is estimated and then the discrete (or building/street) scale where the flow around individual obstacles or small groups of them are considered.

In Section 2.4 we review the concepts and modelling methods for dispersion from typical accident releases in urban areas over the three characteristic scales, but starting from the local obstacle scale, where the release occurs. Then the multi-obstacle and finally the overall dispersion is considered. Following the rationale set out in Section 2.4, different approaches are described, from the most simple and rapid modelling

to the most complex and computationally demanding. The key question is whether dispersion patterns from local sources have some repeatable characteristic forms in canopies as they do over level terrain, following Pasquill and Smith, 1983 [484]. If so, this would enable robust and easily computable formulae to be used for the most common situations. In fact, this methodology has already been applied near closely packed street scale in the elongated obstacles, such as dispersion from steady line sources (of vehicles) in urban street canyons (Berkowicz et al., 1997 [59]; Carruthers et al., [106]; Soulhac et al., 1998 [590]). This review concludes that this approach could be extended to local unsteady sources.

Where obstacles are shaped like cuboids and hemispheres and are isolated, the main characteristic features of the air flow and dispersion are the interactions between the wakes of upwind buildings and the flows around downwind buildings. This is the basis of the UDM model (Hall et al., 2001 [247]) developed for accidental atmospheric releases of pollutants in urban areas DSTL (see also chapter 9).

2.2 Over/through canopies: characteristic regions and flow patterns

Over most canopies/urban areas, with horizontal scale L_c, as shown in Figure 2.1, there are considerable variations in the types, sizes and layout of obstacles, buildings and streets. Over larger canopies/urban areas there are usually also significant variations in the natural topography around the canopy and ground level within the canopy.

The general characteristics of the airflow over different length scales need to be understood and related to each other when developing models for airflow and dispersion, see Tables 2.1 and 2.2. In atmospheric flows with weak or moderate wind speeds (defined in Table 2.1) body forces, such as rotation (or Coriolis) and buoyancy forces affect the direction and speed of the flow within the canopy and beyond it over an outer scale L_0. In the atmosphere, the whole boundary layer flow adjusts to the change of surface conditions: over an outer (or mesoscale) distance L_0 which is typically of order 30-50 times the depth of the boundary layer, i.e., L_0. This distance is usually determined by the Rossby length scale, i.e. $L_U = L_{Ro} = hN/f$ where N is the buoyancy frequency of the stable layer at or above the boundary layer of height h. Typically $N \sim 10^{-2} s^{-1}$. If the size of the canopy is very large, Coriolis forces are large.

As shown in Figures 2.2 and 2.2,b, above the canopy there is an internal layer with the depth $l(x, y)$ above the ground, separating the flow within the layer from the approaching boundary layer flow above it. This layer deepens as a result of turbulence generated in the area where the surface conditions change, e.g. due to temperature or surface roughness (see, for example, Garratt, 1993 [205]; Hunt and Simpson, 1982 [283]). Over a long enough outer scale, distances L_0 the internal layer reaches the top of the boundary layer and so the whole boundary layer velocity and temperature profiles are changed. Where the lengths of the canopies are less than about $10h$, $L_0 > L_c$.

Note that the disturbance produced by the canopy on the outer scale flow affects the approach flow, e.g. the direction of the wind. Over shorter horizontal scales of less than L_0, the internal layer depth l_0 is much less than h, the depth of the boundary

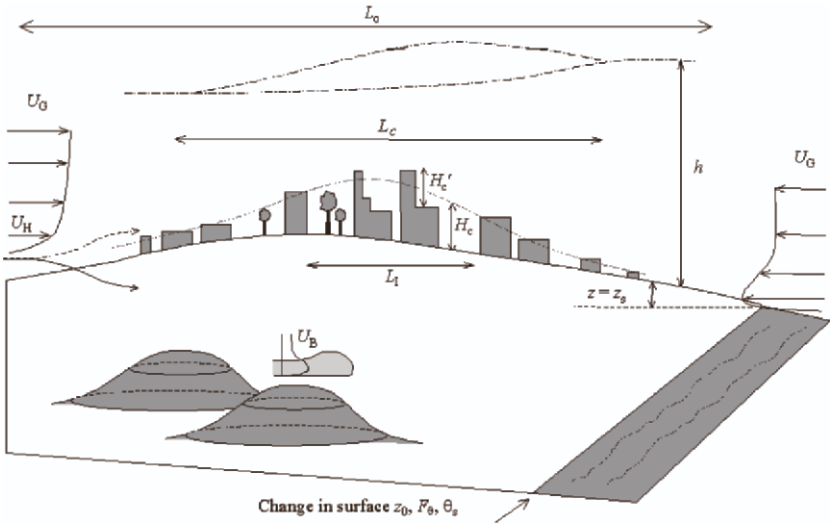

Figure 2.1: Characteristic features of canopy flows (especially urban canopies). L_0 is outer- or meso- (regional) scale on which the canopy affects the dispersion. L_c and L_I are the canopy and inner length scales, respectively. Note that U_G is the approach geostrophic wind speed above the boundary layer, U_B is the typical wind speed associated with local buoyancy effects, e.g. downslope winds from nearby mountains. H_c is the canopy height and $H_c^{'}$ is the standard deviation of building height.

layer. The internal layer depth l is greater than the height of the envelope or canopy of the buildings H_C. On the canopy scale the perturbed flow both within and above the canopy has separate characteristics over the intermediate continuum canopy scales L_{CC} and over the shorter discrete (obstacle) scales L_b. The former continuum scale L_{CC} extends over groups of obstacles of similar size and type. The properties of the canopy of the continuum scale, e.g. its average porosity, and resistance (Jerram et al. 1993 [318]), are determined by the average geometric and flow properties on the discrete obstacle scale. Note that there is significant mass, momentum and energy transfer between the flow in and above the canopy on all scales (outerscale). But where the canopy varies greatly in height (e.g. at the upwind/downwind edge, or in the inner part of an irregularity) there can be significant mean flow entering/leaving the canopy which affects the transport processes (Belcher et al. 2003 [51]). The physical features of the flow and the horizontal and vertical length scales for the three flow regions are related to each other in Table 2.1.

For flow related to large canopies in the atmosphere such as urban areas there are three characteristic flow regions. We begin with those on the outer/mesoscale. These are broadly categorised in Table 2.2 according to the relative effects of buoyancy to inertial forces produced by orographic or heat island effects on the one hand, and the effects of Coriolis forces acting over the overall scale L_0 of the urban area on the other. The former influences are essentially indicated by the value of the Froude number, defined as the ratio of the geostrophic wind U_G to the average velocity U_B produced

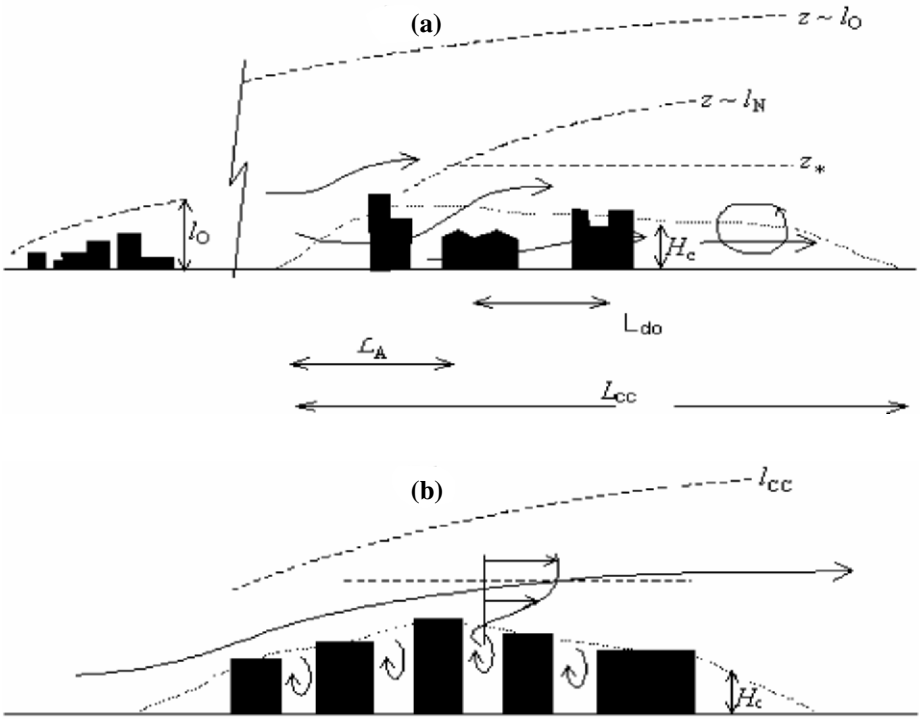

Figure 2.2: Characteristic features of canopy envelopes and zones of air flow on continuum scale. (Note that the definition of this scale depends partly on the level of detail of the computation.) (a) 'Porous' canopy with isolated buildings. l is the height of the perturbed layer above the canopy; z_* is the height, $\mathcal{L}_A$ is the adjustment distance. (b) Non-porous canopy, where the mean flow passes over canopy.

by the buoyancy forces acting over the urban area, i.e. $F = U_G/U_B$. U_B is driven by the horizontal temperature (and density) changes $\Delta\Theta$ (that may be natural or caused by the urban heat island) and is defined by $U_B = \sqrt{gl\frac{|\Delta\Theta|}{\Theta}}$, where l is the internal layer thickness (or H, the height of nearby mountains, if they dominate the local flow) and g is gravitational acceleration. Note that as a result of urban heat island effects $\Delta\Theta/\Theta$ increases with the scale of the urban area, but it also depends on the type of vegetation inside and outside the area. In European and North American cities, typical heating and albedo change cause $\Delta\Theta$ to be positive, up to 10^oC, except those in desert areas - for green cities in desert areas $\Delta\Theta$ can be negative, typically -1^oC (Oke, 1978 [472]; Mestayer and Anquetin, 1995 [425]). Since typically $|\Delta\Theta|/\Theta \sim 0.01$, $U_B \sim 3\ m/s$. Coriolis effects are significant if the mesoscale length scales, defined as L_f and L_{Ro}, are comparable with or less than L_0.

Referring to Table 2.2, we see that for case (i), typical small to medium scale urban areas, buoyancy and Coriolis effects are negligible and $F > 1$, and $L_R > L_c$. For case

Table 2.1: Scale ranges of flow and dispersion over/through canopies (urban areas).

Range	**Determining factor(s)**	**Relations between scales**
1. Boundary Layer (Outer) Scale L_0	Flow over obstacles/buildings. Significant orographic / Coriolis effects (but affected by smaller scales). Surface influences and pollutants mixed through boundary layer.	L_0 for large urban areas $\ell(x \sim L_0) \sim h$
2. Continuum (Neighbourhood) scale L_{CC}	Flow and dispersion above and between obstacles. Average geometrical (and smaller scale) features dominate mean flow/dispersion. Growing internal layer above obstacles.	$d < L_{cc} \leq L_0$ Typically $L_{cc} \sim$ Inner City Scale for urban areas $\ell(x \sim L_{cc}) \lesssim h$.
3. Discrete (Building/street) scale L_{D0}	Flow and dispersion determined by features below building level (except for elevated releases). Mean geometrical and flow features on scale L_{D0} (not smaller) mainly determine dispersion. Internal mixing layers below/above buildings are of order of obstacle/spacing dimensions.	$d, 10H \gtrsim L_{D0} \gtrsim w, b, d$; $\ell(x \sim L_{DO}) \lesssim H$ (this defines magnitude of L_{D0}).

(ii), as the canopy/urban area scale L_C increases, and if there are no thermal effects, the Coriolis force begin changes the wind speed around the canopy. Case (iii) corresponds to where there are significant thermal effects and the buoyancy velocity increases. This is associated with changes in the atmospheric stability and boundary layer depth over urban areas. But if, as in case (iv), the area is even larger, so that $L_R < L_c$, then the heat island and Coriolis effects are larger. This induces convergence and causes the flow moving towards the urban area to turn cyclonically (i.e. anticlockwise in the northern hemisphere), as has been measured, especially at night (Hunt and Simpson, 1982 [283], Bornstein, 1987 [68]).

In the presence of mountains and sloping terrain the wind speeds can be lower, especially at night. Buoyancy forces tend to dominate over inertial effects so that $F < 1$, leading to marked diurnal variations in the wind speed and direction, over the urban area and outside it. Such areas are associated with sudden changes in the airflow, internal fronts and pooling of the air in valleys, all of which greatly influence dispersion of air pollution and products from accidental releases (Hunt, Fernando and Princevac, 2003 [297]).

Table 2.2: Main types and features of canopy flows on the mesoscale (urban, forests).

Increasing effects of orography / heat island →				
Increasing scale	F $L^{'}$ $L^{'}$	> 1 (typically windy environment over flat plain).	~ 1 (typically moderate wind over flat surface).	< 1 (hilly terrain; near coast).
↓	$\lesssim 1$	(i) Roughness slow down; boundary layer depth varies.	(iii) Weak flow convergence, change in stability over urban area.	(v) Slope flows in open valleys; sea breezes; slope flows and pooling in bounded valleys.
	$\gtrsim 1$	(ii) Also anticyclonic turning of wind; weak convergence/ divergence on left/right.	(iv) Strong central convergence and cyclonic turning.	(vi) Interactions between orographic and urban heat island flows. Significant variations in orographic heat island flow across the urban area.

Note: $F = U_G/U_B$; $L' = L_0/L_{Ro}$; U_G is the geostrophic wind speed; $U_B = (gh|\Delta\Theta|/\Theta)^{1/2}$ is the buoyancy-induced local wind speed; L_f is the Coriolis advection length ($=U/f$); L_{Ro} is the Rossby length scale defined by stratification and Coriolis effects ($= hN/f$).

The static stability of the air stream usually changes as it moves into and out of the urban area, typically becoming less and more stable, respectively. However it should not be assumed that the boundary layer profiles over the urban area and downwind are identical to the equilibrium states found in neutral, stable and unstable boundary layers over flat terrain. In fact as the flow adjusts characteristic distortions of the air flow profiles occur on these scales, such as blocked flow, unsteady slope flows, gravity currents and boundary layer jets especially near hills, coasts and urban/rural boundaries. These distorted profiles (which are ignored in most mesoscale atmospheric models) significantly affect dispersion (e.g. Högström and Smedman, [274]; Owinoh et al., [477]).

The characteristic features of the air flow on the neighbourhood scale depend considerably on the distribution of the obstacles dimensions and the patterns of their grouping (continuum/obstacle height H, breadth b, width w, separation distance d). In well spaced canopies, e.g. suburban areas or tower block housing estates, the obstacles are effectively isolated. However, in closely packed canopies, e.g. dense suburbs and inner city areas, there may be a 'canyon' construction with long rows of obstacles separated by narrow gaps or streets (e.g. Grimmond and Oke, [237]). The former are essentially porous to the oncoming boundary layer; the airflow slows down as it passes between the buildings, as a result both of their bulk displacement of the flow over and around the 'envelope' or canopy of the buildings and as a result of their drag. The former effect is often overlooked, is particularly important with densely packed solid obstacles or in two phase flow (Eames et al. [294], see also chapter 7).

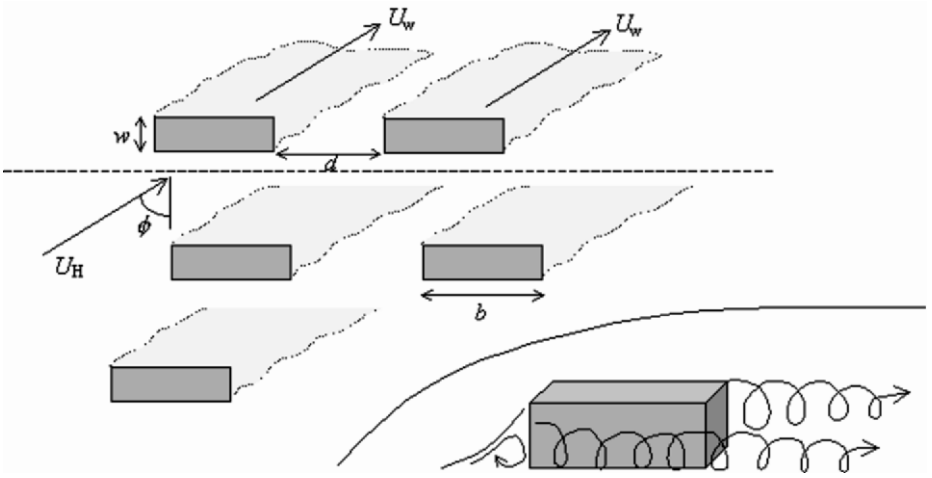

Figure 2.3: Typical configurations on discrete/obstacle scale. Normal approach angle ϕ small enough (i.e. $\cos\phi > 2w/d$) for independent wakes to be formed (approximately parallel to the approach wind). Note the complex forms of obstacle wakes, in which swirl may persist.

Downwind of a characteristic adjustment distance L_A (which is of the order of $H(d^2/wb)$ or H/β where β is the porosity, e.g. 10-30 building widths (Belcher et al., 2003 [51])), the drag force dominates but is weakened by the sheltering effect of upwind buildings (see Figure 2.3). Also over this adjustment distance the air flow above the obstacles first accelerates as a result of the vertical displacement by the buildings, and over this distance the air flow within the canopy begins to decelerate as slow moving fluid is expelled from below the level of the building envelope or canopy. Downwind of this adjustment distance, if the continuum scale is large enough (i.e. $L_{cc} >> L_A \sim 30H$) the air flow within the canopy, with wind speed U_c, is driven intermittently by turbulent shear stresses near the top of the canopy. These are generated by growing instabilities in this region in the intense fluctuating shear layer whose elevation fluctuates above and below the tops of the buildings (Britter & Hanna, 2003 [81] 2003; Finnigan, 2000 [187]).

Note the similarity with the intermittent behaviour of the turbulent boundary layer with polymers. This may be relevant to the flow over very flexible plant canopies (Ptasinski et al., 2003 [511]). There is a finite 'jump' in velocity across this fluctuating layer. The external turbulence is blocked by the vorticity of the layer (Hunt and Durbin, 1999 [292]). This is why there is only a very weak effect of large eddies moving above the canopy. The layer is analogous to that at the outer edge of jets, wakes and boundary layers (Bisset et al., 2002 [63]).

The mean reference height of the layer is z_d which has to be below the mean height of the building (see Jackson, 1981 [311]). Above the buildings the wind speed $U(z)$ rises from its average value U_H at the top of the buildings to a value close to U_G the geostrophic wind speed at a height just above the inner layer, where $z \sim l(x)$. Because

of the variability $H_c^{'}$ in the heights of the buildings and the energetic gusts into and out of the urban canopy, there is an intermediate or roughness 'sublayer' ($H_c < z < z_*$) whose thickness ($z_* - H$) is of the order of the height of the canopy, H_c. It lies between the canopy and the bottom of the upwardly-displaced surface layer which has most of the same characteristics as in the layer over a level surface. Thus for $l_{cc} > z > z_*$

$$U(z) \cong \frac{u_*}{\kappa} \ln\left(\frac{z - z_d}{z_0}\right) \tag{2.1}$$

where z_d is the displacement height (which is of order H), z_0 is the roughness length, which depends on the resistance provided by the buildings in the canopy, and κ is von Karman's constant (Grimmond & Oke, 1999 [237]; Britter & Hanna, 2003 [81]; Belcher et al., 2003 [51]).

Downwind of the canopy where the average drag of any obstacles effectively decreases to zero, the mean air flow descends and accelerates. Typically in neutral conditions the mean velocity adjusts to within 10% of its ultimate (rural) value within about 30 canopy heights (e.g. Counihan et al., 1974 [132]). But if the air flow is stably stratified the well mixed turbulent wake experiences low friction and continues further downwind, with a jet tending to form in the mean velocity profile (Owinoh et al., 2003 [477]).

When a canopy is so densely packed with obstacles, there may be no net flow between them. Then on the continuum scale, the flow largely passes above the canopy envelope (with average height H_C), such as in the central area of some cities (Mestayer et al., 2002 [427]). The flow below the canopy height must depend on the particular street and building configuration at that scale. The flow above the canopy is essentially equivalent to airflow over a change in elevation H_C with length L_{CC}. The roughness length z_0 of this elevated surface is of the order of the thickness of the shear layer over the obstacles and the 'canyons' between them (Soulhac, 2000 [591]). The flow in the inner layer above the obstacles and in the wake downwind of the continuum region are similar to those for porous canopies.

On the discrete/obstacle scale L_{d0} there are also characteristic features of the flow corresponding to different patterns of shapes and spacing of the obstacles. Various concepts have been proposed for defining these categories, for example rugosity (or mean canopy height H_c), relative rugosity (defined by height variability $H_C^{'}$), sinuosity (of canyons), contiguity (e.g. Adolphe, 2001 [5]). These and related concepts have guided our suggested categorisation shown in Table 2.3 for canopy configurations and the consequences for air flow illustrated in Figure 2.4.

Fluid mechanical studies have shown how flows around individual obstacles become significantly distorted in the presence of nearby obstacles depending on the ratio b/d of the breadth b to separation distance d from the nearest obstacle, on the ratio b/w of breadth b to the width w of the obstacle and on the relative height to width ratio H/w. When there are many obstacles, as in an urban areas or in engineering flows, these flow interactions build up into characteristic flow patterns, which we now examine.

In category (vi) of Table 2.3, as Figures 2.3 and 2.5 show, the separation distanced, for cube-like obstacles are large enough that $b/d \leq 1/5$, the flow around each structure does not qualitatively affect others. In other words the flow pattern has approximately

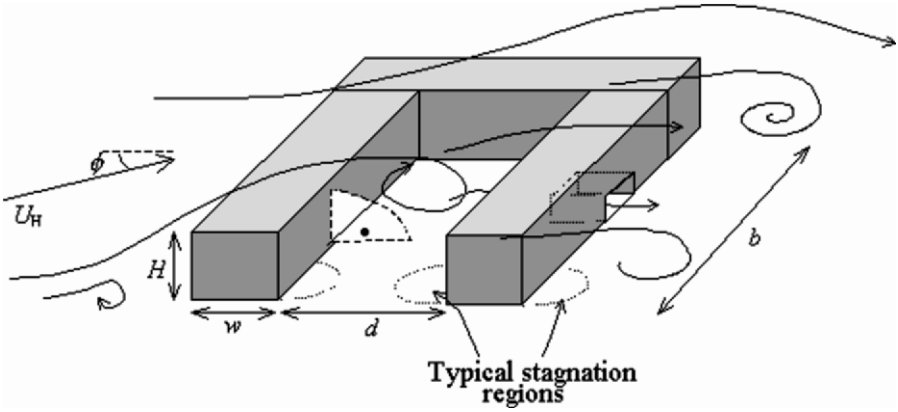

Figure 2.4: Enclosed spaces between connected cuboid obstacles, e.g. courtyards. Typical instantaneous streamlines of the large scale flow in a 'courtyard', where $b/d \sim 1$, $b/w \sim 3$, $H/d \sim 1/3$, $H/w \sim 1$. The shaded area indicates the region of highest concentration of matter released in the 'courtyard'.

the same form as that of an isolated building, with recirculating flow regions, wakes and horseshoe vortex structures around its base.

Where the downwind buildings are almost aligned with the wind Figure 2.5 (i.e. $\cos\phi \leq w/d$), they block the oncoming wake which effectively strengthens it. This is why the wakes of cube shaped obstacles extend to 5 heights downwind in the presence of a downwind obstacle. The downwind obstacle also distort the wake's vorticity so that the wakes tend to be aligned with the obstacle (see examples in Eames and Hunt, [162]). This leads to significant mean flow between obstacles if they are aligned parallel to the oncoming flow (with significant effects on dispersion, Davidson et al., 1995 [143]).

When there are marked variations in the height of adjacent obstacles, the wake vorticity shed from upwind buildings can produce sharp down-flows and increased trailing vorticity in the flow direction, (see Lawson, 1980 [360]). These effects contribute to mixing between the canopy and external flow, Figure 2.6. When tall cuboid obstacles are closely packed (i.e. H/w $\geq$ 1, b/d $\geq$ 1/2), as the air flow passes around them the wakes tend to disappear (because of cancellation of vorticity) and the streamlines are determined simply by the displacement or 'blocking effects' of the buildings (Davidson et al., 1995 [143]; Moulinec et al., 2003 [436]).

For wide obstacles the separation distance d for no interaction is considerably greater, i.e. $d/b < 7$. Even when the separation distance is large enough not to affect the structure of the flow around downwind obstacles, the turbulent wakes from upwind obstacles can affect the flow around those downwind, for example enhancing or diminishing the mixing.

Categories (i), (ii), and (iii) correspond to different types of obstacle shapes and spacing separated by relatively narrow canyons. Here the boundary layer flow mainly passes over the buildings and the canyon, but also drives recirculating flow with a strong mean flow component along the canyon Figure 2.7. Theoretical analysis and

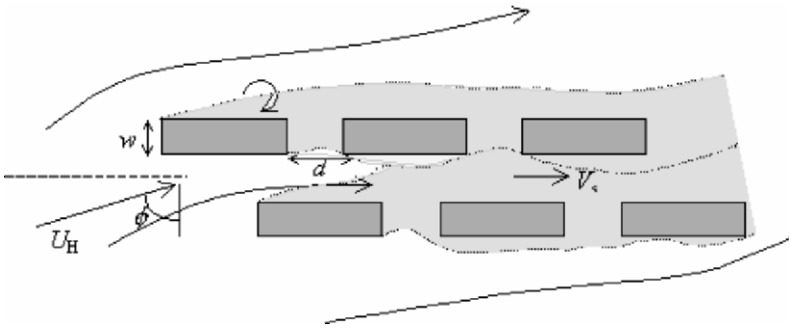

Figure 2.5: Normal approach angle ϕ large enough (i.e. $\cos\phi \lesssim 2w/d$) for wakes to merge and 'canyon' flow to develop in 'streets' between the obstacles.

Table 2.3: Typical configurations of obstacles (e.g. in urban canopies).

Increasing separation, $d \rightarrow$			
Increasing width w $\downarrow$	b/d	$\gtrsim 2$	$\lesssim 1$
	$b/w \gtrsim 10$	(i) Canyon ($H/w > 2$) Residential street ($H/w \lesssim 1$)	(iv) City squares*, parksides
	1-5	(ii) Long blocks (e.g. industrial estates)	(v) Enclosed spaces (e.g. courtyards)
	$\lesssim 2$	(iii) Closely-packed industrial sites, ancient settlements**	(vi) Square blocks (e.g. houses), $H/w \lesssim 1$. Office blocks, $H/w \geq 1$.

In the above, d is the distance to the nearest obstacle (building).
*Long buildings with large space (Le Corbusier Habitation!) are rare except for city squares/courtyards.
**Wide buildings close together are rare except on certain industrial estates.

preliminary computations (by Dr. S.E. Belcher at Reading University) confirm the wind tunnel results of Bottema (1993) [71] that the wind speed tends to increase along the street, and that the effects of upwind side streets tend to amplify this acceleration (by inducing a down flow). This mechanism is analogous to that for the increasing wind speed downwind of bluff obstacles in boundary layers produced by strong longitudinal vortices (Kothari et al., 1986 [345]). Intense vortices tend to form in the streets on the downwind side of the canyon, and where major streets intersect. But locally formed vortices tend to break up at the end of the canyon or downwind of an isolated building, because of their self-destructive tendency in high turbulence (Miyazaki and Hunt, 2000 [434]; A.G. Robins, private communication). Isolated obstacles, especially in slightly stable conditions can produce swirling wakes, far downwind (Kothari et al., 1986 [345]).

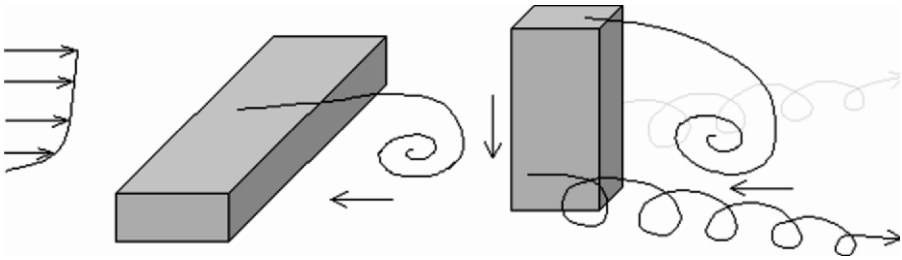

Figure 2.6: 'Tall' obstacles ($H/b > 2$): Effects of uneven obstacle heights. Note strong reverse and downdraft winds (e.g. Lawson, 1980 [360]; Britter and Hunt, 1979 [78]).

In categories (iii) and (v) when $b/d < 1/3$, corresponding to long cuboid obstacles that are sufficiently separated from each other, the flow over an upwind building can descend into the space between them (Lawson, 1980 [360]). This flow is significantly sheltered and stagnation areas are larger than for isolated buildings. Where the separation distance is small, i.e. $b/d \geq 1$, the flow is sensitive to local complicating geometrical factors, such as openings, which can lead to sufficiently high local winds that they affect the overall flow pattern, Figure 2.4 (Hunt et al., 1988 [286]).

In conclusion it has been shown that most of the usual patterns of cuboid obstacles in boundary layers, such as of building/street shape and configurations found in urban areas, can be categorised in geometrical terms. These also determine the characteristic air flow patterns found in these situations for typical wind conditions. In particular there is a major distinction between flows determined by random interactions of wakes of well separated obstacles and highly organised 'canyon' like flows that occur when the buildings form street canyons or, if they are separated, when they are positioned along streets. In very densely packed flows wake analyses are least relevant.

2.3 Computational models and physical concepts, especially for meteorology and air flow in urban areas

2.3.1 Different types of model

Here we review those computational models for predicting dispersion from local releases in canopy flows, especially those characteristic of urban areas. The numerical and physical basis and operational attributes are summarised in Table 2.4 for the three ranges of length scale introduced in Section 2.1, and for the different types of model, ranging from off-line, fully computational models (FCM) to the fastest approximate models (FAM) that can be run on PC's. The choice of the model depends on their practical purpose (especially in relation to dispersion modelling), the required level of spatial/temporal detail and scientific understanding involved, and on the detail and accuracy of meteorological and topographical input data. For research and for off-line validation studies, a variety of types of model tend to be used: some studies

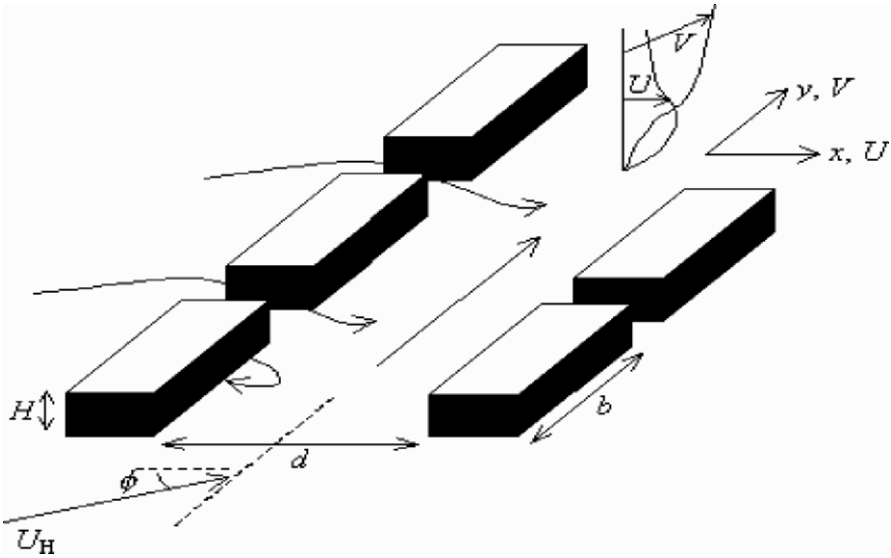

Figure 2.7: Low obstacles aligned in rows with angled cross wind (e.g. main and side streets in urban areas). Note that if $H/d \leq 10$ a street canyon vortex forms, the wind is deflected along the 'main street' and typically increases with x (complicated by effects of gap between adjacent obstacles e.g. side streets).

require great detail and accuracy about particular or commonly-occurring situations; others require simpler models for rapidly calculating a wide range of meteorological and topographic boundary conditions. When such models are analytically-based, their predictions can be easily understood and may be expressed in useful formulae.

The reason why it is necessary to have different types of model for the different distances is because every type of model can only represent a finite range of length scales, with ratio R of the largest to smallest, e.g. R_0 for the overall scale. This ratio is limited by the capacity and speed of the computational systems and data input. Typically, in an FCM R_0 may be as large as 100-300 (so that about 10^7 grid boxes might be included in a calculation). In the FAM used in practice, R_0 may be of the same order ($\lesssim$100), but the discretised methods are much faster than in the FCM, (some FAM use $2d$ Fourier methods and represent obstacles as porous bodies, or others models that aggregate individual elements and represent them as a change in level).

Thus for example the smallest scale represented for each region is the ratio of the length of the region, e.g. L, to the ratio R, so that for the continuum and discrete/obstacle models these scales are L_0/R_0, L_{cc}/R_{CC}, and L_{DO}/R_{D0}. Usually there is some overlap, so that the smallest scales of one range are smaller than the largest scales of the next smaller range, i.e. $L_O/R_0 > L_{cc}$, $L_{cc}/R_{cc} > L_{DO}$.

2.3.2 Boundary layer (or overall scale)

On the overall scale range the inputs to the models are the representation/parameterisation of the surface necessary for computations down to the smallest scale L_0/R_O

Table 2.4: Types of computational model for urban meteorology and air flow. See also Tables 2.5 and 2.6 for continuation.

1	i	**Outerscale** Full computational models (FCM). Based on grid box numerical methods; full physics (fluid dynamics and thermodynamics). Input: from outer boundary conditioner synoptic (or regional) numerical weather prediction models; local surface conditions, e.g. surface fluxes for heat, F_Θ, water vapour, F_v, roughness length, $z_0(x, y)$ and surface elevation $z_s(x, y)$, and special effects e.g. emissions, dust, snow, and coastal surface data. Output: mean flow and turbulence statistics above canopy envelope. Typical number of grid boxes for $(1/3)h$ resolution on $30 - 100h$ grid is $10^6 - 10^7$. Takes about 3 hours per 1 hour run, faster for lower resolution model.
	ii.	Fast approximate models (FAM). (*a*) Flow perturbation models (suitable where buoyancy effects are small $U_G/U_B \gtrsim 1$) using fast/approximate numerical and analytical methods, simple physics (for turbulence, stratification profiles), input from observational data (reduced) or NWP models and from local surface conditions. (*b*) Characteristic flow models are applied where buoyancy effects are significant ($U_G/U_B \lesssim 1$) using scaling formula and continuity equations for special conditions/physics, e.g. slope winds, sea breeze, thermal convection; often adjusted for local conditions. (*c*) Mass consistent models to compute flow fields given data at several points in the flow domain and surface elevation z_s. (Only suitable if such data exist for all relevant cases.) (*d*) Typical resolutions can be on a horizontal scale of $h/10$ or less. (*e*) These models can be run over a few minutes on PC's for each case. Current simplified models do not account for unsteady conditions over large canopies (where $L_0/L_f, L_0/L_{Ro} \gtrsim 1$, and $L_0/h >> 1$).

(which typically is of order of the boundary layer depth h or $h/10$) This is therefore the scale over which the surface conditions are averaged, including ground surface elevation $z_s(x, y)$ (averaged over this scale), roughness length $z_0(x, y)$, surface heat flux $F_\Theta(x, y, t)$, surface temperature $\Theta_s(x, y, t)$ (in operational mesoscale meteorological models). In fully computational models, FCM's, the boundary conditions at the edges of the domain (and, in some models, above the domain) have to be specified. In meteorological/environmental models these are usually derived from real time larger scale regional or global numerical models, which are continually updated at regular intervals, e.g. every 3-12 hours, with observational data taken at all levels in the atmosphere. This process of 'data assimilation' is also beginning to be applied directly to mesoscale models, for example in urban areas with many measurement sites.

A critical feature of any FCM, especially in the boundary layer and when the flow is influenced by mountains, buildings, surface heating, is the representation of the effects

Table 2.5: Table 2.4 continued. See also Table 2.6.

2		**Continuum scale**
	i.	FCM using CFD methods. Grid point numerical models with approximate representation of buildings and open spaces (as porous medium; or distributed forces; as approximate shapes); approximate turbulence and heat transfer models; input from mesoscale models or assumed data. Output: mean and turbulence profiles within the building envelope and up to the boundary layer/inversion layer height. Typical horizontal resolution is greater than the spacing between buildings. For a continuum canopy of $5km$ of order $h - 10h$ with $10^6 - 10^7$ points, the resolution would be comparable to $10W$ or $10d$ for an 'accurate' computation.
	ii.	FAM. (*a*) Flow perturbation models (applicable where $\ln z_0$ or F_Θ vary significantly) using fast/approximate numerical and analytical methods with obstacles and spaces between them described by average properties and their relative fluctuations (e.g. average canopy height H_C, spacing d, and also typical rms fluctuations H_C^1 and d^1); simple turbulence and heat transfer models for canopy flows; input from mesoscale models or local data, and estimates of distributed effects of buildings. Output: mean flow within and above the canopy and turbulence above the canopy. (*b*) Local flow/thermal models (where $\ln z_0$ or F_Θ are approximately uniform). Formulae based on local dynamical and thermodynamic balance and estimates of distributed effects of buildings; input based on average wind, thermal flux and estimates of distributed effects.

on residual (or computed) scales greater than L_0/R_O of the turbulence at the smaller space and time scales. Some meteorological mesoscale models, such as HOTMAC (Brown and Williams, 1998 [87]), contain quite complex sub-models of the turbulence statistics (with extra equation for the turbulent energy and dissipation rate ($\kappa - \varepsilon$)), while others e.g. COAMPS (Hodur, 1997 [272]), MM5 (Anthes and Warner, 1978 [12]), MESONH (Cuxart et al., 2000 [139]), UK Met. Office unified models (Cullen, 1993 [138]), use eddy viscosity or even simpler parameterisations (e.g. assuming the form of the velocity profile). The experience from field studies in the USA is that for urban areas located on sloping terrain where buoyancy forms are significant (i.e. $F \lesssim 1$), the models with the more complex turbulence models are more accurate in these conditions. For example these models can now simulate the delay in these transitions, which may be as long as 5 hours after sunset/dawn. An even more difficult problem to simulate is the elongated eddies in the surface layer, unless large eddy simulations models are used, e.g. Carlotti, 2002 [101], which is only possible in research mode. Without such detailed flow models, calculations of dispersion have to be parameterised to allow for the complex effect.

Table 2.6: Tables 2.4 and 2.5 continued.

3		**Discrete obstacle scale**
	i.	FCM using CFD methods. Grid box numerical models with accurate representation of obstacles, approximate turbulence and heat transfer models; input from continuum models or assumed upwind conditions. (Very fast versions using idealised (e.g. inviscid) equations with finite numerical diffusion and approximate boundary conditions for buildings.) Output: mean flow and turbulence profiles around obstacles. Typical computational domain is several times greater than obstacle scale/spacing W, d with grid size of order $W/100$ or less. Note sensitivity to inflow conditions from other obstacles and atmospheric turbulence. Models better for clusters of obstacles than isolated buildings (where large scale atmospheric turbulence has less influence). Simpler methods are accurate/fast enough for practical use in off-line diffusion calculations.
	ii.	FAM Local flow models (used for diffusion models). (a) Turbulent wakes of individual obstacles based on typical flows near obstacles and perturbation methods for the far field. (b) Close-packed obstacles modelled by ideal (potential) flow (c) Idealised models for interactions when wakes of upwind building impinge on downwind structures. (d) Canyon models (semi-empirical formulae - not yet well established). (e) Canyon/street intersection models (e.g. ideal potential flow).

As explained in Table 2.4, these mesoscale models take many hours to compute a single meteorological situation. Nevertheless, they are sufficiently reliable that they are used operationally in the USA for short term forecasts and for computing the future scenarios of air quality in large urban areas. For complex dispersion e.g. from a localised source, stochastic simulations are sometimes used, (e.g. NAME model of UK Met Office, Maryon and Buckland [396] (1995)). Even then their predictions have to be supplemented with more detailed input on the properties of the turbulence.

Theoretical analysis together with the results of field experiments and numerical simulations are fast approximate models, FAM's, over mesoscale distances are being developed even when the air flow and meteorology is quite complex. These models are useful as estimates and provide input velocity fields for practical dispersion computations Section 2.4 when many scenarios are needed in a short time.

As shown in Table 2.4, when local buoyancy effects are weak (i.e. $U_G/U_B \approx 1$), the air flow over an urban area is generally a perturbation of the oncoming flow. Then from semi-analytic models using perturbation methods faster computational schemes have been devised, e.g. for lee-wave prediction scheme 3DVOM over mountains (Vosper and Mobbs, 1996 [639]), and are being developed in a general way to allow for

orography, roughness change and some effects of surface heating (Owinoh et al., 2005 [477]; Hunt et al., 2004 [299]). Although these are perturbation methods, the changes in wind speed and direction predicted (and verified) by these models can be quite large (~50% or more). (Indeed this modelling approach is the basis for many of the parameterisations used in numerical weather prediction for global/regional models at resolutions of 30-50 *km*.) The perturbation modelling approach being adopted in this range of meteorological flows is similar to that used for sub-mesoscale/neighbourhood scale orographic flows (e.g. in FLOWSTAR model (Carruthers et al., 1988 [105]), RIMPUFF (Thykier- Nilesen et al., 1999 [613])), the main difference being that over the larger scale the internal layer l reaches the top of the boundary layer h. Then the inversion height is affected as in hydraulic flows and Coriolis effects have to be included (which for example significantly influences flows along coasts and up and down large river valleys, e.g. Wippermann, 1984 [650]). Typically these models are run in the steady state. Once the time dependence over several hours is significant, a fully computational model is necessary.

When buoyancy forces are significant, $U_G/U_B < 1$, no FAM is yet available to cover all the most significant type of air flow and meteorological condition that might be needed for dispersion calculations. However, models and physical estimates have been derived for some particular situations, especially when Coriolis forces play a small role. For example, upslope/down flows in confined Alpine-scale valleys, and, rather differently, in wide valleys with low slopes, large heat island effects, and sea/lake breezes (Blumen 1990 [64]; Hunt et al., 2003 [296]; Ohashi and Kida, 2002 [471]. Not only are the quasi-steady features of these flows now quite well described, but also their time/space dependence over the diurnal cycle. In the absence of strong geostrophic winds (or very stable local conditions) the local diurnally varying buoyancy forces control the flow and therefore they are quite predictable (e.g. a valley wind, or sea/lake breeze on a still day). Since the single most important aspect of the air flow needed for dispersion calculations is the direction of the wind, such physically-based models provide vital information for estimating the effect of accidental releases in complex terrain.

2.3.3 Continuum (or neighbourhood) scale

On this scale, (say more than 100-1000 times the distance between obstacles/buildings), fully computational models even with the latest computing systems cannot generally resolve the details of turbulent flow around every obstacle/building. Typically for computations with 10^6–10^7 grid boxes the horizontal grid boxes are comparable with or greater than the distance between obstacles. To resolve the velocity field round each obstacle/building so as to calculate accurately its drag effect on the overall flow, the grid boxes would have to be of the order of $1m$ or less. Therefore even FCM's can, at present, only calculate average features of the flow over these grid box scales, by estimating the average effects of obstacles (buildings and streets) onto the model.

As explained in Section 2.1 different modelling approximations are needed (even with an FCM) depending on whether the obstacles distributed over the continuum scale are effectively porous or non-porous regions of resistance. If they are porous (Figure 2.5), i.e. lie in the category (i) of Table 2.3, the average effect of the obstacles is

estimated by an average drag coefficient averaged over the whole volume occupied by the buildings and the space between them (typically this is of the order of the porosity β. The same approach has been used for FCM computations of flows through forests and agricultural crops (Finnigan, 2000 [187]).

The input to any continuum scale model is the outer scale flow field approaching the region (or the flow leaving the adjoining neighbourhood), as in Figure 2.1. The output is the mean flow and basic turbulence statistics that depend on the particular closure model used, e.g. mixing length, turbulent energy-dissipation ($\kappa - \varepsilon$) closure, or Reynolds stress closure (e.g. Pope, 2000 [506]; Hunt et al., 2001 [293]). All three of these models lead to estimates of turbulent energy, but only the latter also provide estimates of length scale, and the space/time dependent evolution of turbulence structure, which is significant where the areas of building density or height change sharply. Reynolds stress models allow for the marked variation in the length scale and anisotropy of turbulence in these transition zones. Such models predict the mean velocity field everywhere (spatially averaged over the grid box), and the turbulence outside the canopy. Within the canopy, turbulence is generated locally on the scale b of the buildings, and is transported downwards by large-scale inhomogeneous eddying generated by the shear layer over the top (Finnigan, 2000 [187]). Both effects have to be represented in models of eddy viscosity and eddy diffusivity. In the analogous mechanical engineering problem of flow perpendicular to tubes in heat exchangers, the velocity field is simpler because the flow does not vary greatly along the tubes. In order to estimate the average properties of the flow and turbulence (see Eames and Hunt, 2003 [162]) within the array of obstacles the flow is computed in detail over a typical sample volume, e.g. surrounding 5 typical obstacles. A similar approach is now being considered in the numerical modelling of neighbourhood scale flows (Koutsourakis et al., 2003 [346]; JIAWE *No*. 95, April 2003).

If over the continuum scale, the canopy is effectively non-porous, the mean air flow passes over the obstacle envelope as if over a rigid surface with elevation $z_s(x, y)$. The roughness length z_0 also changes as a result of turbulence and recirculating flows in the courtyards, streets, etc. between the buildings. Estimating these parameters z_s, z_0 in terms of the building layout is only approximate (e.g. $z_s \simeq H_c$, $z_0 \sim H/30$). As with porous canopies, the parameterisations for calculating average flow properties can be estimated approximately by detailed computation of typical local areas. These calculations can also provide estimates of the local turbulence, needed for dispersion computations (e.g. Soulhac, 2000 [591]). FCM's using turbulence closure models have been extensively applied to the kinds of recirculating flows that occur between buildings in non-porous urban areas; most validations have been for wind tunnel tests and engineering flows, where the kind of very large-scale eddies and downdrafts found in atmospheric flows are absent. Such motions can lead to more rapid exchange between the upper flow above and within the canopy layer (see review by Mestayer and Anquetin, 1995 [425]).

As shown in Table 2.4, and reviewed by Britter and Hanna 2003 [81], most FAM's for the neighbourhood scale tend to focus on equilibrium flows within and just above the canopy. In a 'porous' canopy (Figure 2.2), the mean velocity within the canopy $U_c(z)$ is driven by the turbulent shear stresses generated in the intense shear layer just above the canopy. Here the ratio of $U_c/U(z_*)$, where $U(z_*)$ is the velocity at the top of

or above the roughness layer (Figure 2.2,b), depends on the porosity – a typical value being 0.3. In a non-porous canopy, typically in the inner city, where flows are determined by canyon and downdraft effects, this mean velocity ratio varies considerably over the range 0.3 to 1.0 (e.g. Soulhac, 2000 [591]).

Above $z = z_*$, but within the internal layer, the mean velocity profile is found in many experiments to have the form of equation (2.1). Despite the unevenness and inhomogeneity of these boundary layer flows, the ratios of the r.m.s. values of the three components of turbulent velocity to the friction velocity u_* are quite comparable with their values over level terrain, i.e. $\sigma_u/u_* \simeq 2.5$, $\sigma_v/u_* \simeq 1.3$, Rotach, 1995 [547].

The approximate average velocity profile (2.1) is not applicable at the edges of continuum regions, where the density and heights of obstacles vary, or in the interiors of such regions, if these are major variations in the spacing of obstacles (such as near parks, squares, etc.) in urban areas. At the edges of porous canopies, where the air flow in the canopy varies rapidly, an FAM approximate model has been developed based on the same approach as FCM by representing the canopy as a porous layer and (as for the FAM in the mesoscale range) solving perturbation equations semi-analytically to provide fast computation of the mean velocity and shear stress (Belcher et al., 2003 [51]; Coceal and Belcher, 2003 [127]). These have been verified against field and wind tunnel studies.

Over non-porous canopies (typically categories (i)–(v) in Table 2.3), the determining parameters ($H_c, z_0(x, y)$) are the same as for FCM over these elevation/roughness changes. The linearised FAM approaches give very similar results to those using FCM's (e.g. Belcher et al., 1990 [49]; review in Hunt et al., 1999 [292]). An operational model for porous and non-porous canopies is available from CERC[1] as part of the FLOWSTAR-ADMS system. However, the use of this kind of FAM for neighbourhood scale urban canopies needs to be extensively tested, especially the average estimates of the recirculating flows and turbulence amongst the buildings. For this purpose it would be necessary to use detailed data (experimental or computational) about typical flow on the building/street scale, and then investigate whether these are characteristic for the neighbourhood scale. (This assumption is effectively the basis for the UDM and ADMS-Urban models.)

2.3.4 Discrete obstacle or the building/street scale

In this review we particularly consider how detailed flow modelling in and around individual buildings and the surrounding streets is useful for understanding dispersion. Also, detailed studies of these local scale flows are necessary, as explained in the previous section, to develop models over neighbourhood scales for flow and dispersion.

(i) Weak interactions between well separated obstacles.

Fully computational methods (FCM), using a variety of turbulence modelling methods, have been extensively applied to computing flows around single buildings in turbulent boundary layers. Using turbulence closure methods many models have predicted mean

[1] *http://www.cerc.co.uk*

velocities near the buildings within one or two widths; but such models (e.g. $\kappa - \varepsilon$ models) have tended to over-predict small- scale turbulence around the structure (Murakami, 1992 [438]) and under-predict the large scale atmospheric eddies. This leads to an over/under-prediction of the mean velocity defects in the wakes downwind of $3d/2d$ structures in the atmospheric boundary layer. Only the computationally intense method of Large Eddy Simulation, or LES (or unsteady modelling of the fluctuating flows using turbulence closure models), can represent accurately the distortion of the large scale eddy motion around the building and its effect on downwind wakes (Rodi, 1997 [541]; Kim and Boysan, 1999 [334]).

Calculations using FCM with turbulence closure have also been performed on flow around small groups of buildings using resolutions down to about $0.1H$. The predictions of the turbulence in these flows are more reliable than those of isolated structures because here most of the turbulence is generated locally between the buildings and is of smaller scale. (Similarly, wind tunnel models of dispersion around buildings are generally more reliable when the buildings are in groups than when isolated because wind tunnels cannot simulate the low frequency fluctuation in wind direction.) This is because the primary interactions between the wake of one building and its impact on adjacent buildings are not sensitive to the structure of turbulence; however, the wakes of isolated or well- separated buildings are strongly affected by the form of the low frequency spectrum of turbulence. This is why in some institutions (e.g. Boris et al., 1992 [67]) work is being undertaken on dispersion in dense urban areas with fast FCM's in which approximate velocity fields are computed using classical grid box methods of finite size (say 1m) but neglecting completely any modelling of turbulent stress. This reduces the number and the order of the equations to be solved and speeds up the computation by a factor of 10 or more. The finite size of the grid effectively introduces numerical diffusion that simulates many of the same flow mean features developed using the more complex turbulence closures.

This approach of neglecting or greatly simplifying turbulence modelling has been used for many years in the Japanese construction industry for design studies on new large buildings (see Murakami, 1992 [438]) and in the aircraft industry for computing very complex flow around helicopters and in certain aero engine flows (Prof. W. Dawes, private communication).

Another simplification to speed up the computation of the mean velocity field is to represent the effects of the individual buildings as a distributed force acting on the flow (or source/sink distribution) and thereby only approximately representing the shape of the building (Moulinec et al., 2003 [436]). (In most FCM calculations considerable computational resource and time is spent on exactly representing the building shape, while at the same time making considerable approximations in the flow. This is justifiable for aircraft design but not for most aspects of environmental modelling.)

An approximation that is useful for computational modelling, especially circulation flow regions, is to simulate the vorticity in terms of the unsteady motion of many discrete vortices. This flow technique can be combined with Lagrangian unsteady dispersion modelling involving the tracking of particles (e.g. Turfus, 1988 [622]). This method may still provide useful techniques for investigating unsteady dispersion in two-dimensional recirculating flows such as street canyons.

There are at present no general FAM's that are capable of calculating the detailed flow around any isolated building or group of buildings, or even calculating those broad features of the flow needed for modelling dispersion close to the building. The main reason is that the unsteady separated shear layers that control the flow are much smaller scale than that of the obstacle or building. This means that the recirculating flow region, which greatly affects the magnitude and time scale of concentration fluctuation, is not only highly unsteady but also very sensitive to the effects of nearby buildings. Nevertheless, the main features of the mean flow patterns and typical magnitudes of the mean and fluctuating velocity have been classified and partially quantified (e.g. the size of the recirculating region) for many types of buildings and groupings. Therefore, although no practical FAM for the mean flow is available at present, these features of the flow field are now well enough known to derive useful quantitative FAM's for the dispersion as described in Section 2.4.

However for certain aspects of the flow/dispersion quantitative FAM's have been developed that are found to be useful in practice. Firstly when obstacles are far enough apart (i.e. b/d is small) that their near flow fields and their wakes are approximately independent, the wakes can be approximated as a perturbation to the approach flow, (Counihan et al., 1974 [132], Robins and Apsley, 2000 [539]). The same model can be used approximately with linear superposition when buildings are separated by about $3H$ where H is their height. As the ratio of breadth, b, to height H, b/H, increases from 1.0 to 10 this minimum separation distance $d_m in$ increases linearly to about $10H$ (Figure 2.3).

(ii) Strong interactions between closely separated obstacles

When d is less than d_{min}, Figure 2.5, it is found that the wakes of the upwind bluff obstacles are blocked by the downwind building and become elongated, so that the recirculating regions extend to the nearest downwind obstacle (e.g. Stoesser et al., 2003 [596]). For obstacles located in rows nearly parallel with the wind direction, the flow structure consists of turbulent recirculating regions in the spaces downwind of the buildings and relatively high-speed streams in the open streets between the buildings (Davidson et al. 1995 [143]). Describing the flow structure in this way provides the basis for FAM for dispersion calculations (see next section).

By contrast, when the buildings are placed in a staggered pattern relative to the wind direction, the flow between downwind buildings tends to destroy the wakes. Then the mean flow between the buildings consists largely of uni-directional bifurcating patterns of diverging and converging streamlines, with small regions of recirculating flow. Such flow can be computed by fast potential flow methods (Davidson et al., 1995 [143]), which are even faster if the buildings shape is approximated (Moulinec et al., 2003 [436]). This approach needs to be tested more thoroughly for cube-like buildings. Soulhac, 2000 [591] has shown that potential methods are also useful for street junctions.

For tall structures (where $H/b > 1$) in turbulent boundary layers the recirculating flow field in the wake is a region where streamlines enter and leave from the external flow (Lawson et al., 1988 [361]). Although in general there is no closed streamline 'bubble', because of the high turbulence there is strong mixing in the horizontal

plane and, to a lesser extent, in the vertical direction. These streamline patterns are significantly affected by surrounding obstacles (Figure 2.6). For example interactions between the wake of a low structure and a tall downwind tends to cause downwash (Britter and Hunt, 1979 [78]) and strong swirl around the sides of tall buildings. This enhances vertical mixing in the lower part of the downwind wakes and, through lateral convergence, may reduce the downwind extent of the wake of the downwind building. Structures placed sufficiently close downwind of other tall structures (where $d < d_{min}$) affect the vortex shedding and thence the whole wake structure. These wake-wake interactions are still not well understood qualitatively or quantitatively.

When the cuboidal structures are long enough and close enough, i.e. categories (i), (ii) and (iii) of Table 2.3, and the wind is at any angle, or if they are situated in rows and the wind is at a small glancing angle to the row, Figure 3a(ii), then characteristic canyon flows are formed in the streets between the structures. The mean flow has a component along the 'street' and a swirling motion in the perpendicular direction tends to extend up to the top of the buildings. The peak mean and fluctuating velocities near the ground are comparable with those at the level of the top of the structures. The key quantitative parameter for dispersion modelling in this situation is the ratio of the mean wind along the 'street canyon' V_c to the mean wind U_H above the buildings at the height H (in the approach flow). Soulhac 2000 [591] suggests (on the basis of computation and wind tunnels in a canyon without side streets) that V_c/U_H is about 0.3 when the angle of the approach flow lies between 0^o and 60^o. However, perturbation theory (extending the work of Belcher et al., 2003 [51]), the recent numerical simulation work of Dr. S.E Belcher (private communication) and informal observations in London suggest that this ratio lies in the range 0.5-1.0 for typical urban situations, at least with wide streets (i.e. for $b/d \lesssim 1$ and $75^o \lesssim \phi$). When $\phi < 30^o$, the along-street flow V_c takes a greater distance along the street to develop. This suggestion of larger values of V_c/U_H is in accord with the field observations of Soulhac (2000 [591], p. 188), which, as he notes, differ in some important respects with his own idealised simulations. The analysis suggests that the value of V_s can be quite sensitive to the value of V_c at the upwind end of the canyon. Thus a major crossroads can have a large effect on the canyon flows downwind.

When the buildings either side of the street are of comparable height, a strong feature of the helical canyon flow is that it does not extend above the buildings. Therefore, as we showed, and following in some respects Soulhac, 2000 [591], the appropriate FAM for these flows is to assume a canyon flow below the building level and a rough wall boundary layer flow above it. There are also mean velocities along the side streets, but these are only significantly smaller if $b/d \gtrsim 3$.

Finally we consider the air flow in typical courtyards and 'squares' connected to adjoining streets (Figure 2.7). Here the interaction between the vorticity layer leading from the top of the buildings and impacting on surrounding buildings leads to even more complex recirculating flows than in street canyons. However, because of the finite extent of these flow regions, it can generally be assumed that (unlike elongated street canyons) there is only a small mean velocity component V_c below the obstacle height, i.e. $Vc/U_H \lesssim 0.1$. However, the turbulence level is quite high in these recirculating flows, with $\sigma_u \sim \sigma_v \sim (0.5 - 1.0) \cdot \sigma_u(z_*)$ $1.2 - 2.5u_*$, so that $\sigma_u \sim V_c$ (Soulhac, 2000 [591], p. 222).

Simulations confirm that these are regions where fluid trajectories are well- mixed. This provides a basis for constructing FAM's for dispersion in these regions using semi-analytical diffusivity models.

In urban areas, especially street canyons and in courtyard/squares, turbulent motions are also produced by the exhaust of local heating/ventilation systems and by traffic movement (Britter and Hanna, 2003 [81]). Those contributions, which are significant in low wind speed conditions, can simply be added to the turbulence generated by the air flow. The contribution of vehicle turbulence tends to be confined to the lowest 5–10 m near the ground. Where the vehicle breadth is bv and speed is Uv, the vehicles' average contribution to the turbulence velocity squared averaged over the width of the street is of order $\Delta\sigma_w^2 \sim \beta_v^2 \cdot U_v^2(b_v/d)$, where the semi-empirical factor β_v is of order 1/10, but depends on the density of the traffic. Typically $\Delta_w \sim 0.2\ m/s$ for $U_v = 8\ m/s$, $b_v/d \simeq 0.2$. This factor, which is included in ADMS-Urban, has been shown to the significant in reducing peak concentration of traffic induced air pollution in field experiments.

2.4 Dispersion in canopies

2.4.1 Discrete/obstacle scale

FCM and FAM methods

In Section 2.2 it was explained how boundary layer flow over obstacles had different characteristic forms depending on their distribution. These characteristic flows correspondingly produce a number of different characteristic patterns of dispersion at the discrete scale, and fewer characteristic types at the continuum scale. On the smaller scales the mean displacement and the dispersion of a cloud of contaminant released from a small source with scale $l_S \leq b$, H are strongly influenced by the local flows around obstacles, i.e. the cloud/plume dimensions are small enough that σ_x, σ_y, $\sigma_z \leq H$, d. As with the air flow modelling, understanding and describing these patterns is the basis for fast approximate models (FAM). These are well developed for certain situations, but are in a formative stage for other situations as explained below. (For many engineering problems the key question is to estimate heat and mass transfer. This is not addressed here.)

Information about these (or any other airflow) patterns is not used as input in the fully computational models (FCM) because these models are determined by general equations and boundary conditions. However flow feature information can be used to judge and interpret the correctness and sensitivity of their predictions.

In this section we begin by reviewing FCM methods at varying levels of complexity that can be applied on this scale before considering the different methods of FAM and their application for the different types of building/street/source configuration. Table 2.7 summarises the main points.

The first stage in FCM calculations for complex flows is to compute the mean flow and the turbulence statistics and then to use these data in computations of the concentration distribution. As explained in Section 2.3, for well separated buildings, ($b/d << 1$), in the atmospheric boundary layer (e.g. in the suburban situation), the usual methods

based on mean flow turbulence closure models do not completely represent the flow and dispersion process in highly unsteady eddying motions in the wake or the effects of large scale eddy motion in boundary layer turbulence. Typically these models make errors of order of 100% in the dimensions of separated flow regions or growth rate of wakes. They are significantly less accurate than the more computationally intensive large eddying simulation methods (e.g. Murakami, 1992 [438]; Rodi, 1997 [541]) or stochastic simulation models (e.g. Turfus, 1988 [622]). However when the buildings are closer together, as in most of the cases of Table 2.3, the mean and turbulent flow fields and dispersion process are dominated by the interactions between the vorticity in the wakes shed off upwind buildings impinging on those downwind. The dispersion is more sensitive to the spacing and orientation of the buildings/streets than to the turbulence structure – as shown by various numerical and experimental studies.

These general principles explained why a commercial CFD code FLUENT was better for these situations than for isolated sources (e.g. Riddle et al., 2004 [534]). Moulinec et al., 2003 [436] quantified the 'topological' mechanism described in Davidson et al., 1995 [143] in which the splitting of the streamlines as the flow passes between buildings effectively diffuses matter released from a local source. The longitudinal or streamwise dispersion is also enhanced as a cloud impacts on a building, slowing up on the stagnation line and passing more rapidly around the sides. This process also slows down the cloud as it moves through the canopy (Eames et al., 2003 [163]). The wakes also amplify this process (Fackrell, 1984 [174]). Hunt, 1985 [284] reviewed earlier studies showing that in these converging and diverging flows around obstacles the mean concentration fields are less sensitive to the turbulence structure (e.g. length scale) than in the unobstructed turbulent boundary layer.

One might conclude that because these effects of dispersion are less sensitive to turbulence structure in complex urban flows, CFD models results should be reasonably accurate provided they are applied with just sufficient detail to represent the mean flow features. This is why CFD methods are used with large computer resources by certain laboratories in the USA (e.g. Brown and Williams, 1998 [87]). On the other hand, it also means that FAMs are appropriate, using approximate models of the turbulence and mean flow for the different types of topology and pattern of the buildings and street. This is the rationale for the fast and easily-understood methods, now being used/developed in the UK and elsewhere, which we describe below.

FAM: Dispersion very near the source

Assuming the location of the source $\mathbf{x_S}$ is known (Figures 2.3, 2.5, 2.10, 2.11, 2.12 and 2.13) calculations of the near field dispersion first depend on the effective source scale L_{Se} (which determines where the matter is dispersed by atmospheric motion) in relation to the separation distance between the buildings d. A finite volume of source material is initiated at time t_S. If $l_S \leq d$, then the matter disperses as if from a small isolated source. Given the time variation of the source strength $Q(\mathbf{x_S}, t)$ the average concentration at a point $\mathbf{x}$ and time t can be calculated as a time integral from the initiation of the source to the measurement time t:

$$C(\mathbf{x}, t) = \int_{t_s}^{t} Q\left(\mathbf{x}_s, t'\right) C_C\left(\mathbf{x}, t - t'; \mathbf{x}_s\right) dt' \tag{2.2}$$

Table 2.7: Types of computational model for dispersion prediction. See also Table 2.8 for continuation.

1.		**Discrete/Obstacle Scale (relevant for diffusion for local sources near obstacles)**
	i.	Full Computational Models (FCM). *a* Steady/unsteady C.F.D models. *b* Unsteady, Large Eddy Simulations - mainly for research use. Note: these types of models are also applied on continuum scale, given enough computer resources or acceptance of approximation.
	ii.	Fast approximate models (FAM) for practical application. *a* Eddy diffusion computations using approximate or idealised flow and obstacle geometry (scenario studies/research). *b* Stochastic modelling. Computational methods, allowing for eddying motions in the wakes of obstacles and concentration fluctuation (scenario studies) (using approximate flow/topology models). *c* Approximate modelling of ensemble average concentration based on ideal/simplified flow/dispersion models for relevant types of situations (as in Table 3) and meteorological conditions. Usually based on interpolations between different types of idealised distorted puff/plume structure. These are fastest methods appropriate for operational conditions. Note: all models either require input for source strength, location(s), size; or else concentration distribution (in order to deduce source information).
2.		**Continuum Scale (usually applied with insufficient computational resources/time to calculate on obstacle scale) (diffusion upp to depth of inner layer $l(x)$)**
	i.	Both FCM and FAM approaches involve approximate modelling of average diffusion process to account for the turbulence and flow between the large numbers of buildings on this scale. eg. porous medium to represent average effects of buildings (as for flow) plus effective diffusivity to represent dispersion processes around individual buildings, or aggregation of dispersion process around individual obstacles to produce average process on continuum scale. In FCM concentration fields are computed. In FAM idealised plume/puff/box model structure is assumed.
	ii.	All methods require input concentration field from building/street scale, e.g. virtual source location/scale/distribution (often asymmetric).

Table 2.8: Table 2.7 continued.

3.		**Outerscale (relevant for distant sources or for down wind sources located within the canopy)**
	i.	FCM Eulerian grid box or Lagrangian particle tracking methods using turbulence models (not suitable for real time emergency response computation), above canopy. Input: from obstacle or continuum scale data (for local sources). Upwind data for distant sources. Output: mean and fluctuating concentrations.
	ii.	FAM *a* Advection and eddy diffusion or Lagrangian stochastic models above canopy with simplified (but time-dependent) flow fields and turbulence profiles (scenario studies/research). *b* Approximate, fast models suitable based on idealised models of flow field turbulence profile (above the canopy) allowing for time dependent flows. *c* 'Box' model (well within boundary layer). *d* Puff/plume models (with segmentation into smaller puffs/grid boxes as time progresses). *e* Combining simplified Eulerian grid box and puff/plume models.

Note: fluctuations (rms and pdf) in concentration can be estimated.

Here, C_C is the concentration at $\mathbf{x}$ in an initially small cloud produced by unit source strength emitted at $\mathbf{x_S}$ at time $t_S^{'}$. Many experiments have shown that provided the energy and/or scale of the turbulent velocity components do not vary greatly (say more than a factor of 2) over the volume occupied by the 'cloud' of contaminant released from the source in the presence of mean wind speed U, C_C can be approximated (near the source) by the basic Gaussian cloud profile $G_{C,o}$, i.e.

$$C_C = G_{C,o} = \exp\left(-\left[X^2 + Y^2 + Z^2\right]\right) / \left[(2\pi)^{3/2}\sigma_x\sigma_y\sigma_z\right] \tag{2.3}$$

with $\sigma_x(\Delta t^{'}), \sigma_y(\Delta t^{'}), \sigma_z(\Delta t^{'})$ being the dimensions of the cloud in the directions parallel and transverse to the local mean flow at time t after the release at time $t_s^{'}$ where

$\Delta t^{'} = t - t^{'}$,

$X^2 = \left[x - (x_S - U\Delta t')\right]^2 / 2\sigma_x^2$,

$Y^2 = (y - y_S)^2 / 2\sigma_y^2$,

and $Z^2 = (z - z_S)^2 / 2\sigma_z^2$.

The reason for this form of profile is because of the essentially Gaussian nature of large scale turbulent eddying motions. The profile is not greatly affected by mean velocity gradients when the cloud travels over flat or undulating surfaces (e.g. Pasquill and Smith, 1983 [484]; Hunt et al., 2002 [294]).

The Gaussian cloud formula can be applied in terms of the distance $\widetilde{x}$ along and distances $\tilde{y}$, $\tilde{z}$ perpendicular to Ψ_S the mean streamline through the source, so that

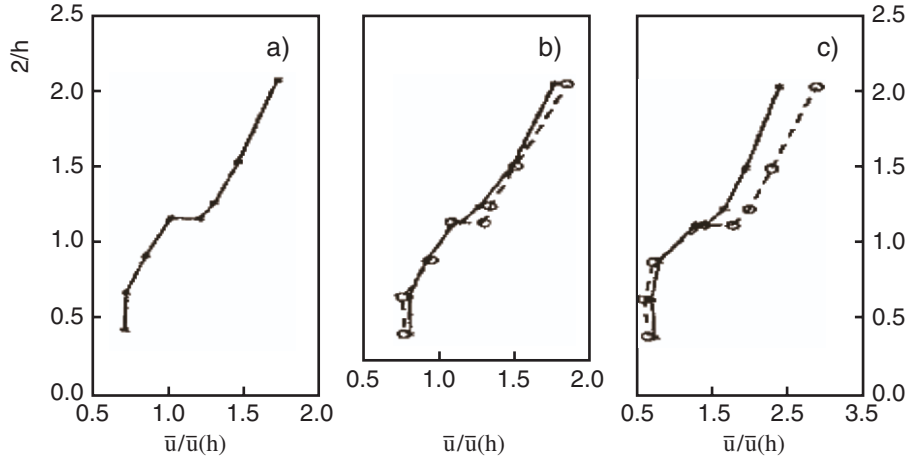

Figure 2.8: Typical mean velocity/turbulence distribution. Average profiles of the magnitude of wind speed, scaled by its value at $z = h$ (canyon height): (a) averaged over all available data; (b) approaching flow normal to the canyon (from SW, full line and stars) and parallel to the canyon (dashed line and circles); (c) approaching flow normal to the canyon from NE (full line and stars) and the same but only runs with wind speed larger than 3 m/s at position 21R [canyon roof] (dashed line and circles). (From Rotach, 1995 [547]).

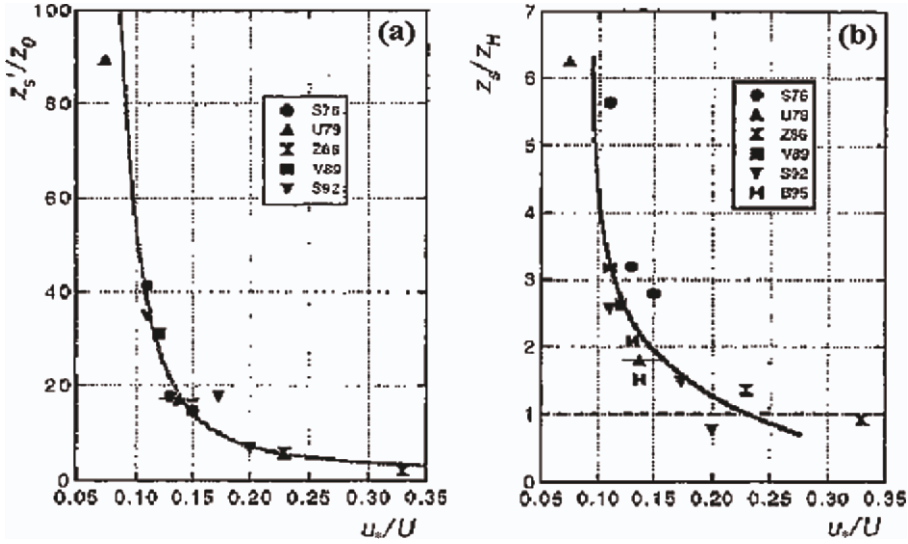

Figure 2.9: Typical mean velocity/turbulence distribution. Variation of u_*/U for neutral conditions with non-dimensional heights: (a) z_s'/z_0 and (b) z_s/z_H where z_s is sensor height above ground; $z_s' = z_s - z_d$, z_d is zero-plane displacement height. The line in (a) is based on the log-profile, and the line in (b) is an empirical fit. (From Roth, 2000 [550]).

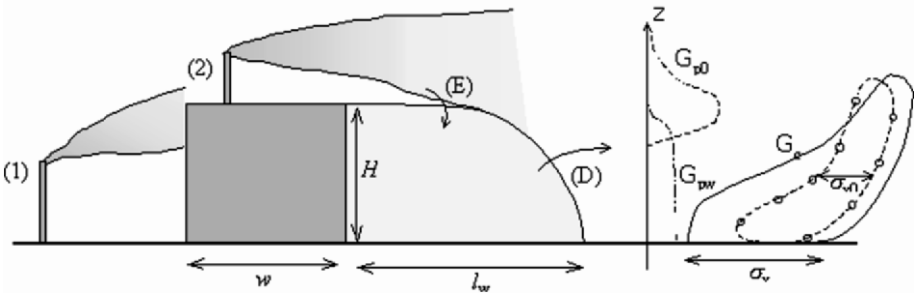

Figure 2.10: Characteristic dispersion mechanisms in canopies from local sources close to an isolated obstacle: source outside wake/canyon, showing impaction of the plume from Source (1), wake entrainment (E) and detrainment (D) from Sources 1 and 2. Note how the plume profile G(z) has a split structure in the wake with unentrained component G_{p0} and detrained component G_{pw}. G_c denotes the typical outline of a cloud emitted upwind, showing the additional longitudinal dispersion associated with the blocking and wake effects. Here the reference cloud outline in the absence of buildings is shown as a dashed line with small circles, with streamwise dimension σ_{x0}.

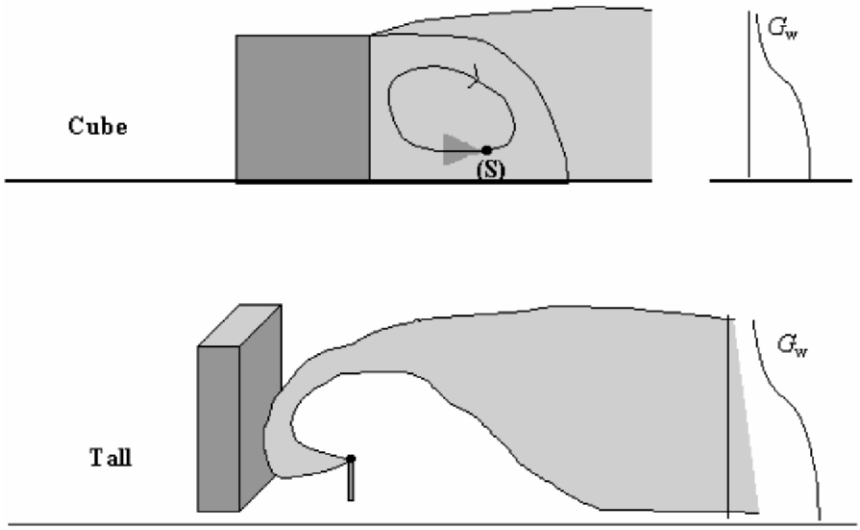

Figure 2.11: Source inside wake/courtyard, canyon/building with a single wake component in the plume profile downwind of the recirculatingregions for cube-like and tall cuboidal building. In the latter case, the concentration may not be well-mixed over the whole height.

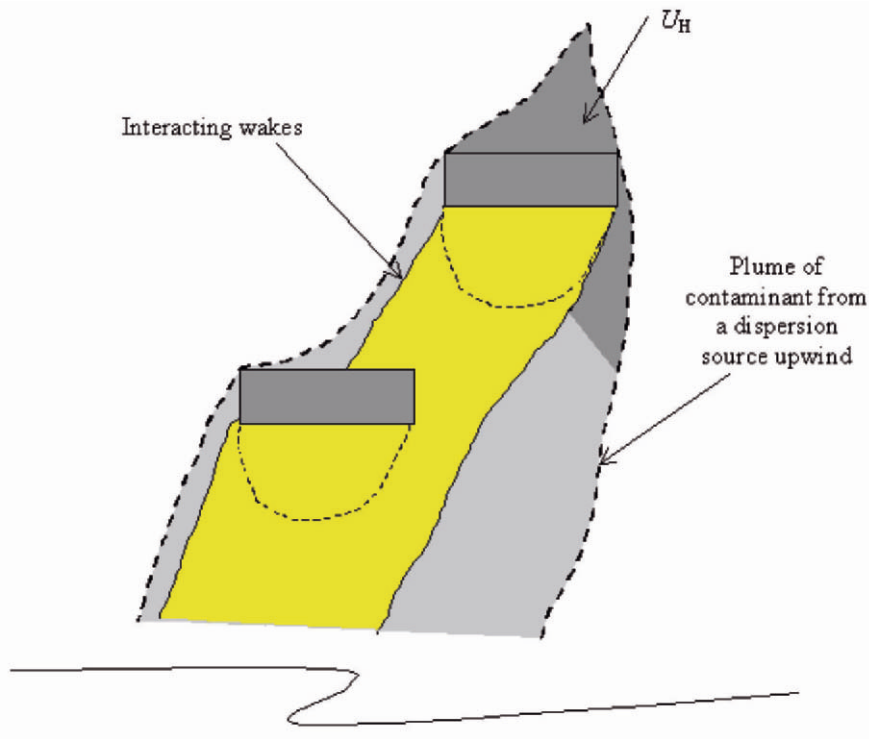

Figure 2.12: Characteristic dispersion mechanisms in canopies in the case of multiple buildings (see also Figure 2.3): On discrete/obstacle scale (for well-separated buildings, $b/d \sim 1$); plume dimensions less than obstacle width.

$X^2, Y^2, Z^2 = \left(\tilde{x} - \tilde{U}t\right)^2/\sigma_x^2,\ \tilde{y}^2/2\sigma_y^2,\ \tilde{z}^2/2\sigma_z^2$, respectively. Note that $\tilde{x} = 0$ at $x = x_S$ and $\tilde{y}$ can be calculated in terms of the coordinates of the mean streamline $y_c(x)$, $z_c(x)$ (see Figure 2.14). The mean velocity along the mean streamline is $\tilde{U}(\tilde{x})$. The magnitudes of $\sigma_x, \sigma_y, \sigma_z$ depend on the variances of the turbulent velocity components and their integral length scales (assuming that the velocity components have similar statistical structure in the different directions).

Very near the source (say within 100 m),

$$\sigma_x \cong \sigma_u \Delta t', \qquad \sigma_y \cong \sigma_v \Delta t', \qquad \sigma_z \cong \sigma_w \delta t' \tag{2.4}$$

Because of the anisotropy of the turbulence these widths can differ by a factor of 2 or more.

Far from the source, where $(t - t') \gtrsim L_x/\sigma_w$ these cloud dimensions are approximately equal to integrals of the diffusivity components $K_x, K_y, K_z\left(\Delta t'\right)$ taken along the trajectory, i.e.

$$\sigma_x^2\left(\Delta t'\right) = 2\int_0^{\Delta t'} K_X\left(\Delta t''\right) d\Delta t'' \tag{2.5}$$

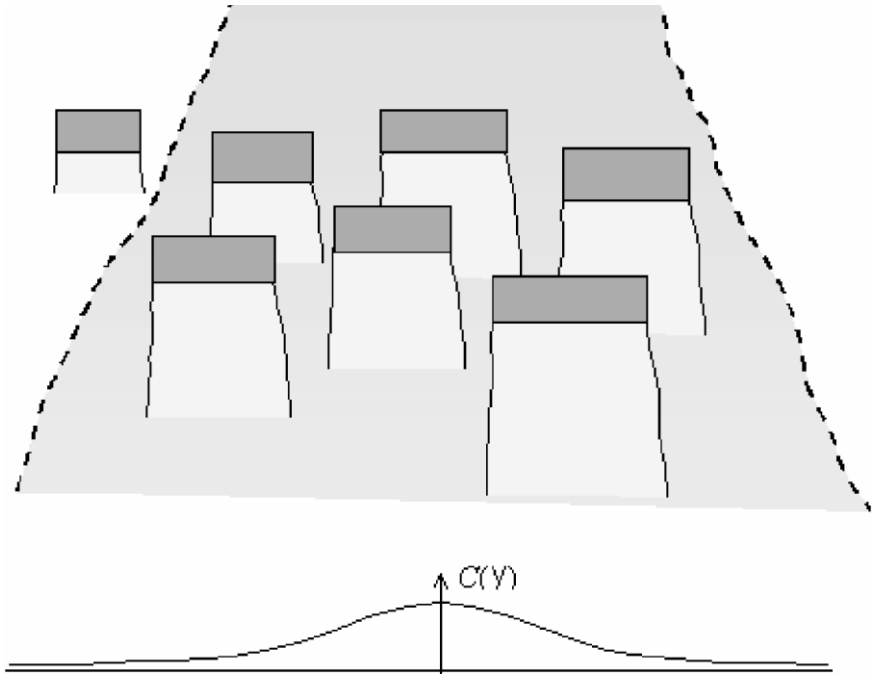

Figure 2.13: Characteristic dispersion mechanisms in canopies in the case of multiple buildings (see also Figure 2.3): Far from the source, on continuum scale; plume is much wider than the building width.

A modified form of this expression can be used when the mean velocity varies along the plume (Hunt, 1985 [285]).

For sources on level ground, as the cloud's vertical dimension grows to greater than its source height z_S, it impacts on the ground. The resulting increase in the concentration is approximately modelled as a 'reflected' Gaussian profile by adding the solution $G_{C,r}$ for an image source at $z = -z_S$. Thus for $\sigma_z > z_S$,

$$C_C = G_{C,0}\left(X, Y, Z, \Delta t^{'}\right) + G_{C,r}\left(X, Y, Z, \Delta t^{'}\right), \tag{2.6}$$

where $G_{C,r} = G_{C,o}\left(X, Y, Z_R, \Delta t^{'}\right)$ and $Z_r^2 = (z + z_s)^2 / 2\sigma_z^2$, and also note that $G_{C,r} = G_{C,o} e^{\left(-2z_S z/\sigma_z^2\right)}$.

It is useful to note that if the source steadily emits q_S units per unit time in a wind with mean velocity U and there is a steady mean wind, the source leads to a steady plume downwind with concentration

$$C_p(\mathbf{x}) = q_s(\mathbf{x}_s)\, G_p(\mathbf{x} - \mathbf{x}_s) \tag{2.7}$$

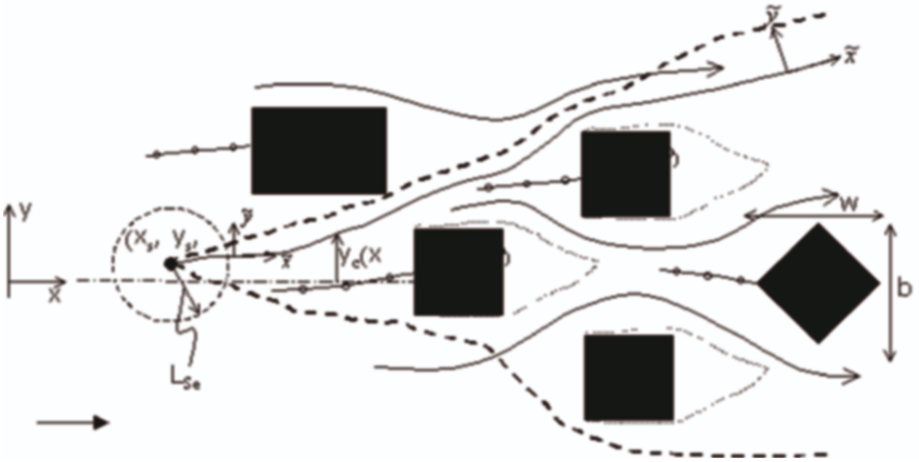

Figure 2.14: 'Tall' obstacles, $H/b > 2$: Staggered obstacles (all of comparable height), located at $\left\{y_B^{(i)}, x_B^{(i)}\right\}$, close to each other. Note how wakes can 'disappear' through converging streamlines, while lateral diffusion is enhanced by diverging streamlines ('topological' diffusion). Streamlines are indicated by solid arrowed lines. The streamline through the source at $(x_S,\ y_S,\ z_S)$ is $y_c(x)$; $\tilde{x}$, $\tilde{y}$ are coordinates parallel and perpendicular to this streamline. Streamlines marked with small circles are mean streamlines Ψ_{stag} passing through stagnation points where plumes split. The cloud/plume resulting from the source is the shaded area enclosed by heavy dashed line. L_{Se} is the effective size of the source outside which ambient turbulence determines the dispersion.

where

$$G_p = \int_{-\infty}^{t} C_C dt' \cong G_p\left(\mathbf{x} - \mathbf{x}_s\right). \tag{2.8}$$

Here the Gaussian plume formula for uniform flow conditions above the ground

$$G_{p,0}\left(Y, Z, \tilde{x}\right) = \exp\left[-\left(Y^2 + Z^2\right)\right] / \left(2\pi U \sigma_y \sigma_z\right). \tag{2.9}$$

After 'reflection' off the ground,

$$G_p = G_{p,0}\left(Y, Z, \tilde{x}\right) + G_{p,0}\left(Y, Z_r, \tilde{x}\right). \tag{2.10}$$

FAM: Dispersion with large separation distances between buildings ($b/d \leq 1/3$ – multiple cloud splitting models)

In a canopy with well-separated obstacles, after the cloud/plume has travelled a distance of order d it will impinge on to or pass over downwind obstacles located at $\underline{\mathbf{x}}$, where k=1,2 (see Figures 2.6 and 2.13). The diffusive and advective processes involved greatly affect the form of the profile of concentration at a given value of X, and the dimensions of the cloud/plume, depending on the cloud parameters in relation to

the building scale H, b i.e. the mean height ratio $\hat{z_c} = z_c/H$, cloud dimensionless ratio $\hat{\sigma} = max(\sigma_y, \sigma_z)/min(H, b)$ and grazing distance ratio

$$\hat{n} = \frac{\min \left| x_c - x^{(k)} \right|}{\max(\sigma_y, \sigma_z)}$$

(Fackrell, 1984 [174]). Hunt and Castro, 1981 [282] extended the work of Vincent, 1977 [636] to dispersion of clouds in building wakes. The basic concepts for plumes were developed by Hunt and Mulhearn, 1973 [280], Puttock and Hunt, 1979 [513], Hunt et al., 1979 [281] and Davidson et al., 1995 [143]. Robins and Apsley, 2000 [539] brought many of the results together for dispersion from local sources near cuboid obstacles in the Buildings Module of the ADMS model. Hall et al., [243, 247] extended the results to cover dispersion around many obstacles in their code UDM. We describe the characteristic processes below and outline the simple models that have been developed.

Impacting low level cloud

As the cloud approaches the cuboid shaped obstacle, if its location is within about one plume width of the centreline (i.e. $\hat{n} \leq 1$) it is swept round and over the obstacle and is entrained into the recirculating wake.

If the cloud is wider than the width of the obstacle (i.e. $\hat{\sigma} > 2$), and so its width and peak concentration are not significantly changed by the impact. If $\sigma_z > H$, its depth is also not much changed. But for a tall obstacle, if $H/b > 2$ and if the plume is narrow plume, defined by $\sigma_z < b$, then the cloud is diffused vertically in the wake, so that σ_z is increased by about b as the cloud passes around the building, but is not completely mixed up to the height of the building.

Also, for the 'puff' cloud the time taken for the cloud to detrain from the wake is of the order of min(6H, 3b)/U, so that the length of the plume σ_x is increased to about $\min(6H, 3b)$ if σ_x is less than this length (Fackrell, 1984 [174]). Thus if the cloud impacts centrally on the obstacle, i.e. $\hat{n} \leq 1$, the change in the cloud dimensions downwind are approximately given by

$$\Delta\sigma_x \sim max\{min(6H, 3b) - \sigma_x, 0\}, \tag{2.11}$$

$$\Delta\sigma_y \sim max\{b/2 - \sigma_y, 0\}, \tag{2.12}$$

$$\Delta\sigma_z \sim max\{H - \sigma_z, 0\} \quad \text{if} \quad H \lesssim 2b, \tag{2.13}$$

$$\Delta\sigma_x \sim max\{b - \sigma_z, 0\} \quad \text{if} \quad H \gtrsim 2b. \tag{2.14}$$

(Upwind of a tall obstacle the 'downwash' can reduce σ_z and reduces entrainment into the wake and $\sigma_z < H$.)

Note that if the cloud 'grazes' the building, i.e. if $\hat{n} \sim 1$, then a proportion α of the cloud first is entrained and then detrained from the recirculating wake (see Figure 2.12). This leads to a changed concentration profile downwind of the wake with length l_W that approximates to a double plume structure as in the ADMS Building Module consisting of the depleted original $G_{C,0}$ and the Gaussian cloud/plume that detrains from the wake.

Thus for $x > x_b + l_w$ and $\Delta t > \Delta t_b$

$$\begin{aligned} G_C &\cong (1-\alpha) G_{C0}\left(\tilde{X}, \tilde{Y}, \tilde{Z}\right) + \alpha G_{C,w}\left(\tilde{X}_w, \tilde{Y}_w, \tilde{Z}_w\right), \\ G_p &\cong (1-\alpha) G_{p,0}\left(\tilde{X}, \tilde{Y}, \tilde{Z}\right) + \alpha G_{p,w}\left(\tilde{X}_w, \tilde{Y}_w, \tilde{Z}_w\right) \end{aligned} \tag{2.15}$$

where

$\tilde{Y}^2 = \tilde{y}^2/2\sigma_y^2$, $\tilde{y} = y - y_c$ and $y_c \cong y_b + b/2 - y_s$,
$\tilde{x_w} = x - x_b$ and $\tilde{X}_w^2 = (x - x_{cw})^2/2\sigma_{xw}^2$,
$\tilde{Y_W}^2 = \left(y - y_b\right)^2/2\sigma_{yw}^2$, $\tilde{Z_W}^2 = z^2/2\sigma_{zw}^2$,
$x_{cw} = x_\kappa + U_w\left(\Delta t - \Delta t_b\right)$, $\Delta t_b = \left(x_b - x_S\right)/U$.

The cloud/plume dimensions are functions of the wake turbulence and the distance downwind from the k^{th} obstacle $(x - x_{(k)})$ and travel time from detrainment i.e. $\Delta t - \Delta t_{(k)}$. Their effective values at $x = x_{(k)} + l_w$ are determined by the scale of the wake, for example $\sigma_{y,w}^2 \cong b^2/4 + \sigma_y^2\left(x - \left(x_{(k)} + l_w\right)\right)$. Note that the wake cloud displacement $x_{c,w}$ depends on the slower wake velocity U_w.

The entrainment factor α decreases as the mean streamline moves further from the centreline of the obstacle. If the instantaneous source is released in the near wake then $\alpha = 1$.

Note that within the recirculating wake, i.e. $x_b < x < x_b + l_w$, the mean concentration $\langle \overline{C}_{c,w} \rangle$ is approximately constant and determined by the value in the approach puff/plume where it touches the wake, and

$$\begin{aligned} G_{C,w} &\cong G_{co}\left(\tilde{X}_{o,w}, \tilde{Y}_{o,w}\tilde{Z}_{o,w}, \Delta t_w\right), \\ G_{p,w} &\cong G_{po}\left(\tilde{X}_{o,w}, \tilde{Y}_{o,w}\tilde{Z}_{o,w}\right) \end{aligned} \tag{2.16}$$

where the displacement parameters are:

$\tilde{X}_{o,w}^2 = 0$ and $\Delta t_w = \left(x_{(k)} + l_w/2 - x_s\right)/U$,
$\tilde{X}_{o,w} = x_{(k)} + l_w/2 - x_s$, $\tilde{Y}_{0,W}^2 \cong \left(y_{(k)} - y_b - b/2\right)^2/2\sigma_{yw}^2$,
$\tilde{Z}_{wo}^2 \cong (z_s - h/2)^2/2\sigma_{zw}^2$ $(x \cong x_{(k)} + l_w/2)$,
and σ_{xw}, σ_{yw}, $\sigma_{zw} = \sigma_x\left(\tilde{x}_{0,W}\right)$ etc.,
$\alpha_c = \left(\langle G_{c,w} \rangle\right) / \left[G_{c,w}\left(y \approx b/2, z, \Delta t_w\right)\right]$,
$\alpha_p = \left(\langle G_{p,w} \rangle\right) / \left[G_{p,w}\left(y \approx b/2, z, \tilde{X} = l_w/2\right)\right]$.

Such expressions can be refined and calibrated for different types of buildings, and for different source positions relative to the source. The example given here shows how even for one particular situation of a puff impacting on a building there are several distinct stages in the dispersion process. But even though the plume structure changes quite markedly many of its characteristic features recur for dispersion around most types of obstacle. In some codes (e.g. Hall et al., 1996 [243]), where many obstacles are considered, these expressions are further simplified, for example by ignoring the lateral displacement of the streamline through the source, i.e. assuming $y_c \approx y_S$.

This approach can be satisfactory even when wakes of structures impact on each other by modelling appropriately the changed cloud dimensions. However, even with

extensive empirical modification it is probably not an accurate or efficient model when buildings are close to each other and the wind is not perpendicular to the buildings. A downwind vortex can cause the air flow to be significantly deflected some distance downwind of the obstacle. The combined effect of many such building wake interaction leads to the characteristic dispersion pattern in 'canyon' flows considered in Section 2.3.3.

Impacting elevated clouds

If the effective source of the puff is at a height z_S above the ground, the puff impacts on a downwind obstacle if $\hat{n} \leq 1$, or in more detail if $y_S - y_{(k)} - b/2 \lesssim \sigma_y$ and $z_S - H \lesssim \sigma_z$. If the vertical cloud depth is small compared to the height (i.e. $\sigma_z < H$) then the puff grazes the top of the obstacle and is entrained into the wake. As with the laterally displaced low level cloud, this leads to a 'double' puff structure, as shown in Figure 2.7. So that for $x \geq x_{(k)} + w/2, \Delta t \, \Delta \, t_{(k)}$

$$G_c \cong (1-\alpha)\, G_{c,0}\left(\tilde{X}, \tilde{Y}, \tilde{Z}\right), \Delta t) + \alpha G_{c,w}\left(X_w, Y_w, Z_w, \Delta t\right). \tag{2.17}$$

Here $\tilde{Z} = (z - z_c)^2 / 2\sigma_z^2$, $z_c \cong z_S + \zeta H$ ($\zeta \cong 1/2$ due to streamline convergence over the building). The functions G_{c0} and G_{cw}, α, and dimension parameters are constructed as in (2.10) by matching the wake concentration in the grazing plume to that in the wake.

This simple form shows how the concentration field varies markedly as the height of the source varies near an obstacle. The results are consistent with wind tunnel concentration measurements of steady plumes in and near obstacle wakes (Robins and Apsley, 2000 [539]).

FAM: Dispersion with moderate spacings between rows of obstacles – canyon model ($H/d \gtrsim 1/3$)

As explained in Section 2.2, where obstacles are located in rows with separation gaps d that are comparable with their height H, (i.e. streets), the recirculating flow in the wake of the upwind row tends to extend across the gap or 'street', and there is usually a significant mean velocity V_s along the street (see Figures 2.5 and 2.15. Note that for convenience separate streamline coordinate systems are used within and above the canyon, with denoting the coordinate relative to the canyon flow. First consider a cloud/plume released below the top of the obstacles.

(a) For a cloud released below the top of the obstacle, the initial phase of dispersion, described in Section 2.4.2 (for $\Delta t < t_1$) ends when the cloud width (defined relative to the local mean wind spread along the street) is comparable with the 'street' width (i.e. $\sigma_y \sim 5$).

(b) For $\Delta t > t_1$ before the vertical growth of the puff reaches the tops of the buildings, i.e. $\sigma_z + z_S < H$ the cloud grows in the flow direction as it is advected along the 'street'. In this phase the puff profile has an approximately Gaussian 'street' form in the vertical and longitudinal directions i.e.

$$C \sim Q_S \left[G_{C,0}\left(\tilde{X}, \tilde{Z}, \Delta t\right) + G_{C,r}\left(\tilde{X}_C, \tilde{Z}_r, \Delta t\right)\right] \tag{2.18}$$

where

$$G_{C,0} \sim \frac{exp\left[-\left(\tilde{X}^2+\tilde{Z}^2\right)\right]}{(2\pi)\, d\sigma_x\sigma_z} \tag{2.19}$$

and the second term is caused by ground reflection as defined in (2.6). The values of σ_x, σ_z are greater (by typically a factor of 2 or more) than their values in open country for the same value of u_* (because of longitudinal dispersion in the streamwise direction and recirculating flows with vertical components).

If the source is effectively steady the resulting plume profile in the canyon (from (2.7)) is

$$G_p \sim \exp\left(-\tilde{z}^2\right) / \left(2\pi V_s d\sigma_z\right) + \exp\left(-\tilde{z}_r^2\right) / \left(2\pi V_s \cdot d \cdot \sigma_z\right). \tag{2.20}$$

(c) In the third phase, where $\sigma_z(\tilde{x}) > H - z_s$, $\tilde{x} \geq l_H$ and $\Delta t > \Delta t_2$, the puff reaches the tops of the obstacles and then is dispersed by the wind moving at speed U_H at an angle Θ to the street. The concentration decreases rapidly (in fact exponentially) along the street. If the source is near the ground (and $\sigma_z \gtrsim H$) the cloud is well mixed and dispersing upwards. But if the source is elevated (i.e. $z_S \sim H$) there continues to be downward vertical dispersion in this phase. The following approximate analysis is derived from the basic solution of Turfus, 1986 [621] for dispersion from a steady localised course where the mean velocity reverses near the ground (see Sections 2.6 and 2.7).

The profile for a puff released below the top of the obstacles $z_S < H$, for $\tilde{x}_c \gtrsim l_H \sim (U/u_*)(H - z_s)$ and $z < H$,

$$G_{C,c} \cong \exp\left(-\frac{\tilde{x}}{10H}\right)\gamma_z(z/H)\,\gamma_C\left(\tilde{X};\tilde{x}_c\right) \tag{2.21}$$

where

$$\tilde{x}_c = y - y_S$$

$$\text{and} \qquad \gamma_z(z/H) = \cos(\mu/H) \tag{2.22}$$

where μ varies slightly with the angle θ of the approach wind (see (2.56)). Also

$$\gamma_c = \frac{10\exp\left(-\tilde{X}^2\right)}{Hd\tilde{\sigma}_x} \tag{2.23}$$

where $\tilde{X} = \left[\tilde{x}_c - V_s\Delta t\right]^2 / 2\tilde{\sigma}_x^2$, and $\tilde{\sigma}_x$, as usual, is a function of $\tilde{x}_c$, the distance from the source along the canyon.

For a steady source, the formula for a plume is similar where

$$G_{p,c} \approx \gamma_p G_{C,c} \tag{2.24}$$

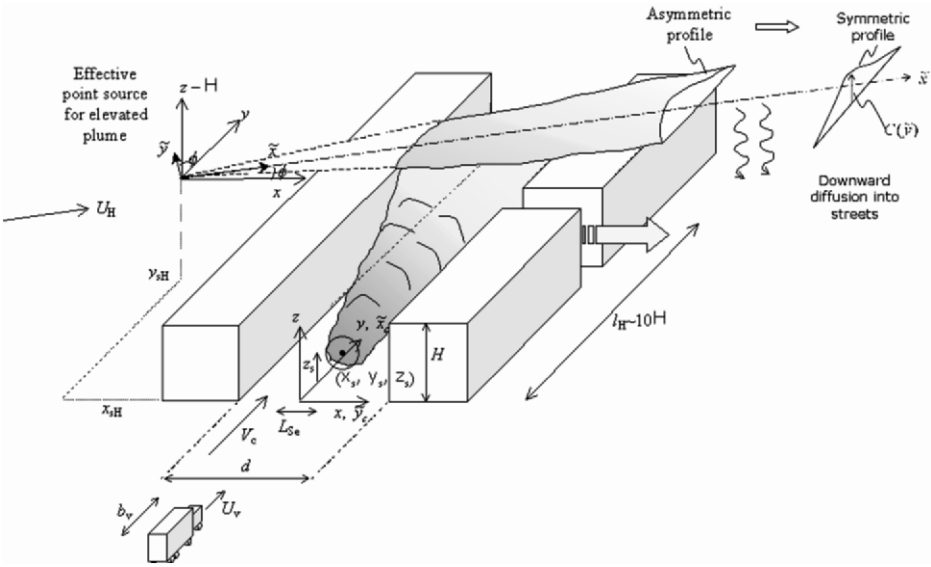

Figure 2.15: Accidental release at $(x_s,\ y_s,\ z_s)$ of initial scale L_{Se} in a canyon of width d and height H with crosswind, showing how on the discrete/obstacle scale the plume is advected along canyon a distance y_{sH} and then carried downwind in a cloud/plume that initially is skewed (along the street). But far downwind on the continuum scale the puff/plume reverts to standard Gaussian form. $(x_{sH},\ y_{sH})$ is the location of the virtual source for dispersion over the continuum scale. Note that vehicles with scale b_v and speed U_v also affect the turbulence.

where

$$\gamma_p \approx \frac{1}{\gamma_c}\frac{2.5}{V_c H d}.$$

Above the level of the buildings over the canyon, where $z = H$ and $-d/2 > \tilde{y}_c > d/2$,

$$G_{C,c} \approx G_{C,c}\,(x_c, z \cong H)$$

where

$$\gamma_z(1) = 0.4\sqrt{10\cos\Theta}. \tag{2.25}$$

(Note $\tilde{y}_c = x$ is here the horizontal coordinate perpendicular to the street axis.)

Just downwind of the canyon, the concentration is given by (2.71), (2.68) for cloud/plume sources (i.e. $x > d/2$).

(d) Further downwind in the fourth phase $\Delta t > t_3$ the puff is advected over the buildings and disperses as if it had been released from a virtual source position at (x_{sH}, γ_{sH}, H)) upwind of the street (see Figure 2.15) at time t_{sH}. Estimates of this position and release time are $x_{sH} \cong x_S - 25H$, $t_{sH} \cong t_S$, i.e.

$$G_{C,H} \cong \frac{2}{(2\pi)^{3/2}\sigma_{xH}\sigma_{yH}\sigma_{zH}} \exp\left(-\left(\tilde{X}_H^2 + \tilde{Y}_H^2 + \tilde{Z}_H^2\right)\right), \tag{2.26}$$

for a continuous source

$$G_{p,H} \cong \frac{G_{C,H}}{U_H} \sqrt{2\pi}\sigma_{x,H}. \tag{2.27}$$

(Note that the dimensions of G_c, G_p are different). Here the coordinates for the cloud/plume through the source are given by:

$$X_H = \frac{(\tilde{x} - U_H\,(t - t_S))}{2\tilde{\sigma}^2_{x_H}}, \tag{2.28}$$

where

$$(\tilde{x} \cong (x - x_{sH})\cos\theta + (y - y_{sH})\sin\theta \;\text{ and }\; \sigma^2_{x,H} \cong \sigma^2_{\tilde{x}}\,(\tilde{x}));$$

$$\tilde{Y}_H \cong \frac{\tilde{y}^2}{2\sigma^2_{y,H}}$$

where

$$\tilde{y} \cong (y - y_{s,H})\cos\theta - (x - x_{s,H})\sin\theta,$$

and

$$\tilde{Z}_H = \frac{(z - H)^2}{2\sigma^2_z}.$$

Note that the cloud/plume dimensions match each other at x = 0, $y = \tilde{x}_c \sim \ell_H$, where phase 3 becomes phase 4, so that

$$\begin{aligned}
\tilde{\sigma}_{x,H}\,(\tilde{x} = -x_{s,H}\sin\theta) &\sim \left[\tilde{\sigma}^2_x\,(\tilde{x} \sim l_H)\sin^2\theta + d^2\cos^2\theta\right]^{1/2}, \\
\tilde{\sigma}_{y,H}\left(\tilde{X} = -x_{s,H}\cos\theta\right) &\sim \left[\tilde{\sigma}^2_x\,(\tilde{x} \sim l_H)\cos^2\theta + d^2\sin^2\theta\right]^{1/2}.
\end{aligned} \tag{2.29}$$

From these formulae for the concentrations in the cloud in the canyon and above buildings, estimates can be derived for the concentration in side streets downwind. Where the side streets are quite short and extend over a distance of order $5 - 10H$, matter from the source is advected along the side street and concentration is approximately equal to that in the main street where the accident occurs (in the direction of the wind). But for $x \gtrsim 10H$, matter from the source mainly reaches side streets by being diffused downwards, so that the concentration is approximately equal to the value at the level $z = H$ (given by (2.26), (2.27)).

The main features of the model given here are found in the detailed computation of Soulhac, 2000 [591] of a source released in rectangular grids of streets. (He used a FCM using a numerical solution for the partial differential equation for constant eddy diffusion).

In particular he showed how in a street with an angled wind the effect of a ground level source leads to the concentration at the top level of the obstacles ($z = H$)

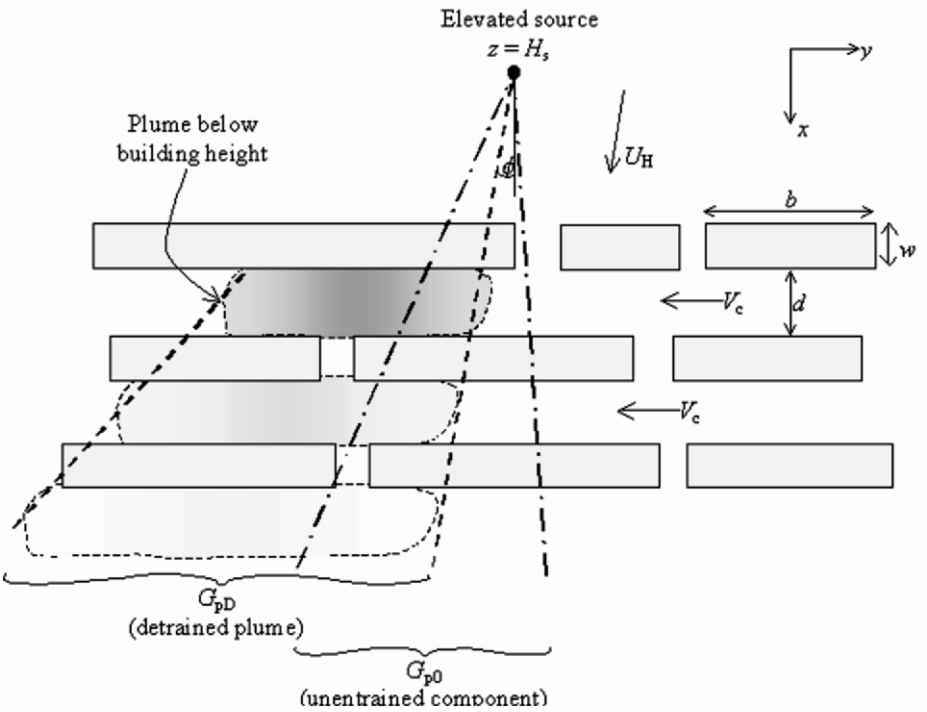

Figure 2.16: Distorted plume caused by 'canyon' winds and diffusion from an elevated source. Plume boundaries (defined a fixed ratio, e.g. 1/10 of centerline concentration at given value of x) in horizontal plane, showing components: unentrained (dash-dot line), detrained (dashed line) and plume in canyon below building height (shading).

increasing slowly and then decreasing quite rapidly, when it is advected away parallel to the wind in a wide plume (with width σ_y much greater than the width of the street). This was consistent with field data in Lyon (Soulhac, 2000 [591]).

If puffs are released above the obstacles ($z_s > H$), then, as shown in Figure 2.16, the puff is carried in a direction parallel to the wind above the buildings. But as it diffuses downwards, it may enter one or more large 'streets' (when $d \gtrsim H$, there will be a significant canyon wind along the streets). Then by a similar mechanism as for low level sources released within canyons the matter will be transported along each of these streets a distance of order $10H$ before diffusing again into the wind above the buildings. This can lead to a split plume structure above the buildings.

This situation approximately corresponds to the field experiment conducted at Dugway, Utah (Griffiths et al., 2002 [235]) with a source placed above one of the elongated cuboids which were aligned in 'streets' The wind direction was not quite perpendicular to the buildings ($\Theta \sim 150^o$); it was observed that the plume did not follow the wind direction but was systematically displaced parallel to the streets by a few obstacle lengths.

This situation needs to be analysed in more detail in future research. Note that the typical peak concentration in the canyon, denoted by $\hat{G}$, is of the order of the concentration at $z = H$ of the unentrained plume, i.e.

$$\hat{G}_C \cong G_{C,o}\,(x, y = y_s, z = H, \Delta t)\,, \tag{2.30}$$

$$\hat{G}_{p,V} \sim G_{p,o}\,(x, y = y_s, z = H) \tag{2.31}$$

where $G_{C,o}$, $G_{p,o}$ are given by (2.4), (2.8). Note that because of the flux downwards into the canyon over short distances (distances where $\hat{\sigma}_y < 10H$ or $\tilde{x} \lesssim 1\ km$), the obstacles do not block the downward diffusion of the plume, and therefore there is no 'reflection' term in (2.30), (2.31). But over a flat surface or over a long distance $\hat{x} > 1\ km$ from an elevated source over streets (when $\tilde{\sigma}_y > 10H$), the matter in the street diffuses up into the plume and then the reflection effect has to be included. This leads to an approximate doubling of the formula in (2.20).

Close packed buildings with no canyon effect ($b/d \gtrsim 1/3$) – topological splitting and lengthening mechanisms

In some flows the spacings between obstacles are within about two or three widths (i.e $b/d \gtrsim 1/3$), and the gaps between them do not form continuous 'canyons'. These situations occur in boiler tubes and engine blades, and in the atmosphere boundary layer in city centres and closely packed industrial plant (such as refineries). Then the streamlines move irregularly between the obstacles, converging and diverging as they do so, as sketched in Figure 2.6. The wake lengths l_w are reduced by converging flows if buildings are staggered or their displacing effects are reduced if the buildings are in lines. Theoretical calculations (e.g. Hunt, Puttock & Snyder, 1979 [281]), supported by numerical simulations (Davidson et al., 1995 [143]; Moulinec et al., 2003 [436]) show how as the streamlines diverge and 'split' near stagnation points, clouds of contaminant that move along or near the stagnation streamlines are advected either side of the building. This process of lateral spreading within the canyon can be so great that the plume width is largely determined by the geometry of the obstacle and the spacing between them, i.e.

$$\sigma_{y_C} \sim \frac{1}{2}\,(b/\,(d + w))\,x, \tag{2.32}$$

where this is larger than the width determined by turbulent diffusion, i.e.

$$\sigma_{y_C} \sim (\sigma_V/\langle U_c\rangle)\,x. \tag{2.33}$$

Also the streamwise longitudinal dispersion is amplified (Eames et al., 2003 [163]).

This shows that if $\sigma_v/U_c \cong 1/10$, then $b/d \gtrsim 1/4$ for the topological spreading to be greater than the turbulent diffusion. When $b/d \lesssim 1/3$ the spreading effect by the wakes (as described in Section 2.4.2 above) is an additive effect. But when $b/d \gtrsim 1/3$, the converging flow between the buildings tends to reduce the sizes of

the wakes by acceleration of the cross-diffusion and cancellation of vorticity from one side of the wake to the other (Hunt and Eames, 2002 [294]; Moulinec et al., 2003 [436]) – see Figure 2.14. This is a further reason why the topological dispersion is the dominant process for closely-packed buildings. The marked difference, by a factor of 2-3, between lateral dispersion of matter released among cuboid buildings placed in staggered, unaligned arrays compared to that of an isolated source over a flat surface was observed in the laboratory and field experiments repeated by Davidson et al., 1995 [143]. The photographic evidence showed quite clearly the splitting of the plume near the front stagnation point. Note that because the mean velocity is reduced it follows from mass conservation the mean concentration is not necessarily reduced by greater spreading.

These experiments showed that for closely-packed structures whose width is comparable to their height (i.e. $b \sim H$) when the source height z_S is less then the height of the obstacles ($z_s < H$) the concentration is well-mixed in the vertical direction both as a result of mean streamline displacements, and because of recirculating flows in the wakes and enhanced turbulence on the upwind faces of buildings (see Figures 2.6 and 2.11). In general (unlike the canyon case) the average wind speed in the 'canopy' below obstacle height, $\langle U_c \rangle$, is in the same direction as the wind over the buildings. The cloud is detrained into the upper flow above the obstacles for $z_s < H$ and $l_H \geq \tilde{x} > d$. Hence the concentration in a puff or cloud has two components, one below the canopy height ($G_{C,b}$) and the other where it is detrained above the canopy ($G_{C,H}$), i.e.

$$G_{C,c} \cong G_{C,b} \quad \text{for} \quad z < H, \quad G_c = G_{c,H} \quad \text{for} \quad z > H \tag{2.34}$$

(Figure 2.17), where

$$G_{C,b} \cong \alpha_C(t) \frac{\exp\left[-\left(\tilde{X}_c^2 + \tilde{Y}_c^2\right)\right]}{2\pi H \sigma_{xc} \sigma_{yc}}. \tag{2.35}$$

Here

$$\tilde{X}_c = (x - x_s - \langle U_{CH} \rangle t)$$

where the advected speed of the cloud is the weighted average of that in the canopy and in the flow above, i.e.

$$U_{CH} \cong \{\langle U_C \rangle + (\sigma_Z / H)\, U_H\} / 2.$$

The smaller detrained component in the faster moving upper cloud is given by

$$G_C \cong G_{C,b}\,(z = H)\, \frac{1}{\sqrt{2\pi}\sigma_{z,H}} \exp\left\{-\frac{(z - H)^2}{2\sigma_{z,H}^2}\right\}$$

where

$$\sigma_{z_H} \sim \left(\tilde{X} - \frac{\ell_H}{3}\right) \sigma_W / U_H.$$

(Hence the detrained component is only significant when $\tilde{x} \gtrsim \ell_H$.)

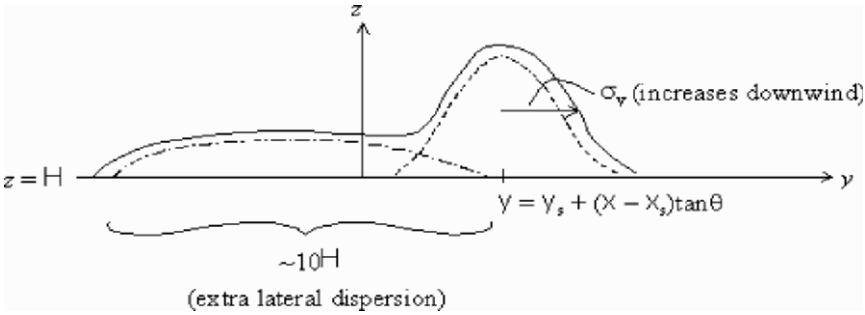

Figure 2.17: Distorted plume caused by 'canyon' winds and diffusion from an elevated source (see Figure 2.16). Plume boundary (for some level of concentration) in a vertical plane above the buildings.

For a plume, the formulae (2.34)–(2.35) are simplified to

$$G_{p,c} \cong \alpha_c \frac{\exp\left(-\tilde{Y}^2\right)}{\sqrt{2\pi} H \sigma_y \langle U_c \rangle}. \tag{2.36}$$

Above the canopy (formula not given) the front of the upper cloud is carried by the faster wind U_H, while the back of the cloud moves at the slower speed of the canopy cloud. Hence the downwind length of the upper cloud σ_{xH} is of order $(U_H - \langle U_c \rangle)\, t$ (Figure 2.18). Its concentration can be calculated explicitly in terms of the flux from the canopy cloud. The typical value in the upper cloud is

$$\hat{G}_{C,H} \sim \frac{\hat{G}_{C,c}}{\sigma_{x,H} \sigma_{z,c}}. \tag{2.37}$$

This is significantly less than in the canopy $\hat{G}_{C,c}$ because σ_{xH} is much greater than σ_{xc} when $\sigma_z \lesssim H$.

The formula for a steady plume is simpler, namely

$$G_{p,H} \cong \alpha_H \frac{\exp\left\{-\left(\tilde{Y}_H^2 + \tilde{Z}_H^2\right)\right\}}{\pi \sigma_{y,H} \sigma_{z,H} U_H} \tag{2.38}$$

where $\tilde{Y}_H^2 = (y - y_S)^2 / 2\sigma_{yH}^2$, $\tilde{Z}_H^2 = (z - H)^2 / 2\sigma_{zH}^2$, and the plume dimensions are calculated in terms of the turbulence above the canopy. Note that above the canopy the wind speed U_H is greater than U_c. To calculate the normalising coefficients α_c, α_H, since the plume flux is unity,

$$\int_{-\infty}^{\infty} \int_{0}^{H} \langle U_C \rangle G_{p,c} \, dy dz + \int_{-\infty}^{\infty} \int_{H}^{\infty} \langle U_H \rangle G_{p,H} \, dy dz = 1. \tag{2.39}$$

It follows that $\alpha_c + \alpha_H = 1$. Since the concentration profile is continuous at $z = H$,

$$\frac{\alpha_c}{H \langle U_C \rangle} = \frac{2\alpha_H}{\sqrt{2\pi} \sigma_{zH} U_H}. \tag{2.40}$$

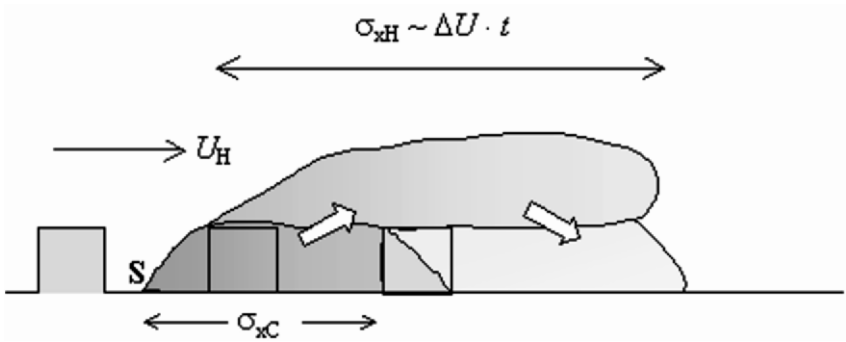

Figure 2.18: Outlines of cloud released in a 'porous' canopy with closely-packed cube-like buildings ($H/w \sim 1$): the case of discrete/obstacle scale where $\sigma_z \lesssim H$, $\sigma_x \lesssim 10H$ with a high concentration cloud in the canopy and a low concentration cloud above it.

Hence

$$\alpha_c = \frac{1}{1 + \frac{\sqrt{2\pi}}{2}\left(\frac{\sigma_{z,H}}{H}\right)\left(\frac{U_H}{\langle U_c\rangle}\right)}. \tag{2.41}$$

Further downwind on the continuum scale, as discussed in Section 2.4.2, the cloud has diffused vertically a significant distance so that its horizontal diffusion $\sigma_{zH} > H$. Its horizontal diffusion caused by the shear is such that the cloud streamwise dimensions σ_z above and below the canopy become approximately equal. Then the expressions (2.9)–(2.41) are no longer valid for the canopy cloud or plume.

A different pattern of diffusion occurs when obstacles are closely packed and tall (i.e. $b/d > 1/3$) and $H \gtrsim 2b$. Then, even though there is an amplified rate of vertical dispersion as a result of vertical swirling and turbulent motion around the obstacles (Figure 2.18), neither the average vertical concentration profiles nor the detrainment from their wakes are uniform over the depth of the average canopy layer H.

Given an approximate estimate for the rate of growth of σ_z in terms of the vertical turbulence $\sigma_W (\cong \langle U_c\rangle/10)$ and the spatial average of the variation of the mean vertical velocity $\sim 1/3\langle U\rangle b^2/d^2$ leads to (by considering detrainment from their wakes)

$$\sigma_z \sim x\left\{\frac{1}{10} + \frac{1}{3}(b/d)\right\}. \tag{2.42}$$

This shows that if $b/d \sim 1/3$, the puff/plume grows at about twice the rate as over a flat surface, so that the distance downwind of the source for the cloud to reach the tops of the obstacles would be about $10H$, Figure 2.19.

FAM: Dispersion in enclosed spaces

If dispersion occurs in an enclosed space such as a courtyard surrounded by moderate to tall cuboid obstacles in an urban area, where typically $H/d \geq 1/3$ (see Table 2.3, Figure 2.4). The competing dispersion mechanisms that chiefly have to be considered are

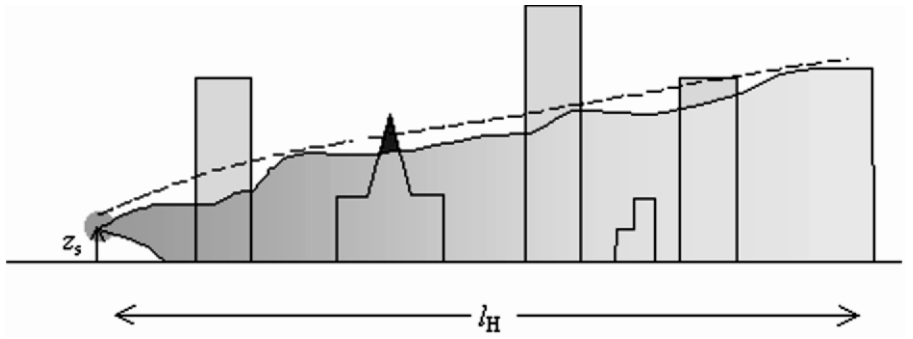

Figure 2.19: Vertical growth of a cloud/plume with outline (solid line) and average over the whole area (- - - dashed line). The source is in an urban area with high closely-packed buildings ($(H/w \gtrsim 2,\ b/d > 1/3)$ showing how the wakes disperse the plume up to height H_C over a horizontal distance l_H (as seen in field trials - see Section 2.4).

(a) mixed by the recirculating flow in the enclosed space with typical velocity $\langle U_c \rangle \sim 1/3 U_H$, and

(b) detrainment from the courtyard into the flow above the buildings with a typical detrainment velocity $u_* \sim U_H/10$. (This detrainment rate would be even smaller if the space is partially covered.)

These estimates imply that any material released is well-mixed in the courtyard before it is significantly dispersed over a time $T_{DC} \sim 10\, d/U_H$. Thus if the total quantity M_S of matter in the source is rapidly released (on a timescale $H/\langle U_c \rangle$ – say 10 seconds) the typical concentration in the enclosed space from the release of a cloud, is inversely proportional to the volume of the courtyard i.e.

$$\hat{C}_{C_E} \sim M_S / \left(d^2 H\right). \tag{2.43}$$

If the source material is continuously released at a rate Q_S on a time scale that is long compared with the typical dispersal time T_{DC}, then the concentration depends on the detrainment rate, so that

$$\hat{C}_{p_E} \sim \hat{C}_{C_E} \sim Q_s / \left(u \star d^2\right) \sim Q_s / U_H d^2 / 10. \tag{2.44}$$

These estimates of concentration levels may be significantly greater (by a factor of 3 or more) than would occur in a street canyon with a steady source (after the matter has spread across the street) where

$$\hat{C}_{p\dot{E}} \sim \frac{Q_s}{V_S d^2} \sim \frac{3 Q_s}{U_H d^2}. \tag{2.45}$$

Clearly more detailed calculations and experiments are needed to test these predictions because of their serious implications. If, as sometimes occurs, the courtyard has a sizeable opening (of width b) the high velocity winds V_0 passing through it contribute to the ventilation of the courtyard space (e.g. Lawson, 1980 [360]). But this will still be less than the detrainment at the level of the buildings (because $V_0 b^2 \sim U_H b^2 \leq u_* d^2$ since $b^2/d^2 \leq 1/10$). See Hall et al., 1999 [246].

2.4.2 Continuum (or neighbourhood) scale dispersion models

Length scales and processes

Once a cloud or continuous plume has been advected from the source within or above a canopy and passed over and around several obstacles, its dispersion is then determined by the average properties of the mean velocity field and turbulence within and above the 'canopy' of buildings. On the continuum scale the larger effects of the mesoscale meteorological and even chemical processes can be neglected: see Table 2.1. Hence the distances and plume dimensions lie within the following ranges defined by the length scales L_{CC} of the continuum region and depth h of the atmospheric boundary layer,

$$\begin{aligned} L_{CC} &\gtrsim X - X_S \gtrsim 3d, \\ L_{CC} &\gtrsim \sigma_x \gtrsim 3d, \\ H &> \sigma_z > H. \end{aligned} \tag{2.46}$$

Typically these regions might include 10^3 individual obstacles.

The key physical mechanisms of dispersion on this scale are the differences in mean wind speed and velocity $\langle U_c \rangle, U_H$ within and above the canopy. In 'porous' canopies, the mean wind speed normalised on U_H, i.e. $\langle U_c/U_H \rangle$ is greater than the turbulence intensities σ_v/U_H, $\sigma_w/U_H \sim 1/10$, so that the cloud/plume is advected by the main wind within as well as above the canopy. In addition the topological and wake dispersion processes (described in Section 2.4.2) are as significant as turbulent eddying for dispersing matter both horizontally and vertically within the canopy.

Note that the scales of the largest horizontal eddying motions of the turbulence within the canopy are of the scale of the obstacles (~d) and are much smaller than those in undisturbed boundary layers (which recent research show range up to 2 *km*, Högström et al., 2002 [275]).

This is why, although the turbulent intensities may be higher than in the undisturbed boundary layer, over the large distances of the neighbourhood scale the lateral dispersion σ_y above the buildings is likely to be comparable with the lateral dispersion in the canopy (see Davidson et al., 1995 [143]). Note that in the region downwind of an area with high buildings and a deep canopy, where the building heights decrease, matter dispersed in the canopy is advected as a wake cloud/plume, just as behind a single building. Its depth where it leaves the deep canopy is comparable with the obstacle height there.

If the obstacles are very closely-packed the ratio $\langle U_c \rangle / U_H$ may be less than σ_w/U_H. Then the canopy is effectively non-porous, so that the mean streamlines and the cloud/plume pass above the buildings and matter reaches the street and spaces downwind of the source by entrainment and downward diffusion into the street. Because there are mean flows along the street at an angle to the plume, there will be some extra lateral diffusion as a result of this process, see Figure 2.21 (eg. Soulhac [591]).

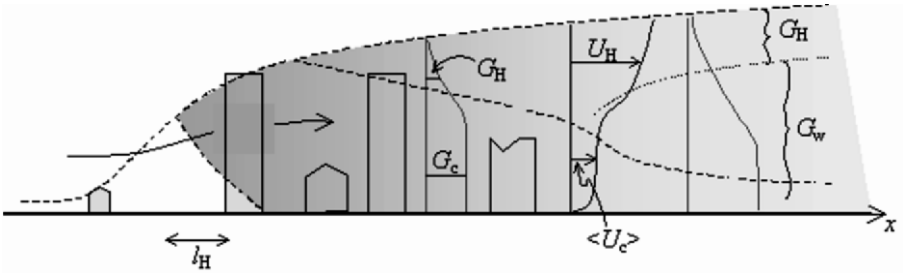

Figure 2.20: Porous canopy. Net air flow through the canopy with average velocity $\langle U_c \rangle$ (e.g. 0.3-0.5 U_H). Plume has double structure within and above canopy structure, and also downwind.

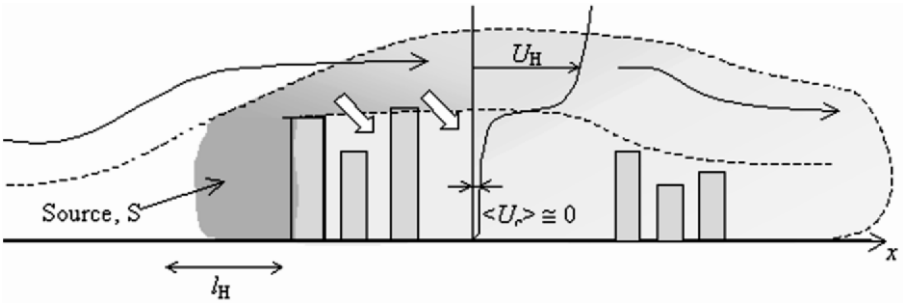

Figure 2.21: Non-porous canopy ($\langle U_c \rangle / U_H < \sigma_w / U_H$), vertical cross-section: Plume disperses from a source within the canopy into the airflow over the canopy and then is dispersed downwards. Note some dispersion upwind of source S. (Here the source material is released in the form of a cloud and the cloud has travelled a few building heights.)

Review of FCM and FAM Models

The continuum scale is an intermediate range in terms of flow modelling, in that some methods are based on detailed or 'discrete' modelling to predict average properties of dispersion, while others are based on 'continuum' modelling approaches using average/statistical descriptions of the aggregated properties of the canopy and the flow (see Table 2.7).

Fully Computational Models

In methods based on the discrete modelling approach, flow fields are calculated for thousands of obstacles and thence the dispersion from arbitrary sources. Basic (mixing length) models for turbulent shear stresses and eddy diffusion fluxes with coarse resolution meshes are likely to provide reasonable estimates for the dispersion within and above the canopy from sources within the canopy (Hall and Cowan, 1998 [245]; Kim and Boysan, 1999 [334]) because the dispersion process above the canopy is largely vertical – which is adequately predicted by such models. Such a modelling approach may take tens of hours on workstations. Faster computational modelling approaches for dispersion are now being explored. Since, as explained in Section 2.4.2, the dispersion is dominated by wakes and the topology of the streamlines passing around the

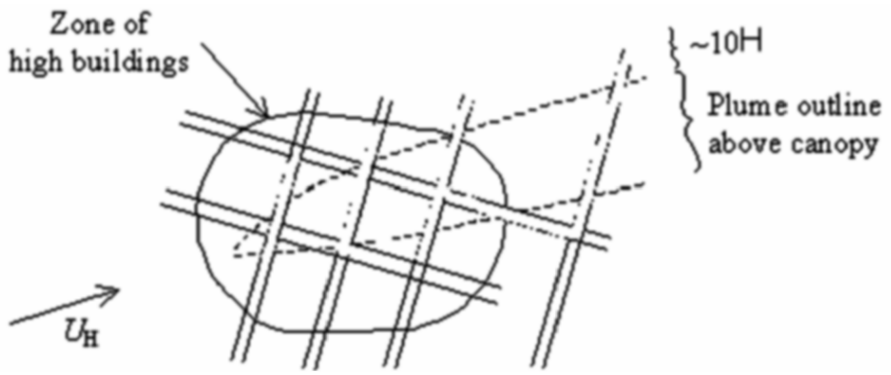

Figure 2.22: Non-porous canopy ($\langle U_c \rangle / U_H < \sigma_w / U_H$): Plan view showing matter being carried along streets in the downwind directions, outside the edge of the upper plume ($z > H_c$).

obstacles, it follows that it is the broad size and overall dimensions of a obstacle that determine divergence/convergence and splitting of streamlines. Also the detailed structure of turbulent eddying has a relatively small influence (if the buildings are closely packed). Therefore computational models can be used with approximate equations, approximate boundary conditions (for the buildings) and quite coarse mesh sizes (e.g. 1/10 the size of the building). Of course some constraints are absolutely necessary such as the finite energy of the flow, mass continuity, zero flux through buildings, etc. One way to reduce these constraints for the dispersed matter is to track Lagrangian particles through the flow, allowing for a turbulent component (Turfus, 1988 [622]). This approach enables small computers to obtain results in a few hours or less.

If such an approach becomes widespread it will be even more necessary to calibrate and understand its merits and drawbacks by using detailed and accurate computational modelling techniques that have been thoroughly validated, such as Large Eddy Simulation methods (Rodi, 1997 [541]), stochastic simulation methods (Hort et al., 2002 [276]; Turfus, 1988 [622]), and time-dependent Reynolds-averaged models.

The more usual approach to speeding up FCM methods for 'multi-body' flow / dispersion calculations such as this is to use the continuum approach. This requires some estimates of turbulence parameters such as mixing lengths or eddy diffusivities for the canopy (on the neighbourhood scale), but these characteristics cannot be deduced from turbulence closure models, although they may be estimated from detailed calculations of flow/dispersion around a few 'typical' obstacles - not a straightforward or accurate process (see Moulinec et al., 2003 [436]).

Since the way that aligned obstacles can deviate the wind direction leads in canyons to the dominant process for dispersion in closely-packed city centres, in that case, as Soulhac, 2000 [591] demonstrated, FCM can be used for dispersion from sources in urban areas by computing the dispersion along the major streets and in the open flow above the buildings. In urban areas this would be similar to the widely-adopted method of modelling traffic-generated pollution by calculating the concentrations in a few key street canyons with the rest of the urban area being regarded as a rough surface. (e.g. Carruthers et al., 2000 [107]).

In order to have even faster models to estimate dispersion for many possible source scenarios, source positions and meteorological conditions, it is necessary to have even faster models even if they are more approximate. These are considered in Section 2.4.2.

Note that provided the models are incorporated into computational systems, whether they are 'fully computational' or 'fast approximate', either may be suitable for the inverse calculation problem of estimating (by successive iterations) the location and nature of the source from measurements (or inferred measurements) of the concentration distribution. However this requires special programming methods to optimise the search algorithm.

FAM Models for Discrete/Obstacle and Continuum Scales

For dispersion from sources in suburban areas with detached buildings and where street canyon effects can be neglected, the multiple cloud splitting models described in Section 2.4.2 have been developed to apply to large numbers of buildings. In order to simplify and speed up the computation time, groups of overlapping split plumes are merged and formed into new, larger plumes. This is a standard computational procedure of 'rediscretisation' that has been used in puff models of diffusion (e.g. in RIMPUFF). This technique enables the FAM model to be applied on the continuum scale (Hall et al., 1996 [243]).

Despite the fact that the model's assumptions formally preclude its application to closely-packed obstacles, a comparison can be made with plumes even in these parts of urban areas because, as explained in Section 2.4.2, the cloud/plume on the neighbourhood scale is broadly Gaussian and similar to that over level ground. But there are significant differences between actual and Gaussian plumes, e.g. in how the plume penetrates into canyons between obstacles and is transported along them over a finite distance (as Soulhac's simulations showed). These differences could only be introduced into the multiple cloud splitting model by considerably distorting the basic models. Nevertheless, comparisons with field data have shown (Brook et al., 2002 [83]) that FAM models can describe many of the observed plume features. Perhaps following the analysis made here about the canyon processes and other aspects of dispersion in canyons and in the presence of close-packed buildings, it will be possible to look at this comparison again in more detail to generalise their model further.

The alternative approach to computing the concentration distribution over the continuum/neighbourhood scale is to consider that the canopy is a porous space with a lower wind speed $\langle U_c \rangle$ and different turbulence structure to that in the boundary layer flow above the obstacles. We differentiate between the situation where $\langle U_c \rangle / U_H$ is large enough for the canopy to be considered porous. Then over the neighbourhood scale for a short-period accidental release the resulting cloud diffuses above the canopy and travels over it at a speed U_H. In most cases where the canopy is non-porous, the cloud/plume dispersion over the building/street scale takes place in a canyon or an enclosed space/courtyard.

The dimension $\tilde{\sigma}_x$ in the direction of the mean wind on the continuum scale (where $\Delta t = \Delta t_c$) can be expressed in terms of the length $\sigma_{xb} \sim \sigma_{xH}$ it develops below the canopy height when $\Delta t \sim \Delta t_H \sim l_H / U_H$ and its subsequent growth (when $\Delta t > \Delta t_H$) in the upper boundary layer (e.g. Chatwin, 1968 [115]).

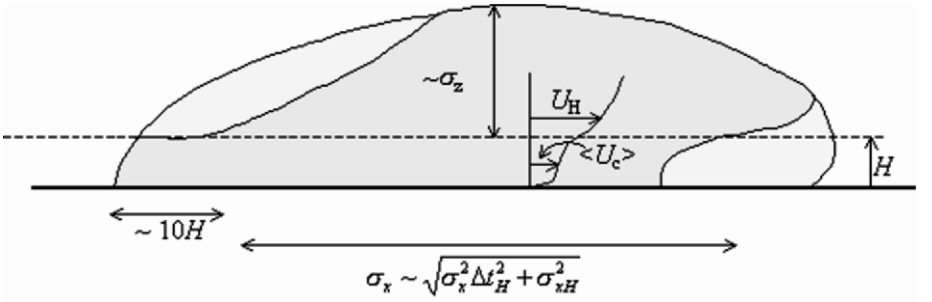

Figure 2.23: Outlines of cloud released in a 'porous' canopy with closely-packed cube-like buildings ($H/w \sim 1$): on the continuum scale, where $H \lesssim \sigma_z h$, $H \lesssim \sigma_x < L_{Cc}$, dispersion above the canopy determines the concentration within it. (Compare with Fig. 2.18).

When $\Delta t > \Delta t_H \sim 10H/U_H$ or $\Delta t_c = \Delta t - \Delta t_H > 0$,

$$\tilde{\sigma}_x^2 \sim \left(\sigma_u^2 \Delta t_c^2 + \sigma_{X_H}^2\right).$$

Porous canopy.
Within a porous canopy (e.g. as described in Sections 2.3.2 and 2.3.4) the puff/cloud travels at a lower speed $\langle U_c \rangle$, see Figure 2.20. Through vertical diffusion, this distorts the front and rear of the cloud (see Figure 2.23) by a finite length $\Delta\sigma_x \sim H^2(U_H - < Uc >)/K_z \sim 10H$. This is of the same order as σ_{xb}. Within a canopy as the flow travels along typical street canyons (even if the buildings are detached – see Section 2.3.3), the obstacles widen the cloud/plume's horizontal dimension σ_y by a fixed distance ($\sim 10H$) along the streets. As the simulations of Soulhac, 2000 [591] demonstrate, over most of the neighbourhood region the plume width $\tilde{\sigma}_y (\sim 0.1\tilde{x} > 0.1 - -1.0\ km)$ is of the same order as this extra sideways displacement (if $H \sim 30\ m$) – see Figure 2.22.

For a steady source, the structure of the resulting plume in the continuum region is primarily determined by its form in the boundary layer above the obstacles as given by (2.38), where $\alpha_H \cong 1$. On the continuum scale the value of $\langle U_c \rangle$ is only significant in determining the virtual origin and $\Delta\sigma_x$. The lateral plume dimensions $\tilde{\sigma}_y$ in and above the canopy are approximately the same as that for a cloud above a rough surface, as discussed above.

We conclude that over the continuum scale the determining parameters are the wind speed U_H and turbulence $\sigma_u, \sigma_v, \sigma_w$ above the canopy and the initial parameters of the cloud/plume when it reaches the top of the canopy or, equivalently, the virtual source at the level of the canopy. Using suitable fast approximate models for the flow field over urban areas (e.g. RIMPUFF, FLOWSTAR), the variation of the mean velocity and turbulence above the canopy can be calculated. The FLOWSTAR code (Carruthers et al., 1988 [105]) has been extended to predict how $\langle U_c \rangle$ varies within the canopy. Dispersion downwind of the canopy can also be estimated using cloud/plume profiles, denoted by $G_{C,W}, G_{A,W}$ which are shown in Figures 2.20 and 2.22.

Non-porous canopy.
When the neighbourhood area is 'non-porous' and consists of closely packed buildings, so that the average canopy velocity is small compared to the turbulent velocity (i.e. $\langle U_c \rangle / U_H < \sigma_w / U_H \sim 1/10$), the mean air flow and transport of the source material on the neighbourhood scale is primarily above the obstacles (Figure 2.20). If the source is below the obstacle height, it first of all disperses upwards (on the obstacle scale) to the tops of the obstacles. Then the concentration of a cloud or plume is calculated as if it were moving over a rough solid surface of height H. The effective source size is d, the distance between the obstacles.

Downwind of a canopy the cloud/plume structure resembles that in the wake of a wide obstacle of height H. Note that the concentration below the canopy is equal to the concentration at the top of the obstacles.

The flow field and dispersion over such a 'non-porous' region is similar to that over a solid obstacle with low slope with roughness change (since the effective surface roughness length z_0 over the central urban area is greater than that upwind). FAM methods are available for point, line and area sources (e.g. ADMS, AERMOD).

2.4.3 Dispersion modelling over the outer-scale

Over a distance of order $L_0 \sim 10\ km$ and travel time L_0/U from the source the turbulent eddies diffuse the source material vertically through the boundary layer up to a height h. However, on this distance and over this time scale the wind speed and temperature profile may change significantly as a result of changes in surface elevation, temperature and roughness and diurnal change. For some kinds of accidental release (e.g. soluble or reactive gases or small particles) there can be substantial changes in the flux of the original material in the cloud/plume, and new material may be created.

The FCM approach is now widely used for engineering purposes and for regulatory predictions of airborne pollutants over large urban areas. Meteorological models provide data for the mean wind field and turbulence that are then used to calculate dispersion. Using at least 10^7 grid boxes (which takes several hours of computation) satisfactory predictions have been made of the broad features of dispersion from localised sources of pollution over mesoscale distances and time scales in urban areas with complex terrain (e.g. Phoenix, El Paso, Salt Lake City in the US). For example, these have shown how pollutants are advected up and down slopes, out of and into urban areas, as the heating of the slopes varies diurnally (Pardyjak et al., 2003 [480]). Some mesoscale codes use simple turbulence models (e.g. mixing length) or even standard boundary layer profiles (as in the UK Met. Office mesoscale code (Cullen, 1993 [138])), while others such as the HOTMAC code used at Los Alamos (Mellor & Yamada, 1974 [406]; Brown and Williams, 1998 [87]) use multi-equation turbulence and eddy diffusion models. Generally it is found that having a small enough grid size in the computation is more essential than the complexity of the turbulence model in determining the accuracy of the code. Only when Δ_x is of order 1 *km* (by comparison with standard codes with 12 *km*) are flow fields in complex terrain reliable enough to compute dispersion on the meso-scale of 10 *km*. But currently this method is only available at the research level (e.g. Capon, 2002 [99]).

For dispersion in flows with significant variation in direction and speed at different heights and different times, the only reliable modelling method is to track individual fluid particles or track many clouds of particles from the source. The former method is now used for regional and synoptic scale dispersion prediction from localised sources, such as nuclear accidents and volcanoes, e.g. Maryon and Buckland, 1995 [396]. Assumptions have to be made about how atmospheric turbulence on scales less than $\sim 3\Delta x$ diffuses particles as they are advected by the 'resolved' flow field on scale Δx. This method requires large computer resources and then can be computed in minutes. For studying critical events in UK urban areas this method should be considered.

A faster and less accurate FCM approach is also used for large scale diffusion, the movement and distorting of larger clouds are computed, with simplifying assumptions about the process. Many field experiments have validated this approach, especially over rather flat terrain in Scandanavia (which includes their urban areas) using the RIMPUFF model. This model includes an algorithm for 're-discretising' the clouds after they have been greatly distorted, mainly through wind shear. They have not been so well-tested in very complex terrain with strong stratification. Thus, in principle, it is well-adapted to mesh with the UDM model for building/street and neighbourhood scales. This kind of Lagrangian puff model is fast enough in practice for emergency response.

In terms of FAM, the most basic method for estimating dispersion on the mesoscale (where σ_z becomes equal to or greater than h) is to assume that the concentration profile is approximately constant below the top of the boundary layer, so that for a continuous source Q_s, and for steady meteorological conditions,

$$C(x,y) = \frac{Q_S}{U_H h \sigma_y \sqrt{2\pi}} \exp\left(-\tilde{Y}^2\right). \tag{2.47}$$

This 'box-model' approach has been used for comparison with urban dispersion experiments by Middleton, 1998 [431]. This has proved satisfactory on neighbourhood scale ($\gtrsim 1$ *km* from source).

To model the transition of the plume between the neighbourhood and mesoscale regions, it is usual (as with other Gaussian plume models, e.g. Pasquill and Smith, 1983 [484]; Hunt et al., 1988 [286, 287]) to estimate approximately the plume profile by one (or more) reflection terms when $\sigma_z h/2$, i.e.

$$G_{p,H} = G_{p,Ho} + G_{p,Hr}$$

where $G_{p,H0}$ is given by (2.38) with $\alpha_H = 1$, and

$$G_{p,HR} = G_{p,Ho} \exp\left[(z-h)^2 - (z-(2h-H))^2\right]/2\sigma_z^2.$$

With such a model it is also necessary to estimate the effects on the cloud/plume dimensions of undulating terrain and any significant changes in stratification over the urban terrain. When, as is usual, the depth of the mixed layer, h, and U_H change over the diurnal period these expressions can be extended by using a FAM for the flow field and turbulence (as discussed in Section 2.2) and thence correcting the values of σ_x, σ_y, $\sigma_z(\tilde{x})$. Also, the time dependence should be considered especially when considering

clouds of contaminant being released. If the wind reverses (i.e. changes direction by 180^o) the concentration can increase with time, over several days (as occurs with sea/land breezes in Los Angeles). On the other hand, the effects of mountains can also lead to dispersion through complex upslope/downslope winds (Pardyjak et al., 2003 [480]). The long-term effect (over several days) of an accidental release can be quite sensitive to the regularity of the cycle of diurnal meteorological conditions, or to the existence of stagnant conditions when $U_H << \sigma_u$ (e.g. Hunt, 1996 [290]).

2.5 Conclusion

In conclusion, in order to use a FAM that calculates $C(\mathbf{x}, \mathbf{t})$ over the three sub-regions of a large urban area, it is necessary to decide what level of output is required in terms of accuracy and computational time and

(a) in which type of urban area the source is located (if it lies within the canopy) by reference to Table 2.3;

(b) which type of flow field model is appropriate for the three sub-regions (also considering the relevant physical factors to include, using Table 2.2 and Section 2.2);

(c) appropriate dispersion model(s) for the sub-regions considering the factors in Table 2.7 and the review in Section 2.4. Some of these models are already available as standard software systems, especially for the neighbourhood and meso-urban scale. (These can also be used as 'screening' models to provide quick estimates, Hanna et al., 2002 [255].) But others, such as those for dispersion in inner city 'canyons', are still in the form of formulae that need to be integrated into dispersion software systems and tested against experiments and detailed simulations (see also chapter 9).

This review has mainly focused on models for mean concentrations. However, fluctuations need to be estimated in order to assess all the risks associated with accidental releases. There is some evidence from the experiments, Davidson et al., 1995 [143], that the intensity of fluctuations is lower in clouds/plumes released among buildings, and are also qualitatively different. There is much less chance of a large scale of wind gust reducing the concentration to zero, so that the probability density function is closer to a log-normal distribution than to a cut-off Gaussian (Mylne, 1992 [440]).

Acknowledgements

We are grateful to many colleagues for their collaboration over many years whose work we have reviewed here. Dr. Roger Kingdon and colleagues at DSTL in the UK and participants at the Kiev NATO Advanced Study Institute [300] who provided helpful input during the compilation of this review. We are also grateful to Dr. David Hall of Envirobods for providing many useful comments on a draft of this report. This study was funded by the UK Atmospheric Dispersion Modelling Liaison Committee. The views expressed in this report are those of the authors, and do not necessarily represent the views of ADMLC or of any of the organizations represented on it.

2.6 Appendix A: dispersion from a steady source between elongated obstacles with cross wind (e.g. street canyon)

The background to this analysis is given in Section 2.4.1. It focuses on the third stage (iii) when the plume from a source at $y_s = 0$, $z_s < H$ moving down the canyon with velocity V_c is well-mixed across the canyon and diffuses up into the cross flow with velocity U_H at an angle ϕ to the x-axis. As shown below, this occurs when

$$y \sim l_H \sim V_c H^2 / K_c.$$

The canyon is assumed to be limited by impervious buildings on each side.

For this steady problem, use eddy diffusion model with constant diffusivities K_c, K_H in the canyon and the upper flow, respectively. The equations are:

In the canyon:

$$V_c \frac{\partial C}{\partial y} = K_c \left(\frac{\partial^2 C}{\partial z^2} + \frac{\partial^2 C}{\partial x^2} \right) \cong K_c \frac{\partial^2 C}{\partial z^2}, \qquad (z < H). \tag{2.48}$$

Above the canyon:

$$U_H \cos\phi \frac{\partial C}{\partial x} + U_H \sin\phi \frac{\partial C}{\partial y} \cong K_H \nabla^2 C, \qquad (z > H) \tag{2.49}$$

which is transformed in terms of coordinates parallel and perpendicular to the upper wind, $(\tilde{x}, \tilde{y}, z)$, as

$$U_H \frac{\partial C}{\partial \tilde{x}} \cong K_c \left(\frac{\partial^2 C}{\partial z^2} + \frac{\partial^2 C}{\partial \tilde{y}^2} \right), \qquad (z > H). \tag{2.50}$$

Let $q_H(y)$ be the average flux of contaminant from the canyon into the upper flow. Total source strength is Q_S in the canyon. Following Turfus, 1986 [621], the solution when $\sqrt{K_c y / V_c} \gtrsim H$ is

$$C = \hat{C} e^{-\lambda y / H} \cos\left(\frac{\mu z}{H} \right). \tag{2.51}$$

Downwind of the source this is the leading order term in an expansion of the form $C = \sum \hat{C}_n e^{-\lambda_n y / H} \cos(\mu_n z / H)$ that matches with the solution in Stage (ii) when the plume depth σ_z is much less than the canyon height H so that $K_c \partial C / \partial z = 0$ at $z = 0$. Substituting (2.51) into (2.48) implies

$$-V_c \lambda / H = -K_c \mu^2 / H^2$$

so that

$$\mu = \sqrt{\frac{V_c \lambda H}{K_c}}. \tag{2.52}$$

Hence the vertical flux at the top of the canyon (per unit area per unit time) is

$$q_H(y) = K_c \hat{C} e^{-\lambda y/H} (\sin\mu)/H. \tag{2.53}$$

Note

$$d \cdot \int_0^\infty \overline{q}_H(y) dy = Q_s.$$

Hence

$$\hat{C} = \frac{\lambda Q_s}{d K_c \sin\mu}. \tag{2.54}$$

Now match with the solution in $z > H$ to calculate λ. Consider the local solution above the canyon: then

$$\text{Canyon flux into the upper flow} = \text{downwind flux at} \quad x = d/2,$$

i.e.

$$d \cdot \overline{q}_H \cong C(z = H) \times U_H \times \sigma_z \quad (x = d/2) \tag{2.55}$$

where

$$\sigma_z(d) \sim \sqrt{\frac{d K_H}{U_H \cos\phi}}.$$

Thence from (2.53), (2.54) and (2.6),

$$\sin\mu \cdot d \cdot K_c/H = \cos\phi \cos\mu \cdot U_H \sqrt{d \cdot K_H/U_H \cos\phi}.$$

Therefore μ is determined by the eigenvalue problem

$$\tan\mu = \left[\frac{d \cdot U_H \cos\phi}{K_c}\right]^{1/2} \sqrt{\frac{K_H}{K_c}} \cdot \left(\frac{H}{d}\right).$$

For typical values

$$K_c(x) \sim 0.4\sigma_w H \sim 0.4 K_c H/10 \sim 0.4 U_H H/20,$$

$$K_H(d) \sim \frac{U_H d}{10}$$

and so

$$\tan\mu \sim (10\cos\phi)^{1/2}/0.4. \tag{2.56}$$

Note that μ is approximately independent of the narrowness of the street, i.e. H/d: from (2.56), when $\phi = 0$, $\mu \cong 1.5$ and when $\phi = \pi/4$, $\mu \cong 1.4$. Hence l_H does not vary significantly with $\phi(\leq \pi/3)$, and is only weakly sensitive when $\phi \gtrsim \pi/3$.

Hence for most orientations of the wind from (2.52)

$$\lambda \cong \frac{K_c\left(\mu^2\right)}{V_c H} \sim \frac{2 \times 0.4}{10} \sim 0.1. \tag{2.57}$$

Hence in the y-direction along the canyon,

$$C \sim \frac{Q_s}{d \cdot K_c} e^{-y/(10H)} \cos(\mu z/H), \tag{2.58}$$

showing that the concentration decays exponentially along the canyon over a scale $l_H \sim 10H$. This is consistent with the computation and experiments of Soulhac, 2000 [591].

Note that the vertical flux

$$\overline{q}_H(y) \cong \frac{Q_s}{dH} e^{-y/(10H)} \tag{2.59}$$

when $y > l_H$ since $\sin\mu \cong 1$. Also,

$$C(y = H) \cong \frac{Q_s}{d \cdot K_c} e^{-y/(10H)} (0.4/\sqrt{10\cos\phi}) \tag{2.60}$$

when $\tan\mu >> 1$.

The approximate solution for the mean concentration in the upper flow ($z > H$), in the upper coordinate system, is

$$C(\tilde{x}_H, \tilde{y}_H, z_H) = \int_{-\infty}^{\infty} \frac{d \cdot q_H \left(\tilde{y}_H'\right)^*}{2\pi U_H (K_H/U_H)\, \tilde{x}^* \left(\tilde{y}_H'\right)} \times \tag{2.61}$$

$$\times \exp\left\{ -\left[\frac{z_H^2}{4(K_H/U_H)\tilde{x}^* \left(\tilde{y}_H'\right)} + \frac{\left(\tilde{y}_H - \tilde{y}_H'\right)^2}{4(K_H/U_H)\tilde{x}^* \left(\tilde{y}_H'\right)} \right] \right\} d\tilde{y}'$$

where $\tilde{x}^*$ is the distance from the upwind side of the canyon, at a displacement $\tilde{y}$, $\tilde{x}^* = \tilde{x}_H - \tilde{y}_H \tan\phi$, U_H is the speed of the upper flow and $\tilde{x}_H$ is the distance parallel to the upper flow from the point $(-d/2, l_H)$. Note that because the buildings either side are impervious, all the plume material lies above $z = H$. Note that in (2.61), in order to simplify the integral,

$$q_H^* \cong \frac{Q_s}{d \cdot l_H \cos\phi} \exp\{-\tilde{y}/(l_H \cos\phi)\} \quad \text{for} \quad \tilde{y} > 0 \gtrsim \frac{H^2 V_c}{K_c}. \tag{2.62}$$

However, for $\tilde{y} < 0$ the plume has not significantly diffused vertically into the upper flow. Hence approximately

$$\overline{q}_H^*(\tilde{y}) \cong 0 \qquad \text{for} \quad \tilde{y} < 0. \tag{2.63}$$

The solution (2.61) shows how the concentration in the upper flow ($z > H$) is effectively dispersing from a source Q_S at $\left(-x_{Hs}^*, y_{Hs}^*\right)$ – see Figure 2.24. This location is estimated by assuming in the upper flow the plume width $\tilde{\sigma}_y \sim \tilde{x}/10$. Since the plume width at the top of the canyon (normal to the mean wind) is $l_H/\cos\phi$, it follows that the distance from the virtual source $S_{(v)}$ to the top of the canyon ($\tilde{x}_H = 0$, $\tilde{y}_H = 0$) is $\tilde{x} = \tilde{x}_{Hc} \sim l_H/\cos\phi$. Since $\tilde{\sigma}_y \sim l_H \cos\phi \sim 10H\cos\phi$ at this point,

$$\tilde{x}_{Hc} \sim 10\tilde{\sigma}_y \sim 100H\cos\phi. \tag{2.64}$$

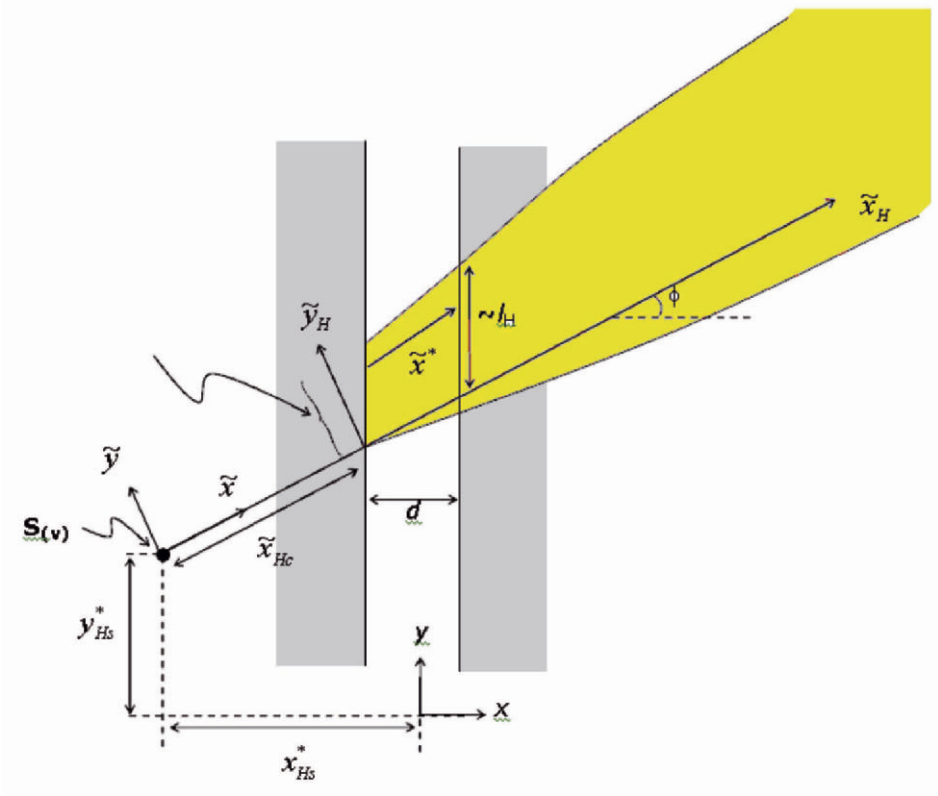

Figure 2.24: Upper plume width that is proportional to $l_H \cos\phi$.

Therefore

$$x_{sH} = -\tilde{x}_{Hc} \cos\phi \cong 100H\cos^2\phi, \tag{2.65}$$

$$y_{sH} = I_H - \tilde{x}_{Hc} \sin\phi \cong 10H(1 - 5\sin 2\phi). \tag{2.66}$$

Therefore, from (2.61), the concentration in the upper flow just downwind of the canyon has the form of a line plume (with variable strength along the line $x = -d/2$),

$$C \cong \frac{\overline{q}^*(\tilde{y})}{U_H \sqrt{\pi\,(K_H/U_H)\,\tilde{x}^*}} \exp\left\{\frac{-z_H^2}{H\,(K_H/U_H)\,\tilde{x}^*}\right\} \tag{2.67}$$

for $\tilde{x}^* > d/\cos\phi$, $\tilde{y} > 0$, $z > H$. This profile has an asymmetric form relative to the centreline.

Far downwind, Stage (iv) of the plume's development, the profile is determined by dispersion from the virtual source, i.e. for $\tilde{x}^* >> l_H \sim 10H$, $z > 0$

$$C \sim \frac{Q_S}{U_H \pi \tilde{\sigma}_y \sigma_z} \exp\left\{-\frac{\tilde{y}^2}{2\tilde{\sigma}_y^2} + \frac{z_H^2}{2\sigma_z^2}\right\} \tag{2.68}$$

where $\tilde{\sigma}_y, \sigma_z$ are functions of the distance from the virtual source. (For uniform diffusivity, $\sigma_y^2 = 2K_H/U_H x$). If the buildings and side streets are porous, this solution is valid below the top of the buildings.

An unsteady source with volume M_s released at time t_s in the canyon leads to the formation of a cloud with length $\tilde{\sigma}_x = \sigma_y \cong \sqrt{2\tilde{K}_{xc}\Delta t} \cong \sqrt{2\left(\tilde{K}_{xc}/U_H\right)y}$, where $\Delta t = t - t_S$, travelling with speed V_S. (Here $\tilde{K}_{xc}$ is the longitudinal diffusivity in the canyon which is typically 2 or 3 times greater than K_c as a result of shear dispersion, e.g. Pasquill and Smith, 1983 [484]). Consequently, the length of the cloud as it reaches the top of the canyon ($\tilde{\sigma}_x\left(\tilde{x} \sim l_H\right)$) is very much greater than the width d of the canyon, i.e.

$$\tilde{\sigma}_x\left(\tilde{x} \sim l_H\right) \sim l_H \sim 10H >> d \ .$$

Therefore the profile within the cloud, $C_{c,c}$ within and above the canyon is similar to that within the plume, $C_{p,c}$, given by (2.58), i.e. for $z > H$,

$$C_{c,c} = C_{p,c} = \frac{1}{\sqrt{2\pi}\sigma_x} \exp\left\{-\frac{(y - V_s\Delta t)^2}{2\tilde{\sigma}_x^2}\right\} \cdot \left(\frac{V_c M_S}{Q_S}\right). \tag{2.69}$$

Now the flux $q_{H,c}$ into the upper flow per unit area per unit time varies with y and time:

$$q_{H,c}(y,t) = \frac{M_S U_H}{Q_S} \frac{1}{\sqrt{2\pi}\sigma_x} \exp\left\{-\frac{(y - V_s\Delta t)^2}{2\tilde{\sigma}_x^2}\right\}. \tag{2.70}$$

The effective virtual source is at the same location as for the plume. The cloud concentration in relation to the plume concentration (2.67) is

$$C_{c,H} = C_{p,c} \times q_{Hc}(y,t)/q_H(y). \tag{2.71}$$

Far downwind,

$$C(\tilde{x},\tilde{y},z') \sim \frac{2M}{(2\pi)^{3/2}\tilde{\sigma}_x\tilde{\sigma}_y\sigma_z} \exp\left\{-\left[\frac{(\tilde{x} - U_H\Delta t)^2}{2\tilde{\sigma}_x^2} + \frac{\tilde{y}^2}{2\tilde{\sigma}_y^2} + \frac{z^2}{2\sigma_z^2}\right]\right\}. \tag{2.72}$$

2.7 Appendix B: notation and abbreviations

b	Obstacle breadth;
b_v	Size of vehicles;
C	Mean (ensemble average) concentration at a point;
$\langle C \rangle$	C averaged over a given volume and time scale;
$\overline{C_{Dx}}$	Average drag coefficient of obstacles in canopy;
d	Gap or separation distance between obstacles;
d'	Standard deviation of separation distance;
f	Coriolis frequency;
F_Θ	Surface heat flux;
g	Gravitational acceleration;
G	Gaussian concentration profiles - subscripts denote particular (e.g. multiple Gaussian) forms to allow for reflection, wakes, within and above canopy, etc.);
h	Boundary layer height;
H	Obstacle height;
H_c	Canopy height;
H_c'	Standard deviation of canopy height, H_c;
$\kappa - \varepsilon$	Kinetic energy and energy dissipation model of turbulene;
K_x, K_y, K_z	Eddy diffusivity components used for dispersion calculations;
l_c	Distance from the source over which the concentration is to be calculated;
l	Length scales of internal layers over the canopy;
l_w	Length of the wake of an obstacle;
L_H	Length of plume/cloud in a canyon (Figure 2.15;
L_A	Adjustment length for mean flow to adjust as it enters the porous canopy;
L_c	Length of canopy;
L_{cc}, L_{DO}	Length scales of the continuum and discrete sub-regions in the canopy;
L_0	Outer length scale (influenced by canopy and boundary layer);
l_S	Length scale over which source material is emitted;
L_{Se}	Effective source size of accidental release;
L_x	Length scale of atmospheric turbulence near the source;
L_ϕ	Distance over which a 'street canyon' changes its direction (Table 2.3);
M_S	Source strength at a point;
$\hat{n}$	Normalised grazing distance between centrelines of plumes/clouds and nearby buildings;
N	Buoyancy frequency in the atmosphere;
$\overline{\mathbf{q}}_H$	Flux per unit area/time at top of canyon;
q_S	Source strength per unit volume;
Q_S	Source strength at a point/per unit time;
R_O, R_{cc}, R_{DO}	Ratio of the length of the sub-regions, L_O, L_{cc} or L_{D0}, to the smallest scales resolved in that region;

t	Time;
T_S	Period of release of source cloud;
u_*	Friction velocity of the turbulent velocity profile of the atmosphere;
U	Mean velocity, with subscripts denoting location/physical process;
U_S	Velocity with which source material is emitted;
U_v	Vehicle speed in a street canyon;
U_c, V_c	Mean wind speed in canopy, along the street canyon;
w	Obstacle length;
$\mathbf{x} = (x, y, z)$	Coordinates of a point;
$X,\ Y,\ Z$	Normalised displacements relative to the source (or mean streamline through the source);
$z_0(x, y)$	Roughness length for wind profile;
z_d	Displacement height for logarithmic wind profile;
$z_S(x, y)$	Surface elevation of the ground relative to adatum level;
α	Factor for weighting different components in double plume/cloud structure (e.g. centreline plume and wake);
β	'Porosity' of canopy [$\beta \sim bw/d^2$];
β_v	Factor for σ_w dependent on traffic (in urban areas);
$\gamma_I, \gamma_c, \gamma_z, \gamma_p$	Functions for modifying Gaussian profiles, G;
$\Delta\sigma_x, \Delta\sigma_y$	Increase in cloud/plume dimensions near a building;
Δt	Time difference;
Θ	Mean temperature;
κ	von Karman's constant;
$\sigma_u, \sigma_v, \sigma_w$	R.m.s velocity components (of the order of $\mathbf{u}_*$);
$\sigma_x, \sigma_y, \sigma_z$	Dimensions of the cloud/plume;
ϕ	Angle between wind direction and normal direction to a street (Figures 2.3, 2.5, 2.14, 2.15), i.e. $\phi = 90^o$ if wind is along the street;
Ψ	streamline;

Subscripts

b	Below top of canopy location/time;
B	Buoyancy;
c	Canyon/canopy
C	Cloud concentration for unit source strength;
Cc	Continuum canopy;
DO	Discrete obstacle scale;
f	Coriolis;
G	Geostrophic;
H	At top of buildins/canyon;
I	Image of undistorted cloud/plume;
o	Undistorted cloud/plume in uniform flow;
o, w	Undistorted cloud/plume at location of wake;
O	Outer scale;
p	Plume concentration for unit source strength
r	Reflected plume;

Ro	Rossby;
S	Source;
Se	Effective source;
$stag$	Stagnation point (streamline);
v	Vehicle;
w	Cloud/plume in wake;
*	Turbulence-related level for log profile, or turbulent source;

Superscripts

*	Along-wind distance from upwind edge of canyon;

Diacritics

~	Coordinates and plume dimensions relative to the mean streamline through the source (or through virtual sources), e.g. $\tilde{X}$;
ˆ	Average value over the central region of a plume or cloud (i.e. 'central' value), e.g. $\hat{C}$;
(k)	Reference to location of an obstacle.

Abbreviations

AERMOD	Atmospheric model for Dispersion (USA);
ADMS	Atmospheric Dispersion Modeling System (UK);
DO	Discrete obstacle sub-region;
DSTL	Defence System Technology Laboratory (UK);
cc	Continuum sub-region;
FAM	Fast approximate model;
FCM	Fully computational model.
RimPUFF	RISO Model for Puff dispersion (DK);
UDM	Urban Dispersion Model (UK).

Chapter 3

Easily Penetrable Roughnesses of different structures

Ye. Gayev[⋆,†1]
[⋆] Institute of Hydromechanics
Ukrainian National Academy of Science,
[†] National Aviation University, Kyiv, Ukraine

In this chapter, several simple flow models will be considered for different structures of the easily penetrable roughness. Generally, two EPR structures will be investigated. In Section 3.1, it will be taken for simplicity that the EPR consists of small spheres 'trapped' in the volume. Therefore, no equations will be required for characterizing the 'medium of obstruction'. This structure is called the "EPR made up of immobile elements". In contrast, the obstructions in Section 3.2 will be allowed to move along the wind ("EPR made up of mobile elements", or "Droplet EPR"). Analytical solutions will be derived whenever it is possible.

3.1 EPR made up of immobile elements

Various flows of gases or liquids in pipelines or in ducts are often met in engineering sciences. Besides the practical importance, such flows represent the simplest possible geometry in fluid mechanics and thus gave base for a number of fundamental investigations of laminar and turbulent flows and their complications with heat and mass processes [380, 566].

The generalization of such problems by introducing easily penetrable layers within the tube or duct, i.e. layers with distributed force (1.7), is oriented to a number of applications and brings also a light to main mechanisms associated with such flows. The applications include the water purification by porous inserts into pipelines, flows in vibrators, in journals and bearings with fibrous insets or brushes, in heat exchangers,

[1] E-mail of the author: *ye_gayev@public.icyb.kiev.ua*

Ye.A. Gayev and J.C.R. Hunt (eds.), Flow and Transport Processes with Complex Obstructions, 89–178.

and biomedical flows in blood vessels and lungs [2, 8, 600]. The consideration of such flows can be useful for meteorological or oceanic problems as a methodological tool.

This penetrable roughness structure resembles a model of 'forest'. The purpose of this section is the consideration of such simple structure in a flow taken in several common arrangements of fluid mechanics.

3.1.1 Fully developed pressure driving flow in a duct with EPR

The flow in a channel with parallel plates (in a duct) is the simplest case allowing the investigation of the most general flow properties. Imagine porous layers near one or both walls of an infinite duct schematically shown in Fig. 3.1. Let the penetrable layers of height h_1 and h_2 contain n_1 and n_2 obstacles in a unit volume, correspondingly. Obstacles are taken of a spherical shape for simplicity, and so n_i, $1/m^3$ is the measure of the obstacle density in a penetrable layer. The coordinates of the flow axis, i.e. the positions of the velocity maximum, are denoted as H_1 and H_2 so that $H_1 + H_2 = H$ which is the duct width. If the two EPR layers are equal and arranged symmetrically in the duct, both heights are equal, $H_1 = H_2 = H/2$.

The flow in the duct takes place due to a longitudinal pressure gradient denoted as p' what is the last input data required. The medium is supposed viscous and incompressible. It is a regular assumption that nothing is changed in the flow along its longitudinal direction x, so that the flow is one-dimensional with the velocity distribution $U(z)$ depending on the normal coordinate z only. Similar, if the flow is accompanied by the heat or mass exchange processes, the distributions of temperature $T(z)$ or concentration $E(z)$ are one-dimensional as well (not shown in Fig. 3.1).

If so, the complete Navier—Stokes equations with the discontinuous force (1.7) can be reduced to two ordinary differential equations each valid on adjoining intervals:

$$\frac{d\tau}{dz} - \rho_1 f(U) = p' \qquad \text{within the EPR,} \qquad z \in [h, H] \tag{3.1}$$

and

$$\frac{d\tau}{dz} = p' \qquad \text{in free stream,} \qquad z \in [h, H]$$

where $\tau = \rho\nu\frac{dU}{dz}$ is the hear stress in the flow. The common non-slip and symmetry boundary conditions have been imposed,

$$z = 0 \quad U = 0 \qquad \text{and} \qquad z = H \quad \frac{dU}{dz}, \tag{3.2}$$

assuming also, naturally, the continuity of the variables $U(z)$ and $\tau(z)$ on the roughness interface level $z = h$.

The problem thus formulated generalizes the textbook problem of the Poiseuille flow and so gives a parabolic velocity distribution and a linear shear distribution for $h = 0$, [380, 566]:

$$U = \frac{p'}{\rho_1\nu} z\left(\frac{z}{2} - H\right) \qquad \tau = p'(z - h).$$

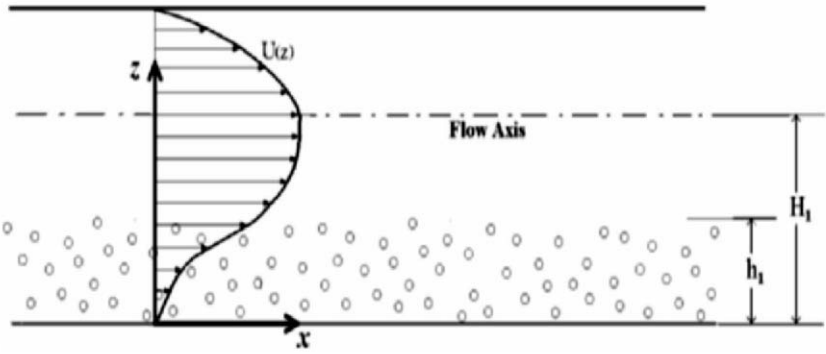

Figure 3.1: Schematic of the flow in a duct with an EPR of a height h_1 and density n_1 near the wall.

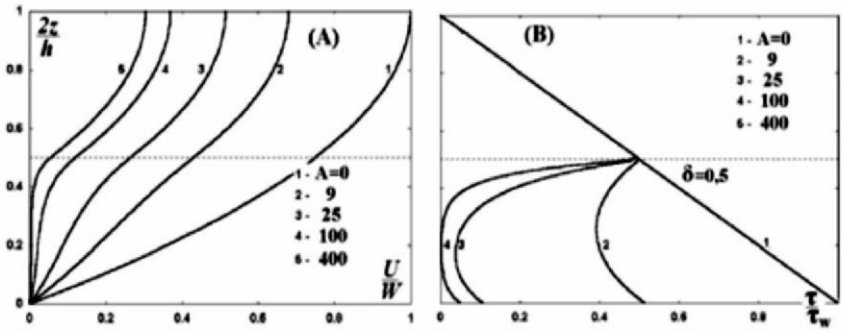

Figure 3.2: Profiles of velocity (A) and shear (B) across a duct with linear EPR symmetrically arranged for various dimensionless densities $A = var$ and $\delta = 0.5$.

Maximum values of the velocity (taking place on the axis $z = H$) and that of shear (on the wall)

$$W = U(H) = -\frac{p'H^2}{2\rho_1\nu} \qquad \text{and} \qquad \tau_W = \tau(0) = -p'H \tag{3.3}$$

are useful to be taken as scales for the solution of (3.1). It is worth to recall that the pressure gradient usually taken over a certain length, $p' = (p_2 - p_1)/L$, $p_1 > p_2$, is negative, and the scales (3.3) are thus positive.

The only linear force law,

$$f = -knU^a, \qquad \text{with} \quad a = 1$$

admits the analytical solution of problem (3.1). Introducing the dimensionless variables

$$\overline{z} = \frac{z}{H}, \qquad \overline{U} = \frac{U}{W} \qquad \text{and} \qquad \overline{\tau} = \frac{\tau}{\tau_w} = \frac{1}{2}\frac{dU}{dz}, \tag{3.4}$$

we get the dimensionless formulation of the problem:

$$\begin{aligned} U^{"} - AU &= -2 \qquad \text{if} \qquad z \in [0, \delta], \\ U^{"} &= -2 \qquad \text{if} \qquad z \in [\delta, 1], \\ z = 0 \quad U = 0, &\qquad\qquad z = 1 \quad U^{'} = 0 \end{aligned} \tag{3.5}$$

(bars over symbols have been dropped). The dimensionless parameters of problem (3.1) are

$$A = \frac{knh^2}{\nu} \qquad \text{and} \qquad \delta = \frac{h}{H}, \tag{3.6}$$

being, correspondingly, the dimensionless density and EPR relative height. The ordinary second-order differential equations (3.6) are easily solved thus giving the velocity

$$U = \begin{cases} \frac{2}{\sqrt{A}}\left(\tau_0 \sinh \sqrt{A}z - \frac{1}{\sqrt{A}} \cosh \sqrt{A}z + \frac{1}{\sqrt{A}}\right), & z \in [0, \delta] \\ U_h - (z-1)^2, & z \in [0, \delta] \end{cases} \tag{3.7}$$

and the shear distributions across the duct

$$\tau = \begin{cases} \tau_0 \cosh \sqrt{A}z - \frac{1}{\sqrt{A}} \sinh \sqrt{A}z, & z \in [0, \delta] \\ 1 - z, & z \in [0, \delta] \end{cases} \tag{3.8}$$

The auxiliary parameters $\tau_0 = \tau(0)$, $\tau_h = \tau(\delta)$ (the shear on the duct wall and on the roughness interface), $U_h = U(\delta)$, and $U_H = U(1)$ (the slip velocity on the EPR level and the maximum velocity on the flow axis) have been found as follows:

$$\begin{aligned} \tau_0 &= \frac{\tau_h}{\cosh \sqrt{A}\delta} + \frac{1}{\sqrt{A}} \tanh \sqrt{A}\delta \\ U_h &= \frac{2}{\sqrt{A}}\left(\tau_0 \sinh \sqrt{A}\delta - \frac{1}{\sqrt{A}} \cosh \sqrt{A}\delta + \frac{1}{\sqrt{A}}\right), \\ \tau_h &= 1 - \delta, \qquad\qquad U_H = U_h + (1-\delta)^2. \end{aligned} \tag{3.9}$$

The solution of this simplest model just obtained brings the credible flow profiles for a duct with symmetric EPRs shown in Fig. 3.2. It can be seen that the velocity distribution varies from a parabolic shape (taking place in the absence of the EPR, $A = 0$ or $\delta = 0$) to a very distorted one which depends on the dimensionless density of the penetrable obstruction layer A. The shear stress keeps linear outside the obstruction layer but significantly bends within it. Both kinds of profiles quantitatively correspond to the experimental distributions measured in, for example, laboratory water flumes [231]. Phenomenon of "drag discontinuity" (Chapter 6) can be observed at the top of the EPR that means that the profile $\tau(z)$ is continuous but not differentiable.

Solution (3.7)–(3.9) has been found for vertically homogeneous EPR, $A = const$. The problem however holds for inhomogeneous EPR, $A(z) = var$. It was solved analytically for $A(z) = az + b$ (linear "forest architecture", and the increasing $a > 0$ or

decreasing $a < 0$ canopy density) and for $A(z) \sim 1/\sqrt{g(h-z)}$ corresponding to the SCS architecture, [214]. It would require the numerical solution of the ordinary differential equation in the general case. It should be pointed out however that, irrespective of the architecture $A(z)$, only the monotonous velocity distributions are possible for $1D$ problems (compare with the results of other sections).

The interesting phenomenon is highlighted by profile 5 in Figure 3.2. Velocities on the extensive bottom portion of the penetrable layer became neglible, which can be explained by the significant flow deceleration caused by obstructions and the insufficient inflow of kinetic energy from the external flow. This phenomenon can be really met in nature and should be of a significant practical importance. Profiles (3.7) obtained allow us to predict a depth, where $U(z)/W \le \varepsilon$. In fact, one finds an estimate how deeply the external energy penetrates:

$$l_z = \delta - \frac{1}{\sqrt{A}} \ln \left(\frac{A\varepsilon - 2 + \sqrt{A}\sqrt{A\varepsilon^2 + 4(\tau_0^2 - \varepsilon)}}{2\left(\sqrt{A}\tau_0 - 1\right)} \right). \tag{3.10}$$

Above the elevation $z = l_z$, the flow speed is significant but equals almost zero beneath it. The wall shear stress τ_0 is taken from (3.9) but ε is a tolerance parameter taken as $\varepsilon = 0.05$ or 0.01.

Hydrodynamic resistance of the obstructed duct

The velocity profile deformation caused by the EPR leads to a significant decrease of the flow discharge in the duct. It is usually expressed through the duct resistance coefficient as

$$\lambda \stackrel{Def}{=} -\frac{p'}{\rho_1 U_{mean}^2} \tag{3.11}$$

where

$$U_{mean} = \frac{1}{2H} \int_0^{2H} V(z) dz$$

is the velocity averaged over the duct. The following relation is obtained:

$$\lambda = \frac{16}{q_1 + q_2} \cdot \frac{1}{\mathrm{Re}} \tag{3.12}$$

where the portions of a discharge are found as

$$\begin{aligned} q_1 = \int_0^{\delta} U(z) dz &= 2\tau_0 \frac{\cosh\left(\sqrt{A}\delta\right) - 1}{A} - 2\frac{\sinh\left(\sqrt{A}\delta\right) - \sqrt{A}\delta}{A\sqrt{A}}, \\ q_2 = \int_{\delta}^{1} U(z) dz &= U_H(1-\delta) - \frac{1}{3}(1-\delta)^3. \end{aligned} \tag{3.13}$$

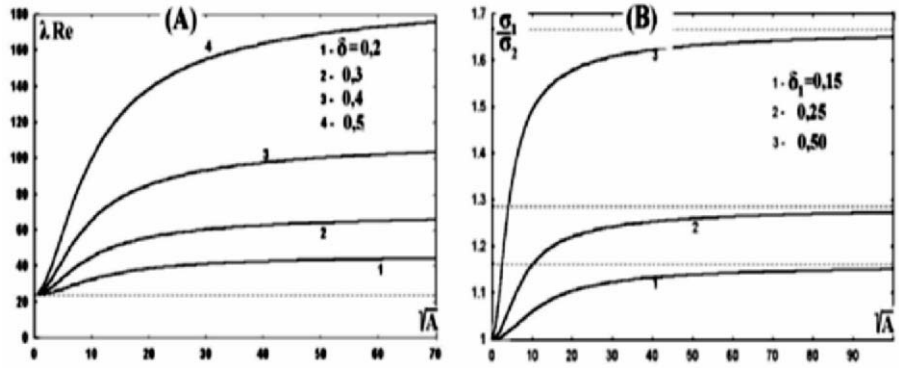

Figure 3.3: Resistance of the symmetric duct with EPR (A) and a shift of the dynamical axis in a non-symmetric case (B) vs the EPR density and height. Dotted lines label limit values.

It was strictly proved for this laminar case that $\lambda \to 24/\mathrm{Re}$ for extreme values $A \to 0$, when the EPR density vanishes. So the model provides the known results as the extreme case. The graphical relation (3.12) is shown in Figure 3.3,A. For each relative EPR height δ given, the resistance increases with the EPR density A. However, a limit exists and corresponds to the resistance of a duct as wide as $2(1-\delta)$.

Non-symmetric arrangement of the EPR in ducts

Profiles (3.7), (3.8) were obtained for symmetric EPRs near both walls in the duct. In practical situations like the experiment in a wind tunnel, EPR is placed, however, non-symmetrically. Because of this, the dynamical axis of the flow (where $\frac{\partial U}{\partial z} = 0$ on definition) does not coincide with the geometric axis of the duct $z = H$. One needs to find the coordinates of the maximum velocity H_1 and H_2, i.e. the distance from both walls to the dynamical axis assuming that (3.7) takes place in each half of the duct so that $H_1 + H_2 = 2H$. This means that one of the shift parameters or $\sigma_1 = H_1/H$ or $\sigma_2 = H_2/H$, or their quotient $\frac{\sigma_1}{\sigma_2}$ must be found.

The solution obtained above can be used independently for the bottom and top parts of the flow, each with its own scales, W_1 and W_2. Because of the flow continuity, dimensional velocity values should be equal on the dynamical axis, $W_1 U(H_1) = W_2 U(H_2)$. This gives the following algebraic equations:

$$\sigma_1 + \sigma_2 = 2, \qquad \sigma_1^2 U_{H1} = \sigma_2^2 U_{H2},$$

where U_{H1} and U_{H2} are calculated from (3.9). The solution can be obtained in a closed analytical form [208] but is dropped here. The graphical dependence of the dynamical axis shift versus the EPR density and height has been shown in Fig. 3.3,B. The case was considered when there is no EPR near the second wall like in Fig. 3.1.

3.1.2 Pulsating laminar flow in a duct with EPR

The laminar pulsatile flow in a plane duct can be treated as the simplest unsteady problem in basic fluid mechanics with applications, for instance, to engineering vibrators [199, 507]. In biological and medical fluid mechanics, one meets the pulsating blood flow in arteries and the air flow in lungs. The generalization of such flows was suggested in literature [598, 601], and is of interest for this chapter.

Let the pressure gradient in a duct between two parallel plates periodically fluctuate,

$$p' = p'_0 + a\rho \cos \omega t \tag{3.14}$$

where ω is the frequency of fluctuations, $1/sec$, and a is their amplitude. The EPR is arranged symmetrically in the duct. Such a problem is valuable both as a further fluid mechanical investigation of penetrable roughness properties [214] and a certain scheme of the turbulence phenomenon. New applications can be found in technical (vibrator drivers, fuel suppliers, etc.) and in biological areas (blood motion in sclerotic veins, air motion in trachea or water motion in fish gills).

The flow under consideration is mathematically more simple in a plane duct than in an axisymmetric round tube. However, no readily solution for smooth walls, i.e. in the case where the EPR is absent, is given in the literature. The formulations and solutions of the problem of a pulsating viscous flow to be taken for a comparison have been presented only for round tubes. The known solutions employ mainly the Laplace transformation and small-parameter methods. The present investigation follows the standard technique of mathematical physics of finding the periodic solutions described particularly by Schlichting [566] with references to some original sources. Their solution for smooth walls will serve for a comparison.

In the general statement of the problem (3.1) and (3.2), a pulsating pressure-driven flow in a plane channel with easily penetrable layers symmetrically placed near both walls can be described by the following equation:

$$U'_t = \nu U''_{zz} - \frac{p'(t)}{\rho} - \begin{cases} kU, & z \in [o, h] \\ 0, & z \in (h, H] \end{cases} \tag{3.15}$$

$$z = 0 \qquad U = 0, \qquad\qquad z = H \qquad U'_z = 0. \tag{3.16}$$

where only the symmetric half of the duct is considered. To make the problem to be dimensionless, the dimensionless time

$$\bar{t} = \frac{\nu t}{H^2} \tag{3.17}$$

should be added to variables (3.4). Separately, we present the following general formulation of the problem (3.6) for the decelerated and free flow parts:

$$\begin{array}{ll} \text{if } z \in [0,\delta] & \text{if } z \in [\delta,1] \\ \begin{cases} U_t = U_{zz} + 2(1 + a\cos\omega t) - AU, \\ z = 0, \qquad U = 0, \end{cases} & \begin{cases} U_t = U_{zz} + 2(1 + a\cos\omega t), \\ z = 1, \qquad U_z' = 0, \end{cases} \end{array} \tag{3.18}$$

$$U(\delta - 0) = U(\delta + 0), \qquad \tau(\delta - 0) = \tau(\delta + 0), \tag{3.19}$$

where two new coefficients

$$\overline{a} = \frac{\rho a}{p_0'} \qquad \text{and} \qquad \overline{\omega} = \frac{\omega H^2}{\nu}$$

have the meaning of, respectively, the dimensionless pressure pulsation amplitude and the frequency and govern the flow along with two coefficients (3.6). (Again, the bars over symbols are dropped hereinafter). In this subchapter, we label solution (3.7), (3.8) for a stationary flow with index "s". The solution of the unsteady problem under consideration (3.18), because of its linearity and the homogeneity of the boundary condition, can be split into a sum of steady (3.7) and unsteady ('fluctuating') terms, with the latter being

$$V(z,t) = U(z,t) - U_s(z) \tag{3.20}$$

It is easy to see that this fluctuating "addition" is to satisfy to the following two problems

$$\begin{array}{ll} \text{for } z \in [0,\delta] & \text{for } z \in [\delta,1] \\ \begin{cases} V_t = V_{zz} + 2a\cos\omega t - AV, \\ z = 0 \qquad V = 0, \end{cases} & \begin{cases} V_t = V_{zz} + 2a\cos\omega t, \\ z = 1 \qquad V_z = 0, \end{cases} \end{array} \tag{3.21}$$

with the conjugation conditions on the interface $z = \delta$:

$$V(\delta - 0) = V(\delta + 0), \qquad V_z(\delta - 0) = V_z(\delta + 0).$$

Here, the dimensionless viscous shear in the flow is related to the transversal gradient of the velocity "addition" as follows:

$$\tau(z,t) = \tau_s(z) + \frac{1}{2}V_z(z,t)$$

Problem (3.21) for "additions" (3.20) describes the periodic back-and-forth motion of the medium with zero mean pressure gradient, p_0', having so its own practical value. That is the case to be investigated here.

It is also useful to investigate the generalization of (3.21) in complex variables:

$$V_t + V_{zz} + 2ae^{i\omega t} - AV,\ z \in [0,\delta] \qquad \text{and} \quad V_t + V_{zz} + 2ae^{i\omega t},\ \ z \in [\delta,1] \tag{3.22}$$

The solution of both equations is sought in the form [566]

$$V(z,t) = Z(z)\exp(\gamma t), \tag{3.23}$$

where γ is a complex exponent and Z is a complex-valued function of the real argument z. It is easy to see that such a solution exists if $\gamma = i\omega$. If so, the first complex-valued equation (3.22) can be solved as

$$\begin{aligned} Z_1(z) = \left(Z(\delta) - \frac{2a}{A+i\omega}\right)\cosh\left(\lambda_1(z-\delta)\right) + \\ + \frac{1}{\lambda_1}Z'(\delta)\sinh(\lambda_1(z-\delta)) + \frac{2}{A+i\omega}, \end{aligned} \tag{3.24}$$

where $\lambda_1 = \sqrt{A+i\omega} = M_1 e^{0.5\varphi_1 i}$, $M_1^2 = \sqrt{A^2+\omega^2}$, and $\cos\varphi_1 = \frac{A}{A^2+\omega^2}$.
Formally substituting $A = 0$, one obtains the solutions also for the second complex-valued equation (3.22) denoted with the subscript "2" here:

$$Z_2(z) = \left(Z(\delta) - \frac{2a}{i\omega}\right)\cosh(\lambda_2(Z-\delta)) + \frac{1}{\lambda_2}Z^{'}(\delta)\sinh(\lambda_2(z-\delta)) + \frac{2a}{i\omega}, \tag{3.25}$$

$$\lambda_2 = \sqrt{i\omega} = M_2 exp(0.5\varphi_2 i), \qquad M_2^2 = \omega \quad \text{and} \quad \varphi_2 = \frac{\pi}{2}.$$

The auxiliary parameters $Z(\delta)$ and $Z-(\delta)$ can be easily derived from the boundary conditions of problem (3.21). We get

$$\begin{aligned} Z(\delta) &= \frac{2a(1-\cosh(\lambda_1\delta_1))e^{-i\varphi_1}}{M_1^2\left(\frac{1}{\lambda_2}\cosh(\lambda_1\delta_1)\cosh(\lambda_2\delta_2) + \frac{1}{\lambda_1}\sinh(\lambda_1\delta_1)\sinh(\lambda_2\delta_2)\right)}\frac{\cosh(\lambda_2\delta_2)}{\lambda_2}, \\ Z'(\delta) &= \frac{2a(1-ch(\lambda_1\delta_1))e^{-i\varphi_1}}{M_1^2\left(\frac{1}{\lambda_2}\cosh(\lambda_1\delta_1)\cosh(\lambda_2\delta_2) + \frac{1}{\lambda_1}\sinh(\lambda_1\delta_1)\sinh(\lambda_2\delta_2)\right)}\sinh(\lambda_2\delta_2) \end{aligned} \tag{3.26}$$

where $\delta_1 = \delta$ and $\delta_2 = 1-\delta$. Expressions (3.24)–(3.26) give a solution of the complex-valued problem (3.22). Separating their real parts from imaginary ones, one gets the solution for pulsations of problem (3.21) as

$$V(z,t) = \Re\left(Z\exp(i\omega t)\right) = \Re\left(Z\cos\omega t\right) - \Im\left(Z\sin\omega t\right). \tag{3.27}$$

The analytical expressions obtained are unwieldy if their real $\Re$ and imaginary $\Im$ parts would have been calculated to the "very end". However, they are easy to be performed by any algorithmic language. Let us start the analysis of the obtained solution (3.24)–(3.27).

Limit case where the EPR is absent

It is evident that, under a harmonically pulsating pressure gradient (3.14), a periodic back-and-forth flow with the oscillation period $T = 2\pi/\omega$ is appeared in the duct. Assuming $A = 0$ or $\delta = 0$, one gets, in the case where the EPR is absent, the known

solution found, for instance, in [566] and useful for a contrast here. The velocity distributions and shear profiles calculated for several consequent time moments within one half-period of the pressure oscillation have been presented in the bottom parts of Figures 3.4 and 3.5.

The only symmetric halves of the profiles within the duct have been shown here. All the velocity profiles cross zero on the wall, because the non-slip condition (3.15) is imposed. For a "small" oscillation frequency, Fig. 3.4, all the velocity profiles have a monotonic parabolic shape that follows closely to the Poiseuille law for each time moments [566]. The motion of the medium is always co-directed with the pressure gradient $p'(t)$. At time moments 1 to 5, the pressure gradient is positive, so the medium flows from the left to the right (the positive direction). At time moment 6, the pressure gradient becomes zero and becomes negative at the next time moments. Velocity profiles 7 to 10 behave correspondingly: velocity values are negative, and the medium flows from the right to the left.

At the subsequent time instances not shown here, the pressure gradient becomes positive again, so the medium moves to the right again. Further, the described medium motion is periodically repeated. It should be noted that, even for this frequency, a small "lag" takes place between the motion and the pressure change: the velocity in the duct does not equal exactly to zero for the zero pressure gradient at the time moments close to 6. The shear stress distributions in the duct follow basically to the stationary law, by reducing linearly from a certain stress on the wall $\tau_0(t)$ to zero on the duct axis; the curve bends near the walls are very small.

Figure 3.5 displays the calculation results for the "high" dimensionless frequency $\omega = 50$. It can be seen in the bottom parts of the figure that, again, the positively and negatively directed flows alternate in the channel. However, the flow picture has drastically been changed. The "lag" between the flow and the pressure change is seen to become much more in the case of "high frequency" oscillations than that in the "low-frequency" case: for example, the velocity profile has just passed the limit right position at time moment 6 while the pressure gradient is zero at that instance; again, the medium still flows in the positive direction, from the left to the right, at time moment 10, while the pressure gradient has almost been reaching its maximum value. Compare this instance with the first case where the "obedient" medium moves to the left with the almost maximum velocity! Of course, such a lag effect is explained by the medium inertia. Because of it, near walls where the medium velocity is lower, the medium follows the pressure gradient more obediently. As a consequence, local maxima appear on the velocity distributions outside the duct axis at time moments 5, 6, 7, and then at moments 11 to 15. What is more, a counterflow, i.e. the zone with the opposite flow direction near walls, appears at time moments 9 and 10. Such a flow behavior was discovered by Richardson [533] and termed as the "annular" effect by him. It can deliberately be used for the ablution of tubes, and the suspension or dusted gas transport. Note that the velocity distribution is near homogeneous in the middle of the duct but is rather complex near walls. The transversal shear distributions in the duct confirm the complexity of the flow for high frequencies once again, Fig. 3.5,B: the shear is almost zero in the middle but is distributed rather complexly near walls. The amplitude of velocity oscillations is twenty five times less than that in the first case,

which means that the hydraulic resistance increases with the frequency. The shear amplitude, however, is reduced only five times.

Complications with EPR present

Let us now compare the complications in the pulsating flow caused by an easily penetrable roughness present near a wall. The flow profiles calculated by (3.24)–(3.27) have been displayed in the top parts of Figs. 3.4 and 3.5 for EPR of the density $A = 50$ occupying a significant portion of the duct's cross-section. (Remember that the disposition of the EPR and, correspondingly, the flow in the duct are symmetric over the axis $z = 1$). The layers near the walls filled with EPR obstacles in a form of small spheres have also been schematically shown in Figures.

The motion of the viscous medium in a duct with EPR can naturally also be thought to alternate periodically with the period $T = 2\pi/\omega$: the medium flows firstly from the left to the right, then in negative direction from the right to the left, and again in the positive direction, etc. The numbering of the profiles in Figures allows one to understand the time moments the distributions are related to; their sequence corresponds generally to the case where the EPR is absent. So, if the EPR is placed in a "slowly" pulsating flow, Fig. 3.4, the amplitude of oscillations reduces by approximately two times. Such a result can be expected because the EPR introduces an additional (to the wall shear) hydraulic drag in the duct. The velocity distribution consists of two portions now: a decelerated flow within the EPR, and a parabolically distributed flow in the free duct's part. At each time moment, the flow has about the same velocity distribution as it would have in the stationary situation (3.7)–(3.8) with the same, but constant, pressure gradient and the same EPR density. The denser the EPR, the weaker is the flow there.

In contrast, placing the EPR in a duct with the "frequently" oscillating medium leads to less expected and radically different results. Figure 3.5 shows that the amplitude of oscillations has not been reduced in comparison with the case where the EPR is absent, but it even has slightly been increased in the free duct's section (the profiles in instants 5 and 6). The magnitudes of the "local maxima" in decelerated flow portions and the dimensions of the zones with counter-directed flows (profiles 8, 9, and 10) grow as well as. One can speak about a reinforcement of the annular effect due to the use of the EPR. The latter is equivalent to a reduction of the hydraulic duct resistance. Increasing the EPR density to $A = 100$ instead of $A = 50$ changes almost nothing, in contrast to the stationary or low-frequency motion. The calculations for frequencies higher than $A = 100$ confirm these conclusions: although the velocity pulsates with a narrower magnitude between 0.045 and +0.045, the EPR makes the limit velocity profiles more "blown out" and increases the dimension of the counterflow zones. The presence of the EPR decreases also the lagging between pressure and velocity oscillations.

The parameter of the EPR δ, $0 \le \delta \le 1$, characterizes the portion of the duct's cross-section occupied by the EPR. The calculations show that its increase does not decelerate the frequently oscillating medium which also differs from the "low-frequency" case. The effects of the easily penetrable roughness on a pulsating flow can be classified, in summary, depending on either the EPR is used for controlling the pulsating flow or, conversely, pressure pulsations are used to influence the flow in a duct with the EPR:

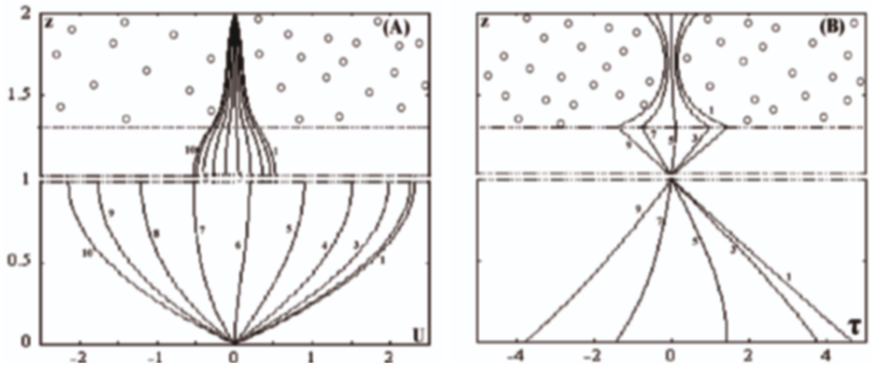

Figure 3.4: Profiles of velocity (A) and shear stress (B) over duct cross-sections at consequent time moments 1 - $t = 0$, 2 - $t = \Delta t = T/20$, 3 - $t = 2\Delta t$, etc. for the periodic pressure change (3.14) with the amplitude $a = 2.5$ and the "low" frequency $\omega = 1$. Bottoms – duct without EPR, tops – with an EPR, $\delta = 0.7$, $A = 50$.

- Placing the EPR in a periodically pulsating flow reduces the duct discharge, i.e., increases its hydraulic resistance if the flow pulsates with a low frequency;
- Placing the EPR in a high-frequency pulsating flow does not reduce the magnitude of velocity variations. That is the possible reason for biological self-controlling systems to react to the appearance of obstructions (because, say, of an illness or senescence) by means of a more frequent oscillating.
- In the last case, however, the near-wall area with counterflows becomes wider, which can negatively affect a biological system.

Applying a pulsating pressure gives thus a possible way to control the flows in ducts with EPRs. One must so account for different flow behaviors under slow and fast pressure fluctuations[2]. More details about the solution can be found in [212].

The other types of unsteady flows in ducts partially filled with a porous material and their numerical investigation can be found, for instance, in [2, 8], where the unsteadiness of the fluid flow was caused by a sudden change in the imposed pressure gradient.

3.1.3 EPR in ducts with non-circular cross sections

In engineering, not only cylindrical pipes are used, but also pipelines with elliptic, square, or triangular cross sections [380]. The area D and the cross section shape are taken constant along the longitudinal flow direction Ox. It is known for this problem that the normal flow velocity components U_y and U_z are equal to zero, and the only non-zero component is the longitudinal velocity $U = U(y, z)$ that depends on two coordinates (y, z)) in D. Therefore, the complete Navier—Stokes equations are reduced to

[2]The performance of the pulsating flow described has been realized as a graphical computer program to be found at *http://www.met.rdg.ac.uk/urb_met/NATO_ASI/Gayev/Pulsation/* or requested from the author.

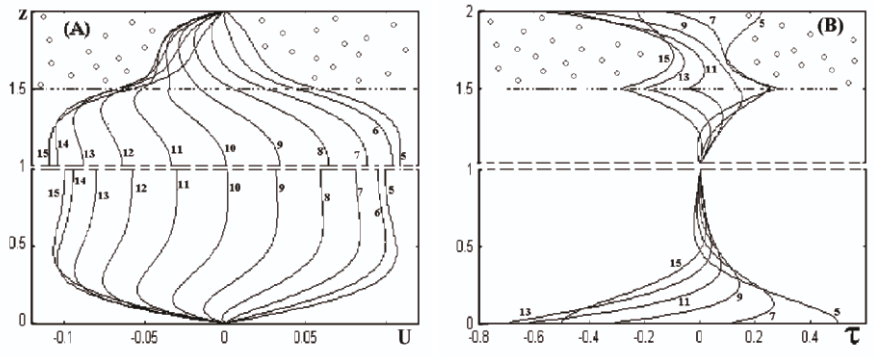

Figure 3.5: Velocity (A) and shear stress profiles (B) for consequent time moments: 5 - $t = 4\Delta t = 4T/20$, 6 - $t = 5\Delta t$, etc. for a half-period of the pressure pulsations with the amplitude $a = 2.5$ and the "high" frequency $\omega = 50$. Bottoms – duct without EPR, tops - with EPR $\delta = 0.5$ and $A = 50$.

the two-dimensional inhomogeneous Laplace equation $\Delta = -2$ that was solved analytically for many crosssectional areas D, [380].

Imagine that the near-wall space with cross section D_1 is filled by small spherical obstructions that form a penetrable roughness along the whole pipeline length, $D_1 \subset D$, Figure 3.6. The same equation can be derived with regard for an additional force proportional to the local velocity that exists within the roughness:

$$\frac{\partial^2 U}{\partial y^2} + \frac{\partial^2 U}{\partial z^2} = -2 + \begin{cases} AU, & \text{if} \quad (y,z) \in D_1, \\ 0, & \text{if} \quad (y,z) \in D/D_1. \end{cases} \tag{3.28}$$

This formulation generalizes problem (3.6). Two boundary conditions are to be imposed, one non-slip condition on the boundary ∂D and the maximum condition $\partial D/\partial l = 0$ on the geometric center of the area D (median intersection point). Isolines of a constant velocity value (isotaches) have been plotted on the bottom of Fig. 3.6. They are parallel lines in the flow between two plates, and are circular ones in a round tube. The isotaches reflect the influence of corners where the obstructed roughness is especially deep.

3.1.4 Boundary layer flow over EPRs

The problems considered so far were one-dimensional in essence. Here, a two-dimensional problem will be considered. It should be also noted that no reduction of any term of the complete Navier—Stokes equations was made yet. This means that no groundless assumptions were employed apart from the representation of EPR by a distributed force. In contrast, the Navier—Stokes equations reduced to the boundary-layer approach (1.4), (1.5) were employed by meteorologists.

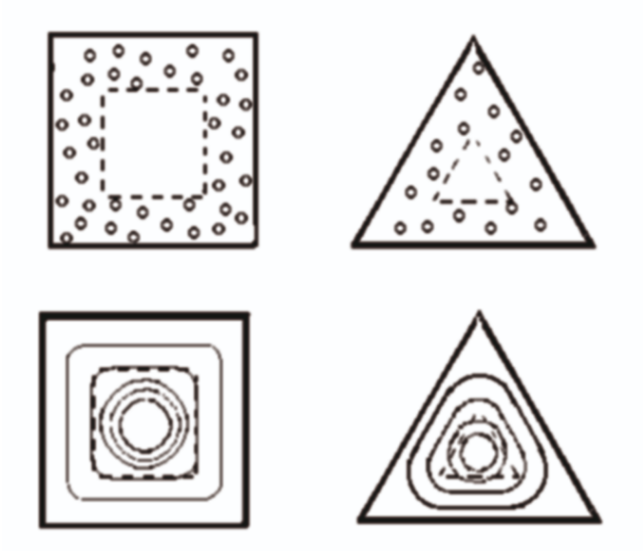

Figure 3.6: Pipelines with squared and triangular cross sections: arrangements of the EPR near walls (top) and isotaches of a laminar flow (bottom).

A boundary layer flow is one of the simplest two-dimensional formulations in fluid mechanics. This approach suggested by Prandtl assumes that the flow properties change very slowly in the longitudinal direction with respect to the normal direction, $\frac{\partial}{\partial x} << \frac{\partial}{\partial z}$. This allows one to drop some terms in the equations, thus having simplified them.

Imagine an initially homogeneous flow in the Ox direction that runs onto the surface $z = 0$ with the easily penetrable roughness of a height h over it. The flow transformation that is schematically shown in Figure 1.15,C is to be performed. The Navier—Stokes equations take the form

$$(\vec{U} \cdot \vec{\nabla})\vec{U} = -\frac{1}{\rho_1} grad\ p + \nu\nabla^2\vec{U} + \vec{f_*}, \qquad div\vec{U} = 0, \tag{3.29}$$

where the force is given accordingly to (3.28) or (1.6)–(1.8) and vanishes outside the penetrable layer. There is one natural scale for the velocity, $W = U_\infty$, the flow speed at the infinitely far distance from the surface, and two length scales. One scale, the diameter of obstructions $2r$, determines the streamline regime; another scale, the height of the EPR h, determines flow's general stability. Correspondingly, there are two possibilities to define Reynolds numbers:

$$\mathrm{Re} = \frac{hU_\infty}{\nu}, \qquad \mathrm{Re}' = \frac{2rU}{\nu}. \tag{3.30}$$

Their ratio is $\mathrm{Re}/\mathrm{Re}^{'} = h/2r \approx 100 - 1000$.

The boundary-layer approach neglects some terms of the momentum equations (3.29) and yields two simplified equations instead of three:

$$U\frac{\partial U}{\partial x}+V\frac{\partial U}{\partial z}=\frac{1}{\rho_1}\frac{\partial \tau}{\partial z}-f_{*x}, \qquad \frac{\partial U}{\partial x}+\frac{\partial V}{\partial z}=0, \tag{3.31}$$

with $\tau=\rho_1\nu\frac{\partial U}{\partial z}$ representing the shear stress in the flow. These are basically the equations (1.5) applied by meteorologists for forest canopies. The talk will be restricted by only the linear force law. Introducing the new dimensionless variables

$$\overline{x}=\frac{1}{\mathrm{Re}}\frac{x}{h},\quad \overline{z}=\frac{z}{U_\infty},\quad \overline{V}=\mathrm{Re}\frac{V}{U_\infty},\quad \text{and}\quad \overline{\tau}=\mathrm{Re}\frac{\tau}{\rho_1 U_\infty^2}=\frac{\partial \overline{U}}{\partial \overline{z}}, \tag{3.32}$$

one arrives at the following conjugation problem:

$0\le z\le 1$

$$\begin{cases} U\dfrac{\partial U}{\partial x}+V\dfrac{\partial U}{\partial z} &= \dfrac{\partial \tau}{\partial z}-AU,\\[2ex] \dfrac{\partial U}{\partial x}+\dfrac{\partial V}{\partial z} &= 0, \end{cases}$$

$z=0\quad U=0,\quad V=0;$
$x=0\quad U=1,\quad V=0;$

$1\le z<\infty$

$$\begin{cases} U\dfrac{\partial U}{\partial x}+V\dfrac{\partial U}{\partial z} &= \dfrac{\partial \tau}{\partial z},\\[2ex] \dfrac{\partial U}{\partial x}+\dfrac{\partial V}{\partial z} &= 0, \end{cases} \tag{3.33}$$

$z\to\infty\quad U=1;$
$x=0\quad U=1,\quad V=0;$ (3.34)

$$z=1\quad U|_{1-0}=U|_{1+0},\quad V|_{1-0}=V|_{1+0},\quad \tau|_{1-0}=\tau|_{1+0} \tag{3.35}$$

(here, the bars over symbols have been dropped). In this problem, the systems of equations (3.33) are considered in the adjacent domains with the interface $z=1$ between them, each system with its boundary conditions (3.34). It is simple to ground that the conjugation conditions (3.35) are sufficient for ensuring the uniqueness of the solution. The solution is determined by the single parameter

$$A=\mathrm{Re}\frac{k_d nh}{U_\infty}=\frac{k_d nh^2}{\nu} \tag{3.36}$$

that accounts for the resistance of individual obstructions, and their size and shape (the resistance coefficient accordingly to (1.8)), and the local density of obstructions. However, the solution in the dimensionless form does not depend on the speed of the flowing medium. The analytical investigation of problem (3.33)–(3.35) is not possible, so it requires numerical methods. A developed finite-difference method was used and brought the detailed data on the flow transformation. The longitudinal velocity $U(z)$ and normal velocity profiles $V(z)$ have been presented in Figure 3.7 for several secant planes. It can be seen that the fluid entering the leading edge of the EPR $0\le\overline{z}\le 1$ experiences a braking by the wall action and the resistance of obstructions. As a result, $V>0$ becomes significant, and the steps are seen on the $U(z)$-profiles. A small local maximum can arise on $U(z)$, but it is quickly smoothed out. The greater the dimensionless EPR density A, the more intensive becomes the transformation. The shear $\tau(z)$

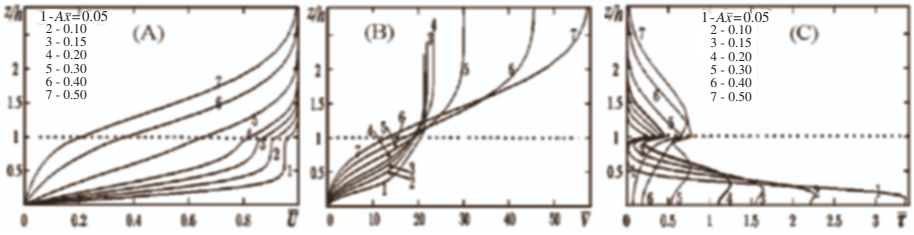

Figure 3.7: Longitudinal (A), transversal velocity (B), and shear stress distributions (C) in the laminar flow over a penetrable roughness with the density $A = 10$ and height $\overline{h} = 1$ (dotted line).

experience a sharp bend on the EPR-flow interface $z = h$ (compare with the drag discontinuity phenomenon, Chapter 6) and is distributed non-monotonically over the flow. For comparison: $\tau(z)$ is strictly monotonous over the conventional boundary layer.

The analysis of the flow picture obtained allows us to distinguish several structural elements of the flow, i.e. *initial region*, main region, and a possible *stagnation zone*, all being represented in Figure 3.8.

Initial region

The initial region extends over an entrance length X_0 and consists of boundary layer 2 over the wall with width $d_0(x)$, internal boundary layer 3 with depth $d_1(x)$, and initial region core 1 between them. External boundary layer 4 with width $d_2(x)$ transports perturbations caused by the EPR far away over it.

The calculations reveal that $\tau \sim 0$ and $\partial U/\partial z \sim 0$ within the initial region core, and thus the drag force (1.6) dominates. This allows us to reduce the governing equation to the following one:

$$U\frac{dU}{dx} = -f_{*x}, \qquad x = 0, \quad U = 1. \tag{3.37}$$

This yields the velocity deceleration law within the initial region. For the linear law, one gets $U_0 = 1 - Ax$, and the length of the initial region is $X_0 = 1/A$. This estimation turns out to be in good agreement with the numerical data. For the quadratic force law (1.7), (1.8), one gets, in the dimensional form,

$$U_0(x) = U_0(0)e^{-\frac{1}{2}C_F S x}. \tag{3.38}$$

The initial region ends, when both boundary layers 2 and 3 contact each other. Its length X_0 reduces with increase in the EPR density (3.36). The velocity distributions $U(z)$ and $V(z)$ across the EPR vary with A. It was discovered, however, that two profiles obtained for A_1 and A_2 can be brought together if we refer them to the corresponding x_1 and x_2. More precisely, this similarity law for the initial region means that the following dimensionless variables suit better than (3.32):

$$\hat{x} = A\overline{x} = \frac{A}{\mathrm{Re}}\frac{x}{h}, \qquad \hat{z} = \overline{z} = \frac{z}{h},$$

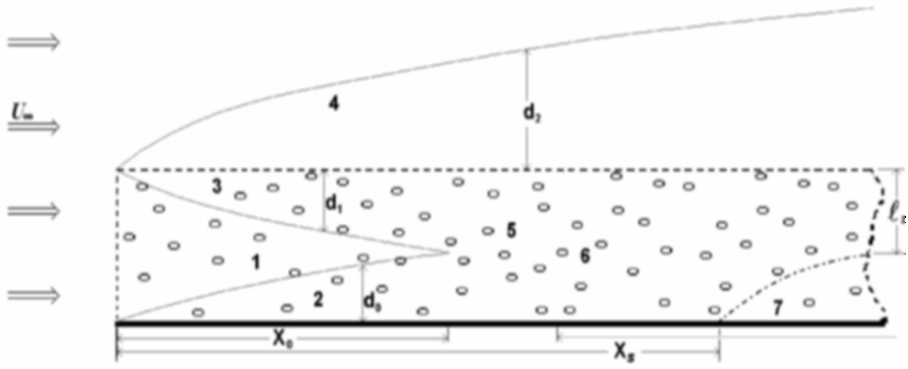

Figure 3.8: General structure of the boundary layer (BL) over an easily penetrable roughness: 1 - core of the initial region with BLs 2 and 3; 4 - external BL; 5 and 6 - main and transition regions; and 7 - possible stagnation zone.

(3.39)

$$\hat{U} = \overline{U} = \frac{U}{U_\infty}, \qquad \hat{V} = \frac{\overline{V}}{A} = \frac{1}{A\mathrm{Re}}\frac{V}{U_\infty}.$$

It is advisable to compare this conclusion with that in Section 3.2.2.

Main region

Main region 6, which begins after some transition 5 of the flow, lasts infinitely and is distinctive by the fact that the internal portions of all the distributions stop changing while the expansion of the external boundary layer $d_2(x)$ is going on. This means that the drag force came to an equilibrium with the shear stress. Imposing the conditions $\partial/\partial z \sim 0$ and $V \sim 0$ on the first system of equations (3.33), the following reduction to one ordinary differential equation takes place:

$$\frac{d\tau}{dz} = f(U), \tag{3.40}$$

$$z = 0 \quad U = 0, \qquad z = 1 \quad \tau = \tau_h$$

with $\tau = \rho\nu\frac{dU}{dz}$. The last problem is similar to (3.1), but the motion on the main boundary layer region is driven by the interface shear τ_h instead of the pressure gradient p' in the duct. The same mathematical technique leads to the solution

$$U = U_h\frac{\sinh(\sqrt{A}z)}{\sinh\sqrt{A}}, \qquad \tau = \tau_h\frac{\cosh(\sqrt{A}z)}{\cosh\sqrt{A}}. \tag{3.41}$$

The auxiliary parameters, the slip velocity $U_h = U(h)$ and the interface shear $\tau_h = \tau(h)$, are evidently matched through the relation

$$\frac{\tau_h}{U_h} = \sqrt{A}\cdot\coth\sqrt{A}.$$

However, their separate values can be obtained by only the consideration of the external boundary layer $d_2(x)$, which cannot be realized so simply.

Stagnation zone

Like in the case of the EPR in a duct, section 3.1.1, for a dense EPR in the boundary layer, one can meet a situation such that there is almost no motion in the bottom part of the EPR near the wall. The shear stress τ_h driving the flow turns out to be not so efficient to provide a sufficient amount of the kinetic energy through all the EPR depth. This phenomenon means the formation of a stagnation zone and is similar to the effect of negative pressure gradient that causes the separation in the regular boundary layer flow. The phenomenon can be crucially important for vegetation canopies or a droplet layer.

Numerical experiments provided the critical EPR density $A_{cr} \approx 2.5$. No stagnation is formed if $A < A_{cr}$; the profiles $U(z)$ in the EPR bottom tend to a constant slop, and $\tau_0 = \tau(0) = const \neq 0$. Stagnation begins at a certain distance X_s (Fig. 3.8) if $A > A_{cr}$ and then ranges to infinity. At this distance, the shear on the wall reaches the value $\tau(X_s, 0) \approx 0$, and the computing program loses its stability.

Profiles (3.41) allow one to estimate the depth l_z, where the kinetic energy is able to penetrate, in the same way as formula (3.10) was obtained.

Self-similarity of the external boundary layer

It is known that the regular boundary layer over a smooth surface turns out to be self-similar [380, 566]. The velocity distributions stretching from the EPR interface $z = 1$ till the boundary layer border $z = d_2(x)$ were also inspected for such a property. It turns out that the numerical profiles of the longitudinal velocity can be brought together if we transform them by mapping

$$\vartheta = \frac{U - U_h}{U_\infty - U_h}, \qquad \eta = \frac{z - 1}{d_2(x)}. \tag{3.42}$$

The uniquenessambient(external) flow of the curve $\vartheta = \vartheta(\eta)$ is broken at the beginning of the initial region or at the distance where a possible stagnation zone starts.

Flow features over an inhomogeneous EPR

Natural canopies such as vegetative covers are mostly vertically inhomogeneous that is accounted for in the mathematical model by means of the density being a function of the vertical coordinate z, $n = n(z) \neq const$. Practical examples of leaf area distributions can be found in [6, 155, 522]; see also Figures 1.7 and 6.3. The same can be expressed by the specific measure of the frontal area $s(z) = nS$ or by the dimensionless canopy density $A = A(z)$ as explained in (3.128). As an example, a function family

$$A(z; a) = 2(A_0 - a)z + a \tag{3.43}$$

that depends on parameter a was investigated. The dimensionless density decreases ($A_z' < 0$) for $a > A_0$, increases for $a < A_0$, and preserves the average measure over the EPR height, $\langle A \rangle = \int_0^1 A(z)dz = A_0$ (see the insert in Fig. 3.9).

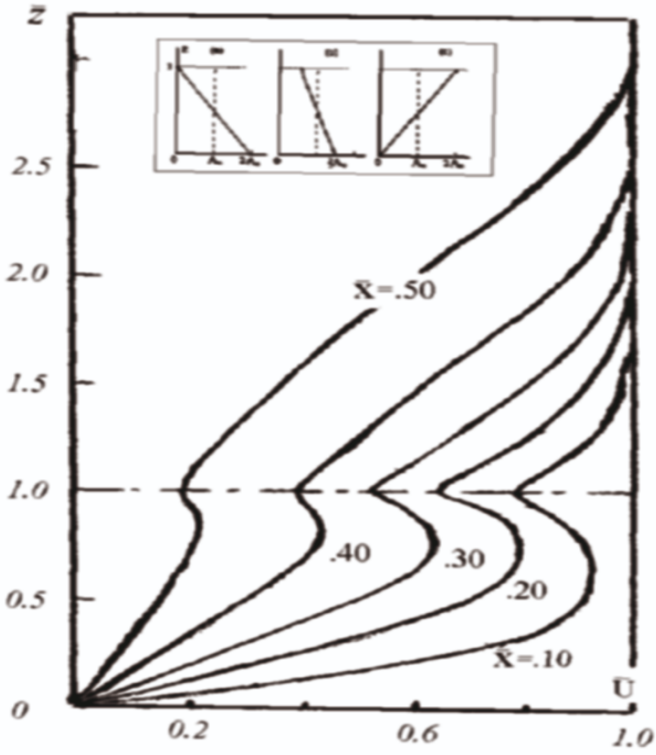

Figure 3.9: Patterns of inhomogeneous EPR densities (3.43) (insert), and velocity distributions on the initial region of boundary layer over the EPR with increasing density. Local extremes are formed on $U(z)$.

The results in Fig. 3.7 correspond to a constant density $A = const$. There are no qualitatively new effects in the case of the vertically decreasing density $A' > 0$ (distributions a and b, inserts in Fig. 3.7). The numerical results for the boundary layer flow that develops over an increasingly inhomogeneous EPR are shown in Fig. 3.9. Local maxima and minima are seen on the longitudinal velocity profiles $U(z)$. The minimum on $z = h$ and maxima within the EPR are explained by the fact that the flow meets a bigger drag force beneath the top of the canopy than that on lower levels. However, this phenomenon takes place only in the initial region. Then the extrema are gradually smoothed over so that the profiles become monotonous in the main flow region. It is known that similar effects can be met in real forests, see Sections 3.3.5 and 5.1.

The profiles obtained were also inspected for the presence of self-similarity in the external boundary layer. Inhomogeneous EPRs (3.43) allow analytical estimations like (3.41) in terms of Bessel functions.

Integral relations for EPR flows

Integral relations are common for the boundary layer approach and express the fundamental conservation laws for momentum, heat, and mass. Similar laws hold in easily penetrable roughness boundary layers.

Equations (3.33) can be rewritten in the following form:

$$\frac{\partial}{\partial x}\left[U(U-U_\infty)\right]+\frac{\partial}{\partial z}\left[V(U-U_\infty)\right]=\frac{\partial \tau}{\partial z}-f_*,$$

where $U_\infty = 1$ and the force f_* depends on the local U within the EPR, but vanishes over it. Integrating this differential equation over the EPR, between $z = 0$ and $z = 1$, and once again between $z = 1$ and $z = \infty$, we get two relations

$$\frac{dI_1}{dx}+V_h\left(U_h-U_\infty\right)=\tau_h-\tau_0-D, \qquad \frac{dI_2}{dx}-V_h\left(U_h-U_\infty\right)=-\tau_h, \tag{3.44}$$

where $I_1 = \int_0^1 U(U-U_\infty)dz$ and $I_2 = \int_1^\infty U(U-U_\infty)dz$ are the momenta of the flow through the EPR and outside it, consequently, and $D = \int_0^1 f(U)dz$ is the momentum dissipation due to the drag on EPR elements. Relation (3.44) expresses the fact that a longitudinal change of the momentum is mutually balanced by the dissipation D, by the shear stress on the boundaries $\tau_0 = \tau(x, 0)$ and $\tau_h = \tau(x, 1)$, and due to the outflow from the EPR, $V_h = V(x, 1)$. However, for the whole flow momentum $I = I_1 + I_2 = \int_0^\infty U(U-U_\infty)dz$, some terms cancel:

$$\frac{dI}{dx}=-\tau_0-D.$$

The integral relations obtained are useful to examine the accuracy of numerical schemes.

3.1.5 Viscous flow entrance to a duct with EPRs

The previous problem made use of the Prandtl's boundary layer approach. Although it is widely applied, it would be worth to examine this approximation on a test problem, where the complete Navier–Stokes equations should be solved. Here is such a test problem that has also its own significance.

Pressure pipelines can often include the inserts of porous or fibrous materials for the accompanying water purification. Two possible arrangements of infinite filtering layers, i.e. near the wall or in the middle of a pipeline, have been illustrated in Fig. 3.10. It takes a certain distance from the duct entrance until the flow reaches the steady state considered in subsection 3.1.1. This part of the chapter focuses on the entrance region of the flow that extends from just the EPR leading edge to the beginning of the steady state region. It gives the example of one of the simplest two-dimensional problems.

We emphasize again that the porous inserts are of infinite length and interpreted as an area $z \in [0, h] \cup [2H - h, 2H]$ with distributed local mass force $\vec{f} = -A\vec{U}|\vec{U}|^{a-1}$, for which $a = 1$ expresses the linear force law, and $a = 2$ is hold for the quadratic law [219]. This kind of a flow generalizes the flow problems for smooth or rough

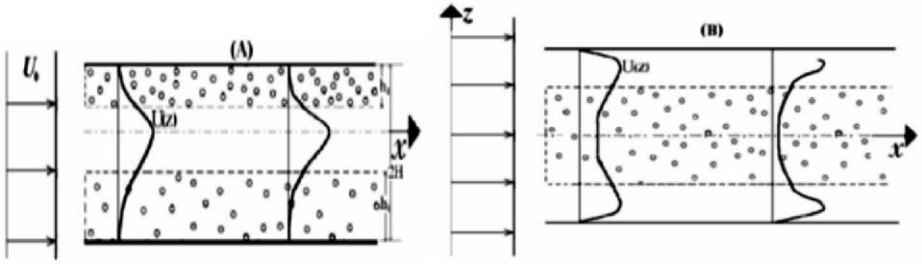

Figure 3.10: Two arrangements for the flow entrering a duct with infinite porous inserts: (A) penetrable roughness near walls, (B) insert in the middle of the duct. An entrance region should be calculated where the flow transforms from the uniform to steady state.

walls earlier studied by Schiller [564], Schlichting [566], and many authors of recent publications.

Schiller gave an engineering solution for how an initially uniform velocity distribution transforms along the tube with a smooth wall yet in 1932. Later on, in the 1950s, Schlichting obtained a more sophisticated solution based on the boundary-layer theory and determined the length of the duct's entrance region length as a function of the Reynolds number. The length mentioned above was found as

$$L_x = c \cdot \mathrm{Re} \tag{3.45}$$

with $c = 0.04$. Later publications gave somewhat different values of the coefficient c. Applicability of the boundary layer approach might be doubted for this problem but will be ascertained here. In the 1970s, the problem of a viscous flow entering a smooth wall duct served as a keystone problem for examining the first algorithms of numerical computer solutions of the complete Navier—Stokes equations [195, 537].

The problem considered here differs from the canonical problem by the presence of a source term (i.e. the force) on the right-hand side of the complete Navier—Stokes equations (3.29). This force vanishes outside the EPR, for $z \in (h, 1-h)$, is opposite to the local flow direction, and is proportional to some power of its velocity (here, we consider the linear or quadratic law). The boundary condition at the entrance $x = 0$ is evident, $U = 1$, $V \equiv 0$ (homogeneous velocity distribution). There are non-slip conditions on the walls $z = 0$ and $z = 1$. The further formulation of the problem is somewhat different for linear and quadratic EPRs.

Linear EPR force

The above boundary conditions are however insufficient for the unique determination of the two-dimensional flow field $U(x,z), V(x,z)$; an additional information about $p(x,z)$ is necessary. For the original problem with smooth walls, the problem closure was suggested by the transition to a steady-state flow solution at a certain sufficient distance L_x called the *entrance region length* [566, 605]. To this end, the pressure gradient can be taken constant $\frac{\partial p}{\partial x} = -\beta$, and the steady-state solution gives the relation $\beta = \frac{1}{1}\lambda = \frac{12}{\mathrm{Re}}$

[380, 566, 605]. In the case under consideration, this function should depend also upon the EPR height h and density A and is given by formulas (3.12), (3.13).

The formula for the duct's resistance coefficient looks as

$$\frac{1}{\beta} = \frac{\mathrm{Re}}{12}\{1 - 2h(4h^2 - 6h + 3) - \frac{24}{\chi^3}(\sinh(\chi h) + \pi\cosh(\chi h) - \pi - \chi h) - \frac{2 + \chi(2h-1)\sinh(\chi h) - 2\sinh(\chi h)}{6\chi^2\cosh(\chi h)}\}, \qquad (3.46)$$

where $\chi = \sqrt{A\mathrm{Re}}$ and $\pi = \frac{\chi(2h-1)-2\sinh(\chi h)}{2\cosh(\chi h)}$. Its graphical representation for different A and Re has been given in Fig. 3.14 (thin curves a). So, the last boundary condition required at the entrance region outlet reads as follows:

$$x = L_x, \qquad \frac{\partial U}{\partial x} = 0, \qquad V \equiv 0, \qquad \frac{\partial p}{\partial x} = -\beta. \qquad (3.47)$$

Problem (3.29) with the formulated boundary conditions possesses a unique solution over the length of the entrance flow region $0 \le x \le L_x$, but the value L_x, the unknown length of the entrance region, is to be chosen at a distance, where no further transformation of the flow field takes place. L_x can be easily adjusted in the course of the numerical performance.

The calculation algorithm was developed using the "artificial compressibility" and "markers and cells" methods [537]. Equidistant steps Δx and Δz as well as a fictitious time step Δt should have been chosen to ensure the accurate numerical results. The last parameters were considered as satisfactory if (*i*) discharge in the duct was conserved with the accuracy of 0.001%, and (*ii*) velocity profiles at the outlet really converged to the steady-state shape. We recall that the latter profile for any parameters δ and A can be represented analytically by formula (3.7) for a linear EPR, $k = 0$, so that this case suits for the examination of the algorithm. The number of numerical cells was chosen 80×40 for moderate values of A and Re; 160×80 cells are required if $A \cdot \mathrm{Re} < 1000$, but one needs 320×160 cells if $A \cdot \mathrm{Re} > 1000 - 2000$. Bigger values of $A \cdot \mathrm{Re}$ caused the algorithmic difficulties which are not overcome yet.

The typical course of the longitudinal velocity for a linear EPR with $A = 100$, $h = 0.3$ and $\mathrm{Re} = 10$ is shown in Fig. 3.12 (solid lines). The dotted lines given for contrast represent the velocity profiles that took place in the duct when the EPR is absent. The distributions of transversal velocities are transformed from a very distorted shape to $V(z) \equiv 0$ at the steady-state region; the shear stress distributions across the duct differ significantly from the case where the EPR is absent (smooth walls) but also approach the shape of steady-state distributions (3.8). Plots can be found in [222]. The following conclusions can be drawn.

The advancement of a flow through the duct is accompanied by its deceleration near the walls and by the EPR drag force, thus displacing the liquid to the center of the duct. This leads to the surprising maxima on the longitudinal velocity profiles, Fig. 3.12. The flow in the middle constantly accelerates, but its value tends to a certain limit reached in the main steady-state region. For this laminar case, $\nu = const$, the dimensionless axial velocity is known to reach the value 1.5 irrespective to Re [380], if the EPR is absent. In the case of interest, it depends upon all the parameters A, δ, and Re, can be

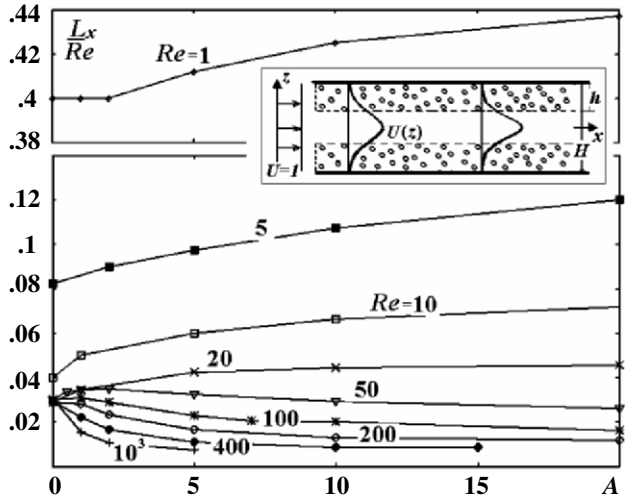

Figure 3.11: Entrance region length for a linear EPR near walls (see the insert) as a function of the EPR density A for different Reynolds numbers.

estimated analytically [222], and is shown in Fig. 3.13. At the end of the initial region, all the hydrodynamic profiles $U(z)$, $V(z)$, $\tau(z)$, and $p(z)$ reach a constant shape. The profile of the longitudinal velocity comes necessarily to a monotonic form.

A number of numerical calculations was carried out for various Reynolds numbers up to 2000, and the duct's initial region length was found as a graphical function $L_x = f(\mathrm{Re}; h, A)$ represented in Fig. 3.11. The dependence L_x vs A significantly differs for small and big Reynolds numbers Re. The value $A = 0$ corresponds to the case where the EPR is absent. It can be seen that, for $A \to 0$, all the curves arrive at the constant value $c \approx 0.03$, but the curves associated with small Reynolds numbers 1, 5, and 10. Hence, it can be concluded that the principal Schlichting's formula (3.45) has been justified for large Re despite it was derived from the boundary-layer approach, rather than from the complete Navier - Stokes equations.

All the formulas and numerical graphical dependences obtained can be verified in some limit cases. The cases $A \to 0$ or $h \to 0$ correspond to the case where the EPR vanishes. For instance, formula (3.46) leads to the known result $\lambda = 24/\mathrm{Re}$, and all the curves in Fig. 3.13 tend to the known value 1.5. If the EPR density A becomes bigger, one gets another limit case: the flow concentrates within the "narrower duct" $h \le z \le 1 - h$ as if the EPR became impenetrable.

Quadratic EPR force

The combination of analytical and numerical methods ensured the reliability of the algorithm, the results obtained, and the conclusions drawn. This is not possible in the case of a quadratic EPR (1.7), (1.8). First of all, condition (3.46), (3.47) was crucial for

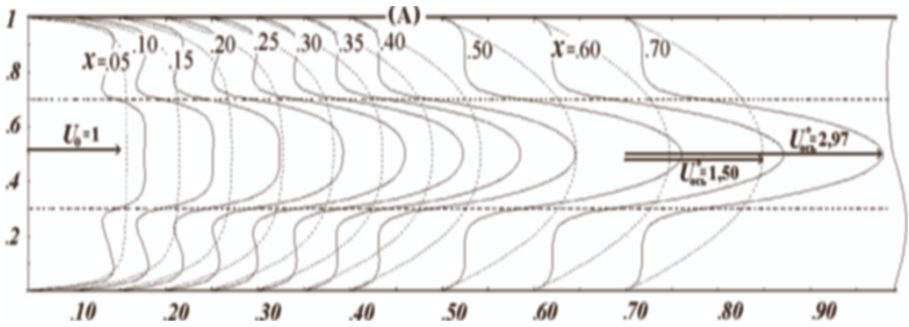

Figure 3.12: Longitudinal velocity transformation behind the leading edge of a duct with the EPR near walls $h = 0.3$, $A = 100$. The flow regime Re = 10 (solid lines) is compared with the case where the EPR is absent (dotted).

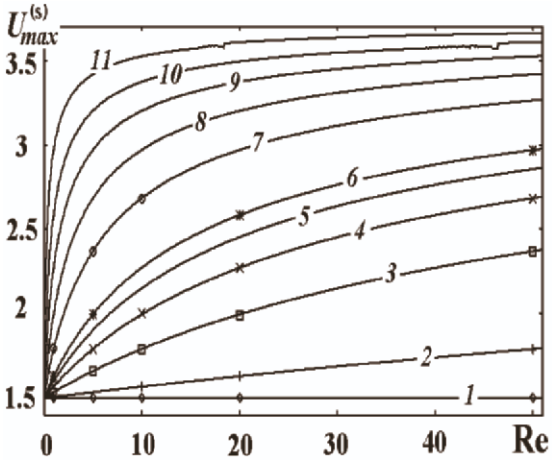

Figure 3.13: Maximum velocity being reached at the axis in the steady-state region of the duct with a linear EPR $h = 0,3$ near the walls: dots numerical solution, lines by the analytical formulae for $A = 0$ (curve 1); $A = 1$ (2); 5 (3); 10 (4); 15 (5); 20 (6); 50 (7); 100 (8); 200 (9); 400 (10) and $A = 1000$ (curve 11).

the mathematical closure of the problem formulation. For the quadratic force law, the value β should be previously found for particular problem parameters h, A and Re by means of the numerical solution of the ordinary boundary-value problem (3.1) with the power $a = 2$. By introducing the dimensionless variables, one comes to the boundary-value problem

$$\frac{1}{\mathrm{Re}}U_s^{"} + \beta = \begin{cases} AU_s^2, & z \in [0,h] \cup [1-h,1], \\ 0, & z \in (h, 1-h, 1) \end{cases} \tag{3.48}$$

$$z = 0 \qquad U_s = 0, \qquad\qquad z = 1 \qquad U_s = 0$$

where the subscript s denotes the relevance to the steady-state flow region.

Let the dimensionless velocity and the shear $\tau = \frac{1}{\mathrm{Re}}U_s^{'}$ take values of $U = U_h$ and $\tau = \tau_h$, respectively, at the symmetric force discontinuity interface $z = h$ and $z = 1 - h$ that are to be determined along with β. The solution of (3.48) in the middle duct's part can evidently be found as

$$\tau = \frac{1}{2}\beta(2z-1), \qquad U = U_h + \frac{1}{2}\beta\mathrm{Re}(z-h)(1-z-h),$$

so that the shear and the velocity are distributed, respectively, linearly and parabolically, which is typical of laminar flows. These give the dimensionless shear at the interface $\tau_h = \frac{1}{2}\beta(2h-1)$ being independent of the flow regime, i.e. of Re. For the flow within the EPR $z \in [o, h]$, one has the boundary-value problem

$$\frac{1}{\mathrm{Re}U_s^{"}} + \beta = AU_s^2, \qquad U_s(0) = 0, \qquad U_s^{'}(h) = \mathrm{Re}\cdot\tau_h, \tag{3.49}$$

what is the same for $z \in [1-h, 1]$. The boundary-value problem (3.49) is solvable for any $\beta > 0$. However, not all the β suit to the condition that the flow discharge through the duct be preserved and be expressed in dimensionless units as $q = \int\limits_0^1 U(z)dz = 2\int\limits_0^{1/2} U(z)dz = 1$. It is now clear that the solution algorithm for (3.49) can be taken as follows: for given h, A and Re, the boundary-value problem (3.49) is solved many times for a sequence of β with the calculation of the integrals $q(h, A, \mathrm{Re}; \beta)$, and β is chosen so that it satisfies the condition $q(h, A, \mathrm{Re}; \beta) = 1$. The graphical dependence $\beta = \beta(h, A, \mathrm{Re})$ calculated in such a way has been presented in the Fig. 3.14 for the quadratic law (thick curves b) in comparison with that for the linear law (thin curves a). The resistance turns out to be even less for the quadratic law than that for the linear one. Note that all the curves tend to $\beta \cdot \mathrm{Re} = 12$ if Re and $A \to 0$. If β is obtained, the numerical flow field performance is possible. They have not been presented here, as no basically new effects were discovered.

Work [2] also focused on the different roles of the linear and quadratic force terms called "macroscopic" and "microscopic retarding forces" in its model of an unsteady flow in a duct partially filled with porous material.

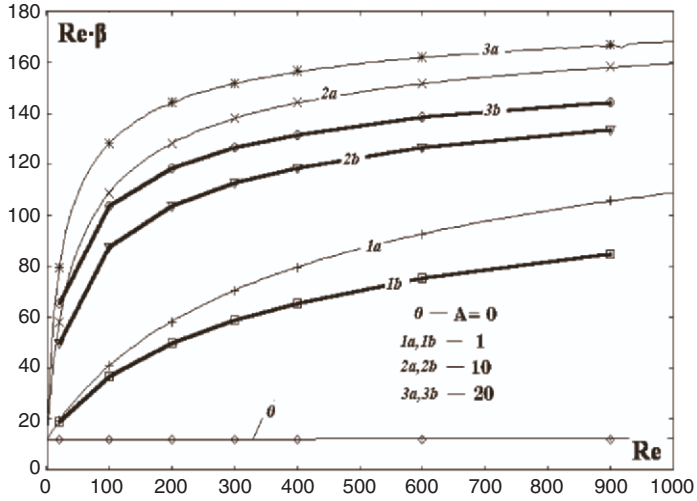

Figure 3.14: Hydraulic resistance $\lambda = 2\beta$ of a duct with EPR vs Reynolds number Re and EPR density A for linear (a) quadratic (curves b) force laws: 1 - $A = 1$, 2 - 10 and 3 - 20; EPR height $h = 0.3$.

3.1.6 Flow entrance into a duct with short EPR inserts

Finite-length porous inserts into a duct are of a special practical importance, Fig. 3.15. The vortical motion can or cannot appear behind the inserts depending on its height h, its length L_h, and the density A. Engineers get thus a means to control the flow. The special case $A = \infty$ can be treated as the well-known problem "backward facing step". The flow under consideration is so a generalization of the well-known problem.

No simplification can be used for the problem of the "backward facing penetrable step" but the full Navier—Stokes equations. Therefore, no solution is available to validate the numerical algorithm. To be aware of it, the numerical algorithm shortly described in the previous section was tested over the whole range of the above-mentioned problems. In this case, the outlet boundary condition $\beta = \frac{12}{\mathrm{Re}}$, which is associated with the steady flow in an infinite duct, was used. The results of two numerical performances for the flow regime Re = 100 and EPR dimensions $h = 0.3$ and $L_h = 1$, are shown in Fig. 3.16; the halves of flows in each case are symmetric. Let us analyze them.

If $A = 0$, one gets the known problem of the flow entering a duct with smooth walls. This flow is known to gradually change from a uniform velocity distribution to a parabolic profile known for the Poiseuille flow at the entrance region outlet $x \geq L_x$. No vortices appear in the flow.

No circulation was found even for penetrable steps with the density $A < 9$. However, yet for $A = 10$, a short circulation zone begins to appear behind the step (the bottom half of the Fig. 3.16). This circulation grows with the EPR density A. It becomes as large as shown in Fig. 3.16, the upper part for $A = 100$. There is the extended circulation zone in this case, and the intensity of the recirculation has also been increased by an order of magnitude.

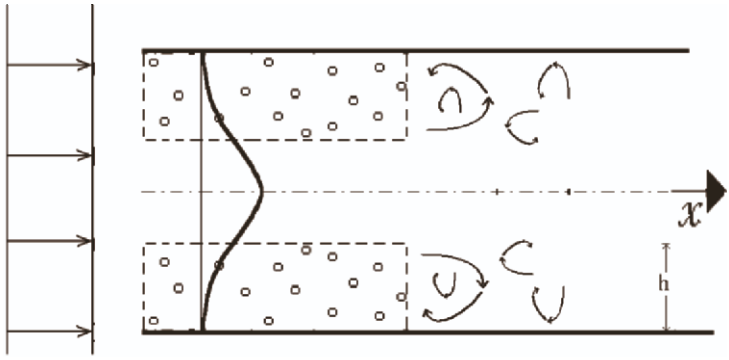

Figure 3.15: Flow entrance into the duct with a short porous insert: the vortical motion is possible after it.

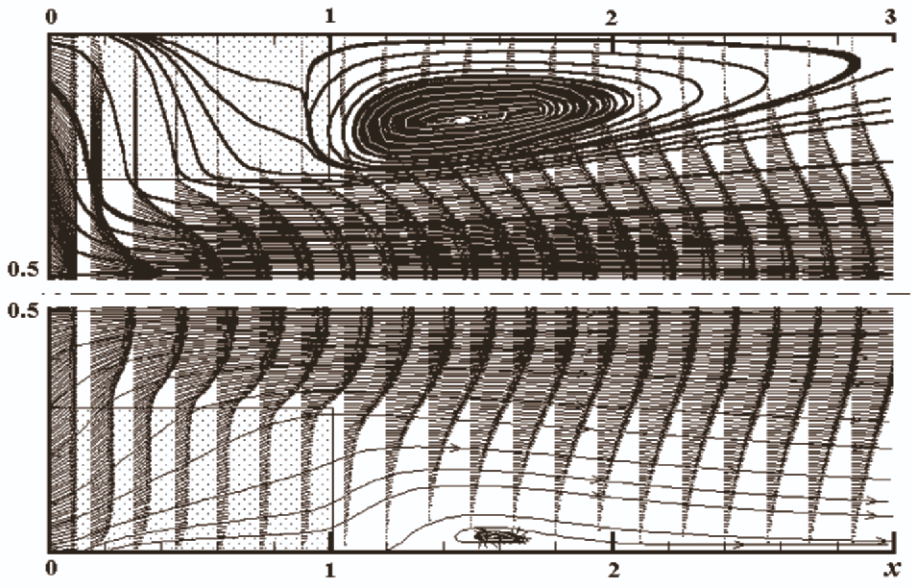

Figure 3.16: Two flow patterns behind penetrable inserts: in the case $A = 10$, bottom, the whirl is only slightly developed; in the case $A = 100$, top, there is a big whirl. Re $= 100$ and $h = 0.3$ (only the halves of the flow picture have been presented).

If the inserts become impermeable, $A \to \infty$, another known limit case appears. There is a number of data for the backward facing step that correlates with the "backward facing penetrable step."

3.1.7 Heat and mass exchange in immobile EPRs

The immobile easily penetrable roughness, EPR, is the heuristic model of a forest or some engineering devices like compact heat exchangers. For such applications, it is necessary to extend the model for including the heat or mass exchange of the EPR with the flow.

Let the flow running onto an EPR over a surface (Figure 3.8) be characterized by some undisturbed temperature $T(0,z) = T_\infty$, and the concentration of an admixture under consideration $C(0,z) = \rho_1 E_\infty$, kg/m^3. Elements of the EPR are still supposed to be small spherical obstacles with their own temperature $t(x,z)$ and to make up of an evaporative material. Heat and mass exchange arises between obstructions and the neighbouring flowing medium. It is assumed that the evaporative material in the gaseous state is always contained near the surface of obstructions with the concentration $c = \rho_1 e(x,z)$ that corresponds to the saturation condition determined by t, the local obstruction temperature. The rate of evaporation from a single obstruction and the rate of local heat exchange are

$$I_E = \alpha_E \rho_1 (e - E) S_0 \qquad \text{and} \qquad I_H = \alpha_H (t - T) S_0 \tag{3.50}$$

where S_0 is the total area of an individual obstruction ($S_0 = 4\pi r^2$ for a sphere), α_H and α_E are the heat and mass exchange coefficients. These coefficients are assumed to be known from handbooks; for the "alive objects" like leaves, they are functions of the vegetation state studied in biophysics. Heat and mass fluxes (3.50) are positive (directed from an obstruction to the flow) if $e > E$, $t > T$.

Fluxes from individual obstructions (3.50) are all radiated into a unit volume of the flowing medium (air), so that they need to be multiplied by the obstacle concentration n to estimate the substance income rate, like it was done for forces by (1.6):

$$\begin{aligned} i_H &= \lim_{\Omega\to 0} \frac{\sum I_{Hi}}{\Omega} = \frac{n I_{Hi}}{\Omega} = \alpha_H (t - T) s_0 \\ &\text{and} \\ i_E &= \lim_{\Omega\to 0} \frac{\sum I_{Ei}}{\Omega} = \alpha_E (e - E) s_0. \end{aligned} \tag{3.51}$$

These sources act within the EPR but vanish outside it. This means that discontinuous terms like (1.7) labelled by a "star" $*$ should be used to write the equations uniquely for the internal and external flows:

$$i_{H*} = \begin{cases} \alpha_H (t - T) s_0, & z \in [0,h], \\ 0, & z > h \end{cases} \qquad i_{E*} = \begin{cases} \alpha_E (e - E) s_0, & z \in [0,h], \\ 0, & z > h \end{cases} \tag{3.52}$$

Note also the difference between the specific frontal area used in (1.8) and the specific full surface area $s_0 = \lim \frac{\sum S_{0i}}{\Omega}$, m^2/m^3 appeared for mass and heat exchange provided the volume under consideration $\Omega \to 0$.

The further transportation of heat energy and the evaporated substance over the whole flow domain takes place due to the convective motion of the surrounding medium, being thus governed by the equations

$$\rho_1 c_1 \left(U\frac{\partial T}{\partial x} + V\frac{\partial T}{\partial z} \right) = \frac{\partial j_H}{\partial z} + i_{H*}(t, T; z), \tag{3.53}$$

$$U\frac{\partial E}{\partial x} + V\frac{\partial E}{\partial z} = \frac{\partial j_E}{\partial z} + i_{E*}(e, E; z), \tag{3.54}$$

where c_1, $J/(kg \cdot {}^oC)$ is the thermal capacity of air, and the local flows of heat and mass in air are

$$j_H = -D_H \frac{\partial T}{\partial z}, \qquad j_E = -D_E \rho_2 \frac{\partial E}{\partial z}, \tag{3.55}$$

where D_H, $Wt/(m \cdot {}^oC)$, and D_E, m^2/s are the heat and mass conductivity coefficients (to be also taken from handbooks).

The following boundary conditions are to be imposed on the system of parabolic partial differential equations of the second order (3.53), (3.54). The flow is homogeneous at the entrance; the temperature and concentration have been prescribed on both horizontal boundaries:

$$\begin{gathered} x = 0 \qquad T = T_\infty, \quad E = E_\infty, \\ z = 0 \qquad T = T_0, \quad E = E_0, \qquad z \to \infty \qquad T = T_\infty, \quad E = E_\infty. \end{gathered} \tag{3.56}$$

Because of the discontinuity of the right-side sources, the conjugation conditions should also be imposed on the interface $z = h$, which means the continuity of substances and their flows:

$$\begin{gathered} T(x, h-0) = T(x, h+0), \qquad j_H(x, h-0) = j_H(x, h+0), \\ E(x, h-0) = E(x, h+0), \qquad j_E(x, h-0) = j_E(x, h+0). \end{gathered} \tag{3.57}$$

Bearing the similarity of the equations for air temperature T and moisture concentration E in mind, we will consider here only heat processes.

The dimensionless variables

$$\overline{T} = \frac{T - T_\infty}{T_\infty - T_0}, \qquad \bar{t} = \frac{t - T_\infty}{T_\infty - T_0}, \qquad \overline{j_H} = \frac{j_H h}{D_H(T_\infty - T_0)} \tag{3.58}$$

are useful along with (3.32), so that the dimensionless fluid temperature varies between 1 and 0, and it is valid for the flow $\overline{j_H} = -\frac{\partial \overline{T}}{\partial \overline{z}}$. One derives finally the following dimensionless boundary-value problem (the bars over symbols are dropped):

$$U\frac{\partial T}{\partial x} + V\frac{\partial T}{\partial z} = \frac{1}{\mathrm{Pr}}\frac{\partial^2 T}{\partial z^2} - \begin{cases} A_H(T - t), & z \in [0, 1] \\ 0, & z > 1 \end{cases} \tag{3.59}$$

$$z = 0 \quad T = 0, \qquad z \to \infty \quad T = 1, \qquad x = 0, \quad T = 1; \tag{3.60}$$

$$T|_{1-0} = T|_{1+0}, \qquad j|_{1-0} = j|_{1+0}$$

with two new dimensionless criteria

$$A_H = \frac{\alpha_H n S_0 h}{\nu} \qquad \text{and} \qquad \mathrm{Pr} = \frac{\nu}{D_H}. \tag{3.61}$$

Prior to the solution of this problem, the fluid fields $U(x, z)$ and $V(x, z)$ should be determined. The numerical investigation of the heat exchange problem was done by the finite-difference method. Its results depend on how the obstruction temperature $t(x, z)$ is parametrized.

First mode of obstruction temperature

The first mode of the obstruction temperature takes place when the latter is kept constant and equal to the wall temperature. In the dimensionless form, we have

$$t = 0. \tag{3.62}$$

In this case, the first fluid motion equation (3.33) and the boundary conditions (3.34), (3.35) are equivalent to the conjugation boundary-value problem (3.60) if $A = A_H$ and $\mathrm{Pr} = 1$, so that the profiles of $U(z)$ and $T(z)$ coincide. This is the so-called Reynolds analogy between fluid mechanics and heat (mass) fields.

If $A \neq A_H$ or $\mathrm{Pr} \neq 1$, the profiles $T(z)$ are separated from $U(z)$, and the Reynolds analogy is not valid furthermore, as it is shown in Fig. 3.17,A. However, the picture of the temperature profile transformation over the surface remains similar to the hydromechanic picture:

- at the entrance cross section, the flowing medium is uniformly warm, $T(0, z) = 1$; having met the "cold" obstructions and the wall, the fluid loses its thermal energy; the zone of cooled fluid widens with x; a heat flow from the warm external flow to the cooled internal one appears;
- at short distances x, the external heat flow influences only the top levels of the internal flow, but its middle levels do not "feel" it; there is the core of the thermal initial region where the main process is the sink of flow heat to cold EPR elements;
- with growing x, the zone of the EPR influenced by the external warm flow grows and involves finally all the EPR; the flow temperature stops to decrease and comes to the equilibrium state with unchanged profiles within the EPR; the thermal main region extends infinitely.

The structure of the thermal flow picture is thus similar to the fluid mechanical structure in Fig. 3.8. It is possible to find out some analytical estimations for particular regions.

Thermal initial region

The thermal initial region is the region just after the EPR leading edge, where the flow velocity decelerates by (3.37), and the flow temperature is changed due to only the sinks on obstructions,

$$U\frac{dT}{dx} = -A_H(T-t), \qquad t \equiv 0.$$

The solution of the last equation gives the law for a temperature decrease on the thermal initial region:

$$T = (1 - Ax)^{A_H/A}. \tag{3.63}$$

In the case $A_H = A$, the length of the thermal initial region equals the hydrodynamic initial region. If $A_H > A$, the temperature decreases faster that the velocity, so the length of the thermal initial region is shorter than that of the hydrodynamic one. The region ends, when T becomes very small, $T = \varepsilon$. The estimation of its length can be made by the formula

$$L_H = \frac{1}{A}\left(1 - \varepsilon^{A/A_H}\right).$$

(If, for example, $A/A_H = 5$ and the tolerance $\varepsilon = 0.005$, the ratio of both lengths is $L_H/L = -0.45$). In the case $A_H < A$, the temperature decreases slower than the velocity; the thermal initial region is longer that the hydrodynamic one.

Note that the Prandtl number has no effect on the initial region. The regularities of mass exchange are similar to those of heat exchange, except for that the criterion number is the Schmidt number Sc.

Main region of EPR

The main region of the EPR is the region where intrinsic profiles do not depend on the longitudinal coordinate x. If so, the left-hand side of Equation (3.60) vanishes, and the latter takes the following simple form:

$$\begin{aligned} &T^{"} - A_H\mathrm{Pr}\cdot(T-t), \\ &z = 0 \qquad\quad T = 0, \end{aligned} \tag{3.64}$$

where $t \equiv 0$ in the case in question. This yields that the flow field does not influence the thermal main region; the single parameter of the problem is

$$\chi_H^2 = A_H\mathrm{Pr} = \frac{\alpha_H n S_0 h}{D_H},$$

as in the relevant hydromechanic problem (3.40). The solution of (3.64) can be presented, similarly to (3.41), in the form

$$T(z) = T_h\frac{\sinh(\chi_H z)}{\sinh(\chi_H)}, \tag{3.65}$$

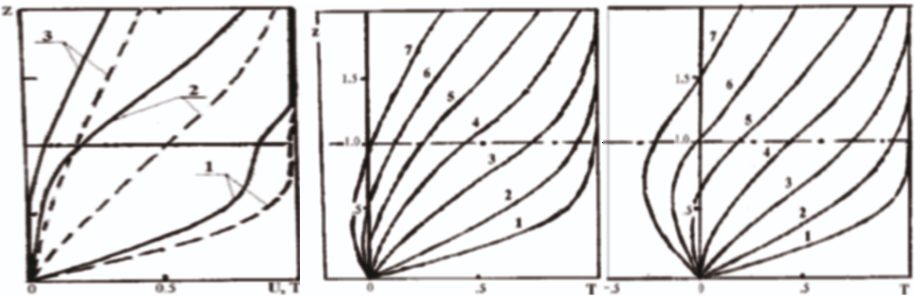

Figure 3.17: Computed flowing medium temperatures (solid lines) for different modes of the obstruction temperature: (A) Comparison with velocities (dashed) in the case of (3.83), Pr = 1, but $A_H = 10$ and $A = 1$; (B) Obstruction temperature by (3.88) with $t_0 = -0.5$; (C) Thermal flow from obstructions by (3.89). Profiles relate to the cross sections: 1 – $x = 0.02$, 2 – 0.05, 3 – 0.1, 4 – 0.2, 5 – 0.4, 6 – 0.8 and 7 – $x = 1.6$.

where the temperature on the EPR top $T_h = T(x, 1)$ is an auxiliary parameter to be found by performance of the whole thermal boundary layer. This profile has been confirmed by numerical performances of the complete problem (3.60). The parameter χ_H has meaning of the "thermal EPR density"; profiles of $T(z)$, for which $T(z) = \varepsilon \approx 0$, become possible (solid line 3 in Fig. 3.17,A), and this zone of "thermal stagnation" becomes thicker with increase in χ_H. In practice of spraying coolers, there is no cooling in this zone, and engineers should avoid the designs with such zones. Formulae (3.65) allow one to find out the EPR level, where the stagnation begins:

$$l_H = \frac{1}{\chi_H} \operatorname{asinh}(\varepsilon \cdot \sinh \chi_H) \approx 1 + \frac{1}{\chi_H} \ln \varepsilon. \tag{3.66}$$

Consequently, the depth of the stagnation zone is $d_H \approx -\frac{1}{\chi_H} \ln \varepsilon$.

Other modes of obstruction temperature

Other modes of obstruction temperature are possible, when the temperature of an obstruction $t(z)$ is governed by some other laws. For instance, this temperature can be kept constant but different from that of the wall $\overline{T} = 0$:

$$t \equiv t_0 \neq 0. \tag{3.67}$$

The temperature distributions in the thermal boundary layer over an EPR with $t_0 = -0.5$ (i.e. obstructions are colder than the wall) have been shown in Fig. 3.17,B. The thermal distributions in such a flow are much complicated. However, analytical estimations are possible if the structure of the boundary layer is taken into account.

One finds that a decrease of the temperature over the initial region core follows the formula

$$T(x) = t_0 + (1 - Ax)^{A_H/A}.$$

On the main thermal region of the EPR, the following vertical temperature distribution has been found:

$$T(z) = T_h \frac{\sinh(\chi_H z)}{\sinh(\chi_H)} + t_0 \left((1 - \cosh \chi_H z) - (1 - \cosh \chi_H) \frac{\sinh(\chi_H z)}{\sinh(\chi_H)} \right).$$

Such profiles can have a point of inflexion.

In another practical case, the temperature of obstructions is controlled to ensure a constant heat flow (for instance, electric current heats obstructions in a wind-tunnel EPR setup). Because of this, the source term in (3.60) has a constant value

$$A_H(T - t) = const = i_0. \tag{3.68}$$

The latter relation means that the temperature of obstructions changes but always reflects the temperature of the flowing medium:

$$t = T - \frac{i_0}{A_H}.$$

The flowing medium itself needs the numerical computations, whose results have been presented in Fig. 3.17,C. The complicated shape of distributions depends on the hydrodynamic and thermal parameters of the EPR: A, Re, A_H, Pr, and i_0. However, some forecasts can be done analytically.

The flowing medium temperature decreases over the initial region core by the law

$$T(x) = 1 - \frac{i_0}{A_H} \ln(1 - Az). \tag{3.69}$$

On the main region, the internal portions of vertical temperature profiles are stabilized as the parabolic profile

$$T(z) = T_h z + \frac{i_0}{2} \mathrm{Pr} \cdot z(z - 1), \tag{3.70}$$

where the auxiliary parameter T_h requires a full numerical computation. Profile 7 in Fig. 3.17,C turned out to be very close to the stabilized shape and fits well the last formula.

Conclusion to section 3.1

The easily penetrable roughness of a rigid structure, e.g. a canopy build from particles or obstructions of the same size that are ‘trapped’ in space, is a simplest possible structure. It resembles a forest canopy. The immobile EPR was considered under the flow conditions in a duct and in boundary layer. A sequence of methodological problems was considered that illustrated how to model penetrable layers in the flow by means of a distributed force and/or heat and mass sources.

Many of the discovered flow features take also place in more complex structures with penetrable roughness, or canopy. Even for forests, one needs to account for bending trees and the motion of leaves. It was mentioned in Section 1.2.1 that several models were suggested for flexible canopies [305, 184, 408, 585, 652], but the problem has unlikely been solved yet. A number of complex structures is considered in the next section.

3.2 EPRs made up of mobile elements

The spraying cooling systems are another example of a "canopy", for which one needs to know not only the flow transformation but also the transformation of the canopy itself. A suggestion was made in Section 1.4 to treat air as a continuous carrier medium and the droplets as another continuous medium being carried by the first one. Several relevant mathematical models for such "*droplet EPR*" are studied in this chapter.

Several peculiarities of real droplet layer media should be accounted for in the models. The most important feature is the ability of droplets to be drifted by the horizontal wind, while they fall vertically under the action of the gravitation force. It has been accounted for in the first model.

Another feature is the diversity of droplet sizes in a real spraying cooling system. The droplets sized from several microns to 1 *mm* "live" in the droplet layer up to several minutes before they fall down on the channel water surface and, because of evaporation, significantly change their radii during the lifetime. However, these droplets do not contribute significantly to the total cooling of water and are so omitted in the consideration. The droplets sized initially more than 7–8 *mm* break up very easily into smaller droplets and are also not accounted for as well. The true spectrum of droplet diameters $2r$ lies between 1 and 6–7 *mm*; these droplets do not change their size being cooled by $7^\circ C$–$15^\circ C$ during their "lifetime" of 2–4 seconds while falling down to the water collector surface. Droplets of the latter range have been taken into account. However, droplets of every radius r have their particular speeds. Therefore, it is worth to consider as many droplet media as many are their sizes. Each of them contributes to the distributed force $\vec{f}$ in the dispersed droplet layer model.

Furthermore, droplets of every radius are in an intricate motion within the spraying system droplet layer. Some of them move from the nozzles up, another ones fall down, by having reached the culmination. Both kinds of droplets are accounted as separate continuous media in the multispeed droplet layer model.

All these models will broaden the conception of easily penetrable roughness, the EPR.

3.2.1 Mathematical model of a "droplet EPR"

In the simplest case, all the droplets are of the same size and the "droplet canopy" affects the wind flow like an easily penetrable roughness mathematically expressed by the conjugation problem (3.33)–(3.35). The boundary layer approach is thus accepted. The distributed mass force $\vec{f}$ should depend, however, not on the local velocity $\vec{V}$ of the carried medium alone, but on the relative velocity between the two media $\vec{V} - \vec{v}$. To get $\vec{f}$, the individual force (1.14) should be multiplied by the concentration of droplets n.

The droplet medium is precisely governed by equations (1.15) and (1.16) which are linked with each other and are very difficult for investigation. Bearing in mind that only "heavy" droplets should be accounted for, let us use the appropriate law of vertical droplet motion instead of the second equation for the vertical droplet speed v. Imagine the simplest situation that the droplets are constantly generated at the height of fountains $z = h$ with intensity q, $1/(m^2 s)$.

After being born, all the droplets fall down towards the water collection surface $z = 0$ with the velocity $v = v(z)$. Several assumptions can be suggested.

Constant fall-down speeds (light droplets)

The motion of a mass in the resistive atmosphere was well studied in connection with rain droplets and cannon shell trajectories. It is known particularly that any body reaches its constant fall-down speed, $v(t) \to \mathbf{v}$, the "pancake speed". If a droplet of radius r with the frontal area $S = \pi r^2$ moves in the vertical direction Oz only, Eq. (1.16) takes the form[3]

$$m\frac{dv}{d\tau} = F_z - mg \tag{3.71}$$

with the aerodynamic resistance force (1.14) in the form $\vec{F}_z = -\frac{1}{2}c_F\rho_1 v^2 S$, where the drag coefficient is often given by the empirical relation [304]

$$c_F = \frac{24}{\mathrm{Re}_v}\left(1 + 0.065\mathrm{Re}_v{}^{2/3}\right)^{3/2}, \qquad \mathrm{Re}_v = \frac{2rv}{\nu}. \tag{3.72}$$

The latter takes the limit forms $c_F = \frac{24}{\mathrm{Re}_v}$ in the case of the linear force law (laminar motion Re << 1, very small droplets) or $c_F = \frac{24}{\mathrm{Re}_v}0.065^{3/2} \approx 0.40$ in the case of the quadratic force law (fully turbulent streamlining, Re >> 1, droplets of a significant size $3\ mm < 2r < 7\ mm$). To find the limit speed value $\mathbf{v}$ such that $v(t) \to \mathbf{v}$, one needs to assign $\frac{dv}{dt} = 0$ in equation (3.71). Analytical solutions with the latter assumptions for $c_F = c_F(\mathrm{Re}_v)$ yield the formulas

for linear force law	*for quadratic force law*
$\mathbf{v} = -\frac{16}{3a}\left(\frac{\rho_2}{\rho_1}\right)\cdot\frac{r^2 g}{\nu}$,	$\mathbf{v} \approx -\sqrt{\frac{20}{3}\left(\frac{\rho_2}{\rho_1}\right)\cdot gr}$

(3.73)

with the coefficient $a = 24$. The "pancake speed" is thus proportional to the droplet radius squared or the root of it depending on the force law assumed. Its value is negative in the coordinate system accepted here, as droplets move oppositely to the Oz direction. The first formula is recommended for very small particles, while the second for big ones. Both formulas, however, give approximately the same dependence on the radius and the density ratio, if assumed formally,

$$a = \frac{8}{\sqrt{15}}\sqrt{\left(\frac{\rho_2}{\rho_1}\right)\left(\frac{r^2 g}{\nu^2}\right)}.$$

The "pancake speed" is reached after the particle (the droplet) passes the distance $z_p \approx 10\ln\left(\varepsilon\left(\frac{\rho_2}{\rho_1}\right)r\right)/3$. However, it is worth to accept the constant fall-down velocity in the coarse model from the very beginning.

[3]Notation τ in the sense of time has been used only in (3.71), (3.83), and (3.93). Otherwise, τ means the shear stress.

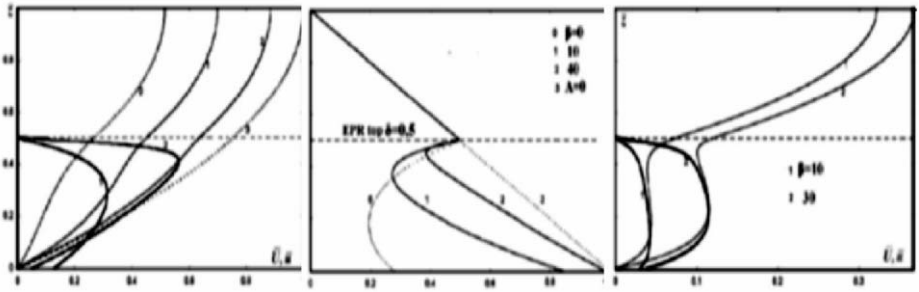

Figure 3.18: Profiles of (A) air (thin lines) and droplet velocities (thick), and (B) shear stress in the duct flow with droplet EPR $A = 25$ and $\beta = var$. (C) Profiles of air (thin) and droplet velocities (thick lines) for $A = 400$. Relative height of the EPR $\delta = 0.5$.

A mathematical model of the flow influenced by the droplet layer with easily penetrable roughness should include the equations for a carrying flow given in Section 3.1.4 along with Eq. (1.15) for the carried medium with the prescribed vertical velocity $v = -v(z)$. Thus, we arrive at the following system of equations:

$$U\frac{\partial U}{\partial x} + V\frac{\partial U}{\partial z} = \frac{1}{\rho_1}\frac{\tau}{\partial z} - nk(U-u), \qquad \frac{\partial U}{\partial x} + \frac{\partial V}{\partial z} = 0,$$

$$m\left(u\frac{\partial u}{\partial x} - v\frac{\partial u}{\partial z}\right) = \rho_1 k(U-u). \tag{3.74}$$

Here, the linear force law has been accepted; "minus" in the last equation emphasises that the prescribed vertical velocity of droplets is always negative. It is worth to examine the model recently obtained for the imaginative simplest situation (see Section 3.2.1).

One-dimensional flow in a duct

The flow model (3.74) takes a simple form if such EPR structures were placed in a plane duct where a pressure gradient $p^{'}$ drives the motion. In this case, one has the one-dimensional motion described by ordinary differential equations; so, similarly to (3.1), the motion within the infinite droplet layer is described as follows:

$$\nu\frac{d^2U}{dz^2} - nk(U-u) = p^{'}, \qquad \nu m\frac{dU}{dz} = -\rho_1 k(U-u).$$

With the scales by (3.3), one derives the following conjugation boundary-value problem that generalizes problem (3.6):

$$\begin{array}{ll} \text{if } z=[0,\delta] & \text{if } z=[\delta,1] \\ U^{"}-A(U-u)=-2, & U^{"}=-2, \\ u^{'}=-\beta(U-u), & z=1 \quad U^{'}=0, \\ z=0 \quad U=0, & \end{array} \tag{3.75}$$

$$U(\delta-0)=U(\delta+0), \qquad \tau(\delta-0)=\tau(\delta+0). \tag{3.76}$$

Here, the dimensionless shear is $\overline{\tau}=\frac{\tau}{\tau_w}=\frac{1}{2}\frac{d\overline{U}}{dz}$, but, in (3.75), (3.76)), the bars over symbols, which stand for dimensionless quantities, have been dropped. The new dimensionless parameter additional to (3.6) is given by

$$\beta=\frac{\rho_1 kh}{mv(z)} \tag{3.77}$$

and is reciprocal to the mass m.

It is very easy to make sure of that the conjugation boundary-value problem (3.75), (3.76) has only a unique solution. In fact, both the left and right systems provide the only solution in each of the adjacent intervals if they are supplemented by the first conjugation condition $U(\delta)=U_h$. For each given value U_h, both solutions give the shear stresses on the interface that become functions of U_h: $\tau(\delta\pm 0)=\frac{1}{2}U^{'}(\delta\pm 0;U_h)$. Only one value U_h can be found to satisfy the second conjugation condition (3.76) that becomes a transcendental equation.

Let us solve problem (3.75), (3.76) now. The right equation (3.75) can be evidently solved providing the linear shear stress in the duct over the droplet layer EPR (its value on the interface $\tau_h=\tau(\delta+0)=1-\delta$ contributes to the internal motion along with the pressure gradient $\overline{p^{'}}=1$) and the parabolic velocity profile in the duct's section free of EPR. The left system of equations admits the first integral

$$\tau=(1-z)-\frac{1}{2}\left(\frac{A}{\beta}\right)u \tag{3.78}$$

with the physical meaning that the droplet EPR changes the canonical shear distribution by an addition proportional to the droplet velocity profile.

The left system of equations (3.75) admits also an analytical solution that can be represented in the form

$$\begin{aligned} U &= 2\tau_0\left[Ag_2(z)+\frac{\beta}{A}-u_0\left[Ag_1(z)-1\right]-2Ag_3(z)+\frac{2}{A}(1-\beta z)+\frac{2\beta}{A^2}\right], \\ \tau &= A\tau_0 g_1(z)-\frac{1}{2}Ag_0(z)-Ag_2(z)-\frac{\beta}{A}, \\ u &= u_0\left[\beta g_0(z)+1\right]-2\tau_0\beta\left[g_1(z)-\frac{1}{A}\right]+2\beta g_2(z)+2\frac{\beta}{A}\left(\frac{\beta}{A}-z\right) \end{aligned} \tag{3.79}$$

with the auxiliary functions generalizing the hyperbolic ones (if $\beta=0$):

$$g_j(z) = \frac{1}{\chi_1 - \chi_2}\left(\frac{1}{\chi_1^j}e^{\chi_1 z} - \frac{1}{\chi_2^j}e^{\chi_2 z}\right), \qquad j = 0,\ 1,\ 2,\ 3$$

and with the characteristic roots $\chi_i = -\frac{1}{2}\beta - (-1)^i D$, $D = \sqrt{\beta^2 + 4A/2}$, $i = 1, 2$. Another auxiliary parameters can be determined from the conjugation condition (3.76):

$$\tau_0 = \tau(0) = \frac{A\{Ag_2(\delta) + \beta g_0(\delta)\} + A(1-\delta) + \beta}{A\{Ag_1(\delta) + \beta g_0(\delta)\}},$$
$$u_0 = u(0) = 2\beta\frac{A^2\{g_1(\delta) - g_2(\delta)\} - A(1-\delta) - 1}{A^2\{Ag_1(\delta) + \beta g_0(\delta)\}}. \tag{3.80}$$

The above-presented formulas give a solution of the conjugation boundary-value problem (3.75), (3.76) for constant coefficients A, $\beta = const$ in the final form. Some typical $1d$-distributions have been shown in Figure 3.18. Dotted line 0 denotes the air velocity distribution if there were no motion of EPR elements, $\beta = 0$. The dotted line 3 corresponds to that if there were no EPR in the duct at all, $A = 0$ or $\delta = 0$. Carrying flow velocity profiles 1 (for $\beta = 10$) and 2 (for $\beta = 40$) lie between them. It can be verified analytically from (3.79) that the case $\beta \to \infty$ corresponds to no EPR at all in accordance with (3.77) (the droplet mass tends to zero, $m \to 0$) and with (3.78).

The same Fig. 3.18,A shows how the droplets change their velocity while moving from "the top of fountains" $z = h$ to the "water collection surface" $z = 0$. The maxima on profiles are typical. The initial horizontal speed of a droplet equals zero at the moment of its appearance at the level $z = h$, so that the droplets are accelerated by the flow. Falling down, the droplets find themselves on levels, where their speed exceed the speed of the carrying medium, so that they are decelerated and return their kinetic energy back to the flow. We may conclude that the mobility of EPR elements results in a new mechanism of energy exchange, from the flow to particles at first, and then from them back to the flow. Such a mechanism was discovered by Bortkovskii in the analysis of the droplet-wind interaction over the storming ocean [70].

Because of the exchange mechanism announced, the maximum and minimum can also appear on the profiles of the carrying medium, as it is seen in Fig. 3.18,C for the EPR density $A = 400$. Note that such a phenomenon was absent in the case of immobile EPRs except for the initial region of the boundary layer (Section 3.1.4). Relation (3.78) can be useful in explaining the following effect: the variation of A/β can force $\tau(z)$ to change its sign. This gives $\tau = 0$ at some points and corresponds to the turning point of the $U(z)$ profile, which is hoped to bring more light to the discussion of the "secondary maximum" phenomenon [572], see Sections 1.1 and 5.1 for comparison.

The one-dimensional analysis like that presented above will be useful for testing the more advanced models of easily penetrable roughnesses.

Constant acceleration fall (heavy droplets)

Droplets with a constant fall-down speed can be figuratively called "light" droplets. Another appropriative law of the vertical droplet motion, say for "heavy" ones, is their fall with the constant acceleration, which leads to the floating model parameters $A(z)$

and $\beta(z)$. Indeed, in accordance with Eqs. (3.71) and (3.72), each particle falls with the constant acceleration at first. However, heavy particles reach the limit speed (3.73) very slowly so that their vertical speed increases as $v = \sqrt{2g(h-z)}$. This causes parameter (3.77) to vary with the coordinate.

Consider now the concentration of droplets on various levels of the droplet layer. The droplets enter "the lid" of a control volume $(z - \Delta z/2, z + \Delta/2)$ with the speed $v_1 = v(z - \Delta z/2)$ but leave its "bottom" with the speed $v_2 = v(z - \Delta z/2)$, $v_1 < v_2$. That is why the local concentration of droplets $n = \frac{q}{v(z;r)}$ turns out to vary with the height along with the dimensionless parameter (3.6). The final forms for both dimensionless parameters are

$$A = \frac{A_0}{\sqrt{\delta - z}}, \qquad \beta = \frac{\beta_0}{\sqrt{\delta - z}} \cdot \tag{3.81}$$

Although they vary with z, the ratio $A(z)/\beta(z)$ remains constant for heavy droplets. Therefore, relation (3.78) still holds as well as some conclusions stated above.

3.2.2 Boundary layer formed by a droplet layer

Consider now the boundary layer flow over the surface with a droplet EPR of the height h over it; Fig. 3.8 illustrates the physical situation. Both the carying and carried media are governed by the system of equations (3.74) determining the two-dimensional fields $U(x,z)$, $V(x,z)$ and $u(x,z)$ in the boundary-layer approach (with $\tau(x,z) = \rho_1 \nu_T \frac{\partial U}{\partial z}$). The non-slip velocity on the surface $z = 0$, and the asymptotics $\lim\limits_{z\to\infty} U = U_\infty$ along with the homogeneous entrance velocity profile $U(z,0) = U_\infty$ are the regular boundary conditions for this problem. For the carried medium described by partially differential equations of the first order, the boundary condition on the interface was accepted earlier,

$$u(x,h) = 0, \tag{3.82}$$

but one more condition for the entrance droplet velocity distribution $u(0,z)$ is required for the boundary layer flow.

Droplets at the flow entrance find themselves in a homogeneous air flow. That is why equation (3.71) can be applied with $U \equiv U_\infty$ in the linear force law. So one gets the droplet horizontal velocity distribution while they fall down for the time τ:

$$u_0 = u\,(0, z(\tau)) = U_\infty \left[1 - exp\left(-\frac{\rho_1 k}{m}\tau\right)\right]. \tag{3.83}$$

This distribution is valid both for the constant, $v(z) = const = v$, and uniformly accelerated, $v(z) = \sqrt{2g(h-z)}$, fall-down speeds. However, the last assumptions give different dependences between the time and the traversed path,

$$\tau = h - \frac{z}{v} \qquad \text{or} \qquad \tau = \sqrt{\frac{2(h-z)}{g}}. \tag{3.84}$$

For the general analysis, the first formula has been accepted.

All the above information is sufficient for the complete formulation of the problem. Introducing the dimensionless droplet velocity

$$\overline{u} = \frac{u}{U_\infty}$$

along with the dimensionless variables (3.32), we obtain two systems of dimensionless equations that generalize problem (3.33):

$$\begin{array}{cc} 0 \le z \le 1 & 1 \le z < \infty \\ \left\{ \begin{array}{lcl} U\dfrac{\partial U}{\partial x} + V\dfrac{\partial U}{\partial z} & = & \dfrac{\partial \tau}{\partial z} - A(U-u), \\ \dfrac{\partial U}{\partial x} + \dfrac{\partial U}{\partial z} & = & 0, \\ u\dfrac{\partial u}{\partial x} - \sigma\dfrac{\partial u}{\partial z} & = & B(U-u) \end{array} \right. & \left\{ \begin{array}{lcl} U\dfrac{\partial U}{\partial x} + V\dfrac{\partial U}{\partial z} & = & \dfrac{\partial \tau}{\partial z}, \\ \dfrac{\partial U}{\partial x} + \dfrac{\partial U}{\partial z} & = & 0, \end{array} \right. \end{array} \tag{3.85}$$

$$\begin{array}{llll} z = 0 & U = 0,\ V = 0; & z \to \infty & U = 1; \\ z = 1 & u = 0; & & \\ x = 0 & U = 1,\ V = 0,\ u = 1 - e^{\beta(z-1)}; & x = 0 & U = 1,\ V = 0 \end{array} \tag{3.86}$$

(the bars over dimensionless variables have been dropped again).

Either of the boundary-value problems can be uniquely solved numerically if any positive value of the slip velocity $U = U_h(x, 1)$ would be prescribed on the common boundary $z = 1$. However, this value is physically suited if it secures the continuity of the transversal velocity and the shear stress. The conjugation boundary condition

$$z = 1 \qquad U|_{1-0} = U|_{1+0}, \qquad V|_{1-0} = V|_{1+0}, \qquad \tau|_{1-0} = \tau|_{1+0} \tag{3.87}$$

is so required to closure problem (3.85) - (3.87).

Two independent dimensionless criteria appear in the problem additionally to (3.36),

$$B = \frac{\rho_1 kh}{m\nu}, \qquad \sigma = \frac{\nu h}{\nu}, \qquad \beta = \frac{\rho_1 kh}{m\nu} = \frac{B}{\sigma}, \tag{3.88}$$

that determine the flow instead of seven physical quantities represented there. The criterion A measures, as before, the density of the EPR: one gets a regular boundary flow over the smooth surface if $A = 0$ (the Blasius flow). Conversely, the limit $A \to \infty$ corresponds to the case of the impenetrability through the section $0 \le z \le 1$ as if there were the regular boundary flow over the surface $z = 1$. The criterion B measures the sluggishness of droplets: $B = \infty$ corresponds to the zero mass of droplets when they are picked up by the flow in a trice and thus have no effect to it (the solution reverts again to the Blasius problem if $B \to \infty$); the case B=0 corresponds to infinitely

heavy droplets, when they cannot be involved in the motion ($u \equiv 0$) and thus model (3.85)–(3.87) reverts to the immobile EPR model. The criterion σ has meaning of the Reynolds number defined by the fall-down speed and characterizes the existence time of droplets, while they move from the top to the bottom. So the extreme cases clarify the essence of model (3.85)–(3.87).

The complete analysis of the boundary layer flow over a droplet layer was carried out within the finite-difference numerical method developed for this conjugation problem, whose results are presented in Fig. 3.19. The initially homogeneous flow runs onto the droplet EPR and is transformed over it: the longitudinal velocities decelerate within the EPR, and the boundary layer grows over it (compare profiles 1, 2, 3, and 4 in subsequent cross-sections in Fig. 3.19,A). The droplets are involved in a motion: the distribution of their velocities at the entrance is presented by the dotted curve 0; however, along with the deceleration of the carried flow, their velocities decrease with increase in x. During their fall down, the droplets initially accelerate and catch up the flow having accumulated a portion of the flow's kinetic energy; then, the droplets become faster than the flow, force (1.14) changes its sign, and they return the kinetic energy back to the flow reducing its deceleration. These are the reasons for the maxima on $u(z)$ and $U(z)$. The transversal velocities in Fig. 3.19,B highlight a displacement of the flow outside the EPR; after a certain distance along the EPR, $V(Z)$ becomes almost zero within the EPR (curve 7). The shear distributions, Fig. 3.19,C, become very complex: they becomes even negative because of the turning points on $U(z)$. The behaviour of the integrated boundary layer parameters is shown in Fig. 3.19,D; it differs from the similar curves $\tau_0(x)$ and $V_\infty(x)$ of the ordinary boundary layer. Understanding the flow structure highlighted in Fig. 3.8 makes it possible to carry out a deeper analysis.

Initial region of the droplet boundary layer

The initial region of the droplet boundary layer can be thought to extend from the entrance section $x = 0$ to a distance $x = X_0$ and to encompass the region where the shear τ is negligible with regard to the drag forces. Since the left carrying medium equations (3.85) can be rewritten in the form

$$U\frac{\partial U}{\partial(Ax)} + \frac{V}{A}\frac{\partial U}{\partial z} = \frac{1}{A}\frac{\partial \tau}{\partial z} - (U-u), \qquad \frac{\partial U}{\partial(Ax)} + \frac{\partial}{\partial z}\left(\frac{V}{A}\right) = 0,$$

and the term $\frac{\partial \tau}{\partial z}$ is taken negligible, variables (3.39) are universal for the longitudinal and transversal profiles in terms of Chapter 3.1.4. In addition, the droplet velocity profiles have the structure $u = u(Ax, z; \frac{\sigma}{A}, \frac{B}{A})$ as the third equation (3.85) allows the form

$$u\frac{\partial u}{\partial \hat{x}} + \frac{\sigma}{A}\frac{\partial u}{\partial z} = \frac{B}{A}(U-u).$$

The dimensionless variables (3.39) have been used in Fig. 3.19,D.

Main region

The main region can be estimated like in Chapter 3.1.4. As all the profiles tend to a certain limiting shape if x grows (to a steady state, $\partial/\partial x \sim 0$) and $V(z)$ vanishes

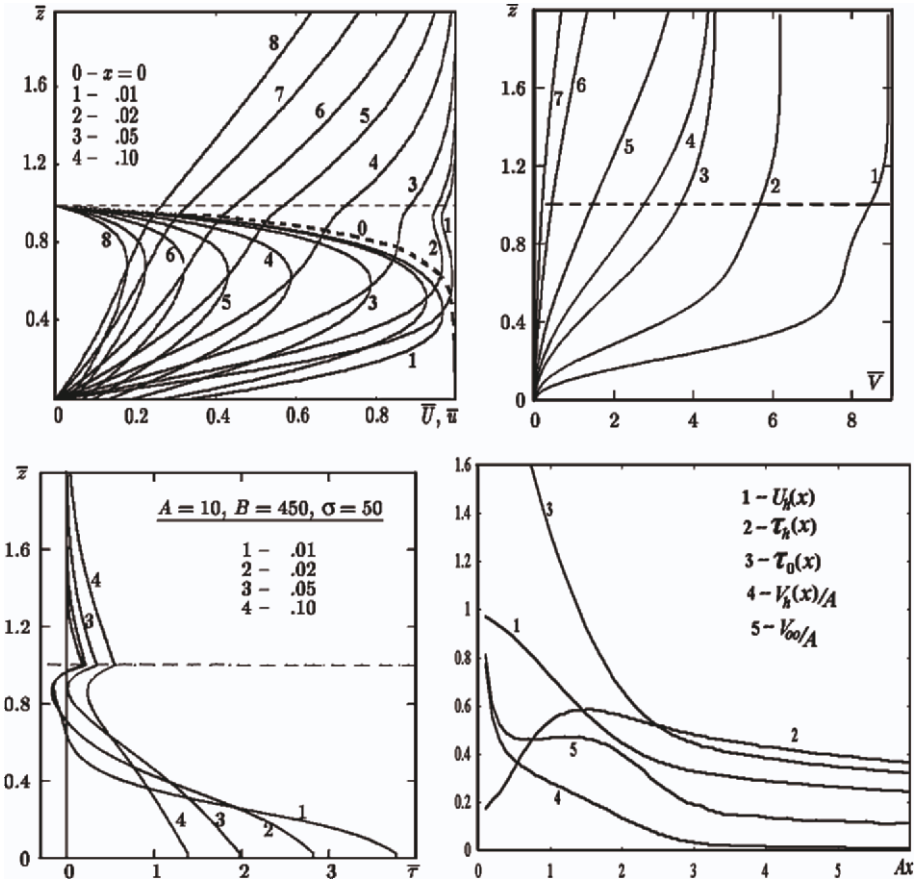

Figure 3.19: Boundary layer flow over a droplet EPR: (A) longitudinal velocities of air and droplets, (B) transversal air velocities, (C) shear stresses in the carrying flow, (D) integrated characteristics of the boundary layer.

within the EPR (curve 7 in Fig. 3.12), the left system of equations (3.85) reduces to the ordinary differential boundary-value problem

$$U'' = A(U-u), \qquad u' = -\beta(U-u), \tag{3.89}$$
$$z = 0 \qquad U = 0, \qquad z = 1 \qquad u = 0$$

that is similar to (3.40). The problem obtained is similar also to the steady-state flow in a duct (3.75), except for the motion is governed not by the pressure gradient but by the shear stress $\tau_h = \tau|_{z=1}$.

It is worth to emphasize that the motion on the main region is determined by only two dimensionless criteria A and β. In this case, the first integral (3.78) takes the form

$$\tau = \tau_h - \frac{A}{\beta}u. \tag{3.90}$$

This means that the shear stress profile is a "mirror reflection" of the $u(z)$-profile. Like before, the solution of (3.89) can be found analytically as

$$\begin{aligned} U &= \tau_0\left[Ag_2(z) + \frac{\sigma}{A}\right] - u_0\left[Ag_1(z) - 1\right], \\ \tau &= A\tau_0 g_1(z) - Au_0 g_0(z), \\ u &= u_0\left[\sigma g_0(z) + 1\right] - \tau_0\left[\sigma g_1(z) - \frac{\sigma}{A}\right]. \end{aligned} \tag{3.91}$$

The auxiliary parameters follow from the boundary conditions as

$$u_0 = \frac{\sigma\left[Ag_1(1) - 1\right]}{A\left[Ag_1(1) + \sigma g_0(1)\right]}\tau_h, \qquad \tau_0 = \frac{Ag_0(1) + 1}{Ag_1(1) + \sigma g_0(1)}\tau_h. \tag{3.92}$$

Finding out the shear stress of the external flow τ_h requires to execute the complete numerical computation of the boundary layer. Such a computation has confirmed approximations (3.91), (3.92). Particularly, a "secondary maxima" can be formed on $U(z)$ (compare with the section 5.1).

Stagnation zone

A stagnation zone within the droplet EPR can also appear in the main region, i.e. a zone near the wall with no longitudinal motion. It would be of significant practical interest for the spraying cooler theory. Self-similarity (3.42) of the external boundary layer has also been confirmed in terms of the variables used in Section 3.1.4.

3.2.3 Heat and mass exchange between the flow and the droplet layer

The easily penetrable roughness made up of mobile elements is a heuristic model of the spraying cooling system (SCS). Therefore, it is important to consider the heat and mass exchange of such an EPR with the flowing medium (air in the case of SCS). Droplets are cooled by the wind, and this "ultimate aim" is practically important for power plant engineers.

Warm droplets release the heat and the moisture into the local flowing air surrounding. The further transportation of these substances is governed by Eqs. (3.53). The problem consists now in the determination of the droplet temperature t. We start from the equation of the heat droplet balance between the change in the individual droplet thermal energy and its removal by the heat exchange and evaporation

$$mc_2\frac{dt}{d\tau} = I_H + \mathcal{L}\cdot I_E \tag{3.93}$$

which is mathematically similar to the droplet motion equation (3.71). (Recall that the symbol τ in the last equation stands for the time). The rate of sensible heat intake I_H (or its withdrawal if $t > T$) and the rate of mass intake I_E (its withdrawal if $e > E$) to (from) an individual droplet are given by (1.18) or (3.50). Their exchange coefficients α_H and α_E will be taken constant. A real case where the coefficients are empirical functions of Re and Pr (or Sc in the case of mass exchange) is considered in Chapter 3.3.

Actually, two quantities, $t(x, z)$ and $e(x, z)$, characterize the aerothermal state of droplets. An approximate empirical relation between the saturation concentration e and the temperature of obstructions t can be found from nomographic empirical charts [60] and, in the first approximation, is a linear function

$$e = \rho_1(b_0 t + b_1), \tag{3.94}$$

with the constants $b_0 = 1.18 \cdot 10^{-3} 1/^o\!C$ and $b_1 = -8.7 \cdot 10^{-3}$. This relation mathematically closes the equations.

Consider the case where the droplets fall down in a homogeneous atmosphere, $T = T_\infty$, $E = E_\infty$. Equation (3.83) is easily solved and gives a formula like (3.94) for the droplet temperature during its fall:

$$t_0(z) = T_{wet} + (t_h - T_{wet}) \cdot e^{-k_* \tau}.$$

The parameters of the last formula are

$$k_* = \frac{1}{mc_2}\left(\alpha_H + \alpha_E \rho_2 b_0 \mathcal{L}\right) S_0 \qquad \text{and} \qquad T_{wet} = \frac{\alpha_H T_\infty + \alpha_E \rho_2 \mathcal{L}(E_\infty - b_1)}{\alpha_H + \alpha_E \rho_2 b_0 \mathcal{L}},$$

the latter being a theoretical limit of the water cooling (the "wet bulb temperature"). The formulae obtained mean that a droplet is cooled during its fall, by changing its temperature from t_h towards the possible least value T_{wet}. The dependence of time τ upon the traversed path $h - z$, either for the uniform or constant acceleration fall (3.94), is to be substituted there to get the entrance droplet temperature distribution which will be used further as one of the boundary conditions.

However, a little way away from the entrance, the surrounding atmosphere ceases being homogeneous so that the relation between the thermal quantities of both moving media cannot be expressed explicitly. Substituting the individual derivative by the local one, equation (3.16) is derived with the prescribed function. Equation (1.17) governs jointly with (3.53) the heat and mass exchange between the carrying medium and the carried one, i.e. the exchange between the flowing air and the droplet EPR in the case of SCS.

The most convenient dimensionless variables for the droplet EPR flow are

$$\overline{\overline{T}} = \frac{T - T_\infty}{t_h - T_\infty}, \qquad \overline{\overline{t}} = \frac{t - T_\infty}{t_h - T_\infty}, \qquad \overline{\overline{E}} = \frac{E - E_\infty}{e_h - E_\infty}, \qquad \overline{\overline{e}} = \frac{e - E_\infty}{e_h - E_\infty} \tag{3.95}$$

that are somewhat different from (3.58) in order to focus more attention on EPR elements. The dimensionless variables for coordinates and fluid mechanical quantities

are the previous ones (3.32). It follows from such a normalization that $\overline{\overline{T}}(\overline{x},\infty)=0$, $\overline{\overline{E}}(\overline{x},\infty)=0$, $\overline{\overline{t}}_h=\overline{\overline{t}}_h(\overline{x},1)=1$, and $\overline{\overline{e}}_h=\overline{\overline{e}}(\overline{x},1)=1$ with

$$\overline{\overline{e}}_h=\overline{\overline{e}}(x,h)=\rho_1(b_0\overline{\overline{t}}_h+b_1)=const$$

because the temperature of droplets was taken constant on the EPR top,

$$t_h=t(x,z)|_{z=h}=const.$$

Though the dimensionless flows are defined differently from (3.58),

$$\overline{\overline{j}}_H=\frac{j_H h}{D_H(T_\infty-t_h)},\qquad\qquad \overline{\overline{j}}_E=\frac{j_E h}{D_E(E_\infty-e_h)},\tag{3.96}$$

they continue to be related to gradients in the simplest way as

$$\overline{\overline{j}}_H=\frac{\partial\overline{\overline{T}}}{\partial\overline{z}}\qquad\qquad \overline{\overline{j}}_E=\frac{\partial\overline{\overline{E}}}{\partial\overline{z}}\tag{3.97}$$

Finally, the relation between the dimensionless droplet vapour concentration and the temperature of droplets takes the form

$$\overline{\overline{e}}=\overline{b}_0\overline{\overline{t}}+\overline{b}_1\tag{3.98}$$

with the coefficients $\overline{b}_0=b_0\frac{t_h-T_\infty}{e_h-E_\infty}$ and $\overline{b_1}=\frac{b_0T_\infty+b_1-E_\infty}{e_h-E_\infty}$.

All these lead to the following formulation of the problem in terms of the dimensionless variables over two adjacent intervals, $z\in[0,1]$ and $\overline{z}\in[1,\infty)$:

for $0\le z\le 1$		for $1\le z<\infty$	
$U\frac{\partial T}{\partial x}+V\frac{\partial T}{\partial z}$	$=\frac{1}{\mathrm{Pr}}\frac{\partial^2T}{\partial z^2}+A_T(T-t),$	$U\frac{\partial T}{\partial x}+V\frac{\partial T}{\partial z}$	$=\frac{1}{\mathrm{Pr}}\frac{\partial^2T}{\partial z^2},$
$U\frac{\partial E}{\partial x}+V\frac{\partial E}{\partial z}$	$=\frac{1}{\mathrm{Sc}}\frac{\partial^2E}{\partial z^2}+A_E(E-e),$	$U\frac{\partial E}{\partial x}+V\frac{\partial E}{\partial z}$	$=\frac{1}{\mathrm{Sc}}\frac{\partial^2E}{\partial z^2},$
$u\frac{\partial t}{\partial x}+\mathrm{v}\frac{\partial t}{\partial z}$	$=B_T(t-T)+B_E(e-E),$		
$e=b_0t+b_1,$			

(3.99)

$z=0$	$\frac{\partial T}{\partial z}=0,\ \frac{\partial E}{\partial z}=0;$	$z\to\infty$	$T=E=0;$
$x=0$	$T=E=0,\ t=t_0(z);$	$x=0$	$T=E=0;$
$z=1$	$t=1;$		

(3.100)

$$T(x,1-0)=T(x,1+0),\qquad J_T(x,1-0)=J_T(x,1+0),$$
$$E(x,1-0)=E(x,1+0),\qquad J_E(x,1-0)=J_E(x,1+0) \tag{3.101}$$

(the bars over dimensionless variables have been dropped). The initial droplet temperature profile takes the dimensionless form

$$t_0(z)=t(0,z)=\frac{\pi_0+\pi_1}{\pi_1}exp\left[\frac{\pi_1}{\sigma}(1-z)\right]-\frac{\pi_0}{\pi_1} \tag{3.102}$$

with $\pi_0=b_0B_E+B_H$ and $\pi_1=b_1B_E$.

The fluid field $U(x,z)$, $V(x,z)$ is assumed to be known from the fluid mechanical problem (3.85)–(3.87), but six new dimensionless criteria have been appeared

$$A_H=\frac{\alpha_H nh^2S_0}{\nu},\qquad B_H=\frac{\alpha_H\rho_2h^2S_0}{\nu mc^{(})_2},\qquad \mathrm{Pr}=\frac{\nu}{D_H}, \tag{3.103}$$

$$B_H=\frac{\alpha_E nh^2S_0}{\nu},\qquad B_E=\frac{\alpha_E b_0\mathcal{L}\rho_2h^2S_0}{\nu mc_2},\qquad \mathrm{Sc}=\frac{\nu}{D_H} \tag{3.104}$$

which determine the heat and mass processes in the droplet EPR flow. The criteria A_H and A_E are proportional to the density of the EPR, whereas the criterion B is related to individual droplets, and the Prandtl Pr (Schmidt Sc) number couples the diffusion of momentum to that of heat (mass). The conjugation condition (3.101) "sews together" the solutions of the left and right boundary-value problems. A few simplified problems should provide a confidence that the coupled problem (3.99)–(3.101) admits a unique solution.

Mass exchange between the flow and the droplet layer

It is well known that, under summer conditions, the latent heat exchange by means of the droplet evaporation constitutes about 80% of the total cooling, [60]. Therefore, let us consider, from the beginning, the only mass exchange of such an EPR. The prevalence of the latent heat exchange (evaporation) allows us to drop the first equations of systems (3.99) and to consider only the second term on the right-hand side of the penultimate equation. One of three unknowns should be eliminated due to the last algebraic relation. To do this, we introduce a new variable, the formal temperature

$$T_E=\frac{E-b_1}{b_0}. \tag{3.105}$$

This quantity is similar to $E(z)$, except for the limit value $T_E(x,\infty)=-b_1/b_0$ is negative; its physical meaning will be clarified later. The problem of mass exchange of the

droplet EPR with the flow is formulated as follows:

$$\begin{array}{lll} \text{for } 0 \le z \le 1 & & \text{for } 1 \le z < \infty \\ U\dfrac{\partial T_E}{\partial x} + V\dfrac{\partial T_E}{\partial z} = \dfrac{1}{\mathrm{Sc}}\dfrac{\partial^2 T_E}{\partial z^2} + A_T(T_E - t), & & U\dfrac{\partial T_E}{\partial x} + V\dfrac{\partial T_E}{\partial z} = \dfrac{1}{\mathrm{Sc}}\dfrac{\partial^2 T_E}{\partial z^2}, \\ u\dfrac{\partial t}{\partial x} - \sigma\dfrac{\partial t}{\partial z} = \dfrac{B_E}{b_0}B_E(t - T_E), & & \end{array} \tag{3.106}$$

$$\begin{array}{llll} z = 0 & \dfrac{\partial T_E}{\partial z} = 0, & z \to \infty & T_E = -\dfrac{b_1}{b_0}; \\ x = 0 & T_E = 0, \quad t = t_0(z); & x = 0 & T_E = 0; \\ z = 1 & t = 1; & & \end{array}$$

$$T_E(x, 1-0) = T_E(x, 1+0), \qquad \frac{\partial T_E}{\partial z}|_{z=1-0} = \frac{\partial T_E}{\partial z}|_{z=1+0} \tag{3.107}$$

with the known entrance profile (3.102).

The number of boundary conditions both for the left and the right second-order parabolic boundary-value problems (3.106) is sufficient to uniquely solve them by any numerical finite difference method, provided they are supplied by an additional condition on the interface at each vertical cross section $x, T_E(x, 1) = T_{Eh}$. However, the left and right solutions do not obviously give the equal derivatives $\frac{\partial T_E}{\partial z}$ on the interface $z = 1$. Therefore, the second conjugation condition (3.107) becomes a one-variable transcendental equation for choosing the proper value of T_{Eh}. The conjugation problems (3.106), (3.107) and (3.85) - (3.87) have computationally been treated in a similar manner.

The results of the numerical solution of the conjugation boundary-value problem for the mass exchange (3.106), (3.107) are shown in Fig. 3.20. The initially homogeneously "cold" air gets the latent heat from the droplet layer and becomes warmer and warmer from cross section 1 to 5, etc. (family (I) of curves in Fig. 3.20,A). In turn, the droplets become cooler: their temperature is reduced especially intensively at the EPR entrance (the dashed curve 0) but less and less intensively in subsequent cross sections (the family of curves (II)). The curves $T_E(z)$ and $t(z)$ attract each other and meet at the theoretical infinity $z \to -\infty$. The complex relation between the two profiles is testified by the local maxima on $T_E(z)$ at early cross sections (curves 1 and 2) and by negative values of the mass flow (3.97) presented in Fig. 3.20,B. A dilative thermal boundary layer grows over the droplet EPR. Its width $d_E(x)$ grows theoretically to infinity over the EPR, but the internal portions of all the variables tend to a certain final position within the EPR, $0 \le z \le 1$.

The cooling of droplets,

$$\Delta t = t_h - t_0 = t_h - t(x, 0),$$

is a very important ultimate parameter in the practice of spraying coolers. The highest possible water cooling $\Delta t(x)$ takes place at the entrance of the droplet layer but

decreases along it. A decrease in the cooling capacity can so be explained as a result of the deceleration and saturation of the flow. However, even very far away from the EPR entrance, the cooling does not vanish but tends to a limit value dependent on the EPR density. The denser the EPR, the lower is the cooling (more comments see in the section 3.3).

The heat exchange between the EPR and the flow (acting separately from the evaporation) is completely similar to the mass exchange as it is generally expressed by the same equations. We will make some generalized conclusions regarding both processes.

Initial mass and heat exchange region

The initial mass and heat exchange region is observed just behind the EPR leading edge where flows (3.97) can be neglected with regard for (3.51). Having neglected also the transversal gradients, one derives the one-dimensional equations for each process:

$$\begin{aligned} &U\frac{dE}{dx} = A_E(e-E), \quad e = e(t), && U\frac{dT}{dx} = A_E(t-T), \\ &x = 0 \quad E = 0, \quad e = e_0(z); && x = 0 \quad T = 0, \quad t = t_0(z). \end{aligned} \tag{3.108}$$

They do not admit an analytical solution, as it was for the immobile EPR, because $e(x,z)$ and $t(x,z)$ vary in both directions. A useful conclusion can be drawn, however, that the processes are independent of the Pr and Sc numbers over the initial region.

Main mass and heat exchange regions

Main mass and heat exchange regions take place sufficiently far after the initial region, where the changes in profiles within the EPR ceased. Because of this, the problems are reduced to the ordinary differential equations similar to (3.75):

$$\begin{aligned} \frac{dj_E}{dz} &= \mathrm{Sc}\cdot A_E(e-E), & \frac{dj_T}{dz} &= \mathrm{Pr}\cdot A_H(t-T), \\ \sigma\frac{de}{dz} &= B_E(e-E), & \sigma\frac{dt}{dz} &= B_H(t-T); \\ z = 0 \quad & j_E = \frac{dE}{dz} = 0, & z = 0 \quad & j_T = \frac{dT}{dz} = 0, \\ z = 1 \quad & e = e_h = 1; & z = 1 \quad & t = t_h = 1. \end{aligned} \tag{3.109}$$

The identity of the systems in (3.109) confirms once more the similarity of both processes; they have been determined by four criteria $\mathrm{Sc}\cdot A_E$, $\mathrm{Pr}\cdot A_H$, B_E/σ, and B_H/σ instead of six criteria (3.103). Each problem admits the first integral. For the mass exchange, for example, we have

$$j_E(z) = j_{Eh} + \frac{\sigma\sqrt{\mathrm{Sc}A_E}}{B_E}(1-e), \tag{3.110}$$

which indicates that the mass flow profile follows the reflection of the droplet temperature profile. It follows that the mass of droplets lost during their fall (it is proportional to their cooling Δt) is completely determined by the mass flow on the interface

$$\Delta m = \rho_2(1 - e_0) = -\frac{B_E}{\sigma\sqrt{\mathrm{Sc}\cdot A_E}}. \tag{3.111}$$

The systems of equations (3.109) admit analytical solutions. For the left system, for example, we get

$$\begin{aligned} E &= e_0 + \frac{B_E}{\sigma}(e_0 - T_0)g_0(z), \\ e &= e_0 - \frac{B_E}{\sigma}(e_0 - T_0)g_1(z), \\ j_E &= \mathrm{Sc}\cdot A_E(e_0 - T_0)g_0(z). \end{aligned} \tag{3.112}$$

The auxiliary parameters $E_0 = E(0)$ and $e_0 = e(0)$ are linked by the relation

$$e_0 = \frac{\sigma + B_E E_0 g_0(1)}{\sigma + B_E g_0(1)},$$

and the computation of the whole boundary layer is required in order to determine one of them.

The analytical solutions for particular regions and the full numerical performance complement each other. The former can be used in the elaboration of an approximate calculation method.

Thermal stagnation zone

The thermal stagnation zone can happen in the lower part of the droplet layer, over which $t(z)$ has almost reached its possible limit, and so there is no cooling of droplets over the lower part of their trajectories. This means that the density of droplets is too high, and the efficiency of the cooling system can be improved by arranging the spraying nozzles to reach a lesser density of droplets.

Integral relations for the mass and heat exchange processes

Integral relations for the mass and heat exchange processes follow from the general equations (3.99). Integrating the first equations from $z = 0$ to $z = 1$ for one relation, and then from $z = 0$ to $z \to \infty$ for the second, one obtains that the mass flow changes over Ox according to

$$\frac{dP_{E1}}{dx} = \frac{j_{Eh}}{\mathrm{Sc}} + D_E - V_h(E_h - E_\infty) \quad \text{and} \quad \frac{dP_{E2}}{dx} = \frac{j_{Eh}}{\mathrm{Sc}} + V_h(E_h - E_\infty).$$

It follows that the total mass flow is completely balanced by the bulk mass income in the EPR,

$$\frac{dP_E}{dx} = D_E, \tag{3.113}$$

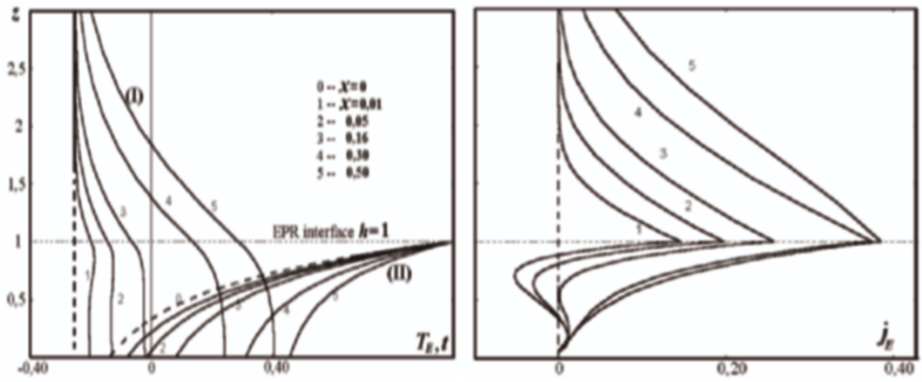

Figure 3.20: (A) Computed profiles (I) of the air "formal temperature" $T_E(I)$ and the droplet temperature (II); (B) the mass flow in the case of only mass exchange $A_E = 2$, $B_E = 450$, and Sc = 1 (fluid mechanics criteria $A = 10$, $B = 450$, and $\sigma = 50$).

where the three mass flows and the bulk mass income are correspondingly

$$P_{E1} = \int_0^1 U(E - E_\infty)dz, \qquad P_{E2} = \int_1^\infty U(E - E_\infty)dz,$$

$$P_E = \int_0^\infty U(E - E_\infty)dz \quad \text{and} \quad D_E = \int_0^1 A_E(e - E)dz$$

(the improper integrals are assumed to exist). Similarly, the integral relation which expresses a balance of thermal energy can be obtained for the heat exchange. The balance relations (3.113) were used for examining the accuracy of the numerical method. They can also be useful in elaborating the approximate semi-analytical "integral" methods.

3.2.4 Joined heat and mass exchange

In practice, under most weather conditions, the mass exchange and the heat exchange act simultaneously. The difficulty in solving the complete problem (3.99)–(3.101) under such conditions lies in the fact that two first left equations become linked due to the third one.

First of all, the method of numerical treatment needs a modification. In the case where each of the physical processes acts independently, the corresponding conjugation boundary-value problems led to one transcendental equation with one unknown. It was natural to expect that, from the physical meaning of the problem, the last equation admits a unique solution.

The left and right boundary-value problems require one boundary condition each on the interface $z = 1$. Like before, let us supply them by two auxiliary values

$$T(x, 1) = T_h(x) \quad \text{and} \quad E(x, 1) = E_h(x)$$

that make each problem uniquely solvable. The left column of the conjugation conditions (3.101) is thereby satisfied. However, the flows, right column of (3.101), being functions of T_h and E_h, cannot be satisfied. Choosing the proper values of T_h and E_h is equivalent to the solution of the system of two transcendental equations

$$J_T(x, 1-0) = J_T(x, 1+0), \qquad J_E(x, 1-0) = J_E(x, 1+0), \tag{3.114}$$

with two unknowns T_h and E_h. The solvability of the system is not so evident, but the simplified problems already discussed provide a confidence of success. The parabolic nature of Eq. (3.99) significantly simplifies the problem since it is possible to calculate cross section by cross section of the boundary layer. An iterative procedure was used to solve (3.114) in each cross section. The results of calculations are presented in Figs. 3.21, A–D.

From the physical viewpoint, the simultaneously acting heat and mass exchanges result in basically new effects. In each cross section of the boundary layer, the profiles of air temperature, curves (II), and of air formal temperature T_E, curves (I), vary from constant values infinitely far away over the droplet layer to certain heightened values within it, the inequality $T_E < T$ always taking place at that; the latter heightened temperatures grow from one to next cross sections because the droplets saturate air with heat and vapour. The droplets themselves are cooled, see the family of curves (III), but the cooling efficiency $\Delta t(x)$ is gradually reduced.

Now, each droplet temperature curve is "attracted" by two corresponding air temperature curves, $T(z)$ and $T_E(z)$. At top levels of the EPR, the droplet temperature exceeds both air temperatures, $t(z) \geq T(z)$ and $t(z) \geq T_E(z)$. Therefore, both the heat and mass flows are directed from droplets to air, and both flows j_E and j_H are positive on these levels z as seen from Figs. 3.14, C and D. However, starting from a certain level labelled by small arrows, the droplet temperature finds itself lower that the air temperature but still tends to the formal temperature, $t(z) \leq T(z)$ but $t(z) \geq T_E(z)$. This means that the evaporation still exists and cools droplets, but air began to warm them. Therefore, the possible minimum droplet temperature lies always between $T(z)$ and $T_E(z)$. The last phenomenon is well known in meteorology.

The content of moisture in air is always less that the saturating content for a given air temperature found via (3.94) as $E_* = e(T)$. If it occasionally turned out that $E > E_*$, it would be dewed that is not accounted for in this model yet. The ratio $\varphi = E/E_*$ is called relative humidity. The distributions of the last over different cross sections of the droplet boundary layer are presented in Fig. 3.21,B. This practically important flow aerothermal characteristic, the relative humidity, reaches the largest values (up to 100%) within the droplet layer but decreases to a certain value far away over it, which has been prescribed by weather conditions T_∞ and E_∞ (or T_∞ and $\varphi_\infty = E_\infty/E_{*\infty}$). There is no further droplet cooling in the zones where $\varphi = 1$.

The flow with heat and mass exchanges acting simultaneously is naturally expected to have the same structure, i.e. the initial and main regions and the stagnation zone. It is so possible to find approximate solutions for them by reducing the problem to one-dimensional models.

To simplify the analysis of the problem, we used hypothesis (3.94) that the function $e = e(t)$ is linear. It is, in fact, weakly nonlinear with an increasing parabolic

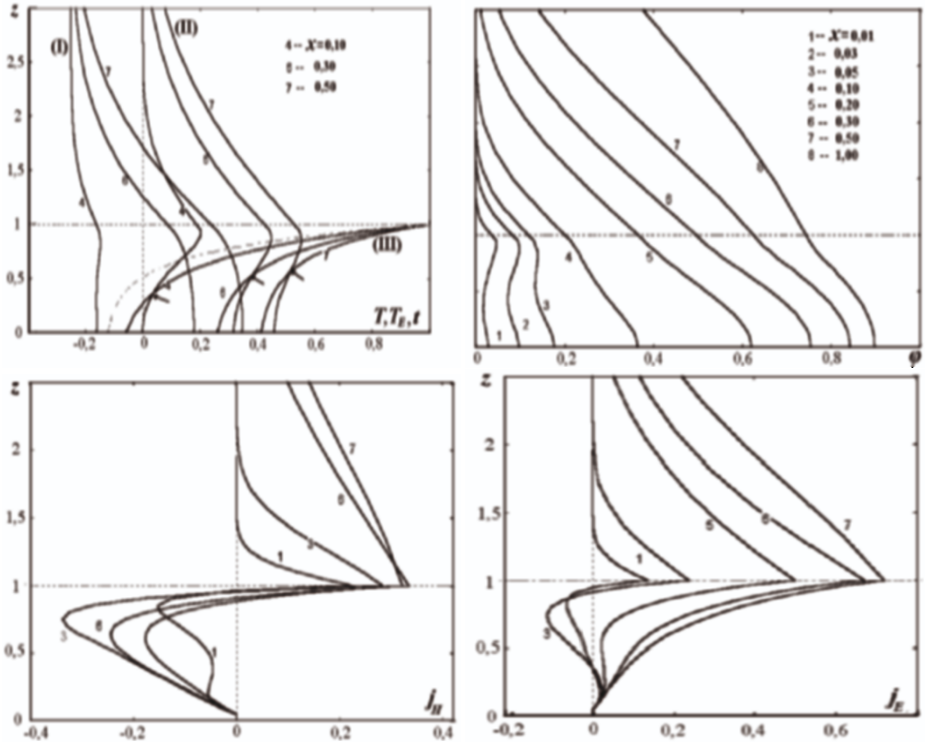

Figure 3.21: Computed aerothermal profiles for the joined heat and mass exchange: (A) temperatures of air and droplets; (B) air humidity; (C) and (D) mass and heat flows (fluid mechanics criteria $A = 0$, $B = 450$, and $\beta = 40$; thermal parameters $A_E = 2$, $B_E = 300$, and $A_H = 10$, $B_H = 100$, Pr = Sc = 1).

shape. Methodological calculations were done with the real empirical function $e(t)$, [217, 223]. The sensitivity of the model to such errors can be estimated as weak.

3.2.5 EPR in the form of a dispersed droplet layer

The previous sections aimed at including the practically important features of real spraying cooling systems as a kind of EPR in the model. Another important feature of the SCSs is the dispersion of droplet sizes. As already mentioned in Section 1.4, the droplet radii vary from several microns to 3–5 *mm*, each droplet size being characterized by its own concentration n, $1/m^3$. The term "*easily penetrable roughness*" assumes the additivity of all forces (1.6) and flows (3.51) in a unit volume, so their "smeared" effect can be expressed by formulas (1.19). The droplets of each size are worth to be treated as a separate carried medium. There is a need to predict the carrying medium flow field along with the fields for each of these carried media. In addition, a natural question arises how to find out a monodisperse medium (characterized by a single radius of all droplets) that would be equivalent to such multidisperse ensemble.

The two-dimensional model, i.e. the boundary layer flow, can be expressed by the following statement of the problem within the droplet layer $0 \le z \le 1$:

$$U\frac{\partial U}{\partial x} + V\frac{\partial U}{\partial z} = \frac{\partial \tau}{\partial z} - \int_0^\infty A(r)(U-u)dr, \qquad \frac{\partial U}{\partial x} + \frac{\partial V}{\partial z} = 0,$$

$$u(r)\frac{\partial u}{\partial x} - \sigma(r)\frac{\partial u}{\partial z} = B(r)(U-u(r)). \tag{3.115}$$

In the external boundary layer $1 \le z < \infty$, the same right equations of (3.85) remain valid. Similar integro-differential equations with integrals in the source terms are valid for heat and mass exchange processes, [217].

Boundary layer over the N-fractional droplet EPR

Considering the dispersed droplet layer, we restrict ourselves by fluid mechanics only. Let the droplet spectrum have been discretized to representative fractions, each with the same radius r_i, $i = 1, 2, ..., K$. A finite sum will represent the integral source term in (3.115), and the equations will govern all the droplet media linked through the first equation. By posing the relevant problem, we substitute the left problem in (3.85) by the following system of $K + 2$ equations:

$$0 \le z \le 1$$

$$U\frac{\partial U}{\partial x} + V\frac{\partial U}{\partial z} = \frac{\partial \tau}{\partial z} - \sum_{i=1}^{K} A_i(U-u_i), \qquad \frac{\partial U}{\partial x} + \frac{\partial V}{\partial z} = 0,$$

$$u_i\frac{\partial u_i}{\partial x} - \sigma_i\frac{\partial u_i}{\partial z} = B_i(U-u_i) \tag{3.116}$$

with the boundary conditions

$$z = 0 \quad U = 0, \quad V = 0; \qquad z = 1 \quad u_i = 0;$$

$$x = 0 \quad U = 1, \quad V = 0, \quad u_i = 1 - e^{\beta_i(z-1)}.$$

The new conjugation boundary-value problem (3.87) that consist of (3.116) and of the equations and boundary conditions from the right column of (3.85) and (3.86) was also solved numerically by the same finite-difference scheme. Again, the problem led to an equivalent transcendental equation

$$R(U_h) = \tau|_{z=1-0} - \tau|_{z=1+0} = 0.$$

It was solved by several iterations, on which two boundary-value problems, (3.116) and (3.85), (3.86) for particular U_h, were solved.

The coefficients of (3.116) are constant in the case of light droplets or can vary according to (3.81) for heavy droplets. Figure 3.22 presents the results of calculations for the constant coefficients in the case of the $K = 3$ fractions in the EPR droplet

ensemble. As before, the boundary layer in the air flow can be seen extending over the droplet EPR (curves 0 in Fig. 3.22). Because of the droplet drift, the extreme points have been appeared on the air velocity profiles within the EPR. Three droplet velocity distributions, curves 1, 2, and 3, have been calculated in each boundary layer cross-section (compare with Fig. 3.19,A); the dimensionless parameters of the droplet ensemble fractions are as follows:

Fraction i=	A_i	B_i	β_i
1	20	550	40
2	10	250	50
3	5	800	30

Remember that B_i expresses the resistance of droplets of the ith fraction to the air flow, A_i accounts for their concentration n_i, and β_i for the speed of their vertical gravitational fall according to (3.36) and (3.88). The velocity profiles have basically the same shape in the case of "heavy" droplets that fall down with acceleration and governed so by coefficients (3.81). There is no big error if these variable coefficients would be substituted by their means.

Similarly, the problem of the joined heat and mass exchange can be formulated (with integral terms like (3.115) or integral sums like (3.116)) and solved. The results presented in Fig. 3.23 highlight the extending aerothermal boundary layer over the EPR along with $K = 3$ droplet temperatures for each fraction under study. The droplet fractions are turned out to be differently cooled: fraction 3 reaches the wet bulb temperature T_* and has not been cooled during the rest of the droplet fall; fraction 2 is cooled so slowly that cannot even reach the air temperature T, and fraction 1 tends to a certain temperature between T_* and T.

The problem can be brought to simplified $1d$ problems for each of the distinctive flow regions. This makes it worth to learn the $1d$ methodological problems.

Droplet EPR in a fully developed duct flow

Like in Section 3.1.1, let us put an infinite droplet EPR into the plane duct and consider the pressure-driven laminar flow, Fig. 3.1. One obtains a generalization of problem (3.6) as

$$\begin{array}{ll} \text{for } 0 \le z \le \delta & \text{for } \delta \le z \le 1 \\ \left\{ \begin{array}{l} 2\dfrac{d\tau}{dz} - \displaystyle\int_0^\infty A(r)\,[U - u(r)]\,dr = -2, \\ \dfrac{du}{dz} = -\beta(r)\,[U - u(r)]\,, \end{array} \right. & \dfrac{d\tau}{dz} = -1, \qquad (3.117) \\ z = 0 \quad U = 0, \qquad z = \delta \quad u = 0, & z = 1 \quad \tau = 0, \qquad (3.118) \end{array}$$

$$U|_{\delta-0} = U|_{\delta+0}, \qquad \tau|_{\delta-0} = \tau|_{\delta+0}. \qquad (3.119)$$

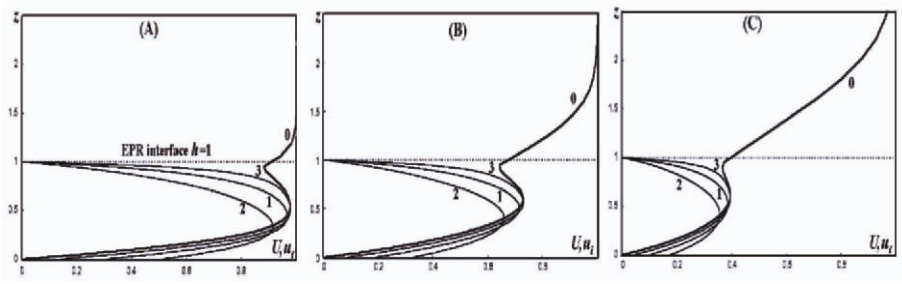

Figure 3.22: Air flow velocity (curves 0, $a = 20$, $B = 550$, $\beta = 40$) over a multidispersed droplet layer $k = 3$ (velocity distributions 1,2,3): (A) cross-section $x = 0,001$, (B) $x = 0,05$, (C) $x = 0,10$.

This is one more conjugation boundary-value problem. It is natural to obtain the linear shear and parabolic velocity distributions outside the EPR in the free flow like in (3.7), (3.8). For the internal portion of the flow, one gets the first integral

$$\tau = (1 - z) - \frac{1}{2}\int_0^\infty \lambda(r)u(z; r)dr.$$

The latter means that the shear stress departs from its conventional linear shape for the deviation caused by a droplet motion like in (3.78). This conclusion is valid also for variable coefficients provided $\frac{A}{\beta} = \lambda$ does not vary with z; the latter condition is satisfied for "heavy" droplets (3.81).

If the droplet size spectrum is represented by K characteristic radii, we replace the left integro-differential system by the following system of ordinary differential equations of the order $K + 2$:

$$\begin{cases} 2\dfrac{d^2U}{dz^2} - \displaystyle\sum_{i=1}^{K} A_i(U - u_i) = -2, \\ \dfrac{du_i}{dz} = -\beta_i(U - u_i), \quad i = 1, 2, ..., K. \end{cases} \tag{3.120}$$

The last problem was in detail investigated in [211].

Problem of an equivalent droplet size

Practice often requires the detailed knowledge or prognosis for different sizes of droplets; for instance, a question can arise about which droplets overcome a certain distance after a spraying system. But mostly the prognosis concerns only the mean droplet size, especially in the course of preliminary investigations. The decision about how to choose the mean size is often made unrigorously. Usually, one of the following definitions of mean diameter is used:

$$d_{mean}^{lm} = 2\frac{\int_0^\infty r^l p(r)}{\int_0^\infty r^m p(r)dr}.$$

Here, $l = m + 1$, and the radius probability $p(r)$ is known. For instance, the case $m = 2$ is known as the Sauter diameter d^{32}_{mean}.

The "*problem of mean value*" with regard to the dispersed droplet EPR (3.115) sounds as the following: to find three coefficients A_{mean}, B_{mean}, and σ_{mean} which determine the monodisperse EPR flow (3.85) and provide the velocity distributions $U(x, z)$ and $V(x, z)$ as close as possible to those of the multidisperse flow (3.115), for which the spectral coefficients $A(r)$, $B(r)$, and $\sigma(r)$ are known.

This problem for three coefficients seems too difficult. However, an analogous problem can be solved quite rigorously for a fully developed flow (3.117)–(3.119) that is governed by only two coefficients $A(r)$ and $\beta(r)$. The following statement can be formulated:

For a fully developed multidisperse flow (3.117)–(3.119), the best choice of the mean coefficients is as follows:

$$A_{mean} = \int_0^\infty A(r)dr, \qquad \beta_{mean} = \frac{A_{mean}}{\int_0^\infty \frac{A(r)}{\beta(r)}dr}. \tag{3.121}$$

If so, the air velocity distribution in the monodisperse flow $U_{mono}(z)$ approaches the multidisperse flow distribution $U_{multi}(z)$ in the best way.

The way to choose the first mean is evident. An EPR with immobile disperse elements is governed by the equation

$$U\frac{\partial U}{\partial x} + V\frac{\partial U}{\partial z} = \frac{\partial \tau}{\partial z} = \frac{\partial \tau}{\partial z} - \int_0^\infty A(r)Udr,$$

where the flow velocity profile does not depend on the radius r and thus can be taken out of the integral. The equation turns out to be equivalent to that with A_{mean} chosen by (3.121). It is not so evident how to choose β_{mean}. A few grounds to this can be found in [223]. Here, the illustration is presented in Fig. 3.24.

Let us imagine that droplets of three sorts are present in the EPR droplet ensemble. We call them figuratively as "big", "small", and "medium" droplets with dimensionless parameters given in the Table below. Let they be present in the ensemble in the proportions (probabilities) $p_1 = 1/3$, $p_3 = 1/2$, and $p_2 = 1/6$ correspondingly, $p_1 + p_2 + p_3 = 1$. Figure 3.24,A presents the droplet velocity distributions within an EPR with the relative height $\delta = 0.5$.

The droplet velocity distributions have been shown in Fig. 3.24,A: curve $i = 1$ for big droplets, $i = 2$ for medium ones, and $i = 3$ for small ones. Big droplets are not as

Table 3.1: Parameters of the numerical example given in Fig. 3.24

Type of droplets	Big, i=1	Medium, i=2	Small, i=3
A_i	25	15	10
β_i	5	10	20

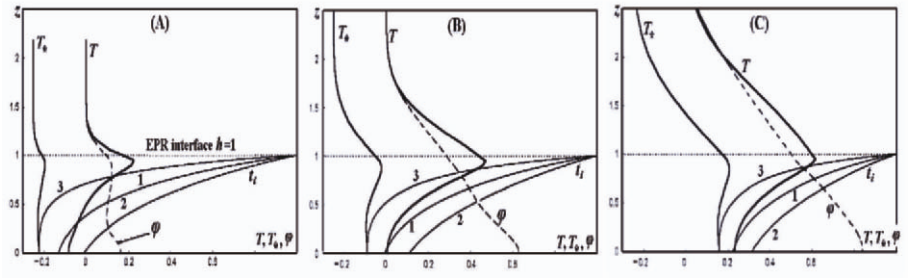

Figure 3.23: Aerothermal profiles over the multidisperse droplet layer with $N = 3$ fractions: air temperatures and humidity (dashed) with droplet fractional temperatures 1, 2, 3 ((A) cross-section $x = 0,001$, (B) $x = 0,05$, (C) $x = 0,10$).

easily movable as other ones, which is the reason for naming them. All three curves are located between two dashed lines; the curve labelled **B** (or **S**) corresponds to the droplet velocity in a monodisperse flow with only **B**ig (**S**mall) droplets.

Curves B and S in right figures 3.24 have the same meaning. The solid line in Fig. 3.24,B displays the air velocity distribution in a multidisperse flow, and the lines **B** and **S** correspond to that of a monodisperse one with only big (small) droplets for the given parameters.

The results of calculations of the monodisperse flow with the parameters determined by (3.121) has been presented by the dotted curves. The droplet velocity distribution of the "equivalent" uniquely sized droplet ensemble is seen in Fig. 3.24,A. By the way, the shape of this curve is strictly given by

$$u_{mean}(z) = \frac{\beta_{mean}}{A_{mean}} \int_0^\infty \frac{A(r)}{\beta(r)} u(z; r) dr.$$

The air velocity distribution for the "equivalent" flow seen in Fig. 3.24,B (dotted line) is very close to that in the multidisperse EPR flow (solid). The similar comparison for the shear stress is given in Fig. 3.24,C. The function $\tau(z) = dU/dz$ is usually very sensitive to errors of any kind; however, the solid (multidisperse flow) and dotted (monodisperse) lines are very close here.

It is thus possible to use monodisperse flow models instead of multidisperse ones. The generalization of "forest models" [155, 187, 522] gives so a tool for solving many problems in spraying cooling.

3.2.6 EPR in the form of a multispeed droplet layer

Engineers would still unlikely be satisfied with many assumptions of the above models of a droplet layer as it is much more complex in reality. However, no results can be obtained without appropriate assumptions.

A shortcoming of the models for droplet layers developed so far is the assumption that the droplets move vertically in only one direction, from the fountain top $z = h$

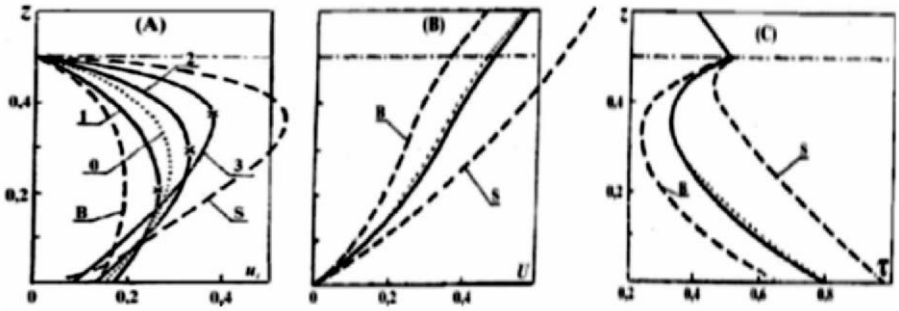

Figure 3.24: To an equivalence between a multidisperse droplet EPR (curves i=1, 2, and 3) and a monodisperse EPR (dotted curve 0): (A) velocities of droplets; (B) air velocities; (C) shear distributions. Dashed lines: B (S) as if only big droplets, $i = 1$ (small, $i = 3$) were present in the droplet ensemble.

where they are assumed to be produced to the water collection surface $z = 0$. In fact, it is easily recognized that the droplets observed in spraying systems rise up from nozzles on a level $z = z_S$ to $z = h$ and then fall down, being simultaneously drifted with the wind. Such an assumption neglects, again, complex perturbations and the break up of water jets and big droplets in a real SCS but was often assumed in the Lagrangian models of droplet layers. This section suggests how to include the above feature into the droplet EPR model, thus giving a closer approach to real spraying systems.

Let the droplets be of the same size. The difficulty of the Eulerian simulation is that one needs associate two droplet speeds to the same space point, one for the droplets rising up and another for the droplets falling down. This ambiguity could be overcome if, again, one introduces two continuous media for both kinds of droplets. Two methodological multispeed droplet EPR models have been suggested here.

Two-speed droplet EPR model

Let the droplets be constantly created (by nozzles) on the level $z = 0$ with intensity $\dot{N}$, $1/(m^2 sec)$, each with the horizontal $u = u_{x0}$ and vertical $v = u_{z0}$ initial velocity components. After the creation, the droplets move up in the air flow field and interact with it. Because of the latter, their horizontal velocity component changes, $u_1(x, z)$. Having reached the droplet layer top $z = h$, the droplets of this kind $i = 1$ "disappear", but new droplets, $i = 2$, "appear" and continue the same horizontal motion but change their vertical motion by the descending one. The force interaction between the flow and droplets is assumed linear. For simplicity, the droplet initial vertical speed is assumed constant, $u_{z0} = a = const$. Figure 3.25,A explains these assumptions.

Droplets of each kind have the same concentration $n(z)$ on each level and contribute to the "smeared" force acting onto the air flow. These three continuous media in the area $0 \le z \le h$ are governed by the equations

$$U\frac{\partial U}{\partial x} + V\frac{\partial U}{\partial z} = \frac{1}{\rho_1}\frac{\partial \tau}{\partial z} - nF_1 - nF_2 - \frac{1}{\rho_1}\frac{\partial p}{\partial x}, \qquad \frac{\partial U}{\partial x} + \frac{\partial V}{\partial z} = 0,$$

$$m_i\left(u_i\frac{\partial u_i}{\partial x}-(-1)^i a\frac{\partial u_i}{\partial z}\right)=F_i,\qquad i=1,2,\qquad (3.122)$$

where $F_i=\rho_1 k(U-u_i)$, $i=1,2$, the pressure gradient should be neglected for the boundary layer but taken into account for the duct's problem. It is also accounted for that the vertical velocities of droplets for $i=1$ and $i=2$ are oppositely directed.

The boundary conditions for the droplet layer are

$$z=0\quad U=0,\quad V=0,\quad u_1=0;\qquad\qquad z=h\quad u_1=u_2,$$

but this multiphase flow must be considered along with the external air flow and thus with the conjugation conditions (3.87).

Consider a methodological $1d$-problem of the flow in a duct to ensure that this problem is well-posed. Assume that such a two-speed droplet EPR has been symmetrically placed near both walls of the infinite duct. The steady-state pressure-driven flow in such a duct is governed by the following boundary-value problem for the internal flow:

$$\text{for}\qquad 0\le z\le\delta$$

$$\begin{cases} 2\dfrac{d\tau}{dz}=A(U-u_1)+A(U-u_2)-2,\\[2ex] \dfrac{du_1}{dz}=B(U-u_1),\\[2ex] \dfrac{du_2}{dz}=-B(U-u_2), \end{cases}\qquad (3.123)$$

$$z=0\quad U=0\quad u_1=u_{x0};\qquad\qquad z=\delta\quad u_1=u_2,\quad \tau=\tau_h=1-\delta.$$

The analytical solution of (3.123) can be found in [215, 223]. Here, only the illustration to the problem has been given in Fig. 3.26.

The model allows one to investigate the influence of the initial droplet "impulse" u_{x0}. This "nozzle impulse" was taken as $u_{x0}=-0.6$ in Fig. 3.26,A, i.e. oppositely to the wind from the left to the right. Therefore, the droplets cause a very strong deceleration of the air flow (thick curve 3), are decelerated themselves during their rise (curve 1), change the motion direction to the right one, and began to fall down. During this stage (curve 2), they leave the flow behind and decelerate. If $u_{x0}=+0.6$ in Fig. 3.26,B, the droplets become faster than air, decelerate, but then change their behaviour and accelerate (curve 1); on the descending way, they accelerate from the beginning but then decelerate and return the kinetic energy back to the flow (curve 2). The carrying medium velocity distribution is shown by thick solid curves 3. In the last case, a much more amount of air passes the EPR. The shear stress distribution (curve 4) emphasizes its complex shape caused by the interaction with droplets.

This model explains so the variety of droplet trajectories that can be met in real spraying systems.

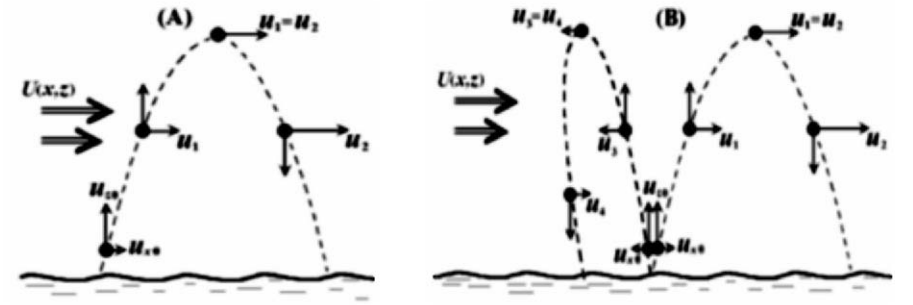

Figure 3.25: Schematic to the multispeed droplet EPR problem statement: (A) two-speed model; (B) four-speed droplet EPR model.

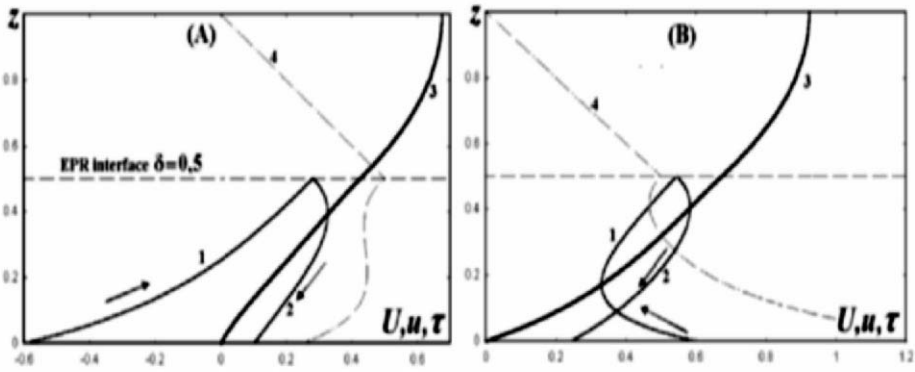

Figure 3.26: Calculated results for the two-speed droplet EPR: (A) droplets start against, and (B) down the wind (1, 2 - rising and descending droplets; 3 - air velocities; 4 - shear).

Four-speed droplet EPR model

The above-considered model encourages one to develop a more complex model of the real behaviour of droplets in spraying systems. In fact, nozzles produce droplets in different directions, some downwind and another upwind.

Consider now four continuous droplet media. Droplets of the kinds $i = 1$ and $i = 3$ rise up after being born at $z = 0$ with the same vertical velocity $u_{z0} = a = const$ but with opposite initial horizontal velocities with regard to the wind, $u_{1x} = u_0$ and $u_{3x} = -u_0$. Consequently, these droplets have different "histories" in the flow. After having reached the top $z = \delta$, droplets of the first kind "re-incarnate" into droplets of the second kind $i = 2$, and the third-kind droplets become those of the fourth kind $i = 4$, both falling down, as this has been schematically explained in Fig. 3.25,B. Expressing this mathematically, one comes to the following boundary-value problem involving the system of sixth-order ordinary differential equations

$$\text{for} \quad 0 \le z \le \delta$$

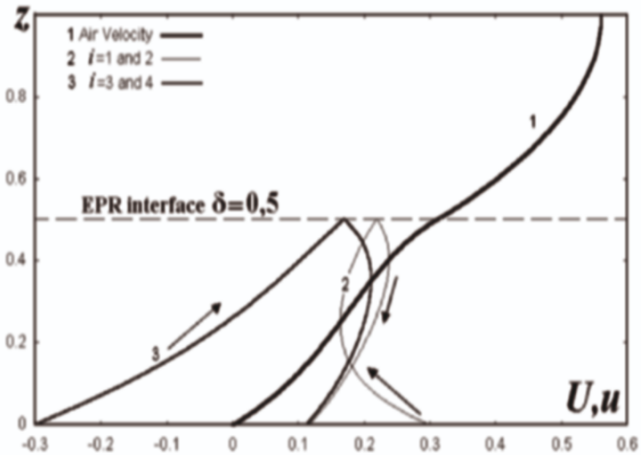

Figure 3.27: Four-speed droplet EPR and air velocity 1 through it ($A = 20$, $B = 5$ and $u_{x0} = \pm 0.3$).

$$\text{for} \quad 0 \le z \le \delta$$

$$\begin{cases} 2\dfrac{d\tau}{dz} = \sum\limits_{i=1}^{4} A_i(U - u_i) - 2, \\ \dfrac{du_i}{dz} = (-1)^{i+1} B(U - u_1), \quad i = 1, 2, 3, 4 \end{cases} \tag{3.124}$$

$$z = 0 \quad U = 0, \quad u_1 = u_0, \quad u_3 = -u_0; \qquad z = \delta \quad u_1 = u_2, \quad \tau = 1 - \delta. \tag{3.125}$$

Since the system of equations admits the first integral

$$\tau = (1 - z) + \frac{A}{2B}(u_1 - u_2) + \frac{A}{2B}(u_3 - u_4),$$

its order can be reduced by one. A semi-analytical solution was found in [215, 223]. The result of computations is shown in Fig. 3.27.

The complex velocity distribution 1 has been formed in the air flow under the influence of droplets of four kinds. A half of them has the initial momentum $u_{x0} = +0.3$ (curves 2); these droplets hands the kinetic energy to the air flow until they become slower it (cross the curve 1). Another half of droplets starts with the $u_{x0} = -0.3$ (curves 3) but contributes to the deceleration of air. After the droplets of both kinds reach the fountain top $z = \delta$ and fall down, their "histories" are quite common: they decelerate air accumulating its kinetic energy but later return the energy back accelerating air.

The model allows one to vary the initial impulse, $u_{x0} = var$. Each time, one will obtain differing "loops" of $u_i(z)$. It can however be strictly proved that the distributions of the air velocity $U(z)$ and the shear $\tau(z)$ do not depend on u_{x0}! This means that the oppositely moving droplets compensate their effect on the carrying medium.

Conclusion to section 3.2

Several models of the "droplet easily penetrable roughness" were suggested to demonstrate that the Eulerian mathematical description of a canopy flow can be generalized to represent the more complex structures met in practice. Linking the numerical methods with the analytical solutions of simplified models, one examines the correctness of the models and obtains the analytical estimations useful for engineering purposes.

3.3 Turbulence in EPRs

The above theoretical analysis of penetrable roughnesses and their interaction with the flow was based on the introduction of a distributed momentum sink (i.e. the force) and heat and mass sources, and was sufficient for discovering some important features of the phenomenon under consideration. It was a simplified consideration with mainly constant coefficients. However, in order to be applied to real environmental and engineering problems, realistic exchange coefficients are to be known.

The coefficient of turbulent viscosity ν_T is the most important among them. A number of scientific efforts were spent for estimating it with respect to the whole wide spectrum of problems of fluid mechanics and heat and mass exchange. Thousands of lengthy papers have been devoted to the "problem of turbulence". However, we still have no any sufficiently grounded and generally accepted theory. Turbulence still remains to be the most serious challenge to theoretical physics.

In the study of the penetrable roughnesses of any kind, it seems reasonable to issue from the already known facts and the theories of roughness-associated turbulence. However, the turbulence in EPRs has its own pronounced features. Learning it can give a new light to "old" problems and researches.

3.3.1 Heat and mass exchange coefficients

The exchange coefficients introduce real scales into theoretical models. They are normally measured under precise laboratory conditions for the key stone problems and can often be found in handbooks. The basic role for a developed theory is played by the drag force of the flow acting on the individual elements of the EPR. There is a number of empirical formulas gleaned for the drag coefficient c_F. The formula (3.72) is one of them; its linear and quadratic extreme cases were investigated with regard for the EPR models. The drag coefficient depends on the shape of obstructions. For the developed turbulence (quadratic resistance law), it is usually taken as $c_F = 0.4$ for a sphere and $c_F = 1.0$ for a cylinder.

The heat and mass exchange coefficients α_H and α_H were taken constant in (3.50). However, they often depend on local flow circumstances. Their simplified description is given in what follows.

The heat and mass exchange coefficients are determined as the proportionality coefficients in the Newton laws (1.18) between the heat delivery into the flow I_H, Wt (admixture mass delivery $I_E,\ kg/s$) and the temperature difference (concentration difference) multiplied by the value of the surface area S_0 of the whole body. It is known

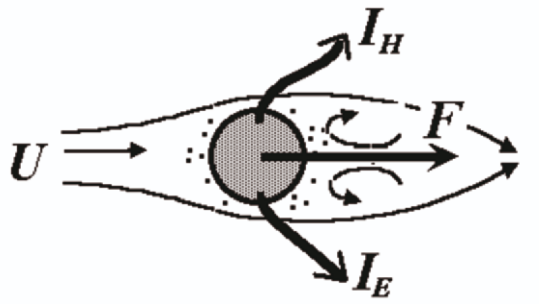

Figure 3.28: Schematic of the forces and the heat and mass fluxs from an individual EPR element to the flow.

that these coefficients vary over the body, but here one needs to know an overall value. Figure 3.28 explains the relation between the flow and an obstruction.

With regard for the evaporation, one often uses the ratio of the vapour mass to the mass of dry air in the same control volume (moisture content, dryness) e and E, kg/kg instead of the concentrations c and C, kg/m^3, so that the relations between them are $c = \rho_1 e$ and $C = \rho_1 E$. To determine $e(t)$, it is normally assumed that the dryness in the close vicinity to the droplet surface equals the saturation vapour content at a droplet temperature t. Figure 3.28 explains the parentage of the force and sources from an obstruction.

The heat and mass transfer coefficients are normally expressed as criterial relations for the thermal and diffusion Nusselt numbers

$$\mathrm{Nu} = \frac{\alpha_H 2r}{D_H} = \begin{cases} 2 + C\mathrm{Re}^m\mathrm{Pr}^n, & \mathrm{Re} < 150, \\ C\mathrm{Re}^m\mathrm{Pr}^n, & \mathrm{Re} > 150, \end{cases} \tag{3.126}$$

and

$$\mathrm{Nu}_E = \frac{\alpha_E 2r}{D_E} = \begin{cases} 2 + C\mathrm{Re}^m\mathrm{Sc}^n, & \mathrm{Re} < 150, \\ C\mathrm{Re}^m\mathrm{Sc}^n, & \mathrm{Re} > 150. \end{cases} \tag{3.127}$$

The local Reynolds number $\mathrm{Re}' = 2rU/\nu$ used in the studies of EPRs varies between 100 and 2 000, so that one often takes $n = 1/3$, $m = 1/2$, and $C = 0.6$. The Prandtl and Schmidt criteria express the properties of interacting substances. For the systems "heat in air" and "water vapour in air", they are $\mathrm{Pr} = (\nu\rho_1 c_p)/\lambda \approx 0.7$ and $\mathrm{Sc} = \nu/D \approx 0.6$ [60]. Having transformed these basic empirical relations, Berman [60] suggested a relation for spraying systems $\alpha_E = 3\sqrt{U/2r}$, provided the local velocity U is taken in m/s and the droplet diameter $2r$ in m. The latter was used in the following performance of SCSs.

The transportation of heat and a substance in the air flow is governed by the Fourier and Fick laws (3.55). The thermal conductivity coefficient $D_H/(\rho_1 c_p)$ and the mass transfer coefficient D_E, both possessing the dimension m^2/s, determine the intensity

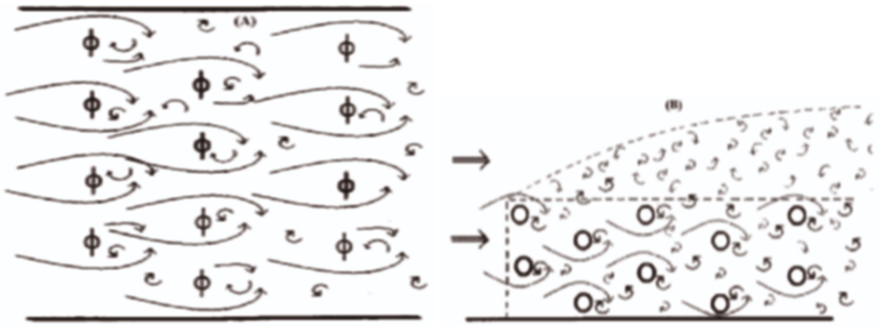

Figure 3.29: Expected appearance and the further behaviour of vortices in EPRs: (A) their spreading and interaction from the plane view, and (B) diffusion of vortices outside the EPR from the side view.

of the substance propagation. They were taken constant in the above basic modeling, though they significantly depend on the flow regime, laminar or turbulent. In fact, the effective turbulent values of these coefficients, D_{TH} and D_{TE}, should be taken. However, many experiments give evidence for that the coefficients are proportional to the effective turbulent viscosity,

$$\mathrm{Pr}_T = \frac{\nu_T}{D_H/(\rho_1 c_p)} = 1, \qquad \mathrm{Sc}_T = \frac{\nu_T}{D_E} = 1.$$

The problem focuses so on the determination of the effective turbulent viscosity ν_T, which is the essence of turbulence theory.

3.3.2 Laboratory investigation of the mean properties of the EPR turbulence

Several important investigations of the turbulence in penetrable roughnesses of different nature were carried out during three last decades. Some experimental works of meteorologists [6, 155, 343, 520, 654], hydrologists [52, 53, 54, 338, 348, 350, 377, 462, 463, 470], and power engineers [209, 216] have already been mentioned. However, the most important meaning is provided by the measurements on laboratory wind tunnels under the idealized conditions. A number of them were carried out by Seginer, Cermak and Meroney, Raupach, Finnigan and Shaw [88, 188, 278, 522, 568]. Here, the results of investigations at the Institute of Hydromechanics UNAS (Ukraine) and at Surrey University (UK) by Gayev and Savory [220, 221] will be overviewed as well.

It was natural to expect from the very beginning that a real turbulent penetrable roughness flow of any kind is associated with a number of vortices shed from individual obstructions within the PR. The visualization of such a flow has been shown in Fig. 1.18. A number of vortices “born” within the PR can brake up or coalesce during their spreading down and diffuse into external boundary layer. Figures 3.29,A and B display this expected behaviour. This should result in the especially intense mixing of any properties. However, the real behaviour of vortices turns out to be somewhat

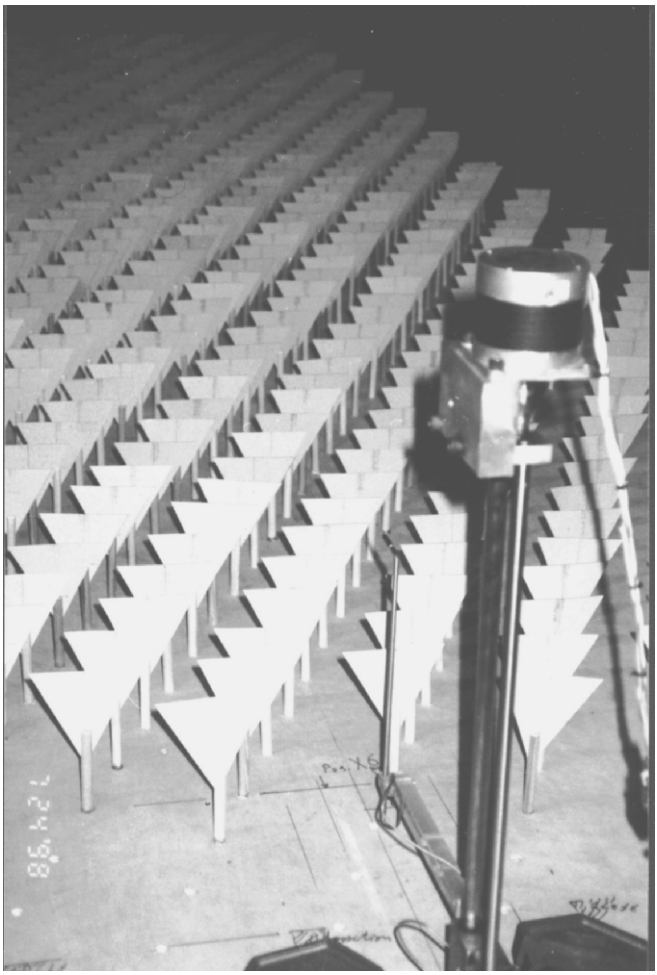

Figure 3.30: Experimental setup with 60 rows of "D-trees".

different as this is explained in Chapters 4 and 5. Let us consider the results of a real experiment.

The experiments were carried out in a wind tunnel at University of Surrey, UK. A model canopy was installed on the ground plane of a wind tunnel which has a working section with dimensions of 1.37 *m* in width and of 1.68 *m* in height. The canopy was formed from an extended array of obstacles. Earlier, cylindrical wooden pegs [411] and metal rods [213] were used as individual obstacles. In this experiment, it was aimed to vary the vertical distribution of the projected area of obstructions.

Each obstruction was constructed with a wooden cylindrical "stem" of 9 *mm* in diameter and of $h_1 + \Delta h_1 = 40\ mm + 30\ mm = 70\ mm$ in height. Into its top, a flat-plate "crown" in the shape of an equilateral triangle (with the height h_2=80 *mm* and a base side of 80 *mm* in length) was slotted to the depth Δh_1 =30 *mm*. Hence, several types of obstructions were possible.

First, the canopy with only "stems" of 70 *mm* in height. Then, the canopies recalling trees with the total height equal to that of a canopy, that is the PR, $h = h_1 + h_2$=120 *mm*. The obstacles were arranged in 60 staggered rows, with the spacing between neighboring "trees" being Δx=60 *mm* in the longitudinal direction and Δy =60 *mm* across the wind tunnel (the latter is also the period of obstacle placement T). This arrangement allowed for a detailed diagnostics of the flow field within the canopy by means of thermal anemometry. The geometric orientation of the "crowns" can be varied, to give either a "point down" (D-orientation) or "point up" (U) shape. The flow direction can also be varied by rotating the trees to give directions normal to, parallel to (0^o), or to be at 45^o to the plane of the "crowns". The photo of the experimental setup with D-trees is presented in Fig. 3.30. The possible canopies are enumerated in the head of Table 3.2. Thus, it was possible to examine a wide range of geometric and flow conditions. Two kinds of hot-wire probes were used, namely single-wire and crossed-wire ones in order to obtain the mean velocity distribution values $U(z)$, $V(z)$, and $W(z)$, as well as the one-point correlations $U'U'$, $U'V'$, $U'W'$, $V'V'$, and $W'W'$ at various elevations within and above the canopy, as well as at various distances from the canopy leading edge. The overview of the data collected for 5 distances along the canopies of the above types (listened in the left column) are given in Table 3.2 together with the indication of the wind speed regimes investigated. The additional measurements were made to estimate the drag coefficients, c_f, of a single "tree" and the array of 18 "trees" by installing models on the ground plane force balance mechanism. The measurements of turbulence spectra in several locations were also performed for some canopy types.

The projected area S facing the flow, associated with each "tree", was 6.3 cm^2 for stems, 36 cm^2 for D-trees, and 35.6 cm^2 for the U-trees. Hence, the averaged value of the specific area distributed over the EPR volume $\Omega = hL_xL_y$ above the ground plane was $\overline{s} = S\frac{L_x}{\Delta x}\frac{L_y}{\Delta y}/\Omega = 4.17\ m^2/m^3$ for the D-canopy. However, this area was not uniformly distributed over the canopy height because each horizontal layer with the infinitesimal depth included different areas ΔS from "trees". Hence, the following distributions describe the area variation with the height z:

$$s(z) = \frac{\Delta S}{\Delta x \cdot \Delta y \cdot \Delta z} = \begin{cases} 1.25\ m^2/m^3, & \text{within stem space, } 0 \le z \le h_1 \\ 11.1\left(1 + \dfrac{\overline{z}-1}{\overline{h}_2}\right), & \text{within D - crowns, or} \\ 11.1\left(\dfrac{1-\overline{z}}{\overline{h}_2}\right), & \text{within U-crowns, } h_1 \le z \le h \end{cases} \tag{3.128}$$

These are the functions increasing with the height for the D-canopy and decreasing for the U-canopy. The last feature distinguishes both kinds of a canopy and also the uniform canopy consisting only of "stems" with the density distribution $s(z) = const$ = 1.25 m^2/m^3 (column 6 in Table 3.2). Either or should be applied to characterizing such an architecture of the PR structure. They simulate the non-uniformity of the leaf area density in forest canopies (see Section 3.1.4).

Table 3.2: Overview of cases investigated with regard to position, type of measurement and that of canopy, and velocity regime

X, *No* of rows	D-canopy	U-canopy	U-canopy, "crown" angles 45^o to flow	U-canopy, "crown" angles 0^o to flow	Stems h = 70 *mm*
10	Si: 8 m/s	–	–	–	–
	Cr: 6 m/s	Cr: 8 m/s	Cr: 8 m/s	Cr: 8 m/s	Cr: 8 m/s
	–	Sp: 8 m/s	–	–	–
20	Si: 8, 6 m/s	Si: 8 m/s	–	–	–
	Cr: 6 m/s	–	–	–	–
	–	Sp: 8 m/s	–	–	–
30	Si: 8,6 m/s	–	–	–	–
	–	–	–	–	–
	–	–	–	–	–
40	Si: 8 m/s	–	–	–	–
	–	–	–	–	–
	–	–	–	–	–
55	Si: 8, 6 m/s	–	–	–	Si: 8 m/s
	Cr: 8, 4, 2 m/s	–	–	–	–
	Sp: 8 m/s	–	–	–	–

Abbreviations: Si – single-wire, Cr – crossed-wire, Sp – spectrum measurements with respect to the canopy type and fetch length.

Results for the D-canopy

The prime purpose of the experiments was to understand the relationship between the theory, resulting in the unique distributions of canopy flow parameters, and the inhomogeneous 3d structure of a real flow, in which one can expect the presence of wakes periodically spanning the flow. That is why each full record of any vertical distributions included the measurements on four verticals: (*i*) one immediately behind a "tree" at a distance of Δx, and others shifted in the y-direction by (*ii*) 30 *mm*, thereby 2Δx downstream of another "tree"; (*iii*) 60 *mm*, thereby 3Δx downstream of another "tree" and (*iv*) 90 *mm*, thereby 4Δx downstream of another "tree". Such profiles obtained at each X-location of 10, 20, 30, 40, and 55 rows of "trees" provided the information from different positions of the wake structure within one period of the canopy array. These distributions are generally required for performing the space-averaging according to Raupach and Thom, [522].

Together, these profiles characterize the turbulent flow transformation along the canopy, as shown in Fig. 3.31. There are several distributions at each x-location; it was explained above why the y-shifted profiles do not coincide. No available theory can predict such a periodic 3d flow structure. However, fortunately, there is the practical interest in profiles which have been averaged in a spatial sense [522]. It is very significant that the measurements further downstream along the canopy show less differences between individual profiles, thus validating the continuous approach of mathematical modeling.

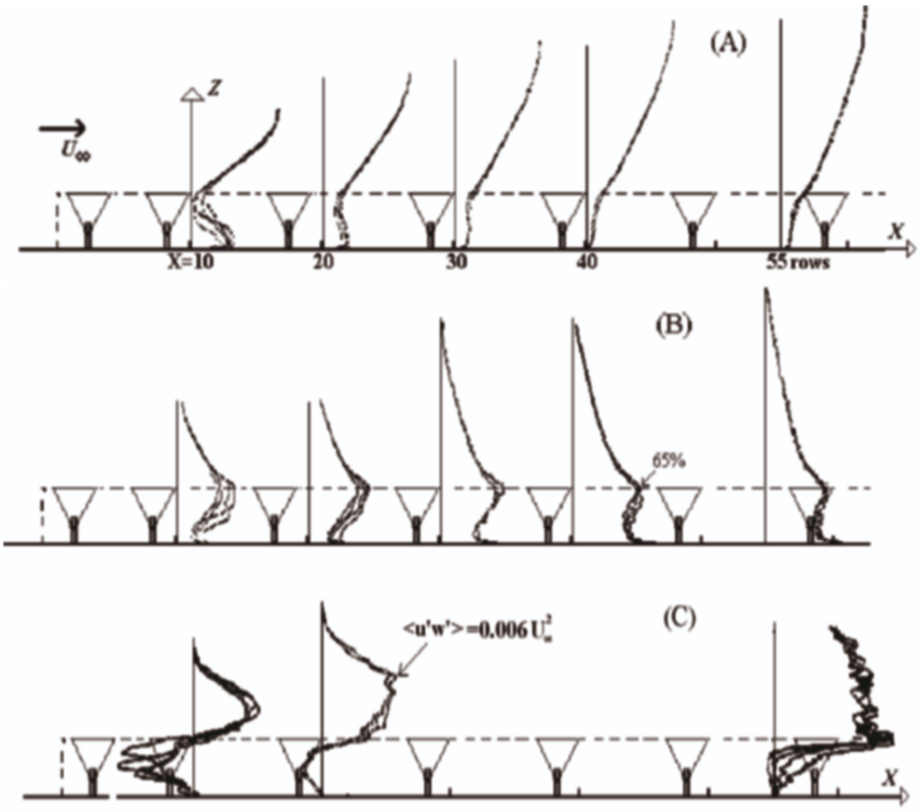

Figure 3.31: Transformation of the mean velocity $U(z)$ (A), its fluctuation $U'(z)$ (B), and turbulent shear stress (C) along the D-canopy with the "crowns" normal to the air flow.

On the basis of the y-shifted profiles, the longitudinal mean velocities (Fig. 3.32,A) and their fluctuations (Fig. 3.32,B) have been presented in the form of dimensionless isolines at a location of X=10 rows =5h from the start of the fetch. The periodic wakes spanning the wind tunnel are clearly seen here, but their structure becomes almost homogeneous further downstream. The level of turbulence was extremely high within the canopy. In addition to Figs. 3.31,B and 3.32,B, it can be noted that the velocity component fluctuations within the canopy were found to have values up to:

$$U'U' \propto 0.36U_\infty^2, \quad U'V' \propto 0.04U_\infty^2, \quad W'W' \propto 0.07U_\infty^2, \quad U'W' \propto 0.09U_\infty^2.$$

It should be mentioned that the hot-wire measurements cannot exactly determine the flow parameters in such extreme turbulence, and so the present results must be considered as preliminary.

The development of the external turbulent boundary layer $d_2(x)$ is also seen in Fig. 3.31, but it is more precisely defined and presented in Fig. 3.33, solid curve 1 for

tree-canopies and 2 for stem-canopies. The boundary layer growth is notably much greater than that associated with a more "usual" roughness. It is quite unexpected that this curve isn't sensitive to the wind tunnel velocity regime U_∞.

The question arises whether the canopy flow validates the above theory? The maxima and minima data points for the $U(z)$-profiles are presented in Fig. 3.34 and connected by dotted or dashed lines. Both sets of curves tend to each other, as the extreme variations attenuate for long x-distances. In addition, both sets of curves are compared with the solid line representing the internal velocity decay (3.37) for which approximately averages the distribution (3.128) and is, thereby, reasonably well validated. The initial region can be stated to extend to the distance $x = L \approx 35$ rows $\approx 17h$ for the canopy density investigated here. The x-locations of 40 and 55 rows (20h and 27h, respectively) are associated with the start of the main region. It is interesting that the internal wind speed slightly increases here after its deceleration in the initial region.

Results for other canopy types

The data gathered for other four types of canopies were not so complete (see 3.2). Nevertheless, they give some useful points to compare with the above analysis.

The U-canopy represents a monotonically decreasing density of the distribution of obstacles over height, contrary to the previous D-canopy, and this is in agreement with the general tendency of the $U(z)$-profiles towards a monotonic shape. Because of this, the longitudinal air motion decays more rapidly within the canopy; such that the $U(z)$ maxima have almost completely disappeared by $x = 20$ rows, and the isolines, like those in Fig. 3.32, highlight the fairly homogeneous flow. It is quite natural that the wakes spanning the flow behind 10 rows of "U-trees" are situated about $0.25h$ lower than those behind the "D-trees" shown in Fig. 3.32.

For the canopy consisting only of "stems" (the "crowns" were removed), the measurements immediately downstream of 10 and 55 rows (Table 3.2) display only monotonic distributions in the mean longitudinal velocity. The boundary layer height was estimated in two x-locations and shown by line 2 in Fig. 3.33. There are, unfortunately, not enough data for this canopy to reliably confirm that the flow immediately downstream of 55 rows (47 h) is within the main region.

The so-called "0^o-canopy" consisted of "Up"-orientated "trees" rotated to the wind direction $\alpha = 0^o$ (that is, parallel to it). Hence, the resistance to the flow was mainly caused by the pressure drag force acting within the "stem" space and, within the "crown" space, by the surface shear stress on the triangular surfaces. No significant features of this canopy flow were found at the location X=10 rows to distinguish it from the flow associated with the canopy consisting only of "stems".

The same "U-trees" rotated to an attack angle of $\alpha = 45^o$ constituted the "45^o-canopy". The angled "crowns" naturally resulted in a modification of the internal flow so that its direction was very different from the direction of the external flow along the wind tunnel.

Despite such variations in the architecture of the canopies, their influence on the external flow can be thought to be not very different in all cases. All of the "tree" canopies produced external boundary layers with approximately the same depth, as can be seen in Fig. 3.33.

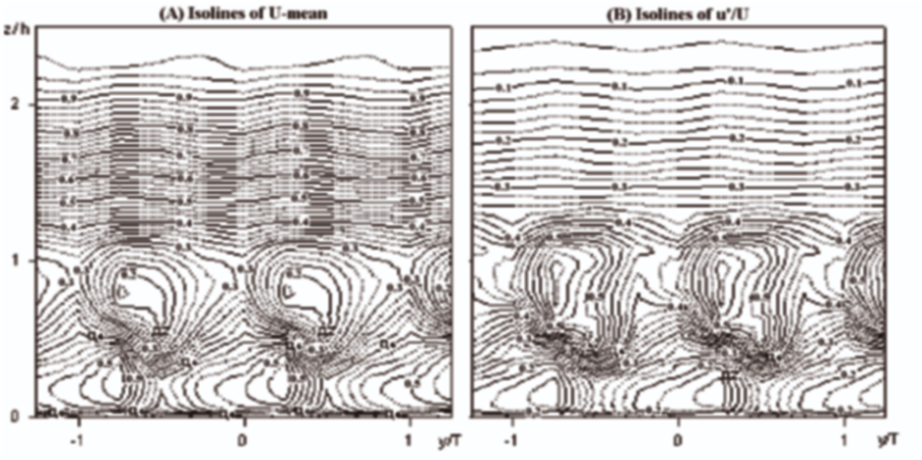

Figure 3.32: Isolines of the normalized mean velocity (A) and longitudinal fluctuations (B) behind the D-canopy fetch of X =10 rows.

3.3.3 Algebraic turbulence model for EPR

It makes clear after the experimental experience that two Reynolds numbers (3.30) should be responsible for the turbulence in EPRs, global and local ones, correspondingly:

$$\mathrm{Re} = \frac{WH}{\nu} \quad \text{and} \quad \mathrm{Re}' = \frac{2rU}{\nu}.$$

The first one is defined by the characteristic length H (the width of a duct or the height of the EPR h) and the velocity (the mean velocity in a duct or the undisturbed boundary layer velocity U_∞) and should determine the stability of the flow as a whole. The second one is defined by the dimension of an individual obstruction $2r$ and the local flow velocity around it U. Just the local Re' determines the vortices shedding from the obstruction. It is known [304] that

(i) the flow streamlines the body if $\mathrm{Re}' < 1$;

(ii) a circulation behind the body appears if $1 < \mathrm{Re}' < 40$;

(iii) this vortex breaks up in two vortices in the region $50 < \mathrm{Re}' < 200$;

(iv) the vortices escape the circulation zone behind the body and form the extended ordered vortex street for Re' up to 1500;

(v) vortex street becomes more and more disordered with the further increase in Re';

(vi) finally, since $\mathrm{Re}' > 8 \cdot 10^6$ the body wake becomes completely stochastic and turbulent.

The "working range" of the local Reynolds number can be estimated as $1000 < \mathrm{Re}' < 30000$, so the vortices behind individual obstructions are still ordered with only

a tendency to stochasticity. At the same time, a huge number of vortices interacts within the EPR that definitely makes the flow highly disordered and thus turbulent. The laboratory experimental data, Fig. 3.31,B, and the field measurements highlight that the intensity of turbulent pulsations can reach even 65%. Mainly meteorologists suggested theoretical models for determining the effective turbulent viscosity in obstructed geometries

$$\nu_T = \nu_T(x, z; U, \partial U/\partial z, ...),$$

and their experience overviewed briefly in Section 1.1 is extremely important for the general theory of EPR.

Over the EPR

Over the EPR all their works postulated the logarithmic mean flow distribution (1.1) with a roughness coefficient z_0 to be determined empirically. Several relations were suggested for the latter [155]:

$z_0 = 0.136h$ (Paeschke, 1937 and Plate, 1971),
or $z_0 = 0.132h$ (Tanner and Pelton, 1960),
or $z_0 = 0.058h^{1,19}$ (Kung, 1961).

Another formulas tried to represent the density of a forest:

$z_0 = 0.5\frac{s}{s_0}h$ (Lettau, 1964),
or $z_0 = 0.36(h - d)$ (Thom, 1971).

Seginer (1974) stated however that the real dependence $z_0/h = f(c_d s \cdot h)$ turns out to be much more complex with $f(c_d s \cdot h)$ even changing a growth by a decrease.

The above discussion doubts the reality of z_0 in formula (1.1). It is worth therefore to eliminate this parameter from the formula. Subtracting the slip velocity $U_h = U(h) = \frac{U_*}{\kappa} \ln \frac{h-d_0}{z_0}$ from (1.1), we obtain the relation

$$U(z) = U_h + \frac{U_*}{\kappa} \ln\left(\frac{z-h}{h-d_0} + 1\right) \tag{3.129}$$

that is more convenient, as the slip velocity U_h can directly be determined from measurements. For the "zero-plane displacement" d_0, another fitting parameter in (1.1) or (3.129), the additional empirical relations are found, see formulas (8.7)–(8.9), chapter 8.

Inside the EPR

Inside the EPR, many works issue from the gradient representation of the effective turbulent shear in the flow

$$\tau = -\rho_1 \langle U'V' \rangle = \rho_1 \nu_T(z, U, ...)\frac{dU}{dz}, \tag{3.130}$$

so that the problem focuses on a suitable parametrization of the effective kinematic viscosity $\nu_T(z, U, ...)$. Some hypotheses were suggested directly for ν_T [155]:

$\nu_T = const$;

$\nu_T = az + b$, Tan,1961; Ordway and Lemon,1963;

$\nu_T \sim U(z)$, Cowan, 1968.

Other suggestions were done for the mixing length $l(z)$ present in the Prandtl's "mixing length hypothesis" $\nu_T = l^2|\partial U/\partial z|$, some of them link the length with the forest density s [155]:

$l(z) = const$, Inoue, 1963;

$l(z) = az + b$, Lemon,1963;

$l(z) = \dfrac{0.6}{s(z)}$, Perrier, 1969;

$l(z) = z\Big(a_1(z)(h - z) + a_2(z)\Big)$, Barr, 1972;

$\dfrac{1}{l(z)} = \dfrac{1}{l_0(z)} + \dfrac{s}{a}$, Menzhulin, 1970;

$l(z) = \min\left\{\kappa(z_0 + z), l_{max}\right\}$, *Seginer*, 1974; *Bickova*, *Dubov*, 1974.

Some of the above hypotheses lead to analytical formulas like (1.3). They can also be applied to a general penetrable roughness.

Two algebraic parametrizations for the effective kinematic viscosity, that generalize the Prandtl's hypothesis, were investigated by the present author:

- for the mixing length

$$\nu_T = \begin{cases} ??, \\ \\ l^2 \frac{dU}{dz}, \end{cases} \qquad l = \begin{cases} const = l_h, & z \in [0, h] \\ \\ l_h + \kappa(z - h), & z \geq h, \end{cases}$$

- and for the viscosity

$$\nu_T = \begin{cases} const = \nu_{T0}, \\ \\ l^2 \frac{dU}{dz}, \end{cases} \qquad l = \begin{cases} ??, & z \in [0, h] \\ \\ l_h + \kappa(z - h), & z \geq h. \end{cases} \tag{3.131}$$

In the first hypothesis, the effective viscosity within the EPR has not been prescribed, but the mixing length has. In the second, the viscosity is prescribed, but the mixing length has been not. It is postulated however that the mixing length in the outer flow linearly continues its value at the EPR height, thus generalizing the Prandtl's mixing length hypothesis. The "universal von Karman coefficient" is usually taken as $\kappa = 0.40$. The advantage of the second model (3.131) is in that it provides some analytical formulas. The effective turbulent viscosity is taken constant within the EPR, $\nu_T = \nu_{T0}$, as the mixing is highly intense and homogeneous there. It is assumed that the parameter ν_{T0} can be found from experimental data. To find the undetermined parameter l_h, the mixing length on the EPR interface $z = h$, the viscosity is assumed to be a continuous function with a conjugation condition $\nu_T(h - 0) = \nu_T(h + 0)$. It follows that

$$l_h = \nu_{T0}\kappa U_*, \tag{3.132}$$

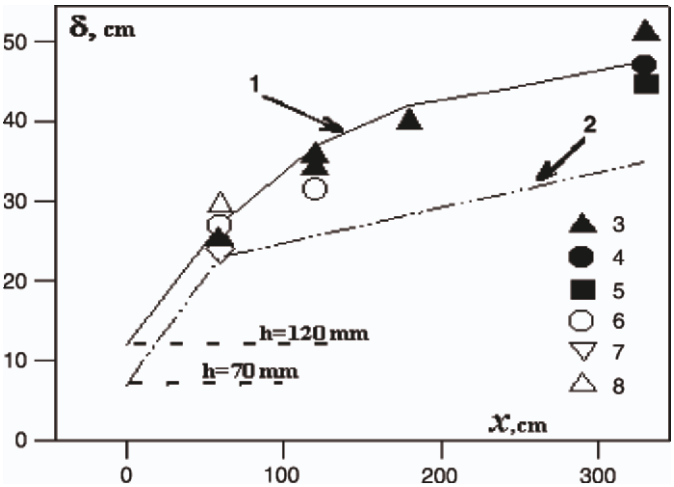

Figure 3.33: The height of the external boundary layer over different canopies investigated: curve 1 – D-canopy, 2 –"stems"-only canopy, $U_\infty = 8\ m/s$. Filled symbols for wind regimes: 3 – 6 m/s, 4 – 4 m/s, 5 - 2 m/s over the D-canopy. Empty symbols: 6 – U-canopy, 7 – 45^o-canopy, and 8 – 0^o-canopy with a wind speed of 8 m/s.

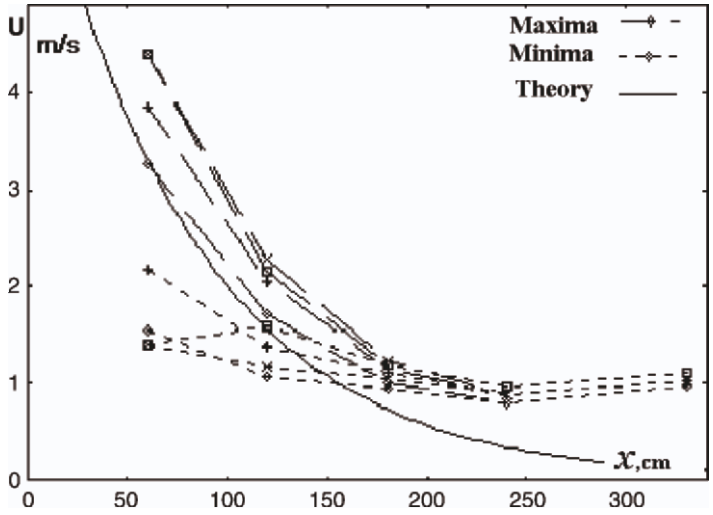

Figure 3.34: Variation of the longitudinal velocity within the D-canopy compared with the theoretical prediction using equation (3.38).

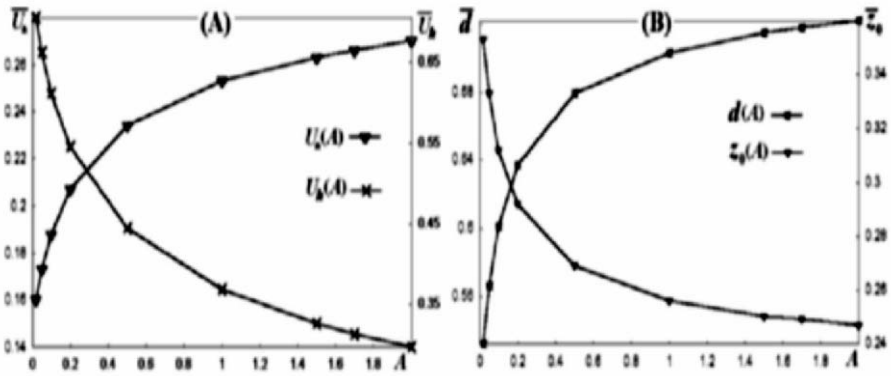

Figure 3.35: Parameters of the logarithmic velocity distribution (1.1) obtained by the EPR boundary layer linear theory for the varying EPR density and the turbulence constant $\overline{\nu}_{T0} = 0.03$.

where the shear velocity is $U_* = \sqrt{\frac{\tau_h}{\rho_1}}$.

The turbulent shear (3.130) is often taken constant in the approximate performances of boundary layers; in fact, Fig. 3.31,C highlights that it is constant over a significant depth H of the main EPR region. The flow obeys the following equation:

$$\frac{d\tau}{dz} = \begin{cases} \frac{1}{2}\rho_1 c_f s U^2, & z \in [0, h] \\ 0, & z \in [h, H] \end{cases} \tag{3.133}$$

where $\tau = \rho_1 \nu_T \frac{dU}{dz}$ and the turbulent viscosity is given by (3.131).

The velocity distribution over the EPR, $z \in [h, H]$, can be immediately obtained as

$$U(z) = U_h + \frac{U_*}{\kappa} \ln\left(\frac{z-h}{z_h} + 1\right). \tag{3.134}$$

The parameter z_h of the formula obtained looks like the roughness coefficient z_0 in formula (1.1), but it has just another physical meaning being proportional to the mixing length on the EPR level, $z_h = l_h/\kappa$. To distinguish, it is called the *mixing length parameter*.

Parameters of the logarithmic law (3.134) were found by fitting to the laboratory experimental data by means of the graphical software Gnuplot and are displayed in the Table 3.3. The velocity distribution (3.134) coincides with the modified logarithmical formula (3.129) if the displacement height is set to $d_0 = h - z_h$. By transforming to the formulae (1.1), the "usual" roughness coefficient z_0 may be calculated as

$$z_0 = (h - d_0) \exp\left(-\kappa \frac{U_h}{U_*}\right).$$

The parameters of (1.1) have also been presented in the right column of Table 3.3. Another way of determining the shear velocity U_* is the use of the correlation profiles

$\langle u'w' \rangle$ measured by the crossed-wire method. Those values, where available, are displayed in brackets. Both methods can differ up to 80%. For the canopy consisting of "stems" only, the related parameters for the logarithmic law have been presented in the last line of Table 3.3.

It is known that logarithmic profiles like (1.1) or (3.134) are proved however for only neutral stratification conditions. Some changes in the formulas are required to account for stable or unstable stratification conditions what will be discussed in the Section 3.3.3, formulae (3.141).

The velocity distribution inside the EPR, $z \in [0, h]$, can be obtained by means of a solution of the second-order ordinary differential equation (3.133). As the equation uses the quadratic law for the distributed drag force, it allows a numerical solution only. The following algorithm can be suggested:

- the equation requires two boundary conditions to be solved. The common non-slip condition $U|_{z=0} = 0$ is supplemented by any trial value of the boundary shear $\tau|_{z=0} = \hat{\tau}_0$ and the profiles $\hat{U}(z)$ and $\hat{\tau}(z) = \rho_1 \nu_{T0} \frac{d\hat{U}}{dz}$ are found by, say, the Runge—Kutta method. The trial boundary values $\hat{U}_h = \hat{U}(h)$ and $\hat{\tau}_h = \hat{\tau}(h)$ are to be found;

- the trial mixing length parameter $\hat{z}_h$ can be calculated by (3.132) and the trial velocity at the boundary layer top $z = H$ can be estimated as $\hat{U}_H = \hat{U}_h + \frac{\hat{U}_*}{\kappa} \ln\left(\frac{H-h}{\hat{z}_h} + 1\right)$;

- Compare the last value obtained with the velocity prescribed $U(H) = U_\infty$, correct the trial value, and repeat calculations again until $\hat{U}_H$ is close to U_∞ with sufficient tolerance.

The model contains the empirical constant ν_{T0}. Its value was found as $\nu_{T0} \approx 0.02 U_\infty \cdot h$ to satisfy the Allan's data for air velocity profiles in a larch forest [6, 223]; it exceeds the laminar air viscosity by up to 10^3–10^4 times.

An approximate "linear theory" can also be developed to make the above solution more transparent, provided the empirical turbulence coefficient ν_{T0} is known. The mass force $\frac{1}{2} c_f s U^2$ in (3.133) can approximately be represented as $k_1 U$ with $k_1 = \frac{1}{2} c_F s \langle U \rangle$, $1/sec$ and with mean velocity value $\langle U \rangle = \frac{1}{h} \int_0^h U(z) dz$. The flow within the EPR obeys the linear equations

$$\frac{d\tau}{dz} = \rho_1 k_1 U, \qquad \tau = \rho_1 \nu_{T0} \frac{dU}{dz}.$$

They provide the analytical forms for the velocity and shear distributions similar to (3.7), (3.8) or to (3.41):

$$U = U_h \frac{\sinh\left(\sqrt{A}\bar{z}\right)}{\sinh\left(\sqrt{A}\right)}, \qquad \tau = \tau_h \frac{\cosh\left(\sqrt{A}\bar{z}\right)}{\cosh\left(\sqrt{A}\right)} \tag{3.135}$$

where $\bar{z} = z/h$ and $A = \frac{k_1 h^2}{\nu_{T0}}$. Both profiles are independent of the wind tunnel velocity regime U_∞. This means that U_h is a universal normalizing scale for the internal velocity

Table 3.3: Parameters for the log-law functions (1.1) and (3.134)

X, rows, U_∞	U_h, m/s	z_h/h	U_*, m/s	z_0
D-canopy				
40 rows, 8 m/s	1.87	1.38	2.0	0.95
55 rows, 8 m/s	2.2	0.86	1.30	0.44
8 m/s	2.7	1.48	1.37 (0.73)	0.67
6 m/s	1.7	0.74	0.88	0.34
4 m/s	1.3	0.69	0.52 (0.35)	0.25
2 m/s	0.66	0.55	0.24 (0.16)	0.18
Stems				
55 rows 8 m/s	4.8	4.1	2.3	1.78

profiles. A relation exists between U_h and τ_h similar to (3.42) that provides the shear velocity

$$U_*^2 = \sqrt{k_1 \nu_{T0}} \cdot \frac{\cosh\left(\sqrt{A}\right)}{\sinh\left(\sqrt{A}\right)} U_h.$$

This relation along with (3.132) and with the relation $U_\infty = U_h + \frac{U_*}{\kappa} \ln\left(\frac{H-h}{z_h} + 1\right)$ constitute the algebraic system sufficient for the determination of all three integral boundary layer parameters U_h, U_*, and z_h. The latter equation set reduces to one transcendental equation for the mixing length parameter $\overline{z}_h = z_h/h$

$$\overline{z}_h^2 = \left(\frac{\nu_{T0}}{\kappa^2 U_{\infty h}}\right) \cdot \ln\left(\frac{\overline{H}-1}{\overline{z}_h} + 1\right) \cdot \overline{z}_h + \left(\frac{\nu_{T0}}{\kappa^2 U_{\infty h}}\right) \frac{\sinh\sqrt{A}}{\sqrt{A} \cdot \sinh\sqrt{A}} \tag{3.136}$$

that can be solved graphically or by a numerical method.

The numerical results for the flow characteristics $\frac{U_h}{U_\infty}$, $\frac{U_*}{U_\infty}$ and $\frac{z_0}{h}$ have been presented in Fig. 3.29 as functions of the EPR dimensionless density A. The calculations were also performed for the empirical turbulence constant $\nu_{T0} = 0.03 U_\infty h$. The shear velocity $U_*(A)$ and the displacement height $d(A)$ turned out to increase, but $U_*(A)$ and $z_0(A)$ decrease with increase in the EPR density. It is possible to vary ν_{T0} in order to fit these theoretical profiles to experimental data, thus determining the empirical constant.

One of the drawbacks of the above one-dimensional theory is that the boundary layer height $\overline{H} = \frac{H}{h}$ is, in fact, unknown and was taken as $\overline{H} = 2 - 3$. This difficulty does not occur for the pressure-driven duct flow. Therefore, the similar calculations were performed for the latter, [223] although no measurements are known for such a

geometry. It should be emphasized that managing such an experiment can give a useful further impetus for this research field.

3.3.4 Performance of the spraying cooling system as an EPR

Laboratory modeling and theoretical investigations of an abstract easily penetrable roughness, as well as the in-situ measurements overviewed in Section 1.4, were carried out to perform a real object, an extended spraying cooling system for a project of the Zaporizhzhya nuclear power plant shown in Fig. 1.12. The interpretation of its droplet layer as an EPR was done in Section 1.4. It is the aim of this section to briefly present the main results of a one-dimensional theory.

From an engineering point of view, the spraying cooling system (SCS) is determined by two groups of factors. Environmental factors determined by meteorological measurements include

- the wind speed outside the boundary layer U_∞, m/s;
- temperature of the approaching air flow T_∞, ^oC;
- air moisture content in the approaching air E_∞ (the mass of vapor in the unit mass of dry air, kg/kg);
- angle of the wind attacking the SCS γ ($\gamma = 90^o$ if the wind is perpendicular to the system being rectangular in a plane, and $\gamma = 0^o$ if the wind blows along the SCS).

Design factors that are of a major importance for engineers include

- longitudinal and transversal lengths of the SCS, l_1 and l_2, m;
- height of spraying fountains h, m
- mean diameter of dispersed water droplets $2r$, m;
- total water output through the SCS Q, m^3/s;
- initial temperature t_h, ^oC of the sprayed water.

The ratio of the water output to the irrigation area $A_0 = l_1 \cdot l_2$ is called the *irrigation density* $q = Q/A_0$ by power engineers, and it is measured in $m^3/(m^2 \cdot s)$; it is one of most important design parameters to determine. The final aim of the performance is the forecast of the SCS thermal behavior, i.e. the final water droplet temperature t_2 and the cooling of water $\Delta = t_h - t_2$, in prescribed and in changeable weather for various SCS designs. The latter allows one to choose an optimal construction.

Recall that this theory is valid under only windy conditions. Under windless conditions, a special theoretical scheme should be developed, [211]. The field experimental data given in Fig. 1.14 confirm that the droplet layer decelerate the wind like it happens in canopy. The first attempt to perform the SCS with an account of the air flow transformation through it was done by Chaturvedi and Porter [114]. Like here, they interpreted the SCS as a droplet layer that decelerates the flow and saturates it by heat and

moisture. However, they considered the outer flow in an isolation from the internal one without their suitable linking. The theory being presented overcomes that drawback by a special attention to the conjugation conditions.

The general theoretical analysis of the flow formed by an obstacle layer shows that the transformation of the flow is confined by only the initial region with an extension of order $(10-20)h$. Over the initial region, the conditions for the droplet cooling become gradually worse so that the cooling is a function of the longitudinal distance, $\Delta t = \Delta t(x)$. However, it is sufficient for practice to account for only the mean cooling over all the initial region length that will be designated here as Δt_1 (subscript '1' labels this first region). If the wind deceleration and the moisture saturation continued to be the dominant mechanism, the further wind would stop within the SCS, the saturation would reach limiting values, and the further cooling of droplets would stop as well, [114]. The above theory of the EPR disproves this, as it accounts for the kinetic energy exchange with the undisturbed external flow, as well as for heat and mass exchange. The rates of the above exchange is measured by the turbulent shear stress τ_h and the heat and mass flows j_{Hh} and J_{Eh} on the interface of the fountain level $z = h$. An equilibrium arises on the main SCS region, the aerothermal profiles become steady, the droplet cooling does not change anymore and will be designated as Δt_2 (this subscript '2' labels the second region). Solutions for the main region will be used here; the variety of meteorological situations will be restricted by summer conditions when evaporation makes the main contribution (about 80%, [60]) to the cooling process.

The flow and exchange processes within the droplet layer

The flow and exchange processes within the droplet layer can be analyzed with the above mathematical models of the EPR in view, especially that for the mobile elements, Section 3.2. It is reasonable to assume that all the droplets continuously appear at the fountain level $z = h$ over the irrigation area $l_1 \times l_2$ with the rate $\dot{N} = \frac{3Q}{4\pi r^3}$, droplets per second. If $\mathbf{v}$ is the typical droplet fall-down speed and $h/\mathbf{v}$ is the typical time of its existence, then the mean concentration of droplets over the irrigation volume $\Omega = l_1 \cdot l_2 \cdot$ is

$$n = \frac{3}{4\pi l_1 \cdot l_1} r^{-3} \mathbf{v}^{-1}, \quad 1/m^3. \tag{3.137}$$

(It can be estimated that the mean number or droplets varies between 10 000 and 1 000 000 in m^3 depending on their size and the irrigation density $q = \frac{Q}{l_1 \cdot l_2}$. The specific frontal area of droplets that is commonly used for canopy descriptions is $s = \pi r^2 n = \frac{3q}{4r\mathbf{v}}$ and can so be estimated as about $0.02 - 0.10\ m^2/m^3$ that is at least by an order less than that in forests).

In fact, some droplets fall down with a continuously accelerated velocity $\mathbf{v}(z) = \sqrt{2g(h-z)}$, so that their density has not been distributed uniformly across the droplet layer: they are denser on higher levels and sparser on lower ones in accordance with (3.81). This leads to velocity local maximum in the initial region like those in Figs. 1.14,A and 3.22 that disappear however in the main flow region.

The above theoretical analysis discovered also that all the dynamical and heat and mass exchange processes in the main region of the EPR flow are governed by several

dimensionless parameters (3.36), (3.88), and (3.103). With the application to spraying systems, they have been found in the form

$$A = \frac{k_d n h^2}{\nu_{T0}} = 15.5 \cdot 10^{-4} \frac{hq}{r^3}, \qquad B = \frac{\rho_1 k_d h}{m\mathbf{v}} = 11.75 \frac{h^{1/2}}{r^2},$$
$$A_E = \frac{\alpha_E k_d n h^2 S_0}{\nu_{T0}} = 0.73 \frac{h^{5/4} q}{r^{5/2}}, \qquad B_E = \frac{\alpha_E b_0 \mathcal{L} \rho_2 h^2 S_0}{\mathbf{v} m c_2} = 3.2 \cdot 10^{-3} \frac{h^{1/2}}{r^2} \tag{3.138}$$

(the calculations are carried out in units SI). The most significant design parameters q, h, and r have been represented in (3.137). On the other hand, no meteorological parameters are seen here. This is because the solutions of Sections 3.2.2 and 3.2.3 are represented in the universal dimensionless form. To distinguish dimensionless quantities from dimensional ones, the bars over symbols will not be dropped.

For the given parameters (3.138), the model predicts all the aerothermal profiles in the main flow region, i.e. the air velocity profile $U(z)$ and the vapour concentration $E(z)$, droplet velocity distribution $u(z)$ and the vapour concentration near their surfaces $e(z)$ which is in an empirical relation (3.94) with the droplet temperature t. The approximate formulas were found as

$$\begin{aligned}
\overline{U}(\overline{z}) &\approx \frac{1}{\chi_{11}} \left\{ B - \chi_{12} \exp\left[\chi_{12}(\overline{z} - 1)\right] - B \exp\left[\chi_{12}\overline{z}\right] \right\}, \\
\overline{\tau}(\overline{z}) &\approx \frac{A}{\chi_{11}} \exp \chi_{12}(\overline{z} - 1) - \frac{\chi_{12}}{\chi_{11}} B \exp \chi_{12}\overline{z}, \\
\overline{E}(\overline{z}) &\approx \frac{B_E}{\chi_{21}} - \frac{\chi_{22}}{\chi_{21}} B \exp \chi_{21}(\overline{z} - 1), \\
\overline{j}_E(\overline{z}) &\approx \frac{A_E}{\chi_{21}} \exp \chi_{12}(\overline{z} - 1) - \frac{\chi_{12}}{\chi_{11}} \exp \chi_{22}\overline{z}, \\
\overline{e}(\overline{z}) &\approx \frac{B_E}{\chi_{21}} - \frac{B_E}{\chi_{21}} \exp \chi_{21}(\overline{z} - 1),
\end{aligned} \tag{3.139}$$

where $\chi_{11} = \frac{1}{2}B + D$, $\chi_{12} = \frac{1}{2}B - D$, $\chi_{21} = \frac{1}{2}B_E + D_E$, $\chi_{22} = \frac{1}{2}B_E - D_E$ are the coefficients of characteristic ordinary differential equations with $D^2 = \frac{1}{4}B^2 + A$ and $D_E = \frac{1}{4}B_E^2 + A_E$. The main vapour mass flow through the droplet layer initial region can be calculated with such distributions in view, which gives

$$\begin{aligned}
j_{1E} &= \frac{1}{h} \int_0^h \rho_1 (E - E_\infty) U dz \approx \\
&\approx \rho_1 \left\{ \frac{E_h}{\chi_{11}} + \chi_{21} - \frac{B+1}{\chi_{11}} E_\infty + \left(\frac{B+1}{\chi_{11}} - \frac{1}{\chi_{11} + \chi_{21}} \right) e_h \right\} U_h, \quad kg/(m^2 s)
\end{aligned} \tag{3.140}$$

(the subscript '1' relates this flow to the initial flow region where it was completely formed).

The flow outside the droplet layer

Profiles (3.139) highlight a detailed flow picture, but mainly integral values U_h, E_h, $U_* = \sqrt{\tau_h/\rho_1}$ and $E_* = -\frac{j_{Eh}}{\rho_1 U_*}$ are required for an engineering performance. They have not been known yet, but the relations for them should be pointed out as

$$U_*^2 h = \nu_{T0} U_h \frac{A}{\chi_{11}}, \qquad E_* U_* h = \nu_{T0}(E_h - e_h)\frac{A_E}{\chi_{21}}$$

that inferred from the second and fourth equations in (3.139) by substituting $\bar{z} = 1$ there.

Consider the external atmospheric flow now, $z \geq h$. The external profiles $U(z)$ and $E(z)$ are formed by the impulse flux τ_h and by the moisture flux j_{Eh} from the "rough surface" $z = h$ that are taken constant over it, $\tau(z) = \tau_h$ and $j_E(z) = j_{Eh}$. The algebraic turbulence model (3.131) links the turbulence exchange coefficients with the air velocity gradient

$$\nu_T = D_T = l^2 \frac{dU}{dz}, \qquad l = l_h + \kappa(z - h).$$

These hypotheses lead to logarithmic distributions (3.134). One can obtain such additional equations for integral parameters:

$$\begin{aligned} U_\infty &\approx U(H) = U_h + \frac{U_*}{\kappa}\ln\left(\frac{H-h}{z_h} + 1\right), \\ E_\infty &\approx E(H) = E_h + \frac{E_*}{\kappa}\ln\left(\frac{H-h}{z_h} + 1\right) \end{aligned} \tag{3.141}$$

where the boundary layer height is assumed to be $H \approx 2h$.

The air over the SCS is highly unstable, because it contains heated and light humid air portions causing buoyancy and natural convection, and thus an additional turbidity (an unstable stratification). Monin and Obukhov [435] suggested to account this by adding a linear term to the logarithmic one (1.1). Here, an alternative way of Nickitin [466] is used that suggests the "universal" Karman constant to be a known empirical function of the Richardson number:

$$\kappa = \kappa(\mathrm{Ri}), \qquad \text{where} \quad \mathrm{Ri} = -\frac{gH}{(U_\infty - U_h)^2}\frac{\Delta\rho_1}{\rho_1}. \tag{3.142}$$

The linear EPR boundary model of Section 3.3.3 was used. An approximate solution of the equation (3.136) for the mixing length parameter was found as:

$$\frac{z_h}{h} \approx \frac{1}{2\kappa(\mathrm{Ri})\cdot \mathrm{Re}}\left\{\left(\frac{4.9}{\kappa(\mathrm{Ri})}\right)^2 + \sqrt{\left(\frac{4.9}{\kappa(\mathrm{Ri})}\right)^2 + 4\mathrm{Re}\left(9.2\cdot 10^{-3} + \frac{\chi_{11}}{A}\right)}\right\}. \tag{3.143}$$

This immediately yields that

$$E_h = \frac{E_\infty h + \ln\left(\frac{H}{h}\frac{h}{z_h} + 1\right)\frac{A_E}{\chi_{21}}}{h + z_h \ln\left(\frac{H}{h}\frac{h}{z_h} + 1\right)\frac{A_E}{\chi_{21}}}, \qquad E_* = -\kappa(\mathrm{Ri})\frac{z_h}{h}\left(E_h - e_h\right)\frac{A_E}{\chi_{21}}.$$

So the integral parameters U_h, U_*, z_h, E_h, and E_* can be found for any κ. The calculations are to be carried out iteratively to satisfy the empirical relation $\kappa = \kappa(\mathrm{Ri})$. The single empirical constant $\nu_{T0} \approx 1.6 \cdot 10^{-2}\ m^2/s$ was determined from the measurements in a SCS (Section 1.4) and substituted into (3.138).

Engineering estimation of cooling

A power engineer is interested in the SCS water cooling Δt at the end, and thus in the final water temperature $t_2 = t_h - \Delta t$. For the summer conditions when evaporation dominates, the latter may be determined now.

Let the droplet layer have a prismatic form with dimensions $l_1 \cdot l_2 \cdot h$. The vertical mass flux $j_{Eh} = \rho_1 E_* U_*,\ kg/(m^2 s)$ takes out an amount of vapor $M_2 = j_h \cdot l_1 \cdot l_2$ and of latent heat $\mathcal{L}M_2$ through the upper SCS' border. The latter is taken out from water droplets so that their cooling is

$$(\Delta t)_2 = \frac{\mathcal{L} \cdot j_h}{\rho_2 c_2 q}.$$

This cooling of droplets is not changed over the main region.

The horizontal component of the mass flow (3.140) and the corresponding latent heat flow were formed in the first (initial) region. So the mass leaving the prismatic droplet layer through its side borders depends on the wind direction and is $M_1 = h(l_1 \sin\gamma + l_2 \cos\gamma) j_1,\ kg/s$. One gets another component of cooling due to the existence of the initial region in the form

$$(\Delta t)_1 = \frac{\mathcal{L} \cdot M_1}{\rho_2 c_2 Q}.$$

The total water cooling by the SCS is thus $\Delta t = (\Delta t)_1 + (\Delta t)_2$. It depends on the whole complex of meteorological and design factors. An example of calculations is given in [210, 216, 223]. The comparison with the empirical nomograph of Berman [60] used to be applied by Soviet power engineers proved some advantages. We also give a few graphical illustrations.

Thermal behaviour of SCSs

Figure 3.36 presents the typical dependence of the water cooling on various meteorological conditions for three variants of the wasted water temperature t_h. The cooling generally increases with the wind intensity (Fig. 3.36,A) and decreases with increase in the atmosphere humidity (Fig. 3.36,B). Under the meteorological conditions given, the temperature can be found to ensure a certain exploitation level of cooling (say, $\Delta t = 8.8^{o}C$ for Soviet turbines).

The cooling significantly depends also on the wind direction, Fig. 3.36,C. The wind strictly across the SCS is the most favorable. The wind along the system should be compensated by rising the temperature of the output water from turbines. (Design parameters of the SCS were taken typical of the Zaporizhzhya nuclear power plant).

SCS design parameters themselves have been very important to be properly chosen by mathematical modeling. The more is the irrigation density, the better is the

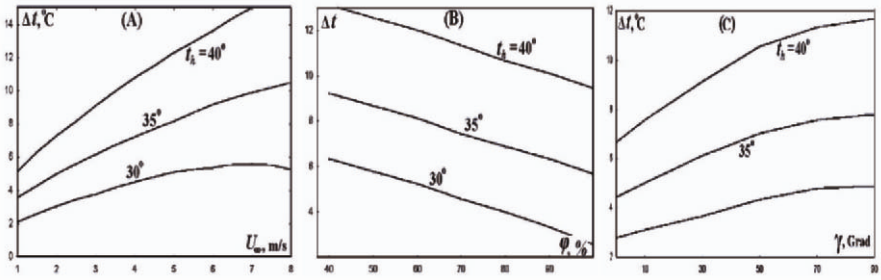

Figure 3.36: Typical dependence of the SCS water cooling upon (A) the wind speed, (B) air humidity, and (C) wind direction.

water cooling. Accounting also for economical reasons, this value was chosen as $q = 1\ m^3/(m^2 \cdot hour)$. Figure 3.37,A shows that the cooling rises linearly with the height of spraying fountains. Such a conclusion must be refined, however, if the mutually acting processes of heat and mass transport are accounted for what is important for autumn and winter conditions.

Figure 3.37,B presents the most distinguishing result. Engineers used to think that the smaller the droplets, the better is the cooling, because the exchange contact area rises as r^{-2}. However, the dimensionless droplet layer density A increases faster, as r^{-3} accordingly to (3.138), and that is the reason that prevents the ventilation of the droplet layer. It is so not surprising that the cooling does not almost depend on the diameter, or it even has a fuzzy maximum.

It can be concluded that the modeling of spraying systems as a kind of the penetrable roughness, or canopy, successfully leads to important practical results. It should also be stressed that many questions still remain unsolved by the one-dimensional half-analytical performance method. Short spraying coolers or large-scale SCSs constructed with relatively short sections with ventilation corridors between them require a more attention to the SCS initial region. Winter weather conditions, as well as the behaviour of tall fountains, require the simultaneous consideration of heat and mass exchange. The SCS' impact on the environment focuses attention to the dispersion of droplet sizes. It was proved over that the initial simple models of immobile or mobile EPR elements have been sufficiently pliable to include new physical phenomena.

However, the most fundamental problem for the theory of EPR is the amendment of the exchange coefficients by means of the in-depth study of the turbulence within the EPR.

3.3.5 Fine structure of the turbulence in EPRs

It can be seen from the above consideration that the theory of EPR flows based on the introduction of the distributed force and sources of substances agrees well with experimental data, at least qualitatively. At the same time, the notable scattering can motivate looking for a refined theory, especially as concerned to the algebraic turbulence model (3.131). Second-order turbulence models that are expressed in terms of the differential equations for ν_T and the associated quantities should certainly fit better,

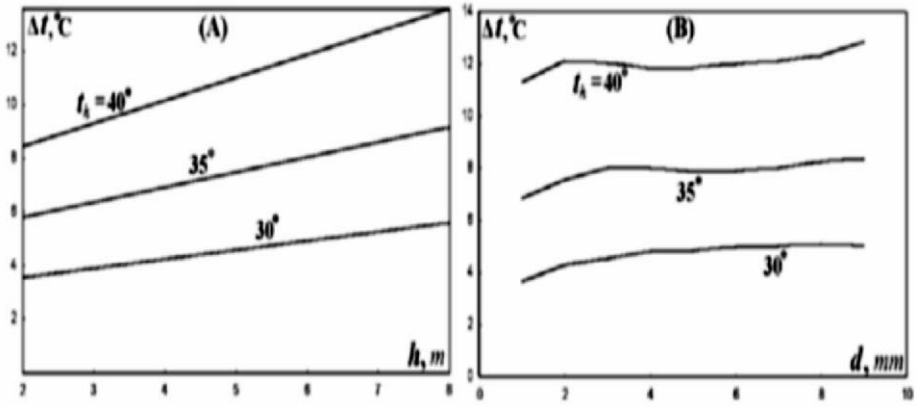

Figure 3.37: Typical dependence of the SCS water cooling upon design parameters for several output water temperatures: (A) height of spraying fountains; (B) droplet size.

for example, for the initial region of an EPR or for EPRs composed of several sections like a spraying system with ventilation corridors between sections. However, several significant circumstances that contradict the common view are to be pointed out. Just these phenomena called here 'paradoxes' should be learned by basic science in the first turn. Indeed, they were widely discussed by meteorologists in the 1980s - 1990s but are unknown in fundamental fluid mechanics yet.

Paradoxes of turbulence in the EPRs

Some paradoxes of the turbulence in canopies, or EPRs, were pointed out by Raupach and Thom in their state-of-art review of 1981, [522]. The first phenomenon is the value of the drag coefficient of elements that constitute the EPR. The highly precise measurements in aerodynamic tubes brought values that depend on the obstacle shape, the flow turbulence level, and the mutual disposition of obstacles but vary near $c_f \approx 0.5$ for spheres and $c_f \approx 1$ for cylinders in the "working range" of the local Reynolds number $10^3 < \mathrm{Re}' < 10^5$. The same coefficient determined from the field measurements in forests turned out to be several times less (in this case, the indirect calculations were performed). A similar paradox takes place for the exchange coefficients.

Raupach and Thom [522] explained this fact by shading some EPR elements by another ones ("shelter effect"). However, the mechanism of this effect has not been clarified: is it a result of the vorticity behind obstacles, or of the extreme turbulence level, or of the basic difference between the natural forest canopy and laboratory models? A possible consequence of aeroelasticity of canopy elements was also listed, [522]. All these mean that the purposeful experiments should still be carried out as well as the mathematical models should be developed that account for a particular behavior of EPR elements (like the freedom of droplets to be drifted by the flow).

The models presented above, as well as models developed by the majority of other authors, forecast the presence of local extreme on the mean velocity profiles in the initial region. Though, after the flow penetrates sufficiently far through the EPR, all the $U(z)$ become monotonic, being growing from the bottom towards the external flow. In addition, no extremes were also found in the wind-tunnel experiments, where the initial extremes were specially managed. It is paradoxical that the maxima (though rather weak) were many times discovered in natural forests even very far away from the forest edge. Shaw pointed out this phenomenon in 1977, [572] and called it the "*secondary maximum phenomenon*", see also Section 5.1 of this book. A number of authors tried to explain this by blowing through effect or attributing the measurement site to the initial flow region, by the incorrect interpretation of the cup anemometer or sonic anemometer readings, by an inclination of real surfaces, and by natural vertical convection jets [155, 522, 572]. A disputable "transilient theory" explanation was suggested by Stull [599] that lies, in short, in following: a turbulent vortex can act from a point A to a remote point C more stronger than to an intermediate point B.

A question appears from the viewpoint of the general EPR theory: is the secondary maximum phenomenon a specificity of forest canopies only, or can something similar be found in other types of EPR flows? "Bulges" on the velocity profiles were found in some measurements in SCS droplet layers, [209, 216, 217, 223]. No similar discoveries were reported for EPRs of another nature, except for the publication of hydraulician Nuding [470]. The last work presents the experimental investigation of the plane hydraulic problem, Section 1.2. The depth-averaged velocity profile in a flume with an artificial vegetation (an array of cylinders) near the left bank has been shown in Fig. 3.38. A local minimum near the interface between the decelerated and free streams is clearly seen.

There is no explanation for the phenomenon mentioned. It is aimed to attract an attention to it again.

Spectral properties of the turbulence in EPRs

Spectral properties of the turbulence in EPRs were investigated to gain an insight of the vortical nature of the EPR turbulence [219, 221]. The same experimental set-up described in Section 3.3.2 was used, with triangle crowns producing large wakes. A single hot-wire anemometer was used to collect the velocity time-histories. A computer-controlled traverse placed the probe at various locations $z = 2, 10, 20, 30\ mm, ...,\ h = 120\ mm, ...\ , 2h = 240\ mm, ...$ along the same vertical from the ground plane highly enough to the free stream. At each location, the probe measured the instantaneous velocity values over a time period τ. The array of instantaneous values $\{U(\tau_i)\}$ was processed by the fast Fourier transformation (FFT) [77] after the measurement. The resulting curve $E = E(f)$ presented the density of the turbulence energy E, m^2/s at frequencies in a diapason $0 < f < \frac{1}{2} f_s$ corresponding to a particular height above the ground plane and a location regarding the wake or the canopy.

The accuracy of each final curve $E = E(f)$ depends on the parameters of the measurement procedure described. Most important is the "sampling frequency" f_s that determines the time interval between samples, $\Delta\tau = 1/f_s$. The block size was taken as $N = 2^8 = 4096$ and so the sampling time was $\tau = N \cdot \Delta\tau$ (the power of 2 being dictated

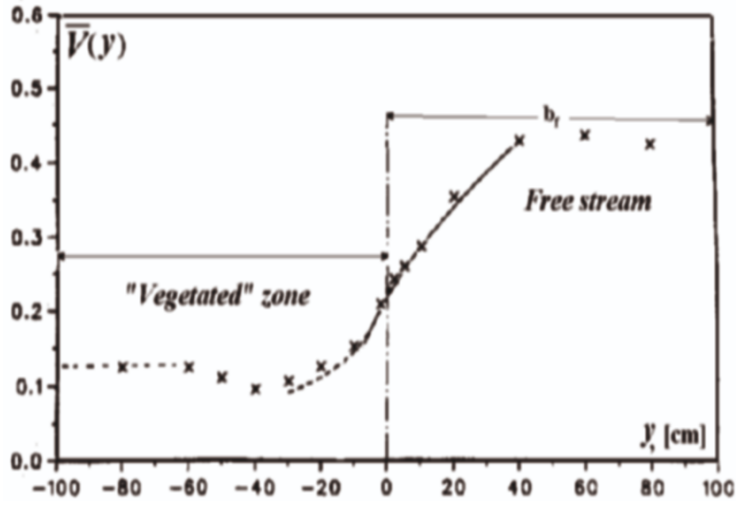

Figure 3.38: Depth-averaged velocity distribution (signs) measured by Nuding in flume experiment *No* 11004, [470]: there is a local minimum near the interface between vegetated (left) and free streams.

by the FFT-algorithm [77]). This gave about $\tau = 20.5\ s$ for the sampling frequency $f_s = 200\ Hz$ and $\tau = 4.1\ s$ for $f_s = 1000\ Hz$. To increase the statistical reliability, several blocks were collected at each measurement point, with good repeatability.

It was important that, for the larger sampling frequency f_s, the spectrum curve $E = E(f)$ included few points in the region of the low-frequency vortices $0 < f < 30\ Hz$. It was found that the spectra obtained with only $f_s = 5000\ Hz$, [220, 221] did not capture the details of these important flow features. In the experiments reported here, two sets of measurements were taken at each location, at the sampling frequencies $f_s = 200\ Hz$ and $f_s = 1000\ Hz$. One data set gave a good resolution for the large vortices, and the other for the small ones.

The examination of the measurement procedure was done by test measurements over the smooth surface before the penetrable roughness model was installed, as well as behind a single tree-like obstruction. The results agreed well with those known from the literature. However, the data also emphasize the urgent necessity of further investigations of EPR flows.

Results for the smooth surface boundary layer

The first test case, useful for future comparison, involved the measurements without any obstructions. That is, a typical boundary layer over a relatively smooth surface (the wind tunnel ground plane covered with plywood) was studied. No unexpected phenomena were found, thereby validating the thermal anemometry technique and acquisition algorithms employed, for flows with a predominant wind direction. For a freestream speed of U_∞, the time-averaged velocity and turbulence intensity distributions are shown in Fig. 3.39,(A). These data allow the determination of the boundary

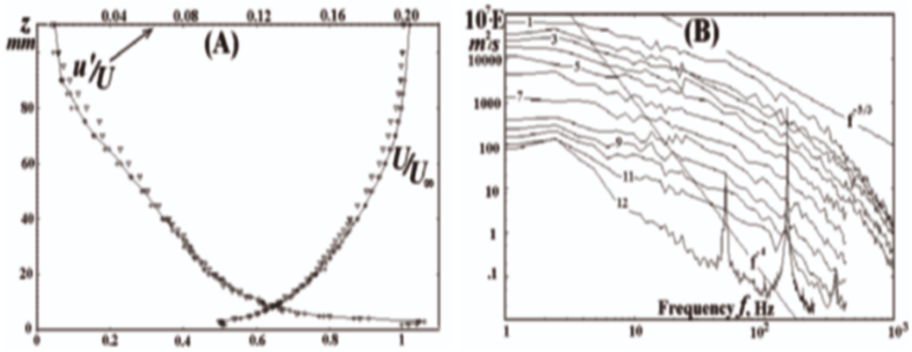

Figure 3.39: Typical vertical distributions over the smooth surface flow: (A) mean velocity and pulsation intensity; (B) energy spectra of velocity pulsations in logarithmic coordinates on various elevations (1 – z=2 *mm*, 2–20, 3–40, 4–60, 5–70, 6–80, 7–90, 8–100, 9–110, 10–130, 110–150 and 12–200 *mm*).

layer depth to be $\delta \approx 78$ *mm* where $U(z)/U_\infty = 0.98$. The maximum of the turbulence intensity of about 20% is at 2 *mm* above the surface. Three types of markers correspond to three verticals across the wind tunnel: one on the centerline, and others 100 *mm* to the left and right.

Figure 3.39,(B) presents the energy spectra of longitudinal pulsations. Each spectral curve is related to a certain elevation over the ground and decreases with increase in the frequency f. The highest curve 1 is related to the elevation $z = 2$ *mm*; the greatest portion of the whole energy of pulsations $0.0055 - 0.0065\ m^2/s$ comes to frequencies about 5–10 *Hz*. Then, the reduction in energy follows the law $f^{-5/3}$ in the energy-containing region $20 < f < 300Hz$, and the law f^{-4} in the so-called dissipation region $f > 400$ *Hz*. It is important to emphasize that all the spectral curves decrease in energy with increase in the elevation above the surface up to $z \approx 2\delta$. This is in compliance with the known data. For instance, the most energetic eddies with frequencies of $5 - 10$ *Hz* on the level $z = 40$ *mm* (curve 3) carry the energy of only $0.0015 - 0.0030\ m^2/s$. However, in the external flow, some peaks can be seen, as on curve 12. These peaks in the free flow are related to frequencies multiple to 50 *Hz* and are certainly due to the electrical noise because the overall turbulence intensity falls to 2–5% on that elevations.

Results for single obstacle wakes

The second case is the wake behind a single obstruction in the form of a "D-tree" described earlier. For a freestream speed of $U_\infty = 8\ m/s$, the measurements were carried out along several vertical lines within the wake behind the "tree", as shown in Fig. 3.40,(A). The mean velocity and turbulence intensity profiles over the vertical line (9,1) that lies in the wake at a distance of $2.5h$ behind the D-tree are shown in Figs. 3.40,(B) and (C), curves 2, along with the corresponding profiles in the oncoming flow upstream of the obstruction (curves 1) for the purpose of comparison. The aerodynamic wake results in the velocity reduction to $U_w \approx 6\ m/s$ and the increased

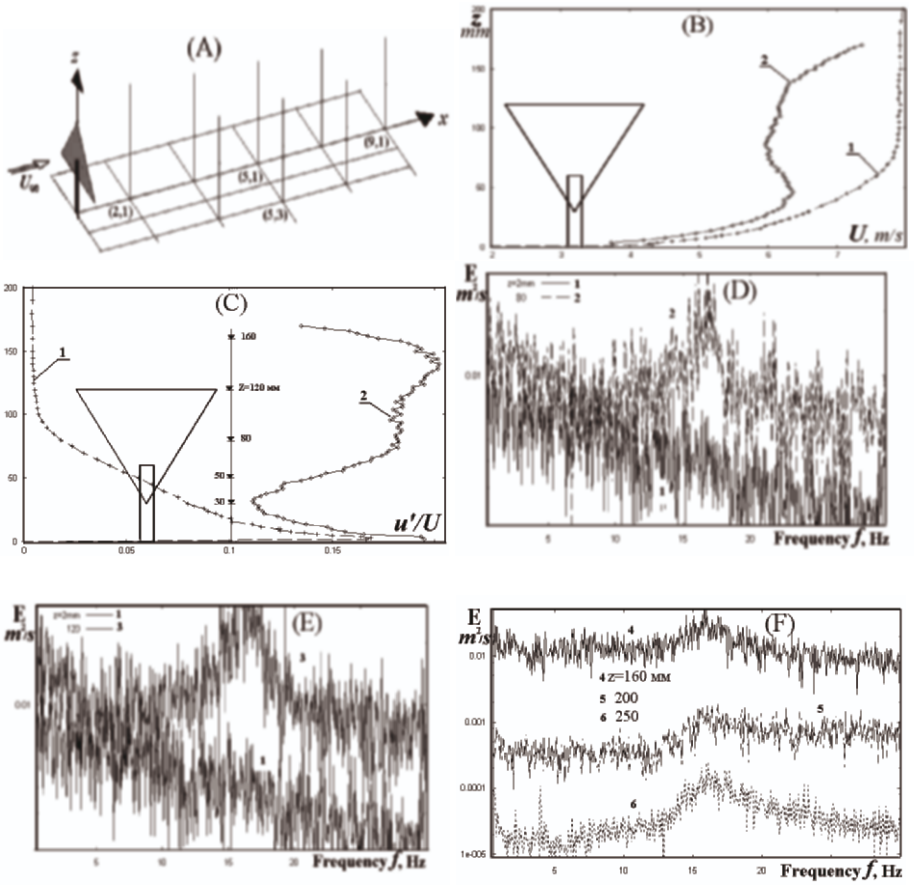

Figure 3.40: Wake investigation verticals (A) and some characteristics within a single wake over the vertical (9,1) located behind a D-tree: (B), (C) mean the velocity and turbulence intensity distributions; (D)-(F) spectrum curves for several elevations shown in (C), 1 – z =2 *mm*, 2–80, 3 – $z = h$ = 120 *mm*, 4–160, 5–200, 6 – z = 2.08 *mm*, h = 250 *mm*.

turbulence within a significant volume of the wake. A silhouette of the obstruction relates the wake directly to the triangle "crown". Note that the crown's equivalent diameter is about $d_e = 5.6\ cm \approx 0.7\delta$.

The spectral curves of longitudinal pulsations at the same vertical (9,1) have been shown in Figs. 3.40,(D)–(F). The levels, at which the measurements were taken, have also been shown in Fig. 3.40,(C). There are no additional features in the spectral curve 1 just $z = 2$ *mm* above the surface, nor in any of the other curves within the trunk space up to $z = 40$ *mm*; this means that the single trunk influences the flow very weakly. However, at the elevation $z = 80$ *mm* and higher within the "crown" wake (curves 3, 4, 5, and 6), the spectral curves behave differently from those in the smooth wall

boundary layer. These spectral curves show a rise that indicates an increase in the turbulent kinetic energy. The energy in the frequency band $1 - 30\ Hz$ is approximately 20 times more than that in the boundary layer. The curves begin to decrease in energy above the elevation $z = 160\ mm$ (curves 4, 5 and 6), these being outside the main wake volume.

Another distinguishing feature of the spectral curves can also be analyzed. The pronounced peaks on curves 2–6 indicate that there is a significant energy at frequencies about $f \approx 17\ Hz$, corresponding to a Strouhal number $\mathrm{St} = \frac{d_e f}{U_w} \approx 0.17$. Above the wake and far enough to its sides, the energy reduces and the spectral curves come to the shape obtained in the smooth wall boundary layer. Such peaks in wake spectra immediately downstream of individual obstructions have been found by other authors, see, for instance, [197].

Results for the canopy vorticity

Consider now what happens to the vorticity within and over a penetrable roughness. In Figs. 3.31, the mean flow quantities and the one-point correlations $\overline{u'^2}$ and $\overline{u'v'}$ were measured along vertical lines through a PR of several fetch lengths, and their rapid tendency towards homogeneous turbulence distributions was shown. The focus of the spectrum measurement is the vortical structure of the canopy turbulence. Figure 3.41 presents the spectral curves measured on several levels on a vertical line through a PR, 5 "tree" rows behind the leading edge. It can be noted that the spectral curves almost coincide everywhere within the canopy depth, say, for elevations $z = 2,\ 20,\ 40,\ 60,\ 100$ and $z = h = 120\ mm$ (only some of these are shown in Fig. 3.41 for clarity). This fact indicates a homogeneous vorticity over the whole space layer $0 < z \leq h$ despite an inhomogeneous drag area distribution (3.128). It can be also mentioned that there is the equal energy distribution between the low frequencies $0 < f < 10 - 15\ Hz$, and this differs from both of the above test cases. No principal differences have been noted at high frequencies when compared to the smooth wall boundary layer case. In particular, there are no peaks, and this indicates the absence of any discrete dominant vortical structures.

The same homogeneity feature characterizes the external flow just above the top of the canopy $z = h$, where the spectral curves begin to gradually reduce in magnitude up to the elevation $z = 220\ mm \approx 1.8h$. The curves can be thought to tend towards those of the freestream (curves 11 and 12 in Fig. 3.39). However, their real behavior becomes quite different at higher elevations. At an elevation of $z = 240\ mm = 2h$, a small peak appears on the spectral curve 5, corresponding to the frequency $f \approx 17\ Hz$, and such peaks grow for next elevations z (see curve 6 for $z = 360\ mm = 3h$) up to the elevation $z = 420\ mm = 3.5h$ (not shown).

The drastic change in the behavior of vortices above the canopy was confirmed by other measurements, at the distance of 20 rows from PR's leading edge, for example. The only difference was that the frequency of peaks was shifted to $f \approx 5\ Hz$.

The question is how to explain the phenomena found. For example, why do the vortices untwist over a relatively calm space layer $h \leq z \leq 1.5h$? The recent advances in fluid mechanics have included the discovery of manifold coherent structures that can constantly be produced in shear flows, thereby contributing to the turbulence [18].

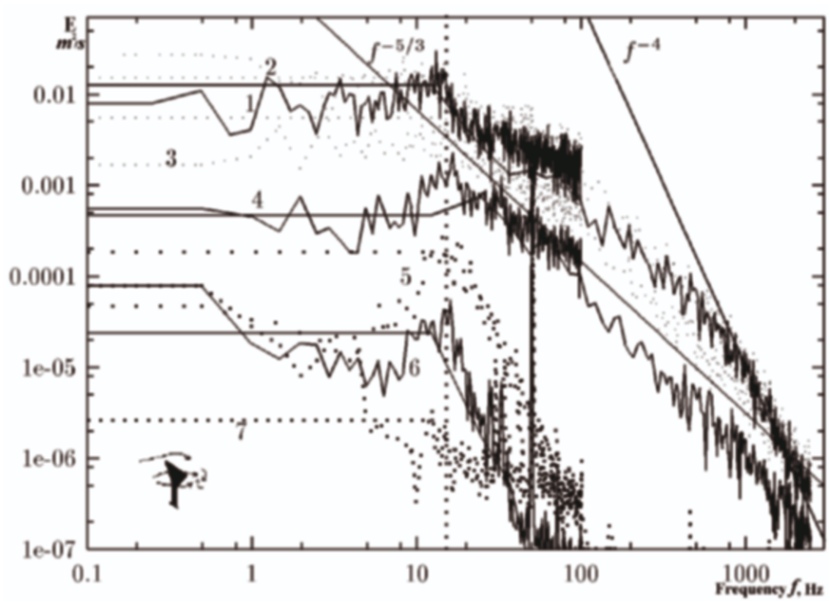

Figure 3.41: Velocity spectra on various elevations within and over the PR from 5 rows of D-"trees": 1–z = 20 mm, 2–z = –120 mm = h, 3–220, 4 – z = 2h = 240 mm, 5 – 300, 6–360, 7–605 mm. Flow speed U_∞ = 8 m/s.

In particular, a hypothesis was recently formulated for canopy flows [186, 187] that, because of an inflexion point on the mean velocity profile $U(z)$ between the internal and external flows, an instability occurs over the PR's leading edge that creates coherent vortices. This hypothesis and its explanation is discussed in Chapters 4 and 5.

3.3.6 Conclusion

It can thus be thought that the intensive turbulence within EPRs, i.e. canopies, reveals some features that are very distinguishing from the common "unobstructed" turbulence. Such kind of the turbulence attracted an increased attention of researchers in last years, [81, 155, 186, 187, 305, 318, 410, 462, 500, 522]. Despite the simplified first-order turbulence closures (algebraic models) or second-order ones (with differential equations for ν_T) turned useful and lead to some plausible results in practical areas, many its phenomena remains unexplained. Further information about basic turbulence laws is provided in Chapters 2, 4 to 9 along with further practical applications.

Acknowledgements

The author of Chapters 1 and 3 dedicates this publication to the blessed memory of Prof. I.K. Nickitin who kindly approved the author's initial ideas about EPR. A corresponding member of UNAS, Dr. Yu. Savchenko, and an academician of UNAS, Prof.

V. Grinchenko, also promoted Dr. Gayev's research under difficult Ukrainian circumstances.

Research grants from Badenwerk Stiftung (Karlsruhe, Germany), the German Research Society, The Royal Society (UK) and US National Science Foundation are gratefully acknowledged in support of the author's work. He is also thankful to Prof. G. Ernst and Prof. W. Rodi (Karlsruhe, Germany), Prof. R. Meroney (Fort Collins, USA), Prof. R. Shaw (Davis, USA) and Prof. J. Hunt (UK) for many fruitful discussions.

A special gratitude is extended to Dr. Eric Savory (Western Ontario, Canada) who collaborated with the author on some of the experimental results presented here in Sections 3.3.2 and 3.3.5.

Chapter 4

Observation and simulation of flow in vegetation canopies

R.H. Shaw[1]
University of California,
Davis, USA

4.1 Introduction

Terrestrial vegetation canopies are obvious examples from the natural world of flow and transport in complex obstructed geometries. Observations of turbulence structure in vegetation canopies date back almost forty years (Wright and Lemon, [654]; McBean, [402]; Allen, [6]; Baines, [19]; Isobe, [307]; Shaw et al., [571]). One of the earliest observational studies of the budget of turbulent kinetic energy inside a forest is that of Lesnik [369]. This latter author appears to have been the first to illustrate the importance of the diffusion of turbulent kinetic energy between levels in the canopy, and to point to the significance of the large difference in scale of turbulence between that created by large-scale shear near the canopy top and that resulting from wakes behind individual canopy elements. It is now clearly apparent that turbulence over and within plant canopies differs significantly from that over smoother surfaces. In particular, velocity spectra are more sharply peaked, streamwise and vertical velocities are strongly (negatively) correlated and are each highly skewed, and transport is dominated by organized structures with ejections from the canopy preceding downward sweeps of high momentum fluid. Excellent reviews of flow and turbulence in plant canopies can be found in Raupach and Thom [522] and, more recently, in Finnigan [187].

An immensely complicated array of leaves, branches, and other plant components, both living material and dead, forms a highly porous barrier to air flow. Despite the visual impression of high density, the actual volume occupied by plant material is a very

[1]E-mail of the author: *rhshaw@ucdavis.edu*

Ye.A. Gayev and J.C.R. Hunt (eds.), Flow and Transport Processes with Complex Obstructions, 179–198.

small fraction of the total canopy volume, usually less than 1%. For this reason, the canopy micrometeorologist can generally neglect the small fractional volume not occupied by the fluid. Yet, in most situations the canopy itself, rather than the underlying ground surface, acts as the primary sink for the momentum of the air.

Air carries away from the canopy and brings to the canopy a wide range of quantities of importance to the biosphere. Aerodynamics creates the microenvironment in which leaves function, in which a host of insects and fungi reside, and in which other biotic activity takes place. Knowledge of the physical nature of canopy exchange is essential to sound analysis and modeling of processes important to agriculture, forestry, land management, and climate change or assessment. While field observations form the basis of our understanding of canopy turbulence, many recent scientific advances in knowledge of such flows stem from computational studies, and they form the major component of this chapter.

4.2 Flow above the canopy

Surface roughness causes a drag on the wind expressed as a shear stress (where stress is force per unit surface area). The square root of the surface kinematic stress $\sqrt{\tau_0/\rho}$ is the friction velocityg u_*. Dimensional arguments lead us to a logarithmic form for the wind profile such that:

$$\overline{u} = \frac{u_*}{\kappa} \ln\left(\frac{z}{z_0}\right), \tag{4.1}$$

where κ is von Karman's constant and z_0 is an expression of the roughness of the surface termed the roughness length. The influence of atmospheric stability can be included using a modified version of the surface layer wind profile:

$$\overline{u} = \frac{u_*}{k}\left[\ln\left(\frac{z}{z_0}\right) + \Psi_m\left(\frac{z}{L}\right)\right], \tag{4.2}$$

where the stability factor Ψ_m is a unique function of the ratio of the height z to the Obukhov length L. Specific forms are available for the ψ-function for both stable and unstable stratification. The proviso here is that the terrain and flow are reasonably horizontally homogeneous, and that observations are conducted at heights that are small compared with the full boundary layer depth yet relatively large compared with the dimensions of the elements of which the surface is composed.

For many situations, this is too restrictive and a modification must be made to account for the fact that exchanges between the atmosphere and the canopy occur at levels elevated from the ground surface by plant components. The common procedure is to introduce a quantity called the zero-plane displacement to adjust the level at which momentum, or the variety of scalar quantities, are exchanged. Whereas all levels within the canopy might be active and the various sources or sinks are distributed through the depth of the canopy, they are represented in this case by a single level. The wind profile can then be written:

$$\overline{u} = \frac{u_*}{\kappa}\left[\ln\left(\frac{z-d}{z_0}\right) + \Psi_m\left(\frac{z-d}{L}\right)\right], \tag{4.3}$$

and the effective origin of the wind profile is elevated to the level d within the depth of the canopy. Typically, the zero-plane displacement is approximately 2/3 the total height of the canopy ($d = 2h/3$) but should also be dependent on canopy density, with d a smaller fraction in more sparse canopies, and a larger fraction in more dense ones. One might also consider vertical distribution of plant material as a factor in determining the value of the zero-plane displacement. Since the sink for momentum does not reside at a single level but, rather, is distributed through the full depth of the canopy, it is clear that this equation cannot be applied to the layer immediately overlying the canopy. In theory, it is appropriate only for levels for which $z >> d$, but it is common to find that the expression is applied to the mean wind profile at relatively short distances above the canopy. The layer immediately overlying the canopy, and extending to $2h$ or more, is generally called the roughness sublayer, and is a region in which departures from general surface layer theory are encountered.

4.3 Flow within the canopy

Vertical profiles of wind, temperature and scalar concentration within the canopy differ markedly from those found above the canopy. If above-canopy flow can be approximated as logarithmic, flow within the canopy is to be characterized as exponential (see upper left portion of Figure 4.1). The rate of depletion of wind with depth into the vegetation is directly related to the density of the canopy, which is usually expressed as the leaf surface area plus the cross-sectional area of cylindrical plant parts, such as branches and trunks, per unit volume that the material occupies. The curvature of the profile reverses in sign and creates an inflection point, which occurs close to the top of the stand when the canopy is sufficiently dense. If the stand is relatively open in its lowest levels, as is often the case in the trunk space of a forest, the wind profile can exhibit a secondary maximum before diminishing to zero at the ground surface.

Real terrestrial surfaces are rarely horizontally extensive, and are most often characterized by frequent changes in vegetation type and height. Particularly in naturally vegetated lands, the terrain commonly exhibits a complexity in slope and elevation that has major influences on the aerodynamics of plant canopies. Nevertheless, it is an essential first step to establish an understanding of flow through "uniform" canopies as a basis from which to study flows in even more complicated situations.

The primary aerodynamic influence of the canopy is, of course, the drag imposed by vegetative elements on the wind field. This drag is composed of viscous drag (skin friction) and form or pressure drag but, at the Reynolds numbers characteristic of leaves in the upper part of the canopy (where the bulk of the momentum is absorbed), the latter component is the more important. Form drag imposed on the air stream by an individual element is approximately proportional to the square of the wind speed and to the exposed cross-sectional area, leading us to introduce a drag force F_i (force per unit mass acting in the x_i-direction) into the equation of motion to represent the influence of the canopy, where

$$F_i = -c_d a U u_i. \tag{4.4}$$

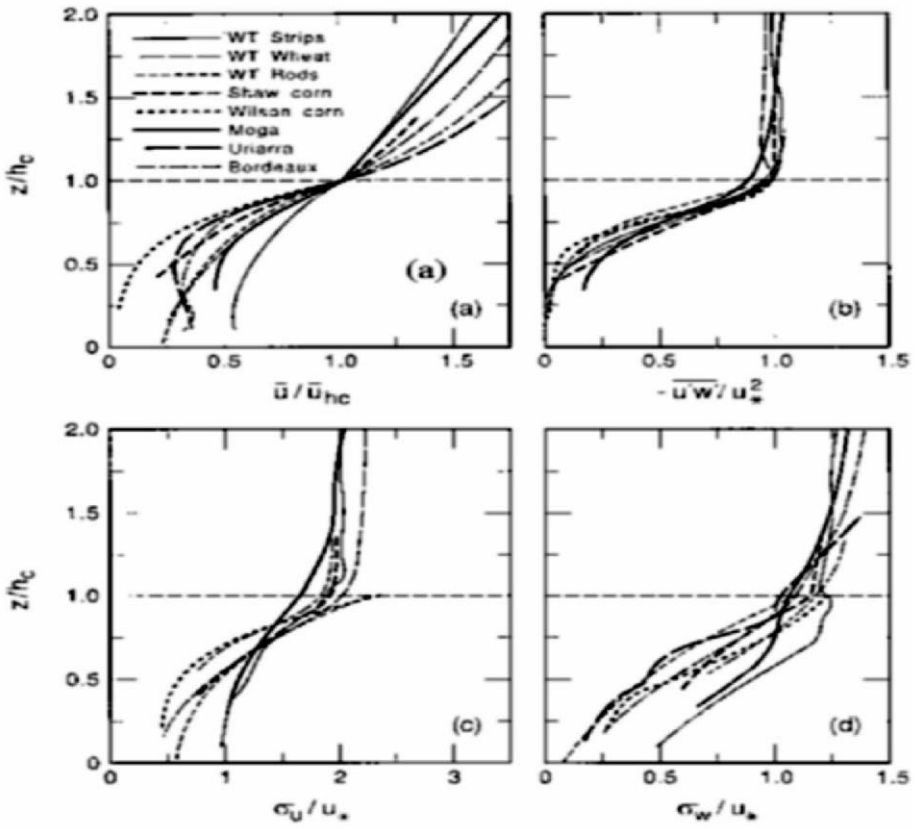

Figure 4.1: Vertical profiles of mean wind (top left), Reynolds stress (top right), streamwise velocity standard deviation (bottom left), and vertical velocity standard deviation (bottom right) within and above various plant and artificial canopies. Wind speed is normalized by its value at canopy top, other velocity statistics by the friction velocity, and height is normalized by canopy height. (From Kaimal and Finnigan,1994 [324]).

The dimensionless drag coefficient c_d (in meteorological practice the usual factor of 1/2 is omitted) is treated as isotropic and includes the influence of leaf and branch orientation, since the quantity a is the one-sided plant area density (m^2/m^3), not the cross-section exposed to the wind. Here, U is the scalar wind speed, while u_i is the velocity vector in the x_i-direction.

Canopies display large relative intensities of turbulence, although the magnitude of the turbulent fluctuations diminishes with depth in the canopy just like the wind speed. This is because the drag elements suppress both the mean wind and the fluctuations but diminish the former more rapidly. The turbulence generated in the wakes behind flow obstructions, so-called wake turbulence, is of a small scale, dissipates relatively quickly and generally contributes little to the turbulent kinetic energy or to the diffusing power of the air flow. Except in sparse canopies, little momentum diffuses to the soil surface

and the ground shear stress is usually insignificant. Virtually all of the momentum of the flow diffusing from aloft is absorbed by the elements of the canopy.

Plant canopies exhibit remarkable turbulence statistics, which makes canopy aerodynamics a topic of substantial scientific interest. Of particular note are the degree to which vertical and streamwise velocities are correlated, and the high degree of skewness in these two velocity components. The correlation coefficient that relates streamwise and vertical velocities, defined as

$$r_{uw} = \frac{\overline{u'w'}}{\sigma_u \sigma_w} \tag{4.5}$$

is typically of the order of -0.35 at levels above the roughness sublayer but reaches values as high as -0.6 near the top of tall vegetation. The negative values imply downward transport of horizontal momentum, while the larger magnitude measured at the vegetation surface is a strong indication that the flow is of a more highly organized nature.

Strong skewness of the velocities

$$Sk_u = \frac{\overline{u'^3}}{\sigma_u^3} \qquad Sk_w = \frac{\overline{w'^3}}{\sigma_w^3} \tag{4.6}$$

also suggests that the flow is dominated by structures that link the two velocity components, and link velocity components with distributions of scalar quantities such as temperature, humidity and carbon dioxide concentration. Inside the canopy, streamwise velocity skewness tends to be large and positive because the flow is dominated by brief but large positive perturbations, while vertical velocity skewness is large and negative because large downbursts accompany high momentum fluid from aloft. Other analytical procedures such as quadrant analysis (Finnigan [183]) have helped to clarify the picture of a flow that is dominated by structures with strong downward "sweeps" of high momentum air linked to relatively weak "ejections" of low momentum. This characteristic is illustrated most clearly by traces of the locus of the u, w turbulent velocity vector. Figure 4.2 is an example of the velocity field above and just within a deciduous forest. The trace within the canopy exhibits strong correlation between velocity components, and an anisotropy between sweeps and ejections.

Careful examination of turbulence in canopies using multiple sonic anemometry, mostly in forests but also in agricultural crops, has provided further detail, and an image now exists of coherent structures consisting of an ejection of low momentum air followed by a more intense downward sweep of air from aloft engulfing the canopy with "fresh" air. At the point of convergence between the ejection and the sweep, scalar quantities exhibit strong gradients (microfronts) that are tilted in the downstream direction. This sequence of events creates time traces of scalars (temperature, humidity etc.) that form a ramp-like pattern. During the day, for example, temperature and humidity measured near the canopy top steadily increase over periods of several seconds or tens of seconds but then rapidly fall with the onset of the sweep (Figure 4.3). The sweep refreshes the canopy with air from aloft. Combining the temperature and velocity records averaged over a number of ramp events, Gao et al.[204] were able to demonstrate the close relationship between scalar and vector fields in the time-height domain. This is

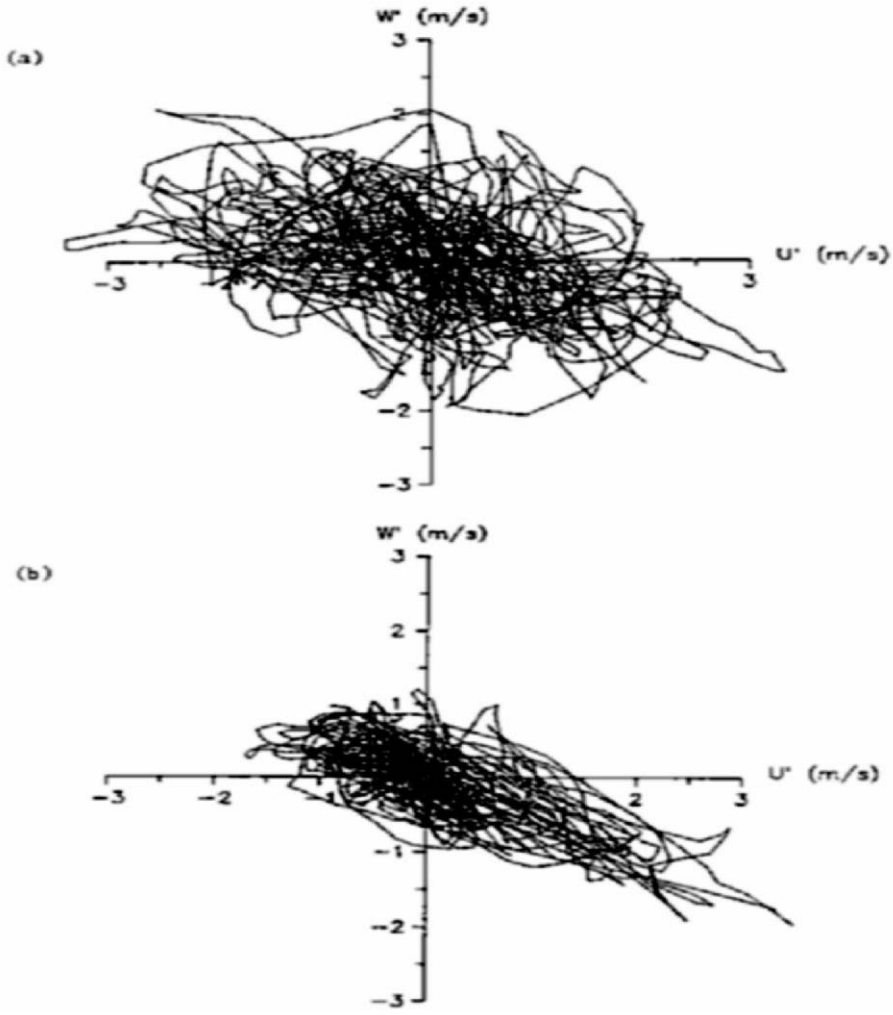

Figure 4.2: Locus of the vector turbulent velocity u', w' at two heights at a deciduous forest site: (a) 2.4 times canopy height; (b) 0.86 times canopy height. (From Shaw and Patton, 2003 [578]).

shown in Figure 4.4, in which the authors reverse time on the horizontal axis to give an impression of the spatial arrangement of the structure. This characteristic has encouraged some researchers to invoke a "surface renewal" approach to the modeling and analysis of canopy exchange.

Field observations have shown that pressure perturbations are also closely connected to coherent structures. Large-eddy simulations (LES) have been extremely useful in this regard and it is now recognized that a relatively large, positive pressure perturbation is centred at the scalar microfront and the top of the canopy. This pressure

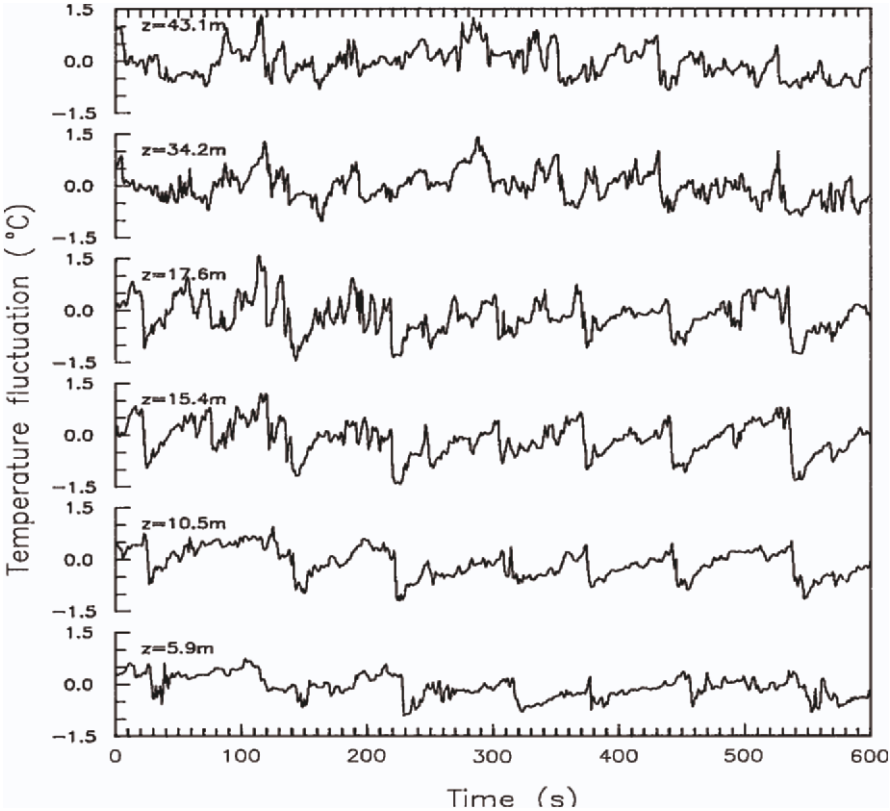

Figure 4.3: Time traces of air temperature at six levels within and above an $18m$ tall deciduous forest at Camp Borden, Ontario, Canada.

pulse is certainly a consequence of the convergence in the flow field, and is a dominant influence on the airflow in the lower reaches of the canopy.

4.4 Computational representations of canopy flow

The first attempts to model flow and transport in plant canopies that accommodated (i) the distinct microclimates of different stands of vegetation; (ii) the separation of soil surface and layers of canopy as distinct sources and sinks of heat and mass; and (iii) the influence of atmospheric stability or advection effects, applied gradient transfer to diffusion within the canopy space ([493]). In this procedure, a flux density is expressed as the product of a diffusion coefficient (turbulent or eddy diffusivity) and the gradient of the time average of the quantity of interest, as in the following examples:

$$H = -\rho C_p K_h \frac{d\overline{\Theta}}{dz}, \qquad \lambda E = -\rho \lambda K_w \frac{d\overline{q}}{dz}, \tag{4.7}$$

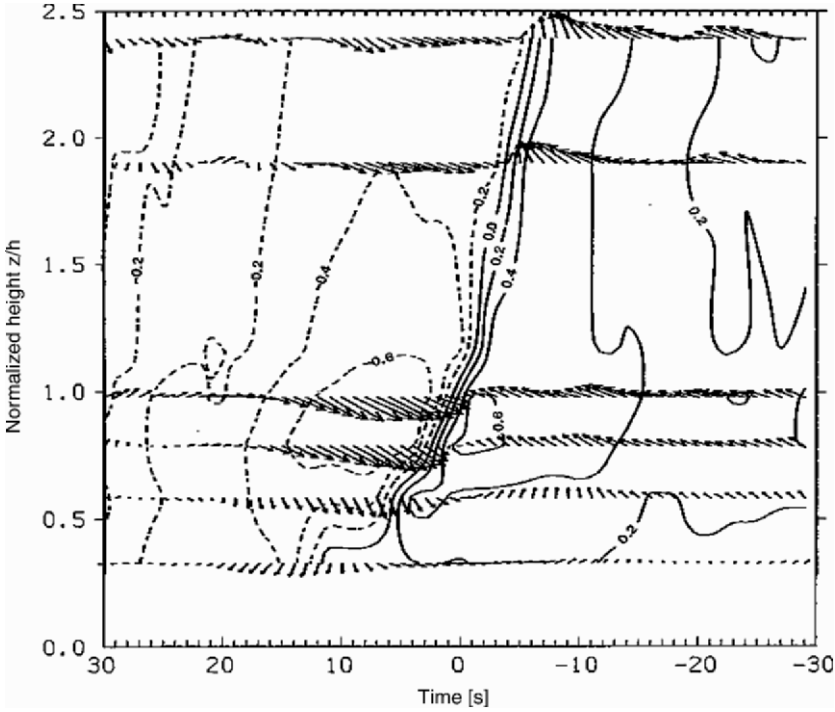

Figure 4.4: Height/time cross-section of temperature fluctuation (contour lines) and the u', w' turbulent velocity vector. The temperature field exhibits a sloping microfrontal boundary between warm air being ejected from the canopy (right side), and cool air being swept into the canopy (left side). (From Gao et al., 1989 [204].)

where H and λE are energy fluxes per unit horizontal area (flux densities), ρ is air density, Θ is temperature, q is specific humidity, and the overbars signify time averages. Incorporated into conservation equations for heat and water vapour, these expressions have formed the basis of many simulations of the plant-atmosphere continuum.

The shortcoming of such descriptions of exchange is that diffusion is not a local phenomenon, as implied by these formulations, and eddy sizes most important to exchange within the canopy can be many times larger than scales associated with the distribution of sources and sinks of heat, water vapour, etc. As an obvious example, gradient diffusion would not permit a secondary maximum in the wind profile in an extensive canopy, because such a profile would require a counter-gradient flux of momentum.

4.5 Higher-order closure schemes

Some of the difficulties associated with gradient diffusion are alleviated by further manipulation of the basic conservation equations to create equations for the time rate of

change of the fluxes themselves. This is a straightforward mathematical procedure that, in itself, does not introduce any new physics into the problem but allows a more direct treatment of the turbulent nature of the flow. As an example, the following equation represents the time rate of change of kinematic heat flux:

$$\frac{\partial \overline{w'\Theta'}}{\partial t} = -\overline{w'^2}\frac{\partial \overline{\Theta}}{\partial z} + \frac{g}{\overline{\Theta}}\overline{\Theta'^2} - \frac{\partial \overline{w'^2\Theta'}}{\partial z} + \overline{\frac{p'\partial\Theta'}{\rho\partial z}}, \tag{4.8}$$

where g is gravitational acceleration, and p is static pressure. Here, we have made the assumption that molecular diffusion is negligible, and that conditions are horizontally homogeneous. With the incorporation of equations such as this, it is no longer necessary to parameterize the flux density via a gradient-diffusion approximation. The terms on the right hand side of the above equation represent processes that act to increase, decrease or physically move the kinematic heat flux. In order, they are gradient production, buoyant production, turbulent transport, and return-to-isotropy. This latter term is the primary sink for kinematic heat flux and expresses the rate at which the flow becomes scrambled, and velocity and temperature become uncorrelated.

The construction of second moment equations, such as the one above, naturally introduces other unknowns and terms of third order. This is to be expected, of course, because the manipulation of the governing conservation equations did not add new information. To close the equation set, it is necessary to either parameterize the higher-order terms that appear on the right hand side of the equations, or construct a set of even higher order equations. It is quickly seen, however, that this latter is a never-ending process with terms of even higher order. Examples of the application of higher-order closure to modelling plant canopies can be found in Wilson and Shaw [647], Meyers and Paw U [430]), and Wilson [648].

4.6 Large-eddy simulation

Large-eddy simulation (LES) was pioneered by Deardorff [146] and is now employed extensively in many fields of engineering and environmental fluid dynamics. A compromise is made such that the largest eddies are directly resolved by a three-dimensional grid network, while parameterisations are applied only to the smallest scales (subgrid-scales - SGS), which remain unresolved. The grid network is selected so that resolved eddies are responsible for a large fraction of the kinetic energy content of the flow, leaving only a small contribution from SGS motions.

Shaw and Schumann [576] were the first to apply LES to the canopy environment in attempts to reproduce characteristics of the flow through and above a deciduous forest. The code numerically solves the basic conservation equations for momentum and heat with options for additional scalars. For flow through a horizontally homogeneous canopy on uniform terrain, the momentum equation appears in the following manner:

$$\frac{\partial \overline{u_i}}{\partial t} + \overline{u}_j \frac{\partial \overline{u_i}}{\partial x} = -\frac{1}{\rho}\frac{\partial \overline{p}}{\partial x_i} - \frac{\partial \overline{u_i'' u_j''}}{\partial x_j} + \frac{g}{T}\overline{\Theta}\delta_{i3} + F_i, \tag{4.9}$$

where the canopy drag force is parameterised as $F_i = -C_d a \overline{V}\overline{u_i}$, and $\overline{V}$ is the scalar wind speed. Here, an overbar refers to a resolved variable whose value changes from grid point to grid point and from time step to time step through the numerical integration. Double primes denote unresolved SGS contributions. Thus, $\overline{u_i'' u_j''}$ represents the SGS contribution to the turbulent stress and must be parameterised. Most efforts to further develop large-eddy simulation centre on schemes to model subgrid-scale fluxes.

Large-eddy simulation output is a three-dimensional, time-dependent flow and scalar field. The results are unique in reproducing most aspects of the turbulent flow field and its interaction with a layer of vegetation. Due to the considerable demand on computational resources, it is not yet reasonable to utilize a grid network that can sufficiently resolve a vegetation canopy and, at the same time, extend both horizontally and vertically to simulate a full atmospheric boundary layer. Nevertheless, even simulations with quite limited vertical extent, as few as three canopy heights, have been successful in accurately reproducing the features described earlier.

4.7 Contribution of canopy elements to small- and large-scale turbulence

Since, in general, individual elements of the canopy are not directly resolved by the numerical grid array, drag effects must be parameterized. Thus, in the resolved-scale momentum equation, the influence of the canopy elements appears as a drag force constructed from an element area density, a drag coefficient, and the local instantaneous velocity. Leaves and branches also create small-scale turbulence in their wakes. An important question arises regarding this wake-scale turbulence in a large-eddy simulation. Is its main action to contribute to the pool of subgrid-scale (SGS) energy, or does it have the overall effect of enhancing kinetic energy dissipation and reducing both SGS and resolved-scale energy? How wake turbulence is treated will strongly influence SGS energy within such numerical simulation, and will establish the relative importance of resolved-scale and SGS processes within the canopy.

It can readily be shown that very substantial amounts of kinetic energy are transformed into wake scales as the mean and turbulent parts of the resolved-scale flow perform work against drag elements (Raupach and Shaw, [523]). It might not be immediately clear how to treat turbulence at this scale. One option would be to combine it with SGS energy arising through the action of SGS viscosity on resolved-scale shear in a cascade process. The problem this presents is the potential disparity in scales between energy arising from the two sources. One could imagine similar contributions to the kinetic energy in unresolved scales from inertial cascade and from wake motions but the much smaller wake scales would contribute much less to SGS viscosity, and the

energy at the wake scales would dissipate much more quickly. Shaw and Patton [578] held wake-scale energy as a separate energy pool in their large-eddy simulation, and were able to evaluate the magnitudes of terms in the budgets of the various kinetic energy pools, the relative contributions to total kinetic energy, and the relative importance of different scales to the diffusion process.

Shaw and Patton [578] performed large-eddy simulations based on a code initially developed by Moeng [441] but modified to include conservation equations for both SGS energy and wake-scale energy, with the former containing an additional term to represent the action of canopy elements in accelerating dissipation, and the latter containing production terms representing contributions from both the resolved-scale velocity field and from SGS turbulence.

As previously known (Shaw and Seginer, [574]), the creation of turbulent wakes behind canopy elements has the very large effect of transferring energy from the mean flow and from larger-scale turbulence to small scales, which dissipate quickly. The simulations by Shaw and Patton [578] confirm this action and also demonstrate the importance of considering the influence of wakes on kinetic energy classified as subgrid-scale within a large-eddy simulation. Considering that SGS energy in their simulation is present at the large-scale end of this range, as determined by the grid dimension, wake scales in a typical vegetation canopy are at least one order of magnitude smaller again. While drag effects on resolved-scale kinetic energy are implicit through the inclusion of a drag term in the momentum equation, the impact on SGS energy must be treated explicitly.

Shaw and Patton [578] showed that the rate of production of wake-scale kinetic energy is large but that the small scale of wake turbulence ensures that it dissipates rapidly with the result that, for a typical element dimension, the energy content of the wake scales matches that of SGS energy within the canopy (Figure 4.5). On the other hand, the effective diffusivity of wake motions is small because this quantity is constructed from the product of turbulent velocity and a length scale that is related to the dimension of individual canopy elements. They deduced, therefore, that it is not necessary to carry a variable to represent wake-scale energy in the simulation, as Wilson [648] concluded in a higher-order closure model. However, the action of canopy elements on SGS energy, when element dimensions are an order of magnitude or more smaller than grid dimensions, is important and it is essential to include a term to represent this energy transfer in the SGS energy budget, as shown in Figure 4.6. Because canopy drag is strongly dissipative to the resolved-scale flow, it was proposed that, for LES of canopy flows, the nature of the SGS model employed is of secondary importance compared to the importance of SGS models in simulations of wall boundary layer flows.

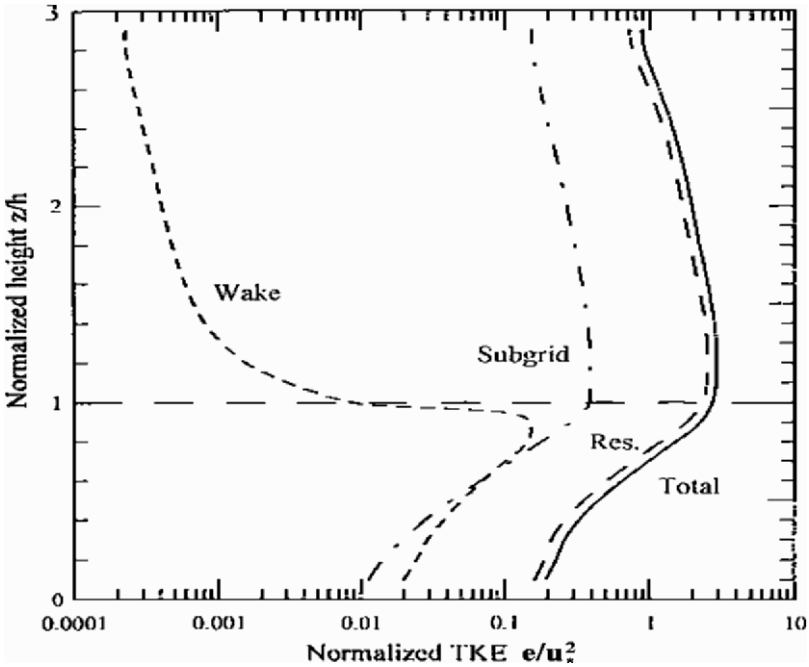

Figure 4.5: Vertical profile of normalized turbulent kinetic energy (solid curve) and its components from a large-eddy simulation: resolved-scale flow (long dash line); SGS energy (dash-dot line); wake kinetic energy (short dash line). Calculations were performed for an element dimension of 0.1 *m* and a canopy height of 10 *m*. (From Shaw and Patton, 2003 [578]).

4.8 Conditional sampling and composite averaging of large-eddy simulations

Large-eddy simulations of flow within and above plant canopies are found to be useful tools for the investigation of the characteristics of turbulence in such regimes. Canopy turbulence is dominated by relatively large three-dimensional structures, yet field observations are necessarily limited to a small number of instruments on an even smaller number of fixed towers. Remote sensing techniques, such as LIDAR provide only partial help, since they can only operate above the vegetation and because scanning to obtain three-dimensional images is currently too slow a process. A further problem arises due to the known importance of atmospheric pressure perturbations, and the difficulty in making direct measurement of static pressure except at the ground surface. Thus, contributions made by LES are thought to be of extreme value in elucidating canopy turbulence.

Gao et al. [204] formed an ensemble average of field observations of temperature and of streamwise and vertical velocities (Figure 4.4) using the scalar ramp as

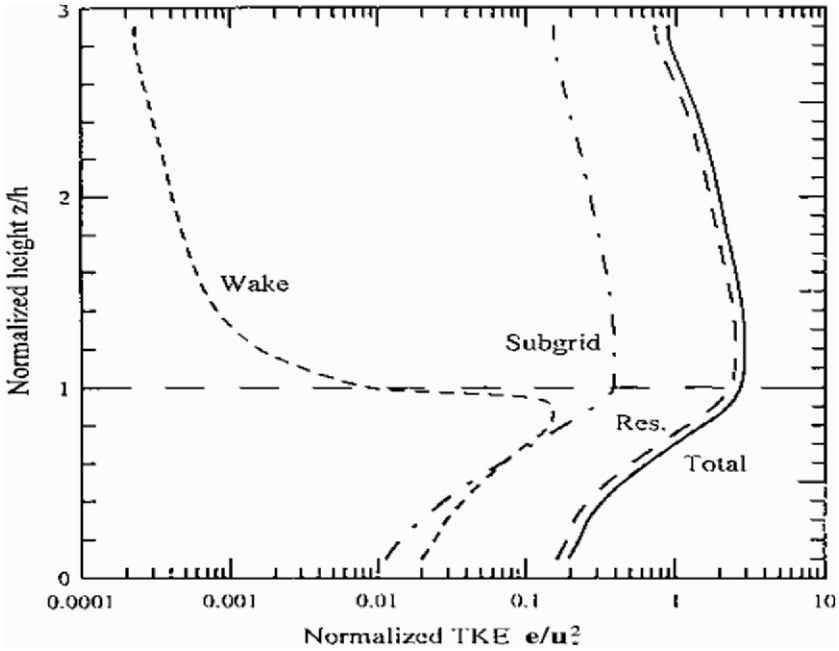

Figure 4.6: Budget of large-eddy simulation SGS kinetic energy normalized by friction velocity and canopy height: energy cascade from resolved flow (solid line); viscous dissipation (long dash line); transfer of SGS energy to wakes (thin solid line); diffusion by resolved and SGS motions (short dash line). (From Shaw and Patton, 2003 [578]).

the detection function and aligning and averaging a series of coherent structures that occurred during a single 30-minute period. No information was provided concerning the lateral features of the composite structure, and longitudinal structure could only be inferred by assuming Taylor's frozen turbulence hypothesis with a height-invariant translation velocity. In contrast, large-eddy simulations provide a wealth of three-dimensional data together with the full turbulent pressure field.

Taking advantage of this, Fitzmaurice et al. [194] and Watanabe [642] have each presented composite averages of structures detected in large-eddy simulations of canopy flows. Fitzmaurice and co-authors based their detection scheme on the positive pressure perturbation centred near the canopy top, while Watanabe used a wavelet transform procedure to detect scalar ramps. Despite the difference in detection procedure, the results are remarkably similar. Both studies examined simulated flows in thermally neutral stratification. Common features of the two investigations are (i) a sweep or gust of high velocity air from aloft upwind of an ejection of low momentum canopy air, (ii) a sloping interface or microfront in scalar concentration between ejected air from the canopy and fresh air from above, (iii) a positive perturbation in static pressure more or less coincident with the microfront and the canopy top, and (iv) strong lateral outflow in line, longitudinally, with the pressure maximum.

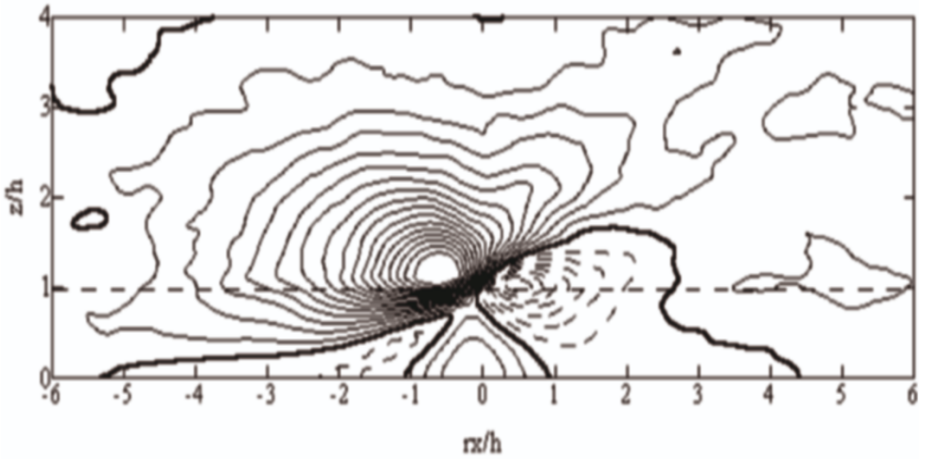

Figure 4.7: An x, z slice through the centre of the composite average structure showing contours of streamwise velocity fluctuation from the local horizontal mean. Contour interval is 0.05 with positive contours as solid lines, and negative contours as dashed lines. Zero contour shown as bold.

These features are illustrated in Figures 4.7 to 4.11 obtained by applying the composite average scheme of Fitzmaurice et al. [194] to a large-eddy simulation of flow in a vegetation canopy and overlying surface layer. The LES output includes the three orthogonal velocity components, u, v, w, a passive scalar c and static pressure p. It was based on the scheme of Moeng [441] and Moeng and Wyngaard [442] and integrated a set of three-dimensional, filtered Navier-Stokes equations under the Boussinesq approximation. A pseudospectral differencing technique was employed for the horizontal derivatives, and a second-order centred-in-space finite difference scheme determined vertical derivatives. The domain comprised 228x144x100 equally spaced grid intervals in the x-, y-, and z-directions. The canopy occupied the lowest ten grid intervals according to an assigned element area density to match the wind tunnel canopy of Finnigan and Shaw [188]. Lateral boundary conditions were periodic, while the upper boundary of the domain was rigid but frictionless. A uniform driving force was applied throughout the domain.

Since the computational flow fields are not driven convectively, the most likely scenario is that a gust from aloft triggered by the high velocity shear immediately above the vegetation, impinges on the canopy and forces an ejection of canopy air. Because wind velocity increases with height, the interface between air from aloft and air ejected from the canopy forms a downstream-sloping boundary. At the same time, the gust creates streamwise convergence, and results in a region of overpressure, which drives the lateral outflow. The static pressure increase peaks close to the canopy top but is felt throughout the depth of the domain and is vertically coherent. One subtle outcome is that flow at the base of the canopy is caused to accelerate prior to the arrival of the sweep at treetop height, and peak wind velocity in the lower half of the canopy is coincident with the maximum pressure. This shows clearly in Figure 4.7, which is a vertical slice of the streamwise velocity perturbation through the centre of a composite

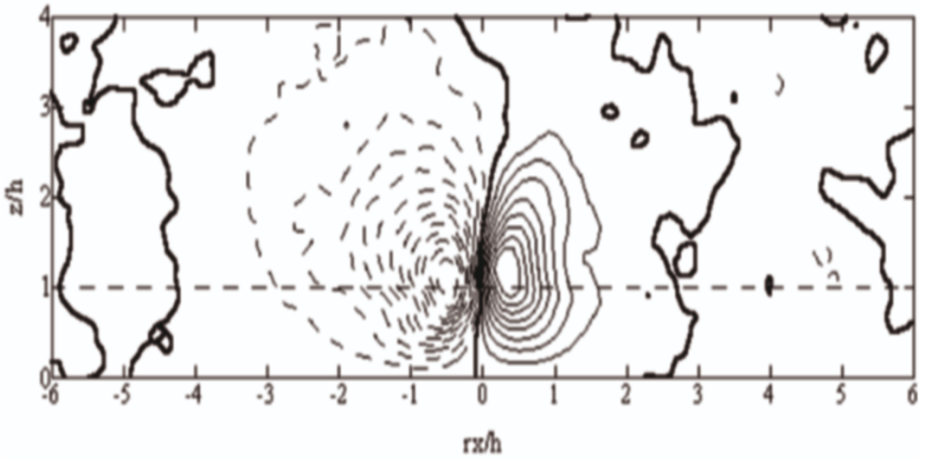

Figure 4.8: An x, z slice through the centre of the composite average structure showing contours of vertical velocity fluctuation from the local horizontal mean. Contour interval is 0.05 with positive contours as solid lines, and negative contours as dashed lines. Zero contour shown as bold.

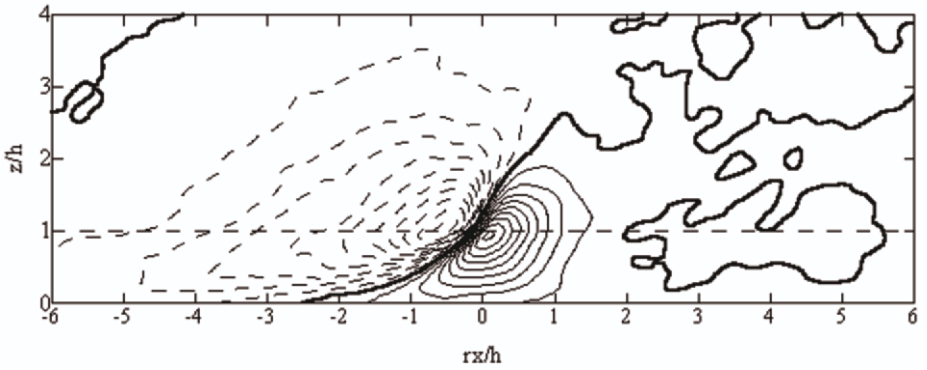

Figure 4.9: An x, z slice through the centre of the composite average structure showing contours of scalar concentration fluctuation from the local horizontal mean. Contour interval is 0.02 with positive contours as solid lines, and negative contours as dashed lines. Zero contour shown as bold.

average coherent structure. There is a distinctive separation between the maximum wind velocity in the relatively sparse trunk space and that in the region of the canopy top and levels immediately above.

Of significant interest are the strong counter-rotating vortices observed in lateral cross-sections. In the region of the sweep, these vortices rotate such that the central area between them is one of downward flow, as shown in Figure 4.11. Following the vortex pair in the streamwise direction, the centres of rotation are observed to be tilted upwards.

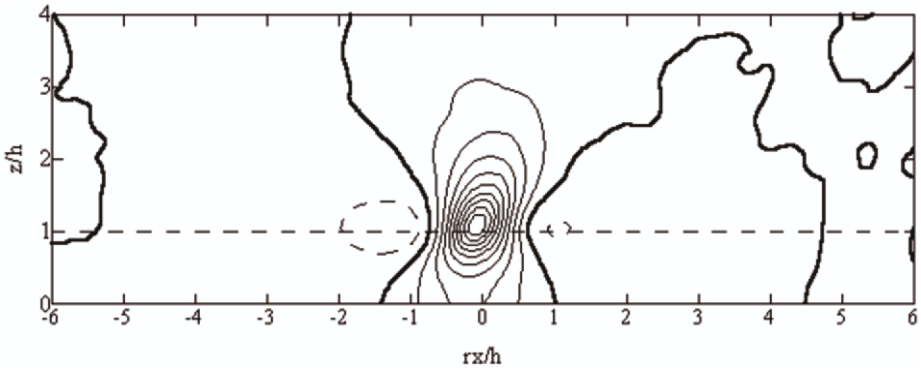

Figure 4.10: An x, z slice through the centre of the composite average structure showing contours of static pressure fluctuation from the local horizontal mean. Contour interval is 0.2 with positive contours as solid lines, and negative contours as dashed lines. Zero contour shown as bold.

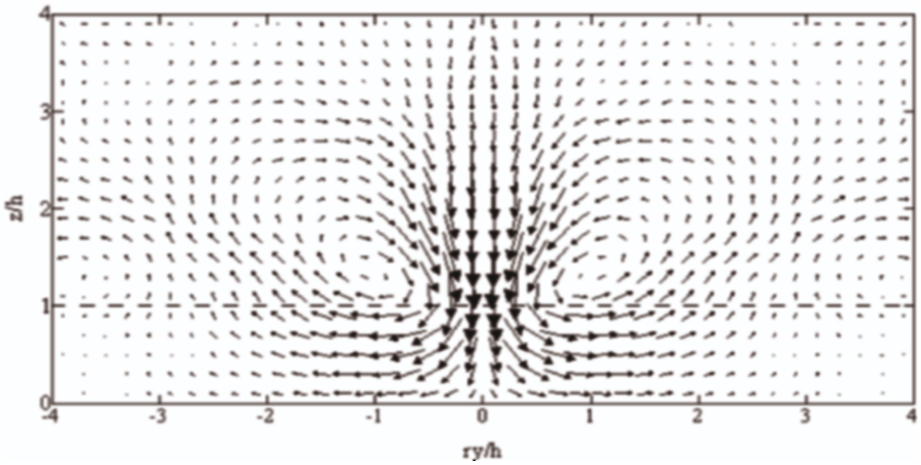

Figure 4.11: A lateral y, z slice across the composite average structure at $rx/h = -1$ showing vectors of lateral and vertical velocity fluctuation.

4.9 Empirical orthogonal function (EOF) analysis

Finnigan and Shaw [188] conducted an Empirical Orthogonal Function (EOF) analysis of an extensive wind tunnel data set obtained in a model wheat canopy. The same authors have recently performed an equivalent analysis based upon the output from the large-eddy simulation described above.

EOF analysis in the context of turbulent flows was introduced by Lumley [381]. It consists of finding the sequence of orthogonal eigenfunctions and associated eigenvalues that converges optimally fast when the variance of the turbulent field is represented

as the sum of this sequence. In horizontally homogeneous flows, this requires the solution to the following eigenvalue problem:

$$\int_D \Phi_{ij}\left(k_x, k_y, z, z'\right)\hat{\phi}_j^*\left(k_x, k_y, z'\right) = \lambda\left(k_x, k_y\right)\hat{\Phi}_j\left(k_x, k_y, z\right) \tag{4.10}$$

where Φ_{ij} is the spectral density tensor defined as

$$\Phi_{ij}\left(k_x, k_y, z, z'\right) = \frac{1}{4\pi^2}\int\int e^{-ik_x r_x - ik_y r_y} R_{ij}\left(r_x, r_y, z, z'\right) dr_x dr_y. \tag{4.11}$$

R_{ij} is the spatial covariance, where r_x and r_y are separations in the streamwise and spanwise directions. There is a denumerable infinity of solutions, ϕ_i^n (eigenvectors), each associated with a real positive eigenvalue λ^n.

The spatial structure of the turbulent field is contained in the eigenvectors. We see that the eigenvectors are expanded as a Fourier series in the directions of flow homogeneity, x and y. The rate of convergence of the sequence of eigenvalues is a sensitive indicator of the presence and relative importance of coherent structures. EOF analysis provides not only an objective measure of the existence of dominant, spatially-extensive structure but, with minimal additional assumptions, allows us to deduce the 3-dimensional structure of the dominant eddies in their 'mature' phase.

The spatial structure derived by Finnigan and Shaw [188] matched measured time-height profiles of velocity in the xz plane and also revealed a double-roller vortex structure in the yz plane that was consistent with the mixing-layer hypothesis of canopy turbulence (Raupach et al., [530]. The study was limited, however as only two velocity components were available from the wind tunnel study and the two-point measurements necessary for the EOF analysis were only performed in the $y = 0$ and $x = 0$ planes.

The recent analysis has been applied to the full three dimensions, and was formulated to include all five variables u, v, w, c, p. In general, a large fraction of the total variance is captured by the first few eigenmodes and only a few wavenumbers, and they adequately capture the structure of the turbulent field. An example of the relative contribution to the total variance by the first five eigenmodes is shown in Figure 4.12 for the 3-dimensional EOF analysis of the u, v, w velocities. The first three wavenumbers of the first eigenmode exceed any wavenumber contribution from the second eigenmode.

An example of the reconstruction of the streamwise and vertical velocities of the *characteristic eddy*, based on the first three wavenumbers of the first eigenmode and the first two wavenumbers of the second eigenmode, is illustrated in Figures 4.13 and 4.14. The eddy is interpreted as a downward sweep of high momentum air penetrating the canopy from above. The structure shown by the characteristic eddy reflects many of the features present in field observations of instantaneous distributions of velocity and scalar quantities, such as those of Gao et al.[204]. The reconstructed eddy also matches most elements of the composite average structure extracted from the same large-eddy simulation output. Based on two-point covariance fields, and seeking to converge optimally fast on the total variance of the turbulent field, the EOF analysis emphasizes the sweep component of the eddy and does not adequately represent the microfrontal boundary between sweep and ejection. The tilted counter-rotating vortex

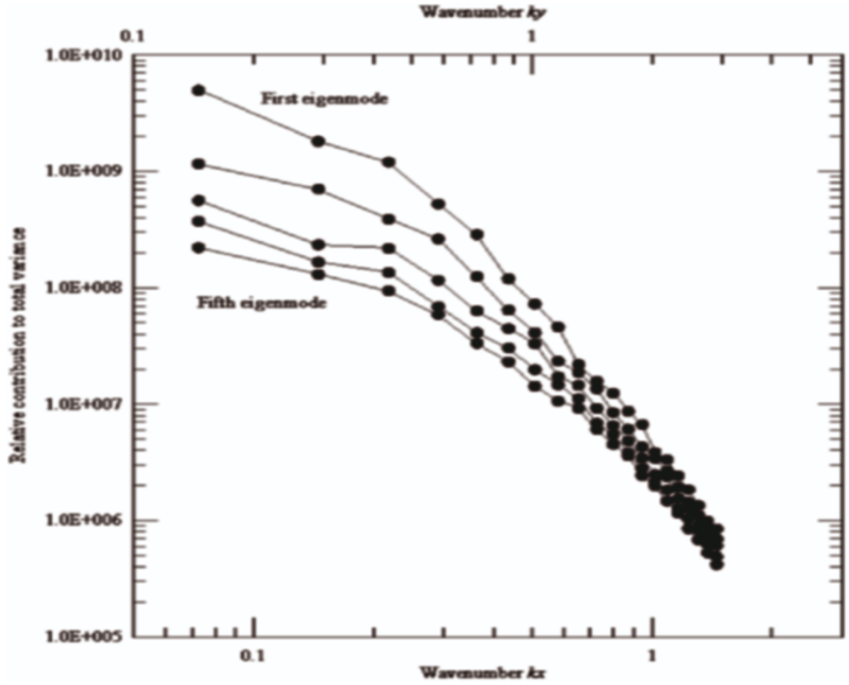

Figure 4.12: Spectra of the relative contribution to the total variance from the first five eigenmodes from a 3-dimensional EOF analysis of the three velocity components, scalar concentration, and static pressure.

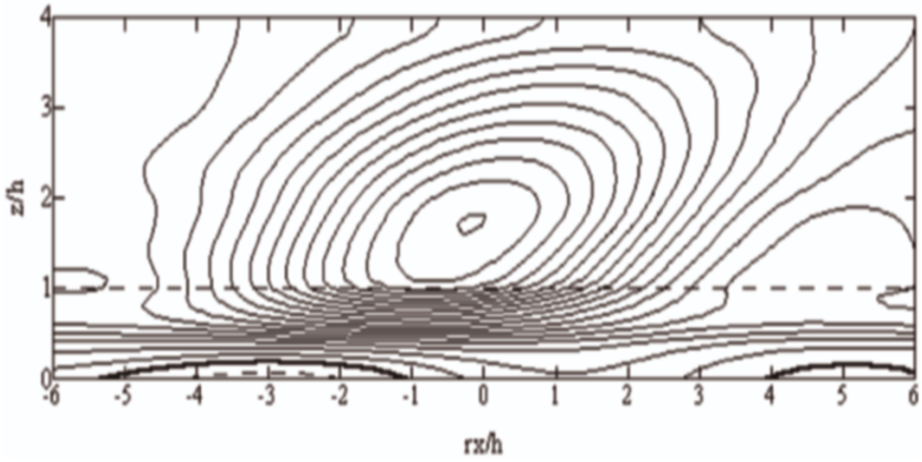

Figure 4.13: Characteristic eddy constructed from the first two eigenmodes and first three wavenumbers of a 3-dimensional EOF analysis of the three velocity components, scalar concentration, and static pressure. Contours of streamwise velocity fluctuation. Solid lines - positive; dashed lines – negative; bold line – zero.

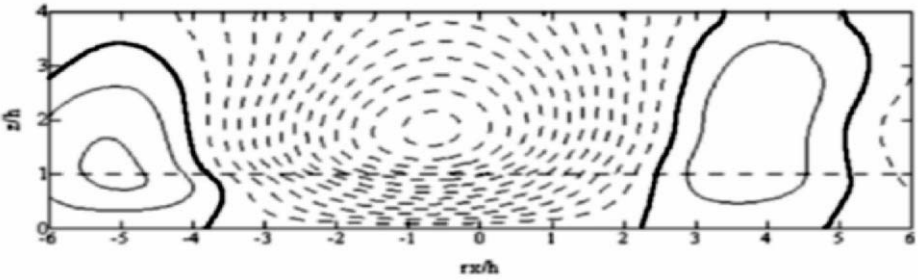

Figure 4.14: Characteristic eddy constructed from the first two eigenmodes and first three wavenumbers of a 3-dimensional EOF analysis of the three velocity components, scalar concentration, and static pressure. Contours of vertical velocity fluctuation. Solid lines – positive; dashed lines – negative; bold line – zero.

pair is observed, however. The EOFs provide the 3-dimensional structure of canopy coherent structures with only trivial *a priori* assumptions, and provide further evidence of the importance of large coherent structures in canopy turbulence.

4.10 Summary

The distributed array of drag elements in vegetation canopies creates a mean wind profile that contains an elevated shear layer centred near the canopy top that more closely approximates a plane mixing layer than a wall layer. This velocity structure is responsible for turbulence characteristics that differ substantially from those over a smooth surface. Velocity spectra are sharply peaked, streamwise and vertical velocities have probability densities that are strongly skewed, streamwise and vertical velocities are correlated more strongly that would be expected over a smoother surface, and transport is dominated by coherent flow structures with sweeps more important than ejections.

Contributions to our understanding of canopy flow and turbulence have derived from field observations, particularly in forests, from wind tunnel simulations, from ensemble average models of canopy flow, and, more recently, from large-eddy simulations. Experimental studies reveal that coherent structures contribute a very large fraction to the total exchange of heat, mass and momentum between the vegetation and the overlying atmospheric surface layer. Such motions are accurately reproduced in the wind tunnel and by computer simulations. An ejection of low momentum air immediately precedes a downward sweep of high momentum air from aloft. The zone of streamwise convergence creates a sloping microfrontal boundary between canopy air and air from aloft. The effect of this was first seen in the ramp-like temperature traces observed within and immediately above forest stands. The convergence also creates a region of overpressure, which is centred at the canopy top but vertically coherent. This positive pressure perturbation has a strong influence of flow in the lower canopy or trunk space.

Composite averaging of structures detected in large-eddy simulations, and EOF analysis of wind tunnel data and of large-eddy simulations reveals a double vortex structure to the turbulent flow. Counter-rotating vortices on either side of the sweep are tilted in the downstream direction in much the same manner as the scalar microfront. It is anticipated that findings such as these will lead to significant advances in our understanding of canopy exchange processes and of our ability to model canopy physics.

Chapter 5

Turbulent flow in canopies on complex topography and the effects of stable stratification

J. Finnigan[1]
CSIRO Marine and Atmospheric Research,
Canberra, Australia

5.1 Introduction

Over the last twenty five years a consistent picture of the structure and dynamics of canopy turbulence has emerged. We now know that there are fundamental differences between the structure of turbulent flow through uniform vegetation canopies and that in a boundary layer. The flow in and above the canopy, that is, in the 'roughness sublayer' resembles that in a plane mixing layer rather than a boundary layer. Turbulence production rates near the canopy top are much higher than in a boundary layer and characteristic large, energy-containing eddies, quite distinct from those in the boundary layer above are generated there by a hydrodynamic instability process. In the canopy, the dissipation rate of turbulence is also enhanced because boundary layers on the vegetation surfaces provide a source of intense shear layers with thicknesses of order the Kolmogorov lengthscale, augmenting those in the normal eddy cascade. This paper describes the way that this 'standard' picture of canopy turbulence is modified by topography so it is appropriate to set the scene with a brief history of how this standard picture was constructed. As scientific histories generally are, this will be a personal account, reflecting the line of discovery followed over the last three deacdes by the group

[1]E-mail of the author: *John.Finnigan@csiro.au*

Ye.A. Gayev and J.C.R. Hunt (eds.), Flow and Transport Processes with Complex Obstructions, 199–219.

at the Pye Laboratory, of CSIRO[2] in Canberra, Australia and their direct collaborators. Other research groups will almost certainly have a very different perspective on these developments.

Many of the earliest detailed studies of canopy turbulence were motivated by questions of biology, especially the water use and carbon uptake of field crops. In fact studies of canopy micrometeorology from the 1960s are as likely to be found in the *Agronomy Journal* as in the more conventional meteorological literature. Physical ecologists faced a crippling sampling problem when they tried to infer whole-canopy behaviour by sampling gas exchange across individual leaves and patches of soil. Not surprisingly, they embraced the alternative approach offered by aerodynamics. This consisted of applying the mass conservation equation in horizontally homogeneous flow thereby obtaining a balance between the source/sink strength of a biologically active scalar and the divergence of its vertical flux. These early workers such as Wright and Lemon, 1969 [366], Denmead, 1964 [148], and Inoue, 1963 [306] were the first to see that the turbulent mixing of the atmosphere could be used as a convenient spatial averaging operator.

Direct measurement of turbulent fluctuations in canopies was not possible until relatively recently so their first recourse was to simple, first-order eddy diffusivity or 'K-theory' models of turbulent fluxes. Typically the vertical eddy flux of a scalar, C, or of mean momentum, that is windspeed, $\overline{U}$, was written as[3]

$$\overline{w'c'} = -K_c \frac{d\overline{C}}{dz}; \qquad \overline{u'w'} = -K_m \frac{d\overline{U}}{dz}, \tag{5.1}$$

and the task became that of finding plausible forms for the diffusivities, K_c, K_m so that the fluxes could be deduced from the more readily measured mean concentrations or velocities. A variety of methods was devised to find these diffusivities and to bound them with global constraints, using the surface energy balance in the case of scalars and the overall surface drag in the case of momentum. The ruling paradigm for the turbulence structure was that canopy turbulence was effectively boundary layer turbulence augmented by the extra mixing caused by eddies shed in the wakes of leaves, stems and branches. In dense canopies it seemed reasonable to assume that a single mixing length, representative of the canopy elements could be used to form the diffusivity so that,

$$K_m = l^2 \left| \frac{d\overline{U}}{dz} \right|. \tag{5.2}$$

And inserting this assumption of a constant mixing length for the momentum flux into the one-dimensional, steady momentum conservation equation,

$$\frac{D\overline{U}}{Dt} = 0 = \frac{d}{dz}\left[K_m \frac{d\overline{U}}{dz} \right] - C_d a \overline{U}^2, \tag{5.3}$$

[2]The Commonwealth Scientific and Industrial Research Organisation (CSIRO) is Australia's major publicly funded research body.

[3]We use conventional micrometeorogical notation in this chapter so that time mean quantities are denoted by overbars and departures therefrom by primes.

produced the exponential velocity profile characteristic of uniform canopies like cereals [306]. In equation (5.3), D/Dt denotes the Eulerian derivative, C_d is the dimensionless drag coefficient of a foliage element and a the area of elements per unit volume of space. Evidently the aerodynamic drag of the canopy is assumed dependent on the square of the velocity, an implicit statement that the drag force on the foliage is primarily pressure or 'form' drag.

This stage of canopy studies culminated in some excellent treatments that gave complete and consistent accounts of momentum and scalar transfer within this eddy diffusivity framework. The most noteworthy perhaps were those by Cowan [136] and Thom [610], while later the excellent review by Raupach and Thom [522] both summarized the understanding then current and foreshadowed the cracks that were starting to appear in that consistent description. One such problem was that while theories were being constructed based on eddy diffusivities and assumptions of leaf-scale eddies dominating canopy turbulence, occasional measurements such as the space-time correlations of Allen [6] were making it clear that the dominant canopy eddies were in fact much larger. Typical integral lengthscales of fluctuations were of order the canopy height, much larger than the scale of the eddies in leaf wakes.

By the end of the 1960s a new wave of studies of laboratory turbulent flows using a variety of conditional sampling methods had changed the conventional picture of boundary layer turbulence, emphasizing the importance of coherent structures in the flow. Several workers started to apply these methods to canopy turbulence. Adapting the quadrant-hole technique and other conditional sampling approaches, Finnigan [182, 183] showed that canopy momentum exchange, $\overline{u'w'}$ was dominated by infrequent energetic 'sweeps' $\{u' > 0; w' < 0\}$ of high momentum fluid while ejections $\{u' < 0; w' > 0\}$ played a lesser role, the reverse of the situation in boundary layers except very close to rough surfaces. These results were soon confirmed by Shaw et al [573]. Over the next decade work exemplified by Bradley and Denmead [149] and Shaw et al. [575] demonstrated that these sweeps were coherent over the whole canopy, suggesting that they were similar to the coherent large eddies already seen in boundary layers.

These findings raised a theoretical objection to the use of eddy diffusivities to model turbulent fluxes in canopies. Corrsin [131] had pointed out that the concept of a diffusivity was only valid if the process responsible for the transport-mixing by turbulent eddies in this case-was of much smaller scale than that over which the mean concentration gradient changes. This latter scale was usually measured as $L_s = \overline{C}/\overline{C}'$ or $L_s = \overline{U}'/\overline{U}''$, where a prime denotes d/dz. In most canopies it was seen that $L_s \sim h_c$, the canopy height. This was not a problem when eddies were supposed to be of leaf scale but if the energetic eddies responsible for transport were also of order h_c then Corsinns's condition was not satisfied and problems could be expected. These problems were masked as long as it was impossible to measure mean gradients and turbulent fluxes independently but once combinations of sonic anemometers and fast response scalar sensors began to be deployed in canopies, regions of 'counter-gradient' flux began to be observed.

This counter-gradient behaviour, which would have required the diffusivity to be negative, was demonstrated unequivocally for scalars by Denmead and Bradley [149,

150], but Wilson and Shaw [647] had already noted that the secondary maximum in the windspeed profile that often occurred in the open trunk space of forests with closed crowns would also require K_m to be negative. Furthermore, Wilson and Shaw showed that the secondary maximum could be satisfactorily explained by moving the level of closure of the flow equations to second order rather than the first order represented by K-theory. To do this though they had to address a problem in the formulation of the canopy flow equations that had been hitherto ignored.

It is clearly impractical to account explicitly for the spatial variability imposed on the airflow by the complexity of the within-canopy airspace. Instead standard free-air Reynolds equations had been adapted for use in canopies by the *ad-hoc* addition of a source or drag term, which was regarded as a smooth function of space. When attempts to write second order closure models of canopy flow were made, however, the limitations of this approach quickly became apparent. At second order, the aerodynamic drag term appeared as a strong non-Newtonian viscous damping of the turbulence, augmenting regular viscous dissipation and some orders of magnitude larger. In reality, as was well known, the interaction of the windfield with the foliage ought to produce large amounts of fine scale turbulence in the wakes of canopy elements.

The paradox was resolved when Wilson and Shaw [647] showed that a rigorous spatial averaging procedure applied to the velocity moment equations that obtain at a point in the canopy airspace produced equations for the area-averaged windfield containing the required smooth source and drag terms as well as terms corresponding to the production of fine scale 'wake turbulence'. The equations also contained extra 'dispersive flux' terms that had not been formally included in analyses up to that point and which were the spatial analogues of the Reynolds stresses that attend time averaging. The spatial averages used by Wilson and Shaw [647] and further developed by Raupach and Shaw [523] were averages over a horizontal plane. The more general volume average was subsequently introduced by Finnigan [184] and Raupach et al. [524].

By the mid to late 1980's a good deal of evidence had been assembled by a range of workers using both wind tunnel and field experiments confirming that the turbulent eddies responsible for transport of momentum and scalars within and just above plant canopies were large and coherent and that their existence formally contradicted the assumptions of K-theory. Furthermore, in extreme cases, this contradiction could not be ignored as clearly counter-gradient fluxes were observed that could not be accommodated in the diffusivity framework, although these cases were the exception, not the rule. Second or higher order closure models could be devised that avoided these problems but only at the expense of complex parameterizations, which were clearly not universal. What was not available was either a simple and physically correct alternative to K-theory or an explanation of the origin of the large eddies.

The first of these was supplied by Raupach [525] with his 'localized near field' (LNF) model. This cast the problem of canopy fluxes in the Lagrangian framework which is widely used in the modelling of atmospheric dispersion from point sources such as factory chimneys. The basic physics of scalar dispersion from a point source were worked out by G.I. Taylor in the 1930's. He showed that during dispersion in a steady wind, U, 'near' to the source the width of a scalar plume grows at a rate proportional to Ut, the distance from the source but further downwind, 'far' from the source, it spreads as $\sqrt{Ut}$ the square root of downwind distance. Raupach pointed

out that *near to* and *far from* the source in this context are measured in terms of the Lagrangian integral scale of the turbulence. Since this was of order the canopy height, h_C any point in or just above a canopy will be in the *near field* of nearby sources or sinks and the *far field* of the rest of the upwind canopy.

The diffusion from the far field sources is well described by the diffusion equation, that is, by K-theory and sets the background concentration of the scalar as well as dominating the vertical flux of the scalar. In the near field, however, the scalar plume is spreading more slowly so that the plume is concentrated and variations around the background concentration are strongly influenced by the local source-sink distribution. Hence the much larger number of upwind sources dominates the flux while nearby sources set the details of the gradient, thereby decoupling the flux and the gradient. Raupach's LNF theory provided a physically correct and readily applicable model for scalar fluxes in canopies that was effectively of the same order of closure as K-theory, albeit in a Lagrangian framework. Unfortunately, it cannot be readily extended from scalars to the velocity field.

A satisfactory explanation for the dominance of large eddies in canopy turbulence had to wait a little longer until Raupach et al. [526, 530] proposed that they were the result of a hydrodynamical instability process at the canopy top rather than being associated with the momentum, deficit behind canopy elements. Raupach et al., [526, 530] pointed out that key characteristics of canopy and roughness sub-layer turbulent structure were more closely matched to a plane mixing layer than a boundary layer. Eddy generation in a plane mixing layer is the result of an inviscid instability of the inflected mean velocity profile that, in the case of a canopy, develops at the top of the foliage. It was showed in [526, 530] that large eddies measured in a range of canopies from 50 *mm* wind tunnel models to 30 *m* forest canopies scaled on the vorticity thickness at the canopy top, $\delta_\omega = U(h_c)/U^{'}(h_c)$ as predicted by mixing layer instability theory. Since the original analysis by Raupach et al., [526, 530], a series of measurements in the field, in wind tunnels and in water flumes (e.g. Ghisalberti and Nepf, [228]) have both confirmed the essentials of the mixing layer analogy for canopy or roughness sublayer (RSL) flow and established bounds on its applicability.

A final distinguishing feature of canopy flows that sets them apart from those in the free air is the greatly increased rate of viscous dissipation, ε in vegetative canopies (although not necessarily in urban canopies). This large value of ε is inferred by balancing measured turbulence kinetic energy (TKE) budgets and is one feature of the more general area of canopy spectral dynamics. Unlike free-air turbulent shear flows, where tke is produced at large scale by the working of turbulent stresses against the *mean* rates of strain and then proceeds down the Richardson 'eddy cascade' to the dissipation scales, where it is converted to heat as viscous stresses do work against *fluctuating* rates of strain, two other processes are active in canopies. The first is the 'shortcutting' of the eddy cascade as small scale eddies are generated in the wakes of canopy elements. The second is the direct dissipation of TKE in the attached boundary layers of canopy element. For leaves with length scales $\sim$ 0.01m, these attached boundary layers are of order the Kolmogorov scale so that in dense canopies dissipation in these fine scale shear layers vastly outweighs that at the end of the eddy cascade. These processes have been well described by Shaw and Seginer [574] and incorporated in LES models (Shaw and Patton, [578]) and 2nd order closure models (Wilson, [648]; Ayotte et al.,

[17]) of canopy flow. The way that these altered spectral dynamics modify the shapes of measured frequency spectra has been calculated by Finnigan, 2000 [187] and shows that values of ε in the canopy inferred from standard Kolmogorov theory without these modifications can be wrong by factors of 3–4.

The picture of canopy turbulence set out above is strictly only applicable to steady homogeneous conditions. While it provides a solid base for extrapolation we are only now beginning to set out general principles around which to describe the behaviour of strongly perturbed canopy flows such as those on hills, around forest edges or behind windbreaks. Neither do we yet have a satisfactory way of accounting for diabatic effects in canopy flows. In this talk we concentrate on perturbations to canopy flows caused by hills and the extra complications that arise when the flow is stably stratified. We rely heavily on analytic models, which, although they require simple parameterizations, provide greater insight than all-out numerical simulations. The motivation for much of this work has been the problem of measuring land-atmosphere fluxes of carbon and energy continuously in Programs like 'FLUXNET' (Baldocchi et al., [40]) but the results are also finding application in wind energy prospecting and weather prediction models.

5.2 The windfield over a canopy covered hill

The basic physics of neutrally stratified flow over hills were elucidated by Hunt, Liebovich and Richards, 1988 [287], building on earlier work by Jackson and Hunt, 1978 [310] and others. In order to obtain the explanatory power of an analytic solution they restricted their attention to low hills. Despite this, the insights they obtained can be applied to general topography. Finnigan and Belcher, 2004 [189] have extended the model of Hunt, Liebovich and Richards, replacing the rough surface of the model [287] with a plant canopy and their approach also yields an analytic solution in the limit of a 'tall canopy'.

We use the following notation: $\overline{U}_B(z)$ is the undisturbed upwind flow (or the areally averaged flow in a region of continuous topography) while $\Delta\overline{p}(x,z)$, $\Delta\tau(x,z)$ and $\Delta\overline{u}(x,z)$ are the perturbations caused by the hill in the mean kinematic pressure, kinematic shear stress and streamwise velocity, respectively. Hence,

$$\begin{aligned} \overline{u} &= U_B(z) + \Delta\overline{u}(x,z); \qquad \overline{w} = \Delta\overline{w}(x,z); \\ \overline{p} &= P_B + \Delta\overline{p}(x,z); \quad \tau = T_B(z) + \Delta\overline{\tau}(x,z). \end{aligned} \tag{5.4}$$

We also define the parameters H, the height of the hill, L its horizontal length-scale (distance from crest to half-height point) and h_C the canopy height. C_d is the dimensionless aerodynamic drag coefficient[4] of the canopy foliage and $a(z)$ is the foliage area per unit volume of space. The momentum absorption distance is defined as $L_c = 1/(C_d a)$.

The model of Finnigan and Belcher, 2004 [189] considers the perturbations caused by the hill to a background flow that consists of a logarithmic profile above the canopy

[4] In this chapter C_d is defined by the expression $F_D = C_d a\overline{u}|\overline{u}|$, where F_D is the aerodynamic drag and so differs by a factor of 2 from some definitions.

and an exponential profile within the canopy. These profiles are solutions to the one-dimensional momentum equations with a constant mixing length within the canopy and a mixing length proportional to $z + d$ above the canopy, where d is the displacement height of the logarithmic profile. Matching these two solutions at the top of the canopy, which is taken as $z = 0$, the origin of the vertical coordinate, we find,

$$U_B(z) = \begin{cases} \frac{u_*}{\kappa} \ln\left(\frac{z+d}{z_0}\right), & z > 0 \\ \\ U_h \exp\frac{\beta z}{l}, & z \leq 0 \end{cases} \tag{5.5}$$

where $U_h = U_B(0)$ is the mean wind speed at the top of the canopy, u_* is the friction velocity, $l = 2\beta^3 L_c$ is the mixing length in the canopy $l = \kappa u_*(z-d)$ is the mixing length above the canopy and $\beta = u_*/U_h$ quantifies the momentum flux through the canopy. Matching both mean wind and shear stress at the canopy top also fixes the following relationships,

$$U_h = \frac{u_*}{\kappa} \ln\left(\frac{d}{z_0}\right); \qquad d = \frac{l}{\kappa} \; ; \qquad z - 0 = \frac{l}{\kappa} e^{-\kappa/\beta}. \tag{5.6}$$

Although directly matching the log-law in the surface layer to the exponential solution in the canopy provides a convenient and mathematically tractable approach flow, it ignores the fact that close to the top of tall canopies, in the so-called, 'roughness sublayer' (RSL), the logarithmic law must be modified. This is because the more efficient turbulent mixing that results from the mixing-layer type instability at the canopy top (Raupach et al., 1996 [530]), can transport the same amount of momentum down a smaller gradient in mean velocity than the turbulence characteristic of the surface layer above the RSL can accomplish. Since, in the horizontally homogeneous approach flow we require a momentum flux constant with height, the result of the more efficient mixing in the RSL is a velocity gradient that is smaller than in the log layer above. Also, when we match the log layer and surface layer directly, we find that $\beta = \kappa/2$, where κ (≈ 0.4) is von Karman's constant. In reality observations in neutral stratification over a wide range of tall dense canopies suggest that, $\beta \approx 0.3$. (Raupach et al., 1996 [530]). Models for the effect of the RSL on horizontally homogeneous flows are available, (eg. Physick and Garrett, 1995 [494]; Harman and Finnigan, 2006 [261]) but their effect on the analytic solutions presented next have not yet been evaluated and we proceed with this caveat.

The analyses of Hunt, Liebovich and Richards, 1988 [287] and of Finnigan and Belcher, 2004 [189] divide the flow in the canopy and in the free boundary layer above into a series of layers with essentially different dynamics. The dominant terms in the momentum balance in each layer are determined by a scale analysis and the eventual solution to the flow field is achieved by asymptotically matching solutions for the flow in each layer. The model applies in the limit that $H/L << 1$. By adopting this limit, Hunt, Liebovich and Richards [287] were able to make the important simplification of calculating the leading order perturbation to the pressure field using potential flow theory. This perturbation to the mean pressure, $\Delta\overline{p}(x, z)$, can then be taken to drive the leading order (i.e. [$O(H/L)$]) velocity and shear stress perturbations over the hill.

Higher order corrections to the leading order terms can then be obtained using standard methods of perturbation analysis. See for example Van Dyke, 1975 [629].

Hunt, Liebovich and Richards, 1988 [287] also showed that $\Delta\overline{p}(x,z) \sim O\left[U_o^2 H/L\right]$, where $U_o = U_B(h_m)$ is the streamwise velocity well above the surface (more precisely at the 'middle layer' height defined below). Furthermore, they showed that

$$\frac{\partial \Delta\overline{p}}{\partial x},\ \frac{\partial \Delta\overline{p}}{\partial z} \sim O\left[U_0^2 H/L^2\right].$$

These deductions lead to important simplifications that permit an analytic solution to the flow field. The restriction to 'tall' canopies in the theory of Finnigan and Belcher, 2004 [189] can be interpreted as a requirement that almost all the momentum flux is absorbed as aerodynamic drag on the foliage and not as shear stress on the underlying surface.

In the free boundary layer above the canopy the flow divides asymptotically into an outer layer, where the flow perturbations caused by the hill are essentially an inviscid response to the pressure forcing, and an inner or *shear stress* layer where *changes* to the shear stress caused by the hill play a role at first order in the momentum balance. The momentum balance in the outer layer to $O[H/L]$ becomes,

$$\overline{U}_B \frac{\partial \Delta\overline{u}}{\partial x} + \Delta\overline{w} \frac{\partial \overline{U}_B}{\partial z} = -\frac{\partial \Delta\overline{p}}{\partial x}. \tag{5.7}$$

The middle layer height h_m divides the outer layer into a lower part, where vorticity in the background flow is dynamically important, and an upper part where the flow perturbations can be calculated by potential flow theory, is defined by the relationship,

$$\frac{h_m}{L} \ln^{1/2}\left(h_m/z_0\right) = 1. \tag{5.8}$$

In the shear stress layer of depth h_i the perturbation in shear stress divergence becomes important so the streamwise momentum balance is,

$$\text{Shear stress layer (of depth } \ h_i): \qquad U_B \frac{\partial \Delta\overline{u}}{\partial x} + \Delta\overline{w} \frac{\partial U_B}{\partial z} = -\frac{\partial \Delta\overline{p}}{\partial x} + \frac{\partial \Delta\tau}{\partial z}. \tag{5.9}$$

The depth of the shear stress layer is defined by the implicit relation,

$$\frac{h_m}{L} \ln\left(h_m/z_0\right) = 2\kappa^2. \tag{5.10}$$

The canopy flow itself breaks down into upper and lower canopy layers. In the upper canopy the linearised momentum balance to $O[H/L]$ is,

$$\text{Upper canopy layer}: \qquad 0 = -\frac{\partial \Delta\overline{p}}{\partial x} + \frac{\partial \Delta\tau}{\partial z} - \frac{2U_B \Delta\overline{u}}{L_C}, \tag{5.11}$$

and we see that in the canopy advection is small compared to the retained terms. As we get deeper into the canopy, the shear stress gradient, $\partial\Delta\tau/\partial z$. becomes weaker and the lower canopy flow reduces to a balance between the pressure gradient and the drag,

$$\text{Lower canopy layer}: \qquad 0 = -\frac{\partial \Delta\overline{p}}{\partial x} - \frac{1}{L_C}\left(U_B + \Delta\overline{u}\right)\left|U_B + \Delta\overline{u}\right|. \tag{5.12}$$

The form of the aerodynamic drag term follows because the drag force always opposes the velocity and we see also that in the lower canopy the momentum balance is nonlinear. This is because the background velocity U_B decays exponentially into the canopy (5.5), while the driving pressure gradient $\frac{\partial \Delta \overline{p}}{\partial x}$, which varies on a lengthscale L in the vertical, penetrates the canopy relatively undiminished so that in the lower canopy it must be balanced primarily by the perturbation drag force, $L_C^{-1}\Delta\overline{u}|\Delta\overline{u}|$.

Equation (5.12) is, consequently, an algebraic equation with the solution,

$$\text{Lower Canopy Layer:} \qquad \Delta\overline{u}(x) = -\sqrt{L_C^{-1}|\frac{\partial \Delta \overline{p}}{\partial x}|} \cdot \text{Sgn}\left(\frac{\partial \Delta \overline{p}}{\partial x}\right). \tag{5.13}$$

We can see from equation (5.13) that the largest velocity perturbations in the lower canopy will coincide with the position of the largest negative pressure gradient over the hill, which is well upwind of the hillcrest.

We can also see from equation (5.7) that to first order, the velocity perturbations in the outer layer will vary as the square root of (minus) the pressure perturbation, that is,

$$\text{Outer Layer:} \qquad \Delta\overline{u}(x,z) \propto -\sqrt{|\Delta\overline{p}|} \cdot \text{Sgn}\,(\Delta\overline{p})\,. \tag{5.14}$$

As we travel over a low hill in neutrally stratified flow, the pressure falls, reaches a minimum just before the crest and then rises again in the lee but doesn't regain its upwind magnitude until well behind the hill. The minimum pressure, therefore, occurs almost at the crest and the minimum pressure gradient occurs about half way up the windward slope of the hill. From equations (5.13) and (5.14) we can see that the perturbation in the outer layer flow peaks roughly over the hill crest and the deep-canopy flow perturbation peaks on the upward face of the hill and is passing through zero on the hill crest, becoming negative on the lee side.

The solutions of equations (5.9) and (5.11) for the shear stress layer and the upper canopy layer are more complicated as we now have to account for shear stress divergence but we can note the following points. Because the shear stress layer is a region of local equilibrium (turbulence production $\sim$ dissipation) it is feasible to model the shear stress with a mixing length model,

$$\text{Shear Stress Layer:} \quad \tau = -\left|l^2\frac{\partial \overline{u}}{\partial z}\right|\frac{\partial \overline{u}}{\partial z} \quad \text{with} \quad l = \kappa(z-d). \tag{5.15}$$

Within the canopy, surprisingly, it is also feasible to use a mixing length model for the perturbations although not for the background flow, hence the use of a mixing length for the background flow solutions (5.5) must be regarded as merely a convenient heuristic, Finnigan and Belcher, 2004 [189]. Within the canopy, in keeping with the 'mixing layer analogy' for canopy turbulence (Finnigan, 2000 [187]), the dynamically correct mixing length is a constant. Finnigan and Belcher, 2004 [189] show that the shear stress in the upper canopy can be written,

$$\text{Shear Stress Layer:} \quad \tau = -\left|l^2\frac{\partial \overline{u}}{\partial z}\right|\frac{\partial \overline{u}}{\partial z} \quad \text{with} \quad l = 2\beta^3 L_C. \tag{5.16}$$

The matched solutions to the four layers tell us that the shear stress layer and upper canopy layers form a region of adjustment across which the mean flow perturbations

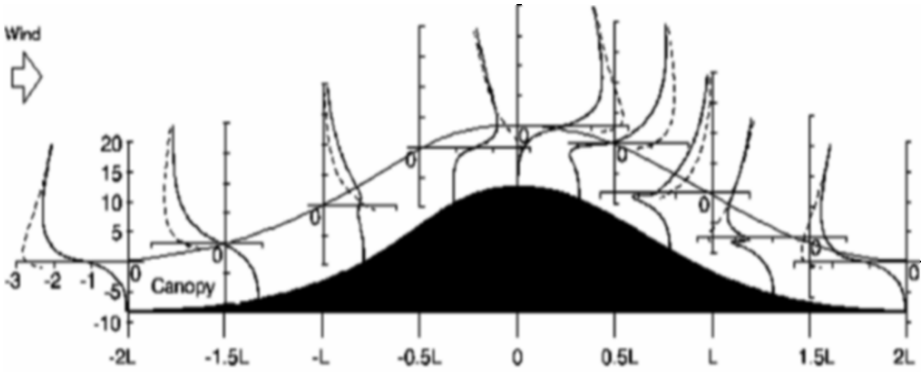

Figure 5.1: Comparison of dimensionless canopy velocity perturbation from the theory of Finnigan and Belcher, 2004 [189] (solid line) with the no-canopy, solution of Hunt, Liebovich and Richards, 1988 [287] (dotted line). Variable plotted is $\frac{\Delta\overline{u}}{U_{SC}}$, where $U_{SC} = \frac{H}{L}U_0$. Note the solution [287] is only valid to $z = -d + z_0$. Profiles are plotted at a series of x/L values between $X/L = -2$ (upwind trough) and $X/L = 2$ (downwind trough) on one of a series of sinusoidal ridges. The units of Z are (m) and the vertical range is from $2h_i > Z > L_c$.

change from being in phase with (minus) the pressure well above the surface (5.14) to being in phase with (minus) the pressure gradient deep in the canopy (5.13). This adjustment strongly modulates the shear across the canopy top. These features are clearly illustrated in Figure 5.1 from Finnigan and Belcher, 2004 [189] where the streamwise velocity perturbations at a series of stations across one of a range of sinusoidal ridges are plotted. Included for comparison are solutions for a rough surface with the same z_0 from the theory of Hunt, Liebovich and Richards, 1988 [287]. We can see that the extra turbulent mixing generated by the canopy reduces the sharp speed-up peak on the hillcrest predicted by Hunt, Liebovich and Richards, 1988 [287] and moves it from around $z \simeq h_i/3$ to $z \simeq h_i$.

In Figure 5.2 we show consecutive vertical profiles from the wind tunnel model study of Finnigan and Brunet [186]. Although this hill is too steep to satisfy the $H/L << 1$ limits of linear theory, upwind of the hillcrest we can still see the main features predicted by the model of Finnigan and Belcher, [189]. The maximum velocity in the lower canopy occurs well before the crest and is falling by the hilltop. The difference between lower canopy and outer layer velocities is a maximum at the hilltop and maximizes the canopy top shear at that point with consequences for the magnitude and scale of turbulence production. Conversely, the difference is at a minimum halfway up the hill, where the lower-canopy velocity is maximal but the outer layer flow has not yet increased much. This effect is so marked that the inflexion point in the velocity profile at the top of the canopy has disappeared. Note also that on this steep hill we observe a large separation bubble behind the hillcrest.

One final prediction made by the theory of Finnigan and Belcher, [189] must be mentioned as it turns out to have important consequences for scalar transport. This is that even on hills of low slope, $H/L << 1$ a region of reversed flow will appear within the canopy on the lee side of the hill, if the canopy is sufficiently deep and dense. This is

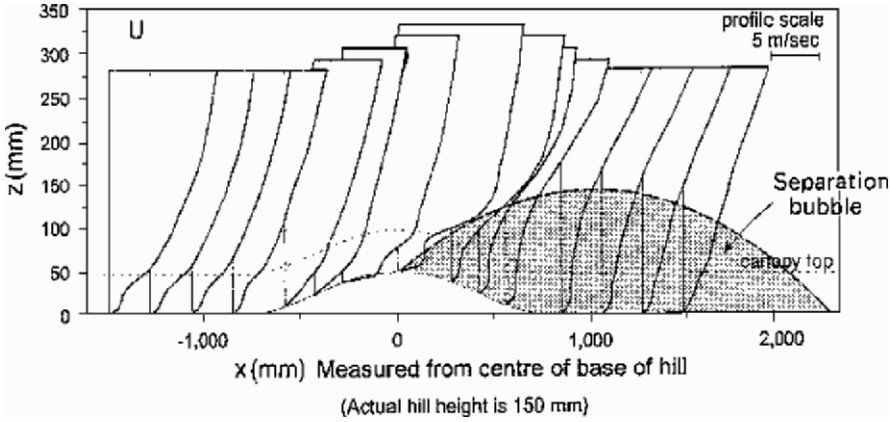

Figure 5.2: Mean velocity profiles on a wind-tunnel model study of flow over a steep two-dimensional ridge covered with a plant canopy. Figure reproduced from Finnigan and Brunet, [186].

illustrated in Figure 5.3, where we have plotted the total velocity over the same hill and canopy as in Figure 5.1. As noted above, the driving pressure gradient, $\partial\Delta\overline{p}/\partial x$ passes essentially undiminished through the canopy and will produce a velocity perturbation $\Delta\overline{u}$ that is negative behind the hillcrest where $\partial\Delta\overline{p}/\partial x > 0$, (5.10). Sufficiently deep into the canopy we can expect that $|\Delta\overline{u}| > U_B$ because $U_B(z)$ decays exponentially into the canopy. The condition for this region of flow reversal to appear (Finnigan and Belcher, 2004 [189]) is,

$$h_c > \frac{l}{2\beta} \ln\left[\frac{U_0^2}{U_h^2}(H/2)k^2 L_c\right]. \tag{5.17}$$

The appearance of this reversed flow region in a deep canopy on a shallow hill has now been confirmed by several laboratory experiments. Figure 5.4, taken from a wind-tunnel model study[5] shows profiles of total velocity $U_B + \Delta\overline{u}$ at three x stations ($x = -2L;\ 0;\ 2L$) over a model hill. The hill parameters were $H/L = 0.1;\ h_c/H = 1.0$. The measurements were taken with a laser-doppler anemometer so that the reversed flow region could be properly resolved. Full details of the experiment can be obtained from the author. A comparable experiment has been conducted in a large water flume ($18\ m \times 0.9\ m \times 1\ m$) by Poggi et al., 2006 [504] over a train of 4 sinusoidal hills with $H/L = 0.1$ and $h_c/H \sim 1$. Their results revealed essentially the same behaviour. While the extent of the region of reversed flow was somewhat smaller in their experiment than in the prediction of Finnigan and Belcher, 2004 [189], the canopy depth and density of their model meant that it did not quite fall the domain of applicability of [189]. Nevertheless, the two sets of experimental results confirm the existence of this phenomenon.

[5] J.J. Finnigan and D. Hughes, personal communication.

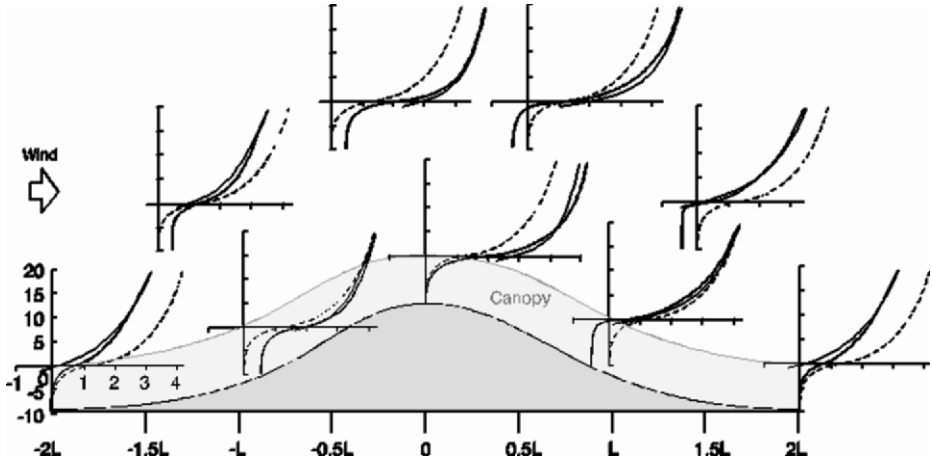

Figure 5.3: Comparison of dimensionless total velocity, $U_B + \Delta u$ in the canopy (heavy solid line) with the no-canopy solution [287] (thin solid line) from the theory of Finnigan and Belcher, 2004 [189]. The background velocity $U_B(Z)$ is shown as a dashed line. Note the solution of Hunt, Liebovich and Richards, 1988 [287] is only valid to $z = -d + z_0$. Profiles are plotted at a series of X/L values between $X/L = -2$ (upwind trough) and $X/L = 2$ (downwind trough). Profiles at fractional X/L values are displaced upwards for clarity. The units of Z are (m) and the vertical range is from $2h_i > Z > L_c$.

5.3 The scalar field over a canopy covered hill

The windfield solution of Hunt, Liebovich and Richards, 1988 [287] was extended to scalar flow and transport over a low hill by Raupach et al., 1992 [528]. They analyzed the exchange of a general scalar with a rough hill and then applied their theory to calculate radiant energy partition into sensible and latent heat. It was assumed that the driving windfield was provided by the theory of [287]. In this section we briefly describe an extension of the approach of Raupach et al., 1992 [528], in which the rough surface is replaced by a canopy and the driving windfield is given by Finnigan and Belcher, 2004 [189]. In the spirit of [528] we analyze the transfer of a generic scalar with a simple concentration boundary condition on the canopy surface.

The mean scalar concentration $\overline{c}$ and its eddy flux $\overline{f}$ are divided into background and hill-induced perturbations as follows,

$$\overline{c} = C_B(z) + \Delta\overline{c}(x,z); \qquad \overline{f} = F_B(z) + \Delta\overline{f}(x,z). \tag{5.18}$$

The background scalar field in the canopy $C_B(z)$ is the solution of the one-dimensional mass conservation equation,

$$0 = -\frac{\partial F_B(z)}{\partial z} + \chi(z). \tag{5.19}$$

The scalar source term is expressed as

$$\chi(z) = a(z)\, g\,(U_B(z))\,[C_0 - C_B(z)] \tag{5.20}$$

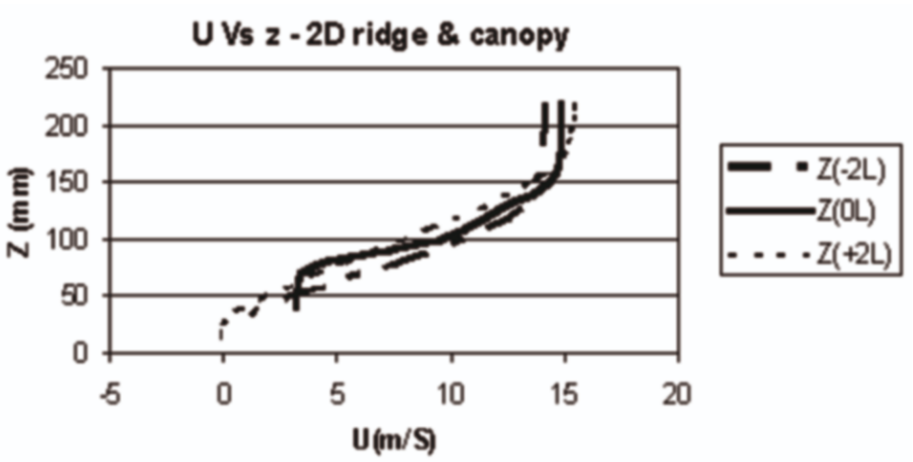

Figure 5.4: Laser-doppler anemometer profiles of mean velocity in and above a wind tunnel model study of flow over an isolated sinusoidal two-dimensional ridge covered with a tall canopy. Profiles are located upwind ($x = -2L$, dot dash line); on the hilltop (solid line) and downwind ($x = +2L$, dotted line). The hill parameters were $H/L = 0.1$; $h_c/H = 1.0$. Full details of the experiment can be obtained from the author (Finnigan and Hughes, pers. comm.)

where C_0 is a reference concentration assumed constant on the surface of the foliage. $g\,(U_B(z))$ is the leaf-level boundary layer conductance, which has a power law dependence on windspeed, $g = AU_B^n$. When the leaf boundary layer is laminar, $n \simeq 0.5$ and when it is turbulent $n \simeq 0.8$ (Finnigan and Raupach, 1987 [185]). It is convenient to define a parameter γ such that, $g = \gamma U_B$, whence $r = 2\gamma/C_d$ is a leaf level Stanton (Nusselt) number, characterizing the relative efficiencies of scalar (heat) and momentum transfer to the leaf. In most situations involving the transfer of biologically interesting scalars in natural canopies, $r \sim 0.1$.

We parameterize the background scalar flux $F_B(z)$ using the same mixing length model that we used for momentum,

$$F_B = -l^2 \frac{\partial U_B}{\partial z} \frac{\partial C_B}{\partial z}. \tag{5.21}$$

As was the case for momentum also, the use of a mixing length is merely a convenient heuristic in the mean flow but is physically correct when used to model the scalar perturbations caused by the hill. Using (5.5), (5.20) and (5.21), the mean canopy mass conservation equation (5.19) becomes,

$$\frac{\partial^2 C_B(z)}{\partial z^2} + \frac{\partial\, C_B(z)}{\partial z} = r\,[C_0 - C_B(z)]\,. \tag{5.22}$$

The solution to (5.22) for small r applies within the canopy[6] and above the canopy

[6]Note that (5.23) applies in the limit of $n \to 1$, i.e. well mixed canopy airspace but the overall form of the solution is relatively insensitive to variation of n within the limits $1 > n > 0.5$.

is matched smoothly to the conventional logarithmic profile to give,

$$C_B(z) = C_0 + \frac{c^*}{\kappa}\ln\left(\frac{z+d}{z_c}\right); \quad z > 0$$
$$C_B(z) = C_0 + (C_h - C_0)\, e^{\frac{r\beta z}{l}}; \quad z \le 0 \tag{5.23}$$

where $C_h = C_B(0)$ and the other parameters are fixed by matching the scalar profiles and fluxes at the canopy top whence,

$$\begin{aligned} F_c(0) &= -u^* c^* = -r\beta^2 (C_h - C_0)\, U_h; \\ c^* &= r\beta (C_h - C_0); \\ d &= \frac{l}{\kappa}; \quad z_c = d e^{\frac{-\kappa}{r\beta}}. \end{aligned} \tag{5.24}$$

When we compare exact and numerical solutions of (5.22) for $n = 0.5$, 0.8 and 1.0 we see minor quantitative but no qualitative changes in the profiles of $C_B(z)$. Similarly, for $r \sim 0.1$, there is little difference between the exact profiles and the 'small r' approximation. Exact solutions will be compared with these approximations in a forthcoming publication.

By comparing (5.23) and (5.24) with the comparable expressions for the wind-speed, (5.5) and (5.6) we see that the leaf-level Stanton number, r plays a significant role in the scalar solution and that since r is small, the background mean scalar concentration through the canopy varies substantially more slowly than the background wind speed.

Above the canopy we adopt the solution of Raupach et al., 1992 [528] for the scalar perturbations. This follows the pattern of Hunt, Liebovich and Richards, 1988 [287] by dividing the flow-field into an outer layer and a shear stress layer of depth h_i. In the outer layer, scalar perturbations are governed by inviscid dynamics while in the shear stress layer, changes to the scalar flux also play a role at first order. The linearised equation for the scalar perturbation induced by the hill in the outer layer is,

$$\textit{OuterLayer}: \qquad \overline{U}_B \frac{\partial \Delta\overline{c}}{\partial x} + \Delta\overline{w}\frac{\partial C_B}{\partial x} = 0 \tag{5.25}$$

which implies that $\Delta\overline{c}(x,z)$ in the outer layer is entirely the result of distortion of the isopycnals of $\overline{c}$ as streamlines converge and diverge.

In the shear stress layer the divergence of the eddy flux of $\overline{c}$ becomes important so the linearised mass balance is,

$$\text{Shear stress layer of depth } h_i: \qquad \overline{U}_B \frac{\partial \Delta\overline{c}}{\partial x} + \Delta\overline{w}\frac{\partial C_B}{\partial x} = -\frac{\partial \Delta\overline{f}}{\partial z}. \tag{5.26}$$

Raupach et al., 1992 [528] showed that in this region two other mechanisms become important in determining $\Delta\overline{c}(x,c)$. The first is the changes induced by the hill in the eddy flux field $\Delta\overline{f}(x,z)$ and hence in its divergence. The second is the change to the flux of $\overline{c}$ from the surface that occurs because the surface shear stress $\Delta\overline{\tau}(x,z)$ varies as the hill is traversed. The mechanism for this in the rough hill model of [528] is the

representation of the surface flux by a flux-gradient expression, $\overline{f}(x,0) = -K_c \partial\overline{c}/\partial z$, involving the scalar diffusivity $K_c(x,z) = \kappa u^*(1 + \Delta\overline{\tau}/2)z$. In the shear stress layer this modulation of the surface flux boundary condition is the dominant influence on $\Delta\overline{c}(x,z)$ but when a canopy is present, this boundary condition is supplanted by the canopy dynamics.

As was the case for the momentum field, the scalar perturbation in the canopy divides asymptotically into a linearised upper-canopy solution and a non-linear, lower-canopy solution. In the upper canopy the perturbation mass balance to $O[H/L]$ becomes,

Upper canopy layer:

$$0 = -\frac{\partial}{\partial z}\left[l^2\left(\frac{\partial U_B}{\partial z}\frac{\partial \Delta\overline{c}}{\partial z} + \frac{\partial \Delta\overline{u}}{\partial z}\frac{\partial C_B}{\partial z}\right)\right] - \frac{r}{2L_c}\left[U_B\Delta\overline{c} + \Delta\overline{u}C_B\right], \tag{5.27}$$

and we see that in the upper canopy advection is small compared to the flux divergence and source terms.

In the lower canopy the flux divergence becomes small as both $U_B(z)$ and $C_B(z)$ decay exponentially. However, a sensible velocity perturbation $\Delta\overline{u}$ continues to drive the scalar source term so that the lower-canopy mass conservation equation becomes,

$$\overline{u}\frac{\partial\overline{c}}{\partial x} = \frac{r}{2L_c}|\overline{u}|\,\overline{c}. \tag{5.28}$$

Equation (5.28) like its momentum equivalent (5.12) is non-linear but for a different reason. At leaf level the boundary layer conductance g depends only on the magnitude of the wind velocity, $\overline{u}$ not on its direction so that we must write $g = A|\overline{u}|^n$. In the upper canopy, where $U_B > \Delta\overline{u}$ it this dependence on absolute velocity need not be made explicit, vide (5.28) but in the lower canopy, where $\overline{u} \simeq \Delta\overline{u}$, it is critical.

We will not develop the full solutions for the scalar perturbation field here but we can describe the results of the different dynamics in the various layers qualitatively. We will take the case of a canopy sink, that is $S_0 < S_B(z)$. For a canopy source, $S_0 > S_B(z)$, the signs of the perturbations are reversed.

Outer layer: In this layer the dynamics are inviscid and streamline convergence over the hillcrest brings isopycnals of $\overline{c}$ from higher in the boundary layer closer to the surface. With the canopy a sink, $\overline{c}$ increases with height so above h_i we see a positive (increased) value of $\Delta\overline{c}$ over the crest in phase with the perturbation in velocity described by combining equation (5.14) with continuity condition.

Lower canopy layer: In the lower canopy the velocity field is dominated by $\Delta\overline{u}$ which is a maximum around $x = -L$. (upwind of the crest) and a minimum at $x = +L$ (downwind of the crest). However the sink (negative source) term depends on the absolute magnitude of $\Delta\overline{u}$ through $g = A|\overline{u}|^n$ so that the sink is large both upwind and downwind of the crest at $x = \pm L$ and small on the hillcrest $x = 0$. At the same time the velocity is $+ve$ upwind and $-ve$ downwind of the crest, leading to flow convergence towards the hilltop. Through the advection term $\overline{u}\,\partial\overline{c}/\partial x$ of (5.25), this convergence combines with the maxima in the sink strength upwind and downwind to effect a minimum in $\Delta\overline{c}$ at the hill crest, see Hunt, Liebovich and Richards, 1988 [287].

Upper canopy layer: The dominant term in the upper canopy is the effect on the sink of the velocity perturbation through the last term of (5.27), $r/2L_C\,[\Delta\overline{u}C_B]$. Since $\Delta\overline{u}$ peaks at the hillcrest, this produces a minimum in $\Delta\overline{c}$ there. This effect can be interpreted as the canopy counterpart of the dominant role played by changes in surface stress on a rough hill in modulating the surface flux boundary condition, and thereby $\Delta\overline{c}$, as discussed earlier. Hence, as a result of quite different dynamics, the dominant influences on $\Delta\overline{c}$ in the lower and upper canopy layers are in phase leading to a minimum in $\Delta\overline{c}$ at the hillcrest. This simple picture is modulated by other effects in the upper canopy layer, however. The eddy flux divergence couples the upper canopy to the shear stress layer above where advection is important at first order (5.26) and within which the contributions to $\Delta\overline{c}$ that are caused by canopy dynamics must decay to match the inviscid, streamline convergence effects around $z = h_i$.

The overall analysis yields the typical magnitudes of the velocity and scalar perturbations within the canopy, U_c and C_c, respectively,

$$U_c = \frac{U_0^2 H L_c}{U_h L^2}; \qquad C_c = rU_c\frac{C_h}{U_h}. \tag{5.29}$$

Note that the magnitude of the velocity perturbation depends on the driving pressure gradient which is $O\left[U_0^2 H/L^2\right]$ and is determined by the outer layer flow as well as by the momentum absorption in the canopy, characterized by L_c and U_h. For the case we have analyzed, the scalar perturbations are caused entirely by the windfield and not by variations in the biological source/sink strength and we have ensured this by choosing a constant concentration boundary condition C_o on the foliage surface. We see then that the scalar perturbations are relatively smaller than the velocity perturbations that drive them, the proportionality factor being the leaf-level Stanton number, r.

The foregoing analysis together with (5.26) now allows us to non-dimensionalize the mass balance equations in a way that permits us to compare the expected magnitude of the advection terms with the eddy flux, $F_B + \Delta\overline{f} = \overline{w'c'}$:

$$\begin{array}{cccccccc}
\textit{Horiz. Adv.} & & \textit{Vert. Adv.} & & \textit{Eddy Flux Divergence} & & \textit{Scalar Source/Sink} & \\
U_B\dfrac{\partial\Delta\overline{c}(x,z)}{\partial} & + & \Delta\overline{w}\dfrac{\partial C_B}{\partial z} & + & \dfrac{\partial F_B(z)}{\partial z} & + & \dfrac{\partial\Delta\overline{f}(x,z)}{\partial z} & = \quad \chi_B(z) \; + \; \Delta\overline{\chi_B}(x,z), \\
\left[\dfrac{U_0^2}{U_h^2}\dfrac{H}{L}\dfrac{L_C^2}{L^2}\right] & & \left[\dfrac{U_0^2}{u_*^2}\dfrac{H^2}{L^2}\dfrac{L_C}{L}\right] & 1 & \left[\dfrac{U_0^2}{u_*^2}\dfrac{H^2}{L^2}\dfrac{L_C}{L}\right] & 1 & \left[\dfrac{U_0^2}{U_h^2}\dfrac{H}{L}\dfrac{L_C}{L}\right]. & \\
0.09 & & 0.09 & 1 & 0.09 & 1 & 0.08 &
\end{array} \tag{5.30}$$

The dimensionless groups are formed by scaling the terms in the equation using L as the characteristic scale of horizontal variation so that $\partial/\partial x \sim 1/L$ and taking l as the scale of vertical variation. We see that the divergence of background eddy flux and the background canopy source/sink are both of order one as expected on a low hill. Note also that, although the Stanton number r plays a significant role in determining the absolute magnitude of the individual terms in the mass balance, it disappears from their ratio. Finally we see the horizontal and vertical advection terms and the vertical divergence of the perturbation eddy flux are of the same order. The magnitude of these

dimensionless groups is calculated in the bottom row of (5.31) for a canopy-covered hill with the following parameter values:

$$L = 100\ m; \qquad H = 10\ m;\ \ L_c = 5\ m; \qquad u^* = 0.5\ m/s; \tag{5.31}$$
$$U_h = 1.67\ m/s; \quad U_0 = 6.85\ m/s.$$

For this particular choice of canopy density, $L_c = 5\ m$ the magnitude of the perturbations induced by the hill are of order the hill slope, H/L. In a canopy with $h_c = 20\ m$ this corresponds to a Leaf Area Index (LAI) of 4. If $LAI = 2$ but the other parameters remain unchanged, the magnitude of the perturbation terms all double because the ratio of the momentum absorption distance L_c to the hill lengthscale L plays an important dynamic role in determining the velocity perturbations that drive the scalar fluctuations in the canopy.

While these dimensionless groups are useful in signaling when topographically driven advection may be a problem at a given flux site, they do not tell the full story because the streamwise variation of the various terms in (5.31) may lead to them cancelling or reinforcing at different positions on the hill. We illustrate this in Figure 5.5, where we have plotted the streamwise variation of the terms in (5.31) calculated at the canopy top with the parameter values as in (5.31) above with the exception of L_C, which is set to $10\ m$.

In Figure 5.5a we plot the individual terms for the case of a canopy sink. We see that the horizontal and vertical advection terms are of the same order and vary roughly in antiphase while the eddy flux reaches its maximum negative value just ahead of the hillcrest, which is where the velocity peaks as we saw in Figure 5.1. In Figure 5.5b we present these results in a different way by taking the ratio of $F_B(0)$ the background or area averaged eddy flux to the sum of the integral over the canopy height of the first, second and third terms on the left hand side of equation (5.31), that is the sum of the horizontally varying terms. The canopy height is taken as $h_c = 20\ m$. We can take this ratio as a rough measure of the error incurred in estimating $\overline{\chi}$ in an advective situation when only the vertical eddy flux is measured. Clearly, the position of the measurement relative to the hill is critical with a possible error of ±40% depending on wind direction.

In this section we have used an analytic theory to understand the advection caused by flow distortion and the corresponding changes to the eddy flux structure and source/sink strengths in the most basic case, where a generic scalar has a constant concentration on the foliage surface. To maintain an analytic solution we have made a series of somewhat draconian simplifying assumptions. Within these limitations, it seems that even relatively gentle topography can have a significant effect on the mass balance and especially on the terms used to deduce canopy-atmosphere exchange at flux towers. A similar calculation using a numerical model that permits a biologically realistic carbon sink distribution in the canopy has been performed by Katul et al., [330] and confirms these analytical conclusions.

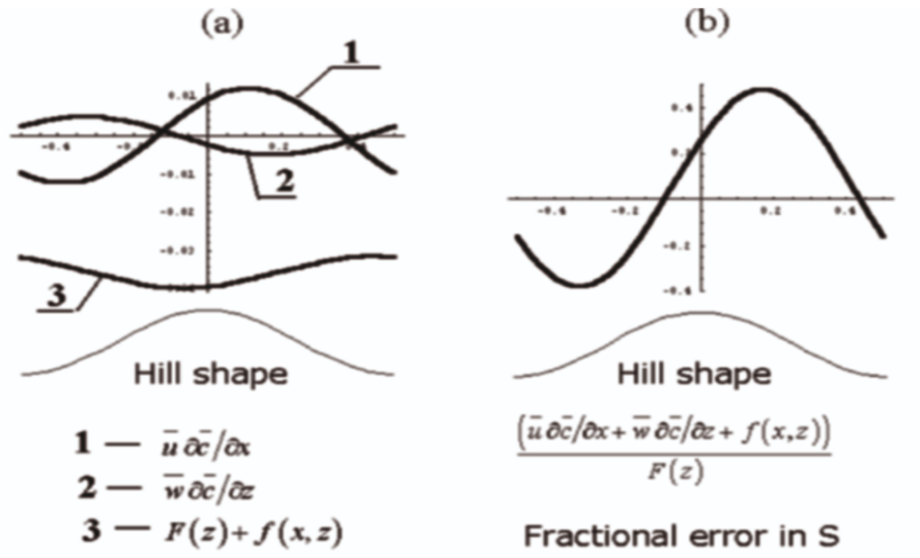

Figure 5.5: a) Variation of the horizontal and vertical advection terms and the eddy flux over a sinusoidal hill covered with a tall canopy. b) Fractional error entailed in estimating the canopy sink S from the background eddy flux, $F(z)$ alone.

5.4 Stable stratification

A pervasive problem at long-term flux measurement sites such as those in the FLUXNET (Baldocchi et al., [40]) is the failure to close the mass balance in nighttime, stably stratified, low-wind conditions. Usually the measured vertical flux of CO_2 plus the accumulation of CO_2 between the sensor and the ground is less than the CO_2 being respired by soil and vegetation. This problem has lent a strong impetus to the study of canopy flows on topography in stable conditions and the analytic models of the wind and scalar fields, described above, provide a natural way to attack the problem. Wind tunnel simulations already referred to (Finnigan and Hughes, *pers. comm.*), in which heat was used as a passive tracer for scalar exchange, have been extended to simulate katabatic flow in a deep canopy on an isolated hill. The canopy was mounted upside down on the tunnel roof, reversing the sign of gravity, and the windspeed and heat flux adjusted to attain a Froude number, Fr for the entire flow of close to one, where the Froude number is defined as the ratio of hydrodynamic to buoyant forcing of the flow parallel to the hill surface, hence,

$$\mathrm{Fr} = \left[\frac{H}{L^2}U_o^2\right] \Big/ \left[g\frac{\Delta\theta}{\Theta_0}\sin\alpha\right] \approx \mathrm{Fr} = \frac{U_o^2}{gL}\frac{\Theta_0}{\Delta\theta}. \tag{5.32}$$

With Fr $\sim$ 1 globally, the flow in the Wind Tunnel model study divided into two distinct flow regimes. Above the canopy the flow remained fully turbulent but stably stratified with a gradient Richardson number Ri $\sim$ 0.1. Within the canopy, the flow was laminar with Ri $\sim$ 10 and flowed downhill as gravity currents on both the windward

and lee sides of the hill. The interface between these two regimes was a thin, strongly sheared layer at the canopy top. This decoupling of the flow within and above the canopy under stable stratification has also been reported anecdotally in field data for some time and was recently quantified by Hammerle et al., 2006 [252].

Adapting the windfield model for stable stratification requires solution of the coupled equations for the windfield, the potential temperature field and the canopy energy balance as it is the radiative cooling of the canopy at night that produces an anomaly in potential temperature $\Delta\overline{\theta}$, which in turn drives the gravity current. However, in the limit of low hills and for times short compared to the timescale of radiative cooling (about 4 hours for forest canopies) it is possible to decouple the problem. We can calculate the $\Delta\overline{\theta}(z)$ field caused by radiative cooling of the canopy on flat ground and then displace this over the hill. The additional changes in $\Delta\overline{\theta}(z)$ that are caused by the scalar flow that results from the gravity current are of second order in the limit described above. The modifications to the windfield model follow directly by first adjusting the pressure forcing by adding a hydrostatic component corresponding to $\Delta\overline{\theta}$ and secondly adjusting the mixing lengths to reflect the stable stratification. We will not describe this analysis here but we note three key results.

First, we find by matching the simple mixing length models for the wind $U_B(z)$ and scalar $\theta_B(z)$ background fields that even for moderately stable conditions, as characterized by Ri ~ 0.1 in the surface layer, the presence of aerodynamic drag in the canopy produces strongly stable flow there. Above the canopy Ri $\propto 1/(z-d)$ while within the canopy Ri $\propto \exp\left(-z^2\right)$. Hence the large values of Ri and consequent laminar flow observed in the canopy in the wind tunnel simulation can be explained quite simply. Second, the Froude number, Fr that characterizes flow over canopies on topography can be defined as the ratio of the hydrodynamic to the hydrostatic contributions to the driving pressure gradient, yielding,

$$\mathrm{Fr} = \frac{U_0^2}{gL}\frac{\Theta_0}{\Delta\theta},$$

where g is the acceleration due to gravity and Θ_0 the reference temperature. We see that Fr does not depend on the hill slope H/L but only on the hill's horizontal length scale, L and the magnitude of $\Delta\overline{\theta}$, giving a possible reason why flux tower sites in gentle terrain are nevertheless subject to advective flows at night that preclude closing the mass balance locally. Finally, we find that when the ratio of hydrostatic to hydrodynamic forcing reaches a critical value, the region of reversed flow near the ground on the lee slope disappears and is replaced by a region of reversed flow on the windward side of the hill.

5.5 Summary and conclusions

A consistent theory of turbulent flow in horizontally homogeneous canopies has been developed over the last twenty five to thirty years. This theory asserts that the origin of the large energy-containing eddies that dominate canopy TKE and transport is an

inviscid instability of the inflected velocity profile that develops at the canopy top. The turbulent structure, as a result, more closely follows that of a plane mixing layer than a boundary layer. Spectral dynamics in the canopy are also altered relative to a free-air boundary layer with shortcutting of the eddy cascade because of the production of small eddies in plant wakes and high rates of dissipation facilitated by the many attached boundary layers on leaves. Many of the large scale features of this picture are modified in canopies on hills.

A theory of flow in canopies over low hills has been developed by extending the asymptotic matching approach of Hunt, Liebovich and Richards, 1988 [287] that was developed for hills covered by short roughness. This shows that the flow in the canopy asymptotically splits into two layers: an upper canopy layer that can be linearised and a lower canopy layer that must be modeled non-linearly. In the upper canopy layer and in the shear stress layer just above the canopy, the velocity perturbations caused by the hill are closely in phase with (-) the perturbation pressure and a velocity maximum occurs just ahead of the hill crest. In the lower canopy layer, the velocity perturbations are in phase with the perturbation pressure gradient, which for a single Fourier mode is $\sim \pi/2$ out of phase with the pressure perturbation.

Two effects result from this. The first is strong modulation of the canopy-top inflection point, which is weakened on the upwind slope and accentuated over the crest. The effect of this on the inflection-point instability that generates turbulent eddies is as yet unknown. The second effect is that in the lower canopy, the negative velocity perturbation on the lee slope can easily exceed the mean velocity, even on gentle hills if the canopy is sufficiently deep and dense. Hence separation can occur within the canopy, even on low hills. As the hill becomes steeper the separation bubble can escape the canopy and global separation may occur on hills covered with tall canopies at much lower angles than if the same hills were covered with short roughness.

Treating the background scalar field with the same heuristic mixing length model as the background velocity field reveals that the variation of the mean scalar concentration profile, $\overline{C}_B(z)$ in a canopy with a simple concentration boundary condition on the foliage is much slower than that of the velocity, $\overline{U}_B(z)$. The different mechanisms of leaf-air transport (molecular diffusion for scalars and mainly pressure drag for momentum) are captured in the leaf-level Stanton number, r, where $r \sim O[0.1]$ for biologically active scalars like heat, water vapour and CO_2. The small value of r ensures this difference in mean profiles and r is an important parameter in the analysis of the scalar perturbations also. The scalar perturbations over the hill are relatively smaller than the velocity perturbations by this factor r. As was the case for the velocity, the scalar perturbation field in the canopy divides into an upper and lower layer but these are not coincident with the velocity layers. Advection becomes important in the lower canopy and advection is important in the scalar budget overall. This has practical implications, making it very difficult to measure accurate surface-atmosphere fluxes using eddy correlation instruments on a single tower, even on quite gentle hills.

The scalar solution for heat transfer can be used to calculate the intensity of the cool layer that develops in a canopy that is cooling radiatively at night. Over low hills, this cool layer provides a hydrostatic term that modifies the hydrodynamic pressure

gradient in stable nighttime conditions. The strength of the resulting gravity current is characterized by a Froude number, which can be expressed as the ratio of the hydrodynamic to the hydrostatic pressure gradient. This Froude number is a function of the buoyancy deficit in the cool layer and the length of the hill slope but not its steepness. Hence hills that are not subject to significant advective effects in neutral or unstable daytime conditions can suffer advective drainage flows at night.

Chapter 6

Transport in aquatic canopies

H. Nepf[1], **B. White, A. Lightbody and M. Ghisalberti**
Parsons Laboratory,
Dept. of Civil and Environmental Engineering
Massachusetts Institute of Technology,
Cambridge, MA 02458

6.1 Introduction: comparison of aquatic and terrestrial canopies

As a bridge to Chapter 4 in this book, it is useful to begin with a comparison of terrestrial and aquatic systems. The range of flow condition observed in aquatic systems is depicted in Figure 6.1. Conditions span from the unconfined canopy, in which the flow depth is much greater than the canopy height, to the emergent canopy, in which the canopy fills the entire flow depth. Consider Figure 6.1a, which depicts an unconfined canopy that closely resembles terrestrial conditions (see also Figure 4.1a). The discontinuity in drag at the top of the canopy creates a region of strong shear. This region of the velocity profile resembles a free-shear-layer and includes an inflection point just within the canopy. A free-shear-layer is characterized by large coherent vortices that form via Kelvin-Helmholtz (K-H) instability and which dominate the transport across the layer [86, 649]. In terrestrial canopies, these coherent structures have been shown to play an important role in transport between the canopy and overlying atmosphere [187, 194, 530]. Far above the canopy the flow returns to a boundary layer structure. The in-canopy flow is driven by the turbulent stress at the top of the canopy, and it decays with distance from the top of the canopy due to the significant momentum

[1]E-mail of the corresponding author: *hmnepf@mit.edu*

Ye.A. Gayev and J.C.R. Hunt (eds.), Flow and Transport Processes with Complex Obstructions, 221–250.

absorption by the canopy [522]. There are three distinct scales of turbulence. The boundary layer turbulence (large dashed circles in Figure 6.1) has the largest scale, but contributes little to vertical transport at the canopy interface. The K-H vortices at the canopy interface (shown as solid black ovals) has the most impact on vertical transport. Observations in terrestrial canopies has suggested that interaction between the boundary layer and K-H eddies causes the K-H structures to be intermittent [194, 204]. Finally, the turbulence produced within the canopy at the scale of the canopy elements is too small to contribute to transport, but its production drains energy from both the mean flow and larger turbulent scales [574], and discussed in Section 4.2.

Aquatic canopies that are deeply submerged have flow structure that is similar to terrestrial canopies, in that a mixing-layer and K-H vortices are present at the canopy interface [227, 305]. However, unlike terrestrial systems, in aquatic systems the K-H vortices are very persistent. Indeed, their strong coherence has allowed exact, positive comparison between the observed vortex frequency and that predicted from instability theory (Ghisalberti and Nepf, 2002 [227]). The persistence of K-H vortices is permitted by the limited submergence depth ($H/h <\approx 5$) at which the aquatic observations have been made. The presence of the water surface (Figure 6.1b) constrains the maximum scale of the boundary-layer turbulence. Because the boundary-layer and mixing-layer eddies are of similar scale, the boundary-layer eddies appear to have little impact on the coherence of the K-H vortices. Indeed, the K-H vortices dominate over the entire flow depth. It is likely that if the depth of submergence were to increase, that the intermittency in the K-H vortices would return, even in the aquatic canopies. The numerical model described in Fitzmaurice et al., 2004 [194], and in Chapter 4 has a domain scale ten times the canopy height ($H/h = 10$), and it produced K-H structures that are intermittent. Thus, it seems that the transition from persistent to intermittent structures occurs between $H/h = 5$ and 10.

The depth of submergence (H/h) also dictates the relative importance of stress-driven and potential-driven flow within the canopy, where the potential gradient includes both pressure gradient and bed slope. From a simple momentum scaling, the relative contribution of stress and potential gradients is proportional to the ratio $(H-h)/h$ [463]. For $H/h >\approx 10$ the flow within the canopy is driven only by the vertical turbulent transport of momentum from the overflow, with negligible contribution from pressure gradients [527]. This defines the unconfined canopy regime (Figure 6.1a) observed in terrestrial canopies, but also observed in some deeply submerged, seagrass meadows. For example, Adbelrhman [1] has successful applied the stress-driven flow model developed for terrestrial canopies [522] to seagrass meadows. Next, for $H/h < 10$, flow is driven by both stress penetration and potential gradient (Figure 6.1b). Finally, in emergent canopies ($H/h = 1$, Figure 6.1c) the canopy flow is driven predominantly by potential gradient. Wind stress may play a small role near the surface, if the sheltering cover provided by the vegetation is weak [317].

The focus of research in terrestrial canopies has been on the vertical exchange between a canopy and the overlying atmosphere, i.e. at the scale of the canopy height, h. In the study of aquatic systems, however, there is interest in processes occurring at several scales both smaller and greater than h – from the stem-scale up to the marsh-scale. For example, the details of flow around an individual stem or leaf sets the length-scale of the diffusive boundary layer that, in many instances, controls the uptake of nutrients

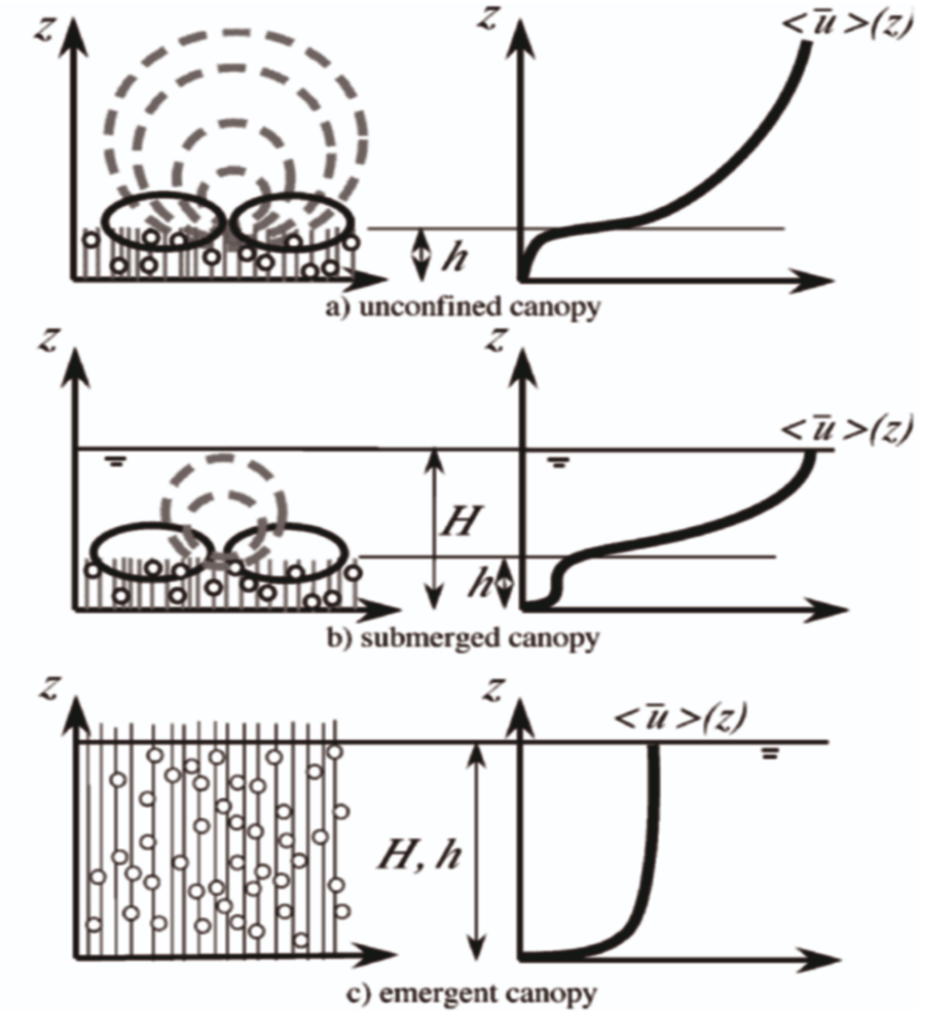

Figure 6.1: Three regimes of canopy flow. Three scales of turbulence are present. The smallest scale (black circles) is set by the canopy morphology, specifically the diameter of and spacing between individual canopy elements, such as stems and branches. Drag discontinuity at the canopy interface generates a shear-layer that produces vortices via Kelvin-Helmholtz (K-H) instability (shown as solid, black ovals). Boundary layer vortices are present above the canopy (dashed gray). When H/h is small the water surface constrains the boundary layer eddy scale.

or the photosynthetic rates [303, 341]. Further, flow structure near the junction of an individual stem and the bed generates exfiltration that enhances pore-water exchange [279, 462]. Velocity heterogeneity exists within a canopy at both the stem-scale (due to the wakes generated by individual stems and branches) and at the canopy-depth-scale (due to vertical variation in canopy density and morphology). Both scales of velocity heterogeneity lead to dispersion that is important to the dispersal of larva [653] , the structure of odor-plumes [181] , and the distribution of particulate matter and nutrients within a marsh. Finally, at the marsh-scale a branching network of channels cuts through regions of dense, largely emergent vegetation. While the channels provide most of the flow conveyance, the vegetation provides most of the ecosystem function and particle trapping. Thus, to describe marsh function one must describe both the transport within the vegetated regions as well as the process of exchange between the vegetation and channels. This chapter will present some overview of the different transport processes occurring at different scales within an aquatic canopy, with emphasis given to emergent conditions, which are unique and prevalent in aquatic systems.

6.2 Emergent canopies

A simple canopy model will be used to describe the flow and transport within and emergent canopy (Figure 6.2). The canopy is represented by an array of vertical, circular cylinders of diameter d. This morphology is a reasonable surrogate in both shape and rigidity for the stem regions of the marsh grasses *Juncus roemerianus* (Needle Rush) and *Spartina alterniflora* (Smooth Cordgrass [339, 367]). The main current is directed along coordinate x, which is parallel to the bed. The bed may have a slope angle Θ relative to horizontal. The coordinate y is lateral and the coordinate z is perpendicular to x toward vertical. The stem density is n = stems per m^{-2}, which defines a mean stem spacing, $\Delta S = n^{-1/2}$. The canopy frontal area per volume is a [m^{-1}]. For the cylindrical morphology,

$$a = nd = \frac{dh}{\Delta S^2 h} = \frac{d}{\Delta S^2}. \tag{6.1}$$

The porosity of the canopy is therefore $n_p = 1 - (\pi/4)ad$. Using stem densities and diameters reported for the short- and tall-form of *S. alterniflora* [627], $ad = O(0.001) - O(0.01)$. In these marsh canopies the solid volume fraction ($\sim ad$) is sufficiently small to make the porosity effectively 1. However, in some freshwater marshes the solid volume fraction can be as high as 15%, corresponding to $ad \approx 0.2$, and $n_p = 0.8$ (Fox et al., 2002 [196]). In mangrove swamps the solid volume fraction can be as high as 45%, $n_p = 0.55$, within the root zone [401].

As described above, the flow within the canopy is heterogeneous at the scales d and ΔS. While this flow structure must be resolved to understand processes that occur at the scale of individual stems, such resolution is not needed, and in fact is quite cumbersome, when describing the flow over larger spatial scales. An averaging scheme is applied to reduce the complexity to tractable equations. The averaging method is nicely described in [522, 523]. Following their notation, the velocity (u, v, w) and pressure (p) field is first decomposed into a time average (overbar) and deviations from the

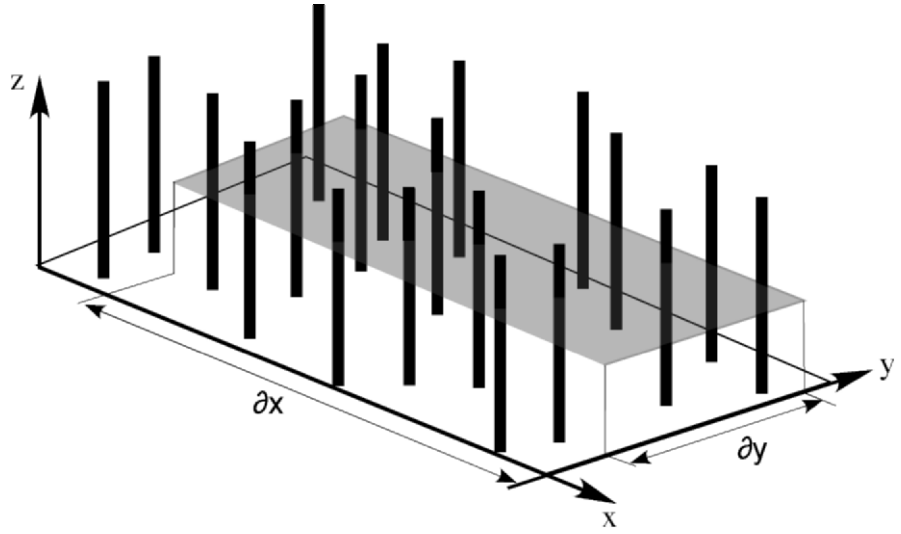

Figure 6.2: Geometry of model canopy. The array consists of vertical circular cylinders of diameter, d, randomly distributed on the x-y plane. Spatial heterogeneity at the cylinder (stem) scale is removed by averaging over a horizontal plane (shown in gray) that is much greater than the cylinder spacing, ∂x and $\partial y >> \Delta S$. Averaging includes fluid volume only, following [522].

time-average (single prime) leading to the familiar Reynolds-averaged Navier—Stokes equations. The time-averaged quantities are then decomposed into the spatial mean in a horizontal plane (angle bracket) and deviations from this horizontal average (double prime). The spatial mean is taken over a scale much greater than ΔS and *only over the fluid volume*, i.e. excludes the volume occupied by the canopy elements. The resulting temporally- and horizontally-averaged momentum equation is

$$\frac{D\langle\overline{u}\rangle}{Dt} = \\ = -\frac{\partial}{\partial z}\langle\overline{u''w''}\rangle - \frac{\partial}{\partial z}\langle\overline{u}''\overline{w}''\rangle - \frac{1}{\rho}\langle\frac{\partial\overline{p}''}{\partial x}\rangle - \frac{1}{\rho}\frac{\partial\langle\overline{p}\rangle}{\partial x} + \nu_m\langle\nabla^2\overline{u}''\rangle + g\sin\theta \qquad (6.2)$$

$$a \qquad b \qquad c \qquad d \qquad e$$

Term a is the horizontal average of the familiar Reynolds stress. Term b is a new stress term arising from spatial correlations in the time-averaged velocity field. Poggi et al. [502] shows that this term, called the dispersive flux, is less than 10% of the Reynolds flux (term a) for $ah > 0.1$. The remaining discussion is restricted to canopies with $ah > 0.1$, so that this term may be neglected. The spatial perturbation in velocity and pressure occurring at the surface of each element gives rise to the viscous and form drag, respectively, of the array. These forces are reflected in terms c (form drag, f_D) and e (viscous drag, f_v). The total drag per fluid mass can be written using a quadratic

drag law.

$$(f_D + f_V) \cdot \frac{\text{drag force}}{\text{fluid mass}} = \frac{1}{2} C_D a \langle \overline{u} \rangle \mid \langle \overline{u} \rangle \mid . \tag{6.3}$$

The absolute value enforces that the drag force acts opposite to the direction of fluid motion. Here C_D is the drag coefficient for the array, and it may differ in magnitude from the drag coefficients of isolated elements of the same form (see, e.g., discussions in [88, 462, 505]). Note that this definition uses a factor 1/2, which is conventional for hydraulic studies. Many air studies exclude this factor as in equation (4.4) in Chapter 4. C_D is a function of stem Reynolds number, as well as canopy density, a. The dependencies of C_D are discussed below.

In free-surface flows the mean pressure gradient is typically hydrostatic

$$\frac{\partial \langle \overline{p} \rangle}{\partial x} = \rho g \frac{\partial H}{\partial x}, \tag{6.4}$$

Applying equations (6.3) and (6.4) to equation (6.2), and making the simplifications described above

$$\frac{D\langle \overline{u} \rangle}{Dt} = -\frac{\partial}{\partial z} \langle \overline{u'' w''} \rangle - g \left(\frac{\partial H}{\partial x} + \sin\theta \right) - \frac{1}{2} C_D a \langle \overline{u} \rangle \mid \langle \overline{u} \rangle \mid \tag{6.5}$$

To discuss some general features equation (6.5) is further simplified by assuming steady, uniform flow, and by integrating over the depth, H. Wind stress is also neglected, although in some instances this can play a role in the momentum balance near the water surface [317]

$$g \left(\frac{\partial H}{\partial x} + \sin\theta \right) H = \tau_{bed} - \frac{1}{2} C_D a \langle \overline{u} \rangle \mid \langle \overline{u} \rangle \mid H. \tag{6.6}$$

Equation (6.6) emphasizes the complementary role of vegetative drag and bed stress. For a given bed and free-surface slope, as the amount of vegetation (a) increases the bed stress (τ_{bed}) decreases. This has important implications for sediment transport within vegetated zones. As an example, consider a typical *S. alterniflora* marsh with $a = 2\ m^{-1}$ and water depth $H = 15\ cm$, such that $aH \approx 0.3$ (Valiela et al. 1978). Lopez and Garcia [378] show that for $aH = 0.3$ the bed stress is reduced to just 20% of the value experienced by a bare bed under the same external forcing. This dramatic reduction in bed stress is the main reason for reduced suspended sediment transport in vegetated flow zones, and the reason that vegetated zones tend to be regions of sediment accumulation [378].

Return to equation (6.5) and consider the magnitude of the Reynolds' stress. Because the length-scale of turbulent eddies within the canopy is small compared to the water depth, turbulent stresses tend to be unimportant within an emergent canopy. From numerical experiments, Burke and Stolzenbach, 1983 [93] estimate turbulent eddy scales 1–3% of the water depth, and turbulent stresses just 2% of the drag for $aH = 0.1$. Observations in model emergent canopies indicate similar ratios [463]. Of

course, in the presence of wind turbulent stress may be important close to the wind-driven surface [93, 317]. With negligible Reynolds' stress and again assuming steady, uniform flow, equation (6.5) becomes

$$g\left(\frac{\partial H}{\partial x} + \sin\theta\right) = -\frac{1}{2}C_D a\langle\overline{u}\rangle \mid \langle\overline{u}\rangle \mid . \tag{6.7}$$

The forcing (left-hand side) is not a function of the vertical coordinate, z. If the canopy density, a, and/or drag coefficient C_D are a function of z, the velocity profile, $\langle\overline{u}\rangle(z)$ will vary inversely, i.e. velocity is highest where $C_D a$ is lowest. For canopies with distinct basal stem regions, this leads to a local maximum in current velocity close to the bed, below the level at which branching begin. This near-bed maximum has been observed in *Spartina alterniflora* [367] under emergent (unsubmerged) conditions. In contrast to *S. anglica* and *S. alterniflora*, the more vine-like *Atriplex portuloides* has leaves (and thus $C_D a$) more evenly distributed over depth, and the resulting velocity profile is fairly uniform over depth [368]. Further, equation (6.7) implies that the velocity profile within an emergent canopy will have a consistent, self-similar form, regardless of absolute current magnitude. That is, taking an arbitrary reference depth,

$$\frac{\langle\overline{u}\rangle(z)}{\langle\overline{u}\rangle\left(z_{ref}\right)} = \sqrt{\frac{C_D a\left(z_{ref}\right)}{C_D a\left(z\right)}}. \tag{6.8}$$

Figure 6.3 demonstrates this scaling using a set of velocity profiles measured in a coastal marsh. The depth-averaged velocity varied from 0.1 to 24 cm/s, but for all conditions the normalized velocity profile $\langle\overline{u}\rangle/\langle\overline{u}\rangle_{15}$ (the reference position $z_{ref} = 15$ cm) agrees very well with the normalized profile of morphology. This normalization provides a useful tool for extrapolating the full velocity profile from records at a single vertical position, in analogy to the use of logarithmic profiles over bare beds. Additional details can be found in [372].

Although the drag coefficient, C_D, will be a function of plant morphology, some general behavior of C_D can be understood by considering the drag coefficient for circular cylinders with diameter, d, equivalent to the stem diameter. The drag coefficient is expected to vary with stem Reynolds number, $\mathrm{Re}_d = \langle\overline{u}\rangle d/\nu_m$, where ν_m is the molecular kinematic viscosity. In marsh systems $\mathrm{Re}_d = O(1 \text{ to } 1000)$ [251, 367], which covers both laminar and turbulent wake structure. For an individual circular cylinder, the drag coefficient decreases with increasing Reynolds number until $\mathrm{Re}_d = 100$ (e.g. Tritton, 1988, Chap. 3 of [616]). This corresponds to the laminar wake regime. For $\mathrm{Re}_d > 100$ the drag coefficient is fairly constant up to $\mathrm{Re}_d = 3 \times 10^5$. The drag coefficient, C_D, is also a function of array density, ad. When stem wakes are turbulent ($\mathrm{Re}_d >> 100$), the wakes of upstream stems can reduce the drag on downstream stems, such that the bulk drag coefficient C_D decreases with increasing stem density (e.g. [462]). However, the relative decrease in C_D is less than the relative increase in ad, such that the total drag increases with ad, as expected. The reduction in drag on downstream stems arises from two effects. First, some downstream stems experience diminished velocity due to the velocity reduction in the wake. Second, the turbulence contributed by an upstream stem wake can delay the point of separation on the downstream stem, resulting in a

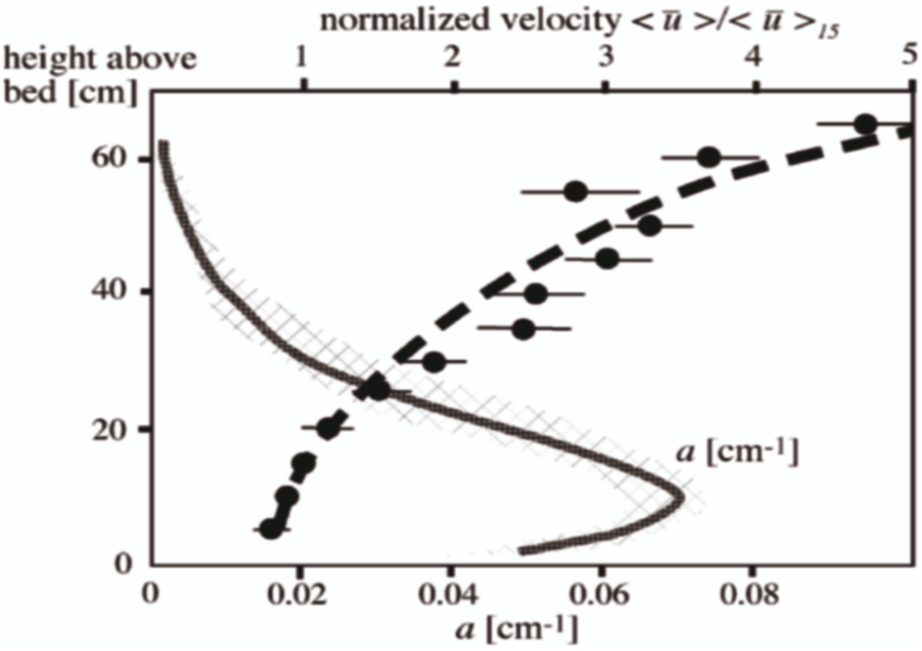

Figure 6.3: Canopy frontal area per volume, a, is shown as a solid gray line with error surrounding line in lighter gray. The velocity ratio predicted from equation (6.8) is shown as a dashed gray line. The reference velocity is taken at $z = 15$ *cm* above the bed. The observed velocity ratio $\langle \overline{u} \rangle / \langle \overline{u} \rangle_{15}$, is shown as solid circles. The horizontal bars indicate the standard deviation of the observed velocity ratio measured at different current speeds. In some cases the bar is covered by the symbol.

lower pressure differential around the stem and thus a lower drag (shown in cylinder arrays by Zukauskas [673] and Luo et al [382]). Both effects contribute to the 'sheltering' described by Raupach [528] and diminish the array drag coefficient relative to the drag coefficient for an isolated array element. The impact of sheltering on C_D is important for $ad \gtrsim 0.03$. For lower stem density C_D can be approximated from the drag coefficient for an individual cylinder at the same stem Reynolds number (Stone, [462]). As mentioned above, $ad < 0.03$ for many, but not all, aquatic canopies.

In contrast, when the stem Reynolds number is small, $\mathrm{Re}_d < 10$, the array drag coefficient increases with increasing array density (decreasing porosity). At low Reynolds number the drag is predominantly viscous, with little or no contribution from inertia (form drag). As the space between stems decreases, the viscous drag increases. This trend is seen in both the linear drag regime ($\mathrm{Re}_d << 1$, e.g. Sangani and Acrivos, 1982 [556]), as well as the quadratic drag regime (Koch and Ladd, 1997 [342]). In random arrays, the drag changes from linear to quadratic at around $\mathrm{Re}_d = 5$, [342].

6.2.1 Turbulence within emergent canopies

Vegetation affects the structure and intensity of turbulence. The presence of vegetation damps large-scale eddies, specifically eddies >> ΔS. But eddies which are comparable in size to the stem spacing or smaller may persist. Indeed, stem wakes can contribute additional turbulent energy at these scales when vortex shedding is present. Vortex shedding is initiated at $\mathrm{Re}_d \approx 50$ for an isolated cylinder (stem). But, within a canopy local shear generated by upstream wakes may delay the onset of vortex shedding to higher Re_d (Dybbs and Edwards, [161]). For canopies of $ad = 0.008$ to 0.07, vortex shedding was not initiated until $\mathrm{Re}_d = 150 - 200$ [460]. Vortex generation drains energy from the mean flow energy (expressed in the vegetative drag) and feeds it into the turbulent kinetic energy. The rate at which turbulent energy is produced in the wake, P_W, is then equal to the rate at which mean flow energy is extracted [523], i.e. the spatially-averaged rate of work done by the flow against the vegetative drag is

$$P_W = \frac{1}{2} C_D a \cdot \langle \overline{u} \rangle^3. \tag{6.9}$$

P_W has units of energy per fluid mass generated per time $[m^2/s^3]$. Note that equation (6.9) represents the spatially-averaged production (averaged over scales greater than ΔS), and it assumes that all energy extracted by stem drag appears as turbulent kinetic energy. In the absence of vortex shedding ($\mathrm{Re}_d \lesssim 200$), viscous drag dissipates mean flow energy without generating turbulence, and equation (6.9) is only an upper limit.

Because wake turbulence is generated at the stem-scale and larger scales are damped, the dominant turbulent length scale within the canopy is shifted downward from analogous conditions without vegetation. For example, in a model canopy constructed from 0.6-*cm* circular cylinders the vertical eddy scale was 2 to 3 *cm*, regardless of water depth, indicating that canopy-geometry and not flow depth was controlling the eddy-scale [377, 378]. Even for sparse canopies the production of turbulence within stem wakes exceeds the production through bed shear over most of the flow depth [93, 377, 460]. Therefore, turbulence levels cannot be predicted from the bed-friction velocity, u_*, as in an open-channel, but rather are a function of the characteristic canopy drag, $C_D a$. Integrating over the depth of an emergent canopy, the horizontally-averaged turbulent kinetic energy budget reduces to a balance between the wake production and the viscous dissipation, ε, i.e. $P_W = \varepsilon$. Assuming the characteristic length-scale of the turbulence is set by the stem geometry, *e.g.* $\sim d$, the dissipation rate will scale as (Tennekes and Lumley, [606], p. 68),

$$\varepsilon \sim \langle \overline{k} \rangle^{3/2} d^{-1}, \tag{6.10}$$

where k is the turbulent kinetic energy. Equating (6.9) and (6.10), the turbulence intensity in the canopy is,

$$\sqrt{\langle \overline{k} \rangle} \sim [C_D a d]^{1/3} \langle \overline{u} \rangle. \tag{6.11}$$

Equation (6.11) indicates that for constant velocity, $\langle \overline{u} \rangle$, the turbulence level increases with array density, ad, because more wakes are present to produce turbulence.

However, the velocity decreases with increasing ad. This creates a non-linear relation between $\langle\bar{k}\rangle$ and ad. With the introduction of a sparse canopy (ad small) the velocity is not strongly affected, and turbulence intensity increases with increasing ad. However, at larger ad the velocity is sufficiently suppressed that $\langle\bar{k}\rangle$ becomes a decreasing function of ad. This non-linear relationship was predicted numerically for flow through emergent vegetation [93] and within bottom roughness elements [164], and was observed in a flume study using *Zostera Marina* [201]. The variation of turbulence intensity with canopy density has important implications for canopy ecology. For example, an increase in turbulence intensity, particularly from turbulence of stem scale, could benefit the vegetation by augmenting nutrient uptake and/or gas exchange [11], and similarly enhance uptake by microbes living on plant surfaces, if uptake is mass-transfer limited [203].

6.3 Diffusion and dispersion within emergent vegetation

Different transport processes are important at different scales within the canopy. At the smallest scales ($<< d$), turbulence is excluded and transport is controlled by molecular diffusion. In the water column turbulence can exist down to the Kolmogorov length-scale, $\eta_\kappa = \left(\nu_m^3/\varepsilon\right)^{1/4}$. Furthermore, a laminar sub-layer exists adjacent to all surfaces, e.g. the bed or a leaf surface, and has the scale $\delta_S = 5\nu_m/u_*$, where u_* is the friction velocity defined for that surface. Transport over scales smaller than η_K or over the distance δ_S from any boundary can only occur by molecular diffusion. Within aquatic canopies flow speeds are typically 1-10 cm/s (e.g. [368]). For these conditions η_K = O(0.1 to 0.01 cm), based on dissipation values measured by Lopez and Garcia [377] and Nepf and Vivoni [463]. Laminar sub-layers measured for macrophyte blades are $\delta_S = 0.4 - 0.7$ mm at 1 cms^{-1} mean flow and 0.05-0.15 mm at 10 cms^{-1} (Hurd, [303]). At scales greater than η_K and δ_S but less than the spacing between individual leaves and stems, transport can occur by turbulent diffusion, if turbulence is present. The turbulence contributing to transport may be generated by the bed-shear, by wind, or by the stem wakes. At scales greater than the stem spacing, but less than the scale of variation in canopy density, L_a, additional mechanism of dispersion arise from heterogeneity in the flow field at the scale of individual stems and leaves. These mechanisms, mechanical diffusion, longitudinal wake-trapping dispersion and longitudinal wake-shear dispersion are described below. Finally, at scales greater than the canopy heterogeneity, L_a, dispersion is controlled by the differential advection created between regions of differing stem-density, i.e. variation in $\langle\overline{u}\rangle$ created by variation in $C_D a$.

The transport produced by turbulent eddies depends on their characteristic length scale, l_e, and velocity scale, u_e. So, the turbulent diffusivity

$$D_t \sim l_e u_e. \tag{6.12}$$

As is discussed above, within a canopy, the turbulence scales are constrained by the size and spacing of the stems and branches. If the stem Reynolds number is high enough, the stem wakes generate eddies of scale d. These eddies may grow, but only

to a size comparable to the stem spacing, ΔS. Thus, within the canopy l_e is between d and ΔS. In a typical canopy d and ΔS differ by less than an order of magnitude, so that we might simply say $l_e \sim d$. Furthermore, since $u_e \sim \langle \overline{k} \rangle^{1/2}$, (6.11) and (6.12) may be combined to write

$$D_t = \alpha [C_D a d]^{1/3} \langle \overline{u} \rangle d, \tag{6.13}$$

where α is an O(1) scale coefficient. Observations from cylinder arrays suggest that the turbulent diffusivity is not isotropic, and that the scale factor, α, differs for horizontal and vertical turbulent diffusion. Specifically, in an array of vertical circular cylinders $\alpha = 0.8$ for horizontal diffusion [462] and $\alpha = 0.2$ for vertical diffusion (inferred from Nepf et al., [460]).

The combination of reduced velocity and reduced eddy-scale will reduce the in-canopy turbulent diffusion relative to regions without vegetation but under the same forcing (e.g. tidal pressure gradient). This reduction has been observed in the field for aquatic grasses (Worcester, [653]; Ackerman and Okubo, [4]; Ackerman, [3]). Turbulent diffusivity in an aquatic canopy differs from the open water in another important way. In the open water there is a wide range of turbulent scales, from the domain width and depth down to the Kolmogorov scale. Therefore, as the scale of a diffusing patch grows, larger and larger eddies contribute to its dispersal, i.e. l_e in (6.12) increases as the patch size increases. And, thus the diffusivity characterizing that dispersal also increases. The dependence of horizontal diffusivity on patch scale is well documented for patch scales from 10 m to 10^5 m (Okubo, 1971 [475]; Lawrence, 1995 [359]). In contrast, within a canopy the range of eddy-scales is quite small, as all scales greater than the stem spacing are damped by the vegetation. The largest eddy-scales contributing to turbulent diffusion are limited to the range $l_e = d$ to ΔS. Once a dispersing patch grows larger than this, the diffusivity describing the dispersal of the patch is given by (6.13), and is independent of patch scale. Because turbulent diffusion is constrained by the canopy eddy scale, other mechanisms of dispersion, described below, become important at larger scales within a canopy.

Mechanical dispersion, D_m, was first defined for porous media flow and represents the spreading of fluid particles due to differences in their individual flow paths imposed by the intertwining pore channels. This concept can be extended to canopy flow, with the variations in flow path generated by the presence of the canopy elements. Consider a cloud of particles released together at $(x, y) = (0, 0)$ and which subsequently advect through an array of vertical stems at a mean velocity, $\langle \overline{u} \rangle$. In each time interval, Δt, each particle moves a longitudinal distance, $\Delta x = \langle \overline{u} \rangle \Delta t$. During this time each particle has probability $a \cdot \Delta x$ of encountering a stem. If a stem is encountered the particle is forced to move laterally, and the lateral step will be $\pm \Delta y = \beta d$, where β is an O(1) scale factor. On average the particles move right and left with equal probability. After M time steps, where M is large, the particles achieve a Gaussian distribution in y with variance,

$$\sigma^2 = \frac{a \Delta x (\beta d)^2 t}{\Delta t} = \beta^2 a d^2 \langle \overline{u} \rangle t \tag{6.14}$$

(e.g. Hoel et al., [271]). Since the variance increases linearly with time, this describes

a Fickian process, with dispersion coefficient $D_m = (1/2)d\sigma^2/dt$. From (6.14),

$$D_m = \frac{\beta^2}{2} ad^2 \langle \overline{u} \rangle. \tag{6.15}$$

To measure the mechanical dispersion experimentally requires conditions in which the turbulent diffusion is negligible, specifically, $\mathrm{Re}_d < 100$ so that no turbulence generation occurs in the element wakes. Two studies, Nepf et al., 1997 [460] and Serra et al., [570], provide observations in this regime. In these studies the normalized diffusivity, $D/\langle \overline{k} \rangle d$, varies linearly with array density, ad, as predicted by equation (6.15), Figure 6.4,b. The observations fit a curve $D/\langle \overline{u} \rangle d = ad$ (shown as a dashed line), suggesting a step-scale $\beta = \sqrt{2} \approx 1.4$, which is physically reasonable. Note that this model implies that mechanical dispersion is not a function of canopy drag (C_D), but only canopy geometry (a and d). Serra et al., [570] suggest a similar model, but the lateral step-scale is a function of C_D which is also physically resonable. More data is needed to clearly distinguish between the two models. Finally, in the model described above and in the observations reported in Nepf et al. [460] and Serra et al., [570], the stems (cylinders) have exclusively vertical orientation, so that only a lateral component of mechanical diffusion is generated. However, real stems and branches may have significant horizontal orientation, so that particles may be diverted vertically as well as laterally, and both vertical as well as lateral mechanical dispersion will exist.

Mechanical and turbulent diffusion are independent processes, so that their contribution to the total diffusivity are additive at scales greater than the stem-scale. The models for diffusivity are compared to laboratory and field observations in Figure 6.4,a. The solid lines indicate the model for turbulent diffusivity given in equation (6.13) with $\alpha = 0.8$ and 0.2 for lateral and vertical diffusivity, respectively. The dashed line indicates the sum of turbulent (6.13) and mechanical (6.15, with $\beta = \sqrt{2}$) lateral diffusivity. Note that the mechanical component only becomes important at high array density. Measurements made in laboratory arrays of vertical circular cylinders (triangles) agree well with the models and demonstrate anisotropy between the vertical (open symbols) and lateral (closed symbols) components of diffusivity. Within a stand of *Spartina alterniflora*, the lateral diffusivity agrees with model predictions, but the vertical diffusivity is higher, such that the vertical and lateral diffusivities are less anisotropic in the field (circles). This is likely because the field canopy contains elements (stems and branches) with varied orientation, and thus produced turbulence that is more isotropic than an array of vertical circular cylinders.

Because mechanical diffusion arises from velocity perturbations at scale d, this mechanism contributes little to mixing at scales smaller than d. A patch dispersing only under the action of mechanical dispersion will appear filamentous and choppy at scales of O(d). With the onset of vortex shedding ($\mathrm{Re}_d >\approx 100$), turbulence of scale d and smaller is introduced, and produces small-scale mixing that smooths the concentration over scales less than d (Dybbs and Edwards, 1984 [161]; Nepf et al. [460]). For processes that depend non-linearly on concentration, there will be a large difference between a smooth ($\mathrm{Re}_d >\approx 100$) versus a spikey ($\mathrm{Re}_d < 100$) concentration profile. In addition, animals that follow odor plumes to locate prey or mates may need different search strategies for smooth and spikey plumes (Finelli, [181]).

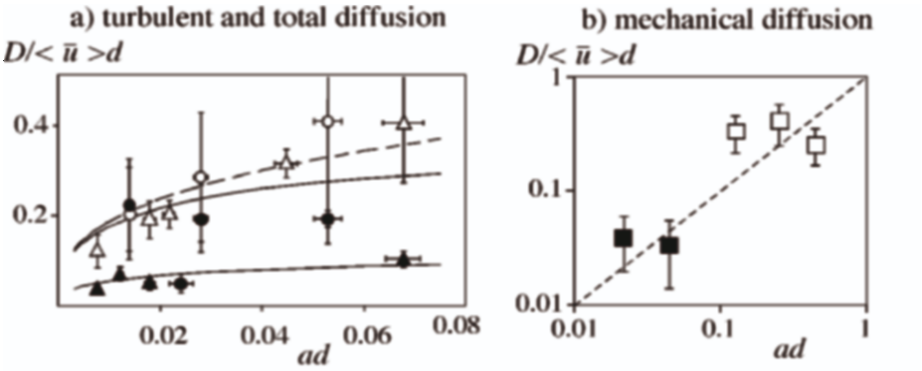

Figure 6.4: Observed diffusivity in a canopy normalized by the mean velocity and stem diameter. Vertical bars indicate one standard deviation among cases conducted at the same canopy density ad, but different velocity. a) $\mathrm{Re}_d > 100$. Vertical (solid) and lateral (open) diffusivity observed in the lab (triangle) and in the field (circle) from Nepf et al. [460], Tarrel [602], and Lightbody [371]. b) $\mathrm{Re}_d < 100$, only mechanical diffusion is present: closed symbol from Nepf et al. [460], open symbol from Serra et al., [570].

6.3.1 Longitudinal dispersion

As discussed above, spatial heterogeneity in the velocity field exists at the stem-scale, created by the overlapping wakes of individual stems, Figure 6.5. The velocity field can be divided into three flow regions. Directly downstream of each stem is a recirculation zone (dark gray in Figure 6.5) of width d and length γd, where γ is an O(1) function of Re_d (e.g. Gerrard, 1978 [225]). In this zone the average longitudinal velocity is zero. In the wake downstream of the recirculation zone (light gray in Figure 6.5), velocity is positive but diminished from the spatially-averaged flow, $\langle\overline{u}\rangle$. The drag imposed by the surrounding array causes the wake profile to decay over length-scale $(C_D a)^{-1}$ [643]. Finally, in the gaps between wakes and stems the flow must, by conservation of mass, be greater than $\langle\overline{u}\rangle$. Consider a group of particles released at time $t = 0$ and longitudinal position $x = 0$. Each particle experiences a different series of velocities along its trajectory, $u''(x(t))$, so that the particles become longitudinally dispersed. Three possible trajectories are shown in Figure 6.5. Particle 3, which passes through several wakes and recirculation zones, makes less longitudinal progress than particle 2, which remains predominantly in the gap between wakes. The central limit theorem provides that after each particle has sufficiently sampled the spatial variability in the velocity field, the ensemble of particles will have a longitudinal distribution that is Gaussian with a mean displacement $\langle\overline{u}\rangle t$ and spatial variance, σ_x^2, that increases linearly with time. The the longitudinal dispersion coefficient is then $K_X = (1/2)\partial\sigma_x^2/\partial t$. The magnitude of K_X depends on the spatial variance of the velocity field, σ_u^2, and the time-scale required to sample this variance. The variance is defined by the velocity characteristics in each flow zone. To define K_X these characteristics are used in a statistical model of particle trajectory through a random distribution of zones. Some elements of the derivation are given here, and the full derivation can be found in White and Nepf, 2003 [643].

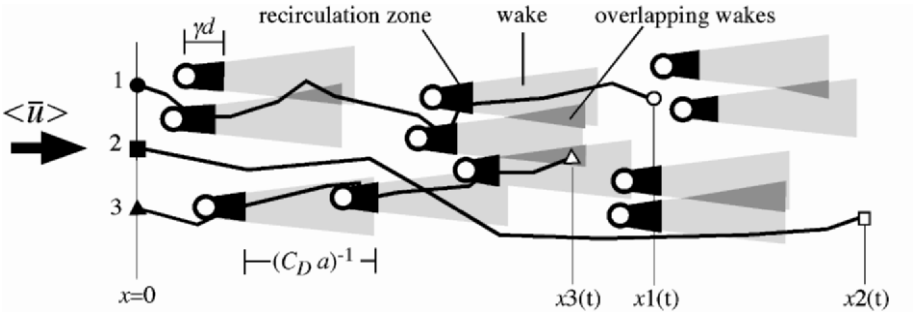

Figure 6.5: Top view of canopy. Circles represent cylindrical stems of diameter d. Behind each stem is a recirculation zone (black) of length γd, where γ is an O(1) function Re_d. The wake downstream of each recirculation zone has length $(C_D a)^{-1}$ (light gray). Where wakes overlap (dark gray), the velocity deficit is the linear sum of individual wake deficits. Particles 1, 2, 3 released together at $x = 0$ and $t = 0$ pass through different velocity zones and travel different longitudinal distances (x_1, x_2, x_3) in time, t, such that the spatial variance in the velocity field produces longitudinal dispersion.

First, consider the recirculation zone. In the absence of vortex shedding, the trapping and release from this zone occurs by diffusion. The mean residence time in this zone is $\tau \sim d^2/(4D)$, where D is the molecular diffusion constant. When vortex shedding is present the creation and subsequent shedding of vortices at frequency f_s controls the trapping and release of tracer from the recirculation zone, and $\tau \sim 1/f_s$ (Gerrard, [225]). In both cases the residence time is longer than the advection time,$\tau > d/\langle\overline{u}\rangle$, so that particles that enter the recirculation zone are delayed relative to particles that merely advect past it. This introduces a form of dead-zone or trapping dispersion.

Next, consider the wakes downstream of the recirculation zone. White and Nepf [643]derived the following expression for the velocity deficit, u_w, in the wake of a cylinder (stem) located at $x = 0$ and $y = 0$ within an array of cylinders,

$$u_w = \frac{C_D\langle\overline{u}\rangle d}{\sqrt{\pi\nu x/\langle\overline{u}\rangle}} \exp\left(-\frac{\langle\overline{u}\rangle y^2}{4\nu x}\right) \cdot \exp\left(-\mathbf{C_D a x}\right). \tag{6.16}$$

The first part of the expression, given in plain font before dot "·", is the familiar wake deficit profile for a single, isolated cylinder (Schlicting, 1960 [565]). Here ν denotes the sum of molecular (ν_m) and turbulent (ν_t) viscosity. The additional factor, given in bold font, arises from the drag associated with the canopy. The momentum absorption scale, $(C_D a)^{-1}$, sets the length-scale of influence for any individual wake. Where the wakes of adjacent cylinders overlap (medium gray in Figure 6.5), the total velocity deficit may be found from the linear superposition of each contributing wake (Bradshaw et al., [74]; Zhou et al., [667]).

Velocity in the gaps is enhanced above the spatial average. Between adjacent cylinders located at $x = 0$ and $y = \pm w/2$, where w is the gap width, the velocity may be

described with

$$u_g = \frac{C_D\langle\overline{u}\rangle ad}{2(1-ad)}\exp\left(-C_D a x\right). \tag{6.17}$$

The gap enhancement also decays downstream with length-scale $(C_D a)^{-1}$. At any point in the canopy the total velocity perturbation, u'', is the linear superposition of the velocity perturbations caused by all upstream wakes, u_w, and gaps, u_g. By considering all possible random arrangements of stems, the spatial variance in can be defined, i.e. σ_u^2 (White and Nepf, [643]). Using σ_u^2 and the detention time in each recirculation zone, τ, the particle tracking experiment represented in Figure 6.5 can be evaluated. The resulting longitudinal dispersion, K_X, to first-order, is

$$\frac{K_X}{\langle\overline{u}\rangle_{\mathrm{d}}} = \sqrt{\frac{C_D^3 \mathrm{Re}_t}{128}} + \frac{C_D ad}{4(1-ad)} + \gamma ad\frac{\tau\langle\overline{u}\rangle}{d}. \tag{6.18}$$

Higher order terms are given in White and Nepf [643]. The first, second and third terms on the right-hand side are the contribution of wake-shear, gaps, and recirculation zones, respectively. To first order the wake-shear contribution is independent of canopy density ad. While the number of wakes increases with the number of stems (increasing ad), each wake decays more rapidly, over scale $(aC_D)^{-1}$, and the two effects cancel. At higher order there is a weak dependence on ad, as discussed in White and Nepf, 2003 [643]. The transport Reynolds number, $\mathrm{Re}_t = \langle\overline{u}\rangle d/(\nu_m + \nu_t)$, describes the rate of lateral spreading of the wakes. For conditions with $\nu_m << \nu_t$, Re_t is nearly constant. Hinze [266] gives $\mathrm{Re}_t \approx 65$, and Schlicting [565] suggests $\mathrm{Re}_t \approx 45$. Fitting wake profiles given in Kovasznay [352] and Zavistoski [664] White and Nepf [643] estimate $\mathrm{Re}_t \approx 35$ for $\mathrm{Re}_d = 50$ to 1000.

Note that the dispersion terms described in equation (6.18) are valid only in the limit of Fickian behavior. From the central limit theorem, this regime is reached when every particle has amply sampled each region (wakes, gaps, recirculation zones). The average time-scale to advect through a wake is $(a\langle\overline{u}\rangle)^{-1}$, and the average time-scale to experience trapping within a recirculation zone is $\tau/(\gamma ad)$. Then, the Fickian limit is reached at time $t >> \tau/(\gamma ad)$ and $(a\langle\overline{u}\rangle)^{-1}$.

The dispersion coefficient predicted by (6.18) is consistent with observations made for $\mathrm{Re}_d = 65$ to 650 and $ad = 0.013$ to 0.082 (Figure 6.6a). For all ad, the normalized dispersion decreases with increasing Re_d, and most dramatically near the vortex shedding transition, $\mathrm{Re}_d \approx 100$. This is consistent with the contributions to dispersion by C_D, γ and τ, all of which decrease with increasing Re_d, up to $\mathrm{Re}_d = 100$. In addition, for all Re_d, the dispersion coefficient changes very little between the lowest two ad values, but increases sharply at the highest ad. This suggests wake-shear dispersion, which to first-order is not dependent on ad, is dominant at $ad = 0.013$ and 0.025. Between $ad = 0.025$ and 0.082 normalized dispersion increases, indicating the contribution of the recirculation zone, which increases with ad. For the range of Re_d and ad considered here, $C_D = O(1)$ and the gap contribution is O(0.01), and thus negligible. The distinction between wake and recirculation zone dispersion is further shown in Figure 6.6b, which depicts conditions at $\mathrm{Re}_d = 100$. For $ad < 0.05$ the wake-shear component dominates and total dispersion is only weakly dependent on ad. For

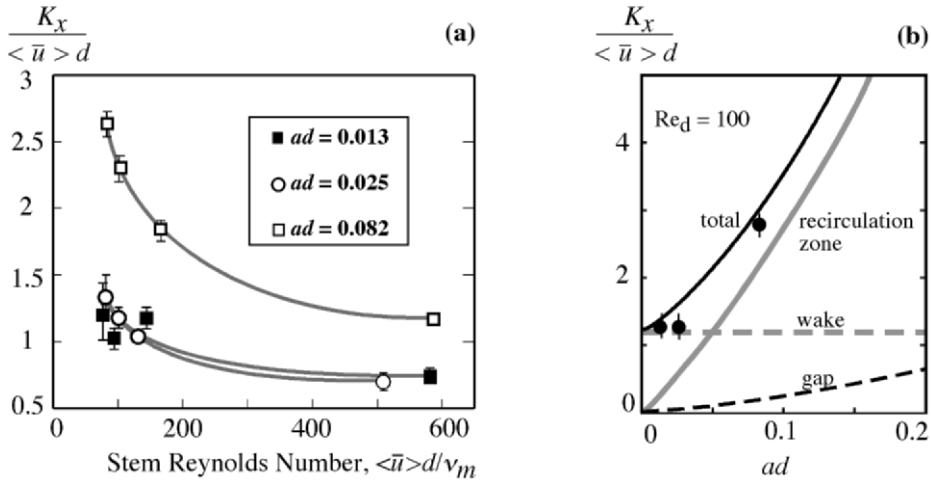

Figure 6.6: Measured longitudinal dispersion normalized by velocity and stem diameter. (b) Comparison of observed (dots) and predicted (lines) dispersion for $\mathrm{Re}_d = 100$. Contribution by the recirculation zones (gray solid line), the wake shear (gray dashed line), and the gaps (black dashed line); and the total dispersion (black solid line) based on equation 6.18 with $C_D = 1.8$, $\nu_\tau = 0.03\ cm^2 s^{-1}$, $\tau = 7.5\ s$. These parameters were based on experimental and literature values and were not adjusted to fit the data. From White and Nepf [643]. Reprinted with permission from Cambridge University Press.

$ad > 0.05$ the recirculation zone trapping dominates and total dispersion is strongly increasing with ad.

The description of dispersion given above assumes a unique wake for each stem. But, at high canopy density neighboring wakes may influence one another. Based on wake studies by Zhang and Zhou [666], wake interference occurs in a random array for $ad > 0.1$. For $ad > 0.1$ individual recirculation zones merge into larger trapping regions consisting of multiple stems and the fluid space between them. The total stagnant water volume is then greater than the sum of recirculation zones for individual stems, *i.e.*γ will increase with ad when wake merging begins. As the trapping zones increase in size, the residence times will likewise increase. Both trends should enhance trapping dispersion. More studies are needed at high array density to fully understand these trends.

The dispersion coefficients described by equation (6.18) assume that the canopy morphology is uniform in space, *i.e.*a and d do not vary in space. If the morphology is heterogeneous, *e.g.* at scale L_a, the velocity $\langle\overline{u}\rangle$ is also heterogeneous at scale L_a, introducing another process of dispersion, namely mean shear dispersion. Recall that the velocity $\langle\overline{u}\rangle$ is defined as a spatial and temporal average of the fluid velocity taken over a footprint that is greater than ΔS but less than L_a. The mean-shear component of dispersion may be predicted from the morphology of the canopy. As a simple example

consider a canopy that is homogeneous in the horizontal, but varies over depth, i.e. $a = f(z)$. The depth-averaged velocity is denoted U. The deviation between the local-average velocity, $\langle\overline{u}\rangle(z)$, and the depth-averaged velocity is denoted, $u'_v(z) = \langle\overline{u}\rangle(z) - U$, where the sub-script v denotes the vertical heterogeneity. This is distinct from the velocity heterogeneity at scale ΔS, denoted $u''(z)$ above. The mean shear dispersion is then (Taylor, [604])

$$K_h = -\frac{1}{h}\int_0^h u'_v \int_0^z \frac{1}{D_z}\int_0^z u'_v\, dz\, dz\, dz. \tag{6.19}$$

The sub-script h is used to denote the dispersion associated with velocity shear at the canopy scale, as distinct from velocity shear at the wake scale. Recall that here $h = H$, as the canopy is emergent. Equation (6.19) can be non-dimensionalized as

$$\frac{K_h}{Uh} = -\frac{1}{h^2 d}\int_0^h \frac{u'_v}{U}\int_0^z \frac{U\langle\overline{u}\rangle d}{\langle\overline{u}\rangle D_z}\int_0^z \frac{u'_v}{U}\, dz\, dz\, dz \tag{6.20}$$

where D_z is the vertical, turbulent diffusion. The ratio $D_z/\langle\overline{u}\rangle d$ is a function of $C_D ad$ (equation 6.13). Following equation (6.8) each velocity ratio in (6.20) can be expressed in terms of $C_D a$. Therefore, the dimensionless dispersion, K_h/Uh, may be predicted from apriori knowledge of the canopy morphology. However, since C_D may vary with velocity, the solution of (6.20) may require iteration. In some cases ($\mathrm{Re}_d > \approx 100$ and $ad < 0.03$) C_D will be relatively insensitive to the velocity and array density, so that a constant $C_D \approx 1$ may be assumed. Then equation (6.20) can be evaluated directly, i.e. without iteration, using only the profile of $a(z)$.

To illustrate the predictive power of equation (6.20), consider a simple canopy consisting of an array of circular cylinders. The frontal area per volume, a, has a step function profile, which produces a step-function velocity profile, as depicted in Figure 6.7. For this canopy (6.19) reduces to the following, in which u_i and D_i represent the velocity and diffusivity, respectively, in the lower ($i = 1$) and upper ($i = 2$) layer of the canopy.

$$K_h = \frac{\left(u_1 - u_2\right)^2 h^2}{96}\left(\frac{1}{D_1} + \frac{1}{D_2}\right). \tag{6.21}$$

Re-arranging equation (6.21) to a non-dimensional form,

$$\frac{K_h}{Uh} = \frac{1}{96}\left(\frac{u_1 - u_2}{U}\right)^2\left(\frac{Ud}{D_1} + \frac{Ud}{D_2}\right)\left(\frac{h}{d}\right). \tag{6.22}$$

Each term in (6.22) can be expressed in terms of the canopy parameters $C_D a$, d, and h. Using equations (6.8) and (6.13), the non-dimensional dispersion is then,

$$\frac{K_h}{Uh} = \frac{h}{120d}\left(\frac{\sqrt{C_{D2}a_2/C_{D1}a_1} - 1}{\sqrt{C_{D2}a_2/C_{D1}a_1} + 1}\right)^2\left(\frac{1}{\left[C_{D_1}a_1 d_1\right]^{1/3}} + \frac{1}{\left[C_{D2}a_2 d_2\right]^{1/3}}\right). \tag{6.23}$$

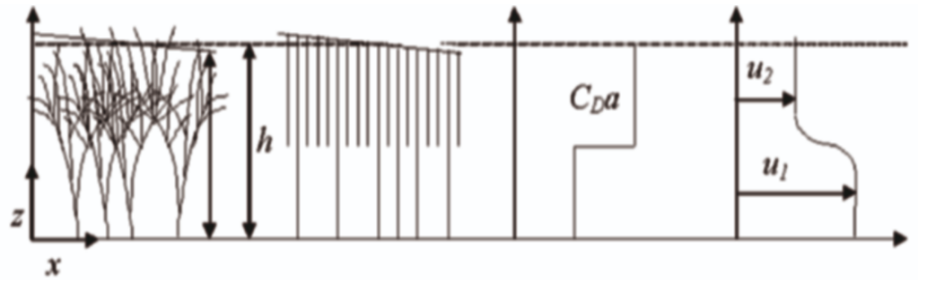

Figure 6.7: Natural vegetation, for which stem density changes over depth, can be represented by a simpler canopy with a step distribution in frontal area density, *a(z)*. This step distribution is generates a step profile of longitudinal velocity, $\langle \overline{u} \rangle$.

This Fickian dispersion coefficient is only realized after the tracer has sampled the full velocity heterogeneity, which in this case requires that the tracer mixed over the full canopy depth, i.e.

$$t_s \sim \frac{h^2}{D_z}. \tag{6.24}$$

Some experiments have been conducted to test the theory for mean shear dispersion in heterogeneous canopies, using a canopy of the form shown in Figure 6.7 with $a_1 d_1 = 0.012$ and $a_2 d_2 = 0.024$ (Lightbody, [371]). Tracer was released as instantaneous slugs at mid-depth in the canopy (i.e. at the interface). The concentration distribution was recorded at several positions between 50 *cm* and 525 *cm* downstream of the release. For each distance multiple releases were performed and the results averaged to form the ensemble-mean concentration distribution, which in turn was used to define the spatial concentration variance, σ_x^2. This study focused on dispersion occurring before the tracer cloud has spread over depth (pre-Fickian). So, for these observations (6.19) is modified to consider only an effective depth, rather than the full canopy (water) depth. The effective vertical scale of the cloud, $\Delta h < h$, is defined as the water depth that would yield the same dispersion coefficient at that longitudinal position. Because the two layers have different vertical diffusivities, D_1 and D_2, $\Delta h = \Delta h_1 + \Delta h_2$, where Δh_1 and Δh_2 are the effective vertical extents of the tracer in the lower and upper regions of the canopy, respectively. Using (6.19), the dispersion coefficient resulting from a step gradient with layer thicknesses Δh_1 and Δh_2 and diffusivities D_1 and D_2 in each layer, respectively, is:

$$K_{\Delta h} = \frac{\left(u_1 - u_2\right)^2}{8\Delta h}\left(-\frac{(\Delta h_1)^3}{3D_{z,1}} + \frac{\left(\Delta h_1\right)^2 \Delta h_2}{D_{z,1}} + \frac{\Delta h_1 \left(\Delta h_2\right)^2}{D_{z,2}} - \frac{\left(\Delta h_2\right)^3}{3D_{z,2}}\right). \tag{6.25}$$

The subscript Δh denotes that this coefficient applies for pre-Fickian dispersion when the cloud has effective vertical scale Δh. This expression appropriately reduces to (6.21) when $\Delta h_1 = \Delta h_2 = h/2$. From diffusion scaling

$$\Delta h_t = R\sqrt{D_t t} \tag{6.26}$$

where R is an O(1) scale constant. A reasonable estimate would be that $\Delta h_i = \sigma_z$, the standard deviation of vertical concentration, which gives $R = \sqrt{2}$, assuming Fickian diffusion occurs in the vertical. Replacing the effective layer depths with the definition given in (6.26),

$$K_{\Delta h} = \frac{R^2}{12}\left(\frac{u_1 - u_2}{U}\right)^2 U^2 t, \tag{6.27}$$

which is valid for $\Delta h < h$.

The observed longitudinal dispersion will also be influence by stem-wake dispersion. However, for $ad < 0.1$ (as is the case here), the recirculation zone and gap dispersion will be negligible (White and Nepf 2003 [643]). Further, the stem-wake dispersion can reach Fickian behavior at $t > (a\langle\overline{u}\rangle)^{-1}$, or $x > a^{-1}$ (see discussion above). For the canopy studied this requires $x > 8$ *cm*. Because all measurements were taken more than 50 *cm* downstream, stem-wake dispersion may be represented by the term shown in (6.18). Additionally using equation (6.8) to replace the velocity ratio in equation (6.27), the total longitudinal dispersion coefficient is,

$$K_x = \sqrt{\frac{C_D^3 \mathrm{Re}_t}{128}} Ud + \frac{R^2}{12}\left(2\frac{\sqrt{C_{D2}a_2/C_{D1}a_1} - 1}{\sqrt{C_{D2}a_2/C_{D1}a_1} + 1}\right)^2 U^2 t. \tag{6.28}$$

The variance in tracer concentration should therefore evolve as

$$\sigma_x^2 = 2\sqrt{\frac{C_D^3 \mathrm{Re}_t}{128}} dx + \frac{R^2}{12}\left(2\frac{\sqrt{C_{D2}a_2/C_{D1}a_1} - 1}{\sqrt{C_{D2}a_2/C_{D1}a_1} + 1}\right)^2 x^2, \tag{6.29}$$

where we have replaced $x = Ut$. Equation (6.29) shows that the variance grows nonlinearly with distance from source. Further, this growth is only weakly dependent on the velocity through C_D. In some cases ($\mathrm{Re}_d >\approx 100$ and $ad < 0.03$) C_D will be relatively insensitive to the velocity and array density, so that a constant $C_D \approx 1$ may be assumed (Nepf, 1999 [462]). For these conditions the variance can more simply be expressed as

$$\sigma_x^2 = 2\sqrt{\frac{\mathrm{Re}_t}{128}} dx + \frac{R^2}{12}\left(2\frac{\sqrt{a_2/a_1} - 1}{\sqrt{a_2/a_1} + 1}\right)^2 x^2. \tag{6.30}$$

Both expressions are compared to observation in Figure 6.8. The predicted curves use $\mathrm{Re}_t = 35$ and $R^2 = 2$, as discussed above. Equation (6.29) does a very good job predicting the trend in the variance, confirming the above theory. Equation (6.30) under predicts the observed variance, but with a maximum error of 40%. Thus, for order of magnitude estimation the simpler equation (6.30) may be applied. Clearly better predictions are possible when the full C_D dependence is included, which again points to the need for better quantification of the dependence of C_D on Re_d and ad.

6.4 Submerged canopies

To flow above a submerged canopy, the canopy appears as additional bed roughness. Sufficiently far above a canopy the profiles are logarithmic (e.g., Thom, [611]; Kouwen

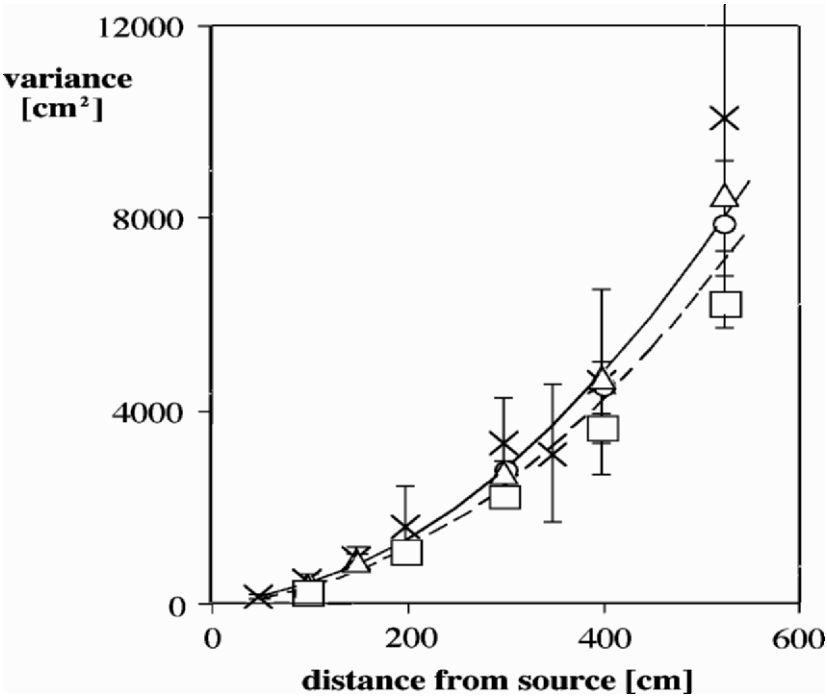

Figure 6.8: Observed growth in tracer spatial variance agrees with theoretical prediction. Velocity is 0.9 $cm \cdot s^{-1}$ (×), 2.0 $cm \cdot s^{-1}$ (○), 3.2 $cm \cdot s^{-1}$ (△), 4.1 $cm \cdot s^{-1}$ (□). Vertical bars indicate standard deviation of multiple realizations for same conditions. Predicted growth based on equation (6.29) (solid line) and equation (6.30) (dashed line).

and Unny, [348]; Gambi et al., [201]; Shi et al., [580]). The velocity profile is defined by the effective momentum boundary, z_m, the friction velocity, u_*, and the roughness height, z_0 (e.g., Plate and Quraishi, [499]; Thom, [611]), see also Section 4.2

$$\langle \overline{u} \rangle (z) = \frac{u_*}{\kappa} \ln \frac{z - z_m}{z_0}. \tag{6.31}$$

For continuity with flow within the canopy, the velocity is taken as a spatial and temporal average, $\langle \overline{u} \rangle$, although above the canopy this spatial average is not needed. The effective momentum boundary is the vertical position within the canopy below which momentum from the overflow does penetrate. That is, for flow above the canopy, $z = z_m$ is an effective lower boundary and $(H - z_m)$ is the effective depth of the overflow. Friction velocity for the overflow may then be estimated as

$$u_* = \sqrt{g \frac{\partial H}{\partial x} (H - z_m)}, \tag{6.32}$$

which indicates the equivalent bed stress provided by the canopy to the overlying flow

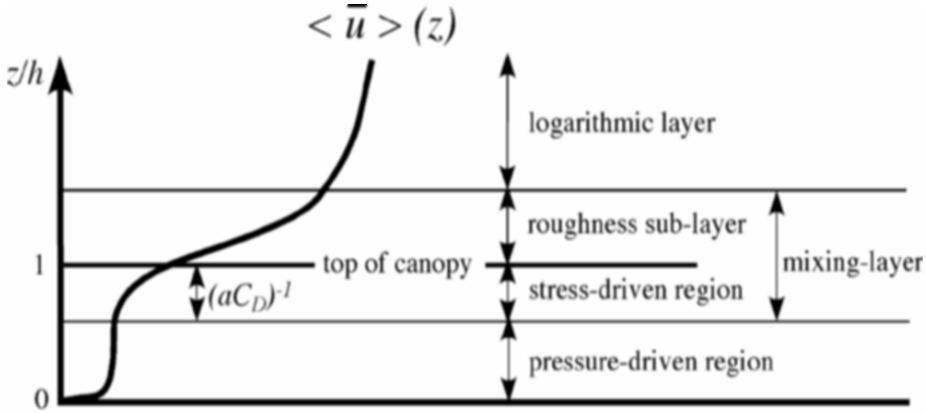

Figure 6.9: Velocity profile in and above a submerged canopy. In the upper portion of the canopy flow is predominantly driven by turbulent *stress*, which penetrates downward into the canopy over attenuation scale $(aC_D)^{-1}$. Below this flow is driven by potential gradients due to bed- or pressure gradients. At the top of the canopy the discontinuity in drag generates a mixing-layer. Above this the profile transitions to a logarithmic boundary layer profile.

and appearing to act at $z = z_m$. Finally, z_o and z_m both depend on the plant height, pronation, stiffness, and stem density (e.g. Businger, [95], Abdelrhman, [1]).

The existence of the logarithmic profile requires equilibrium turbulence, such that dissipation and production are locally in balance (e.g. Tennekes and Lumley [606]). This condition is not met within the canopy or for some distance above it, called the roughness sub-layer (Figure 6.9). Thus, logarithmic profiles cannot exist above canopies that occupy a large fraction of the water depth, such that the roughness sub-layer extends to the surface. In practice, logarithmic structure has not been observed above canopies with depth ratios of $H/h \leq 1.5$, Nepf and Vivoni, [463].

The flow within a canopy is driven by the combination of turbulent stress generated by the overflow and by potential gradients associated with the hydrostatic pressure gradient and bed slope. The relative importance of these drivers depends on the depth of submergence (H/h) and the canopy momentum absorption, aC_D. The pressure-(potential-) driven component is given in equation (6.6). A simple model for the stress-driven, in-canopy flow has been given for terrestrial canopies by Raupach and Thom [522] and applied to aquatic canopies by Abdelrhman [1], see also discussion in Chapter 4. With U_h the velocity at the top of the canopy (at $z = h$), the profile within the canopy is

$$\langle \overline{u} \rangle (z) = U_h \exp\left(\lambda\left(\frac{z}{h} - 1\right)\right). \tag{6.33}$$

Recall that $z = 0$ at the bed and positive upward, so that the above expressions gives a maximum velocity at the top of the canopy (equal to U_h), and an exponential decay of velocity downwards into the canopy. The attenuation of momentum within the canopy is characterized by the coefficient λ. Using model assumptions described in

Abdelrhman [1]

$$\lambda = h\left[\frac{C_D a}{2z_m^2}\right]^{1/3}. \tag{6.34}$$

As expected, the attenuation coefficient is a function of canopy momentum absorption, $C_D a$. Thus, vertical exchange of momentum (and, by analogy scalar constituents) is restricted to a region of length scale $(C_D a)^{-1}$. To model the full velocity profile, i.e. both within and above the bed, some researchers have simply combined models for above-canopy and in-canopy profiles by matching the velocity at the top of the canopy. An example of this is given in Abdelrhman, 2003 [1], who achieves good agreement with measured profiles (after some calibration). Another example can be found in Carollo et al., [102]. By this construction $\langle\overline{u}\rangle$ but not the mass flux $\left(\langle\overline{u}\rangle A n_P\right)$ will be continuous at the canopy interface, because the porosity, n_P, is discontinuous at this interface.

Traditional open-channel flow equations have also been applied with some success to flows with aquatic vegetation. For a comprehensive review one can begin with Kadlec, 1990 [322], Dawson and Charlton, 1988 [145] and Fishenich, 1994 [190]. In these formulations the drag is represented by either the Manning's roughness coefficient (e.g. Ree, 1949 [531]; Kouwen and Li, 1980 [349]; Kouwen, 1992 [351]; Guardo and Tomasello, 1995 [242]), or by the Darcy-Weisbach friction factor (e.g. Chen, [116], Kowen and Unny, 1973 [348]). Predictably, both drag parameters increase with increasing vegetation height, stem density and rigidity. These depth-averaged characterizations work well for systems in which the vegetation is a small fraction of the water depth, e.g. rivers. However, in marshes, wetlands, and mangroves, the vegetation is distributed over a large fraction (or all) of the water depth, so that modeling vegetative drag using a bed friction characterization like Manning's coefficient is ill-posed, as this model assumes that drag is contributed only at the bed. None-the-less, some effort to extend the Manning's roughness coefficient to vegetated flow has been made (e.g. Guardo and Tomasello, 1995 [242]; and discussion in Wu, Shen and Chou, 1999 [657]). Although useful for its simplicity, this depth-averaged approach reveals no information about the vertical structure of flow, or even how flow is distributed within and above a canopy (Kadlec, [322]; Jadhav and Buchberger, [312]). Furthermore, because the vegetation resistance is lumped with the bed drag, there is no way to extract the changes in bed stress which occur as increasing percentages of the total resistance is provided by increasing canopy density. It is the stress at the bed that determines sediment transport and boundary exchange, not the total resistance provided by the combination of canopy and bed (Lopez and Garcia, [378]). Finally, at a single site (i.e. a fixed vegetation height) the Manning's coefficient is a function of water depth (Wu, Shen, and Chou, [657]; USGS [626]), as the total vegetative resistance increases as water depth within the canopy increases.

6.4.1 Scale constraints in a vegetated shear-layer

As discussed earlier, the velocity profile near the top of the canopy is characterized by a region of strong shear arising from the discontinuity in drag. In this region the

velocity profile resembles a free-shear-layer (FSL) or mixing layer, and includes an inflection point just within the canopy (Figure 6.9). A free-shear-layer is characterized by large coherent vortices that form via Kelvin-Helmholtz (K-H) instability and which dominate the transport across the layer (Brown and Roshko, 1974 [86], Winant and Browand, 1974 [649]). A similarity between canopy-shear-layers and FSL has been shown for both terrestrial (Raupach et al., 1996 [530]) and aquatic canopies (Ghisalberti and Nepf, 2002 [227]). And, the K-H vortices control the exchange of scalars and momentum between the canopy and overlying flow. In a FSL, the vortices and the shear-layer width grow continually downstream, predominantly through vortex merging (Winant and Browand [649]). In contrast, in canopy-shear-layers the vortices initially grow, but quickly reach a fixed scale. The constraint on vortex scale is reflected in the arrested growth of the shear-layer. This is depicted in Figure 6.10, which shows the momentum thickness,Θ, reaches an equilibrium value at 4-m from the leading edge of a submerged aquatic canopy (Ghisalberti [226]). A shift in vortex frequency occurs during the initial growth phase, from 0.13 Hz (at 1.6 m) to 0.06 Hz (at 4.8 m). This suggests that one vortex merging occurs in the canopy-shear-layer before vortex growth is arrested (Ghisalberti [226]). Similarly, Cheng and Castro [119] have shown that after a short development region the roughness sub-layer, the top of which corresponds to the top of the canopy-shear-layer (as shown in Figure 6.9), is independent of distance along a model canopy, remaining constant even as the overlying boundary layer continues to develop. In many instances the final vortex size, and the region of rapid exchange it defines, extends to neither the water surface nor the bed. This segregates the canopy into an outer region of rapid exchange with the overlying flow and an inner region of more limited renewal (Nepf and Vivoni[463]).

Constrained shear-layer growth has previously been observed in shallow-water shear-layers or SSL (Chu et al., 1991 [121], Uijttewaal and Tukker, 1998 [624] Uijttewaal and Booij, 2000 [625]). When a vortex within a SSL grows to sufficient scale, the rate of shear-production balances the rate of dissipation by bottom friction and the vortex growth ceases. Subsequently this vortex begins to dissipate (van Prooijen and Uijttewall, 2002 [628]). By analogy, one expects that canopy-shear layers may be controlled by a balance between the production of large-scale vorticity by mean shear and its dissipation by canopy drag. However, an important difference should be noted. In SSL, the bed-friction coefficient, c_f, is presumed to be spatially uniform, such that the bed drag, $\tau_b = -\rho c_f U \mid U \mid$, is stronger on the high velocity side than on the low velocity side. The result is that the normalized velocity difference between the streams,

$$\frac{\Delta U}{U} = 2\frac{\mid u_2 - u_1 \mid}{u_1 + u_2}, \tag{6.35}$$

decreases with downstream distance, which ultimately dissipates the vortices and erases the shear-layer, i.e.ΔU goes to zero (e.g. Uijttewaal and Booij [625], van Prooijen and Uijttewall [628]). In contrast, a canopy-shear-layer is continually reinforced by the drag differential between the vegetated and open layers, which maintains a constant velocity difference after the shear-layer is fully developed (as shown in Figure 6.10). Thus, the final stage of canopy-shear-layer growth will be equilibrium, i.e. the vortices will reach *and maintain* an equilibrium scale without subsequent dissipation.

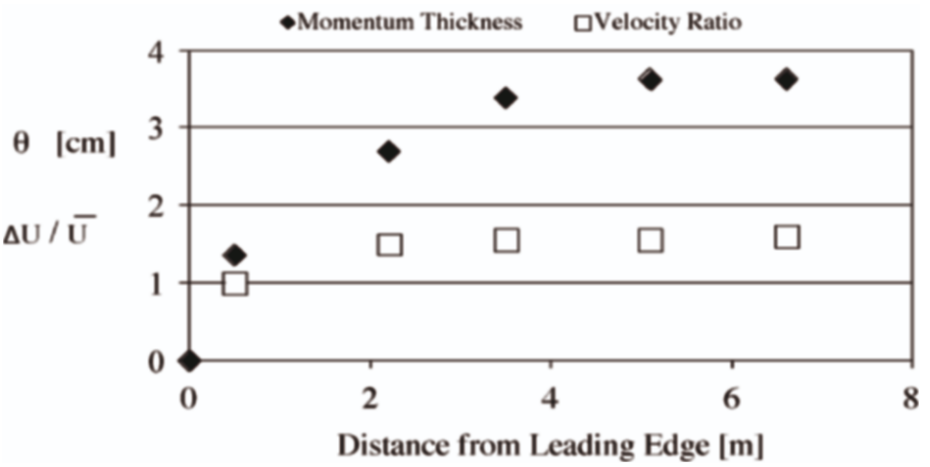

Figure 6.10: Momentum thickness, Θ_m, a proxy for shear layer width, and velocity difference, $\Delta U/\overline{U}$, where $\overline{U} = (U_1 + U_2)/2$. The two parameters are plotted versus distance downstream of canopy edge. Beyond 4-*m* the shear-layer growth has ceased.

Consider again the model canopy depicted in Figure 6.2, consisting of an array of vertical circular cylinders of diameter d and frontal area per volume a. Now, however, the canopy height, h, is less than the flow depth, H, such that unobstructed flow exists above the canopy (Figure 6.11). The canopy interface, $z = h$, is parallel to the flow. In this flow there are two dominant scales of turbulence: the shear (K-H vortex) scale and the stem-scale. The stem-scale turbulence is generated in the wakes of individual stems within the canopy (here of scale d). If the stem-scale (d) and shear-scale (O(h)) are distinct ($d << h$), the turbulent kinetic energy budget can be separated into shear-scale and wake-scale budgets (Shaw and Seginer, 1985 [574]). As the shear-scale vortices dominate vertical transport and govern shear layer growth, only the budget for shear-scale turbulent kinetic energy (k_s) is considered here,

$$\frac{D}{Dt}\langle\overline{k_s}\rangle = -\langle\overline{u'w'}\rangle\frac{\partial\langle\overline{u}\rangle}{\partial z} - \frac{\partial}{\partial z}\langle\overline{w'k_s}\rangle - \frac{1}{\rho}\frac{\partial}{\partial z}\langle\overline{w'p'}\rangle - \frac{\partial}{\partial z}\langle\overline{w''k_s''}\rangle - e_c - e_v. \qquad (6.36)$$

$$a \qquad b \qquad c \qquad d$$

Term a is shear production. Terms b and c are vertical transport associated with turbulence and pressure fluctuations, respectively. Observations in free- and canopy-shear-layers suggest that these terms are comparable in magnitude, but opposite in sign, such that to first order the sum of the pressure and turbulent transport is negligible within the shear-layer (e.g. Rogers and Moser [542], Brunet et al. [88], Raupach et al. [524]). Term d is the dispersive transport (analogous to term b in equation (6.2)), which is negligible relative to term a, as discussed above (Poggi et al. [502]).

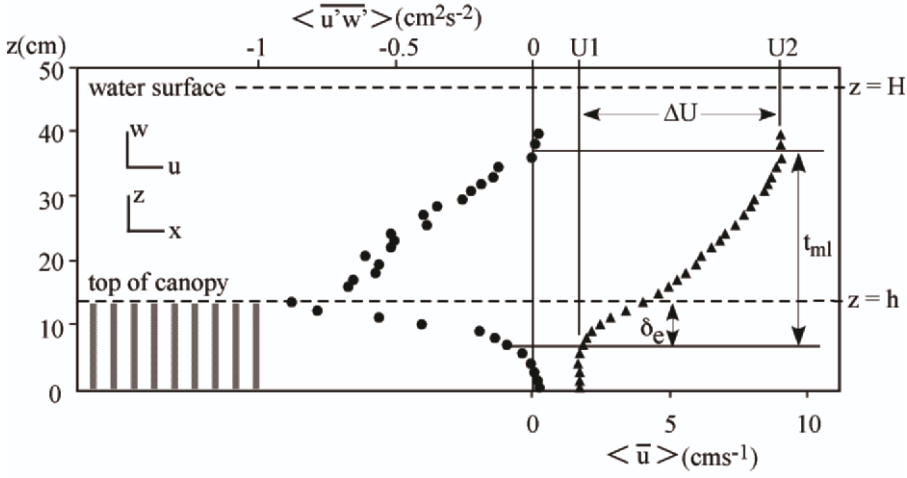

Figure 6.11: The discontinuity in drag at the top of the canopy ($z = h$) creates a shear layer of width t_{ml}. The velocity difference across the layer is $\Delta U = U_2 - U_1$. The layer penetrates downward into the canopy a distance δ_e from the canopy top.

The canopy dissipation, e_c, represents the damping of shear-scale turbulence by canopy drag (e.g. Wilson [648])

$$e_c = \frac{1}{2} C_D a \langle \overline{u} \rangle \left(2\langle \overline{u'^2} \rangle + \langle \overline{v'^2} \rangle + \langle \overline{w'^2} \rangle \right). \tag{6.37}$$

As in equation (6.3), the drag parameterization in (6.37) represents both the viscous and form drag associated with the individual elements. The component associated with form drag, a sink in the shear-scale energy budget, will be a source (called wake production) in the element-scale kinetic energy budget. The component associated with viscous drag dissipates shear-scale energy directly to internal energy, without contributing to smaller-scale turbulence (see discussion in Raupach and Thom, 1981 [522] Shaw and Seginer, 1985 [574]).

Finally, the viscous dissipation, e_V, is generally negligible relative to the canopy dissipation (Wilson, 1988 [648]).

As described above, terms b, c, and d, as well as the viscous dissipation, e_V, may be neglected from a first-order energy budget within the shear-layer. The remaining terms suggest that the vortex (and shear-layer) growth will be arrested $\left(D\langle \overline{k_s} \rangle / Dt = 0 \right)$ when the shear-production balances the canopy dissipation. This balance implies

$$\frac{\langle \overline{u} \rangle C_D a}{\partial \langle \overline{u} \rangle \partial z} = \frac{2\langle \overline{u'w'} \rangle}{2\langle \overline{u'^2} \rangle + \langle \overline{v'^2} \rangle + \langle \overline{w'^2} \rangle}. \tag{6.38}$$

The turbulence statistics included in the right-hand-side of (6.38) have similar profile shapes across a free-shear-layer, with maximum values $\overline{u'w'} = -0.01\Delta U^2$, $\overline{u'^2} = 0.03\Delta U^2$, $\overline{w'^2} = 0.015\Delta U^2$, and $\overline{v'^2} = 0.02\Delta U^2$, where $\Delta U = u_2 - u_1$ is the velocity

difference across the layer (e.g. Wygnanski and Fielder [659]). Recall that in fully-developed, obstructed-shear-layers, ΔU reaches a constant value shortly after initiation (Figure 6.10). To the extent that turbulence statistics in obstructed shear layers are similar to free-shear layers (supported by Raupach et al. [530]), the right-hand side of (6.38) would then have a constant value of 0.21. Indeed, this value is consistent with observations made in real and model terrestrial canopies as well as in model aquatic canopies (Table 6.1). In the Table 6.1 the turbulence statistics are evaluated at the top of the canopy, where data is available for all cases reported. The Table includes only cases for which the shear-layer extends neither to the bed nor to the water surface, to ensure that shear-layer dynamics are not influenced by an upper or lower boundary. The observed turbulence ratio has a mean value 0.21 ± 0.03. The available observations suggest that the turbulence statistics are not dependent on the canopy momentum absorption, aC_Dh. Some dependence on canopy Reynolds' number is implied, as the statistics are notably lower for the cases at $\mathrm{Re}_h \geq 10^6$.

A canopy-shear-layer parameter is defined from (6.38),

$$CSL = \frac{\langle\overline{u}\rangle C_D a}{\partial\langle\overline{u}\rangle/\partial z}. \tag{6.39}$$

This parameter is similar to one derived by Chu et al.[121] for shallow-shear-layers, with C_Da replacing the bed-friction parameter c_f/h. We anticipate that CSL will have a universal value (CSL_{eq}) for obstructed-shear-layers at equilibrium. From Table 6.1 we anticipate $CSL_{eq} = 0.21 \pm 0.03$. If this equilibrium exists, then (6.39) can provide an estimate of the length-scale,δ_e, which defines the region within the canopy that experiences rapid exchange with the adjacent open water (Figure 6.11). The characteristic length-scale of the shear-layer vortices is $L_h = \langle\overline{u}\rangle/\partial\langle\overline{u}\rangle/\partial z$, where the sub-script h indicates evaluation at the top of the canopy (at $z = h$). Substituting into (6.39),

$$CSL = C_D a L_h. \tag{6.40}$$

Additionally, $\delta_e \sim L_h$ and setting $CSL = CSL_{eq}$, equation (6.39) then becomes

$$\delta_e \sim \frac{CSL_{eq}}{C_D a}. \tag{6.41}$$

The penetration length-scale is proportional to the momentum absorption length-scale $(C_Da)^{-1}$, and not directly dependent on the free-stream velocity. Of course (6.40) is only valid for $\delta_e < h$, such that the shear-layer is not influenced by the bottom boundary, specifically the bed-stress does not contribute to the momentum balance. In the limit of a sufficiently sparse canopy (small C_Da), the bed-stress is more significant than canopy drag, and the velocity profile transitions to a rough boundary layer form. The transition from shear-layer behavior (drag dominated by canopy) to rough boundary layer behavior (drag dominated by bed stress) can be inferred from equation (6.41). Setting $\delta_e = h$ implies a transition occurs at $C_Dah = O(0.1)$. This is consistent with the series of canopy densities examined by Dunn et al. [156] and Poggi et al. [503]. The Dunn profiles span $C_Dah = 0.02$ to 0.35, and the Poggi profiles (Figure 3 in Poggi et al., 2004 [503]) span $C_Dah = 0.02$ to 0.6. In both studies cases with $C_Dah < 0.04$ exhibit a boundary-layer form with no pronounced inflection point at the top of the

Table 6.1: Turbulence statistics evaluated at the top of canopy. In all cases $H/h > 2$ and $\delta_e < 1$, to ensure that shear-layer dynamics are not influenced by other boundaries. U_h not available for Katul and Change [329], so an estimated value is based on Amiro Pine [9].

		h *cm*	a cm^{-1}	U_h	Re_h $U_h h/\nu$	$aC_d h$	X
Dunn et al. [156] R4 R8 R10	 cylinders in water in water	 12 12 12	 0.011 0.025 0.025	 59 44 64	 7 x 10^4 5 x 10^4 8 x 10^4	 0.17 0.28 0.36	 0.22 ± 0.02 0.23 ± 0.02 0.22 ± 0.02
Vivoni [637] R6B R7	 Flexi- strips in water	 14 16	 0.55 0.055	 15 7.8	 2 x 10^4 1 x 10^4	 0.52 0.60	 0.21 ± 0.02 0.23 ± 0.02
Seginer et al. [568] Fig.10,14	 cylinders in air	19	0.053	900	2 x 10^6	0.32	0.16 ± 0.03
Wilson [648], Table 1 Wilson et al. [648] Table 3	 corn	225	0.0064	140- -250	5 x 10^6	0.43	0.16 ± 0.01
Katul and Chang [329] Table 3	 pine forest	1400	0.0014	est. 150	2 x 10^7	0.39	0.15 ± 0.03

where $X = -2\langle\overline{u'w'}\rangle/(2\langle\overline{u'^2}\rangle + \langle\overline{v'^2}\rangle + \langle\overline{w'^2}\rangle)$, $\quad U_h = \langle\overline{u}\rangle$ at $z = h\ cm \cdot s^{-1}$

canopy. A pronounced inflection point appears at $C_D ah > 0.1$. Similarly, Belcher et al [51] propose a rough boundary-layer model for $ah \leq 0.1 - 0.01$, which they call the very-sparse-canopy limit. In this limit the canopy has negligible affect on the surface-shear-stress. For $C_D = O(1)$, this limit is consistent with that derived from equation (6.41).

Several laboratory and field studies provide data that supports the equilibrium argument presented here: Seginer et al. [568] – unconfined case; Tsujimoto et al. [617] runs R43, A11, A31, A71; Dunn et al. [156] runs 4, 8,and 10; Nepf and Vivoni [463] runs 6B and 7A; Raupach et al. [524]; Brunet et al. [88], and Ghisalberti [228] runs A – K. Only cases in which $H/h > 2$ were considered, so that flow depth does not restrict shear-layer growth (Nepf and Vivoni, [463]). Further, only cases for which $\delta_e < h$ were selected. These conditions ensure that the evolution of K-H vortices were not influenced by the bottom boundary or water surface, but only by the internal dynamics of the shear-layer itself. Profiles of velocity were used to estimate CSL at the inflection point and at the top of the canopy, with the values differing by around 10%. The penetration length-scale, δe, was taken as the distance from the top of the canopy to the point within the canopy at which the Reynolds' stress decays to 10% of its peak value. C_D was reported or estimated from a momentum balance within the canopy. Additional terrestrial data was drawn from Finnigan ([187], Table 6.1 1) using the reported values of L_S/h and ah to estimate CSL from (6.40). The drag coefficients for these cases were

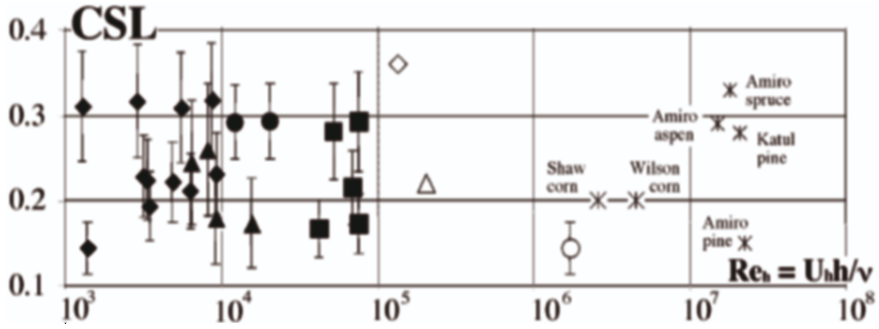

Figure 6.12: Canopy-shear-Layer parameter, CSL, defined in equation (6.39) versus canopy Reynolds number, $\mathrm{Re}_h = U_h h/\nu$. Data sources given in Table 6.2. For Katul Pine U_h is not provided, but assumed to be $U_h = 1.5\ m/s$, as in Amiro Pine.

Table 6.2: Data sources for Figures 6.12 and 6.13. When needed the canopy drag coefficients from field studies are corrected for factor 1/2.

Study	**Canopy form**	**Symbol**
Dunn et al. [156]	cylinder in water	solid square
Vivon [637]	cylinders in water	solid circle
Tsujimoto et al. [617]	cylinders in water	solid circle
Ghisalberti [229]	cylinders in water	solid diamond
Seginer et al. [568]	cylinders in water	open circle
Raupach et al.[524]	rectangular strips in air	open triangle
Brunet et al. [88]	flexible, cylinders in air	open diamond
Katul and Chang [329]	pine forest, $C_D = 0.2$	star with label
Shaw et al. [574]	corn, $C_D = 0.35$	star with label
Wilson [647]	corn $C_D = 0.3$	star with label
Amiro [9]	pine and aspen, $C_D = 0.3$ spruce, $C_D = 0.15$, Fig. 6.1	star with label

drawn from the literature, as listed in Table 6.2, accounting for the studies that drop the factor 1/2 from the drag law.

The measured value of CSL is constant across a range of Reynolds' number, $\mathrm{Re}_h = U_h h/\nu_m$ (Figure 6.12). Further, the mean observed CSL ($= 0.24 \pm 0.06$) is consistent with the equilibrium value predicted from observed turbulence statistics, $CSL_{eq} = 0.20 \pm 0.03$ (Table 6.1). These results support the proposed theory that the size of canopy-shear-layers is controlled by an equilibrium condition in which the shear-production and the dissipation by canopy drag are in balance. The equilibrium condition appears to be insensitive to Re_h over the range 10^3 to 10^8. This range spans the mixing-transition in free-shear-layers, which occurs at $\mathrm{Re}_{ml} = \Delta U t_{ml}/\nu_m = 6 \times 10^3 - 2 \times 10^4$, where t_{ml} is the shear-layer width (Moser and Rogers, 1991 [446], see also Figure 6.11). With $t_{ml} = O(h)$, a mixing transition is expected at $\mathrm{Re}_h = O(10^4)$. The cases above the transition ($\mathrm{Re}_h > 10^4$) have a comparable average value (0.23 ± 0.07) to those cases below this threshold (0.24 ± 0.05), suggesting that the transition to fine-scale structure

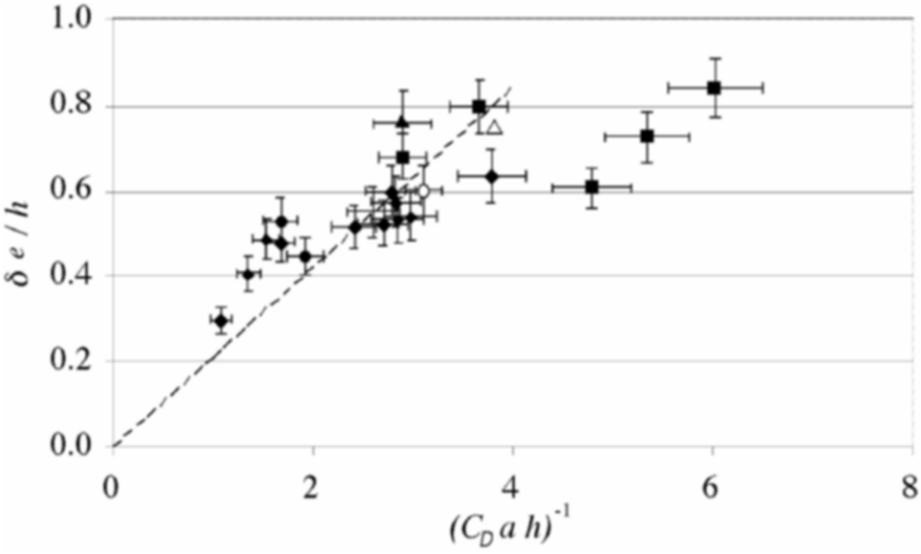

Figure 6.13: Scale of vortex penetration, δ_ε, versus $(C_D ah)^{-1}$. Symbols given in Table 6.2. The penetration scale, δ_ε, is defined as the depth at which the Reynolds' stress has decayed to 10 % of its maximum.

within the layer does not impact the evolution of the larger structures. This is consistent with FSL, in which the evolution of the large-scale (K-H) structures is similar with and without the super-position of fine-scale turbulence (Ho and Huerre [268]).

Figure 6.13 shows that for dense canopies (small $(C_D ah)^{-1}$) the penetration length-scale is a linear function of $(C_D ah)^{-1}$. Deviation from linear behavior begins at

$$(C_D ah)^{-1} \approx 4,$$

as the limit of full-depth penetration is approached. The linear relation $\delta_e/h = 0.21/(C_D ah)$, shown as a dashed line, fits the data well, suggesting that the scale constant is close to one. Further, the observed relation suggests that for dense canopies the region of rapid exchange between the canopy and surrounding water is dictated by canopy morphology, expressed through the momentum absorption scale ($C_D a$), and it is independent of flow speed, except through the dependence of C_D. This result is similar to that obtained by Beavers and Joseph, 1967 [47], who found that the penetration length-scale at the boundary between a channel and a porous medium scales in proportion to $\sqrt{k_p}$, where k_p is the permeability of the medium. Here $(C_D a)^{-1}$ plays the role of the permeability. Similar scaling is discussed in Chapter 3. This analysis provides the basis for predicting the penetration length-scale, δ_E, which is a useful tool for mapping transport zones within the obstructed region of flow (i.e. within the canopy), as it defines the region at the edge of a canopy that rapidly exchanges with adjacent open water. Finally, for $H/h < 2$ the presence of the free surface constrains the shear-layer vortices, and the penetration scale, δ_e, is diminished (Nepf and Vivoni, 2000 [463]).

6.5 Summary

This chapter examined the role of vegetation in modifying flow and transport in aquatic systems. The most important influence of a canopy the heterogeneity it produces in the velocity field at several different scales. At the scale of individual canopy elements, velocity heterogeneity results from the overlapping wakes generated by individual stems and branches. In addition, the canopy morphology may vary over depth or over distinct horizontal scales associated with differences in planting density. The resulting variation in canopy resistance produces velocity variance. Both scales of velocity heterogeneity impact the diffusion and dispersion within a canopy, which is important to the dispersal of larva, the structure of odor-plumes, and the distribution of particulate matter and nutrients within a marsh. As a chemical or larval patch grows, larger scales of canopy heterogeneity can influences its dispersion, and the rate of dispersion increases.

Aquatic canopies also exhibit a range of behavior depending on the depth of submergence. When the canopy is submerged, the drag discontinuity at the top of the canopy produces a shear-layer at this interface. Within the shear-layer, large coherent vortices form via Kelvin-Helmholtz (K-H) instability, and these structures dominate the vertical transport between the canopy and overlying open water. The depth to which these vortices penetrate the canopy is determined by the canopy morphology, and in particular the bulk canopy resistance. In many instances the vortices do not penetrate to the bed, so that the canopy is divided into two layers. The upper canopy is flushed rapidly by the energetic, shear-scale vortices. The lower canopy flushes more slowly through longitudinal advection and the less vigorous vertical mixing derived from stem-scale turbulence.

Acknowledgements

The authors gratefully acknowledge the support of the National Science Foundation under the grants EAR0125056, EAR 9629259, and EAR 0309188. Any opinions, conclusions or recommendations expressed in this material are those of the author(s) and do not necessarily reflect the views of the National Science Foundation.

Chapter 7

Vorticity annihilation and inviscid blocking in multibody flows

I. Eames[•1], **V. Roig**[⋆], **J.C.R. Hunt**[•†] **and S.E. Belcher**[‡]
[•]University College London, London, UK
[⋆]IMFT, Toulouse, France
[†]TU Delft, The Netherlands
[‡]University of Reading, Reading, UK

7.1 Introduction

Many environmental and processing engineering flows consist of collections of fixed or moving bodies (such as buildings, plants, bubbles and droplets). These flows may be unbounded or bounded high Reynolds number flows through groups of bodies, such as crop 'canopies' or buildings in the atmospheric boundary layer, boiler tubes in a furnace, flows through moving objects such as icebergs in the ocean, or bubble swarms in pipes. Examples of buildings in the urban terrain are given in Chapters 2 and 8, while plant canopies are described in Chapters 4 and 6. For many problems, the goal is to model the impact of many bodies on the ambient flow. There is an intrinsic complexity to modelling the flow through and around a group of bodies and estimating the flow signature they generate. In many cases, the huge number of bodies and the range of geometrical lengthscales (eg. from leaf size, to tree size, up to a forest scale, for plant canopies) means that traditional computational models, where the whole flow domain is meshed and solved numerically, are not able to include all the geometrical aspects [596]. As such, average descriptors, such as a distributed drag force introduced into

[1]E-mail of the corresponding author: *I.Eames@ucl.ac.uk*

Ye.A. Gayev and J.C.R. Hunt (eds.), Flow and Transport Processes with Complex Obstructions, 251–270.

the momentum equation, are required to drive computational models, in addition to imposed sources of turbulence. In attempting to model these processes, it is also pertinent to ask what are the geometrical features of the bodies which need to be estimated and included in such problems, as well as dynamical constraints such as the average drag coefficient.

Computational models describing plant canopies as a region of distributed drag, are quite successful at predicting how the mean flow is modified, examples are given in Chapter 3. But, for modelling flows through urban areas, where buildings occupy a significant volume fraction of the flow, this approach is inadequate near the front blocking region of a group of buildings (or indeed close to the bodies themselves), where inertial forces are much larger than for plant canopies and drag effects are greatest. In this region, inviscid blocking by the bodies is as significant as the influence of the drag force in decelerating the flow. How can we include this effect into current computational models?

To answer some of these questions, we need to first look at some of the physical processes which occur within groups of bodies and which are responsible for the flow signature of individual bodies decaying rapidly from the body. The dominant process is vorticity annihilation due to intermingling wakes (in Section 7.2). From this we are able to estimate when a distributed drag model, where local information about individual bodies is lost, is applicable. We develop an inviscid analysis (in Section 7.3) of how the kinematic blocking by rigid bodies is affected by their geometry. The important geometrical quantities identified in part of the analysis are the volume and added-mass coefficients of the bodies. But which of these is important also depends on the overall shape of the group of bodies. We show in Section 7.4 how these processes may be incorporated into future computational models. New measurements of the high void fraction (bubbly) flows are described which lend support to models of these processes (Section 7.5).

7.2 Vorticity annihilation in multibody flows

A schematic of the flow past a collection of bodies is shown in Fig. 7.1. We focus on the effect of bodies on the perturbation created by a 'test' body. As we follow the mean streamlines, they are seen alternately to converge and diverge, leading to regions where the flow is accelerated and decelerated. Even for an isolated body, the rear stagnation point associated with the wake generates a strained flow, albeit very weak. An additional process we can identify is that the wake of the test body intermingles with its neighbours. Broadly speaking, both processes serve to weaken the wake downstream of the test body although intermingling is dominant. We illustrate these processes with linearised calculations.

7.2.1 Flow generated by isolated body

The flow generated by an isolated planar body in an unbounded uniform stream may be surprisingly, far more complicated than the multibody counterpart. Vorticity of opposite signs is continuously shed from the surface of a rigid body (see Fig. 7.2a).

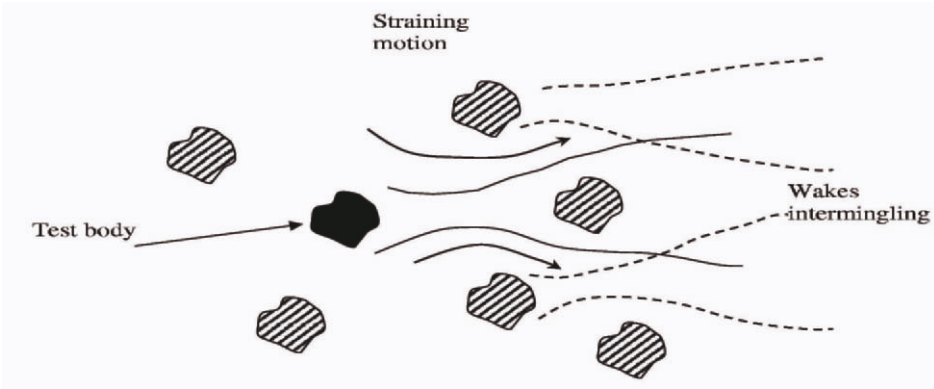

Figure 7.1: Schematic showing the wake of a test body interacting with the bodies downwind.

The presence of a (planar) body located at the origin is equivalent, in the far field, to a point force located at the origin (eg. see [75]). The flow $\mathbf{u} = (u_x, u_y, u_z)$ satisfies the linearised momentum equation,

$$U\frac{\partial \mathbf{u}}{\partial x} = -\frac{1}{\rho}\nabla p + \nu\nabla^2\mathbf{u} + \frac{F_0}{\rho}\hat{\mathbf{x}}\cdot\delta(\mathbf{0}), \tag{7.1}$$

where U is the free-stream velocity, F_0 is the drag on the body, located at the origin, ν is the kinematic viscosity of the fluid, whose density is ρ. $\delta(\mathbf{0})$ is the delta function located at the origin. Taking the curl of (7.1), we arrive at the evolution equation for vorticity $\omega(= \partial u_y/\partial x - \partial u_x/\partial y)$,

$$U\frac{\partial \omega}{\partial x} = \nu\nabla^2\omega - \frac{F_0}{\rho}\frac{\partial \delta(\mathbf{0})}{\partial y}. \tag{7.2}$$

Vorticity is advected downstream and diffuses, primarily, cross-stream. The presence of a point force creates a dipole source of vorticity (last term in (7.2)) – corresponding to a source and sink or equal strength, close together. An exact solution to (7.2) is

$$\omega = \frac{F_0}{\rho U}\frac{\partial C}{\partial y}, \qquad C = K_0\left(\frac{rU}{2\nu}\right)\exp\left(\frac{xU}{2\nu}\right), \tag{7.3}$$

where K_0 is the Bessel function of the second kind, zeroth order and $r = \sqrt{x^2+y^2}$. Far downstream, the velocity perturbation in the wake is

$$u_x - U \approx -\frac{F_0}{\rho U}C \sim -\frac{F_0}{\rho U}\left(\frac{U}{4\pi\nu x}\right)^{\frac{1}{2}}\exp\left(-\frac{Uy^2}{4\nu x}\right), \tag{7.4}$$

and is approximately gaussian. The wake width increases as $Y \sim (\nu x/U)^{\frac{1}{2}}$ downstream of the body. The flow generated by the wake generates a velocity deficit downstream, directed to the body, whose volume flux,

$$Q_0 = \int_{-\infty}^{\infty}(U - u_x)\mathrm{d}y = \frac{F_0}{\rho U},$$

is constant. Thus the volume flux in the wake is related to the drag on the body through

$$F_0 = \rho Q_0 U. \tag{7.5}$$

This provides an alternative explanation of Betz's result [62] (equation (7.5)) which is usually derived using a momentum-integral approach. The volume flux in the wake generates an irrotational source flow, in the far field, located at the origin:

$$\mathbf{u} = U\hat{\mathbf{x}} + \frac{Q_0 \mathbf{x}}{2\pi|\mathbf{x}|^2}, \tag{7.6}$$

(Batchelor [42]). But upstream and within a distance a of the body (where a is a characteristic lengthscale of the body), the flow is dominated by the kinematic constraint that the flow must go around the body and the flow is approximately

$$\mathbf{u} = U\hat{\mathbf{x}} + \mu_b \nabla\left(\frac{\mathbf{x}}{|\mathbf{x}|^2}\right), \qquad \text{where} \quad \mu_b = \frac{UV_b(1+C_m)}{2\pi}, \tag{7.7}$$

is the dipole moment of the body, whose volume is V_b. C_m is a dimensionless geometrical factor called the added-mass coefficient and is principally determined by the cross-sectional area of the body, compared to its volume. Various 'models' have been proposed to capture both the dipole and source solutions (for high Reynolds number separating flows) by a judicious choice of strength and location of point sources and sinks. Estimates by Hunt & Eames [294] suggest that the influence of a separated wake on the far field parameter μ_b is not significant.

To illustrate the difficulty in modelling the flow, we consider a cylinder of radius a. The drag coefficient is related to the drag through

$$\rho a C_d U^2 = F_0. \tag{7.8}$$

The far field and very near field potential flows are

$$\mathbf{u} = U\hat{\mathbf{x}} + \frac{UaC_d\mathbf{x}}{2\pi|\mathbf{x}|^2}, \qquad \mathbf{u} = U\hat{\mathbf{x}} + \frac{(1+C_m)U}{2}a^2\nabla\left(\frac{\mathbf{x}}{|\mathbf{x}|^2}\right), \tag{7.9}$$

respectively. Three natural lengthscales arise in describing the flow:

$$aC_d, \qquad \left(\frac{x\nu}{U}\right)^{\frac{1}{2}}, \qquad \sqrt{\frac{(1+C_m)}{2}}a. \tag{7.10}$$

The first is determined by the drag on the body, the second by viscosity and distance while the last one is determined by the shape of the body. For an isolated body, the first two lengthscales characterise the far field flow which makes the problem more difficult than the multibody counterpart, where only one lengthscale is required.

7.2.2 Effect of straining on an isolated wake

The effect of an external straining flow on a laminar wake caused by other bodies is illustrated with linearised calculations (see Fig. 7.2b). Consider a point source of momentum in a planar linear straining flow,

$$\mathbf{u}_E = (U + \beta x, -\beta y, 0), \tag{7.11}$$

where β is the strain rate. Accelerating/decelerating flows correspond to $\beta > 0, < 0$ respectively. The linearised vorticity equation is

$$\frac{\partial \omega}{\partial \tau} - \beta y \frac{\partial \omega}{\partial y} = \nu \nabla^2 \omega - \frac{F_0}{\rho} \frac{\partial\, \delta(\mathbf{0})}{\partial y}, \tag{7.12}$$

because there is no vortex stretching in planar flows. Here $\tau(x)$, the travel time from the origin to position x, is

$$\frac{U\tau}{\beta} = \log\left(1 + \frac{\beta x}{U}\right). \tag{7.13}$$

Physically, the action of an accelerating flow leads to an inflow of vorticity to the centreline, counteracting the diffusive cross-stream flux. This limits the spreading of the wake, which ultimately tends to a constant width. The diffusion of positive and negative components of vorticity into one another leads to a rapid cancellation of vorticity with the strength of the wake diminished. In a decelerating flow with an initially wide wake, the outflow from the centreline (for $\beta < 0$) dominates over the diffusive flux so that while the wake strength increasing with distance, the strength of the vorticity remaining unchanged.

Equation (7.12) admits similarity solutions of the form $\omega(\tau, y) = \Omega(\tau)\tilde{\omega}(\tilde{y})$ where $\tilde{y} = y/Y(\tau)$ (see Hunt & Eames [294]) and the characteristic vorticity and lengthscales

$$\frac{\Omega}{\Omega_0} = \left(\frac{Y_0}{Y}\right)^2 \exp(-2\beta\tau), \qquad Y^2 = \frac{\nu}{\beta} + \left(Y_0^2 - \frac{\nu}{\beta}\right)\exp(-2\beta\tau), \tag{7.14}$$

where the velocity deficit is still gaussian. For accelerating flows ($\beta > 0$), the wake width tends to a constant with the vorticity strength rapidly diminishing to zero. But for decelerating flows ($\beta < 0$), the wake width increases and the vorticity strength remains constant. A measure of the wake strength is the volume flux,

$$Q(x) = \frac{Q_0}{(1 + \beta x/U)^2}. \tag{7.15}$$

In the absence of strain ($\beta = 0$), $Q = Q_0$ is conserved. But straining flows may either reduce or increase the volume flux (for $\beta > 0, < 0$ respectively). For $\beta > 0$, the reduction of the volume flux generates a flow equivalent to a line distribution of sources of strength $m = -\mathrm{d}Q/\mathrm{d}x (< 0)$ contributing a dipole component to the flow, in addition to that described by (7.7). The flow induced by the wake is

$$\mathbf{u} = \int_0^\infty m(x')\mathbf{S}(\mathbf{x}, x')\mathrm{d}x' = -Q_0\mathbf{S}(\mathbf{x}, 0) + \left[\int_0^\infty Q(x')\mathrm{d}x'\right]\frac{\partial \mathbf{S}(\mathbf{x}, 0)}{\partial x}, \tag{7.16}$$

where $\mathbf{S}(\mathbf{x}, x') = (x - x', y)/2\pi((x - x')^2 + y^2)$ is the flow generated by a unit source at $(x', 0)$. The first and second terms on the right-hand side of (7.16) respectively corresponds to sink and dipolar contributions to the flow. For $\beta > 0$, the flow is irrotational in the far field and is characterised by a dipole moment,

$$2\pi\mu_s = \int_0^\infty Q(x')\mathrm{d}x' = \frac{Q_0 U}{\beta}. \tag{7.17}$$

The total dipole strength induced by a rigid body in a straining flow is approximately the sum of (7.7) and (7.17). The relationship between drag and volume flux is now no longer valid for when the wake vorticity is partially or completely annihilated, and is now determined by the local strain rate through

$$F = 2\pi\rho(\mu_s + \mu_b)\frac{\mathrm{d}u_{Ex}}{\mathrm{d}x} = F_0 + \rho(1 + C_m)V_b\frac{\mathrm{d}u_{Ex}}{\mathrm{d}x}, \tag{7.18}$$

(using (7.7), (7.17)) ie., the combination of viscous drag and inviscid straining force, in agreement with the detailed numerical calculations of Magnaudet, Rivero, and Fabre [388].

It is equally important to consider the effect of large scale diverging flow (ie. where $\mathrm{d}u_{Ex}/\mathrm{d}x < 0$) on the flow around the obstacles and on their wakes. Consider the straining in the adjustment zone where the approach flow enters a 'canopy' of tall thin obstacles. This can be idealised as a straining flow $\mathbf{u}_E = (U - \beta x, 0, \beta z)$. Then the vorticity ω_z shed from the body is stretched by the diverging streamlines. Unlike the disappearing wake case, here the wake is stronger and persists further. Thus over a distance l between the obstacles, the effective momentum deficit increases by a factor βl even though the drag is not affected. To satisfy continuity this extra volume flux deficit in the wake leads to additional entrainment into the wake from the approach flow outside the wake. This increased wake deficit, which persists further downwind, is a noticeable feature of groups of bodies when they are aligned parallel to the wind (and the downwind bodies deflect the flow upwards) ([596]).

7.2.3 Intermingling wakes

The dominant influence of neighbouring bodies is through their wakes intermingling. By bringing together and mixing wake vorticity (consisting of positive and negative components), vorticity is rapidly annihilated and the wake disappears. We illustrate this process by considering a random assemblage of planar bodies embedded in a uniform flow. White & Nepf [643] have also considered this problem, which is described in Chapter 6, but the implications for the far field flow and implications were not discussed. The fraction of the domain occupied by the bodies is α. We attempt to calculate the conditionally averaged velocity field $\langle\mathbf{u}\rangle$ created by the test body (located at the origin) within a random array. For viscously dominated flows, the steady two-dimensional conditionally averaged linearised momentum equation is

$$\rho U\frac{\partial\langle\mathbf{u}\rangle}{\partial x} = -\nabla p + \mu\nabla^2\langle\mathbf{u}\rangle - \overline{\mathbf{F}} + F_0\hat{\mathbf{x}}\cdot\delta(\mathbf{0}), \tag{7.19}$$

(see Hinch [265], Batchelor [43], Koch & Brady [340]). The distributed drag concept requires the localised point force induced by bodies to be smeared over the whole fluid region, so that the distributed drag is

$$\overline{\mathbf{F}} = -\frac{\lambda\alpha a\mu\langle\mathbf{u}\rangle}{V_b},$$

where $F_0 = \lambda a\mu\mathbf{u}$ is the drag on the test body, of characteristic size a and $\lambda = O(1)$. The last term in (7.19) is the force due to the test body. Taking the curl of (7.19), we obtain

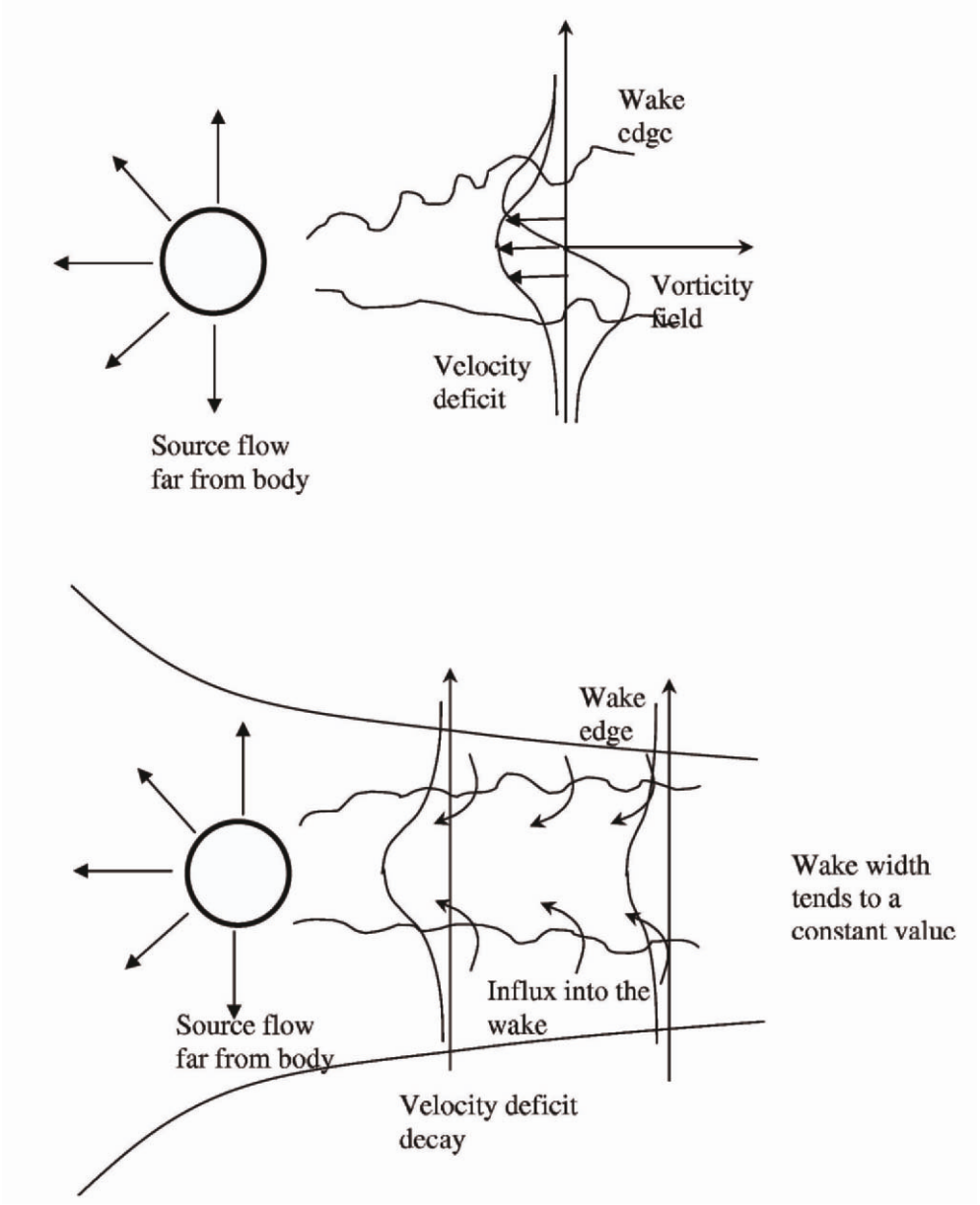

Figure 7.2: Schematic showing the flow generated by a rigid body in (a) a uniform flow and (b) a straining flow.

$$U\frac{\partial\langle\omega\rangle}{\partial x} = \nu\nabla^2\langle\omega\rangle - \frac{\lambda a\alpha\nu\langle\omega\rangle}{V_b} - \frac{F_0}{\rho}\frac{\partial\delta(\mathbf{0})}{\partial y}, \tag{7.20}$$

whose exact solution is

$$\langle\omega\rangle = \exp\left(-\frac{x}{L_d}\right)\omega_0(x,y), \tag{7.21}$$

where the lengthscale L_d satisfies

$$\frac{1}{L_d} = \frac{\lambda a\alpha\nu}{V_b U} + \frac{\nu}{UL_d^2}, \tag{7.22}$$

and

$$\omega_0(x,y) = \frac{F_0}{\rho U}\frac{\partial C}{\partial y}, \qquad C(x,y) = K_0\left(\frac{(\rho U - \frac{\lambda a\alpha\mu}{V_b L_d})r}{2\mu}\right)\exp\left(\frac{(\rho U - \frac{\lambda a\alpha\mu}{V_b L_d})x}{2\mu}\right), \tag{7.23}$$

is approximately the vorticity field generated by an isolated test body. Far downstream, the velocity deficit is approximately gaussian:

$$\langle u_x\rangle - U \sim -\frac{F_0}{\rho U}\left(\frac{U}{4\nu\pi x}\right)^{\frac{1}{2}}\exp\left(-\frac{Uy^2}{4\nu x}\right)\exp\left(-\frac{x}{L_d}\right). \tag{7.24}$$

Thus the wake generated by the test body decays exponentially with distance downstream due to wakes intermingling, and beyond a distance L_d, which we refer to as the wake length, the flow is irrotational (see also the discussion in Chapter 6, eqn 6.16 and the implications for mixing). For $\alpha \ll 1$, the wake length is

$$L_d \sim \frac{V_b U}{\lambda a\nu} = \frac{\rho V_b U^2}{\alpha F_0}. \tag{7.25}$$

Because the wake disappears, the volume flux decreases rapidly from its value Q_0 near the body. From (7.23),

$$Q(x) = \int_{-\infty}^{\infty}(U - \langle u_x\rangle)\mathrm{d}y \approx Q_0\exp\left(-\frac{x}{L_d}\right). \tag{7.26}$$

The disappearance of the wake vorticity leads to an irrotational dipolar flow (see the analysis of (7.2.2)) of strength

$$2\pi\mu_d = \int_0^{\infty} Q(x')\mathrm{d}x' = Q_0 L_d. \tag{7.27}$$

The right-hand side is equal to $V_b U/\alpha$. This result could be calculated from (7.19) by using a momentum integral argument to show $\int_V\langle u_x\rangle\mathrm{d}V \sim UV_b/\alpha$, and since the flow is dipolar.

The wake of the test body therefore disappears after it has interacted with

$$N \sim \frac{L_d}{L_s} = \frac{V_b^{\frac{1}{2}}U}{\alpha^{\frac{1}{2}}F_0} \tag{7.28}$$

bodies downstream (for two-dimensional flows), where the average separation of the bodies is approximately $L_s \sim V_b^{\frac{1}{2}}/\alpha^{\frac{1}{2}}$. The assumption of randomness is not necessary for vorticity annihilation to occur: for a structured array of bodies (eg. aligned or staggered), the same processes occur (see Hunt & Eames [294]), but over a much longer distance $\sim UL_s^2/\nu = UV_b/\nu\alpha$.

The same processes occur in three-dimensional flows. For a random array of fixed rigid spheres (see Koch and Brady, 1985 [340]), the axisymmetric velocity disturbance in the far wake of a test sphere tends to

$$\langle u_x \rangle = U - \frac{Re}{32} C_d \frac{Ud}{x} \exp\left(-\frac{Re(y^2+z^2)}{4xd}\right) \exp\left(-\frac{x}{L_d}\right), \tag{7.29}$$

where C_d is the drag coefficient and $\mathrm{Re} = Ud/(\nu + \nu_t)$ is the effective or turbulent Reynolds number of the wake. The decay distance of the wake is $L_d \sim 2d/3\alpha C_d$. We will use the above results to interpret the experimental results of Section 7.5.

The above calculations show how the local information about the flow from one body, within an array of bodies, is quickly lost downstream. The lengthscale estimated L_d will be much shorter for turbulent flows, where the initial width of the turbulent wake is wider and mixing more vigorous. When the size of the group of bodies is smaller than L_d, the process of vorticity annihilation supports the distributed drag models where local information is lost. But when L_d is comparable to the size of a localised group of bodies, it may be necessary to take into account the flow generated by individual bodies. Referring back to the discussion in Section 7.2 the far field flow is now only characterised the lengthscale L_d.

7.3 Inviscid blocking effects in multibody flows

The kinematic constraint imposed by a rigid body ensures that the flow goes around each body and this flow (on the upstream portion of the body) is strongly determined by the body shape. This blocking effect is not a feature of distributed drag models – its importance is illustrated here using inviscid models (see Eames, Hunt & Belcher [163] for a more comprehensive description). We show in Section 7.4 how inviscid blocking may be included into future computational models.

Consider a group of bodies lying within a perimeter/surface S, denoted by a dashed curve (see Fig. 7.3), in a steady uniform flow, U. The total volume bounded by S and the volume of the bodies, are V and V_b respectively. The average voidage of the bodies within V is $\alpha = V_b/V$. The cross-sectional area (or width) of the streamline tube, which just passes around V, tends to A_∞ far upstream of the cloud.

7.3.1 Potential flow around a rigid body

As with the discussion of the wake generated by an isolated body, which may be understood by introducing point sources into the momentum equation, it is useful to recap how a similar method applies to potential flows. Potential flow problems are solved

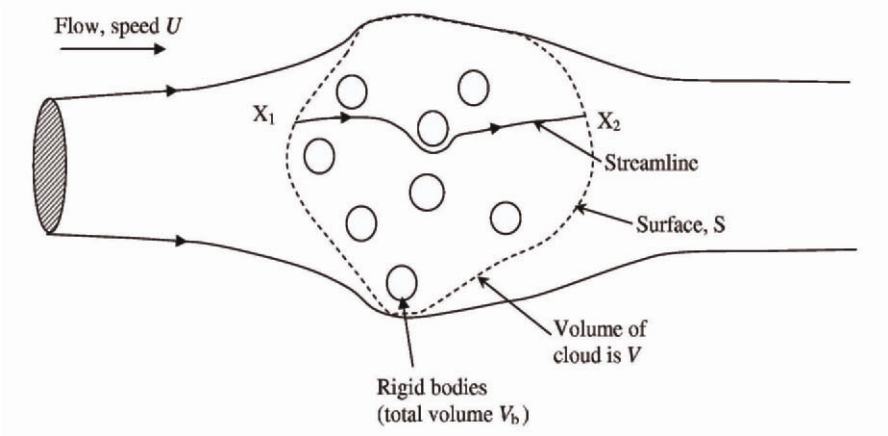

Figure 7.3: Schematic of the flow through/around a group of bodies fixed in a uniform flow.

from the mass-conservation equation

$$\nabla \cdot \mathbf{u} = 0, \tag{7.30}$$

where the flow is expressed in terms of a velocity potential, $\mathbf{u} = \nabla\phi$. The flow around a rigid body may be calculated by introducing point sources and sinks into the flow, judiciously chosen so that a streamline corresponds to the surface of the body. Far from a rigid body (located at the origin), the flow is to leading order dipolar (corresponding to a source and sink placed close together). This corresponds to adding dipole terms to the right-hand side of (7.30), with

$$\nabla \cdot \mathbf{u} = 2\pi\mu_d \hat{\mathbf{x}} \cdot \nabla\delta(\mathbf{0}), \tag{7.31}$$

(eg. Teshukov & Gavrilyuk [607]) where μ_b is given by (7.7). We will use this result in the remainder of our discussion.

7.3.2 The mean Eulerian velocity

The main approach for modelling multiphase flows has been through solving conservation equations described in terms of Eulerian phase-averaged mean quantities – the two-fluid approach [665]. The Eulerian mean velocity in a control volume V (such as the volume within the perimeter S of the cloud of particles) is defined as the velocity u_x (for each component) averaged over the volume occupied by the fluid (ie the fluid space between the bodies),

$$\overline{u}_E = \frac{1}{V - V_b} \int_{V-V_b} u_x \mathrm{d}V, \tag{7.32}$$

[152, 641]. The integral is taken over the fluid space between the bodies, $V - V_b$, and although the velocity decays slowly with distance from the individual bodies, the integral is well-defined because the volume over which the integral is taken is specified. Note that the integral may include regions of the flow with perfectly closed streamlines.

7.3.3 The interstitial Eulerian flow

The definition (7.32) masks the local and non-local contributions from bodies to the flow. A more systematic approach to characterising the Eulerian mean velocity is to decompose the flow into (i) a far field flow contribution – far from each body but still within the group of bodies – and (ii) a near field flow contribution – local to each body. This concept, originally described qualitatively by Kowe et al. [353], is strictly valid for dilute arrays since it formally requires the bodies to be widely separated, so that there is a separation of lengthscales between the near and far field, scaling approximately as $O(a)$ and $O(L_s)$ respectively. The decomposition is defined formally here for potential flows. The far field flow, $\mathbf{u}_E^{(f)}$, is defined mathematically as the sum of the dipolar and source contributions from the bodies, by assuming the bodies shrink to zero, so that (from (7.31))

$$\nabla \cdot \mathbf{u}_E^{(f)} = \sum_i 2\pi\mu_i \cdot \nabla\delta(\mathbf{x}_i) + Q_S, \tag{7.33}$$

where $\delta(\mathbf{x}_i)$ is the delta function and μ_k is the dipole moment associated with a body located at $\mathbf{x}_i$, and Q_S is the source due, either to the introduction of bodies, the injection of bubbles into the flow, or to satisfy kinematic boundary conditions due to the presence of walls.

The velocity field induced by the dipole and source distribution is

$$\mathbf{u}_E^{(f)}(\mathbf{x}) = U\hat{\mathbf{x}} + \int_V \nabla G(\mathbf{x}, \mathbf{x}')(\nabla \cdot \mathbf{u}_E^{(f)}(\mathbf{x}'))\mathrm{d}\mathbf{x}', \tag{7.34}$$

where $G(\mathbf{x}, \mathbf{x}')$ is the Green's function for Laplace's equation and $G = (\log|\mathbf{x} - \mathbf{x}'|)/2\pi$, $-1/4\pi|\mathbf{x} - \mathbf{x}'|$ for two- and three-dimensional flows. When the bodies are widely separated, the bodies within the group of bodies are subject to an interstitial flow, $\overline{\mathbf{u}}_E^{(I)}$, which is defined to be the average of $\mathbf{u}_E^{(f)}$ over the whole flow in V, so that

$$\overline{\mathbf{u}}_E^{(I)} = \frac{1}{V}\int_V \mathbf{u}_E^{(f)}\mathrm{d}V. \tag{7.35}$$

Thus the interstitial velocity, as described by Kowe et al. [353], is effectively the average velocity field experienced by a test body introduced into the flow, which is not located close to any other bodies. Notice that $\overline{\mathbf{u}}_E^{(I)} \neq \overline{\mathbf{u}}_E$ because $\overline{\mathbf{u}}_E$ includes contributions from the near field flow from each body. The dipole moment associated with each body moving parallel to the stream is $(1 + C_m)(v - \overline{u}_E^{(I)})V_B/2\pi$, where V_B is the volume of a body and C_m its added-mass coefficient.

Boundaries and global mass conservation impose important constraints on the interstitial velocity. To relate these concepts to experimental measurements described later we focus on bounded channel flows generated by a stream of speed U through a cloud of bubbles injected into a channel and moving vertically with a speed v. When the average separation between the bodies is small relative to the separation of the channel walls, the dipole field and average flow is equivalent to a distributed dipole moment, and averaging (7.34) over the whole volume yields,

$$\overline{u}_E^{(I)} + C_m\alpha(v - \overline{u}_E^{(I)}) = U. \tag{7.36}$$

In Section 7.5, this relationship is applied to interpret experimental results.

7.3.4 Mean potential flows through groups of fixed bodies

Far upstream of the bodies, the flow is a uniform stream of speed U. Due to the linearity of Laplace's equation, the flow generated by N bodies, labelled as 1, ..., k, ..., N, of volume V_{Bk}, can be decomposed as the sum of the contributions from a uniform flow and from the individual bodies,

$$\phi = Ux + \sum_{k=1}^{N} \phi_k, \tag{7.37}$$

where ϕ_k is the velocity potential associated with the k-th body. ϕ_k includes interactions between bodies, so that mathematically ϕ_k is composed of an infinite number of (image) dipoles within the k-th body to satisfy the boundary conditions on the surface of each body and rest of the array, or equivalently, an infinite distribution of multipoles (Saffman, 1992 [555]). The bodies are fixed in a uniform flow so that the kinematic condition imposed on the surface of each body is

$$\nabla\phi \cdot \hat{\mathbf{n}} = 0, \tag{7.38}$$

where $\hat{\mathbf{n}}$ is directed out of the fluid domain. In general, the dipole moment associated with the k-th body, μ_k, is determined by the added-mass tensor, $\mathbf{C}_{mk}$, through

$$\mu_k = -(\mathbf{I} + \mathbf{C}_{mk})V_{Bk}U\hat{\mathbf{x}}/2\pi$$

(Taylor [603]). Although we focus on bodies which are symmetric about the mean flow $U\hat{\mathbf{x}}$, so that $\mu_k = -(1 + C_{mk})V_{Bk}U/2\pi$, where $C_{mk} = \hat{\mathbf{x}}^T\mathbf{C}_{mk}\hat{\mathbf{x}}$ is the added-mass coefficient which characterises the shape of the body, these results may be easily extended to arbitrarily shaped bodies. The dipole moment is negative, indicating that the dipoles are pointing in the opposite direction to the mean flow. In the far field, the velocity potential associated with the k-th body, located at $\mathbf{x}_k$, is dominated by the dipole contribution:

$$\phi_k \to 2\pi\mu_k \frac{\partial G(\mathbf{x}, \mathbf{x}_k)}{\partial x}. \tag{7.39}$$

The interaction between each body is implicitly included through the added-mass coefficient (or dipole strength) which increases with α – this increase was explicitly calculated for groups of cylinders by Dalton & Helfinstine [140]. In an unbounded flow, the outside flow $\mathbf{u}_E^{(0)}$ is characterised by a total dipole strength which is equal to the sum of the individual contributions from all the bodies, so that for $|\mathbf{x}| \gg |\mathbf{x}_k|$,

$$\mathbf{u}_E^{(0)} \equiv \mathbf{u}_E^{(f)} \to \nabla\left[Ux + \left(\sum_{k=1}^{N} 2\pi\mu_k\right)\frac{\partial G(\mathbf{x}, \mathbf{0})}{\partial x}\right]. \tag{7.40}$$

The Eulerian mean velocity is computed by averaging over the whole fluid region between the bodies, as in (7.31). It can be expressed, using Gauss's Theorem, as

$$\overline{u}_E = \underbrace{\frac{U}{1 - V_b/V}}_{\text{blocking}} \left[1 - \underbrace{\sum_{k=1}^{N} \frac{(1 + C_{mk})V_{Bk}}{V}}_{\text{near-field}} + \underbrace{\sum_{k=1}^{N} \int_S \frac{\phi_k n_x}{UV} \, \mathrm{d}S}_{\text{far-field}} \right], \tag{7.41}$$

where $\hat{\mathbf{n}} = (n_x, n_y, n_z)$ is a unit vector normal to the body surface and directed out of the control volume and $V_b = \sum_{k=1}^{N} V_{Bk}$. The Eulerian mean is thus a linear operator and is formed by the sum of the contributions from each body. A distinction is made between the three terms in (7.41), which are interpreted as a blocking contribution which causes the flow to speed up and does not depend on the shape of the bodies. The second term is a near field contribution to the Eulerian mean arising from the impulse of the body and its volume. The third term is a far-field contribution to the Eulerian mean because the velocity potential decays sufficiently slowly that, even in the far field, boundary conditions on the whole flow domain are still important.

To illustrate the sensitivity of the mean flow within a groups of bodies and their impact on the ambient external flow, we consider the influence of the shape of bodies on the mean flow estimates. For simplicity, in the ensuing calculations, the bodies are assumed to be identical (with volume V_B and added-mass coefficient C_m) and the volume fraction, α, is small.

Example (a): Rectangular array of bodies. Consider a planar rectangular array of bodies randomly positioned in a region $|x| \le l$, $|y| \le w$, where the rectangular region V has length $2l$ and width $2w$, with end edges perpendicular to the undisturbed mean flow. For short wide arrays of bodies ($l/w \ll 1$), the mean Eulerian velocity is $U(1 - \alpha)^{-1}$ and is faster than U due to a blocking effect which accelerates the flow through the obstacles. As the aspect ratio of the rectangular array (l/w) increases, $\overline{u}_E \to U(1 - (1 + C_m)\alpha)/(1 - \alpha) \approx U(1 - \alpha C_m)$ and is slower than U because the residence time is increased by the stagnation regions. Thus there are two important contributions to the average velocity: a blocking effect which speeds up the flow and a local added-mass or drift effect which retards the flow near the stagnation points.

Example (b): Circular array of bodies. For a circular array of bodies, the Eulerian mean velocity is

$$\overline{u}_E = U\left(\frac{1 - \frac{1}{2}(1 + C_m)\alpha}{1 - \alpha}\right) \approx U\left(1 - \frac{1}{2}(C_m - 1)\alpha\right),$$

which is faster or slower than U depending on whether the bodies are bluff ($C_m > 1$) or streamline ($C_m < 1$).

Example (c): Bounded channel flow of bodies. The Eulerian mean velocity is

$$\overline{u}_E = U(1 - \alpha)^{-1}, \tag{7.42}$$

which is independent of body shape and only depends on the fraction of the flow occupied by bodies.

The above examples illustrate how the mean flow through the group of bodies depends both on the shape of the bodies and the group itself.

7.4 Modelling drag forces and inviscid blocking

It would seem natural to ask how both drag forces and inviscid blocking may be included in current incompressible computational models of multibody flows. To demonstrate this for the case of an isolated body, we first note that that the inertial terms in the momentum equation may be expressed as

$$[(\mathbf{u}\cdot\nabla)\mathbf{u}]_i = \frac{\partial}{\partial x_j}(u_i u_j) - [\mathbf{u}(\nabla\cdot\mathbf{u})]_i. \tag{7.43}$$

The momentum equation is now

$$\rho\left(\frac{\partial\mathbf{u}}{\partial t} + \nabla\left(\frac{1}{2}u^2\right) - \mathbf{u}\times\omega\right) = -\nabla p + \mu\nabla^2\mathbf{u} + F_0\hat{\mathbf{x}}\cdot\delta(\mathbf{0}) - \rho\mathbf{u}(\nabla\cdot\mathbf{u}). \tag{7.44}$$

The mass-conservation equation has a dipolar source contribution (from 7.30), so that in total we have

$$\rho\frac{\mathrm{D}\mathbf{u}}{\mathrm{D}t} = -\nabla p + \mu\nabla^2\mathbf{u} + F_0\hat{\mathbf{x}}\delta(\mathbf{0}) - \rho\mu_T\hat{\mathbf{x}}\frac{\partial\delta(\mathbf{0})}{\partial x}. \tag{7.45}$$

The term μ_T is

$$\mu_T = \mu_d u_x(0) \sim \frac{u_x(0)^2 V_b(1+C_m)}{2\pi}, \tag{7.46}$$

for planar flows. Thus inviscid blocking may be included into current computational models through force dipoles (last term in 7.45). We estimate the relative size of the source and dipole contributions in the momentum equation. The dipole contribution is equivalent to a source and sink, separated by a distance $s \sim a$ (so that $\partial\delta(\mathbf{0})/\partial x \sim 1/s$). The dipole term is then of approximate strength $\rho U^2(1+C_m)V_b/2\pi s \sim \rho U^2 a$ This term is comparable to the drag force $\rho C_d a U^2$, where $C_d \sim 1$. This suggests that the drag coefficient needs to be approximately doubled to account for blocking and this is consistent with the value of $C_d \sim 3$ applied by Belcher, Jerram & Hunt [51] to describe the deceleration and blocking effect by a group of bodies on a uniform flow.

These calculations illustrate how inviscid blocking may be included into the momentum equation through the use of force-dipoles. For continuum models, where bodies (or group of bodies) are replaced by a uniform drag force, inviscid blocking is modelled by including an asymmetric contribution to the drag force related to the geometry of the bodies. Physically, this corresponds to the distributed drag force being larger at the front of the group of bodies, than at the rear.

7.5 High Reynolds number bubbly flows

To highlight the importance of vorticity annihilation and inviscid blocking in multibody flows, using experimental observations. The multiphase flow example we present, of rising high-Reynolds number bubbly flows, has the same physical ingredients as flows past groups of fixed rigid bodies, but with the advantage of being able to reconstruct a conditionally averaged velocity by only looking at a fixed point past which bubbles

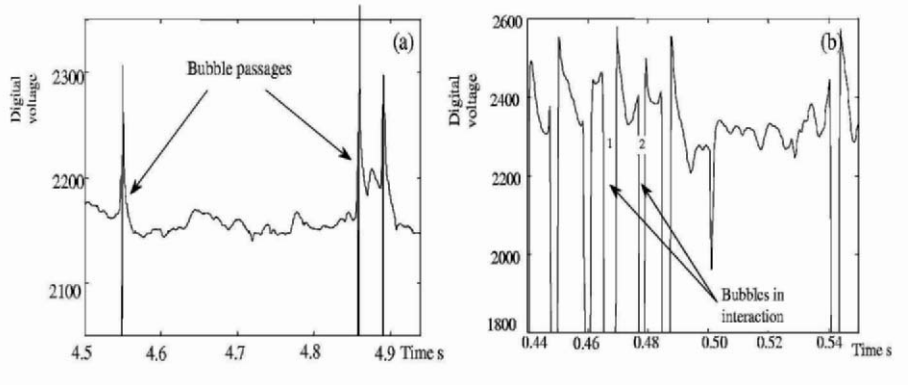

Figure 7.4: Typical times series of a hot-film anemometer for (a) low (α = 2%) and (b) high (α = 13%) void fractions.

are convected randomly. For low void fraction (< 0.2%) high Reynolds number bubbly flows, Risso & Ellingsen [535] studied experimentally the statistical properties of the flowand showed that the conditionally averaged flow induced by a bubble, may be separated into two zones. In the vicinity of the bubble, the flow is similar to that of an isolated bubble. But far downstream, the flow is controlled by the non-linear interactions between the wakes. At higher void fractions, (up to 20%), typical of many industrial problems, the influence of vorticity annihilation and blocking is much more pronounced, as we shall see.

7.5.1 Experimental method and diagnostics

The experimental apparatus consists of a vertical channel flow into which bubbles are injected. A vertical liquid flow was introduced to ensure that a hot-film system could be used to measure velocity at points. The vertical channel is of height 3.1 m and 0.3×0.15 m^2 cross-sectional area. A 576 capillary tube network was placed at the entrance of the channel to generate bubbles. The tubes are uniformly spaced on a grid and are distributed across the whole section of the channel.

Measurements of the vertical velocity, far from the injection site, were made at a fixed position using a hot-film system (e.g. [108]), from which the bubble diameter and rise speed could be calculated. The accuracy of the measurements have been extensively tested at low void fractions using LDV and optical methods. The time-series of the velocity measurements were converted into spatial information using a Taylor hypothesis that a mean flow advects disturbances past the probe. Examples of the velocity time-series is shown in Fig. 7.5. A more thorough description of the experimental technique and diagnostic tools applied to the data is given in [358].

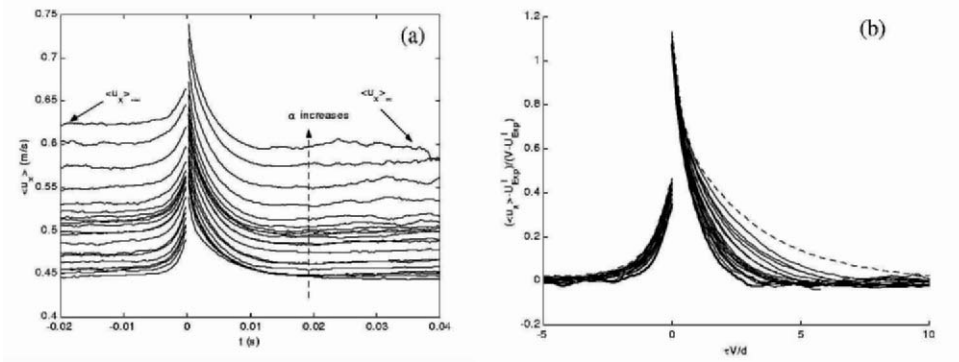

Figure 7.5: (a) Unfiltered conditional average vertical velocity for increasing void fraction. The up- and down-stream asymmetry in the profiles are clearly present. The symmetry in the velocity profile is restored in (b), where the filtered conditional average vertical velocity is plotted (with the interstitial component, $\overline{u}^{(I)}_{Exp}$ subtracted). In both (a) and (b), the velocity is plotted against time t from the up and downstream surface of the bubble. In (b), the time is normalised by v/d, where v is the vertical bubble velocity and d the bubble diameter.

7.5.2 Conditionally averaged velocity field

The vertical velocity component of the flow, conditional on a bubble being located at the origin, were constructed by collecting signal parts until the interface of the next bubble is encountered for the downstream average (or until the interface of the previous bubble for the upstream average). We call this the unfiltered conditional average, which is shown in Fig. 7.5(a). There is a noticeable asymmetry between the upstream and downstream portions of the velocity field. Upstream of the bubble, the flow is to leading order determined by the inviscid blocking by the bubble and decays rapidly. But downwind of the bubble, the flow is dominated by the wake flow and decays more slowly. Both the wobbling of the bubbles as they rise (see [536]) and the presence of small amounts of surfactant (in the water), ensure that the initial wake width is initially comparable to the bubble diameter. The centreline wake velocity appears to decay exponentially with distance. This is in part due to the averaging process but also due to vorticity annihilation due to intermingling wakes (see 7.24). By truncating signal sections after a fixed distance up and downstream of each bubble, we are able to construct a filtered conditionally averaged velocity field could be constructed. The filtering restores the up and downstream symmetry of the measured velocity, and is insensitive to the cut-off distance.

The relaxation lengthscales, non-dimensionalised using the bubble diameter d, for up and downstream distances from the bubble surface are denoted by L^*_u and L^*_d respectively and are plotted in the Fig. 7.7. These distances are estimated by exponential fitting of the up and downstream sections of the filtered conditional average. The upstream distance L^*_u is weakly dependent on void fraction, and larger than the inviscid estimate of $0.2d$. The downstream distance L^*_d extends further than the upstream distance, and is smaller than the wake disappearance length, estimated from equation (7.29), $L_d = 2d/3\alpha C_d$.

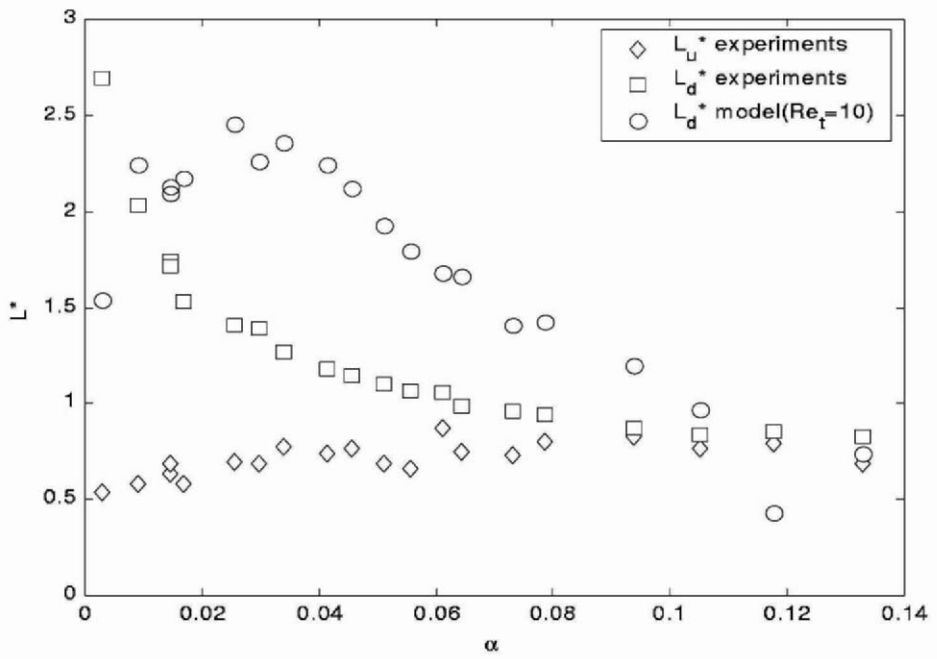

Figure 7.6: Relaxation lengthscales of the unfiltered conditional average velocity field normalised by the bubble diameter d as a function of void fraction. (The difference from estimates based on the filtered conditionally averaged velocity field, are negligible). L_u^* and L_d^* correspond to decay distance for up and downstream velocity. The theoretical prediction, from (7.29), of the relaxation lengthscale is $L_d/d = 2d/\alpha C_d$, for $Re_t = 10$.

7.5.3 Interstitial velocity measurement

The filtered conditionally averaged measurements picks up the flow between the bubbles. Far from the test bubble, the filtered conditionally averaged velocity tends to a constant value which corresponds closely to the interstitial flow concept introduced in 7.3.3, i.e.

$$\overline{u}^{(I)}_{Exp} = \lim_{x/d \gg 1} \langle u_x \rangle. \tag{7.47}$$

The inviscid model (7.35) suggests that the interstitial Eulerian velocity is related to the bubble rise velocity (v) and bulk fluid velocity U through,

$$\frac{\overline{u}^{(I)}_{Exp} - U}{\overline{u}^{(I)}_{Exp} - v} = \alpha C_m, \tag{7.48}$$

where α is the bubble void fraction, and C_m is the added-mass coefficient associated with the ellipsoidal bubbles. The concept of an interstitial velocity requires a separation of scales between the size of the bubbles and their average separation. For widely separated bubbles, the local flux transported by the bubbles $C_m(v - \overline{u}^{(I)}_E)$ is dominated by inviscid blocking, even if vorticity is shed from the bubbles. But at high void fractions,

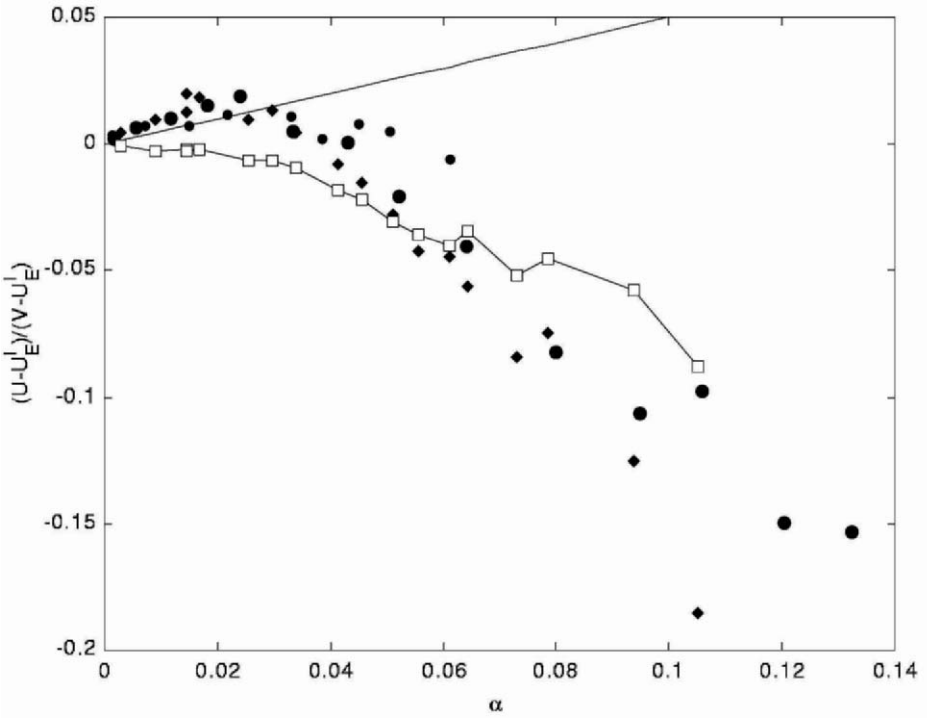

Figure 7.7: Normalised interstitial velocity versus voidage. The closed symbols are experimental measurements. The inviscid prediction (7.48), is plotted as a full line, while the wake corrected model (7.49) is plotted as open symbols.

the distinction between near and far field is blurred, and an additional contribution will arise from the wake which tends to increase the experimental measurements of the interstitial velocity and decrease the right-hand side of (7.48).

The contribution to the interstitial velocity is estimated from the flux transported by the wakes, i.e.

$$\overline{u}^{(I)}_{Exp} - U = \alpha C_m(\overline{u}^{(I)}_{Exp} - v) - \frac{\alpha}{V_B}\int_0^{L_m} Q(x)\mathrm{d}x, \tag{7.49}$$

where L_d is the 'wake length' of the test bubble, $Q(x) = Q_0 \exp(-x/L_d)$ is the volume flux in the wake and L_m is the measurement volume. The volume flux Q_0 is estimated using Betz' formula (7.5) to be $Q_0 \approx g/(v - \overline{u}^{(I)}_{Exp})$ while L_d is determined experimentally (see Fig. 7.6). For low void fractions, $L_m \ll L_d$ and (7.48). is recovered. For higher void fractions, the measuring region is comparable to the wake length and the second term on the right-hand side of (7.49) is comparable to the inviscid contribution. Figure 7.7 shows a comparison between the experimental results and the predictions (7.48) and (7.49).

For $\alpha < 0.2\%$, the comparison with the inviscid blocking solutions appears quite satisfactory. For $0.2 < \alpha < 10\%$, the influence of the wake is appreciable, but the

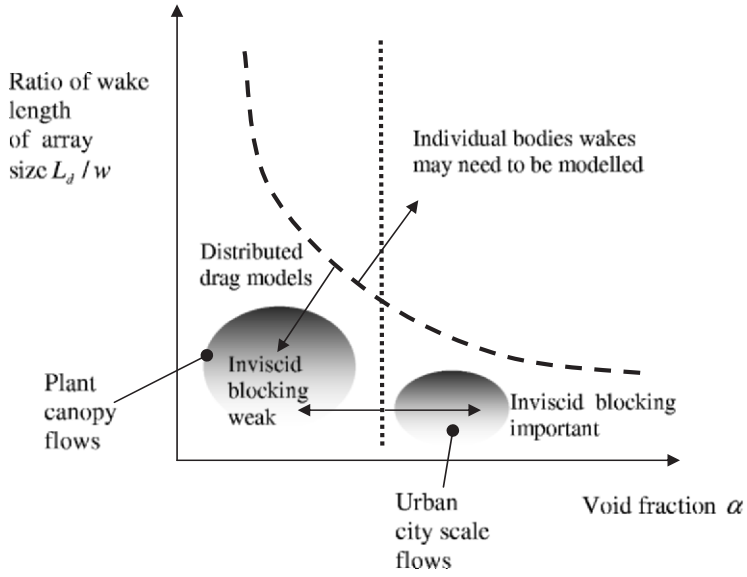

Figure 7.8: Schematic summarising when vorticity annihilation and blocking are important, in terms of the two parameters L_d/w (ratio of wake length L_d to a representative size of the group of bodies, w) and voidage, α. The dashed curve is approximately $L_w/w \sim a/\alpha w$. We have indicated approximately where plant canopy and urban city-scale flows lie.

wake model appears to also provide practical estimates of the interstitial velocity measurement. Both the vorticity annihilation and inviscid blocking solutions are broadly confirmed by these experiments. A more detailed description is given by Larue de Tournemine and Roig [358].

7.6 Concluding remarks

In this chapter, we have discussed two dominant processes in multibody flows relevant to flow through groups of buildings and vegetation: vorticity annihilation and inviscid blocking. These processes are characterised by the dimensionless quantities: the ratio of the 'wake lengths' (over which the wakes 'disappear') to size of group of bodies L_d/w, and the voidage, and are summarised in Fig. (7.8).

Vorticity annihilation occurs largely through wakes interminging with their neighbours over a distance L_d. Our analysis has shown that in order for a distributed drag model to be strictly valid, where there is no local information about the characteristics of a body is lost, the size of the group of bodies must be smaller than L_d. This appears true for plant canopy problems, but possible not for the urban terrain. Nepf [464] has suggested that the 'wake length' L_d, is a better measure of the distributed drag force, rather than separately estimating a representative body lengthscale and C_d. The measurement of this lengthscale certainly requires the development of new diagnostic tools to estimate conditional velocity profiles behind bodies, some of which have been

developed for multiphase flows by Roig and described in Section 7.5. An alternative strategy may be to use integral invariants (such as the volume flux deficit) to estimate a bulk drag coefficient (or L_d).

The influences of the shape of rigid bodies and of the group itself on the ambient flow and on the average flow through the group has been estimated using an inviscid analysis. These results broadly illustrate how the flow may be faster through a wide (in the cross-stream direction) or slowed down as it passes through a long thin group. The influence of inviscid blocking in decelerating the mean flow near to the front of a group of bodies or individual bodies can be as significant as the drag force.

The theoretical analysis has shown how singularity methods, where sources and sinks of force and mass, are useful for developing a physical understanding some of the salient features of multibody flows. This analysis indicates how drag and inviscid blocking mechanisms might be included into practical computational models. A future challenge remains how to include these effects into a rational continuum model. The experimental study described here has provided some support for the theoretical work presented, but they have also indicated the need to develop new diagnostic methods to interpret experimental results in these complex flows.

Chapter 8

Fires in porous media: natural and urban canopies

R.N. Meroney[1]
Colorado State University,
Fort Collins, CO, USA

8.1 Introduction

Uncontrolled fires and their associated smoke have been part of mankind's hazard environment since prehistoric times. Fires caused by lightening or volcanic activity moved across the earliest vegetative landscape whether grassland or forest scourging away all life before its path. Later, as man collected into groups and tribes, villages, towns and cities were routinely wiped away as natural, accidental, war or arson sources provided ignition. Most cities were not burned to the ground once, but multiple times. Even today massive wild fires in forests occur every year all over the world, and the threat of mass fires in cities haunt the minds of those concerned by large petrochemical accidents, wars or terrorism.

Large fires (or mass fires) occur at infrequent intervals, but are capable of causing immense loss of life and property. Mass fires occur where heavy fuel loadings exist over extensive areas; hence, they are observed in both wildland and urban areas. Given the distribution of trees, vegetation and buildings within these regions, the flow regime is essentially over and within a porous canopy. "Natural" urban or forest fires occur at widely spaced intervals, and the costs are such that it is not appropriate to create them deliberately in order to study their physics. Most reports of such fires tend to be anecdotal in nature, and very little quantitative information is generated. Their infrequency has made it difficult to generate the public awareness and support for long term research. Nonetheless, concerns about the results from war such as Fire Storms and

[1]E-mail of the author: *Robert.Meroney@Colostate.Edu*

Ye.A. Gayev and J.C.R. Hunt (eds.), Flow and Transport Processes with Complex Obstructions, 271–310.

Nuclear Winter, terrorism, as well as the increased incidence of rural/urban wildfires as the public penetrates previously unsettled regions makes the situation urgent.

Given the cost and difficulty of studying mass fires, it is apparent that analytic, physical and numerical models of fire and flow behavior in such situations are necessary. Unfortunately, fire itself is an extremely complicated phenomena, and when combined with the almost infinite range of combinations of fuel type, fuel size, geometry of needles, leaves, vegetation and dwelling shape, atmospheric condition (wind, temperature, humidity), terrain variations and ignition source (lightning, cigarettes, explosives, etc.) the problem begins to look untenable. Nonetheless, a great deal has been learned by studying the individual components of fire scenarios, and conclusions have been reached that guide strategies to mitigate, contain and reduce the impact of massive fires. This chapter will examine the historic character of mass fires, the nature of fire spread, the character of fire whirls as a significant aggravating component of such fires, full-scale field and scaled physical model studies, and the use of numerical models to investigate fire and fluid physics systematically.

8.2 Forest and wildland fire statistics

Throughout the world it is more and more common to see homes and other types of structures in wildland environments. This trend is creating an expansion of wildland/urban interface areas where structures are located next to large amounts of vegetation. Because of their location, these structures are extremely vulnerable to fire should a wildland fire occur in the surrounding area. For example, the wildland fires in southern California, U.S.A., burned 2,985 km^2, killed 22 people, and destroyed some 4,810 structures. The most costly fire in California history occurred in October 1991 in the Oakland Hills fire storm in which there were US $ 2.3 bn in insured property losses. Applying a simple least-squares logarithmic curve fitting to the inflation-adjusted California wildfire loss data (annual aggregates) yields an estimated return period of five years for US $ 100 m, ten years for US $ 650 m, and 25 years for an aggregate loss of US $ 2bn., (Munich Re, 2004 [437]).

Recent publication of world fire statistics reveals that costs of fires currently runs around 1% of GDP in most advanced countries. Deaths and losses in the United States tend to be the most extreme with annual losses of $ 10bn/year [224]. The annual review performed by Munich Re of world disaster losses reveals that world-wide forest fire losses alone exceeded $ 5.5bn and insured losses exceeded $ 2.5bn during 2003. Such losses exceed the sum of all losses from volcanic eruptions, hailstones, flash floods, Tsunamis, landslides, avalanches, water drainage, frost, and local and winter storms combined! (Of course the Baran earthquake, the European heat wave, floods, and severe and tropical storms individually exceeded forest fire losses, Munich Re [437].

The most catastrophic US fire disaster was the Peshtigo, WI, wildfire in October 1871 in which 1,500 lives were lost and 3,780,000 acres (15,300 sq km) burned. The death toll was four times higher than the famous Great Chicago Fire which ignited the same day [490]. The second most significant US fire was probably the Big Blowup of August, 1910 in Idaho and Montana during which 78 fire fighters lost their lives and 3,000,000 acres (121,100 sq km) burned. This fire led to a century long policy in

the U.S. to put out all fires in all situations irregardless of the long-term consequences [514]. An average of 140,000 wildfires per year took place in the United States from 1916 to 1996. The number of acres burned each year fell from a peak of 52.3 million in 1930 to 3.6 million in 1958 (212,000 to 14,600 sq km). Since then, the number of acres burned each year by wildfires has remained fairly steady between 1.6 to 7.4 million (6,500 to 30,000 sq km). Historical wildland fire statistics compiled by the US National Interagency Fire Center indicates the number and acreage burned of wild fires has decreased since the1920s, and remained more or less constant since 1960, but total loses and suppression costs have nearly doubled. The long-term decline in the area burned reflects fire suppression policies after the Big Blowup of 1910 aimed at suppressing all wildfires quickly, but one unintended consequence has been that brush and litter have accumulated increasing the potential for higher intensity fires. Meanwhile population shifts have moved more people and greater building infrastructure into heavily vegetated areas where wildland meet urban development. Today there are fires outside of homes every 38 seconds in the United States [308, 325, 456, 457].

8.3 Historic large urban fires

Literature and history record many famous forest and urban fires [82, 634]. Urban fires also exist in myth and legend. Stories about the Fall (burning) of Troy about 1200 BC were told orally for several hundred years before Homer composed his brilliant epics, the *Iliad* and the *Odyssey*, about the Greek heroes who conquered Troy and the Trojan heroes who attempted to defend it.

The Roman historian Tacticus in his book *Anals* reported that during the night of July 18, 64 AD, fire broke out in the merchant area of the city of Rome. Fanned by summer winds, the flames quickly spread through the dry, wooden structures of the Imperial City. Soon the fire took on a life of its own consuming all in its path for six days and seven nights. When the conflagration finally ran its course it left seventy percent of the city in smoldering ruins [173, 249].

The Great London Fire of September 1666 was one of the world's worst urban conflagrations until the twentieth century. It lasted for five days and nights destroying five-sixths of the city, 13,000 homes were burned, 100,000 were left homeless, and most business and public buildings were destroyed. Incredibly, the death toll included only four to six people by fire, while falling walls, fright or exertion killed others, but many of the homeless froze, starved or died of disease [98].

Another great fire occurred in Moscow, Russia, in 1812 when Napoleon entered the city after the battle of Borodino. Shortly after Napoleon entered Moscow, the Russians set fires across the entire city. Fighting of the fire was complicated by both soldiers of Napoleon's Great Army and Russian criminals and looters [449].

In the United States one can identify at least thirteen major fires between 1835 and 1991 during which between 400 and 28,000 buildings were destroyed and up to 2,300 lives were lost. On Sunday, 8 October 1871 the Great Fire of Chicago and the Peshtigo forest fire (which started the same day) killed 3,600 and burnt over an area of 5,900 square miles (15,300 square kilometers). In Chicago burning planks were lifted by fire whirls and dropped as far as three-eights of a mile (~1km) ahead of the main fire.

Musham [452] attributes a large part of the destruction of the city to burning material carried by the fire whirlwinds.

The San Francisco earthquake of 1905 caused fires, which destroyed 28,000 buildings and killed 1,200. More recently, the Oakland Hills Tunnel Fire during 1991 shocked California with its economic impact (US $ 3 bn), and the Cerro Grande, New Mexico, fire near Los Alamos in 2000 displayed how a prescribed fire set to mitigate fire loads can quickly get out of control [129, 482, 552].

The 1923 Kanto earthquake in the Yokohama/Tokyo area produced mass fires that killed over 100,000, injured over 40,000 more and destroyed property up into the Hakone Mountains. One gigantic fire whirl killed 38,000 in fifteen minutes in the Hifukusho-Ato region of Tokyo [314].

Fires started by bombing during World War II caused incredible damage and hardship and damage in urban regions. During the fires storm caused by bombing in Dresden, Germany, in 1943, some 250,000 were believed to have died (which exceeds the death toll at Hiroshima, Japan, by a factor of three). Fires in Dresden, Hamburg, Hiroshima, and Tokyo would be classified as mass fires, whose size were sufficient to generate their own wind fields associated with massive thermal updrafts of air [65, 103, 331].

Post WW II concerns about the impact of mass fires led to studies in Europe and the United States of the physics and behavior of very large fires. A joint research effort called Project Flambeau by Australian, Canadian and United States foresters and civil defense agencies examined fire development over simulated urban regions in the late 1960s. They created simulated housing areas by creating 10 ft (2 m) high piles of pine and juniper wild-land fuels distributed in checkerboard patterns. Measurements were made of wind speeds, temperature, and fuel consumption rates. Fire whirls and fire tornadoes were observed to frequently occur [133, 422].

During the mid 1980s studies of large fires were renewed due to the concern that the insertion of large amounts of ash and debris into the stratosphere from large fire or nuclear explosion might bring about a "Nuclear Winter", 1985 [103]. Predictions were primarily based on atmospheric computational models, and some scientists argued these models were inadequate since they did not reflect the observed physics seen in large fire experiments such as Project Flambeau. The January 1994 fires in Sydney, N.S.W., Australia exemplify how wildfires can invade urban and suburban areas imbedded in forested hilly terrain. These fires demonstrated how fires in urban and forest canopies can produce unexpected explosive spread conditions [615].

An almost infinite set of case examples both old and recent could be provided; however, this selection should provide an introduction to the nature and extent of fires in the wild land-forest/urban interface. The causes of these fires range from accidental to arson, and artificial to natural (lightning). The extent of the fires can be assigned to unfavorable meteorological conditions, multiple arson and terrorist actions, inadequate city planning, failure to recognize or understand the physical mechanisms of fire moving through vegetative or urban canopies, or even fire-fighting inexperience or ineptitude. The challenge here is to focus on the fluid mechanics of fires in order to predict and plan for future conflagrations.

8.4 Fire classification

Fires are often classified by materials burnt or their size. Composition categories include Class A: Ordinary combustibles like wood, cloth, or paper; Class B: Flammable or combustible liquids, gases, or greases; Class C: Energized electrical equipment; and Class D: Combustible metals like magnesium, phosphorous or sodium. A large body of research exists which has studied how the composition of the fuel bed limits fire growth. These studies include the fire chemistry or pyrolysis, ignition sources, ignition susceptibility, and influence of radiation [518]. These concepts will not be discussed further in this paper. Large or mass fire sizes are classified as conflagrations, fire storms, or moving fire storms. The large mass fires initiated by nuclear war are feared to contribute to possibilities of "Nuclear Winter".

8.4.1 Mass fires

There is no precise definition of a "mass fire", but it is generally accepted to be a flaming region at least 100 m in diameter in which the flame heights are small compared to the diameter. Such fires can produce storm-like winds and a rotating cloud column. Very large-scale or mass fires are classified by their burning characteristics. A *conflagration* is a fire that develops moving fronts under the influence of wind or topography, and the hot, burning area is usually confined to a relatively narrow depth. A *fire storm* is defined as a fire in which many parts of the entire fire area are burning simultaneously. Conditions for firestorm genesis are generally accepted to include a fuel loading of $> 4g/cm^2$, a building density of $>$ 20 to 30 percent, a fire area of $> 3km^2$, initial fires in $>$ 20 percent of the buildings, and ambient winds of $< 10\ km/h$. Such a fire is essentially stationary, with little outward spread, and can be identified by a towering convection column extending up to several kilometers. A *moving firestorm* is a firestorm that spreads under the influence of wind or topography. This latter type is often observed in wild-land fires that produce firebrands, which can be carried by fire-whirls further downwind to ignite additional regions. Moving fire storms and associated fire-whirls were present in the Great Fires of London, Chicago, Peshtigo, and at Hifukusho-Ato [363].

8.4.2 Nuclear winter

Although large-fire research in a war and wildland context has been going on for many years, a popularized study of the supposed effects of large fires, directed toward support of the anti-nuclear weapons movement, was written and first published in Europe as *"The atmosphere after a nuclear war: Twilight at noon"*, by Crutzen and Birks [137]. The idea was subsequently reworked, a new computer model was developed, and the results were published in the U.S. by Turco et. al. [620]. In 1985 the U.S. National Academy Press published a summary report. The report did not consider the radioactive or biological implications of a Nuclear Winter, only the extent to which the atmosphere would be modified by a major exchange of nuclear weapons. They concluded a major nuclear exchange would insert significant amounts of smoke, fine dust and undesirable chemical species into the troposphere, but they were uncertain as to the

amount which would reach the stratosphere. They emphasized the high level of uncertainty in available models, and recommended further research. The report includes a chapter on large fires and an excellent summary of the observations of large fire plume heights and smoke characteristics [180].

8.5 Modeling methodologies

Predicting smoke and flame behavior can be based on full-scale field experience, analytic integral approximations that capture the gross flow behavior, fine-scale numerical modeling and/or physical modeling at reduced scale. These methods are typically called full-scale, zone, field (numerical), and physical modeling, respectively.

8.5.1 Full scale fire tests

Full-scale modeling tends to be prohibitively expense, and other than a few post-disaster studies of actual fires is not frequently utilized. During the 1960s and 70s a joint agency program called Project Flambeau studied large fires set among piles of forest slash. The slash was set into piles approximating the geometry of suburban housing areas. Measurements were made of fire temperatures, velocities, radiation, and fire load burning rates. Movie film and photographic sequences were collected for each test [134, 478]. Some qualitative evidence from the Flambeau series does exist. Fire whirls were observed in every test burn carried out during the Flambeau fire tests. Fire whirls tended to form on the lee side of these fires. This is the position of strong vortex activity due to fire-blocking effects on the ambient wind. Often two fire whirls of opposite rotation were observed. Fire whirls are more likely for fires where the convection column is leaning due to the presence of ambient wind [134, 135].

In Operation Euroka, based at Langley in Queensland, Australia, two square kilometers of scrub was flattened by two bulldozers towing a giant ball on a chain. The uprooted trees (approximately 6000 tonnes) were then pushed into rows in a 50-acre area to simulate the fuel loading and pattern of an urban environment. This area was then set alight. Scientists studied the patterns of winds induced by a large fire, assessed the rate of burning, analyzed the effects of large fires on electromagnetic communications and identified the degree of protection needed for human survival [645].

Another significant field test was the Canadian Mass Fire Experiment of 1989 [516]. The U.S. Defense Nuclear Agency worked with Forestry Canada and the Ontario Ministry of Natural Resources to instrument a large prescribed burn in forest debris near Hill Township, Ontario. The fire covered about 480 *ha* in area (4.8 *sq km*). Measurements included estimations of energy release rate, emission factors for smoke particulates and species, ground level winds and temperatures, and some aspects of cloud dynamics. The fire caused a capping cloud to form up to 6.5 *km*. Rain, snow, hail and lightning were reported along with ground level fire whirls and water spouts.

8.5.2 Zone modeling

This method predicts the vertical and horizontal motions of a well-mixed smoke layer continuously supplied from a fire plume. The method assumes there is a large volume available in which turbulence and relatively small lateral velocities distribute the heated gases into a homogeneous mixture. The analytic relations used are based on laboratory and field scale fires for a limited range of volume configurations. They are popular as a means to perform smoke management inside of building structures, and for calculating simple isolated plume behavior. Many factors can make a zone model prediction unrealistic. Special consideration must be given to situations where irregular boundaries, inhomogeneous materials, and secondary flows occur (like in urban street canyons) [337, 478].

8.5.3 Field modeling

Computational fluid dynamics (CFD) provides a design technique to examine the relative merits of various fire suppression strategies. Such programs can inherently consider irregular building and terrain geometry, heat transfer due to variable properties and radiation, time varying fire strength, fire chemistry, affect of fire suppression operation, and variations in weather phenomena. While CFD represents a significant improvement in the predictive capability of smoke control modeling, uncertainties in the predictions remain. The smoke layer boundaries suggested by CFD simulations, just like those of the zone models, are best estimates, and as such have no conservativeness or "safety factor" built in. It is prudent to examine solutions to ensure that they are robust, that is that the flow patterns predicted are insensitive to small changes in boundary conditions such as external wind environment, fire strength, and even fire location [336]. In Section 8.7.3 several idealized calculations of fire behavior are considered for both two and three-dimensional fires ignited in porous canopies immersed in a deep atmospheric shear layer.

8.5.4 Physical modeling

Another option to simulate smoke movement is physical modeling at reduced scale. The concept of similitude is basically simple. Two systems at different geometric scales will exhibit similitude if a one-to-one correspondence exists in space and time between fluid particle kinematics (locations, velocities, accelerations and rotations) caused by fluid particle dynamics (pressures, gravity, viscous forces, etc.), when properly scaled by characteristics scales of fluid properties, force, length and time. To achieve this similarity, however, is not trivial. The specification of dimensionless parameters which guarantee similarity has historically been the subject of much discussion and debate [415, 416, 582]. Williams [644, 646] identified twenty-nine dimensionless groups required to simulate large fires based on normalization of the governing equations of motion, energy and concentration. A subset of eleven dimensionless groups were considered important, and seven were designated as critical for even partial simulation:

- Geometrical similarity,
- Convection (Reynolds number),

• Radiation groups (2) (Ratio of L to radiation absorption length and blackbody radiation flux to enthalpy convection),

• Gas-phase heat release (Enthalpy of formation to ambient enthalpy),

• Fuel gasification energy (Total heat required to gasify a unit mass of fuel to ambient enthalpy), and

• Fuel loading or burning rate group (Time average mass burn rate to convective mass flux).

Of lesser importance were listed dimensionless ambient velocity, vorticity, and atmospheric lapse rates. These dimensional considerations lead to several possible strategies for simulating mass fires. They are the following.

Standard scaling: Keep some groups constant. Usually Froude number and mass burning rate are chosen which leads to distortions in radiation, convection, turbulence and fuel bed geometry. Basically one is just looking at a buoyant plume.

Pressure adjustment: Varying pressure might preserve scaling of all but radiation parameters. Unfortunately to scale a 1 *mile* fire to 50 $feet$ would requires use of 1000 *atm* pressure.

Pressure and body force adjustment: Varying pressure and G (centrifuge) simultaneously allows consideration of all core variables except blackbody radiation.

Adjustment of composition and temperature of ambient atmosphere: Varying pressure and temperature could permit scaling of all core variables except absorptive radiation.

Adjust pressure, temperature and body force: All core variables satisfied, but maximum LSR variation probably limited to about 10. The conclusion must be that satisfactory physical model scaling of all aspects of mass fires is not likely.

Froude modeling (Fr) using either air or saltwater is probably the most common kind of physical modeling for hot smoke transport. Smoke movement away from the vicinity of a flame can be reproduced, but chemical kinetics, flame dynamics, and heat transfer scaling is not preserved. Unfortunately, due to scaling constraints it is difficult to simultaneously simulate buoyant plume movement and wind induced pressure distributions about the external urban building envelope. Nonetheless, physical modeling has been successfully used to study flow through forest and urban canopies in the absence of fires, and with fires for flow and fire movement through ground litter, idealized ignition concepts, fire whirl dynamics and compartment fires. Quintierre [515] provides a variety of examples of how physical modeling has been used to model various aspects of fires including simple fire plumes, ceiling jets, burning (pyrolysis) rate, flame spread, and enclosure fires. Heskestad, 1975 and others included cases of sprinklered fires [202, 263, 335, 515].

8.6 Forest and urban climate meteorology

The dynamics of fire growth is strongly influenced by the kinematics of flow through porous vegetation and urban structures (the canopy). The local wind and turbulence environment at the source determines the initial spread of a fire. Wind profiles vary depending upon the density (porosity) of the surrounding objects, their distribution vertically or laterally, the presence of below canopy open regions, and the distance

from the canopy edge [410, 458]. Wind approaching across less obstructed surfaces initially penetrates the upstream edge of the porous region, but subsequently the flow is deflected upward and flows within the media diminish. This process is reversed as flows move out of a canopy into clear areas.

Thus, fires starting near the edge of a canopy see larger horizontal crosswinds and turbulence which produce plumes that lie close to the ground; whereas, fires that ignite within the center of a canopy tend to rise vertically until deflected by winds at the upper edge or roof of the porous region. Fire and smoke spread within the forest or urban canopy is subsequently strongly influenced by canopy composition, density and distribution. These parameters are the proper subject of further research by analytic, physical and numerical modeling.

Once a hot smoke plume rises above the underlying canopy the buoyant force of a large fire leads to significant plume rise. The plume rise trajectory and the dispersion of its materials can be predicted. The effect of small-scale atmospheric turbulence, initial plume cross-sectional aspect ratio is minimal on plume trajectory, but the magnitude of atmospheric turbulence, atmospheric stratification, and ground terrain on rate of dispersion can be significant [363, 634].

8.6.1 Agricultural/forest canopy behavior

Previous chapters in this monograph have considered the physics of easily penetrable roughness (EPR) flow within vegetative canopies in some detail. Hence, only those aspects that relate to further understanding of the development and spread of fire and smoke within plant canopies will be repeated here emphasizing those features related to the author's personal experience using wind tunnel modeling. Arrangements of pegs, flexible strips, artificial trees and vegetation over hills studied are shown schematically in Figure 8.1.

Flow within and downwind of an individual tree

Even a single tree can significantly reduce wind speeds and increase turbulence downwind of its stem and crown. Gross [240] used a three-dimensional nonhydrostatic numerical model to investigate the air flow and turbulence around a single tree. For turbulence closure he used the Prandtl-Kolmogorov exchange coefficient and the Blackadar mixing length relation. The presence of the tree was simulated by an additional drag coefficient associated with tree foliage density or leaf area density. Cone and ball shaped crown tree regions, with and without elevating trunks, neutral and stable air stratification, and a tree porosity of 0.934 was assumed based on field measurements. Calculations produce the anticipated wake deficits, turbulence excess, and a drag coefficient of $\sim$1.0 which are similar to individual tree values measured by Meroney [410, 411]. All simulations show a reduction of wind speed inside the tree foliage, an accelerated flow over and around the tree and a wake region in the lee. The geometry of the crown seems to be the dominant factor. In a stable stratified atmosphere, the flow around the canopy is enhanced, while vertical motion is suppressed, and the strength and length of the reverse flow region behind the tree increases.

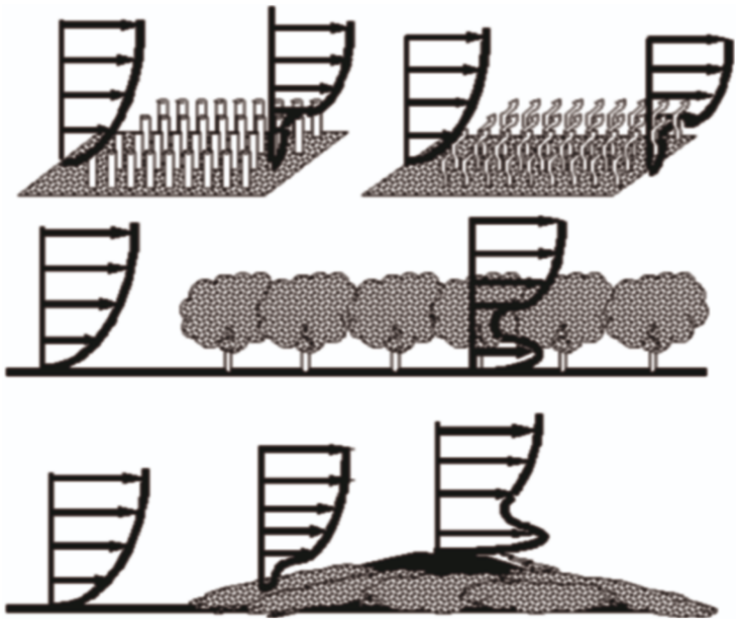

Figure 8.1: Schematics of peg canopy, flexible strip canopy, plastic tree canopy, and indoor-outdoor carpets on sinusoidal hill shapes (Meroney, [418]).

The superposition of individual tree wakes results in the under-forest and above-forest velocity features found in extensive areas of forests or woods. The initial growth of wake deficits and the subsequent decay at greater downwind distances are characteristics of both individual tree and forest measurements. Yano [663] developed a concept of momentum defect superposition in the wakes of an array of roughness elements to reproduce velocity, turbulence and shear distributions within and above canopies.

Under-canopy forest flow field

The presence of tree trunks, branches, stems and leaves (or needles) in a forest produces a barrier to air flow caused by form drag and skin friction which reduces the under-forest flow velocities substantially compared with wind speeds which occur above the canopy. Surface layer streamlines are displaced vertically, flow beneath the canopy is driven by shear from the flow above the canopy, and maximum winds occur at the top of the average height of the vegetation. Mean wind speeds typically decrease within the canopy as one approaches the ground to about 20% of the tree-top wind values. Turbulence levels beneath the canopy may be similar to those found at ground level over small roughness surfaces (5-15%), but are significantly less than those which can occur in the strong shear which occurs above the canopy roof (20-40%). Meroney [418] summarizes field measurements, and fluid model and numerical estimates of flows through vegetative canopies.

Different profiles have been proposed using first order closure models which specify a simple eddy diffusivity, K, and a drag coefficient, C_d, to describe that portion of the mean wind profile which exists beneath the forest ceiling for constant foliage distribution:

$$\frac{U}{U_h} = \sqrt{\frac{\sinh(\beta\xi)}{\sinh\beta}} \tag{8.1}$$

(Cowan, [136, 185]),

$$\frac{U}{U_h} = \exp\left(-\beta(1-\xi)\right) \tag{8.2}$$

(Inoue, 1963 [306]; Cionco, 1965 [124]), and

$$\frac{U}{U_h} = \sqrt{\frac{\cosh\beta\xi}{\cosh\beta}} \tag{8.3}$$

(Massman,1987 [397]),
where $\xi = z/h$, U_h is the mean horizontal wind speed at the top of the canopy, h; and β is a maximum value of the foliage area density and the extinction coefficient given by:

$$\beta = \left[2C_d \cdot LAI \cdot \sigma\mu)\right]^{1/2} \tag{8.4}$$

which is a combination of the drag coefficient, C_d, the leaf-area-index, LAI, a measure of foliage distribution, σ, and a normalized eddy diffusivity, $\mu = K_h/hU_h$. Only the expression proposed by Massman [397] is consistent with the frequently observed zero wind gradient within the lower region of the canopy. Other authors have produced velocity profiles for non-constant foliage distributions and using higher order turbulence closure. Once a velocity distribution model is specified it is possible to solve by iteration for shear stand drag coefficient, $C_f = 2(U_*/U_h)^2$, displacement height, d and surface roughness, or roughness length z_0, parameters useful to characterize above canopy flow dynamics as functions of $C_d \cdot LAI$ and foliage structure. Massman [397] concluded that $C_d \cdot LAI$ values from 0.25 to 0.5 characterize most full foliage canopies. Over this range almost any under-canopy model gives results very close to the following expressions:

$$\begin{aligned} 0.10 < z_0/h < 0.13, \\ 0.67 < d/h < 0.75, \text{ and} \\ 0.17 < C_f < 0.20. \end{aligned} \tag{8.5}$$

Above-canopy forest flow field

The atmospheric boundary layer (ABL) is that portion of the atmosphere where surface drag due to the motion of the air relative to the ground modifies synoptic-scale motions caused by horizontal pressure gradients, Coriolis forces, and buoyancy. The depth of the ABL is highly variable (50 to 2000 m), but it generally increases with proximity to the equator, with wind speed, and as the earth surface roughness, but it decreases

at night, and is strongly modified by thermal winds, inversions, and stratification. The lowest 10% of the atmospheric boundary layer is called the surface layer. It is characterized by the sharpest variations of wind speed, temperature, humidity, and turbulence characteristics with height. Counihan [132] concluded the surface (or constant flux) layer would be about 100 m deep during adiabatic conditions. In diabetic (stratified) situations the surface layer depth is about equal to the absolute value of the Monin-Obuknov length, $L_{mo} = T{u_*}^3/(6gw't')$. For a summary of surface layer behavior for both neutral and stratified flows combined with both smooth and rough surfaces see [414, 417].

Within the surface layer the mean wind-speed profile is commonly described by logarithmic expressions. For situations when stratification has only a minor influence a modified logarithmic law has been proposed:

$$u(z) = \frac{u_*}{\kappa} \ln \frac{z - d + z_0}{z_0} \tag{8.6}$$

where $u_* = (\tau/\rho)^{1/2}$ is the surface friction velocity, d is the zero-plane displacement, κ is von Karman's shear layer constant, and z_0 is the surface roughness. The displacement thickness, d, is important for tall roughness elements such as agricultural crops, forest and cities. When the roughness elements are short, such that $z_0 < 0.2\ m$, one can set $d = 0$. The parameters can be determined from representative field measurements; however, fitting an expression which permits three free parameters to field measurements of wind speed in/above agricultural canopies is not trivial. It is not uncommon for some least-square fitting routines to produce negative displacement heights – which is, of course, inappropriate.

No exact definition of high roughness has been offered, but roughness of a height exceeding 10% of the surface layer is generally viewed as high roughness, see also Section 1.5. Generally, the von Karaman universal constant κ is assumed equal to 0.4 based on extensive experimental study of fully developed turbulent flow through pipes and its relationship to the Kolmogorov dissipation constant. Some experimentalist treat the constant as another free parameter to improve curve fit to data; hence, values ranging from 0.15 to 0.5 have been recorded.

Jaeger [313] recorded wind speed measurements over a ten year period over stands of Scotch pine located in southern Germany as they grew from 3 to 8 m height. He made estimates of the variation in u_*, z_0, d, β (Deacon parameter), and Richardson number, Ri, from wind and temperature data collected from meteorological towers placed within the forest stand. He found that the following correlations described the measurements:

$$d = 0.63h \quad \text{regression coefficient, } r = 0.73 - 0.93; \tag{8.7}$$

$$z_0 = 0.174h + 0.227 \text{ regression coefficient, } r = 0.44; \tag{8.8}$$

and

$$u_* = (0.027h + 0.062)U_{10} + b \text{ regression coefficient, } r = 0.84. \tag{8.9}$$

The expressions are functionally similar to those derived from under canopy flow. Artificial plastic trees were selected by Meroney [410] to reproduce the median behavior of measurements made about live trees (Colorado Blue Spruce, Juniper, Pine, and

Spruce). These model trees were randomly positioned on support boards with approximately one tree per 36 cm^2 (see Figure 8.2 and 8.3). The total canopy was 2 m wide and 11 m long when installed in the Meteorological Wind Tunnel at Colorado State University. Figures 8.4 and 8.5 display typical mean velocity and turbulence profiles found within and above the model plastic tree forest canopies. Notice the initial intrusion of the approach flow into the trunk space within the canopy at the upwind edge which diminishes with distance until the flow reaches an equilibrium state. Then as the flow approaches the down wind edge of the forest, the streamlines dip down into the canopy again and accelerate the air closer to the ground [411].

Wind flow near clearings, clear-cut and forest edges

When airflow passes from a cleared area into a forest, winds initially penetrate into the canopy space, but then the streamlines are lifted upward to the canopy roof. The penetration distance among the trunks space in the canopy under story may persist for 5 to 10 tree heights. Subsequently the wind rises above a recirculation region and re-enters the forest about $20h$ from the windward forest edge. Figure 8.6 from [410] displays the effect of such initial wind penetration at the windward forest edge and the subsequent flow acceleration before the downstream forest edge on canopy drag. Thus, embers carried from fires at ground level near the upwind of a forest will have a strong tendency to rise into the upper canopy and initiate crown fires; whereas embers released by ground fires near the windward edge of a forest will be deflected downward. If a crown fire exists near the windward edge of a forest, the embers may be immediately deflected down into yet unburnt ground cover downwind of the forest.

Eimern, 1964 [166] considered the aerodynamics of shelter belts and summarized the influence of density, shape, surface roughness, thermal stratification, wind angle and tree arrangement on downstream wind speed, turbulence, soil moisture, etc. The micrometeorology of shelter belts and forest edges are reviewed by McNaughton, 1989 [404]. There are similarities as well as differences between flow downstream of thin shelter belts and forest edges. The foliage density of the forest canopy replaces the porosity used for narrow shelter belts. Upwind profiles must be characterized by the upwind forest roughness, displacement height, forest friction velocity, and foliage density. McNaughton sought a comparison to the flow over a forest canopy edge and the flow that occurs when a boundary layer passes over a solid backward facing step. For solid steps a recirculating eddy occurs of downwind extent of about $(6–7)h$. But permeability often allows the wind to penetrate the forest upwind of the forest edge. In coniferous forests researchers detect upwind penetration over several heights upwind, but in denser foliage other researchers see little penetration at all. Nonetheless, little evidence exists to support the presence of a recirculating eddy downwind of the forest edge. The flow velocities and surface shear appear to adjust to the immediate absence of the forest edge by $20h$; however, the wind continues to accelerate over a longer distance as a deeper layer of the atmosphere adjusts to the change of surface roughness.

Fowler et al. [198] examined the effects of shelter wood cutting (30-percent canopy removal) and clear cutting clearings from 0.8 to 8.5 ha on climatic variables of the High Ridge Evaluation Area within the Umatilla National Forest in northeastern Oregon.

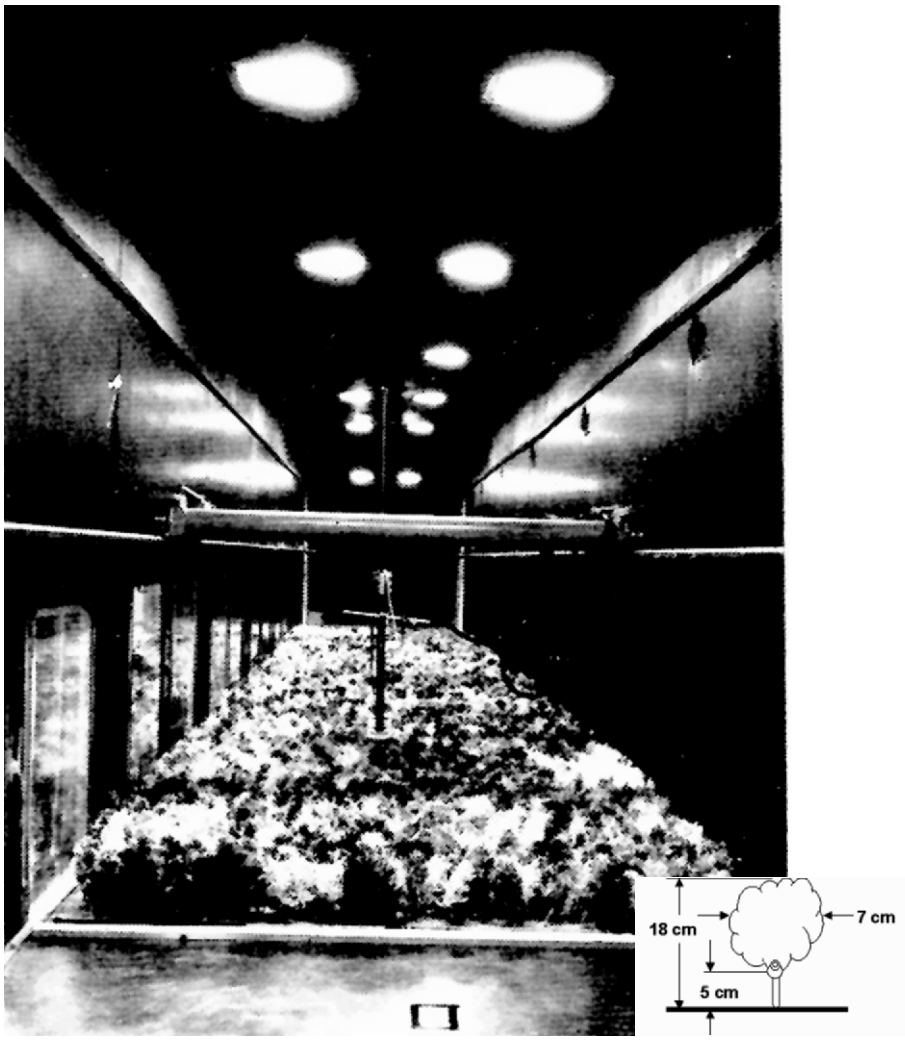

Figure 8.2: Plastic-tree canopy 2 *m* wide 11 *m* long installed in Meteorological Wind Tunnel, Colorado State University with parameters of a single "tree".

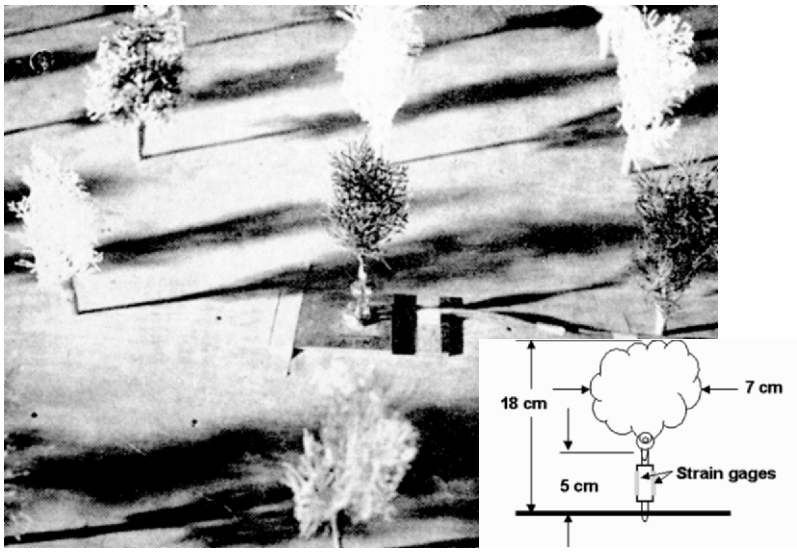

Figure 8.3: Strain gage balance installed in model trunk of individual test tree.

Areas were harvested in 1976 after nine years of pre-logging calibration. The wind speeds increased substantially in all classes of clearings.

Homogeneous surface roughness over hills/mountains

Complex hilly terrain may exist with a variety of vegetative surface cover. For example the approach terrain and a hill itself may be either bare or vegetation covered. Alternatively then, the upwind surface may be smooth (farmed plains or meadows)and the hills may be rough (tree covered, or the upwind surface may be rough (tree covered) and the hill bare. In some cases only portions of the hill may be bare due to selective shelter wood cutting or clear cutting. The presence or absence of high roughness may lead to lower/higher wind speeds, higher/lower turbulence, or attached/separated streamline flow. Such open regions are often deliberately provided in forested regions as "fire breaks". The distance fires can propagate across such open areas is of primary interest to fire engineers.

The linear-perturbation theory approach to predict effects of sudden roughness changes of airflow over 2-dimensional hills can be reduced to a few simple algebraic algorithms. These equations can be used to estimate the effect of forest clear cutting on winds above hills and ridges. Jensen [315] proposed that perturbations in mean wind velocities induced by surface roughness change could be calculated from:

$$Du(z)_{\text{roughness}} = \frac{u_{*1}}{\kappa} \ln \frac{z_{02}}{z_{01}} \cdot \frac{\ln z/z_{01}}{\ln l_{zr}/z_{01}} - 1 \tag{8.10}$$

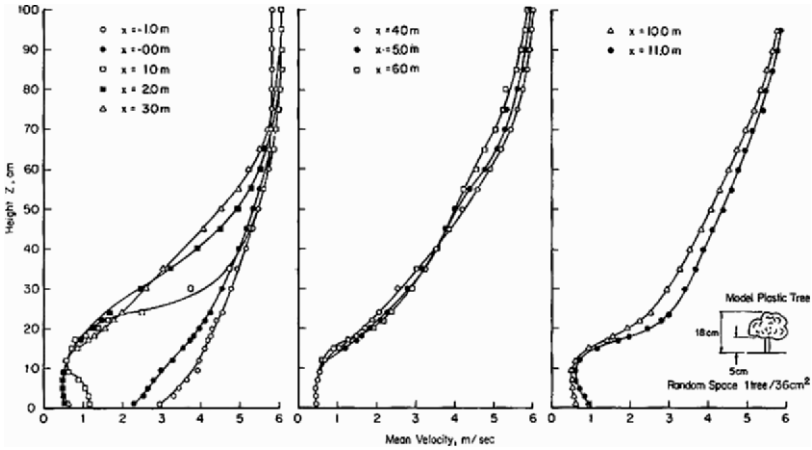

Figure 8.4: Mean velocity profiles measured above and within a model plastic-tree canopy (Meroney, [411]).

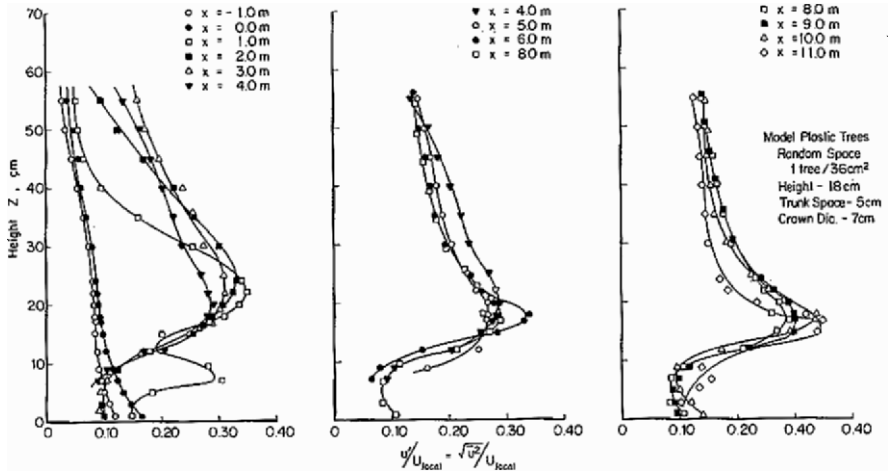

Figure 8.5: Turbulence intensity profiles measured above and within a model plastic-tree canopy (Meroney, [411]).

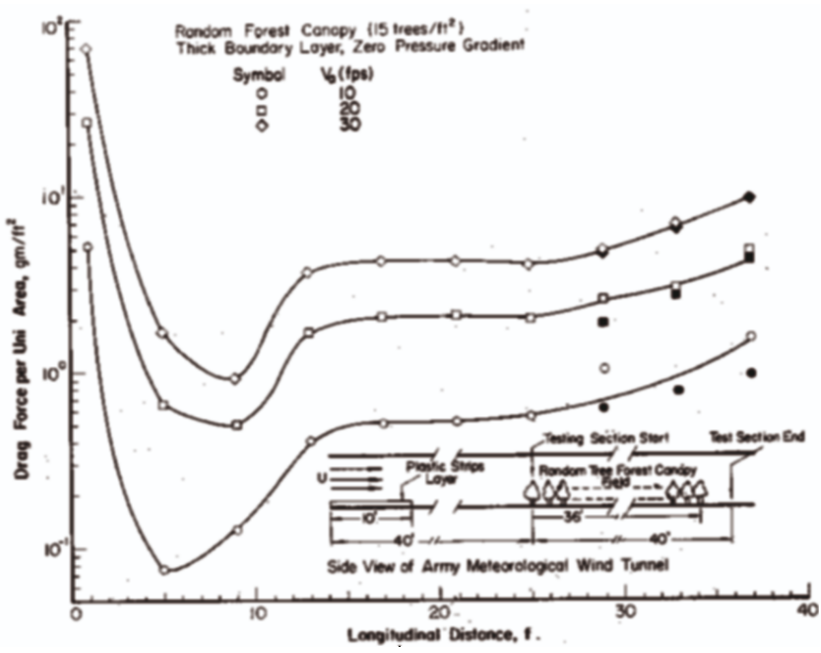

Figure 8.6: Shear plate drag for model forest canopy (Meroney, [410]).

where $l_{zr} \ln[l_{zr}/z_{01}] = 2\kappa^2 x$. Jensen and Petersen [316] recommended perturbations induced by surface elevation change for triangular shaped hills could be calculated from:

$$Du(z)_{\text{hill}} = (u_{*1}/\kappa)[1 + (h_{\text{hill}}/L)\Big(\ln[L/z_{01}]/\ln[l_{zh}/z_{01}]\Big)^2 \ln[z/z_{01}] \tag{8.11}$$

where $l_{zh} \cdot \ln[l_{zh}/z_{01}] = 2\kappa^2 L$. Since the solutions are separately linear their perturbations should be additive; thus,

$$u(z)_{\text{hill\&roughness}} = u_0(z) + Du(z)_{\text{roughness}} + Du(z)_{\text{hill}}. \tag{8.12}$$

These expressions are sufficient to calculate wind speeds over hills for different clearcut options over alternative slope triangular hills. Meroney, 1993 [418] presented figures based using the above relations for effects of various size forest clear-cuts on hill top flowfields. These measurements were subsequently compared with windtunnel measurements of wind fields over various two-dimensional hill shapes covered with model forest canopies simulated by different depths of plastic indoor-outdoor carpeting, Meroney, et al., 1993 [419].

Change in roughness effects

It has long been observed that when the wind flows from one surface texture to another a transition takes place in wind speed and turbulence within an inner boundary layer,

that grows in depth with downstream distance from the surface change. When the surface change is associated with roughness height, and downstream wind profiles are plotted semi-logarithmically with height, then a distinct "kink" in the slope of the plot is observed which can be associated with this inner-boundary-layer depth, l_z. The wind profile near the ground will adjust to surface roughness changes as it moves downwind from the ground cover transition. Above l_z the profiles will correspond to the wind profile for the roughness before the change in cover. Various field measurement programs over smooth-to-rough and rough-to-smooth roughness transitions provide justification for empirical plots of the sort proposed by Park and Schwind [481] together with several others.

More elegant analytic and numerical models exist to predict the resultant variation in wind profiles which exist at different fetch distances downstream of a transition of roughness. The subject is extensive enough that a literature review has been prepared on the topic by Hunt and Simpson, 1982 [283]. Unfortunately, little data exists for roughness variations as large as the abrupt change that occurs from a forest edge to a meadow or from rural to urban areas.

Wu and Meroney, 1995 [656] measured flowfield responses over modeled roughness changes of smooth, rough and very rough boundaries (equilibrium power law coefficients of $\alpha = 0.12$, 0.16 and 0.34, respectively) for smooth-to-rough and rough-to-smooth transitions in the Meteorological Wind Tunnel at Colorado State University. Separate internal boundary layer depths were defined based on mean velocity, turbulent intensity and shear stress profiles. Flow predictions from several first-order turbulence closure schemes were compared to the wind-tunnel data. Since the log velocity profile was not found to exist in the transition region at all, the assumption that local eddy diffusivity varies as $K = \kappa z$ is not acceptable. Similarly mixing assumptions associated with mixing length theory and $\tau/E = \text{const}$ are not valid. On the other hand, mixing assumptions that $K = c_o \kappa z E^{1/2}$ or $(u^2 - w^2)dU/dx = 0$ seem justified.

8.6.2 Urban canopy behavior

Again the reader is referred to earlier chapters in this monograph related to air movement within urban canopy layers. Only those details related to the growth and spread of mass fires within a suburban, urban or wildland/urban interface will be discussed below.

A good summary of urban behavior is contained in the recent book edited by Moussiopoulos, 2003 [448] titled *Air Quality in Cities*. This book summarizes some of the results of Project SATURN a European Union effort under EUROTRAC-2. Although the book emphasizes air pollution meteorology over cities, several chapters consider details of air flow over and within cities based on field, windtunnel and numerical models. Researchers considered air flow in geometrically simple cases (arrangements of $2d$-rectangles, blocks and cubes) as well as data from actual city streets geometries. Some 20 local, urban scale and meso scale models were evaluated and compared to field and laboratory measurements of wind speed and concentration.

The authors concluded that field conditions could be reproduced by both wind tunnel and numerical models, but the numerical models were very sensitive to alternative specifications of grid resolution, wall boundary conditions, source size and turbulence

model. Indeed, one author noted during one comparison "*this example shows how easily model results can be manipulated by merely varying the choice of parameters which are accessible to the user* ". In another case four experienced user groups predicted the dispersion of dense gas releases around simply shaped building by using the same commercially available CFD code. The concluded "*the variability between different modeller's results was shown to be substantial*".

Urban flow styles: classification

Plate [501] provides a review of flow over uniformly rough boundaries, with special applications to urban areas. For neutral stratification in the absence of elevated inversions the flow is found to be very similar in character to vegetative canopy flows. Many of the same characteristics of porosity, permeability, displacement height, and effective surface roughness are used to describe the boundary layer over the suburbs and city center. But a critical difference between uniform and homogeneous canopies and the typical city is that wind blowing from open country onto a city complex meets different types of building formations. These range from the open rural and usually uncluttered country at the edge of the city, to suburb regions with single family and one or two story houses, to light industry regions, to high rise buildings in the city center. At the same time there is often an increase in building density, closed street canyons and quite irregular building heights. Thus, the urban boundary layer grows as a superposition of inner boundary layer flows driven by roughness changes occurring in the windward direction.

A very comprehensive study of urban boundary layer characteristics was made by Theurer, 1992 [608] to summarize what is know about these parameters and to correlate them with building dimensions. Theurer used two parameters to describe the distribution of roughness elements:

$\lambda_{\text{ar}} = \sum$ of areas covered by buildings/total urban area, and
$\lambda_{\text{fa}} = \sum$ of average building areas normal to the wind/total urban area.

These two parameters combined with a pictorial description of the roughness pattern are sufficient to classify the roughness height, z_0, and the displacement height, d, for each configuration.

The lower part of the urban boundary layer has its own flow field driven by the shear from the boundary layer above the structures. It is extremely difficult to parameterize the flow beneath the building height, H, since it is strongly driven by local arrangement of the streets, the building density, trees and vegetation, parks, lakes, hills and even traffic. Nonetheless, it is in this "penetrable" region that fires ignite, flames spread, plumes grow and eventually large "mass" fires can develop. Once the fire's buoyant plume penetrates into the boundary layer above the city structures, then the "aerodynamic" boundary layer described earlier can deflect and transport the smoke, flames and embers downwind.

Oke [472, 473] differentiated the flows within urban street canyons based on the street width to building height ratio (B/H). The flow was classified as skimming flow ($0 < B/H < 1.2$), wake interference flow ($1.25 < B/H < 5.0$), or isolated roughness

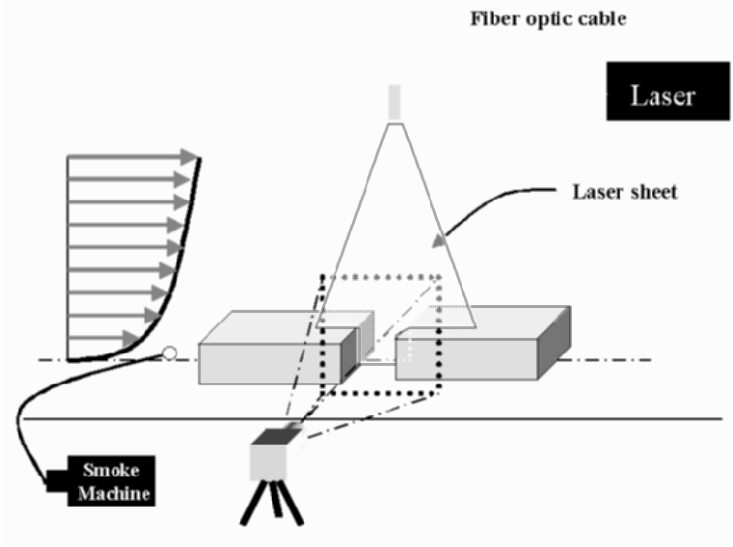

Figure 8.7: Schematic of visualization setup; 5-watt Argon Laser illuminates smoke for capture on digital video.

flow ($B/H > 5.0$). Wind tunnel simulations provide an opportunity to examine the linear and nonlinear effects of various parameters individually and/or in combination. The case of an isolated $2d$ street canyon in open country was examined by Meroney et al. [420]. Similarly, the case of arrays of 3-d street canyons made of rectangular blocks was examined by Chang and Meroney [111, 112]. The same street canyon geometries were subsequently studied in an urban environment, i.e., with additional canyons of similar geometry upstream and downstream of the test section. In each case various street canyon aspect ratios, (B/H),were tested under different wind conditions.

For the open country case visualization using smoke and a vertical light sheet revealed that clean air is sucked into the canyon by an intermittent eddy circulating down into the canyon. These smoke eddies change character with canyon aspect ratio as proposed by Oke (Figures 8.7 and 8.8). This eddy circulates upwind at street level. A roof top eddy which begins at the upwind upstream building roof corner sucks canyon gases onto the roof. In the open country case, the first building alters the flow locally quite dramatically, promoting separation from the floor. On the other hand, in the urban roughness case the surrounding buildings raise the displacement height to the urban canopy level, almost to the roof of the buildings. The shear zone thus formed at the ceiling of the canyon induces a permanent eddy recirculating inside the canyon. As a result, vertical mixing across this shear layer is suppressed and pollution is trapped inside for longer times, until upstream turbulence in the main flow may cause sufficient disturbance to break down the recirculating eddy. The flow inside the canyon in open country is much more nonstationary than in the urban canyon case. A recirculating eddy forms only intermittently in the former, whereas it is clearly much more stable amidst urban roughness.

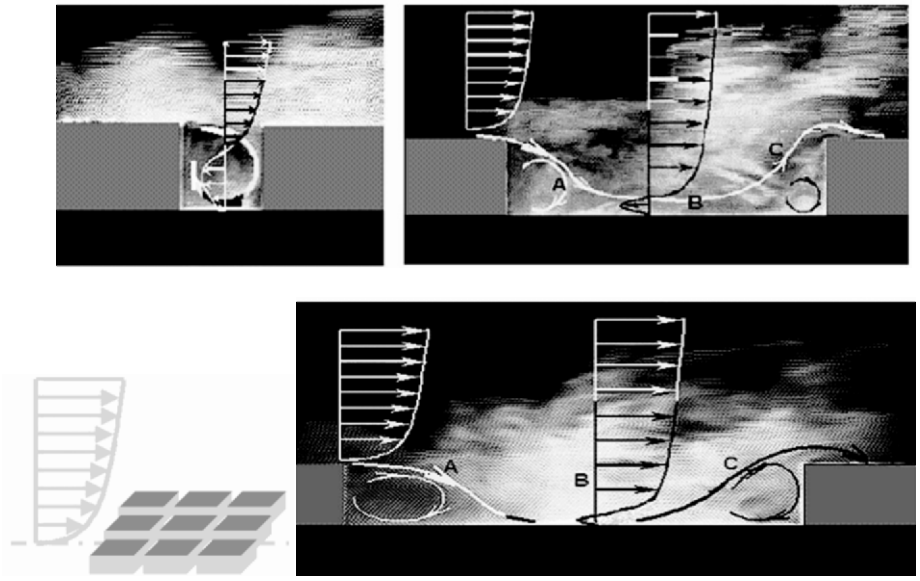

Figure 8.8: Skimming, Interference Flow and Isolated Roughness Flow visualizations using Laser light sheet (Chang and Meroney, 2003 [111, 112]).

Smoke and fire from sources ignited within a street canyon at ground level will tend to follow streamline trajectory patterns. Thus, smoke will be drawn against the upwind wall side of a canyon oriented normal to the wind to roof levels. Smoke and fire may even propagate upwind along the roof for situations where separation occurs on the upwind corner of a building. Similarly roof-top or upper level fires will tend to travel along recirculating street canyon eddies to impact the upwind faces of downwind buildings.

Typical smoke propagation scenarios seen during visualization are shown in Figures 8.9 to 8.12. Rural or open country building ($N = 1$) complexes tend to produce an extended separation zone from the upwind corner of the upwind building, resulting in upwind roof contamination and more energetic canyon breathing, Figure 8.9. Urban building complexes ($N > 1$) tend to produce less frequent canyon breathing, and stronger canyon vortex circulations. Building orientations with approach winds directed perpendicular to a building face or street canyon axis produce flows with augmented lateral growth but no shift in the plume axis (Figure 8.10). Building orientations with approach winds oblique to a building face or street canyon axis produce flows with augmented lateral growth and significant shift in the plume axis (Figure 8.11).

Canyon breathing plays an important role in street canyon dispersion. Vortices establish within the street canyons and are maintained by the shear flow over the street canyon top at roof level, but occasionally the turbulent flow above the building roofs penetrate downward into the canyon and lift or wash the vortex out of the canyon. Subsequently, a new vortex appears and is sustained until the canyon breathes again (Figure 8.12).

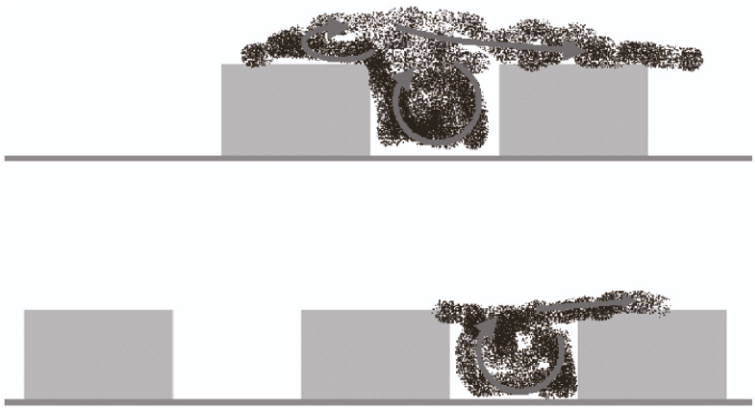

Figure 8.9: Canyon eddies for open country and urban skimming flow situations.

Numerical models show that for steady-state type calculations although general flow field behavior is reproduced, predicted concentrations are often too large. This is believed to be caused by the fact that the "average" flow and transport predicted by a steady-state calculation did not realistically reproduce the combined dispersion and diffusion effects of an intermittently fumigating street canyon.

Urban flow characteristics

A limitation of direct field measurements of atmospheric phenomena is that all possible governing parameters are simultaneously operative; thus, it is not simple to determine which are governing, which are secondary or which are insignificant. In addition if nonlinear interactions occur their role may not be clear. Thus, independent influences of building geometry (building height, width, roof shape), street dimensions (breadth, width, intersection location), thermal stratification (solar insolation and orientation, building and street thermal capacitance), vehicular movement (size, number, frequency), plume buoyancy, vegetation or landscaping, and surface roughness are all intertwined. Consequently, many of the qualitative and most of the quantitative conclusions about urban canopy flow result from systematic physical and numerical model studies.

Kastner-Klein and Rotach [327] investigated a detailed 1:200 scale model of a portion of the city of Nantes, France in a neutral boundary-layer wind tunnel at the University of Karlsruhe, Germany. They used laser-doppler anemometry to measure all components of velocity, turbulence intensity, and turbulent shear at different locations within the city. Subsequently, they compared their data with various parameterization schemes and concluded that in the roughness sub-layer (RSL),

$$u_{RSL}(z) = \frac{u_*}{0.6\kappa}\left\{(1 - 0.6\ln(0.12) - \exp\left(0.6 - 0.072\frac{z - d_0}{z_0}\right)\right\}, \tag{8.13}$$

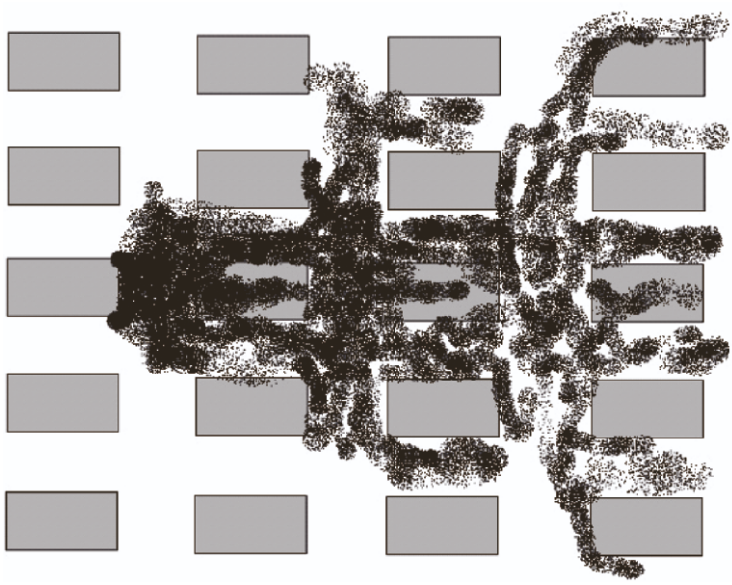

Figure 8.10: Lateral smoke growth for wind fields aligned to street canyon rows.

whereas above the canopy layer,

$$u(z) = \frac{u_*}{\kappa} \ln \frac{z - d_0}{z_0}, \tag{8.14}$$

where u_* is friction velocity, d_0 is displacement height, z_0 is roughness length, just as for forest canopies. Consequently, they propose parameters for these relations which depend on local building geometry:

$$do/H = 1 + 4.43^{-\lambda_p}(\lambda_p - 1), \text{and} \tag{8.15}$$

$$z_0/H = 0.12(z_s - d_0) = 0.072(z_s - d_0) \tag{8.16}$$

where H = average building height, where the plan areal fraction $\lambda_p = A_P/A_T$ is the ratio of average frontal plan area of roughness elements to total surface area, and where z_s = height of the maximum shear stress. Similarly, turbulent shear stress scales as:

$$\frac{u'w'}{(u'w')_s} = F\left(\frac{Z}{Z_s}\right). \tag{8.17}$$

Here $(u'w')_s \sim (u'w')_{max}$, $Z = (z - d_s)$ and $Z_s = (z_s - d_s)$, z_s is height of maximum shear stress, and d_s is height of region inside canyon with nearly zero shear stress equal λ_p. Hence, an empirical fit gives:

$$\frac{u'w'}{(u'w')_s} = \left(\frac{Z}{Z_s}\right)^2 \exp\left[2 \cdot \left(1 - \frac{Z}{Z_s}\right)\right]. \tag{8.18}$$

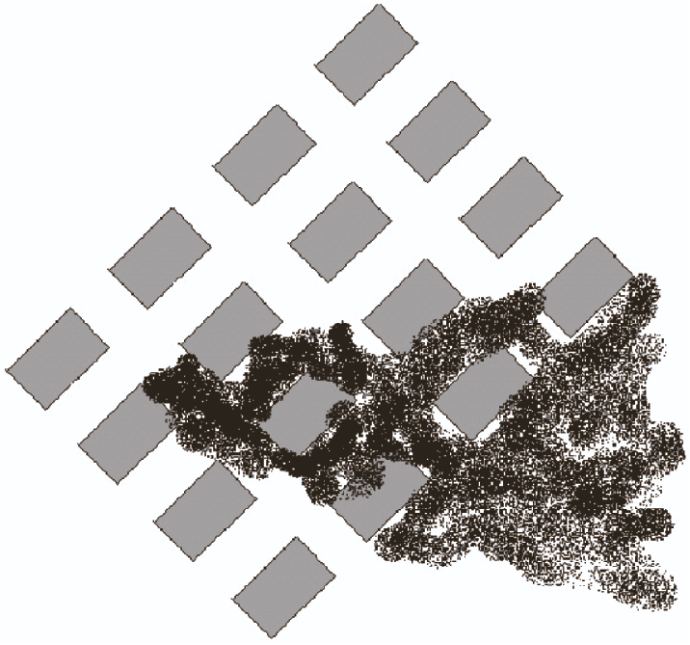

Figure 8.11: Smoke trajectories for wind allined oblique to street canyon rows.

From the review provided in Sections 8.6.1 and 8.6.2 it is apparent that the average flow characteristics over forest canopies and urban canopies are very similar. Almost identical expressions are found to correlate profiles of velocity, turbulence and shear stress. Nonetheless, structural differences inside canopy elements are expected to strongly affect the propagation of fire and smoke, since urban structures have large regions of impenetrable wall; whereas, the resistance of trees and vegetation is spread more uniformly through the canopy volume as many small elements of leaves, twigs, needles and boughs.

Joint wildland/urban configurations

Tree windbreaks have long been known to modify the wind field downwind, and they have frequently been used to mitigate extreme winds and modify the flow around groups of buildings. Sometimes the trees are arranged to modify snow drift patterns, in other cases they are intended to reduce wind forces or reduce heating or air-conditioning loads. Recently, Rehm et al., 2002 [532] proposed a grid-free way to model individual trees for study of flow over a wooded building complex. Their proposal is to represent the trunk and branches of each tree by a collection of spherical particles strung together like beads on a string. The drag from the tree, determined as the sum of the drags of the component particles, produces an oscillatory, spreading wake of slower fluid.

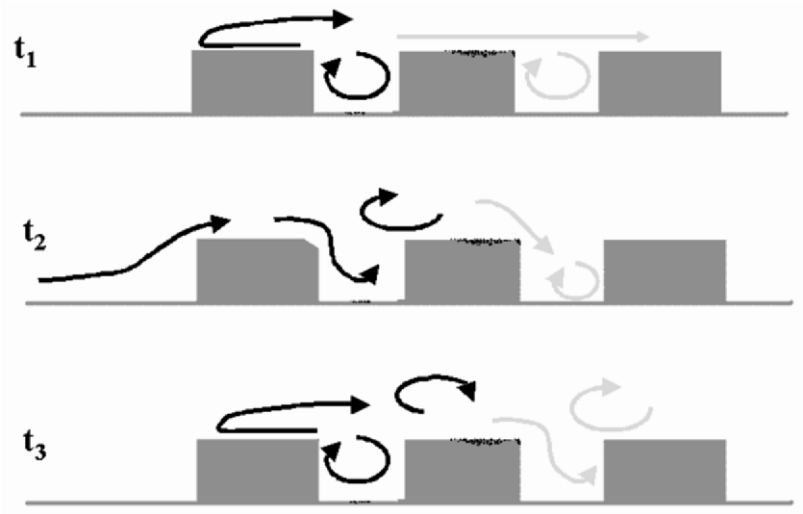

Figure 8.12: Visualization evidence for intermittent nature of street canyon vortex rolls, ie. street canyon "breathing" in the case $t_1 < t_2 < t_3$.

The authors tested their concept through a CFD simulation of the flow around an eleven story target building made up of a cluster of ten buildings, surrounding buildings and trees on the NIST (National Institute of Standards and Technology) campus near Gathersburg, Maryland. They used a large eddy simulation (LES) turbulent model over a grid made of ~600,000 cells using the FDS (Fire Dynamics Simulator) code which can be downloaded free from the URL: *http://fire.nist.gov*. Time dependent simulations produced realistic looking velocity fields and unsteady pressure spectra for probes placed on target buildings. One case examined a typical result for a row of 20 *m* high trees located upwind of the 49 *m* tall building. The wakes of the trees oscillate and spread laterally and produce fluctuations at low levels on the target building.

8.7 Fluid mechanics of fires and porous canopies

When a solid or liquid fuel burns, the molecular structure of the fuel is modified by the action of the heat resulting in the production of a combustible vapor. This process, called *pyrolysis*, precedes the actual burning of fuel like a wave moving ahead of the flame. Once pyrolysis has occurred *ignition* is possible. Ignition usually depends on the presence of an ignition source (spark, cigarette, lightning, existing fire) that has a sufficiently high temperature to initiate combustion in the fuel vapors. The process of the spread of fire through a fuel canopy is then a multi step process:

- Preheating and out gassing region (pyrolysis),
- Intermittent deflagration (ignition),
- Flame attachment region, and
- Steady burning region.

Spontaneous or self-ignition is also possible if external heating is sufficient to raise the vapor temperatures above critical levels (eg. in wood pyrolysis occurs between 65–340°C, piloted ignition between 200–350°C and selfignition can occur between 250–600°C depending on wood species, humidity, and exposure time [362, 363, 498]). Pyrolysis and ignition can occur even without a flame present if radiation is sufficiently large. By proper forest thinning and building structure separation radiation intensity levels can be reduced low enough to limit the propagation of fires.

One dominant source of ignition in wildland/urban fires is due to firebrand activity. This method is most effective when wind speed is great. Showers of large numbers of burning embers ignite spots in areas ahead of the primary burning region. These areas coalesce and add to the forward movement of the fire front. The wind also tilts the convective column generated by the fire and brings it closer to downwind unburnt fuels; thus, increasing radiation intensities and initiating pyrolysis ahead of the moving fire front.

Most forest fires begin at ground level among layers of dead leaves, needles and other litter. The propagation of the fire through this porous fire bed (or canopy) has been extensively studied in fire wind tunnels. Many studies use actual forest litter; whereas, others use idealized porous structures including arrays of match sticks, circular rods of rolled paper, incenses sticks, vertically supported index cards, wooden dowels, Popsicle sticks, strips of cardboard, strips of paper, beds of torn newsprint, wooden teepee arrangements, and even computer card punching (chad) [363, 508, 638].

Unfortunately, these ground fires can extend up into the crown regions of trees if dry dead branches extend beneath the living crown along the trunks down to the ground. The fires are said to "jump" into the crown region. Once crown fires exist forest fires tend to grow almost explosively with flames leaping from tree-to-tree top, embers become lofted to great heights ahead of the fire, and fire whirls develop among the strong crown fire updrafts.

Finally a column of buoyant combustion products, ash, embers, and smoke are produced which rise above the flames. This often spectacularly visible plume of exhaust products can itself be very hazardous since it contributes to pyrolysis, firebrands, suffocation, and loss of visibility. The behavior of this plume has been the subject of extensive analysis and research, but in most cases the plume is presumed to rise independent of any surrounding terrain, structures or porous surroundings. Little attention has been given to the motion of the plume in the immediate vicinity of a fire as it is modified by surrounding forest or building structures. Once the plume penetrates the surface layer above the canopy it is presumed to follow conventional plume/jet mixing, trajectory, and kinematic under the influence of buoyancy and cross flow winds [82, 180, 363, 498, 635].

8.7.1 Field scale experiments

This section provides some additional information about a few of the field scale experiments introduced in Section 8.5.1 under Modeling Methodologies: Full Scale Fire Tests.

Probably the most extensive and ambitious mass fire experiments were performed during the Flambeau project between 1964 to 1975. Approximately 25 separate large

scale field experiments were performed of sizes ranging from 2 to 20 *ha* on both flat and inclined slopes to examine the behavior of very large fires [133, 134, 478]. During Test Fire Number 5(1966) 240 piles of pinyon pine and juniper tree debris approximately 15 *m* square were arranged in 15 x 16 rows, 7.5 *m* apart, and 1.5–2 *m* tall. The region covered was approximately 350 *m* square ($\sim$ 12.5 *ha*). The test region was instrumented with heat protected anemometers, radiometers, aspirated thermocouples and fuel bed weighing platforms. Outside the fire perimeter were mounted pulsed-Doppler radars, smoke visibility measurement equipment, infra-red spectral scanners, and still and cine photographic equipment.

The lower 100 to 200 *m* of the Project Flambeau convection columns contracted because of the inflow of the air to the fire. This inflow was horizontal at ground level, but contained a considerable downward component. Winds typically occurred as single line spiraling columns or dual vortex fire whirls. Maximum measured winds were 56 m/s. This fire had a maximum energy release rate of 500 kW/m^2. Given the limited height of the fuel beds and the simultaneous ignition of the entire region few conclusions are possible with respect to fire spread through a porous canopy.

During 1970 Operation Euroka was performed in Queensland, Australia [645]. This fire was principally of brigelow, a heavy dense hardwood. The slash was arranged by bulldozers into fire beds that had very little fine material; hence the peak combustion rates were considerably later and lower than those of the U.S.A. fires. The fire had peak energy release rates of about 120 kW/m^2. During Operation Euroka maximum winds were 20 m/s, and after 30 minutes a fire whirl developed. Winds tended to spiral inward from around the fire which covered an area of about 2 *ha*.

8.7.2 Laboratory scale experiments

As noted earlier there have been extensive studies in fire wind tunnels of fire propagation through porous fire beds made of a variety of different depths of natural and artifical materials. Unfortunately, little of this work is directly applicable to the simulation within urban fires or forests including crown fires. One minor exception is the limited work of Lee and Otto, 1975 [364].

In urban areas, buildings of various shapes and heights are grouped together to form city blocks separated from each other by the open streets. Consequently, fire propagation is strongly affected by the unique relationship of the buildings. Lee and Otto [364] chose to simulate how fires develop about just two rectangular buildings simulated by identical wood piles of length L, width $L/2$ and height $L/3$ with the long sides parallel to each other. These fuel piles were separted by a distance $L/2$ with an overlap of equal magnitude. The wood cribs were set afire at the same time, and velocity, temperature, and heat flux measurements were made, while ordinary and infrared photography were used to monitor the flames. The fire developed in five stages related to heat flux levels as noted below:

- During Stage 1 both piles burned independently, ambient indrafts were controlled by each pile separately with no evidence of gross vortex activity.
- During Stage 2 the heat flux became strong enough to produce weak interaction between the induced airflow about the two fuel piles. Discretely separate

multiple fire whirls extended from each corner. Individual fire whirls strengthened and heat flux increased.

- During Stage 3 the individual whirls of eah pile coaesce almost instantaneously into one single flame leaning towards the open street with a single strong vortex column.

- During Stage 4 the vortex becomes so strong that flames are actuallydrawn out from the openings on the opposing sides of the piles facing the streets towards the vortex column. Heating no longer occurs primarily in the vertical, but lateral and horizontal heating causes fire to move along the model building. Secondary vortices appear.

- During Stage 5 the fuel is exhausted, the piles start to collapse, the main vortex column dissipates, and vortex shedding into a wake region predominates. The vortices shed so frequently and violently that this may indicate a primary period of fire spread to other structures.

The interaction of the fire between the two structures that resulted during fire whirl formation and subsequent sucking of flames out of openings (windows and doors) is similar to that assumed by the Himmoto and Tanaka [264] fire propagation model.

As noted earlier a number of wind tunnel studies have examined flow within arrays of building like blocks placed in arrays to simulate generic and actual urban districts. Cermak [109] concluded that the general nature of above city flow including distributed roughness and the effects of the heat island can be simulated when Richardson number similarity exists and for sufficiently large model Reynolds numbers. Plate, 1995 [501] and Theurer, 1992 [608] demonstrated that similarity of flow exists for a wide range of roughness arrangements including actual city geometries. Quintela and Viegas, 1995 [517] and Meroney, 1978 [412] concluded that even thermal effects to buildings can be simulated given equality of the parameter $\mathrm{Re}/\mathrm{Gr}^{1/2}$. Finally, dispersion of neutrally buoyant scalar plumes from point or line sources, which might represent the dispersion of cool smoke, was studied by Theurer, 1992 [608], Meroney et al., 1996 [420, 111], among many others.

No additional examples of intense heat sources or actual fires released within model forest or simulated urban environments are known to this author.

8.7.3 Numerical experiments

Fortunately, numerical modeling despite its many limitations associated with grid resolution, choice of turbulence model, or assignment of boundary conditions is not intrinsically limited by similitude or scale constraints. Thus, in principle, it should be possible to numerically simulate all aspects of fires within canopies for which realistic models exist for combustion, radiation, fluid properties, ignition sources, pyrolysis, etc. In addition it should be possible to examine all interactions of fire properties individually, sequentially and combined to evaluate nonlinear effects. Thus, computational fluid dynamics may well provide a greater understanding of the behavior of small, medium, and mass fires in the future.

Realistically, however, many of our computational submodules for combustion, radiation, pyrolysis, etc. are still primitive, and even inclusion of all models within a computation becomes cumbersome to calculate, and excessive in use of computational resources and time. Continued verification and validation is required at almost every level of CFD prediction. These caveats notwithstanding, there does exist exciting progress in the use and interpretation of numerical predictions of fire behavior.

Zone model based fire spread model

Himoto and Tanaka[264] describe calculations of fire spread in a simulated urban district by combining a modified zone model and a model for pyrolysis and ignition. Once a fire is ignited in a room, the combustibles inside the building burn filling the room uniformly with combustion products, heat and radiation; then the conditions in the first room communicate to surrounding rooms or buildings through convection plumes and radiation. Once the new space heats to a sufficient temperature, it also ignites, and the process proceeds.

The model was supplied with an idealized urban district of 49 identical buildings arrayed at a uniform separation distance of 3 m. The buildings chosen were assumed to be light weight concrete two-story houses composed of ten rooms. Some openings were open, others closed by window glass. The simulation was carried out for two wind speeds, 0.0 and 6.0 m/s. For no-wind the fire spreads in a symmetric pattern, but with a prevailing wind to the north the fire induced plumes were blown down by the wind and ignited downstream buildings earlier. For both cases the growth rates of fire in the 2^{nd} floor compartments were faster than that of the 1^{st} floor due to *a*) effects of plume buoyancy and *b*) 2^{nd} floor compartments were closer to the external fire plume centerline and exposed to more outside heating.

Field model based fire spread models

Baum and McGrattan [46] considered a fire growing from the exposed top of an oil storage tank in a 3 x 3 matrix of large cylindrical tanks. Each tank was 84 m diameter and 27 m high. The geometry was chosen to represent a portion of the oil storage facility of the Japan National Oil Corporation at Tomakomai. A approach velocity profile with a power law distribution of 0.15 and a wind speed at tank height of 6 m/s was stipulated. They used the LES program FDS to calculate time dependent combustion, plume rise and radiation exposure of the nearby tanks. The model included the effects of radiation from smoke particle back to tank surfaces.

Morvan and Dupuy [445] predicted fire propagation in Mediterranean shrub land by representing the vegetation as a collection of solid fuel particles distributed with appropriate size, moisture content, density, etc.. Separate layers were created to represent ground cover, crown canopy regions, thinning, and fire breaks. The model captures the degradation processes (dryng, pyrolysis, char combustion) and ignition. Calculations were performed over a domain 5 m tall by 20 m long. The authors considered different cell sizes (5, 10 and 20 cm) and compared rate of spread, mass fluxes, contributions of radiation and convection. The model predicted the temperature and velocity field

for fires with canopy top wind speeds of 1 and 5 m/s. Their model is intended for incorporation in the EU FIRESTAR system forest fire prediction tool.

Researchers are beginning to add complex terrain into their predictions of fire spread behavior. Viegas [635] calculated fire spread rates over a simplified canyon geometry consisting of a horizontal plane and two inclined planes that intersect each other along a line that exists in the vertical plane. Canyon centerline slopes varied from 16.1^o to 30^o. A constant heat flux over a small area represented a fire at the base of the canyon. A fire propagation algorithm was incorporated in the flow field to estimate the movement away from the ignition point at the base of the canyon. It was found that fire driven convection processes modified the shape of the thermal plume depending on the ambient wind speed and fire intensity.

Coen and Clark [128] has coupled a fire model into a three-dimensional non-hydrostatic terrain-following numerical mesoscale model developed at the US National Center for Atmospheric Research, Boulder, CO. The model includes rain and cloud physics. Calculations predict the growth and spread of a fire line moving across a two dimensional small Gaussian hill (height 200 m, half-width 300 m) for a wind speed of 3 m/s, and a stable atmospheric lapse rate ($10^oC/km$). The head of the fire propagated quickly uphill in the direction of the environmental wind. Once the fire reaches the top of the hill, the updrafts tend to inhibit the forward movement of the fire front, and the fire spreads faster laterally in the lee of the hill.

Hot plume behavior in generic porous canopies

One of the features of the forest fire problem making rigorous analysis difficult is the presence of individual trees, shrubs, bushes, trunks, branches, leaves and occasional human structure. To simulate these elements in detail with sufficient accuracy to replicate individual vortical motions would be intractable. Over a region of even a few acres there must be thousands of individual unequally sized and spaced objects.

A number of authors, however, have represented forest or urban canopy layers by porous regions of distributed force (or drag) [206, 213, 217, 318, 320, 576, 662]. The advantage of such an approach is that it permits inclusion of a canopy sublayer without the use of excessive and costly grid resolution. Yamada [662] and Shaw and Schumann [576] introduced the approach in order to add vegetation to meso-scale models of complex terrain. Jeram et al. [320] used the concept in $2d$ calculations for inviscid flow and constant eddy diffusivity flow estimates of the up and downwind penetration of flow within simple urban areas.

Garzan et al. [206] treated a $2d$ forest as a highly inhomogeneous and very permeable porous medium. The heat generated in the burning part of the forest was simulated through the addition of an area source term to the equation of thermal energy. The resulting velocity field was then used to estimate the position and velocity of firebrands. They simulated an atmospheric region 800 m high and 1000 m long with a 20 m high porous forest region also 1000 m in extent along the ground boundary. A constant heat flux of 50 kW/m^2 was imposed over a 20 m high and 100 m long region some 100 m downwind of the domain inlet. Turbulence was modeled by the standard $k-\varepsilon$ model. The plume height is deflected downward and the firebrands ae blown further downwind at the higher wind speed.

Numerical model calculations using the CFD code FLUENT 6.1 were performed to evaluate the time dependent behavior of fires ignited within a homogeneous porous canopy. These were compared with flow behavior from a similar fire in the absence of the canopy. Consideration was given to the effects of grid resolution, turbulence model (κ-RANS versus LES), wind speed (U_h = 0, 1, 2, 5 m/s), fire intensity (Q = 20, 50, 100 kW/m^3), and inlet velocity profile (α = 0 or 0.14). The development of velocities, turbulence intensity, static pressure, and temperature fields were examined for such examples. Typical results are discussed below.

Fire in $2d$ porous canopies

Calculations considered a fire domain 60 m tall and 300 m long including a porous canopy 100 m from the entrance along the ground 6 m high and 100 m long. The associated computational grid consisted of 9000 rectangular cells. A buoyancy source was placed 10 m inside the canopy 2 m tall and 4 m long that dissipated 100 kW/m^3. A power law velocity profile approached the canopy with a power-law exponent of 0.14 and a velocity at canopy height of 1 m/s. Inlet turbulence levels were 10%. Calculations were completed for fires with *a*) no canopy present and *b*) a canopy present with porous material having inertial resistance coefficients of 1 m^{-1} in both coordinate directions.

For the case of a fire ignited along a smooth ground surface, the thermal plume calculated by a transient LES turbulent model tended to grow downwind in time, creeping along the surface occasionally releasing unstable buoyant puffs of heated air upwards from the downwind tongue of the plume into an ascending turbulent thermal plume. The thermal plume along the ground was instantaneously rather shallow but mixed into regions above intermittently, Figure 8.13. The thermal plume calculated by a steady state $\kappa - \varepsilon$, RANS model produced a ground level plume of greater depth but which decayed exponentially in the vertical and downwind directions in a Gaussian manner. For the no-canopy fire plume situation, the laid over behavior of the plume resembles the visualizations of line source plumes photographed by Maruyama and Tanaka, 2002 [395] during their study of the high temperature field behind a flame in a turbulent boundary layer. Measurements of downwind velocity profiles also produced similar wall-jet behavior near the ground.

For the case of a fire ignited within a porous canopy region, the thermal plume calculated by a transient LES turbulent model was initially laid over slightly by the approach winds, but then separated from the wall and accelerated upward in the low speed regions within the canopy. When the plume reached the canopy ceiling it had substantial vertical velocity and lofted above the canopy in a conventional bent-over turbulent plume, Figure 8.14. The plume calculated by a steady state $\kappa - \varepsilon$, RANS model also lofted from within the canopy, but the RANS average plumes were broader since they represented the average character of the intermittent plume observed during the transient calculations. These results resemble the behavior of a fire ignited within a deep canopy that quickly moves from the ground fire bed into the canopy region.

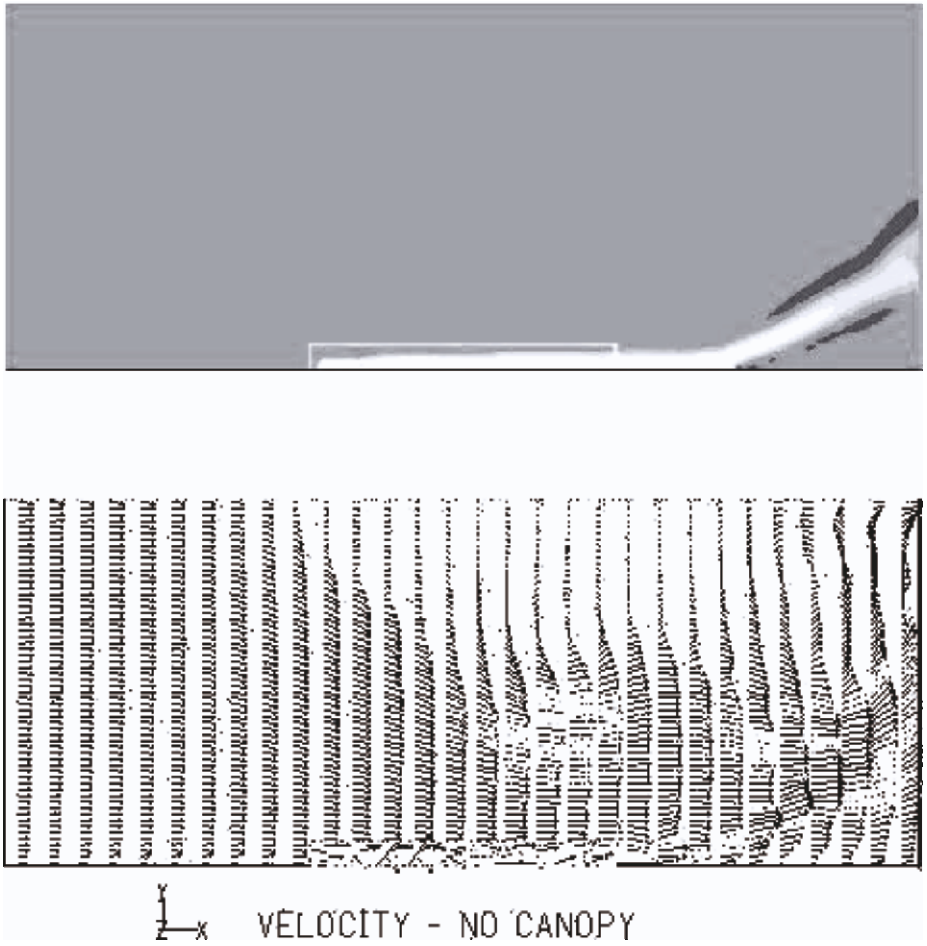

Figure 8.13: LES simulation of 2-d thermal plume growing along ground surface 116 seconds after ignition. No canopy: Top – temperature; bottom – velocity field.

Fire in $3d$ porous canopies

Calculations considered a fire domain 60 m tall, 300 m wide and 300 m long including a porous canopy that existed along the wall 6 m high, 100 m wide and 100 m long. The computational grid consisted of 185,000 hexagonal cells. A buoyancy source was placed 10 m inside the canopy 2 m tall, 80 m wide and 4 m long that dissipated 100 kW/m^3. A power law velocity profile approached the canopy with a power-law exponent of 0.14 and a velocity at canopy height of 2 m/s. Inlet turbulence levels were 10%. Calculations were completed for fires with a) no canopy present and b) a canopy present with porous material inertial resistance coefficients of 1 m^{-1} in all three coordinate directions.

During the 3-d calculations the fire line produced very similar patterns to those observed for the 2-d model. For a fire ignited along a smooth wall the transient plume also spread (creeped) along the ground surface releasing intermittent puffs of heated air from the tip of the plume tongue. However, given a finite lateral extent there was evidence of end effects where air descended from above, and converged laterally inward toward the center of the fire line. Surface temperatures remained high for long distances downwind (See Figure 8.15).

For a fire ignited within the porous canopy the 3-d fire line again produced similar patterns to those observed for the 2-d model. The heated plume rose upwards irregularly along the fire line to the canopy ceiling. When the plume penetrated through the shear zone into the higher wind speed above the canopy it was bent over, but continued to ascend upwards. There was considerably more evidence of lateral convergence downwind of the fire line however, and within the canopy there was an extensive region of reverse flow downstream of the fire line that fed air into the rising heated plume (Figure 8.16).

The consistent and physically realistic behavior of these virtual plume calculations is very encouraging. Future calculations should consider the effects of forest canopy inhomogeneities (ground cover versus crown vegetation), alternative fire locations, and combustible canopy structure. It will also be intriguing to examine those fire configurations which lead to the presence of intense fire whirls and the associated lofting of fire brands.

8.8 Fire whirls and fire tornadoes

Fire whirls are a typically rare but a potentially catastrophic form of fire. They are observed during urban and forest fires, where fire "tornadoes" are characterized by large-scale whirling flames which rise in 2 to 360 m diameter vortices from 10 to 1200 m high. These fire whirls accelerate combustion, produce significant suction pressures and lifting forces, and can carry burning debris, logs and even buildings thousands of meters from the main fire.

The formation of fire whirls requires a source of ambient vorticity, a concentrating mechanism, and a favorable environment for fire whirl stability and growth (augmentation physics). Emmons and Ying [169] wrote the defining paper about fire whirl behavior. They identified the primary mechanisms, performed laboratory scale experiments

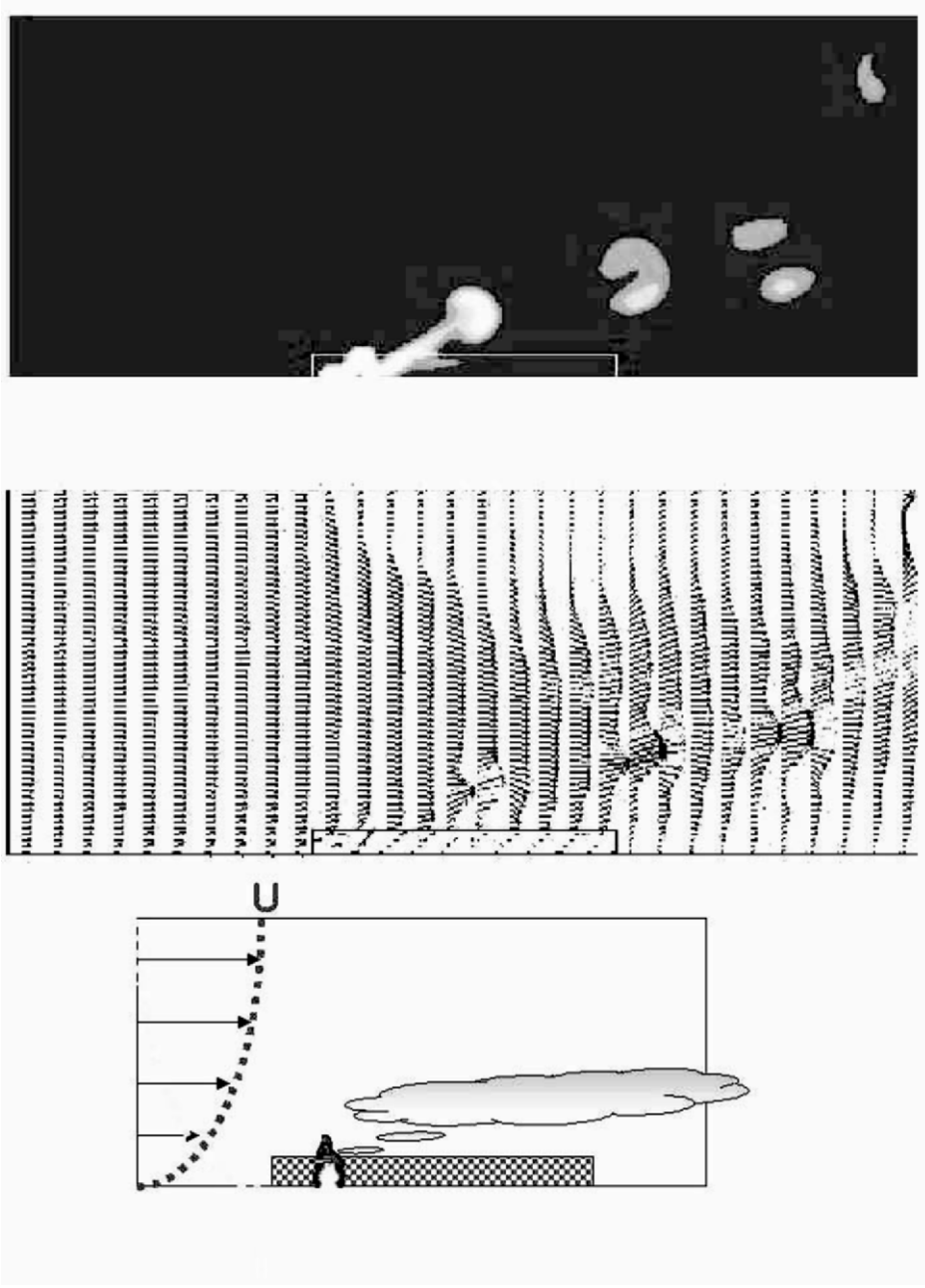

Figure 8.14: LES simulation of 2*d* thermal plume growing within porous canopy 116 seconds after ignition. Canopy case: Top – temperature; middle – velocity field; bottom – schematic of fire position.

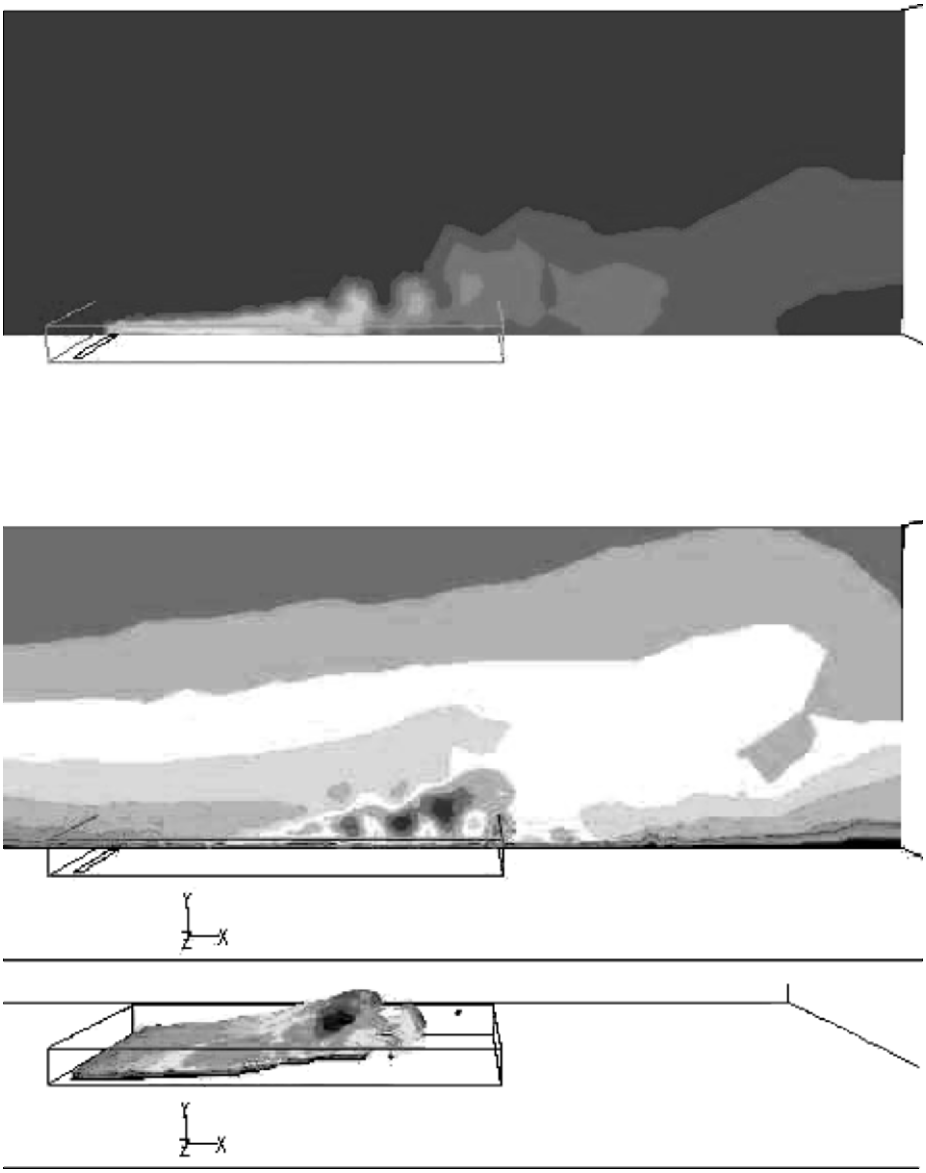

Figure 8.15: LES calculations of 3*d* thermal plume behavior over ground surface 160 seconds after ignition. No porous canopy case: Top – density contours; middle – velocity contours; bottom – geometry of plume.

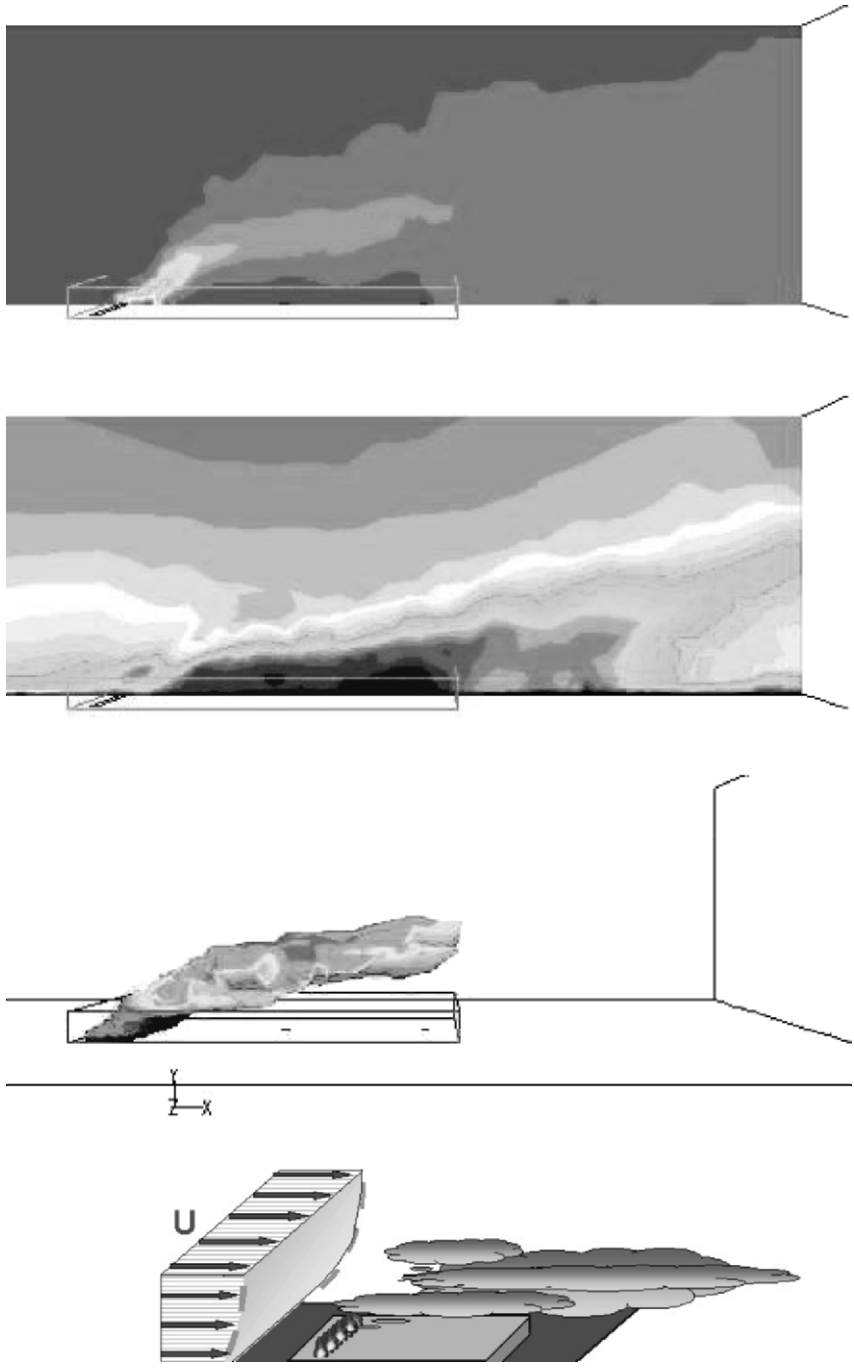

Figure 8.16: LES calculations of 3*d* thermal plume behavior growing within a porous canopy 112 seconds after ignition. Porous canopy case: (a) – temperature contours; (b) – velocity contours; (c) – geometry of fire and smoke; (d) – general schematic.

in a laboratory apparatus 3 m high which used a 2.25 m diameter rotating screen mesh to introduce angular momentum and a pan of burning fuel (acetone) to provide a source of buoyancy. They also proposed a fire plume model based on a one-dimensional entrainment theory, but it failed to reproduce the growth of the fire plume with height.

Later Mayle, 1970 [400] continued their research by performing measurements of velocity and pressure within the fire whirl. He found that the behavior of the plume was governed by dimensionless plume Froude, Rossby, second Damkohler Mixing Coefficient and Reaction Rate numbers. For plumes with a Rossby number less than one the plume is found to have a rapid rate of plume expansion with height. This phenomenon is sometimes called "vortex breakdown", and it is a "hydraulic jump" like phenomena caused by the movement of surface waves up the surface of the fire plume that are greater than the speed of the fluid velocity. Unfortunately, even improved entrainment rate type models do not predict these phenomena very well.

Ambient vorticity can be produced by ground level boundary layers generated by the wind, wind shear from non-uniform horizontal densities, the earth's rotation, or wind shear produced as air passes over a ridge or hill. Concentrating mechanisms include rising air in a buoyant column from unstable layers forming over sun-heated ground, the presence of a storm front, or hot gases from a fire. The concentrating mechanisms rotate the horizontal vorticity into the vertical and stretch the vortex tubes. Through conservation of angular momentum the stretched tubes induce more rapid rotation resulting in lower axial pressures, which in turn encourages further entrainment of ground level vortex-rich air. Finally, the rotational structure of the vortex induces centrifugal forces which dampen turbulence near the vortex core; thus, reducing any tendency for the fire whirl plume to diffuse outward from the core

8.8.1 Physical modeling of fire whirls

Byram and Martin [97] used external vertical cylinders with tangential slots oriented to produce rotating flow about a fire source. They examined two sets of equipment of diameters and heights, 33 and 183 cm, or 66 and 335 cm, respectively. Burning alcohol pools within their apparatus, they reported visible fire whirls up to 300 cm tall with inner fire tube columns 2 cm in diameter. They observed horizontal velocities at the surface of the inner column of about 9 m/sec (~6000 rpm) and vertical velocities to 18 m/sec.

Emmons and Ying [169] used the rotating-screen apparatus described above to systematically evaluate the effects of angular rotation (Rossby number) and plume buoyancy (Froude number) on fire whirl dynamics. They reported that turbulent mixing coefficient decreases with increasing angular momentum, and increases with elevation above the ground. Later Chigier et al., 1970 [120] reproduced their apparatus but used a turbulent jet diffusion flame. Since these early experiments several investigators have re-created similar laboratory apparatus while evaluating the character of fire whirls [450].

Other investigators have reproduced fire tornadoes as they develop in simulated outdoor environments. Lee and Otto [364] examined how city fires might develop by simulating in a wind tunnel a simple urban street arrangement. Their results revealed that strong street level vortices could develop due to building fire interaction. Emori and

Saito [170] simulated a fire whirl formed during a forest fire burning over a mountain ridge top that injured several Japanese fire fighters. Soma and Saito [586] recreated fire tornadoes that occurred during the Kanto earthquake in Tokyo (1923), the Hamburg firestorms during WW II (1943), and oil-tanker fires in Hokkaido bay, Japan (1965).

More recently Satoh and Yang [558, 559] produced laboratory scale fire whirls by adjusting symmetrical vertical gaps separating the square vertical bounding walls surrounding a central fire pan. They examined the effect of gap size, wall height, fuel size, and heat load on the fire whirl. They determined that there is a critical gap size, which is not so large or small that it inhibits the entrainment of air needed to sustain the fire. Stable whirls were generally associated with flame heights smaller than the wall height of the square enclosure. Flame temperatures were primarily affected by the magnitude of the volumetric heat source.

8.9 Numerical modeling fire whirls

Murgai and Emmons [451] and Emmons and Ying [169] describe integral plume models, which are calibrated with experimental data. Satoh and Yang [559] used the UNDSAFE code with associated 3d, compressible, buoyant, and constant turbulent viscosity specifications. Ten cases were considered which included validation exercises and parameter sensitivity studies.

Battaglia et al., 2000 [44] simulated the laboratory experiments of Emmons and Ying, 1966 [169]. Chigier et al., 1970 [120], and Satoh and Yang, 1997 [559], which included cases for fixed circulation and variable fire strength, fixed fire strength and variable circulation, and jointly varied fire strength and circulation. The numerical code used was the NIST shareware FDS (Fire Dynamics Simulator) which includes 3d, compressible, buoyant and LES turbulent models [45]

Meroney [422, 423] and Meroney et al. [421, 424] considered the growth of fire whirls in large building atria and their effects on distribution of smoke and building evacuation. Using the commercial cfd code, FLUENT 6.1, he reproduced the transient growth and stabilization of laboratory fire whirl configurations used by Byram and Martin [97], Emmons and Ying[169] and Satoh and Yang [559]. Figure 8.17 present the transient appearance of fire whirls generated within fire whirl simulation chambers.

8.10 Conclusions and recommendations

The development of large fires in vegetation and building environments continues to be a major concern as population increases results in larger urban areas and the intersection of wildlands and urban regions. Although the total number of fires observed seem to be constant, the proximity of wildlands and urban populations has resulted in steadily increasing economic infrastructure losses. Continued research into the mechanisms of fire spread and their possible mitigation are appropriate. This review suggests that:

- Fire and smoke movement through forests and building arrays are imbedded in flows defined by the porous nature of the burning media. Initially it is the flow

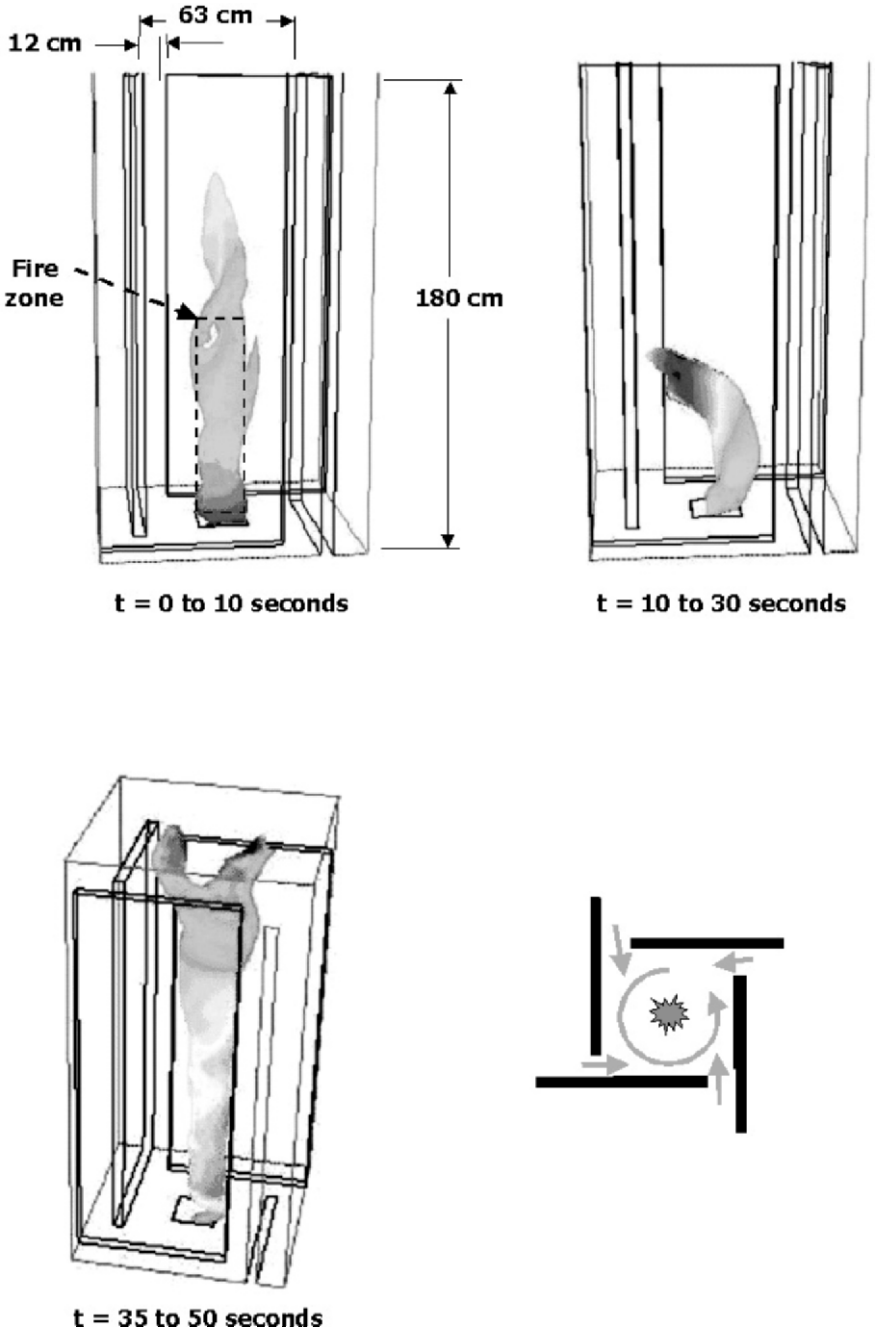

Figure 8.17: Isotemperature surfaces calculated at various times during numerical simulation of fire whirl configuration studied by Satoh and Yang, [559], Case 8.

through the permeable media which determines the nature of the growth and spread of the fire.

- Fires growing within porous media inherently are different from fires burning over flat surfaces.
- Flow through forest canopies and building arrays are very similar with respect to their mean behavior in terms of distributions of velocity, turbulence and shear profiles, but
- Building arrays are NOT locally porous only in the average.
- Improved fire spread models should be developed to determine the effects of street arrangement, street canyon aspect ratio, building heights, etc. on fire propagation. CFD appears to be a valuable tool in investigating these phenomena systematically.
- Simple parameteric models are needed to use in numerical models to permit simulation of fire pyrolis and spread.
- Porous canopy models may be improved by using various degrees of porosity to model individual buildings, vegetation, and other structures.
- Future calculations need to include realistic thermal radiation models to predict drying, pyrolysis and ignition. These same calculations need simple but realistic models for fire spread.

Chapter 9

Urban air flow researches for air pollution, emergency preparedness and urban weather prediction

A. Baklanov[1]
Danish Meteorological Institute,
Copenhagen, Denmark

9.1 Introduction

The quality of the urban air pollution forecast and the Urban Air Quality Information and Forecasting Systems (UAQIFS) critically depends on the: (i) mapping of emissions, (ii) level of urban air pollution (UAP) models, and (iii) quality of meteorological fields in urban areas. The main problem in forecasting of UAP is the prediction of episodes with high pollutant concentration in urban areas. In these areas most of the well-known methods and models, based on in-situ meteorological measurements, fail to produce realistically the meteorological input fields for the UAP models. Many projects are aimed at developing UAP dispersion models and chemical transformation and at improving knowledge about pollutants and emissions. However, no significant efforts were put to improving forecasts of meteorological parameters in UAP models. These would be especially important in air pollution episodes (APEs) with low winds, stable stratification, local air circulations, topographic effects, breeze conditions, and internal boundary layers. Moreover, a reliable urban scale forecast of air flows and meteorological fields is of primary support for urban emergency management systems for

[1]E-mail of the author: *alb@dmi.dk*

Ye.A. Gayev and J.C.R. Hunt (eds.), Flow and Transport Processes with Complex Obstructions, 311–357.

accidental toxic releases, fires, or even chemical, radioactive, or biological substance releases due to terrorist actions, the potential risk of which has been recently emerged.

UAP models in operational UAQIFSs, as a rule, still use simple in-situ meteorological measurements which are fed into meteorological pre-processors (see Figure 9.1). Lacking an adequate description of physical phenomena and the complex data assimilation and parameterisations of numerical weather prediction (NWP) models, these pre-processors do not achieve the potential of NWP models in providing all the meteorological fields needed by modern UAP models to improve the UAQ forecasts.

Historically, UAP forecasting and NWP were developed separately. This was plausible in the previous decades when the resolution of NWP models was too low for city-scale air pollution forecasting. However, during the last decade, substantial progresses in both meso-meteorological and NWP modelling and the description of urban atmospheric processes have been achieved. For instance, state-of-the-art nested NWP models can use land-use databases down to 1 *km* resolution or finer, enabling to provide high quality urban meteorological data. Thus, NWP models are now approaching the necessary horizontal and vertical resolution to provide weather forecasts for the urban scale (e.g. Baklanov et al., [27, 38]).

Many urban features can influence the atmospheric flow, its turbulence regime, the microclimate, and, accordingly modify the transport, dispersion, and deposition of atmospheric pollutants within urban areas, namely:

- Local-scale non-homogeneities, such as sharp changes of roughness and heat fluxes;
- Sheltering effects of buildings on the wind-velocity;
- Redistribution of eddies, from large to small, due to buildings;
- Trapping of radiation in street canyons;
- Effect of urban soil structure,
- Different diffusivities of heat and water vapour in the canopy layer;
- Anthropogenic heat fluxes, including the so-called urban heat island;
- Urban internal boundary layers and the urban mixing height;
- Effects of pollutants (including aerosols) on urban meteorology and climate;
- Urban effects on clouds and precipitation.

Despite the increased resolution and various improvements, current operational NWP models still have several shortcomings with respect to urban areas, such as:

- Urban areas are mostly described by similar sub-surface, surface, and boundary layer formulations as for rural areas.
- These formulations do not account for specific urban dynamics and energetics or for their impacts on the simulation of the urban atmospheric boundary layer (UBL) and its intrinsic characteristics (e.g. internal boundary layers, urban heat islands, precipitation patterns).
- Additionally, NWP models are not primarily developed for air pollution and emergency modelling, and their outputs need to be designed as suitable input for urban and meso-scale air pollution and emergency preparedness models. Therefore, due to the above mentioned reasons, the situation in UAQIFS is changing nowadays and requires a revision of the conventional conception of UAQ forecasting. In response to the above mentioned research needs, two large European Union initiatives have been realised during the last years.

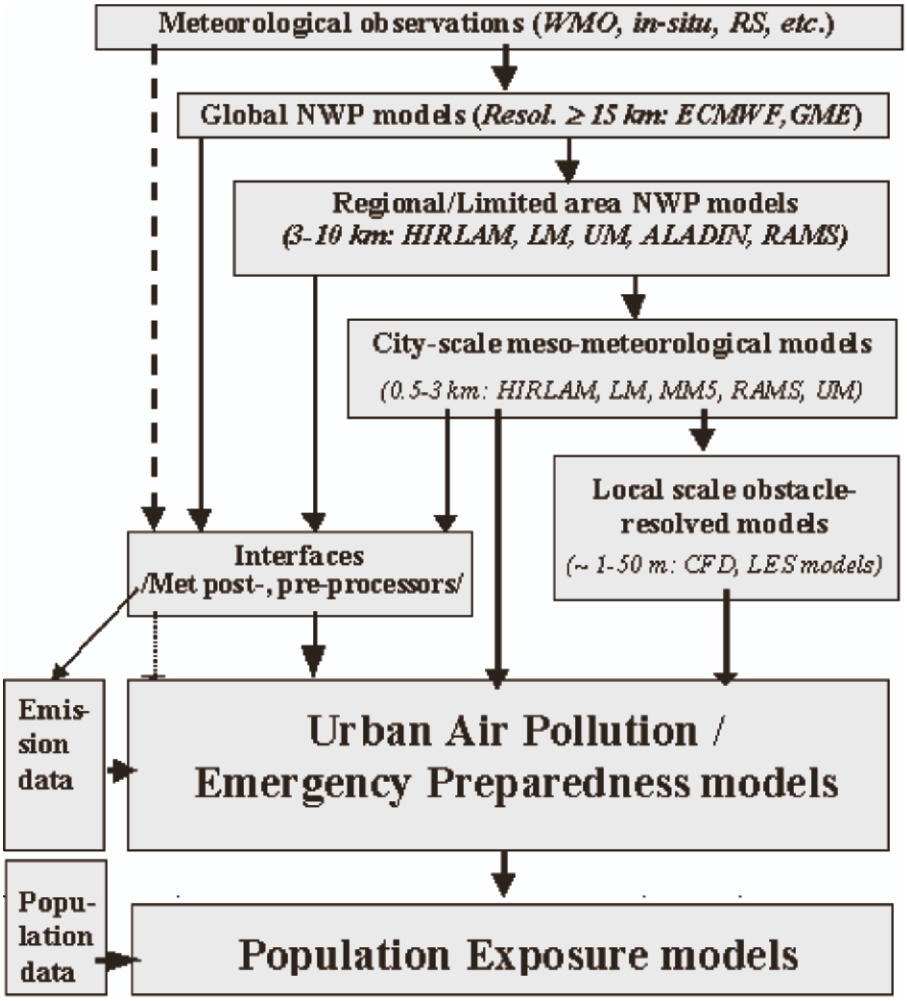

Figure 9.1: Current regulatory (dash line) and suggested (solid line) ways for forecasting systems of urban meteorology within UAQUIFSs by downscaling from the adequate NWP model to the urban scale (Baklanov et al., [38]).

The first one is the European COST Action 715 (http://cost.fmi.fi/wg2): Urban Meteorology 'Meteorology Applied to Urban Air Pollution Problems' (1999-2004) (Chairman Prof. B. Fisher, UK) (Fisher et al., [192]) with the following four working groups (WGs):

WG1: Wind fields in urban areas (Chair Dr. M. Rotach).

WG2: Mixing height and surface energy budgets (Chair Dr. M Piringer) (Piringer and Joffre, 2005).

WG3: Meteorology during peak pollution episodes (Chair Prof. J. Kukkonen).

WG4: Input data for urban air pollution models (Chair Prof. M. Schatzmann).

Two large urban experimental campaigns were also realised within the COST Action 715:

(i) the Basel UrBan Boundary Layer Experiment (BUBBLE), initiated by the Swiss COST organisation (Leader Dr. M. Rotach) (Rotach et al., [549]);

(ii) the UBL/CLU study, Marseille, France, an associated project of ESCOMPTE (Leader Dr. P. Mestayer) (Mestayer et al., [429]).

The second initiative is the European research project called FUMAPEX: "Integrated Systems for Forecasting Urban Meteorology, Air Pollution and Population Exposure" (Leader Dr. A. Baklanov) of the Fifth Framework Programme, Subprogramme: Environment and Sustainable Development, Key Action 4: City of Tomorrow and Cultural Heritage. FUMAPEX started in November 2002 and will continue for a period of three years ($http://fumapex.dmi.dk$). FUMAPEX is a member of the CLEAR cluster of European Urban Air Quality Research ($http://www.nilu.no/clear$).

The main objectives of the FUMAPEX project are the following:

(i) to improve meteorological forecasts for urban areas,

(ii) to connect NWP models to UAP and population exposure (PE) models,

(iii) to build improved UAQIFS and urban emergency modelling system, and

(iv) to demonstrate their application in target cities located in various European climates. The FUMAPEX scheme of the improvements of meteorological forecasts in urban areas, interfaces and integration with UAP and PE models for the UAQIFS is presented in Figure 9.2.

The improvement of urban meteorological forecasts, additionally to a better prediction of urban weather events and improved UAQIFSs, will also provide information to city management regarding additional hazardous or stressing urban climate (e.g. urban runoff and flooding, icing and snow accumulation, high urban winds or gusts, heat or cold stress in growing cities and/or a warming climate). Moreover, the availability of reliable urban scale weather forecasts could be of relevant support for the emergency management of fires, accidental toxic emissions, potential terrorist actions, etc.

The improved forecast techniques can be used in two ways. Firstly, it can be the short-term episode forecasts for the next few days. Secondly, it is an integrated modelling system for long-term air quality management to predict future episodic pollution levels, taking into account estimated trends in local traffic and other emissions. In both ways the modelling system can be employed to evaluate alternative scenarios and to develop efficient strategies to reduce emissions, pollution levels, and PE to prevent health consequences in a cost-effective way.

In order to achieve the innovative project goal of establishing and implementing the improved UAQIFS to assist sustainable urban development, the following steps should be achieved:

1. improve predictions of the meteorological fields needed by UAP models by refining resolution and developing specific parameterisations of the urban effects in NWP models,

2. develop suitable interface/meteorological pre-processors from NWP to UAP models,

3. validate the improvements in NWP models and meteorological pre-processors by evaluating their effects on UAP models against urban measurement data,

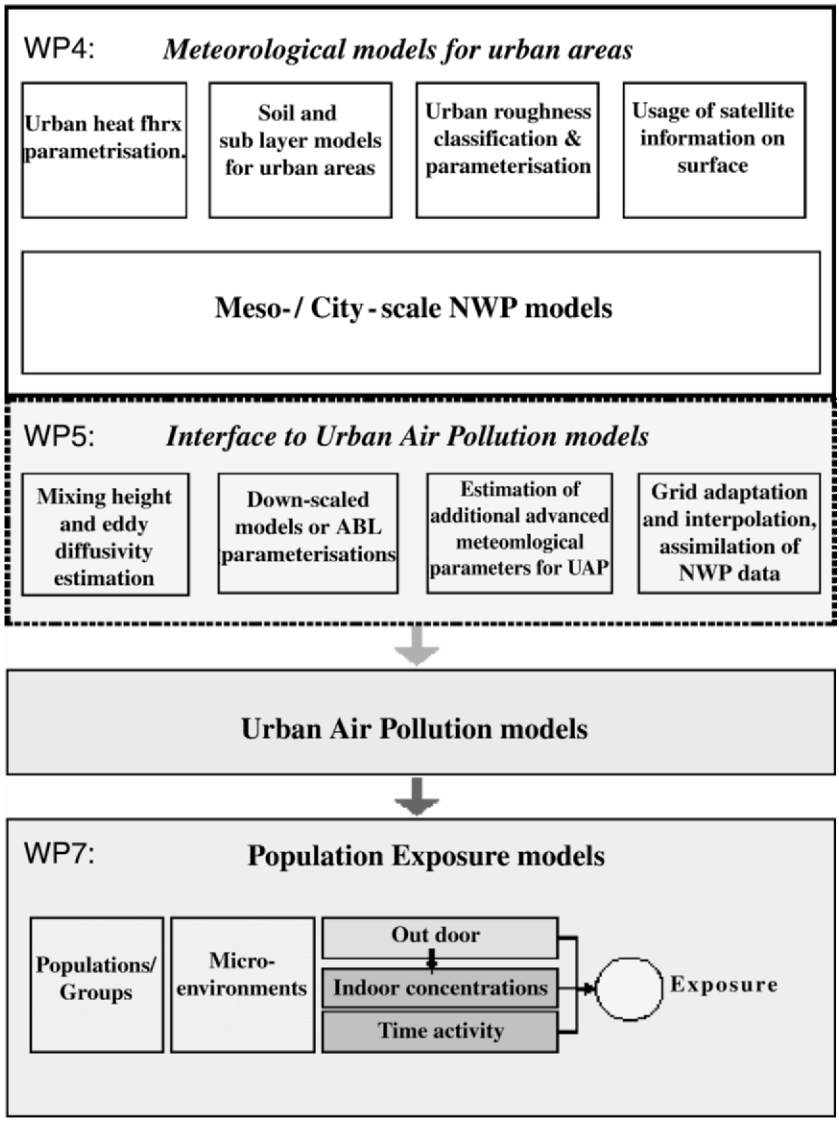

Figure 9.2: Outline of the overall FUMAPEX methodology integrating models from urban meteorology to air quality and population exposure. The main improvements of meteorological forecasts (NWP) in urban areas, interfaces and integration with urban air pollution (UAP) and population exposure (PE) models for the Urban Air Quality Information Forecasting and Information Systems (UAQIFS) are mentioned on the scheme (Baklanov et al., 2005 [36]).

4. apply the improved meteorological data to UAQIFS, emergency preparedness and PE models, compare and analyse results, and

5. successfully link meteorologists/NWP modellers with UAP and public health scientists and 'end-users' of UAQIFS.

The necessary steps are evolved in 10 separate, but inter-linked Work Packages realised by 16 partners and 6 subcontractors[2]. They represent leading NWP centres, research institutions, organisations responsible for UAP, PE forecast and control, and local/city authorities from 10 European countries.

Two new relevant European COST Actions were also started recently; this is COST 728: 'Enhancing meso-scale meteorological modelling capabilities for air pollution and dispersion applications' (http://www.cost728.org/) (Sokhi et al., [584]) and COST 732: 'Quality Assurance and Improvement of Micro-Scale Meteorological Models' (*http* : *//www.mi.uni − hamburg.de/Home*.484.0.*html*) (Schatzmann, [562]).

This Chapter is an overview of several European national and international research activities in the considered field and it is mostly based on the main achievements from the two above mentioned EU actions: FUMAPEX and COST 715.

9.2 Applications to urban air quality forecasting and numerical weather predictions

This Section has been written in cooperation with the FUMAPEX WP4 team: Mestayer, P. (ECN), Clappier, A. (EPFL), Zilitinkevich, S. (UH), Joffre, S. (FMI), Mahura, A., Amstrup, B., Petersen, C. (DMI).

9.2.1 Introduction to the problem

A palette of urban Surface Energy Budget (SEB) schemes and urban sublayer models are now available (e.g., Bortnstein, [68]; Oke et al., [474]; Grimmond and Oke, [237]; Masson, [398]; Dupont, [157]; Martilli et al., [393]; Hunt et al., [298, 302]; Belcher et al., [51]; see also an overview in Chapter 2), but they have not all been tested with meso-meteorological models and validated to the same degree. They range from simple transformations of some key coefficients in exchange schemes developed for natural surfaces to detailed modules computing quasi-explicitly the radiative and turbulent energy exchanges of each built element category, e.g., the ground surface, walls and roofs, treated in group by type. Furthermore, even more detailed models and software are available to compute the thermo-radiative budgets of, or interactions with, elemental building surfaces. These tools may be used to analyse experimental data from validation campaigns, to run numerical experiments for urban areas, or to perform sensitivity analysis studies.

The development and validation of these SEB models brought to light and helped to quantify several specificities of the urban canopy energetics:

[2] See the project web-site: http://fumapex.dmi.dk

• Net radiation varies in time at the local scale with solar orientation and in space with district morphology, which is not much different from its rural counterpart on average;

• The diurnal cycle of the turbulent sensible heat flux is large but highly variable, strongly dependent on district structure, and often positive at night. In the dense city centres, this flux is limited by a strong aerodynamic resistance (high z_{om}/z_{ot} roughness length ratio), favouring heat storage;

• A large heat storage in building materials, rather than in the ground, as a function of building density and morphology;

• A low but highly variable latent heat flux;

• A hysteresis in the diurnal cycles, with phase lags between the energy budget components due to heat being diverted from the budget and provisionally stored in the building materials in the morning at the expenses of the sensible heat, while the stored heat is released in the evening and at night.

Therefore, to improve meteorological forecasts for urban areas and to provide the high-resolution meteorological fields needed by urban air quality (UAQ) models, it is required to implement specific urban surface layer and surface energy balance parameterizations into meso-meteorological and NWP models, or so to speak to 'urbanise' these models.

The improvement of UBL formulations and parameterisations using urban physiographic data classifications in NWP models together with the evaluation of the induced improved simulation of urban meteorology for NWP and UAQ forecasting is one of the main aims of the EU-funded FUMAPEX project (Integrated Systems for Forecasting Urban Meteorology, Air Pollution and Population Exposure; Baklanov et al., [36]). This section reviews works and advances achieved within FUMAPEX (Baklanov et al., [38]) with respect to:

• Finer spatial grid resolution and model downscaling;
• Detailed physiographic data and land-use classification;
• Calculation of effective urban roughness;
• Estimation of urban heat fluxes;
• Urban canopy and soil sub-models.

9.2.2 FUMAPEX methodology for urbanization of city-scale meteorological models

The FUMAPEX strategy to improve NWP and meso-scale meteorological models includes the following aspects for the urbanisation of relevant submodels or processes:

(i) Model down-scaling, including increasing vertical and horizontal resolution and nesting techniques (one- and two-way nesting);

(ii) Modified high-resolution urban land-use classifications, parameterizations and algorithms for roughness parameters in urban areas based on the morphologic method;

(iii) Specific parameterization of the urban fluxes in meso-scale models;

(iv) Modelling/parameterization of meteorological fields in the urban sublayer;

(v) Calculation of the urban mixing height based on prognostic approaches.

Apart a better prediction of the urban weather and the Urban Air Quality Information and Forecasting Systems (UAQIFS) *perse*, improved urban meteorological forecasts will also provide information to city management regarding additional hazardous or stressing urban climate (e.g. urban runoff and flooding, icing and snow accumulation, high urban winds or gusts, heat or cold stress in growing cities and/or a warming climate). Moreover, the availability of reliable urban scale weather forecasts could be a relevant support for emergency management of fires, accidental toxic emissions, potential terrorist actions, etc. The outline scheme of the overall FUMAPEX methodology of integrating models from urban meteorology to air quality and population exposure for the improved UAQIFS is presented in Figure 9.2.

The following meso-meteorological and NWP models of FUMAPEX partners were used for urban conditions or for different variants of the 'urbanisation' scheme (user/developer teams are in brackets): 1. DMI-HIRLAM (DMI); 2. Lokalmodell LM (DWD, MeteoSwiss, EPA Emilia-Romagna); 3. MM5 (CORIA, met.no, UH); 4. RAMS (CEAM, Arianet); 5. Topographic Vorticity-Mode (TVM, Schayes et al., [563]) Mesoscale Model (UCL); 6. Finite Volume Model FVM (EPFL); 7. SUBMESO model (ECN).

Increased grid resolution and nesting of NWP models

Increased computer power and the implementation of grid nesting techniques allowed modern NWP models to approach the resolution necessary for the city-scale. The FUMAPEX strategy for improving UAQIFS includes, first of all, increasing model resolution and down-scaling (with one- or two-way nesting) of NWP models with different resolutions (Figure 9.1).

For example, the recent Danish operational NWP system (Sass et al., 2002) consists of several nested models named DMI-HIRLAM-S05 and -T15, with horizontal resolutions of 5 and 15 *km*, respectively. The previous nested DMI-HIRLAM versions G45, E15 and D05 (operational prior to 14 June 2004) had 45 *km*, 15 *km* and 5 *km* resolution, correspondingly. The vertical resolution of the operational versions is 40 levels, but it was increased up to 60 levels for test runs. Within the FUMAPEX project, DMI run also several experimental versions of DMI-HIRLAM (e.g., U01, I01) with a horizontal resolution of 1.4 *km* over Denmark and the Sjaeland Island, where the city of Copenhagen is located (Baklanov et al., [27]; Fay et al., [176]; Mahura et al., [390]).

The German DWD Local Model LM (Doms and Schattler, 1999 [151]) is currently operated as a nest within the Global Model for Europe (GME). LM has a resolution of 7 *km* for the Central and Western Europe. In 2003, it became operational for that area with a resolution of 2.8 *km*. For the FUMAPEX study, both the horizontal and vertical resolution of LM were increased to 1.1 *km* and 43 layers, respectively, as required by the 1-way self-nesting version of LM (Fay and Neunhaeuserer, 2005 [177]).

In Norway, the non-hydrostatic MM5 model (Grell et al., 1994 [234]) is nested with the HIRLAM NWP model (Berge et al., 2002 [58]). The latter model is operated on a 10 *km* horizontal resolution for North-Western Europe. A domain with a resolution of 3 *km* has been set up for the region around the city of Oslo in which MM5 is one-way nested with HIRLAM. A two-way nesting takes place between the 3 *km* resolution

domain and a 1 *km* resolution area covering Oslo. The output data from MM5 are inputs to the Air Quality Model of the Norwegian Institute for Air Research (NILU).

FUMAPEX partners performed verification and sensitivity studies with their NWP models against measurement data for several episodes in different European cities: Helsinki, Oslo, Bologna, Valencia, Copenhagen (Neunhaeuserer et al., 2004 [465]; Fay et al., 2005 [176]; Baklanov et al., 2005 [38]). Results for the verification of the LM model using different resolutions are discussed by Fay and Neunhaeuserer 2005 [177] and for the Norwegian urban MM5-HIRLAM system by Berge et al. 2002 [58]. Verifications for high-resolution versions of the DMI-HIRLAM modelling system were carried out for Copenhagen by Baklanov et al 2005 [38] and Mahura et al., 2005 [390]).

Figure 9.3 presents one example of the verification results for the DMI-HIRLAM-U01 research model with a 1.4-*km* resolution for May 2005 (Mahura et al., 2005 [390]). It shows better prediction of the diurnal cycle of the average wind velocity at 10 *m* than with the S05-version. On average, the bias for both models was around 1.5 m/s. The verification runs underlined that increasing the resolution (down to 1 *km*) brings some improvement to the skill of the meteorological forecast. Nevertheless, it will be also very important for further improvements to have more detailed surface features databases and to increase the quality of the land-use classification (LUC) for urban areas.

Urban land-use classification
and algorithms for roughness parameters

Surface characteristics such as albedo, thermal properties, roughness, or moisture availability significantly control the surface energy balance partitioning of any type surface. In contrast to most natural surfaces, urban landscapes show a much larger range and variability of surface characteristics. However, most of the NWP and meso-meteorological models still do not consider any urban class at all, or include only one urban class for all types of urban surfaces. In view of the wide range of urban surface types, it is not possible to single out one set of universal urban surface values, which would be valid for all types of urban neighbourhoods worldwide. Therefore, much more detailed surface information than in existing NWP models is needed.

Typical surface characteristics can be attributed to distinct **categories** of urban neighbourhoods. Such a classification can be performed based on land use maps or aerial photos. Digital LUC datasets can help to define different urban classes and are a source of increasing importance. Unfortunately, most LUCs are classified by functional aspects (residential, industrial) and not by surface morphometry or surface cover. Focussing on meteorological aspects, Ellefsen 1991 [167] classified North American cities into 17 Urban Terrain Zones (UTZ) according to building contiguity, construction, and materials. Fehrenbach et al., 2001 [178] have automated the classification of urban climatological neighbourhoods from satellite image analysis. However, no universal classification scheme exists. Historical development results in a huge variety of urban neighbourhood types worldwide. The more complete a description scheme is, the more it is restricted to a specific (historical) region, e.g., UTZs are difficult to apply to European cities because typical morphometry and building materials are different.

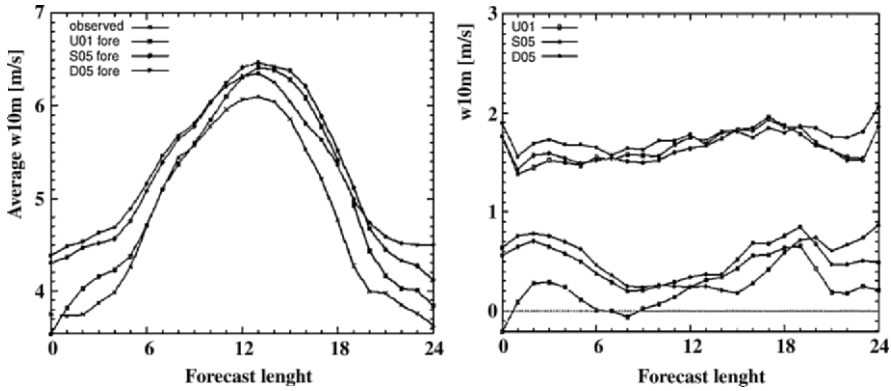

Figure 9.3: Comparison of the diurnal variation of average wind velocity (in m/s at 10 m between observational data and three DMI-HILRAM-S05, -U01, and -D05 model versions for 00 UTC forecasts during May of 2005: (left) comparison with observations, (right) at top - bias, bottom - rms error.

An appropriately chosen set of **surface parameters** can be related to specific physical processes. For example, it is not surprising that the area covered by vegetation drives the magnitude of the latent heat flux, or that morphometric parameters help to describe the roughness and turbulence characteristics over a particular urban surface. Therefore, the following three most important characteristics can be outlined (cf. Piringer and Joffre, 2005 [497], for a summary).

(i) *The Urban cover*: Two dimensional plan aspect ratios ("plan area fractions") describe the 2D surface fraction of a particular surface type per total plan area (as viewed from above), e.g. the plan area ratios of buildings, vegetation, impervious surfaces. It can also include dominant street directions in a grid cell.

(ii) *The Three dimensional structure*: 3D morphometric parameters describe the configuration of urban buildings (it can include vegetation as well). They are used in the BEP model to parameterize drag and turbulence production (see Section 9.2.4) or in the SM2-U model to simulate storage heat flux densities and surface temperatures (see Section 9.2.5). The most important morphometric parameters to be used in urban meteorology models include: the mean building height, frontal aspect ratio, surface enlargement, normalized building volume, characteristic inter-element spacing, canyon width, building breadth, etc. For many cities, authorities provide digital 3D building data sets, which are a powerful tool for the analysis of urban surface forms. Such high resolution data can provide detailed measures of 3D parameters, and additionally vertical profiles, e.g., of building volume density and sky view factors.

(iii) *Urban materials*: This information (e.g., construction materials of buildings roofs and walls) is of great importance especially for the estimation of radiative properties (e.g. surface albedo) and the determination of storage heat flux densities. Detailed analysis of aerial photos or field surveys can provide the necessary information.

Proceeding from the urban LUC, the calculation of the main aerodynamic characteristics of urban areas such as the roughness length and displacement height, can be performed based on the morphometric or morphologic methods.

With morphometric methods, ranking these aerodynamic characteristics depends on the model intrinsic requirements for input data. Bottema and Mestayer 1998 [73] and Grimmond and Oke 1999 [238] reviewed methods to deduce aerodynamic properties from a set of morphometric parameters. Tests of the models against individual datasets showed poor performances. The simplified model of Bottema 1997 [72] gave relatively better results and additionally can be applied across the full range of building density parameters. Considering its relatively low input requirements, it is an efficient alternative. More simple models cannot be recommended, especially due to their limited range of applicability. As to the "recommended rule of thumb" of Grimmond and Oke 1999 [238], one should keep in mind that it does not include any density dependency of roughness and, therefore, will overestimate roughness for low and high densities, and underestimate it at medium densities.

With morphologic methods a more empirical and pragmatic approach can be considered, based on the visual observation of the physical structure of the urban canopy (e.g., from aerial photography). From survey of experimental data, Grimmond and Oke, 1999 [238] offered a first-order evaluation of the roughness parameters of urban zones, separated into only 4 categories. These categories are associated with 4 flow regimes: (1) Low height and density - isolated flow; (2) Medium height and density - wake interference flow; (3) Tall and high density - skimming flow; (4) High rise - chaotic or mixed flow.

Ellefsen 1991 [167] designed a scheme to identify 17 types of urban terrain zones that are defined by a written description and model photography. Furthermore, Grimmond & Oke 1999 [238] adapted this scheme to their proposed 4 urban roughness categories, offering physical description, matrix of typical photographs, and table of the most probable non-dimensional roughness parameters. For the above mentioned categories the classical Davenport classification of effective terrain roughness was revised by including explicitly the urban terrains (Davenport et al., 2000 [142]; Mestayer and Bottema, 2002 [426]).

Depending on the choice of the urbanisation approach (see Section 9.2.2) different urban LUCs are possible. In our studies for different cities, from 3 to 9 types of urban types were considered. Figure 9.4 presents two examples of the urban land-use classification, prepared following the above mentioned improved morphologic method, for the Copenhagen and Marseilles urban areas. The urban topographic databases BDTopo (French National Geographic Institute) for Marseilles and the AIS Land-use database (Danish Environmental Research Institute) for Copenhagen were used to analyse urban structures in order to characterise the morphology of settlements and land coverage (Long et al., 2002 [374]; Mahura et al., 2005 [390]). The accuracy of the computed descriptive statistics was estimated for different sizes of grid cells. It was found that individual cells of 200 x 200 m represent best the structure of each urban district with respect to both high resolution and statistical representativeness (Long, 2003 [375]). Therefore, mean variables describing the buildings morphology and land covers were computed for this size cells onto a grid and composed as layer themes in GIS: building

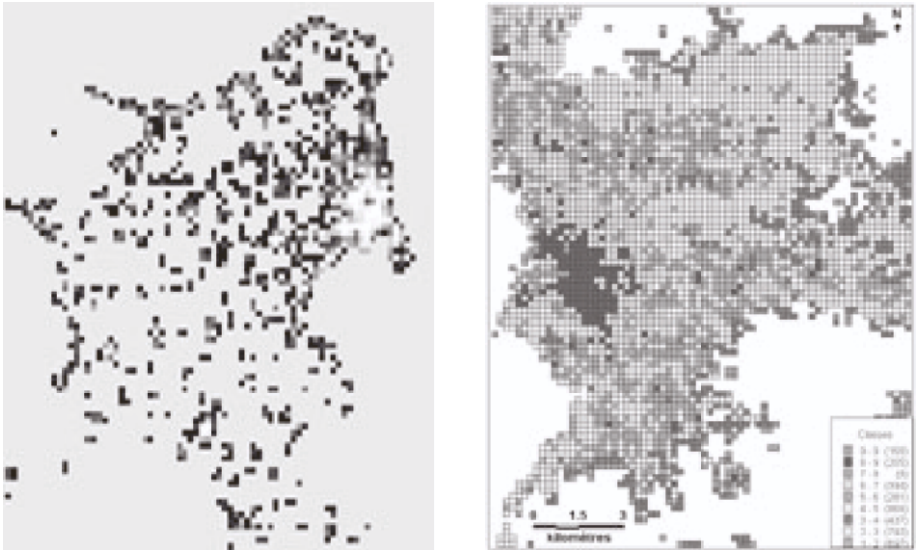

Figure 9.4: Examples of improved urban land-use classifications prepared for: a) the Copenhagen metropolitan area (shown as a percentage of the urban class representation in each grid-cell of the domain) used in the DMI-HIRLAM simulations (Left panel); (b) the Marseilles metropolitan area (shown as a presence of 9 classes in domain, see Long et al. 2003 [375]) used in the SUBMESO/ SM2-U simulations (Right panel).

average height, perimeter, volume, compactness; plan area, vegetation and pavement densities, etc.

For the St. Jerome study area (Long et al., 2003 [376]; Long, 2003 [375]), it was found that the average buildings height is 7.7 *m* with 50% of these buildings having heights within the range 4.8-9.7 *m* (see Table 9.1). Many buildings are small because, on average, the perimeter and volume are 62.5 *m* and 3192 m^3, respectively.

Urban fluxes and sublayer parameterisation

Simulating urban canopy effects in urban-scale NWP and meso-meteorological models can be considered with the following two main approaches (Baklanov et al., 2005 [38]):

1. Modifying the existing non-urban approaches (e.g., the Monin-Obukhov similarity theory MOST) for urban areas by finding proper values for the effective roughness lengths, displacement height, and heat fluxes (adding the anthropogenic heat flux (AHF), heat storage capacity and albedo change). In this case, the lowest model level is close to the top of the urban canopy (displacement height), and a new analytical model is suggested for the urban roughness sublayer which is the critical region where pollutants are emitted and where people live.

Table 9.1: Characteristic parameters of the Marseille districts City centre, Collective buildings, Small collective buildings, and Pericentre from BDTopo analysis - Aver = average, VC = Variation coefficient (in %). Compactness is the perimeter ratio of the building and the circle having the same area (Long and Mestayer, Sect. 1.2 in Baklanov and Mestayer, 2004 [33]).

	City centre		**Collective**		**Small collective**		**Pericentre**	
	Aver	*VC*	**Aver**	*VC*	**Aver**	*VC*	**Aver**	*VC*
Built density	0.46	32.8	0.11	53.6	0.14	37	0.38	25.8
Veget. density	0.01	487	0.17	118	0.08	150	0.01	354
Pavement density	0.16	42.7	0.12	58.8	0.15	41	0.14	44.4
Compactness	0.59	11.4	0.65	11.9	0.71	6.8	0.64	7.2
Space (m)	25	70.9	61.3	44.6	43	34.1	23.3	48.5
Height (m)	15.6	29.6	17.2	34.8	8.9	32.4	9.5	32.1
Build. $nb.$ / 4 ha^2	14.7	46.7	9.7	54.3	17.7	38.8	21.7	42.3
Perimeter (m)	175.9	30.2	07.4	34.9	74.9	27.2	118.2	23.8
Volume (m^3)	27444	51.9	9062	63.1	3207	72.4	7949	49.3

2. Alternatively, source and sink terms are added in the momentum, energy and turbulent kinetic energy equation to represent the effects of buildings. Different parameterizations (Masson, 2000 [398]; Kusaka et al., 2001 [354]; Martilli et al., 2002 [393]) have been developed to estimate the radiation balance (shading and trapping effect of the buildings), the heat, the momentum and the turbulent fluxes inside the urban canopy, considering a simple geometry of buildings and streets (3 surface types: roof, wall and road).

In a first stage, three FUMAPEX modules for NWP model urbanisation (Figure 9.5) were developed for further testing and implementation into NWP models or their post-processors. It included the following modules:

1. The DMI module: Based on the first approach, it includes a new diagnostic analytical parameterisation of the wind profile into the urban canopy layer (Zilitinkevich and Baklanov, 2005 [671]) and corrections to the surface roughness (with the incorporation of the displacement height) for urban areas and heat fluxes (adding the additional AHF, e.g., via heat/energy production/use in the city, heat storage capacity and albedo change) within existing physical parameterisations of the surface layer in NWP models with higher resolution and improved land-use classification. It is realised in the city-scale version of the DMI-HIRLAM model.

2. The EPFL module of the Building Effect Parameterisation (BEP): Based on the second approach and the urban surface exchange parameterisation submodel (Martilli et al., 2002 [393]). It was first tested with the research meso-meteorological FVM and TVM models and now is considered for incorporation into the DMI-HIRLAM and LM NWP models.

3. The ECN module: Based on the detailed urban area soil and sublayer SM2-U model (Dupont et al., 2005 [160]). It was first tested with the large eddy simulation SUBMESO research model and is also considered for incorporation into the DMI-HIRLAM NWP model.

Additionally to the above mentioned approaches, the flux aggregation technique of Hasager et al., 2003 [262] was installed in the DMI-HIRLAM model for non-homogeneous surfaces. However, it has not yet been tested for urban areas.

There are also other modules, for instance one of the most detailed parameterisations of urban effects within current numerical models with explicit consideration of the effects of buildings, roads, and other anthropogenic building materials on the urban surface energy budget, was suggested by Masson 2000 [398] in the Town Energy Balance (TEB) scheme.

The main idea of our urban module architecture was to build it as much as possible independently of the type of NWP models, and to allow a simple implementation into different models. Note that it is not possible to build it as a completely independent module, but the urban modules were modified substantially to satisfy the main requirements and formats of NWP models.

There is also freedom on how to implement the module: either to incorporate it inside the NWP model code or to call the separate module from the NWP code. The algorithm to call the module by the NWP model is presented in Figure 9.5. The initialisation module is called only once when the model is initialised for simulations, and then the urban modules (1, 2, 3 or 4) - on every time step during the simulation.

The urban canopy modules can be built as an interface/post-processor module separated from the NWP model. In such case, the urban sublayer model will be run separately (using previously simulated NWP data as a fist approximation) and will improve the meteorological fields in an area close to and inside the urban canopy with higher resolution (cf. one example in Section 9.2.4). Obviously, such a strategy is less promising, because it does not yield any improvement of the meteorological forecast in urban areas and cannot allow feedbacks. For UAQ modelling/forecasting and improvements of UAQIFS, this approach can, however, be very useful and easier to implement, because it does not require any modification of the operational NWP model (which is usually complex and time-demanding). Thus, in such an approach for improving the FUMAPEX UAQIFS strategy, one can consider the urban sublayer modules (including several upper layers and surrounded areas) as interface modules between the NWP and UAQ models.

9.2.3 Approach based on improved urban roughness and fluxes

The first simplest urban module (the DMI module of the FUMAPEX 'urbanization' scheme in Figure 9.5) is based on the following requirements: (i) to be relatively cheap computationally and as close as possible to the parameterisations of the surface/boundary layer in the parent NWP models, (ii) to split the surface layer over urban areas into two/three sub-layers (see Figure 1.10). This split distinguishes: (i) the roughness layer (including logarithmic layers), where MOST can be used with correction to the urban roughness, and (ii) the urban canopy layer, where MOST does not work and new analytical parameterizations for the wind and eddy profiles have to be considered.

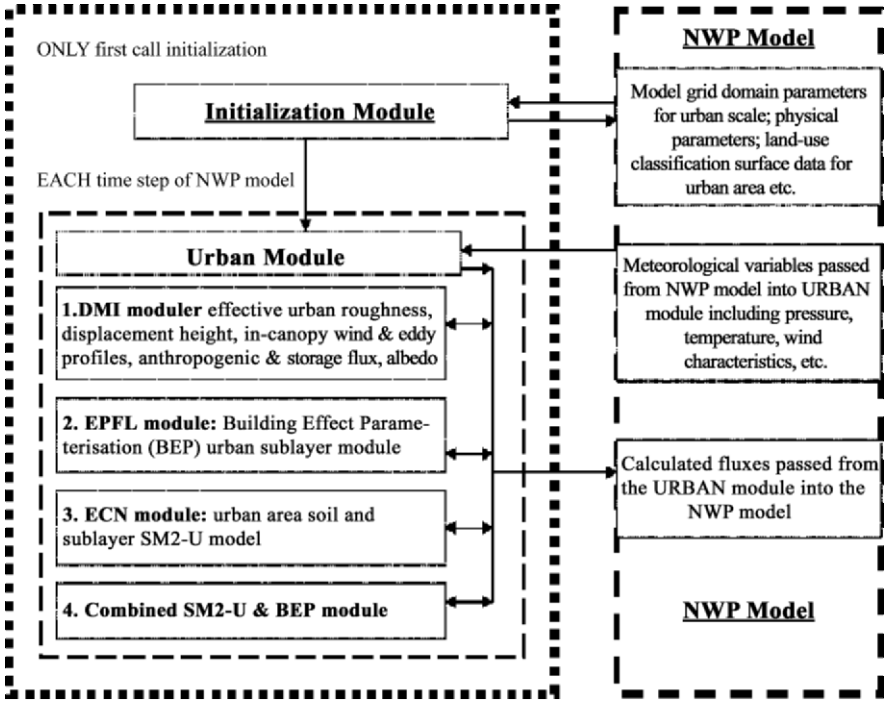

Figure 9.5: General scheme of the FUMAPEX module architecture for NWP model urbanization (Baklanov et al., 2005 [38]).

This module includes algorithms for calculating the following urban parameters for the NWP model and steps for each model grid having urban features:

(i) Land-use classification, including at least one urban class and several urban subclasses;

(ii) Displacement height for the urban (and forest) canopies;

(iii) Urban and effective roughness (and flux aggregation);

(iv) Stability-dependent urban roughness lengths for momentum;

(v) Urban anthropogenic heat fluxes,

(vi) Urban storage heat fluxes by the Objective Hysteresis Model (OHM, Grimmond et al., 1991 [236]) or specific roughness lengths for heat and moisture;

(vii) Albedo correction for urbanised surfaces;

(viii) Prognostic mixing height parameterisations;

(ix) Parameterisation of wind and eddy profiles within the canopy layer.

It is reasonable to use this method for relatively cheap simulations and for NWP models with a low vertical resolution (first computational vertical level higher than 20 m), when other more complex models of the urban sub-layer (e.g., BEP and SM2-U) would not much affect results or would be too expensive for operational forecasting applications. This module, with some simplifications, was implemented and tested

with the city-scale DMI-HIRLAM NWP model for case studies in the Copenhagen metropolitan area and surroundings.

Effect of the urban canopy roughness

The MOST should not be applied inside the urban canopy. Thus, the classical MOST theory with a modified calculation of the urban roughness cannot give a satisfying solution for the urbanisation of NWP model. To avoid or minimise this problem, it is suggested to consider the MOST profiles in NWP models only above an elevated level of the order of the displacement height. Therefore, in the suggested algorithm, the roughness for urban areas is characterised by, at least, two parameters: the roughness length and the displacement height. Theoretical aspects of such an approach were discussed by Rotach [546, 548]), Belcher and Coceal [50], Belcher et al. [51], Zilitinkevich et al. [670] and the COST-715 Action (Fisher et al. [192]).

Roughness parameters for urban areas are calculated by the modified algorithm (see Section 9.2.2) based on the morphological methods. The displacement height is calculated only for grid-cells tagged as urban class following Fisher et al. [192]. The roughness length is calculated for each grid-cell in the following way: (i) constant values in each urban sub-class are tabulated for the urban class; (ii) effective roughness is calculated based on values and percentages of each land-use class and urban subclasses in the cell; (iii) at each time step, the roughness value is recalculated due to effect of temperature stratification.

In the general case of very inhomogeneous surfaces, such as urban areas, in order to include mutual effects of neighbouring cells it would be reasonable to simulate the effective roughness fields for grid-cells of a given city separately for different situations (e.g., for different seasons, wind directions) and to build a kind of effective roughness maps library. For such a strategy, the flux aggregation technique of Hasager et al. 2003 [262] was tested in the DMI-HIRLAM model but at the current stage only for non-urban areas, because there is not enough experimental data to verify urban areas parameterisations and to check the applicability of the linear approximation of the technique for urban conditions.

Nevertheless, most of NWP and meso-meteorological models consider the roughness length as a constant for each grid cell. Experimental data (Arya, 1975 [14]; Joffre, 1982 [321]; Wood and Mason, 1991 [651]) showed that it can depend on temperature stratification. This effect can be considerable especially for very rough surfaces, like the urban canopy. Therefore, using a new stability-dependent parameterisation of the urban roughness length for momentum (Zilitinkevich et al., 2005 [672]), the algorithm includes a recalculation of the roughness for the prevailing stable or unstable stability.

However, just modifying the current rural MOST approaches for urban areas with specific values for the effective roughness lengths and displacement height, still does not solve the main problem, i.e., how to describe the vertical structure of meteorological parameters inside the urban canopy? We can suggest here to apply the new simple heuristic model of Zilitinkevich and Baklanov 2005 [671] (see in Baklanov and Zilitinkevich, 2004 [34]) for the vertical profiles of the momentum flux and the mean wind velocity within the urban canopy. It considers the vertical wind profile inside the canopy (below the displacement height) as an analytical function of the average building height, size and density, as well as of some meteorological parameters.

It is noteworthy that the suggested improvements based on the canopy profile model and displacement height do not required to substantially modify the NWP model itself, because the first computational model level is usually above the canopy, so that the canopy parameterisation can be used only for diagnostic calculation of the wind for higher resolution UAQ modelling outside the NWP model or for diagnosis of 10 m wind in NWP.

Surface energy budget in urban areas

In general, the SEB in urban areas can be written in the following way (Piringer and Joffre, 2005):

$$Q^* = K\downarrow - K\uparrow + L\downarrow - L\uparrow = H + LE + Q_{As} \qquad [W/m^2] \tag{9.1}$$

where Q^* – net all-wave radiation; $K\downarrow$ – incoming shortwave radiation; $K\uparrow = \alpha_0.K\downarrow$ – outgoing, reflected shortwave radiation where α_0 – surface albedo; $L\downarrow$ – incoming longwave radiation from the sky and surrounding environment 'seen' from the point; $L\uparrow = \varepsilon_0\sigma T_0^4 + (1-\varepsilon_0); L\downarrow$ – outgoing longwave including both that emitted from the surface consistent with its emissivity ε_0 and absolute surface temperature T_0, and the reflected incoming longwave;H – turbulent sensible heat flux; LE – turbulent latent heat flux (L is the latent heat of vaporisation); Q_{As} – specific urban anthropogenic surface heat flux. Thus, the urban formulation differs from the non-urban one only by the Q_{As} term.

This formulation is suitable for detailed urban canopy models (see e.g. Sections 9.2.4 and 9.2.5), when the *surface* is just millimetres above ground and the canopy layers are within the simulation domain. For meso-scale meteorological and NWP models in which the *surface* may be high above the urban canopy (average roughness level or displacement height), the SEB can be rewritten in the following form:

$$Q^* = K\downarrow - K\uparrow + L\downarrow - L\uparrow = H + LE + Q_A + \Delta Q_S \qquad [W/m^2] \tag{9.2}$$

where Q_A is the anthropogenic heat flux from sources within the urban canopy and ΔQ_S is an imbalance term, which includes the storage heat flux in the urban canopy elements, the ground and the air layer, extending from the surface to a level where the vertical heat exchange divergence is negligible (i.e., the constant flux layer).

Correspondingly, in the model we need to define and parameterise two new urban terms: Q_A and ΔQ_S as well as the albedo for urban areas.

Urban anthropogenic heat flux calculation

Following estimations of the average anthropogenic heat fluxes (AHFs) for cities in different climatic zones (Oke, 1978 [472]), reference values for a full urban area (100% of urban class; e.g., city centre or high building district) are in the range from 60 to 200 W/m^2, depending on the city size. Information on the spatial distribution of AHFs over a city is not available from monitoring data and is difficult to obtain from measurements (e.g., Pigeon et al., 2005 [496], shows for Toulouse that Q_A estimates are very uncertain and consequently can display negative values during summer months).

Therefore, we suggest calculating the urban AHF based on an assumed dependency on (e.g., proportionality to) other relevant urban characteristics which are available in the models (Baklanov et al., 2005 [38]), e.g.:

1. Population density using maps with a high resolution in urban areas;
2. Nocturnal radiation emissions (brightness) over urban areas based on high resolution satellite images (see Figure 9.6);
3. Land-use classification as a percentage of urban subclasses (central part, urban, sub-urban, industrial, etc.);
4. Emission inventory for specific pollutants typical of urban areas (e.g., NO_x from traffic emissions, etc.);
5. Monitoring or simulation fields of air pollution concentration for such specific pollutants (see above #4).

The first method for AHFs as a function of the population density distribution in urban areas is the one most frequently used and was tested for FUMAPEX NWP models.

For the second method based on the nocturnal brightness of urban areas, it is suggested to use the simple dependence: $Q_A = I_{ln} Q_{Amax}$, where I_{ln} is the normalised light intensity (max value is 1), and Q_{Amax} is a scale (max) value of the AHFs for 100% of urban surface (from 50 W/m^2 for small/medium cities and up to 200 W/m^2 for large mega-cities in industrially developed countries). However, it is important to notice that the brightness of urban areas is different for industrial vs. developing countries, and hence the method should be corrected accordingly. Figure 9.6 displays two examples of the high-resolution satellite images of city lights at night over Europe and Northern America.

The third method using land-use classification as a percentage of urban classes was tested for the Copenhagen and Krakow study in COST-715 (see Piringer and Joffre, 2005 [497]). The anthropogenic part to the urban surface fluxes was approximated according to a coarse urban LUC: (i) 75 W/m^2 for the city centre, (ii) 40 W/m^2 for city periphery areas, and (iii) 20 W/m^2 for other urban-suburban areas.

The last two methods (4 & 5), based on urban emissions or air pollution, can be easily used in atmospheric pollution forecasting models, because such information is usually available in the simulation.

Urban storage heat fluxes

Storage heat fluxes in the urban canopy are considered in our system by two different approaches. First, the heat storage capacity effect can be calculated using specific parameterisations for the temperature and moisture roughness lengths of urban areas. Most of NWP and meso-meteorological models consider for their surface layer profiles that the scalar roughness length, z_{0t}, is equal to the roughness for momentum, z_{0m}. However, for urban areas, they are generally very different (up to 2–3 orders of magnitude). Theoretical studies (Zilitinkevich, 1970 [668]; Brutsaert, 1975 [89]) suggest that the ratio z_{0t}/z_{0m} is a function of the roughness Reynolds number. Thus, the formulation of Brutsaert and Sugita 1996 [91] for example can be suggested for urban areas. However, this and other existing formulations are very uncertain, rarely verified and cannot consider all the mechanisms of the urban heat storage.

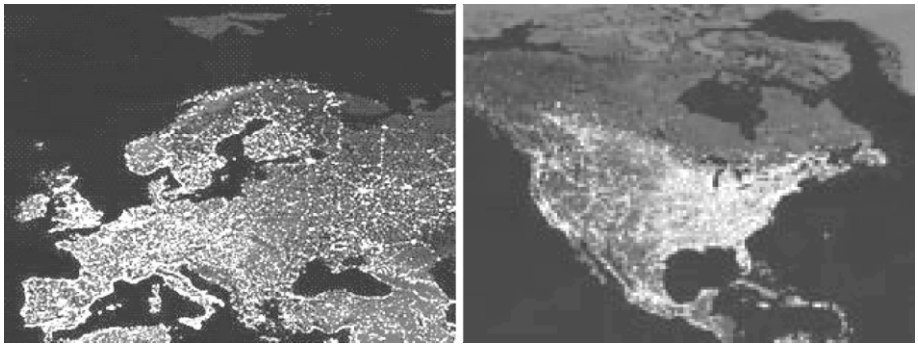

Figure 9.6: Satellite image maps of the night lightness over urban areas of the European countries (left), and Northern America (right) [455].

Therefore, the heat storage in the urban fabrics/buildings, including hysteresis, can be most easily parameterised from the radiation and surface cover information using the empirical objective hysteresis model (OHM) of Grimmond et al., 1991 [236]:

$$\Delta Q_S = \sum_{i=1}^{n} (\lambda_i \alpha_{1i})\, Q^* + \sum_{i=1}^{n} \left(\lambda_i \alpha_{2i}\right) \frac{\partial Q^*}{\partial t} + \sum_{i=1}^{n} \left(\lambda_i \alpha_{3i}\right) \qquad [W/m^2] \qquad (9.3)$$

where the λ_i are the plan fractions of each of the n surface types in the area of interest and the α_{1-3i} are the corresponding empirical coefficients. These α coefficients have been deduced from a re-analysis of the Multi-city Urban Hydro-meteorological Database (MUHD) obtained from ten sites in seven North American cities Grimmond and Oke [237].

Urban albedo effects

Radiative properties (such as albedo and emissivity) of building and ground-covering materials are very different from those of natural grounds and vegetation, while the vertical structure of spaces between buildings provides shade and radiation trapping. In addition, they have not only horizontal but also vertical and/or slanted orientations, which strongly alter the radiative transfers and energy budget. The heat flux to or from the ground changes with surface material: concrete, tarmac, soil, etc. Anthropogenic energy use can be a noticeable fraction of the annual solar input and thus, influences the local air stability.

Sensitivity tests and verification for Copenhagen

Sensitivity tests and verification of this approach of NWP urbanisation were performed by Baklanov et al., [37, 38] using the DMI-HIRLAM research version (1.4-*km* resolution) for the Copenhagen (CPH, Denmark) and Malmo (MAL, Sweden) metropolitan areas and surroundings. Independent runs were performed for several specific cases:

(i) one control run with no modifications in the ISBA surface scheme (Noilhan & Planton, 1989 [469]); (ii) a modified urbanised version including urban roughness (up to 2 m when the urban class is 100% in a grid-cell) and anthropogenic heat fluxes (up to 200 W/m^2).

Following the simulation results (Figure 9.7) it was found that incorporating actual urban **roughness** values modified the structure of the surface layer wind field over urban areas. During daytime, the wind velocities were lower by 1-4 m/s. With a roughness z_{0m} of 2 m, this effect became more visible and pronounced not only near CPH and MAL, but also for other less urbanised areas. At night, this effect was smaller. The average differences in velocities were 2.4 and 2 m/s for CPH and MAL, respectively. For temperature, the urban roughness effect did not contribute significantly compared to the wind effect.

Incorporation of the **anthropogenic heat flux** showed well pronounced differences (starting at 16 UTC) for simulated wind fields over the CPH urban cells. Then, the altered area extended farther inland of the Sjaelland Island, and the difference rapidly increased to 1.5 m/s by 18 UTC. It also became well pronounced over MAL reaching the same value. For MAL, during the late evening - early morning hours the difference became the largest reaching a maximum of 2.1 m/s, and again by 10 UTC no difference was visible. For temperature, AHF increased the temperature above the urban cells, except that it was smaller during the 9-15 UTC-period with a minimum at noon. For both urbanised areas, this increase was on average up to 1^oC (max 2.3^oC) but with a large variance.

The analysis of the diurnal cycle at the urban Vaerlose station (55.77^{o}N, 12.33^{o}E) located in central Copenhagen showed that the diurnal variability of the wind direction was modelled in all runs with practically no differences between the control and modified runs. A similar situation was observed for the suburban Jegersborg station (55.77^{o}N, 12.53^{o}E) and the Kastrup station (55.62^{o}N, 12.65^{o}E) located not far from the seashore (so that urban effects were minimised during the studied day due to eastern winds).

Inspecting the wind velocity daily cycle at an urban station (Fig. 9.8, top) shows that between 07-19 UTC the run with the AHF reflects better the observed local maximum than the run with urban roughness, which alternatively better fits the observed local minimum. This means that the combined effect of both roughness and AHF should be included. It is noteworthy that for the suburban station, the modification including the improved roughness showed a better fit to observational data compared with all other runs. For temperature (Fig. 9.8, bottom), on the other hand, the fit to observations was now better for the urban compared to the suburban station (not shown) for the modified run with the AHF. Modifications of roughness did not improve the fit. Moreover, in this specific example, we did not include the storage heat flux, therefore a time shift of the temperature field is observed in the diurnal cycle, especially during the transitional morning and evening periods. The objective hysteresis model (Grimmond et al., 1991 [236]) improves this shortcoming.

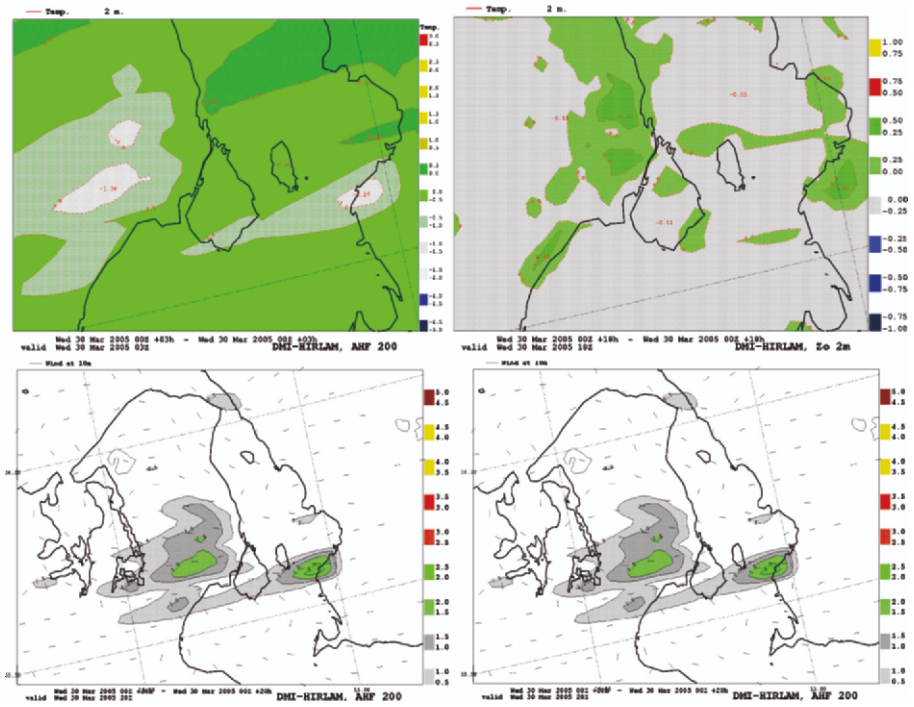

Figure 9.7: Sensitivity tests to urban features with the DMI-HIRLAM high resolution model shown as the difference fields (runs without vs. with modifications) for the 2-*m* temperature (upper row) and 10-*m* wind velocity (lower row) separately with the inclusion of the AHF (left) and urban roughness (right) over the Copenhagen and Malmo metropolitan areas on 30 March 2005.

9.2.4 Building Effect Parameterization (BEP) models for NWP

This Section of the Chapter has been written after Martilli et al., 2002 [393].

The second module option of Figure 9.5 was realised with the Building Effect Parameterization (BEP) model, developed by the Swiss partner EPFL. It includes the urban sub-layer parameterisation suggested by Martilli et al., 2002 [393] with modifications for implementation into NWP models and several further improvements (e.g., Hamdi and Shayes, 2005 [250]; Clappier, Ch. 3.4 in Baklanov and Mestayer, 2004 [33]).

Module description

The aim of the urban sub-layer parameterisation developed at the EPFL (Martilli et al., 2002 [393]) is to simulate the effect of buildings on a meso-scale atmospheric flow. It takes into account the main characteristics of the urban environment:

– the vertical and horizontal surfaces (wall, canyon floor and roofs),

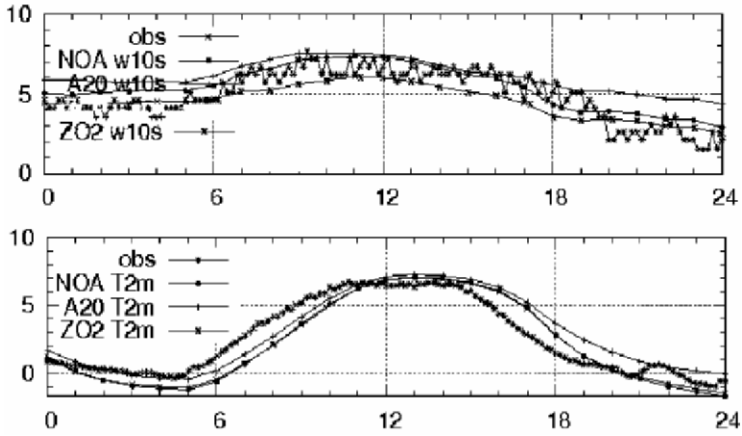

Figure 9.8: Diurnal cycle (30 March 2005) of wind velocity at 10 m (w10s, in m/s; top panel) and air temperature at 2 m (T2m, in deg. ^oC; lower panel) based on the DMI-HIRLAM high resolution control run (NOA), modified runs with added anthropogenic heat flux (max 200 W/m^2) (A20) and urban roughness (max 2 m) (Z02) vs. observational data (obs) at Vaerlose urban station (55.77^{o}N, 12.33^{o}E) located in central Copenhagen (Baklanov et al., [38]).

– the shadowing and radiative trapping effects of the buildings,

– the anthropogenic heat fluxes through the buildings wall and roof.

In this parameterisation, the city is represented as a combination of several urban classes. Each class is characterised by an array of buildings of the same width B located at the same distance from each other (canyon width W), but with different heights H (with a certain probability to have a building with height H, see Figure 9.9). To simplify the formulation we assume that the length of the street canyons is equal to the horizontal grid size. The vertical urban structure is defined on a numerical grid (see Figure 9.9).

In the method developed by Martilli et al., 2002 [393] the contributions of every urban surface type (canyon floor, roofs and walls) on the momentum, heat and turbulent kinetic energy equation are computed separately:

– The contributions of the horizontal surfaces (canyon floor and roofs) are calculated using the formulation of Louis 1979 [379] based on the MOST. The roughness lengths used for this calculation are representative for the local roughness of the specific surface types (roofs or canyon floor) and not for the entire city, as it was considered in the first module (Section 9.3.1).

– The exchange of momentum and turbulent kinetic energy on the vertical surfaces (walls) are parameterised as the effect of pressure and drag forces induced by the buildings. The temperature fluxes from the walls are a function of the difference between the air temperature and the wall temperatures. They are parameterised using the formulation of Clarke 1985 [125] proposed by Arnfield and Grimmond 1998 [13] in their urban energy budget model.

The energy budget is computed for every mentioned surface (canyon floor, roofs and walls):

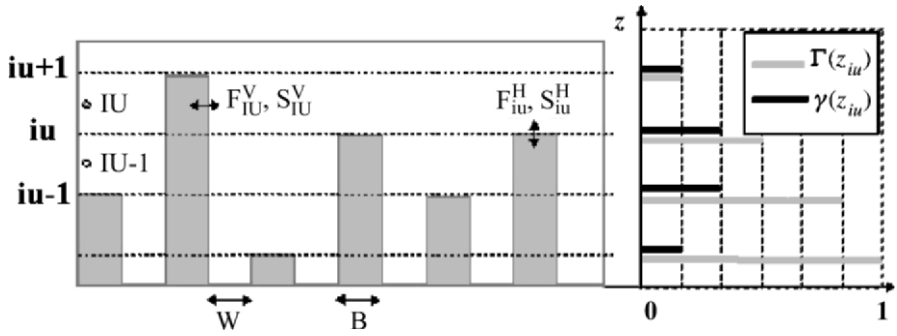

Figure 9.9: Schematic representation of the numerical grid in the urban module. Where W is street width, B is buildings width, iu are the face and IU centre of the urban model levels, $\gamma(z_{iu})$ density of building of height z_{iu} and $\Gamma(z_{iu})$ density of buildings higher than z_{iu} (after Martilli et al., [393]).

– The direct and infrared radiations at the surfaces are calculated to take into account the shadowing and radiative trapping effects of the buildings.

– The surface temperatures of roofs, walls and canyon floor are solved by heat diffusion equation in several layers in the material (concrete or asphalt).

Sensitivity to urban parameters

In order to use the parameterisation of Martilli et al., 2002 [393] in a mesoscale model a number of input parameters have to be evaluated. These parameters characterise the urban environment and they can be classified in three different groups:

– parameters characterising the buildings and streets geometry (street width and direction, building width and height),

– parameters characterising the building and street materials (heat capacity and diffusivity, albedo and emissivity, street and roof roughness length),

– parameters characterising the energy produced inside the buildings (indoor temperature).

These different input parameters producing various effects on the momentum and the energy fluxes, they influence the wind and the temperature (Roulet et al., 2005 [551]).

The wind velocity is mainly affected by the buildings walls drag force, which produces a negative momentum flux. Consequently, highest are the buildings, lower is the wind velocity inside the urban canopy (see Figure 9.10a).

The temperature is influenced by two different energy sources: the anthropogenic sources (building indoor temperature) and natural sources (direct solar radiation and infrared radiation). When the streets are much larger than the buildings, the buildings have almost no effects. The urban area is like a dry smooth ground: the temperatures are especially influenced by the heat capacity, thermal diffusivity, albedo and emissivity of the streets (see Figure 9.11 right).

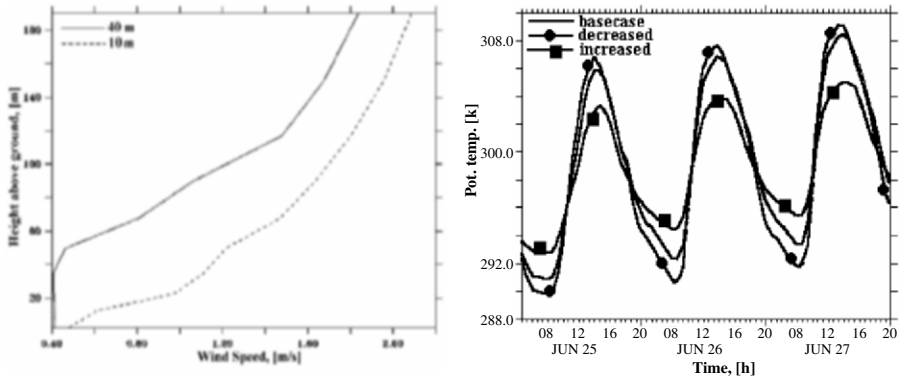

Figure 9.10: Sensitivity of the simulated meteorological fields using the BEP module to urban parameters: a) wind profile simulated with 40 *m* (black line) and 10 *m* (red line) building height; b) Temperature evolution inside the urban canopy for three different street heat capacities: 1.4 (basecase), 14 (line •), 0.14 (line □) $MJm^{-3}K^{-1}$ (EPFL contribution in Baklanov et al., 2005 [38]).

When streets width and buildings width are comparable, the decrease of the night temperatures is attenuated. This can be due to two different effects:

– The radiation trapping between building walls and streets stores the energy inside the urban canopy. Consequently, when buildings are high and streets are narrow the decrease of the night temperatures is low.

– During the day, the energy coming from the sun is always much higher than the energy coming from the buildings. But during the night, the energy produced by the buildings can increase the temperature (if the building is heated). Consequently, the variation of the building indoor temperature will affect the outdoor temperature only during the night (see Figure 9.11 left).

The parameterisation has been tested on the city of Basel (Switzerland), Mexico City (Mexico), Copenhagen (Denmark), and verified versus the BUBBLE experiment (Basel Urban Boundary Layer Experiment: Rotach et al., 2005 [549]). The verification results (Figure 9.11) show that the urban parameterization scheme is able to catch most of the typical processes induced by an urban surface: Inside the canopy layer, the wind speed, the friction velocity and the atmospheric stability are reduced. In the other hand, even if the main effects of the urban canopy are reproduced, the comparison with the measurement seems indicates that some physical processes are still missing in the parameterization. In most of the cases, the model still overestimates the wind speed inside the canopy layer and it can have difficulties to simulate the maximum of the friction velocity which appears above the building roofs.

The urban parameterisation increases the temperature in the urban surface layer and substansionaly improve the air temperature forecast in urban areas (see Figure 9.12).

The BEP module with the Martilli parameterisation was implemented into the Finite Volume Model FVM (EPFL, Martilli et al., 2002 [393]), Topographic Vorticity-Mode (TVM, Schayes et al., 1996 [563]; Hamdi and Shayes, 2005 [250]),

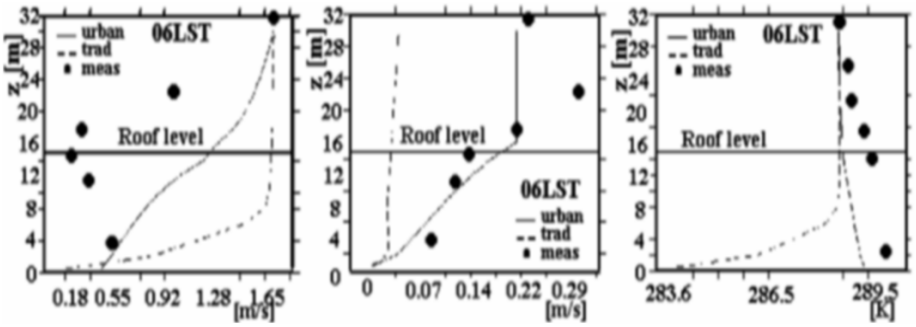

Figure 9.11: Vertical profiles of wind velocity (left), friction velocity (middle), and potential temperature (right) measured (points), simulated with MOST (dashed line) and with the urban parameterization of Martilli et al. 2002 [393] (solid line) (Clappier, Ch. 3.4 in Baklanov and Joffre, [30]).

DMI-HIRLAM (DMI, Baklanov et al., 2005 [35]); and the Local Model (LM) which is used by the Swiss meteorological institute (MeteoSwiss) as the aLMo version. The BEP module was also tested with the aLMo NWP model as an interface/post-processor module, separated from the NWP model. In such case, at the first step, the meteorological fields, produced by aLMo with a 7 $km \times 7km$ resolution, are interpolated onto a 1 $km \times 1$ km grid. At the second step, the meteorological fields are recomputed at the highest resolution solving the momentum, energy and turbulent kinetic energy budget in the boundary layer and in the surface layer using BEP (Baklanov et al., 2005 [38]).

The urban parameterisation developed by Martilli et al., 2002 [393] shows a clear capacity to improve the results of NWP models (like LM or HIRLAM) by taking into account the effect of urban areas. However, the parameterisation should be further tested using different cities and longer periods.

9.2.5 The soil model for sub-meso scales: the urbanised SM2-U model

The third module (see Figure 9.4) modified and tested for the urbanisation of meso-meteorological models includes the detailed urban area soil submodel SM2-U (Soil Model for Sub-Meso scales Urbanized version) module, developed by the ECN team (Dupont, 2001, Dupont et al., 2004, 2005 [157, 158, 160]; Mestayer et al., 2004 [428]).

Model description

The SM2-U model (Dupont and Mestayer, 2004 [158]; Dupont et al., 2005 [160]) is based on the force-restore model of Noilhan and Planton 1989 [469] for the transfers between the atmosphere, one vegetation layer, and three soil layers in its most recent version, ISBA-3L (Boone et al., 1999 [66]). It keeps the principal characteristics of this "soil" model and was developed as a pre-processor for fine resolution sub-mesoscale simulations. The surface dynamic influence is represented through roughness lengths

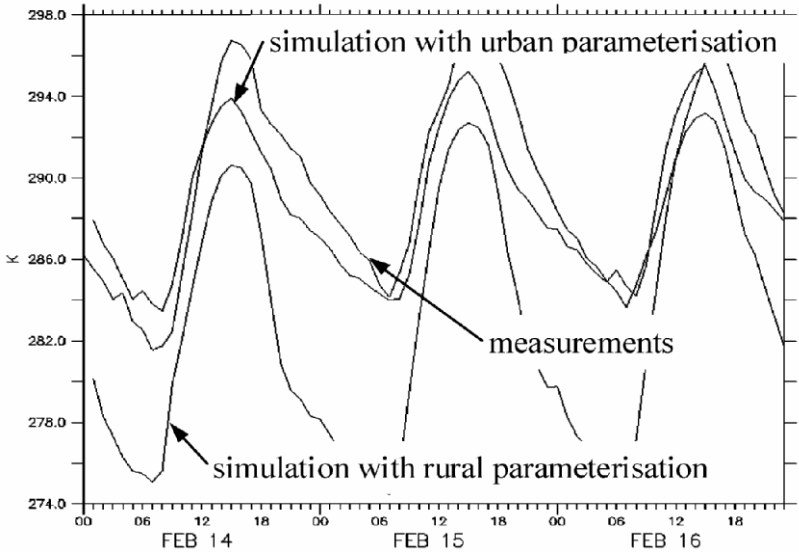

Figure 9.12: Temperature measured and simulated with and without the BEP urban parameterization over Mexico City. The simulation without the urban parameterization underestimates the temperature (Clappier, Ch. 2.16 in Baklanov, 2003 [29]).

and displacement heights. Except radiation reflections and water runoff from saturated surfaces, the horizontal exchanges inside the urban canopy are not explicitly simulated, considering that the effects of wind advection between urban surfaces is accounted for by the atmospheric model above, due to the fine spatial resolution of the computational grid (100-1000 m).

SM2-U separates 8 types of surfaces (see Figure 9.13), namely: bare soil without vegetation (denoted "*bare*"), bare soil located between sparse vegetation elements (*nat*), vegetation over bare soil (*vegn*), vegetation over paved surfaces (e.g., trees on the road side: *vega*), paved surfaces located between the sparse vegetation elements (*pav*), paved surfaces located under the vegetation (*cova*), building roofs ($roof$), and water surfaces (*wat*). Three soil layers are considered: a surface layer for the natural surfaces (nat+vegn and bare), allowing evaluation of the evaporation fluxes from the bare soils; a root zone layer representing the influence area of the vegetation roots; and a deep soil layer used as a water reservoir for dry periods. Roof surfaces are considered fully impervious while paved surfaces are semi-impervious, letting water infiltrate downwards but not upwards. The model includes the constants for 11 soil classes, 11 vegetations, 3 water bodies, 4 roof materials, and 2 paved surface materials.

The time evolution of surface temperature T_{si} in each cell appears as the sum of a forcing term due to the heat storage G_{si}, and to a relaxation term towards the equilibrium with the deep soil temperature T_{soil}:

$$\frac{\partial T_{si}}{\partial t} = C_{Tsi} G_{si} - \frac{2\pi}{\tau}(T_{si} - T_{soil}) \quad for \quad i \in \{bare, nat, vega, vegn\}, \tag{9.4}$$

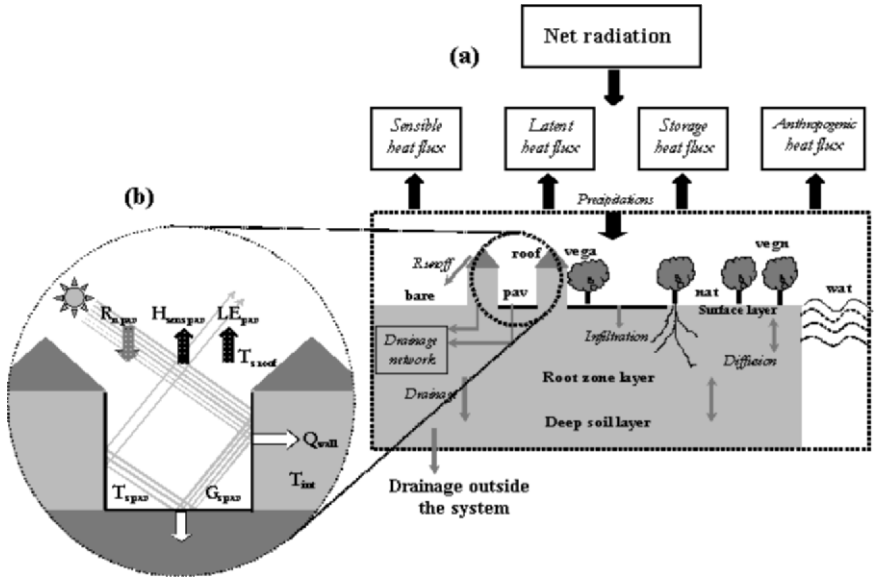

Figure 9.13: Scheme of the SM2-U energy and water budget models: (a) with 7 surface types (pav, bare, nat, roof, vega, vegn, wat) and 3 soil layers. (b) Energy budget of paved surfaces.

where $C_{Tsi}(= \rho_S c_S)$ is the inverse of the surface layer heat capacity and the parameter $\tau = 86400$ s is the day duration. Inversely the deep soil temperature is determined by a return-to-equilibrium equation towards the temperature average of all surfaces in contact with the soil. In this budget the anthropogenic heat flux Q_F may include contributions from vehicles and heat flux through building roofs. The time evolution of the surface layer water content wi is calculated with a similar force-restore equation adding a forcing term due to precipitation and a relaxation term towards equilibrium with the deep soil water content at equilibrium between capillarity and gravity forces.

The three-dimensional structure complexity of the urban canopy is not explicitly simulated at the sub-grid scale: the horizontal effects are expected to be taken into account by the fine resolution of the computational grid, but the canopy vertical dimension influence is accounted for by parameterisation relationships. The building walls are integrated in the paved surface temperature and energy budget equations. Schematically, this consists in solving the energy budget of a street canyon (Figure 9.13) instead of paved horizontal surfaces alone. Thus, T_{spav} corresponds to an effective average temperature of street canyon surfaces while the heat stored by walls and the radiative trapping, which are the principal effects of the canopy thickness, are integrated in the paved surface energy budget. The building walls are actually considered in three ways: first by modifying the surface atmospheric resistance to the heat flux (to account for heat stored by walls); second by modifying the energy budget to include the heat flux through the walls; third by considering the radiative trapping inside the streets by means of a corrective factor to the paved surface albedo, called street canyon effective albedo.

This effective albedo depends on the individual wall and paved surface albedos, the street aspect ratio, and the sun position with respect to the average street axis direction. The computation of the street canyon effective albedo is similar to Masson's 2000 [398] as shown by Dupont et al., 2005 [160]. The effective emissivity of the street canyon is that of the paved surfaces.

SM2-U has been implemented in SUBMESO, a high-resolution atmospheric model developed on the basis of the Advanced Regional Prediction System (ARPS) Version 3 (Xue et al., 2000 [660], 2001 [661]) by Dupont 2001 [157] and in MM5 by Dupont et al., 2004 [159]. Its transposition, implementation and test with operational NWP models (e.g., DMI-HIRLAM, LM) and UAQIFSs is part of the EU-project FUMAPEX (Baklanov and Mestayer, 2004 [33]).

Model validation and test

For a rural area, while ISBA determines only one surface temperature, SM2-U distinguishes vegetation (T_{svegn}) and bare soil (T_{snat}) surface temperatures. This modification has been introduced to allow the evaluation of vegetation influence on paved as well as natural surfaces. Indeed, computing a single temperature for a paved surface and vegetation would be erroneous, since they behave so differently. The representation of sparse vegetation mixed with artificial-surfaces is then as realistic as possible, especially in alternative scenarios of micro-climatology. This modification in the original part of the model generates computational changes in the calculation of the mean surface temperature, sensible and latent heat fluxes: this has been validated against the experimental data from HAPEX-MOBILHY and EFEDA campaigns (Dupont et al., 2005 [160]). The urban hydrological components of the model have been validated against the experimental data obtained during ten years at the Reze suburban site in the Nantes urban area (Berthier et al., 2001 [61]), with tests both on an annual scale and for stormy events (Dupont et al., 2005 [160]). Finally the energy budget urban parameterisations have been validated for a densely built city centre against the measurements of Grimmond et al., 2004 [239] at the Marseilles central site during the campaign UBL-ESCOMPTE (Mestayer et al., 2005 [429]), in a forced mode without soil-atmosphere feedback (Dupont and Mestayer, 2004 [158]), showing an excellent agreement on average.

Figure 9.14 (Dupont et al., 2005 [160]; Baklanov and Mestayer, 2004 [33]) shows examples of simulations with the SM2-U soil model obtained for 4 typical European districts, city centre, residential, industrial-commercial, and high-rise building districts, with their average mixture of building densities, bare and paved soils, and vegetation cover over natural or semi-impervious surfaces. These simulations were obtained without feedback from the lower atmosphere. Feedback effects are currently studied in the ESCOMPTE-simulations for Marseille and idealised cities. Figure 9.14 demonstrates the influence of building density and district structure not only on the magnitude of the heat fluxes but also on the phase lag between the energy budget components, which is a key factor in the urban heat island process: in the first half of the day a large amount of heat is diverted from the budget and provisionally stored in the artificial ground and building materials, at the expenses of the sensible heat, while in the evening and at

night these materials, warmer than air, release the stored heat to provide the nocturnal positive sensible heat flux.

Based on these validation simulations, a series of additional simulations were performed (Baklanov et al., 2005 [38]) to assess the impact on the heat fluxes of the wall parameterisations representing the canopy influence. At first the effective albedo and emissivities of the street canyon were replaced by those of the street canyon floor, i.e. asphalt albedo and emissivity. Most of the results were identical; the main impact is an increase in the root mean square difference between measurements and simulations but the averaged diurnal cycles are very similar to those of Figure 9.14. The net radiation is slightly lower during the day due to the larger albedo (0.08 for the pavement and only 0.04 for the effective albedo at midday) while the replacement of the effective emissivities (0.97 and 0.99, for the atmospheric absorption and infrared emission, respectively, in the basic simulations) by the asphalt emissivity (0.94) has little impact due to compensating influences. The further simulations differ either in aggregating the two layers of the artificial surfaces (roofs, walls and pavements) in only one layer with the same (averaged) transfer coefficients or in suppressing the walls. With one averaged layer the model does not reproduce well the early morning warming of the artificial surfaces because the layer is too thick, impeding the model fast response to environmental forcing variations; in the case when this unique layer has the same thickness as the first, surface layer of the base case the model does respond rapidly to the forcing variations but does not simulate well the amount of heat stored in the artificial materials, because the layer is too thin. Thus, two layers for representing artificial surfaces appear as a necessary compromise, whereby the first thin layer allows the model fast response, and the second layer ensures the storage capacity. When the walls are not simulated, the sensible heat fluxes are much less well simulated: the stored heat is smaller during the day, which results in a larger daytime sensible heat flux and a smaller nocturnal heat release inducing a negative nocturnal sensible heat flux.

After validation of the model, the large eddy simulations employing the SUBMESO model with the urban soil layer model SM2-U were performed for the model domain covering the Danish Island of Zealand and including the Copenhagen metropolitan area (Mahura et al., 2005 [389]). Monthly and diurnal cycle variability were studied for the net radiation, sensible and storage heat fluxes, surface's temperatures, and others. These were evaluated for selected urban vs. non urban related types of covers/surfaces and urban districts such as city center, high buildings, industrial, and residential. Results showed strong effects of urban features on temporal and spatial variability. They are useful and applicable for verification of numerical weather prediction models and development of urban canopy parameterizations.

As seen in Fig. 9.15,a, during this month the maxima of the mean air temperature in CC/HBD and ICD occurred at noon and one hour earlier compared with the RD and non urban areas. Moreover, on a diurnal cycle, the maximum difference between air temperatures in mentioned areas was less than 0.8^{o}C. The diurnal cycle of the mean water vapor specific humidity is shown in Fig. 9.15,b. As seen, the CC/HBD cells had the lowest values compared with all other cells. In opposite, for the non urban areas, the values are the highest.

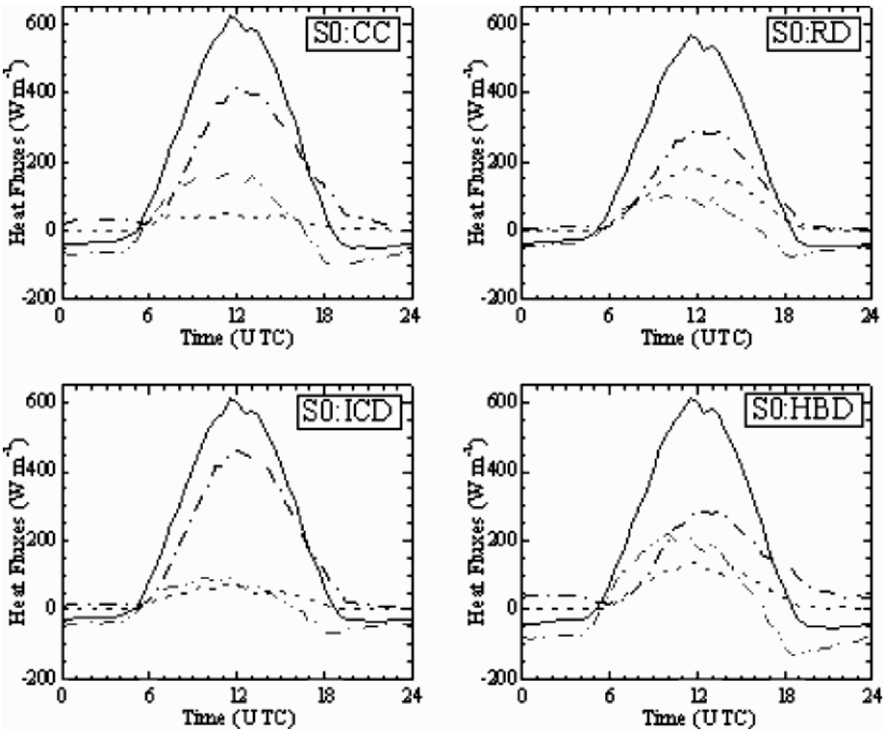

Figure 9.14: Energy budgets over four typical European urban districts (from Dupont et al., 2005 [160]): CC, city centre; RD, residential district; ICD, industrial-commercial district; HBD, high building district. The simulation corresponds to an average diurnal cycle in July in Nantes, France, and S0 indicates no surface-atmosphere feedback computation. The curves —, depict net radiation flux; – – – –, latent heat flux; – · – · –, sensible heat flux; and – · · – · · –, storage heat flux.

9.2.6 Conclusions and recommendations

Different parameterisations of the urban sublayer for NWP and urban-scale meteorological models have been analysed and several options for the integrated FUMAPEX urban module usable with NWP models have been suggested (Baklanov et al., 2005 [38]). The first version of the module includes three main submodels, which can be chosen depending on the specific problem, model resolution or city area:

1. Corrections of the surface roughness for urban areas and urban heat fluxes (adding the anthropogenic heat flux, heat storage capacity and albedo change). This can be complemented with an analytical model for wind velocity and diffusivity profiles inside the urban canopy (Zilitinkevich and Baklanov, 2005 [671]; Baklanov et al., 2005 [38]).

2. The urban sub-layer model BEP (Martilli et al., 2002 [393]; Hamdi and Schayes, 2005 [250]) with special physical parameterisations of the urban surface exchange for the urban sub-layer implemented into (or after) the NWP model.

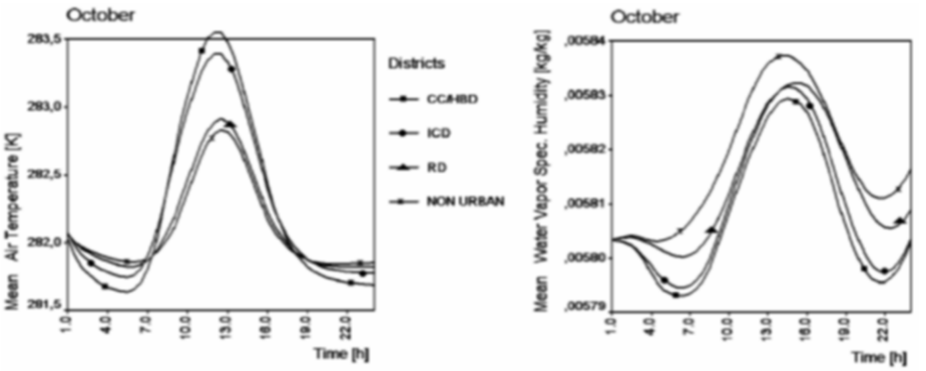

Figure 9.15: Diurnal cycle (in October) variability of the mean a) air temperature and b) water vapor specific humidity for the city center/high building district (CC/HBD), industrial commercial district (ICD), residential district (RD), and non urban areas of Copenhagen, Denmark (Mahura et al., 2005 [389]).

3. The SM2-U full force-restore soil submodel for urban areas (Dupont and Mestayer, 2004 [158]; Dupont et al., 2005 [160]; Mestayer et al., 2004 [428]).

The fourth combined module, including all non-overlapping mechanisms from the SM2-U and BEP models, is under development.

It is shown (Baklanov et al., 2005 [38]) that the implementation of the urban modules can significantly improve the forecasted meteorological fields for urban areas. The first approach (module 1) is the most cheapest way of the model urbanisation and can be easily used in operational NWP models as well as in GCM/RCMs (Global/Regional Climate Models). The second approach (module 2: BEP) is relatively more expensive ($\sim$ 5-10 % computation time increasing), but it gives a possibility to consider the energy budget components and fluxes inside the urban canopy. However, this approach is sensitive to the vertical resolution of NWP models and is not very effective if the first model level is higher than 30 meters, therefore it requests increasing the vertical resolution of current NWP models. The third approach (module 3: SM2-U) is considerably more computationally expensive than the two first modules, however it gives a possibility to study accurately the urban soil and canopy energy exchange including the water budget. Therefore the second and third approaches are recommended to use in advanced urban-scale NWP and meso-meteorological research models. The third module (SM2-U) can be very useful for implementation into research submesoscale or micro-meteorological models (e.g., SUBMESO) for LES or assessment (non-prognostic) studies.

Results with these modules showed that the radiation budget does not differ significantly for urban and rural surfaces, as the increased loss of net thermal longwave radiation is partly compensated by a gain in net shortwave radiation due to a lower albedo. The turbulent fluxes of sensible and latent heat, as well as their ratio are variable, depending in particular on the amount of rainfall that fell during the preceding period. The storage heat flux usually is significantly higher in urban areas compared to densely vegetated surfaces. This cannot be explained entirely by a higher thermal

inertia, as this quantity is only slightly higher for urban as compared to rural environments. Other factors of importance are the low moisture availability and the extremely low roughness length for heat fluxes. The anthropogenic heat flux is a most typical urban energy component as it is absent over rural or natural surfaces.

One sophisticated way to simulate the storage heat flux for urban areas can be realised using the BEP (Section 9.2.4) or SM2-U (Section 9.2.5) modules. One goal is to simplify the parameterisation of the storage heat flux in NWP models simulations for the main types of urban areas and concentrations of urban elements. Using these modules can give a possibility to suggest a simplified classification of the urban storage heat fluxes for the main urban classes to be used in NWP models.

Further improvements in NWP and UAQ forecasting systems

The next step of the project will be the intercomparisons of urban modules with(in) the NWP models (such as HIRLAM and LM) and their verification with respect to urban meteorology forecasts.

The urban canopy models considered in this paper can be also implemented as an interface / post-processor module, separated from the NWP model. In this case, the urban sublayer model will be run separately, using ready NWP data as a first approximation, and will improve the meteorological fields in an area close to the urban canopy and inside the canopy with higher resolution.

Such an approach has of course a clear drawback as it does not improve the meteorological forecast for the urban area and does not allow feedbacks. However, for urban air pollution modelling/forecasting and improvements of the UAQIFS, this approach can be very useful and easier to realise, because it does not request any modification of the operational NWP model (which are usually very difficult and time consuming). This approach for improving the FUMAPEX UAQIFS strategy thus consider the urban sublayer models (together with several upper layers and surrounded areas) as interface modules between the NWP model and UAQ model.

The current versions of the urban modules, considered in the paper, have several shortcomings and have to improved and further developed. For the first approach (module 1), the complemented analytical model for wind velocity and diffusivity profiles inside the urban canopy (Zilitinkevich and Baklanov, 2005 [671]) have to be tested with different NWP models and meteo-preprocessors, and to be carefully verified versus experimental data for different regimes. Besides, it is advisable to extend this model for the temperature and humidity profiles as well. The second module (BEP) in the current version does not consider the moisture and latent heat fluxes and completely considers the anthropogenic heat fluxes, therefore they have to be incorporated into a new version of the BEP module. Besides, recalculation of fields on lowest sub-layers is necessary. The third module (SM2-U) need to be further developed by consideration of the building drag effect (it is realised in the module 4) and snow and ice have to be included in SM2-U to make it suitable for NWP during winter periods especially for northern areas. The existing version of the module, when SM2-U is running for every grid-cell, is too expensive for operational NWP models, therefore the module has to be optimised by calling only for the urban cells.

It is obvious that these developments in process parameterisations and model resolution require more and more adequate data for validating, improving and initialising NWP or meso-meteorological models. There is the need for carrying out urban field campaigns in the future to provide data from which insights may be drawn in order to devise simpler models and parameterizations for complex models. The existing measurements have limitations which arise due to inescapable constraints on field programmes in cities (Baklanov et al., 2005 [38]). There is a real need for long measurement runs, so that a variety of conditions are sampled, and that instrumental techniques can be compared against each other. Potential of remote sensing methodologies and satellite observations should also be better exploited.

9.3 Applications to emergency preparedness for urban areas

This Section has been prepared in cooperation with the Danish ARGOS team: J.H. Sorensen (DMI), S. Thykier-Nielsen, T. Mikkelsen (Riso NL), S. Hoe (DEMA) and A. Mahura (DMI).

9.3.1 Introduction

Nuclear, biological, and chemical (NBC) emergency preparedness and early warning systems require forecasting of the atmospheric transport and deposition of harmful matter and estimation of possible environmental, radiological, health and/or other consequences. The quality of the meteorological and wind flow data for such emergency forecasts, especially in urban landscapes, is one of the most important issues. The possibility of terrorist actions involving dispersion of NBC harmful agents (e.g., dirty bombs) or actions against nuclear or chemical industry objects has considerably increased the needs for improvement of the NBC emergency preparedness systems with higher resolution for urban areas and considering urban features of different scales.

Meteorological fields constitute a main source of uncertainty in urban air quality (UAQ) forecasting models, especially for the NBC emergency preparedness purposes. Historically, UAQ and numerical weather prediction (NWP) models has been developed separately, and there is a little or no tradition for co-operation between the modelling groups. For the long-range transport models in nuclear emergency preparedness systems, operational NWP data has been used during the last two decades (cf. e.g. Galmarini et al., 2004 [200]; Graziani et al., 1998 [233]). But previously the resolution of such data was not suitable for the urban scale, and the NWP models did not consider urban features. Recently the situation is changed, and it is obvious that a revision of the conventional conception of UAQ forecasting is required. Besides, nowadays it becomes possible to downscale or integrate such city-scale meteorological models with micro-scale obstacle-resolved models for separate districts or blocks of buildings (see e.g. Fig. 9.2).

The main problem in forecasting urban air contamination (UAC) is the simulation of accidental release dispersion in the urban canopy or episodes with high pollutant

concentrations in urban areas. In these areas most of the well-known methods and models, based on in-situ meteorological measurements, fail to realistically produce the wind flow structure and meteorological input fields for the UAC models. Many efforts have been devoted to develop UAC dispersion models and to improve knowledge about contaminants and source terms. However, no significant efforts are made so far to improve forecasts of wind-flow structure and meteorological parameters in UAC models. This is especially important for air contamination in situations with low winds, stable stratification, local air circulations, complex topography, street canyons, breeze conditions, and internal boundary layers.

The applicability of different urban wind-flow and meteorological models for UAC emergency modelling depends on types of the risk sources and releases, the scale of the dangers, and purposes of the model use (i.e. for emergency forecasting or risk assessments).

9.3.2 Possible risk sources

Different applications of urban-scale meteorology and wind-flow models to the emergency preparedness systems and issues for city areas can be considered many types of accidental NBC releases in urban or agricultural canopy areas. Possible threats and risks of terror actions in such areas may include: 1) radionuclide releases due to accidents at nuclear power plants, "dirty bombs", nuclear tests explosions, etc.; 2) bio-terror actions; 3) chemical harmful releases due to different kind of accidents or terror acts.

The radioactive releases can be very different in the radionuclides composition (isotopes, gases, and aerosol forms), release type, and scale. Thus, it is relevant to have a classification of main categories of releases (Baklanov and Sorensen, 2002 [27]):

(i) nuclear weapons including "dirty bombs" (atmospheric, underground, and underwater explosions),

(ii) nuclear power plants (normal exploitation; accidental releases for different levels of accidents and types of reactor);

(iii) nuclear vessel reactors (accidents with obsolete or operational submarines/ships for different accident types);

(iv) reprocessing plants (normal exploitation or different accidents);

(v) resuspension of radioactive particles (mining activity or contaminated areas, depending on soil type, recultivation measures, etc.);

(vi) emission and formation of natural radioactive aerosols (radon decay products, etc.).

Important issue for urban dispersion modelling is the characteristics of the release, e.g., radiochemical composition, density for gases, size distribution for aerosols, etc. For radioactive aerosols the particle size distribution (e.g., number of modes, distribution type, average diameter and standard deviation for each mode, density, and nuclides) varies significantly for different release types and from one nuclide to another. The particle size spectrum could be very broad, e.g. 0.001-200 μm.

The information about the source term for a dirty bomb scenario (as well as other types of accidental releases) is a very uncertain issue. In many studies modellers consider roughly estimated parameters of the release, based on literature data and a realistic

value of the release strength, composition of nuclides, and size distributions (e.g., a "dirty bomb" scenario described by Sohier and Hardeman, 2005 [583]). As another option a unit release of ^{137}Cs and other main isotopes could be considered at the first stage of forecasting and further scaled when relevant data about the release strength become available. Therefore, it is important to develop models of air flow and release dispersion in urban areas not only for the direct problem of the contamination forecast or assessment, but also for the source-term estimation using monitoring data and inverse models based on the adjoint equations and variational approach (see Section 9.3.4).

Chemical accidental releases can be very harmful and very active, therefore, the chemical transformation is an important part for emergency modelling. For heavy gases it is important to consider the equations for transport of dense gases and dispersion and transformation equations should be integrated with air flow models including the feedbacks (see e.g., Nielsen, 1998 [467]).

Biological warfare agents are alive microscopic organisms including viruses, bacteria, and mycotoxin producing fungi (Sorensen, 2005 [588]). By e.g. inhalation a human being can acquire an infection dose, which subsequently may propagate in the body causing sickness or death. For some agents, e.g. pneumonic plague and small pox, secondary infection from person to person may take place. In such cases even a small initial bio-terror attack may end up involving a large number of infected people. Other agents like anthrax are not associated with secondary infection.

Biological warfare agents may be spread by use of different release contraptions. These comprise e.g. envelopes containing say 10 g anthrax spores, firework type rockets carrying a load of 100 g up to 100 m above ground where the rocket disintegrates and disperses the load, aggregates spreading aerosols from airplanes or helicopters, and missiles carrying around 500 kg of agents. It has been estimated (Sorensen, 2005 [588]) that 100 kg anthrax spores dispersed under optimum conditions from an airplane in the Middle East may cause between one and three million deaths.

Biological emergencies include naturally occurring diseases and epidemics, and the use of biological warfare agents e.g. in terror actions (Sorensen, 2005 [588]). National meteorological services may have an important role with respect to corresponding emergency response activities. This is due to the fact that certain diseases involve airborne spread, often in combination with other routes of infection. Contrary to most other routes, e.g. spread by direct contact between individuals, the atmospheric dispersion of infective material, e.g. exhaled aerosols, is uncontrollable, but predictable. Thus, real-time assessment of the airborne dispersion of infective material, utilising the available meteorological data, may be helpful to emergency management authorities.

Airborne spread of contagious aerosols at sufficient concentration to infect may take place over long distances provided the following requirements are fulfilled:

1. high liberation of contagious material (virus, bacteria etc.) to the atmosphere,

2. high degree of stability of the contagious material in the atmospheric environment,

3. small infectious inhalation doses required to infect.

Due to the possibility of carrying out experiments on animals, animal diseases are well studied. Airborne animal diseases involve e.g. Foot-and-Mouth Disease (FMD) and Aujeszky's Disease (Gloster and Alexandersen, 2004 [232], Sorensen, 2003 [587]).

9.3.3 Modelling of urban air flows and release dispersion for emergency preparedness

In general sense for emergency preparedness in urban areas it is necessary to realise the modelling of air dynamics and release dispersion in the urban boundary layer. The modelling of airborne transport and contamination in such areas includes the following three main components: (i) modelling of meteorological fields and air flow structure, (ii) modelling of pollutant transport, diffusion, deposition and chemical (or physical, e.g., radioactive decay, aerosol formation) transformation, (iii) possible interaction and feedbacks between the air flow and pollution (e.g., heavy gas dispersion).

Types and simplicities of the models for urban emergency preparedness, first of all, depend on the two main issues: (i) scales of the considered processes, and (ii) aim of the modelling (as a risk assessment or operational forecasting tool).

Depend on the scale of risk / danger three main types of the models are considered: 1) meso- or city-scale, 2) district scale obstacle-resolved, and 3) separate building (group of buildings) outdoor and indoor coupled models. Models in each of the above mentioned types are different for the operational forecasting vs. risk assessment items.

City-scale models

Meso- and city-scale meteorological models or wind fields models, used with emergency preparedness modelling systems for assessments and forecasting aims, are usually similar to the models used for NWP or in the urban air quality information and forecasting systems (UAQIFS). The availability of reliable UAQIFS with urban scale weather and pollution forecasts could be of relevant support for emergency management:

(i) accidental radioactive or toxic emissions,

(ii) potential terrorist attacks with NBC matter releases, etc.,

(iii) fires, etc.

Therefore, the already discussed meteorological model types, methods of their urbanisation, nesting technique and the conclusions, discussed in the previous Section 9.3.2 are relevant here as well, so we send the reader to Sections 9.2.2–9.2.6 and do not repeat them here.

Most of the models for the city scale are not obstacle-resolved, therefore they have to parameterise or simplify the urban structure. Many meso-meteorological models (such as MM5, RAMS, HIRLAM, LM) are used for emergency preparedness for both prognostic and diagnostic modes. Several modelling systems use also diagnostic wind-flow models, e.g. LINCOM (Astrup et al., 1996 [16]; Mikkelsen et al., 1997 [433]), with meteorological observation data or for the higher resolution downscaling using lower resolution NWP data as input. Diagnostic methods are cheaper, but show less promising results for forecasting mode (Baklanov et al., 2002 [28]).

For the research or assessment mode, the models can be more sophisticated, including the large eddy simulations (LES) or other high-order turbulence closure models, down-scaling with obstacle-resolved computer fluid dynamics (CFD) tools, but such models are very expensive computationally (see e.g., Mahura et al., 2005 [389]). For the forecasting mode, the models have to be fast enough; therefore, they use

parameterisations for the urban surface layer (see Section 9.2.3)) or simplify dramatically the formulations of the atmospheric boundary layer (ABL) equations.

The potential use of improved NWP forecasts for nuclear emergency management in urban areas in case of releases of hazardous radioactive matter from nuclear accidents or terror acts were considered and demonstrated by Baklanov et al., 2005c [39]. Such use of urban-scale NWP model data is tested with the Danish nuclear emergency preparedness decision-support system, the Accident Reporting and Guidance Operational System (ARGOS) (Hoe et al., 1999, [269]; 2002 [270]) for the Copenhagen metropolitan area. DMI is running an experimental improved city-scale version of the DMI-HIRLAM meteorological forecast model (see Section 9.2.3) over Denmark including the Copenhagen metropolitan area with a horizontal resolution of 1.4 *km*, and thus approaching the city scale. This involves 1 *km* resolution physiographic data with implications for the urban surface parameters, e.g. surface fluxes, roughness length, and albedo. These data are operationally used by ARGOS in case of terror acts or accidents in Denmark or surroundings for simulation of hypothetical atmospheric releases of toxic or radioactive matters. By using the Local Scale Model Chain (LSMC), developed at the Riso National Laboratory (Mikkelsen et al., 1997 [433]), ARGOS can calculate forecasts of radioactive doses and concentrations. The main item for this work in FUMAPEX was to improve urban high-resolution NWP model forecasting data for the Copenhagen metropolitan area and to make it available for the ARGOS emergency preparedness decision-support system. The scenarios included hypothetical releases of radioactivity, e.g., from the Barseback nuclear power plant, which is located only 20 *km* away from the Copenhagen city centre (Baklanov et al., 2005 [39]).

To demonstrate the improvements of the ARGOS emergency preparedness system for the Copenhagen metropolitan area, let us consider a "dirty bomb" scenario (as described by Sohier and Hardeman, 2005 [583]) with radioactive release from town of Hillerod (located close to Copenhagen). The source was 137Cs released at a constant rate of 1011 Bq/s within the 15 minute interval. For the meteorological situation considered, the hypothetical release took place from 00:00 to 00:15 UTC on 19 June 2005. In Figure 9.16 the corresponding local-scale plume from the hypothetical atmospheric release, as calculated by RIMPUFF/ARGOS using meteorological data from the urbanised DMI-HIRLAM-U01 (resolution of 1.4 *km*) and operational -T15 (resolution of 15 *km*) models and visualised by ARGOS, is shown. 250 *m* resolution land orography data were used for the ARGOS simulations. Figure 9.17 shows the differences in the ABL heights, simulated for the same two versions of DMI-HIRLAM and considered in the above ARGOS simulations. The urban heat island effect, considered by the urbanised version U01, on the ABL height over Copenhagen, Malmo, and other Danish and Swedish cities (marked by arrows) is visible in Figure 9.17a. The ABL height, which is also the mixing height for air pollutants, effected considerably the air concentration and deposition levels of the contaminants.

The sensitivity of the dispersion pattern on the meteorological data (operational non-urbanised vs. urbanised) is considerably higher: the differences in the dispersion lead to different levels of contamination over the city areas and to different areas contaminated by the plume (Baklanov et al., 2005 [39]).

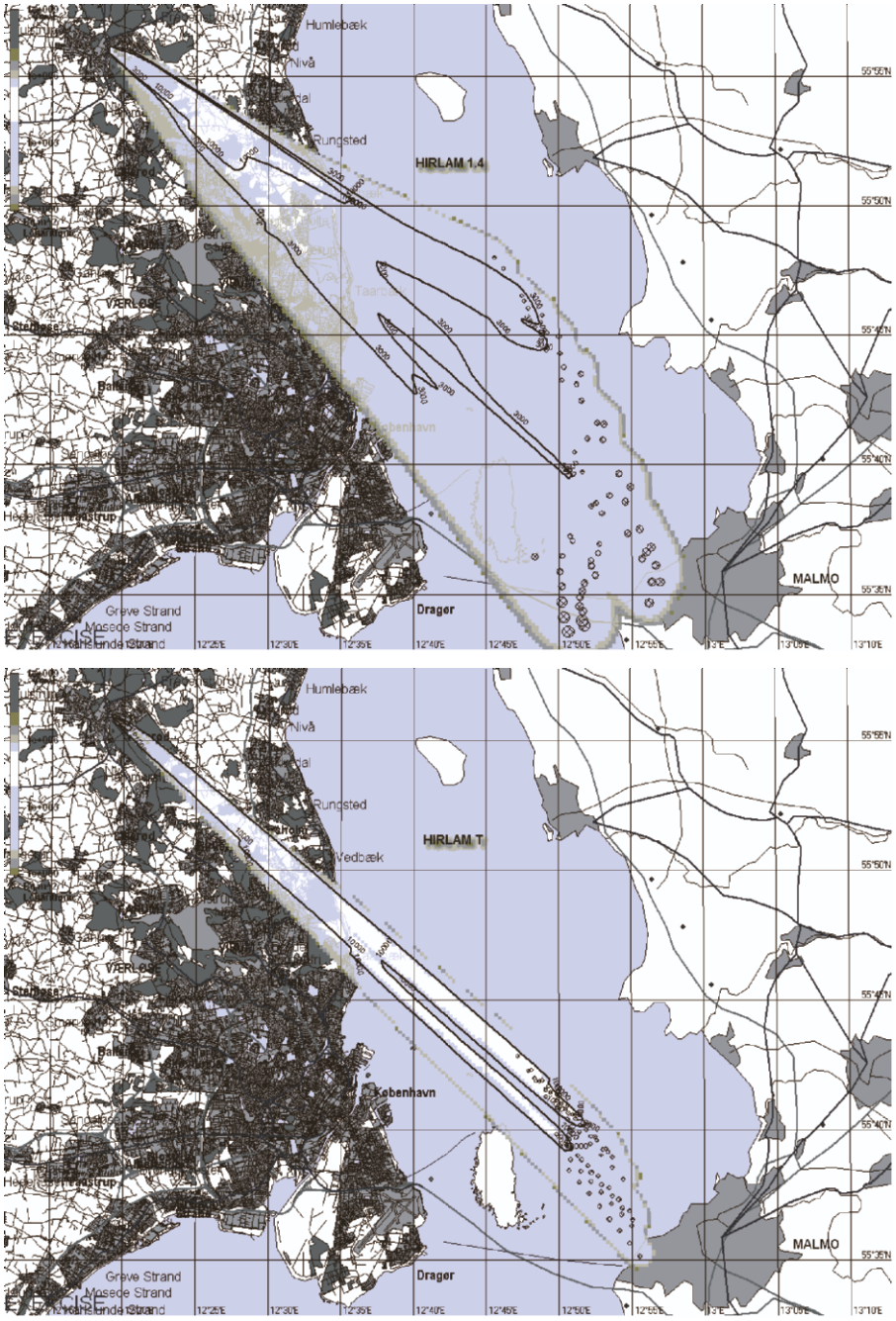

Figure 9.16: Local-scale plume from the ^{137}Cs hypothetical accidental atmospheric release (00:00-00:15 UTC, 19 June 2005) at Hillerod, as calculated by RIMPUFF using DMI-HIRLAM and visualised by ARGOS for the Copenhagen metropolitan area. Air concentration of ^{137}Cs for different DMI-HIRLAM models: a) urbanised U01, and b) operational T15.

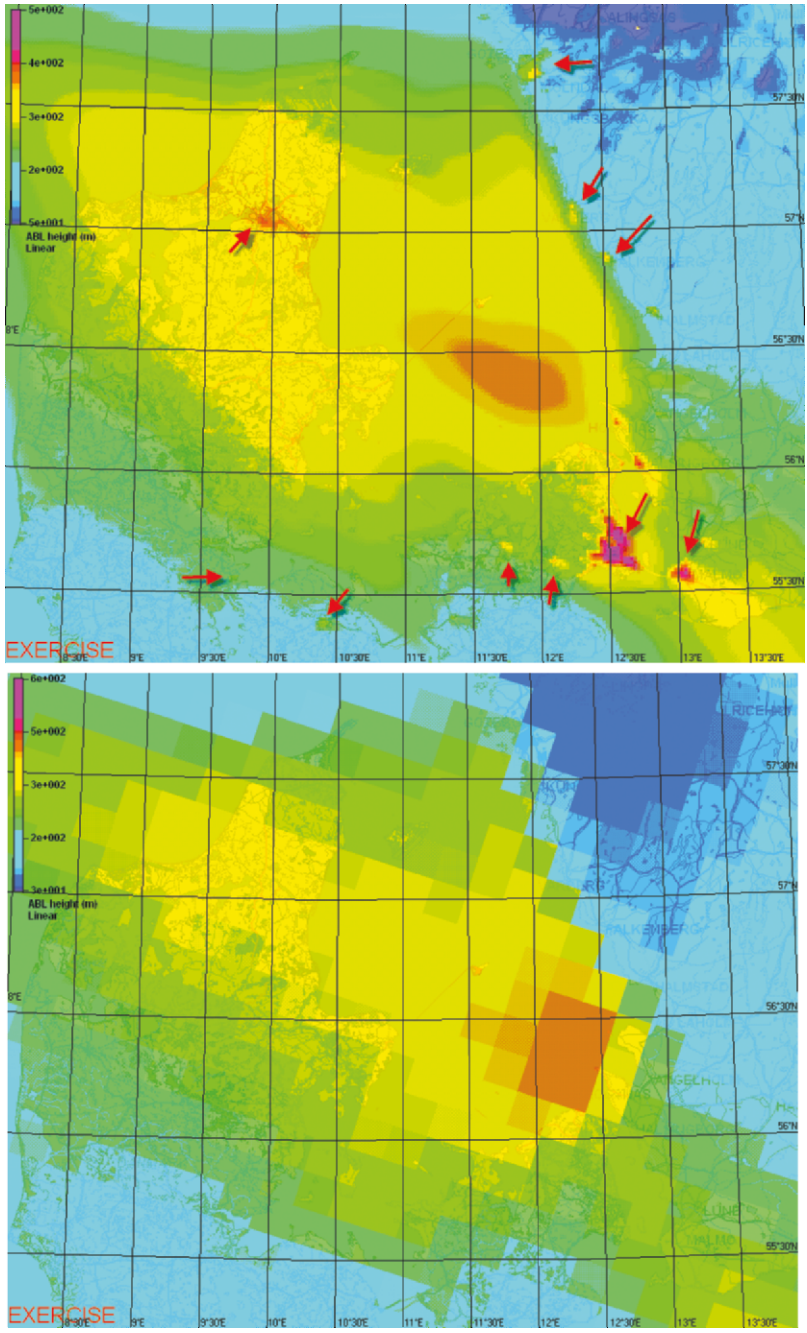

Figure 9.17: The atmospheric boundary layer height over Denmark and surroundings as calculated from DMI-HIRLAM models: a) urbanised U01, and b) operational T15. Main cities are shown by arrows (Baklanov et al., 2005 [39]).

Micro-scale models

Recently there has been an increasing interest of modelling the dispersion of toxic material in local-scale urban areas. The use of increasingly powerful computers enabled the development of tools that have the potential to predict flow and transport processes within the urban canopy layer resolving the individual buildings and street canyon structure (Schatzmann, 2005 [562]). These new tools are micro-scale meteorological models of prognostic or diagnostic types. Prognostic models are based on the Reynolds-averaged Navier-Stokes (RANS) equations, whereas diagnostic models are less sophisticated and ensure only the conservation of mass. These two model types are presently supplemented by even simpler engineering tools. It is to be expected, however, that the latter will sooner or later be replaced by RANS codes or even more complex LES models.

Models have begun to play an important and often dominant role in risk assessment and urban emergency planning studies that are undertaken to investigate and to quantify the effects of accidental releases or other activity on air quality. Their increasing use, however, is paralleled by a growing awareness that the majority of these models has never been a subject of rigorous evaluation. Besides, most of them are too expensive for the operational use in case of the emergency preparedness.

The possibility of a release in an urban environment signifies the importance of having fast robust urban dispersion models available. Comprehensive models involving e.g. CFD and LES are probably not feasible in real time. Due to the influence of the urban environment on the meteorology, it is important to make use of urban-scale numerical weather prediction model data.

Therefore, for emergency forecasting in the local-scale of urban areas very simplified dispersion models with simply urbanised meteo-preprocessors are still used (see, e.g., overview by Hanna et al., 2004 [259]; Britter and Hanna, 2003 [81]; Britter, 1998 [79]). A brief overview of such urban dispersion models is given below:

• AERMOD (Cimorelli et al., 2004 [123]) is the US EPA's updated Gaussian-type plume model for application to industrial and other local sources at downwind distances (less than about 20 km). It automatically handles urban areas through inputs of surface roughness length and building geometries. It assumes nearly-neutral or convective conditions in such areas. Geometry information is usually input only for the buildings near the source.

• Baseline Urban Dispersion Model (Hanna et al., 2003 [257]) is also a Gaussian-type model, using observed average wind speeds in the urban area and assuming nearly-neutral to convective stabilities at all times. Turbulence is parameterized using UBL relations. A key assumption is that, even at low wind speeds, the lateral turbulent velocity does not drop below 0.5 m/s. The latter assumption results in a wide plume spread during light winds.

• BLM (Barrio Logan Model) (Venkatram et al., 2004 [633]) is a Gaussian-type model based on simple parameterizations of the UBL and dispersion in the urban area. It assumes an initial size to the plume due to mixing behind buildings near the source. It assumes that observed wind speeds and turbulence are available from some height above the average building height.

• HPAC (Hazard Prediction Assessment Capability) (DTRA, 2001, 2004 [153, 154]) is a multipurpose code that could be described as a Gaussian puff model. It is widely used for non-urban areas in U.S. Department of Defense (DOD) applications and has been previously evaluated for several field experiments (Chang and Hanna, 2004 [113]). The latest version (DTRA, 2004 [154]) includes also the urban algorithms. HPAC incorporates UDM (Hall et al., 2002 [248]) for distances less than 2 *km*, after which it switches to its standard puff dispersion algorithm.

• SUDC (Simple Urban Dispersion Correlation) (Neophytou and Britter, 2004 [459]) is a one-line urban model formulation developed using observations from several urban field and laboratory experiments. The relation, which states that C/Q is proportional to x^2, has been developed for the range x/H_b less than about 60, where H_b is an average building height.

• UDM (Urban Dispersion Model) (Hall et al., 2002 [248]) is a widely-used model developed by the UK Defence Science and Technology Laboratory (DSTL) based on assumptions of a Gaussian shape and empirical parameterizations developed from special field and laboratory experiments involving obstacle arrays.

The verification of the above mentioned six urban dispersion models versus the Salt Lake City Urban 2000 field data (Allwine et al., 2002 [7]) is analysed by Hanna et al., 2004 [259] and presented in Figure 9.18. The points represent maximum hourly-averaged C/Q for each of 18 trials and 7 monitoring arcs.

In Denmark, for example, a group consisting of representatives for the Danish Emergency Management Agency (DEMA), the Danish National Centre for Biological Defence (NCBD), the Riso National Laboratory and DMI has created the layout for an emergency preparedness system. It deals with the spread of material from Chemical, Biological, Radiological and Nuclear accidents in urban areas. Riso focuses on implementing and developing RIMPUFF (Mikkelsen et al., 1984 [432], 1997 [433]) and UDM (Brook et al., 2003 [84]) models within the ARGOS system. Parameter studies for realistic urban scenarios have been made using release data for nuclear (dirty bombs) as well as biological (anthrax) materials (Thykier-Nielsen and Griffiths, 2005 [614]). Figure 9.19 presents an example of the consequence simulations of dirty bomb dispersed in urban environment by the UDM model by Risoe and Dstl (Thykier-Nielsen and Griffiths, 2005 [614]).

Further work for comparing different models with wind tunnel experiments and their improvement is required. The main weak point of all the above mentioned simple models is that the models' wind flow does not follow building structure. Therefore, the canalling effects (a very important for street canyons) are not reproduced in the models. Instead for the building effects they use an extra dispersion and porosity (e.g., dispersion coefficient corrections and puff splitting) approach, which is very limited. As seen from Figure 9.19, the plume 'penetrates' the buildings, but does not flow round them. Besides, urban sub-layer wind profiles and fluxes are not considered in most of these models.

Further improvements of such simple models can be focused on combined wind-flow and dispersion models (e.g., Soulhac and Perkins, 2005 [594]) considering the building structure. However, such obstacle-resolved numerical models (e.g., CFD) are very expensive computationally for emergency preparedness forecast purposes. Therefore, a simplification of urban structure is necessary. It could be realised by

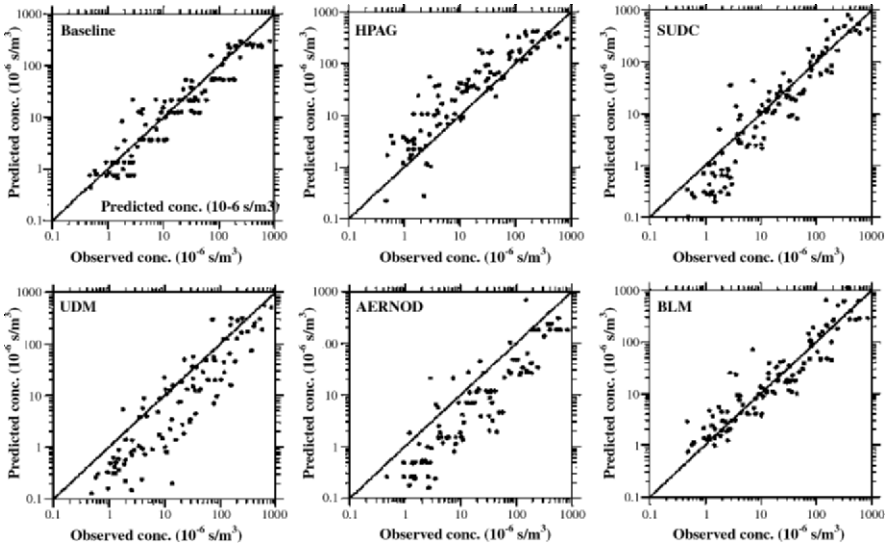

Figure 9.18: Scatter plots of predicted by the above mentioned models versus observed (Salt Lake City Urban 2000, Allwine et al., 2002) maximum hourly-averaged C/Q for each trial and monitoring arc. In general, the largest C/Q values are on the closest arcs (Hanna et al., 2004 [259]).

simple models of potential streaming around the nearest buildings and urban meteo-preprocessors with a parameterisation of the urban effects for longer distances: after 2-3 lines of buildings behind the release. Urbanised high resolution NWP data (see Section 9.3.2) are also relevant for such models.

For research and assessment simulations of NBC agents dispersion, where the CPU time is not a critical issue, different CFD codes and models are broadly used (see Chang and Meroney, 2003 [111]; Vardoulakis et al., 2003 [630]). For example, the Swedish Defence Research Agency (FOA/FOI) uses the PHOENICS code for urban risk assessment modelling, e.g., different scenarios of industrial pollution, accidental releases between buildings, acts of terror, etc. (Burman, 1997 [94]; Baklanov, 1997 [22]; Baklanov et al., 1997 [23]). This code is a general-purpose software package which predicts quantitatively:

- how fluids (air, water, steam, oil, blood, etc.) flow in and around: the engines, process equipment, buildings, human beings, lakes, river and oceans, etc.;
- the associated changes of chemical and physical composition;
- the associated stresses in the immersed solids.

One example of the risk assessment of ammonia intoxication (caused by plant wreck in town conditions) by the PHOENICS CFD model (Mastryukov and Ivanov, 2002 [399]) is presented in Figure 9.20.

Several CDF codes were also used for combined outdoor street canyon air flow and pollution and in-door ventilation. One of such problem-oriented CFD modelling systems was developed by Baklanov (1988 [21], 2000 [24]) and Amosov and Baklanov 1992 [10]. It included the following assumptions, possibilities, and applications:

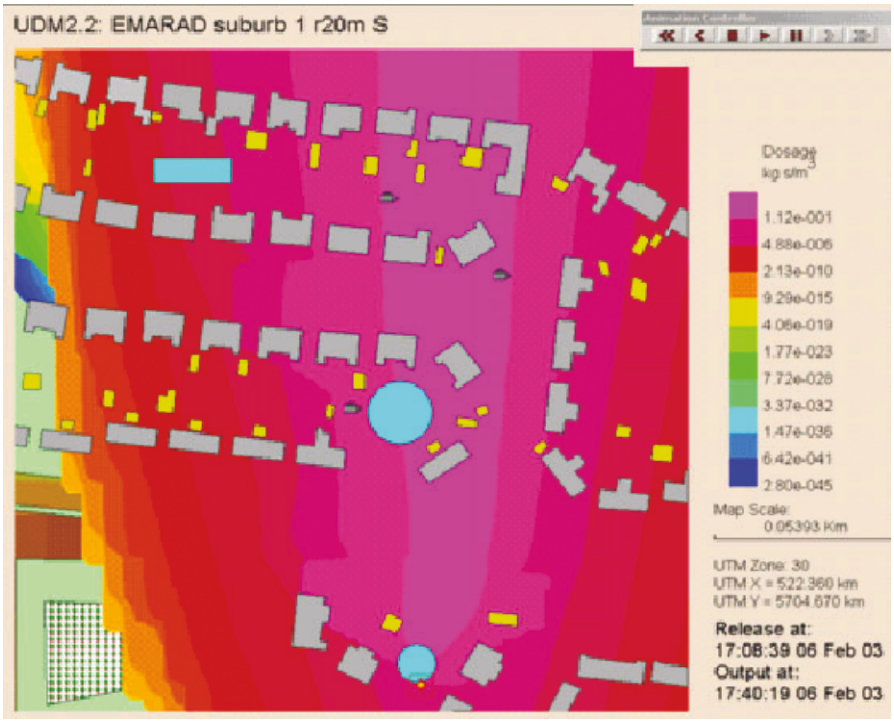

Figure 9.19: Modelling the consequences of dirty bomb dispersed in urban environment by the UDM model. Simulated total dose ($kg\ s/m^3$) (Thykier-Nielsen and Griffiths, 2005 [614]).

- 3D compressible air dynamics and air pollution,
- Complex geometry by the method of fiction domains and σ-coordinates,
- Sub-grid turbulence closure, modified $k-\varepsilon$, k-l models,
- Radiation and thermal budget of arbitrary oriented surface,
- Artificial and ventilation sources of air dynamics and circulation,
- Urban/industrial air flows and pollution problems,
- Indoor air dynamics and ventilation,
- Microclimate and pollution mountain valleys and circuses,
- Mining ventilation and microclimate of open pits.

In general CFD models show a good applicability for risk assessments in urban areas; however, their results can differ depending on turbulent closure models and other assumptions (Schatzmann, 2005 [562]). For practical applications these models contain a substantial amount of empirical knowledge, not only in the turbulent closure schemes but also in the use of wall functions and in other parameterisation schemes. To cast doubt on the results is perfectly justified, as it was shown by systematic studies in which applications of the same model by different modellers to a given problem (Hall, 1997 [244]) and applications of different models by either the same or different modellers to the same problem (Ketzel et al., 2002 [332]) revealed significant differences.

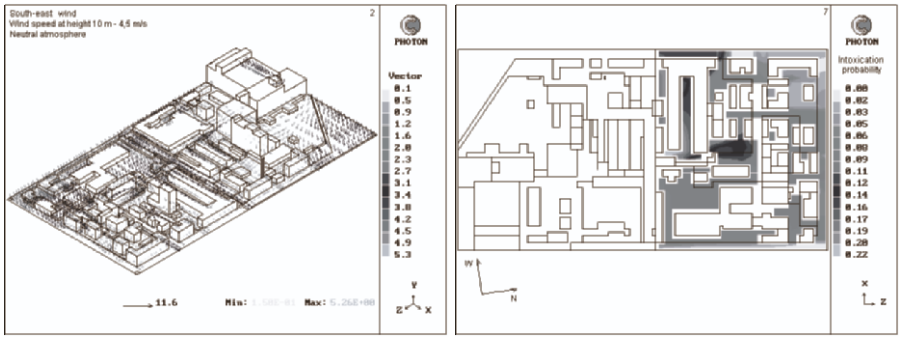

Figure 9.20: PHOENICS example study: risk assessment of ammonia intoxication (Mastryukov and Ivanov, 2002 [399]). Scheme of the building complex and 6 m height horizontal wind velocity fields (left). Emergency produced damage and potential danger fields of the initial response on the intoxication (right). Summation of each damage field with "weight" coefficients representing the realization probability of a relevant wind direction, speed range and atmospheric stability.

Nevertheless, these models are used in the preparation of decisions with profound economic and political consequences. The main objective of the current COST Action 732 (Schatzmann, 2005 [562]) is to improve and assure the quality of micro-scale meteorological models that are applied for predicting flow and transport processes in urban or industrial environments.

Many CFD models, based on the RANS equations, use the standard $k - \varepsilon$ turbulence models, which were originally developed for hydro-dynamical engineering problems. For example, for urban canyons this model with the linear stress-strain relation is violated in complex flow and have to be improved using nonlinear two-equation turbulence models (Ehrhard et al., 2000 [165]). On the upper levels of the boundary layer it strongly overestimates the eddy profile (Baklanov, 2000 [24]). Numerous modifications of $k - \varepsilon$ model just adjust data for specific regimes, but do not provide a good theoretical background. LES models show a substantially better correspondence with measurement data in urban areas (e.g., Walton et al., 2002 [640]) and have good perspectives. But they are more expensive, and therefore, their usage is limited.

9.3.4 Source-receptor problem and inverse modelling

In many cases due to unknown or uncertain parameters of the release, the estimation of source term characteristics, based on environmental pollution monitoring, is a very important issue for emergency response systems. For example, after the Algeciras accident in Spain (30 May 1998) many European monitors measured peaks of air radioactive contamination, but during several days the reason was unknown. Similar situations had happened after the Chernobyl and many others "man-made" accidents. After 11 September 2001 this problem became potentially more important due to the risk of possible terrorist actions followed by atmospheric releases of dangerous NBC matters.

A combination of the forward and inverse modelling approaches allows to solve some environmental and nuclear risk problems more effectively compared with the traditional ways based on the forward modelling. For the inverse modelling problem, most of the western scientists (Persson et al., 1987 [491]; Prahm et al., 1980 [509]; Seibert, 2001 [569]) use the common back- trajectory techniques, suitable only for the Lagrangian models. The Novosibirsk scientific school established by G.I. Marchuk in Russia has suggested a fruitful theoretical method for inverse modelling, based on adjoint equations (Marchuk, 1982 [391], 1995 [392]; Penenko, 1981 [486]) and suitable for the Eulerian models. This approach has further been used and improved by several authors (Baklanov, 1986 [20], 2000 [25]; Pudykiewicz, 1998 [512]; Robertson and Lange, 1998 [538]) for estimation of source-term parameters in the atmospheric pollution problems.

Penenko and Baklanov 2001 [487] described some new aspects of the simulation technique, based on variational principles and adjoint equations, and applicable for Eulerian and Lagrangian models. This methodology is based on both direct and inverse modelling techniques. Variational principles combined with decomposition, splitting and optimization techniques are used for construction of numerical algorithms. The novel aspects are the sensitivity theory and inverse modeling for environmental problems which use the solution of the corresponding adjoint problems for the given set of functionals. The methodology proposed provides optimal estimations for objective functionals, which are criterion of the atmospheric quality and informative content of measurements. Some applications of the suggested methods for source parameters and vulnerability zone estimations are discussed by Penenko et al., 2002 [488] for different regions with environmental risk sites.

Adjoint equations with an original algorithm of illumination / smoothing of measurement functions are considered in (Issartel, 2003 [309]).

Let's consider the problem of source term estimation in case of NBC accidental contamination with unknown release parameters (e.g. co-ordinates, time period and strength). The estimation is based on monitoring data and inverse modelling by the adjoint problem methods. Suppose that several monitoring stations of a radiological monitoring network measured unexpected picks of air pollution concentration or radioactivity. The modelling and measurement area (10×15 km^2) with positions of 10 monitoring stations for measuring meteo-parameters and air pollution during the experiment is given in Baklanov, 2000 [25]. The results of the inverse simulation - the source location probability density function (isolines), and velocity vector fields - are shown in Figure 9.21. As seen, the release source position was estimated quite qualitatively (difference between co-ordinates of the maximum of the probability density function and the release site was less than 1 km), using the inverse adjoint modelling based on measurement data from the monitoring sites.

9.3.5 Concluding remarks

Recently there has been an increasing interest of modelling the dispersion of toxic material in local-scale urban areas. Types and simplicities of the models for urban emergency preparedness, first of all, depend on two main issues: (i) scales of the considered processes, and (ii) aim of the modelling (as a risk assessment or operational forecasting tool).

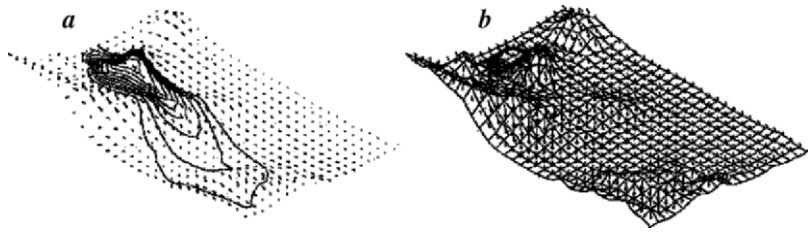

Figure 9.21: Example of source term estimation, based on the forward (a) and inverse (b) local-scale modelling in a case of accidental contamination from an unknown release (Baklanov, 2000 [25]). Simulated wind fields and isolines of: a - air pollution concentration in surface layer based on forward modelling; b - probability density function base on the adjoint problem.

Depending on the scale of risk / danger three main types of the models are considered: 1) meso- or city-scale, 2) district scale obstacle-resolved, and 3) separate building (group of buildings) outdoor and indoor coupled models. These models are different for the operational forecasting vs. risk assessment items.

Meso- and city-scale meteorological models or wind fields models, used with emergency preparedness modelling systems for assessments and forecasting aims, are usually similar to the models used for NWP or in the urban air quality information and forecasting systems (UAQIFS). Most of the models for the city scale are not obstacle-resolved; therefore, they have to parameterise or simplify the urban structure. The availability of reliable UAQIFS with urban scale weather and pollution forecasts could be of relevant support also for emergency management (see conclusions in Section 9.3.2).

The use of increasingly powerful computers enabled the development of tools that have the potential to predict flow and transport processes within the urban canopy layer resolving individual buildings and street canyon structure. These new tools are micro-scale meteorological models of prognostic or diagnostic types for emergency forecasting or risk assessments.

In general CFD models show a good applicability for risk assessments in urban areas; however, their results can differ depending on turbulent closure models and other assumptions. Many CFD models, based on the RANS equations, use the standard k-e turbulence models (originally developed for hydro-dynamical engineering problems), which are violated in complex flow in street canyons and have to be improved and further verified. LES models show substantially better correspondence with measurement data in urban areas and have good perspectives in future, but they are more expensive computationally, and therefore, their usage is limited.

For emergency forecasting in the local-scale of urban areas very simplified and fast dispersion models with slightly urbanised meteo-preprocessors are still used. Further improvements of such simple models can be focused on combined wind-flow and dispersion models considering the building structure. However, such obstacle-resolved numerical models (e.g., CFD) are very expensive computationally for emergency preparedness forecast purposes. Therefore, a simplification of urban structure is necessary.

It could be realised by simple models of potential streaming around the nearest buildings and urban meteo-preprocessors with a parameterisation of the urban effects for longer distances: after 2-3 lines of buildings behind the release. Urbanised high resolution NWP data (see Section 9.3.2) are also relevant for such models. Further work for comparing different models with experiments and their improvement is required. The main weak point of all discussed simple models is that the models' wind flow does not follow the building structure.

In many cases due to unknown or uncertain parameters of the release, the estimation of source term characteristics, based on environmental pollution monitoring, is a very important issue for emergency response systems. A combination of the forward and inverse (adjoint) modelling approaches allows to solve such environmental risk and emergency management problems (e.g., source-term estimation) more effectively compared with the traditional ways based on only the forward modelling.

Conclusion

Flows of air and water associated with complex geometries were reviewed and discussed in this book. The geometries of interest may be extremely different in their types and in the obstructions that constitute them. An immense array of leaves and branches occurs in forests, or in agricultural fields. These form a highly porous medium for air flow, with a wide range of quantities of importance for biosphere, where a variety of biotic activity takes place. This penetrable array is called "the canopy" by micrometeorologists, see Chapters 4 and 5.

Active and vital biological life also occurs within aquatic vegetation. If this vegetation is deeply submerged in the water flow, it affects the flow in a similar manner to terrestrial canopies. Emergent riverine vegetation is also often met in practical hydraulics problems and may also be considered as a "canopy", Chapter 6. Distributions of flow properties in vertical sections, the vertical-plane hydraulic problem, and the horizontal-plane hydraulic problem, Sections 1.2.1 and 1.2.2, distinguish between different aspects of the aquatic and terrestrial canopies. Chapter 6, however, shows a link between them.

Both of the above types of canopy are characterized by a very small fraction of the total canopy volume, so that canopy modelers can generally neglect this volume not occupied by the fluid. The same concept relates to many other types of "obstructed geometries" such as droplet layers, Sections 1.4 and 3.2, windmills, Section 1.4 and bubble flows, Section 7.5. Despite their diversity, many of these flows may, nevertheless, be united by the fact that one needs to account for both the internal decelerated flow within the obstructed geometry and for the external free flow over it. Field experiments in natural forests or in agricultural canopies, in wind tunnels with simulated forests of urban settlements and in water flumes with simulated aquatic vegetation have discovered many common features of these flows. These features are formalized in mathematical models.

The fraction of the total canopy volume that is not occupied by the fluid cannot be neglected for urban building array geometries. However, extensive investigations and measurements have shown many common features with the other canopy flows. Therefore, some of the discoveries made in canopy flow studies have also been successfully applied to "urban canopies".

A consistent theory for the phenomenon of "canopy flows" has been developed over the last twenty five to thirty years. It arose from studies of flows around single isolated obstacles and now accounts for the effects of groups of obstructions and with models for particular canopy types.

Two types of theoretical models of motion within obstructed geometries have been noted in this book. One type considers the way in which the flow and associated exchange processes are affected by individual obstacles and their wakes. The other concentrates more on representation of groups of obstacles along the canopy and in the vertical direction. Introduction of the mass force that represents such canopies in mathematical models ensures a uniform mathematical treatment of all the above flows. This force represents "closeness", or density, of the obstructions. Similar, source/sink terms are required to solve related heat exchange and diffusion problems. The idea of the "distributed force" provides a link with classical hydromechanics theory of roughness and so the canopies may be also called "penetrable roughness", Chapters 1 and 3. The penetrable roughness model showed that as the flow enters and leaves the canopy over a limited length it significantly influences the mixing and exchange processes in the obstructed geometry. Both concepts lead to idealized calculations, but both have the capability of being combined and extended.

The distributed array of drag elements in a penetrable roughness or canopy, creates a mean wind profile that contains an elevated shear layer near the canopy top that resembles closely a plane mixing layer. This velocity structure is responsible for turbulence characteristics that differ substantially from those over a smooth surface. Velocity spectra are sharply peaked, streamwise and vertical velocities have probability densities that are strongly skewed, streamwise and vertical velocities are strongly correlated and transport is dominated by coherent flow structures, with sweeps more important than ejections. Experimental studies reveal that coherent structures contribute a very large fraction to the total exchange of heat, mass and momentum between the canopy and the overlying flow layer. The origin of the large energy-containing eddies that dominate canopy turbulent kinetic energy and transport is an inviscid instability of the inflected velocity profile that develops at the canopy top, Chapters 4, 5 and 7.

Studies in meteorology, hydraulics and wind engineering, as well as general fluid mechanics, have contributed to furthering our understanding of canopy flows and turbulence through field observations, particularly in forests, by wind tunnel simulations, by intricate turbulence closures and, more recently, by extensive large-eddy simulations. They were demonstrated by the NATO Advanced Study Institute # PST.ASI.980064 "Flow and Transport Processes in Complex Obstructed Geometries: from cities and vegetative canopies to industrial problems" held in Kyiv, Ukraine, May 4–15, 2004, [300, 301].

The theory reviewed and discussed here has already found a number of practical applications, particularly in the meteorology of forests and complex topography, Chapter 5, the hydraulics of open water flows, Chapter 6, the thermal performance of spraying coolers, Chapters 1 and 3 and the mitigation of large fire danger, Chapter 8 as well as in urban air pollution, emergency preparedness and prediction of urban climate, Chapter 9.

It is believed that further development of this highly important area of science and engineering will lead to new discoveries and new applications.

Bibliography

[1] Abdelrhman, M.A. (2003) Effect of eelgrass Zostera marina canopies on flow and transport, *Mar. Ecol.-Prog. Ser.* **248**, 67–83.

[2] Abu-Hijleh, B.A., and Al-Nimr, M.A. (2001) The effect of the local inertial term on the fluid flow in channels filled with porous materials *Heat and Mass Transfer* **44**, 1565–1572.

[3] Ackerman, J.D. (2002) Diffusivity in a marine macrophyte canopy: implications for submarine pollination and dispersal, *American Journal of Botany* **89(7)**, 1119–1127.

[4] Ackerman, J., and Okubo, A. (1993) Reduced mixing in a marine macrophyte canopy, *Functional Ecology* **7**, 305–309.

[5] Adolphe, L. (2001) A simplified model of urban morphology: application to an analysis of the environmental performance of cities, *Environment and Planning B: Planning and Design* **28**, 183–200.

[6] Allen, L.H. (1968) Turbulence and wind speed spectra within a Japanese larch plantation, *Journ. Appl. Meteorol.* **v. 7, N 1**, 73–78.

[7] Allwine, K.J., Shinn, J.H., Streit, G.E., Clawson, K.L., and Brown, M. (2002) Overview of Urban 2000: a multiscale field study of dispersion through an urban environment, *Bull. Am. Meteorol. Soc.* **83**, 521–536.

[8] Al-Nimr, M.A., and Alkam, M.K. (1998) Unsteady non-darcian fluid flow in parallel-plates channels filled with porous materials, *Heat and Mass Transfer* **33**, 315–318.

[9] Amiro, B.D. (1990) Drag coefficients and turbulence spectra within three boreal forest canopies, *Boundary-Layer Met.* **52**, 227–246.

[10] Amosov, P., and Baklanov, A. (1992) Room ventilation on the base of numerical modelling of air- and thermodynamics, *in ROOMVENT'92, Int. Conference, Aalborg, Denmark, Sept. 2–4* **v.1**, 273–288.

[11] Anderson, M., and Charters, A. (1982) A fluid dynamics study of seawater flow through Gelidium nudifrons, *Limnol. Oceanogr.* **27**, 399–412.

[12] Anthes, R.A., and Warner, T.T. (1978) Development of hydrodynamic models suitable for air pollution and other mesometeorological studies. *Mon. Wea. Rev.* **106**, 1045–1078.

[13] Arnfield, A. J., and Grimmond, C. S. B. (1998) An urban canyon energy budget model and its application to urban storage heat flux modelling', *Energy and Buildings* **27**, 61–68.

[14] Arya, S.P.S. (1975) Buoyancy effects in a horizontal flat-plate boundary layer, *J. Fluid Mechanics* **68**, 321–343.

[15] ASHRAE (1999) Fire and Smoke Management, *Chapter 51 of ASHRAE HVAC Applications 1999.*

[16] Astrup, P., Jensen, N.O., and Mikkelsen, T. (1996) Surface roughness model for LINCOM. *Riso National Laboratory*, Denmark, *Riso-R-900(EN)*.

[17] Ayotte, K.W., Finnigan, J.J., and Raupach, M.R. (1998) A second order closure for neutrally stratified vegetative canopy flows, *Boundary-Layer Meteorol* **90**, 189–216.

[18] Babenko, V.V., Kanarskiy, M.V., and Korobov, V.I. (1993) *Boundary layer on elastic plates*, Kiev: Naukova Dumka.

[19] Baines, G.B.K. (1972) Turbulence in a wheat crop, *Agric. Meteorol.* **10**, 93–105.

[20] Baklanov, A. (1986) Numerical modelling for normalisation of atmospheric environment on industrial sites, in: Numerical solution of atmospheric hydrothermodynamics problems, *Novosibirsk: Computing Centre RAS*, 30–38.

[21] Baklanov, A. (1988) *Numerical modelling in mine aerology*, Apatity, USSR Academy of Science. (in Russian).

[22] Baklanov, A. (1997) *Modelling of local air pollution processes*, FOA Progress report, Swedish Defence Research Establishment, Umea, Sweden (FOA-D-97–00301-862-SE).

[23] Baklanov, A., Burman, J., and Naslund, E. (1997) Numerical modelling of three-dimensional flow and pollution transport over complex terrain, *PHOENICS Journal of Computational Fluid Dynamics* **10(1)**, 57–86.

[24] Baklanov, A. (2000) Application of CFD methods for modelling in air pollution problems: possibilities and gaps, *Journal of Environmental Monitoring and Assessment* **65**, 181–190.

[25] Baklanov, A. (2000) Modelling of the atmospheric radionuclide transport: local to regional scale. *Numerical Mathematics and Mathematical Modelling*, *INM RAS, Moscow,* **2***, (special issue dedicated to 75-year jubilee of academician G. I. Marchuk)*, 244–266.

[26] Baklanov, A., and Sørensen, J.H. (2001) Parameterisation of radionuclide deposition in atmospheric dispersion models, *Phys. Chem. Earth* **26**, 787–799.

[27] Baklanov, A., Rasmussen, A., Fay, B., Berge, E., and Finardi, S. (2002) Potential and shortcomings of numerical weather prediction models in providing meteorological data for urban air pollution forecasting. *Water, Air and Soil Poll.: Focus* **2**, 43–60.

[28] Baklanov, A., and Sørensen, J.H. (2002) Size dependent characteristics of airborne radioactive particles, *Proceedings from the International Conference on Radioactivity in the Environment, Monaco, 1–5 September*, 400–406.

[29] Baklanov, A. (ed.) 2003: FUMAPEX Integrated Systems for Forecasting Urban Meteorology, Air Pollution and Population Exposure - Project Kick-off Meeting and First Progress Report, DMI Scientific Report 12/03, ISSN 0905–3263. URL: *http://glwww.dmi.dk/f+u/publikation/vidrap/2003/Sr03–12.pdf*

[30] Baklanov, A. and Joffre, S. (editors) (2003) Improved Models for Computing the Roughness Parameters of Urban Areas. / Baklanov, A., P. Mestayer, M. Schatzmann, S. Zilitinkevich, A. Clappier, etc. D4.4 FUMAPEX Report, November 2003. DMI Sci. Report 03–19, ISBN.: 87–7478-495–1, 51 p.

[31] Baklanov, A., Mahura, A., Nielsen, N.W., and Petersen, C. (2005) Approaches to Urbanization of DMI-HIRLAM NWP Model. *HIRLAM Newsletter*, **49**, 61–75.

[32] Baklanov, A. (2006) Overview of the European project FUMAPEX. *Atmos. Chem. Phys.*, **6**, 2005–2015.

[33] Baklanov, A., and Mestayer, P. (editors) (2004) Improved parameterisations of urban atmospheric sublayer and urban physiographic data classification. / A. Baklanov, E. Batchvarova, I. Calmet, A. Clappier, J.V. Chorda, J.J. Dieguez, S. Dupont, B. Fay, E. Fragkou, R. Hamdi, N. Kitwiroon, S. Leroyer, N. Long, A. Mahura, P. Mestayer, N.W. Nielsen, J.L. Palau, G. Perez-Landa, T. Penelon, M. Rantamaki, G. Schayes and R.S. Sokhi. D4.1, 4.2 and 4.5 FUMAPEX Report, April 2004, Copenhagen, DMI, Denmark. DMI Scientific Report: #04–05, ISBN 87–7478-506–0.

[34] Baklanov, A., and Zilitinkevich, S. (editors) (2004) Parameterisation of nocturnal UBL for NWP and UAQ models. *Danish Meteorological Institute, DMI Scientific Report* #04–08, ISBN: 87–7478-510–9. 70 pp.

[35] Baklanov, A. (2005) Meteorological advances and systems for urban air quality forecasting and assessments. *Short Papers of the 5th International Conference on Urban Air Quality Valencia*, Spain, 29–31 March 2005, CLEAR, 22–25.

[36] Baklanov, A., Hanninen, O., Slordal, L.H., Kukkonen, J., Bjergene, N., Fay, B., Finardi, S., Hoe, S.C., Jantunen, M., Karpinen, A., Rasmussen, A., Skouloudis,

A., Sokhi, R.S., and Sørensen, J.H. (2005) Integrated systems for forecasting urban meteorology, air pollution and population exposure. *Atmospheric Chemistry and Physics Discuss.*, 5, 1867–1913.

[37] Baklanov, A., Joffre, S.M., Piringer, M., Deserti, M., Middleton, D.R., Tombrou, M., Karppinen, A., Emeis, S., Prior, V., Rotach, M.W., Bonafe, G., and Baumann-Stanzer, K. (2005) Towards estimating the mixing height in urban areas – Recent experimental and modelling results from the COST-715 Action, *Submitted to Boundary-Layer Meteorol.*, 35p.

[38] Baklanov, A., Mestayer, P., Clappier, A., Zilitinkevich, S., Joffre, S., Mahura, A., and Nielsen, N.W. (2005) On parameterizations of urban atmosphere sublayer in meteorological models, *Atmospheric Chemistry and Physics Discuss.* **5**, 12119–12176.

[39] Baklanov, A., Sørensen, J.H., Hoe, S.C., and Amstrup, B. (2006) Urban meteorological modelling for nuclear emergency preparedness. *J. Envir. Radioact.*, **85**, 145–170.

[40] Baldocchi, D.D., Falge, E., Gu, L., Olson, R., Hollinger, D., Running, S., Anthoni, P., Bernhofer, Ch., Davis, K., Evans, R., Fuentes, J., Goldstein, A., Katul, G., Law, B., Lee, X., Malhi, Y., Meyers, T., Munger, W., Oechal, W., Paw U, K.T., Pilegaard, K., Schmid, H.P., Valentini, R., Verma, S., Vesala, T., Wilson, K., and Wofsy, S. (2001) FLUXNET: A new tool to study the temporal and spatial variability of ecosystem-scale carbon dioxide, water vapour and energy flux densities. *Bull. Amer. Meteorol. Soc.* **82**; 2415–2434

[41] Bartzis, J.G., Venetsanos, A., Varvayani, M., Catsaros, N. and Megaritou, A. (1991) ADREA-I: a three-dimensional transient transport code for complex terrain and other applications. *Nuclear Technology* **94**, 135–148.

[42] Batchelor, G.K. (1967) *An Introduction to Fluid Dynamics*. Cambridge University Press.

[43] Batchelor, G.K. (1972) Sedimentation in a dilute dispersion of spheres. *J. Fluid Mech.* **52**, 245–268.

[44] Battaglia, F., McGrattan, K.B., Rehm, R.G. and Baum, H.R. (2000) Simulating Fire Whirls, *Combustion Theory Modeling* **Vol. 4**, 123–138.

[45] Baum, H.R., McGrattan, K.B., and Rehm, R.G. (1996) Three Dimensional Simulations of Fire Plume Dynamics, *Fire Safety Science- Proceedings of the 5th Int. Symposium*, 511–522.

[46] Baum, H.R., and McGrattan, K.B. (1999) Simulation of Oil Tank Fires, *Interflam 99, June 29-July1* **Vol. 2**, 1117–1128.

[47] Beavers, G., and Joseph, D. (1967) Boundary conditions at a naturally permeable wall, *J. Fluid Mech.* **30**, 197–207.

[48] Beffa, C.J. (1994) Praktische Lösung der tiefengemittelten Flachwassergleichungen, *Mitteilungen VAW* **v. 133**, Zurich.

[49] Belcher, S.E., Xu, D.P., and Hunt, J.C.R. (1990) The response of a turbulent boundary layer to arbitrarily distributed roughness change, *Q. J. R. Met. Soc.* **116**, 611–635.

[50] Belcher, S.E., and Coceal, O. (2002) Scaling the urban boundary layer. In: Rotach M., Fisher B., Piringer M. (Eds.), *COST Action 715 Workshop on Urban Boundary Layer Parameterisations (Zurich, 24–25 May 2001). Office for Official Publications of the European Communities*, EUR 20355, 7–16.

[51] Belcher, S.E., Jerram, N., and Hunt, J.C.R. (2003) Adjustment of a turbulent boundary layer to a canopy of roughness elements, *J. Fluid Mech.* **488**, 369–398.

[52] Bennovitsky, E.L. (1988) Derivation of functional dependences for roughness coefficient of partially vegetated beds, *Water resources (Wodnije resourci)*, **N 1**, 68–74. (in Russian)

[53] Bennovitsky, E.L., and Modzalevsky, A.I. (1990) Effect of submerged higher water vegetation on open bed capacity, *Water resources (Wodnije resourci)* **N 5**, 93–99. (in Russian)

[54] Bennovitsky, E.L., and Sherenkov, I.A. (1990) Effect of higher water vegetation on rated capacity of river and channel beds, *Hydraulic Waterworks (Gidrotehknicheskoje stroitelstwo)* **N 11**, 15–16. (in Russian)

[55] Bennovitsky, E.L., Lvov, V.A., and Factorovich, I.Yu. (1992) Modeling the organic containment extraction by a channel biological plateaus, *Vodni Ressoursi* **N 6**, 88–93. (in Russian)

[56] Bennovitsky, E.L. (1995) Equation of velocity horizontal distribution for flows in beds with near-bank vegetation, *Water resources (Wodnije resourci)* **22, N 4**, 407–412. (in Russian)

[57] Bennovitsky, E.L., and Gayev, Ye.A. (2004) Analysis of flows trough vegetated beds. *Flow and transport processes in complex obstructed geometries, Abstracts of NATO Advances Study Institute PST.ASI.980064*, Kyiv, Institute of Hydromechanics NASU, May 4–15, 2004.

[58] Berge, E., Walker, S.-E., Sorteberg, A., Lenkopane, M., Eastwood, S., Jablonska, H.I., and Koltzow, M.O. (2002) A real-time operational forecast model for meteorology and air quality during peak air pollution episodes in Oslo, Norway, *Water, Air and Soil Pollution Focus* **2**, 745–757.

[59] Berkowicz, R., Hertel, O., Sørensen, N.N., and Michelsen, J.A. (1997) Modelling Air Pollution from Traffic in Urban Areas, *In Proceedings from IMA meeting on Flow and Dispersion Through Obstacles*, Cambridge, England, 28–30 March, 1994, eds. R.J. Perkins and S.E. Belcher, 121–142.

[60] Berman, L.D. (1962) *Evaporative Cooling of Circulating Water*, Pergamon Press, N.-Y.

[61] Berthier, E., Dupont, S., Andrieu, H., and Mestayer, P.G. (2001), Comparison of evapotranspiration in an urban area, as evaluated by both an atmospheric model and a hydrological model, *International Symposium on Environmental Hydraulics*, Tempe, Arizona, 5–8 Dec. 2001, Proceedings CD, 6 pp.

[62] Betz, A. (1925) Ein Verfahren zur direkten Ermittlund des Profilwiderstandes. *Z.F.M.*, **16**, 42.

[63] Bisset, D.K., Hunt, J.C.R., and Rogers, M.M. (2002) The turbulent/non-turbulent interface bounding a far wake, *J. Fluid Mech.* **451**, 383–410.

[64] Blumen, W. (Ed.) (1990) *Atmospheric processes in complex terrain*, American Met. Soc.

[65] Bond, H. (Editor) (1946) *Fire and the Air War, National Fire Protection Association*, Boston, MA.

[66] Boone, A., Calvet, J.C., and Noilhan, J. (1999) Inclusion of a Third Soil Layer in a Land Surface Scheme using the Force-Restore Method, *J. Appl. Meteorol.* **38**, 1611–1630.

[67] Boris, J.P., Grinstein, F.F., Oran, E.S., and Kolbe, R.L. (1992) New insights into large eddy simulation, *Fluid Dynamics Research* **10**, 199–228.

[68] Bornstein, R.D. (1987) Mean diurnal circulation and thermodynamic evolution of urban boundary layers, *Modelling the urban boundary layer*, published by American Meteorological Society, Boston, MA, 53–94.

[69] Borovkov, V.S. (1989) *River bed processes on urbanized territories*, Leningrad, Gidrometeoizdat. (in Russian)

[70] Bortkovskii, R.S. (1987) *Air-See Exchange of Heat and Moisture During Storms*, D. Reidel, Dortrecht.

[71] Bottema, M. (1993) *Wind climate and urban geometry*, Ph.D. thesis, Eindhoven University of Technology, The Netherlands.

[72] Bottema, M. (1997) Urban roughness modelling in relation to pollutant dispersion, *Atmos. Env.* **31**, 3059–3075.

[73] Bottema, M., and Mestayer, P.G. (1998) Urban roughness mapping-validation techniques and some first results, *J. Wind Engineering & Industrial Aerodynamics*, **74–76**, 163–173.

[74] Bradshaw, P., Dean, R.B., and McEligot, N.P. (1973) Calculation of interacting turbulent shear layers: duct flow, *Trans. ASME I: J. Fluids Engng.* **95**, 214–219.

[75] Bretherton, F.P. (1962) Slow viscous motion round a cylinder in a simple shear, *J. Fluid Mech.* **12**, 591–613.

[76] Briggs, G.A. (1973) Diffusion estimation for small emissions. *Paper bf No. 79 Atmospheric Turbulence and Diffusion Laboratory*, NOAA, Oak Ridge, TN.

[77] Brigham, E.O. (1996) The Fast Fourier Transform and its applications, Prentice Hall, New Jersey.

[78] Britter, R.E., and Hunt, J.C.R. (1979) Velocity measurements and order-of-magnitude estimates of the flow between two buildings in a simulated atmospheric boundary layer, *J. Ind. Aero.* **4**, 165–182.

[79] Britter, R. (1998) *Recent Research on the Dispersion of Hazardous Materials. European Commission*, EUR 18198 EN, ISBN 92–828-3048–9

[80] Britter, R.E., Caton, F., Di Sabatino, S., Cooke, K.M., Simmonds, P.G., and Nickless, G. (2000) Dispersion of a passive tracer within and above an urban canopy. *In Proceedings of the Third Symposium on the Urban Environment*, American Meteorological Society.

[81] Britter, R.E., and Hanna, S.R. (2003) Flow and dispersion in urban areas, *Ann. Rev. Fluid Mech.* **35**, 469–496.

[82] Brode, H.L., and Small, R.D. (1986) A Review of the Physics of Large Urban Fires, *The Medical Implications of Nuclear War*, Institute of Medicine, National Academy of Science, National Academy Press., Washington D.C., 73–95.

[83] Brook, D.R., Beck, N.V., Clem, C.M., Strickland, D.C., Griffiths, I.H., Hall, D.J., Kingdon, R.D., and Hargrave, J.M. (2002) Validation of the Urban Dispersion Model (UDM), *In Proceedings of 8th International Conference on Harmonisation within Atmospheric Dispersion Modelling for Regulatory Purposes*, Sofia, Bulgaria, 14–17 October 2002, 8–12.

[84] Brook, D.R., Felton, N.V., Clem, C.M., Strickland, D.C.H., Griffiths, I.H., Kingdon, R.D., Hall, D.J., and Hargrave, J.M. (2003), Validation of the Urban Dispersion Model (UDM), *International Journal of Environment and Pollution* **20**, 11–21.

[85] Brown, K.W., and Covey, W. (1966) The energy budget evaluation of the micrometeorological transfer processes within a cornfield, *Agric. Meteor.* **3**, 73–96.

[86] Brown, G.L., and Roshko, A. (1974) On density effects and large structure in turbulent mixing layers, *J. Fluid Mech.* **64**, 775–816.

[87] Brown, M.J., and Williams, M.D. (1998) An Urban Canopy Parameterization for Mesoscale Meteorological Models. Los Alamos National Laboratory, *Report LA-UR-98–3831*.

[88] Brunet, Y., Finnigan, J.J., and Raupach, M.R. (1994) A wind-tunnel study of air flow in waving wheat: single-point velocity statistics *Boundary-Layer Meteorology*, **70**, 95–132.

[89] Brutsaert, W. (1975) The roughness length for water vapor, sensible heat, and other scalars, *J. Atmos. Sci.* **32**, 2028–2031.

[90] Brutsaert, W. (1982) *Evaporation into the Atmosphere. Theory, History and Applications*, D. Reidel Publ. Co.

[91] Brutsaert, W., and Sugita, M. (1996) Sensible heat transfer parameterisation for surfaces with anisothermal dense vegetation, *J. Atmos. Sci.* **53**, 209–216.

[92] Buchlin, J.-M. (1992) Numerical modelling of liquid sprays, *1st European Computational Fluid Dyn. Conf. Multiphase Flows*, Brussels, Preprint 1992–39/EA, von Karman Inst. Fluid Dynamics, Sept. 1992.

[93] Burke, R., and Stolzenbach, K. (1983) Free surface flow through salt marsh grass, *MIT-Sea Grant Technical Report, MITSG*, Cambridge, Ma, 83–163.

[94] Burman, J. (1997) *A study of the influence of topography and density on the dispersion in a gas cloud*, Scientific report, FOA, Umea, Sweden (FOA-R-96–00304-4.5-SE).

[95] Businger, J.A. (1975) Aerodynmiacs of vegetated surfaces. In: Devries, DA, Afgan, NH (eds). *Heat and mass transfer in the biosphere, PartI. Transfer processes in the plant environment*, Scripta, Washington, DC.

[96] Bykova, L.P. (1983) Numerical modeling a breeze circulation over a city with accounting processes in roughness layer, *Meteorologia i Hydrologia* **No 12**, 36–43. (in Russian)

[97] Byram, G.M., and Martin, R.E. (1970), The Modeling of Fire Whirlwinds, *Forest Science* **Vol. 16, No. 4**, 386–399.

[98] Cannon, D.J. (Editor) (1977) *Heritage of Flames: The Illustrated History of Early American Firefighting*, Doubleday and Company, Inc., New York.

[99] Capon, R. (2003) *Modelling low level winds with the Met Office New Dynamics model*, Internal Report No. 133, NWP Scientific Paper No. 66, Met. Office, JCMM, Reading University, Reading, UK.

[100] Carlotti, P., and Hunt, J.C.R. (2000) Spectra of turbulence in boundary layers near the ground. *In Proceedings of 8th European Turbulence Conference, Barcelona*, Kluwer. Submitted to *Journal of Flow Turbulence and Combustion*, 307–310.

[101] Carlotti, P. (2002) Two point properties of atmospheric turbulence very close to the ground: comparison of a high resolution LES with theoretical models, *Boundary Layer Meteor.* **104**, 381–410.

[102] Carollo, F.G., V. Ferro, and Termini, D. (2002), Flow velocity measurements in vegetated channels, *J. Hydraul. Eng.-ASCE* **128 (7), 664**, doi: 10.1061/0733–9429.

[103] Carrier, G.F. (1985) *The Effects on the Atmosphere of a Major Nuclear Exchange*, National Academy Press, Washington, D.C., *http://www.nap.edu/books/0309035287/html/.*

[104] Carrilho da Graca, G., and Linden, P.F. (2002) Simplified modeling of cross-ventilation airflow. *ASHRAE Trans.* **109**, 1–14.

[105] Carruthers, D.J., Hunt, J.C.R., and Weng, W.-S. (1988) A computational model of stratified turbulent airflow over hills, *FLOWSTAR I. In Computer Techniques in Environmental Studies* (ed. P. Zanetti), Springer-Verlag, 481–492.

[106] Carruthers, D.J., Holroyd, R.J., Hunt, J.C.R., Weng, W.-S., Robins, A.G., Apsley, D.D., Thomson, D.J., and Smith, F.B. (1994) UK-ADMS: A new approach to modelling dispersion in the Earth's atmospheric boundary layer, *Journal of Wind Engineering and Industrial Aerodynamics* **52**, 139–153.

[107] Carruthers, D.J., Edmunds, H.A., Lester, A.E., McHugh, C.A., and Singles, R.J. (2000) Use and Validation of ADMS-Urban in Contrasting Urban and Industrial Locations, *Int. J. Environment and Pollution* **14**, 1–6. CERC (2000) ADMS 3 User Guide, Cambridge Environmental Research Consultants Ltd.

[108] Cartellier, A. (2003) Screening mechanisms and induced agitation in bubble flows at finite particle Reynolds numbers: experiments and preliminary modelling attempts using a hybrid model, *ERCOFTAC Bulletin*. **56**, 27–33.

[109] Cermak, J.E. (1995) Physical Modelling of Flow and Dispersion over Urban Areas, *Wind Climate in Cities*, (J.E. Cermak et al., eds.), Kluwer Academic Publishers, 383–404.

[110] Chang, J.C., Hanna, S.R., Boybeyi, Z. and Franzese, P. (2004) Use of Salt Lake City Urban 2000 field data to evaluate the Urban HPAC dispersion model, To appear in *J. Appl. Meteorol*.

[111] Chang, C.H. and Meroney, R.N. (2003) Concentration Distributions from a Point Source Within Urban Street Canyons: Wind Tunnel and Computational Data, *J. of Wind Engineering and Industrial Aerodynamics* **Vol. 91, No. 9**, 1141–1154.

[112] Chang, C.H. and Meroney, R.N. (2003) The Effects of Surroundings with Different Separation Distances on Surface Pressures on Low Rise Buildings, *J. of Wind Engineering and Industrial Aerodynamics* **Vol. 91, No. 8**, 1039–1050.

[113] Chang, J.C., and Hanna, S.R., (2004) Air quality model performance evaluation, To appear in *Meteorol. Atmos. Phys.*

[114] Chaturvedi, S., and Porter, R.W. (1978) Air-vapor dynamics in large-scale atmospheric spray cooling systems. *Trans. ASME, J. Fluid Engineering* **v. 100, N 1**, 65–72.

[115] Chatwin, P.C. (1968) The dispersion of a puff of passive contaminant in the constant stress region, *Q. J. R. Meteorol. Soc.* **94**, 350–360.

[116] Chen, C.-L. (1976) Flow resistance in broad shallow grassed channels, *J. Hydr. Eng. Div.- ASCE* **102 (3)**, 307–322.

[117] Chen, F., Janjic, Z., and Mitchell, K. (1997) Impact of atmospheric surface-layer parameterizations in the new land-surface scheme of the NCEP mesoscale ETA model, *Boundary-Layer Meteorol.* **85**, 391–421.

[118] Chen, K.H., and Trezek, J.T. (1976) Spray energy release (SER) approach to analyzing spray system perfomance, *Proc. Amer. Power Conf.* **38**, 1435–1448.

[119] Cheng, H. and Castro, I. (2002) Near wall flow over urban-like roughness, *Boundary-Layer Met.* **104**, 229–259.

[120] Chigier, N.A., Beer, J.M., Grecov, D., and Bassindale, K. (1970) Jet Flames in Rotating Flow Fields, *Combust. Flame* **Vol. 14**, 171–180.

[121] Chu, V.H., Wu, J.-H., Khayat, R.E. (1991) Stability of transverse shear flows in shallow open channels, *J. of Hydr. Eng.* **117(10)**, 1370–1388.

[122] Cimorelli, A.J., Perry, S.G., Venkatram, A., Weil, J.C., Paine, R.J. Wilson, R.B., Lee, R.F., and Peters, W.D. (1998) *AERMOD: Description of Model Formulation*, (12/15/98 Draft Document) Prepared for Environmental Protection Agency, Research Triangle Park, NC. (Docket No. A-99–05; II-A-1). 113 pp.

[123] Cimorelli, A.J. et al. (2004) AERMOD: A dispersion model for industrial source applications. Part I: Model formulation and boundary layer characterization. To appear in *J. Appl. Meteorol.*

[124] Cionco, R.M. (1965) A Mathematical Model for Air Flow in a Vegetative Cover, *J. Appl. Meteorol.* **Vol. 4**, 517–522.

[125] Clarke, J.A. (1985) *Energy simulation in building design*, Adam Hilger, Bristol.

[126] Clarke, R.H. (1979) *A model for short and medium range dispersion of radionuclides released to the atmosphere*. National Radiological Protection Board report NRPB-R91.

[127] Coceal, O., and Belcher, S.E. (2004) A canopy model of mean winds through urban areas. *Quarterly Journal of the Royal Meteorological Society*, **130**, 1349–1372.

[128] Coen, J.L., and Clark, T.L. (2001) Coupled Atmosphere-fire Model Simulations in Various Fuel Types in Complex Terrain, *4th Symposium on Fire and Forest, American Meteorological Society*, 13–15 November 2001, Reno, NV, 39–42.

[129] Cohen, J.D. (2000) Examination of the Home destruction in Los Alamos Associated with the Cerro Grande Fire, July 10, 2000, United States National Park Service. (*http://www.nps.gov/fire/download/pub_pub_examlosalamos.pdf*.)

[130] Cooke, K.M., Di Sabatino, S., Simmonds, P., Nickless, G., Britter, R.E., and Caton, F. (2000) Tracer and Dispersion of Gaseous Pollutants in an Urban Area. Birmingham Tracer Experiments. *Technical Paper CUED/A-AERO/TR.27*, Department of Engineering, Cambridge University.

[131] Corrsin, S. (1974) Limitations of gradient transport models in random walks and turbulence. *Adv. Geophys.* **18A**, 25–60.

[132] Counihan, J., Hunt, J.C.R., and Jackson, P.S. (1974) Wakes behind two-dimensional surface obstacles in turbulent boundary layers, *J. Fluid Mech.* **64**, 529–563.

[133] Countryman, C.M. (1964) *Mass Fires and Fire Behavior*, U.S. Forest Service Research Paper, PSW-19, Pacific Southwest Forest and Range Experiment Station, Berkeley, CA.

[134] Countryman, C.M., Project Flambeau...An Investigation of Mass Fire (1964–1967), Pacific Southwest Forest and Range Experiment Station, Berkeley, CA, Vol. 1, 2 & 3, 1969.

[135] Countryman, C.M. (1971) *FIRE WHIRLS...why, when, and where*, Pacific Southwest Forest and Range Experiment Station.

[136] Cowan, I.R. (1968) Mass, Heat and Momentum Exchange between stands of plants and their atmospheric environment. *Q.J. Ror. Meteorol. Soc.* **94**, 523–544

[137] Crutzen and Birks (1982) The atmosphere after a nuclear war: Twilight at noon, *Ambio*, 115–25.

[138] Cullen, M.J.P. (1993) The unified forecast/climate model, *The Meteorological Magazine* **122**, 81–94.

[139] Cuxart, J., Bougeault, P., and Redelsberger, J.L. (2000) A multi-scale turbulence scheme for LES and mesoscale modelling, *Q. J. R. Meteorol. Soc.* **126**, 1–30.

[140] Dalton, C., and Helfinstine, R.A. (1971) Potential flow past a group of circular cylinders, *J. Basic Engr., Trans. ASME.* **93**, 636–642.

[141] Darwin, C.G. (1953) A note on hydrodynamics, *Proc. Cam. Phil.Soc.* **49**, 342–354.

[142] Davenport, A., Grimmond, S., Oke, T., and Wieringa, J. (2000) The revised Davenport roughness classification for cities and sheltered country, *3rd Symp. On the Urban Environment*, 14–18 Aug. 2000, Davis, Ca, AMS Proceedings, 9–10.

[143] Davidson, M.J., Mylne, K.R., Jones, C.D., Phillips, J.C., Perkins, R.J., Fung, J.C.H., and Hunt, J.C.R. (1995) Plume dispersion through large groups of obstacles - a field investigation, *Atmospheric Environment* **29**, 3245–3256.

[144] Davidson, M.J., Snyder, W.H., Lawson, R.E., and Hunt, J.C.R. (1996) Plume dispersion from point sources upwind of groups of obstacles - wind tunnel simulation s. *Atmospheric Environment* **30**, 3715–3725.

[145] Dawson, F., and Charlton, F. (1988), Bibliography on the hydraulic resistance or roughness of vegetated water courses, *Occasional Publication* **No. 25**, Freshwater Biology Association, Ambleside, U.K.

[146] Deardorff, J.W. (1972) Numerical investigations of neutral and unstable planetary boundary layers, *J. Atmos. Sci.* **18**, 495–527.

[147] Defina, A., and Bixio, A.C. (2005) Mean flow and turbulence in vegetated open channel flow, *Water Resour. Res.* **Vol. 41, No. 7**, W07006.

[148] Denmead, O.T. (1964) Evaporation sources and apparent diffusivities in a forest canopy, J. Appl. Meteor. **3**, 383–389.

[149] Denmead, O.T., and Bradley, E.F. (1985) Flux-gradient relationships in a forest canopy. In *The Forest-Atmosphere Interaction* (Eds.B.A. Hutchison and B.B. Hicks), 421–442. (D.Reidel Publishing Co.: Dordrecht, The Netherlands.)

[150] Denmead, O.T., and Bradley, E.F. (1987) On scalar transport in plant canopies, *Irrig. Sci.* **8**, 131–149.

[151] Doms, G., and Schattler, U. (1999) *The nonhydrostatic limited-area model LM, part1: scientific documentation*, R&D Dep. of DWD.

[152] Drew, D.A., and Wallis, G.B. (1992) Fundamentals of two-phase flow modelling. *Third International Workshop on Two-Phase Flow Fundamentals*. (Ed. G.F. Hewitt & R.T. Lahey).

[153] DTRA (2001) *The HPAC User's Guide, Version 4.0*, report HPAC-UGUIDE-02-U-RAC0, Prepared for DTRA by SAIC, 10260 Campus Point Drive, San Diego, CA 92121.

[154] DTRA (2004) *HPAC Version 4.04.011*, (DVD containing model and accompanying data and document files), Available from DTRA, 6801 Telegraph Rd., Alexandria, VA.

[155] Dubov, A.S., Bickova, L.P., and Marrunitch, S.V. (1978) *Turbulence in a Vegetation Canopy*, Leningrad, Hydrometeoizdat. (in Russian)

[156] Dunn, C., Lopez, F., and Garcia, M. (1996) *Mean flow and turbulence in a laboratory channel with simulated vegetation*, Report of Hydrosystems Lab., Univ. Illinois, Urbana, Illinois.

[157] Dupont, S. (2001) *Modelisation Dynamique et Thermodynamique de la Canopee Urbaine: Realisation du Modele de Sols Urbains pour SUBMESO*, Doctoral thesis, Universite de Nantes, France.

[158] Dupont, S., and Mestayer, P.G. (2004) Evaluation of the urban soil model SM2-U on the city center of Marseille (France), *Fifth Symposium on the Urban Environment*, 23–27 Aout, Vancouver, BC, Canada, AMS Proceeding CD (9.14)

[159] Dupont, S., Otte, T.L., and Ching, S. (2004) Simulation of Meteorological Fields within and above Urban and Rural Canopies with a Mesoscale Model (MM5), *Boundary-Layer Meteorol.* **113**, 111–158.

[160] Dupont, S., Mestayer, P.G., Guilloteau, E., Berthier, E., and Andrieu, H. (2005) Parameterisation of the Urban Water Budget with the Sub-Meso Soil Model', *J. Appl. Meteorol.*, submitted.

[161] Dybbs, A., and Edwards, R. (1984) A new look at porous media fluid mechanics, Darcy to turbulent, *In. Fundamentals of Transport in Porous Media*, (Bear and Corapcioglu, eds.), 199–256.

[162] Eames, I., and Hunt, J.C.R. (2003) *Complex flow problems*, ERCOFTAC Bulletin *No.* 56 (Editors).

[163] Eames, I., Hunt, J.C.R., and Belcher, S.E. (2003) Lagrangian and Eulerian properties of steady flows through groups of obstacles, *Journal of Fluid Mechanics*, [Summary version in ERCOFTAC Bulletin *No.* 56.]

[164] Eckman, J. (1990) A model of passive settlement by planktonic larvae onto bottoms of differing roughness, *Limnol. Oceanogr.* **35**, 887–901.

[165] Ehrhard, J., and Kunz, R., Moussiopoulos, N. (2000) On the performance and applicability of nonlinear two-equation turbulence models for urban air quality modelling, *Journal of Environmental Monitoring and Assessment* **65**, 201–209.

[166] Eimern, I. (ed.) (1964) Windbreaks and Shelterbelts, *World Meteorological Organization Technical Note* **59**.

[167] Ellefsen, R. (1991) Mapping and measuring buildings in the canopy boundary layer in ten U.S. cities, *Energ. Buildings*, **15–16 (3–4)**, 1025–1049.

[168] Emeis, S., and Frandsen, S. (1993) Reduction of horizontal wind speed in a boundary layer with obstacles, *Bound.-Layer Meteorol.* **v. 64**, 297–305.

[169] Emmons, H.W., and Ying, S.J. (1966) The Fire Whirl, *11th Int. Combustion Symposium*, Proceedings, U. of California, Berkley, CA, Aug 14–20, 1966, 475–488.

[170] Emori, R.I., and Saito, K. (1982) Model Experiment of Hazardous Forest Fire Whirl, *Fire Technology* Vol. 18, 319–327.

[171] Emtzev, B.T. (1967) *Two-dimensional violent flows*, Moscow, Energy Publ. (in Rusian)

[172] Escartin, J., and Aubrey, D.G. (1995) Flow structure and dispersion within algal mats, *Estuarine, Coastal and Shelf Science* **40**, 451–472.

[173] Eyewitness to History (1999) The Burning of Rome, 64 AD, Eyewitness to History web site, *http://www.eyewitnesstohistory.com*.

[174] Fackrell, J.E. (1984) Parameters characterising dispersion in the near-wakes of buildings, *J. Wind Eng. and Industrial Aero.* **16**, 97–118.

[175] Farouk, B., McGrattan, and Rehm, R.G. (2001) Large eddy simulation of naturally induced fire whirls in a vertical square channel with corner gaps, *Int. Mech Eng. Congress and Exposition Proceedings*, November 5–10, 2000, Orlando, FL.

[176] Fay, B., and Neunhaeuserer, L. (2005) Evaluation of high-resolution simulations with the Lokalmodell of the German Weather Service for urban air pollution episodes in Helsinki and Oslo in the FUMAPEX project, *Atmos. Chem. Phys. Discuss.* **5**, 8233–8284.

[177] Fay, B., Neunhauserer, L., Palau, J.L., Perez-Landa, G., Dieguez, J.J., Odegaard, V., Bonafe, G., Jongen, S., Rasmussen, A., Amstrup, B., Baklanov, A., and Damrath, U. (2005) *Evaluation and inter-comparison of operational mesoscale models for FUMAPEX target cities*, FUMAPEX Report for D3.4, DWD Offenbach, Germany, June 2005.

[178] Fehrenbach, U., Scherer, D., and Parlow, E. (2001) Automated classification of planning objectives for the consideration of climate and air quality in urban and regional planning for the example of the region of Basel/Switzerland, *Atmos. Environ.* **35(32)**, 5605–5615.

[179] Felix, E.N. (1987) Hydrologic and climatic changes in three small watersheds after timber harvest, *Research Paper PNW-PR-379*, Portland, OR, U.S.D.A., Forest Service, Pacific Northwest Research stateion, 13 pp.

[180] Fendell, F.E. (1985) Observation of Plume Heights and Ash Transport in Large Fires, Appendix 5–1 of from *The Effects on the Atmosphere of a Major Nuclear Exchange*, (Carrier, G.F., Chairman) National Academy Press, Washington, D.C., pp. 97–100, 1985.

[181] Finelli, C.M. (2000) Velocity and concentration distributions in turbulent odor plumes in the presence of vegetation mimics: a flume study, *Mar. Ecol. Prog. Ser.***207**, 297–309.

[182] Finnigan, J.J. (1979) Turbulence in waving wheat. I. Mean statistics and honami, *Boundary-Layer Meteorol.* **16**, 181–211.

[183] Finnigan, J.J. (1979) Turbulence in waving wheat. II. Structure of momentum transfer, Boundary-Layer Meteorol. **16**, 213–236.

[184] Finnigan, J.J. (1985) Turbulent transport in flexible plant canopies, in *The forest-atmosphere interaction,* (eds. B.A. Hutchison and B.B. Hicks), D. Reidel publishing Co., The Netherlands, 443–480.

[185] Finnigan, J.J., Raupach, M.R. (1987) Transfer processes in plant canopies in relation to stomatal characteristics, in, *Stomatal Function,* (eds. E. Zeiger, Farquar,G.D and Cowan I.R.), Stanford University Press, Stanford, California, 385–429.

[186] Finnigan, J.J., and Brunet, Y. (1995) Turbulent airflow in forests on flat and hilly terrain, in *Wind and Trees,* 3–40, Eds. M.P. Coutts and J. Grace. *Cambridge University Press.* UK.

[187] Finnigan, J.J. (2000) Turbulence in Plant Canopies *Ann. Review Fluid Mech.* **v. 32** (edited by J.L. Lumley, M. van Dyke and H.L. Reed), 519–571.

[188] Finnigan, J.J., and Shaw, R.H. (2000) A wind-tunnel study of airflow in waving wheat: an EOF analysis of the structure of the large-eddy motion, *Boundary-Layer Meteor.* **96**, 211–255.

[189] Finnigan, J.J., and Belcher, S.E. (2004) Flow over a hill covered with a plant canopy. *Q. J. Roy. Meteorol. Soc.* 130, 1–29

[190] Fishenich, J. (1994) *Flow resistance in vegetated channels: summary of the literature*, Technical Report, HL-94-xx, U.S. Army Corps of Engineers Waterways Experimental Station, Vicksburg, Miss .

[191] Fisher, B.E.A. (2003) Meteorology factors influencing urban air pollution. Presented at 4th International Conference on Urban Air Quality: *Measurement, Modelling and Management*, Charles University, Prague, Czech Republic, 25–27 March 2003.

[192] Fisher, B., Joffre, S., Kukkonen, J., Piringer, M., Rotach, M., and Schatzmann, M. (Eds.) (2005) *Meteorology applied to urban air pollution problems.* Final Report of COST Action 715. Demetra Ltd Publishers, ISBN 954–9526-30–5

[193] Fisher, B., Kukkonen, J., Piringer, M., Rotach, M., Schatzmann, M. (2005) Meteorology applied to urban air pollution problems: results from COST 715, *Atmos. Chem. Phys. Discuss.* **5**, 7903–7927.

[194] Fitzmaurice, L., Shaw, R.H., Paw U.K.T., and Patton, E.G. (2004) Three-dimensional scalar microfront systems in a large-eddy simulation of vegetation canopy flow, *Boundary-Layer Meteor.* **112**, 107–127.

[195] Fletcher, C.A.J. (1991) *Computational Techniques for Fluid Dynamics, Vol. I: Fundamentals and General Techniquess. Vol. II: Specific Techniques for Different Flow Categories*, Second Edition, Springer Verlag, Berlin.

[196] Fox, P., Fernando, H., Rodriguez, R., Serra, T., and Arzabe, M. (2002) Evaluation of flow fields in wetlands using physical models. *US Dept. of Interior. Desalination Research and Development Program*, Report *No*. **49**.

[197] Fox, T.A. (1986) *Turbulence generation in the wake of perpendicular cylinders and bars*, Doctor Phylosophy Thesis, Surrey University (UK).

[198] Fowler, W.B., Helvey, J.D., and Felix, E.N. (1987) Hydrologic and climatic changes in three small watersheds after timber harvest, *Research Paper PNW-PR-379*, Portland, OR, U.S.D.A., Forest Service, Pacific Northwest Research Station.

[199] Gallitzeyskiy, B.M., Rizhov, Yu.A., and Yackush, E.V. (1977) *Heat and hydrodynamics processes in fluctuating flows*, Moscow: Mashinostroyenie. (in Russian)

[200] Galmarini, S., Bianconi, R., Klug, W., Mikkelsen, T., Addis, R., Andronopoulos, S., Astrup, P., Baklanov, A., Bartniki, J., Bartzis, J.C., Bellasio, R., Bompay, F., Buckley, R., Bouzom, M., Champion, H., D'Amours, R., Davakis, E., Eleveld, H., Geertsema, G.T., Glaab, H., Kollax, M., Ilvonen, M., Manning, A., Pechinger, U., Persson, C., Polreich, E., Potemski, S., Prodanova, M., Saltbones, J., Slaper, H., Sofiev, M.A., Syrakov, D., Sørensen, J.H., Van der Auwera, L., Valkama, I., Zelazny, R. (2004) Ensemble Dispersion Forecasting, Part I: Concept, Approach and Indicators, *Atmos. Environ* **38**, 4607–4617.

[201] Gambi, M., Nowell, A., and Jumars, P. (1990) Flume observations on flow dynamics in Zostera marina (eelgrass) beds, *Mar. Ecol. Prog. Ser.* **61**, 159–169.

[202] Gani, R., and Williams, A. (1992), Physical Modeling of Fires, Transport Phenomena in Heat and Mass Transfer, (J.A. Reizes, editor), *Elsevier Publishers*, 1215–1223.

[203] Gantzer, C., Rittmann, B., and Herricks, E. (1991) Effect of long-term water velocity changes on streambed biofilm activity, *Wat. Res.* **25**, 15–20.

[204] Gao, W., Shaw, R.H., and Paw, U.K.T. (1989) Observation of organized structure in turbulent flow within and above a forest canopy, *Boundary-Layer Meteor.* **47**, 349–377.

[205] Garratt, J.R. (1993) *The Atmospheric Boundary Layer*, Cambridge University Press.

[206] Garzon, V.E., McDonough, J.M., and Saito, K. (1998) Time-Dependent Model of Forest Fire Spread in Turbulent Gusting Winds, Very Large-Scale Fires, ASTM STP 1336 (Keltener, Alvares, & Grayson, Eds.), *American Society for Testing and Materials*, 73–83.

[207] Gastellu-Etchegorry, J.P., Martin E., and Gascon, F. (2004) DART: a 3-D model for simulating satellite images and surface radiation budget, *Intern. J. Remote Sensing* **25(1)**, 73–96.

[208] Gayev, Ye.A., and Nickitin, I.K. (1982) Flow Hydrodynamics in the presence of an Easily Penetrable Roughness. Laminar Flow, *Hydromechanics*, Kiev, **45**, 65–73. (in Russian)

[209] Gayev, Ye.A., Tsymbal, V.S., and Nickitin, I.K. (1986) On particular features of interaction of the atmospheric boundary layer with large-scale spraying cooling system for power plants, *Trudi UkrNII Goskomgidromet* **216**. (in Russian).

[210] Gayev, Ye.A. (1987) Heat performance method for largescale spraying cooling systems, *Promishlennaya teplotekhnicka*, Kiev, **9, N 4**. (in Russian).

[211] Gayev, Ye.A., Denisenko, A.I., and Asaturyan, A.Sh. (1990) Mathematical Modeling of Long Spray-Ponds for Cooling of Recycled Cooling Water of Conventional and Nuclear Power Plants Under Windless Conditions, *Fluid Mechanics – Soviet Research*, **Vol. 19, No. 3**, 66–75.

[212] Gayev, Ye.A., and Sabayeva, L.M. (1990) Interaction of stabilized flow with an easily penetrable, particulate roughness, *Fluid Mech – Sov. Res.* (USA) **19, N 3**, 13–21.

[213] Gayev, Y.A., Melenevskiy, V.V., Nikitin, I.K., Tsymbal, V.S., and Prokhorov, V.N. (1990) Turbulent flows in and above a permeable roughness layer, *Fluid Mechanics, Soviet Research*. **Vol. 19, No. 6**,79–89.

[214] Gayev, Ye.A. (1990) Effect of Easily Penetrable Roughness on the hydrodynamics of laminar flow, *Fluid Mech. – Soviet Research*. **v. 19, N 3**, 1–12.

[215] Gayev, Ye.A. (1993) Model of an Easily Penetrable Roughness in a form of Multy-Speed Drop Layer, *Hydromechanicka*, Kiev, **66**. (in Russian).

[216] Gayev, Ye.A. (1994) Large Spray Cooler Theoretical Simulation Based on the Continuum Mechanics Method, *Proc. 9th Cooling Tower and Spraying Pond Symposium*, Rhode-Saint-Genese, Belgium.

[217] Gayev, Ye. (1997) Aerothermal theory of an Easily Penetrable Roughness, *Il Nuovo Cimento*, **v. C20**, 331–342.

[218] Gayev, Ye. (1997) *Theoretical modelling of river flows with penetrable roughnesse*, Report to Institute of Hydromechanics, University of Karlsruhe, March 1997.

[219] Gayev, Ye. (2001) Pulsating laminar flow in a duct with easily penetrable roughness near walls, *Int. J. Fluid Mech. Research* **v. 28, No. 1–2**, 164–172.

[220] Gayev, Ye., Savory, E., Toy, N. (2001) Wind Tunnel Investigation of a Complex Canopy Shear Flow, *Int. J. of Fluid Mech. Research* **v. 28, No. 4**, 484–495.

[221] Gayev, Ye., and Savory, E. (2002) Canopy vorticity derived from spectra measurements, *Int. J. of Fluid Mech. Research* **v. 29, No. 3–4**, 481–486.

[222] Gayev, Ye.A., and Shikhaliev, S.Z. (2002) Numerical investigation of flow entrance to a duct with easily penetrable roughness, *Applied Hydromechanics (Prikladna Hydromekhanica)*. **4(76)** N. 4, (in Russian).

[223] Gayev, Ye.A. *Interaction of flows with easily penetrable roughness in the nature and engineering*, Kiev, Institute of Hydromechanics UNAS (to be printed).

[224] Geneva Association *World Fire Statistics* (2001) **Bulletin 17**, International Association for the Study of Insurance Economics, Geneva, Switzerland.

[225] Gerrard, J. (1978) The wakes of cylindrical bluff bodies at low Reynolds Number, *Phil. Trans. Roy. Soc. A.* **288(1354)**, 351–382.

[226] Ghisalberti, M. (2000) *Mixing layers and coherent structures in vegetated aquatic flows*, M.S. Thesis, Massachusetts Institute of Technology, Cambridge.

[227] Ghisalberti, M., and Nepf, H.N. (2002) Mixing layers and coherent structures in vegetated aquatic flows. *Jnl. of Geophysical Research* **107**, 3–11.

[228] Ghisalberti, M., and Nepf, H. (2004) The limited growth of vegetated shear-layers, *Water Res. Res.* **40**, W07502, doi:10.1029/2003WR002776.

[229] Ghisalberti, M. (2005) *Momentum and scalar transport in vegetated shear flows*, PhD. Thesis, Massachusetts Institute of Technology, Cambridge, Ma, USA.

[230] Ghosh, S., Hunt, J.C.R., Phillips, J.C., and Miller, P.C.H. (1993) Dynamics of turbulent air-flow in droplet driven sprays, *Applied Scientific Resarch* **51**, 257–262.

[231] Ginsberg, A., and Stefan, H.G. (1995) *Hydrodynamics of flow through vegetation in open channels*, A review. Technical report, St. Anthony Falls Hydr. Lab., Univ. of Minnesota.

[232] Gloster, J., and Alexandersen, S. (2004) New direction: Airborne transmission of foot-and-mouth disease virus, **Atmos. Environ. 38**, 503–505.

[233] Graziani, G., Klug, W., and Moksa, S. (1998) *Real-Time Long-Range Dispersion Model Evaluation of the ETEX First Release*, EU JRC.

[234] Grell, G., Dudhia, J., and Stauffer, D. (1994) *A Description of the Fifth-Generation PENN STATE/NCAR Mesoscale Model (MM5), NCAR Technical Note, NCAR/TN-398+STR*, Boulder, Colorado, National Center for Atmospheric Research.

[235] Griffiths, I.H., Brook, D.R., Hall, D.J., Berry, A., Kingdon, R.D., Clawson, K.L., Biltoft, C., Hargrave, J.M., Clem, C.M., Strickland, D.C.H., and Spanton, A.M. (2002) Urban Dispersion Model (UDM) validation, *In Proceedings of the American Meteorological Society Fourth Symposium on the Urban Environment*, Davis, California, May 2002.

[236] Grimmond, C.S.B., Cleugh, H.A., and Oke, T.R. (1991) An objective urban heat storage model and its comparison with other schemes, Atmos. Environ. **25B**, 311–326.

[237] Grimmond, C.S.B., and Oke, T.R. (1999) Heat storage in urban areas: Local-scale observations and evaluation of a simple model, *J. Appl. Meteor.* **38**, 922–940.

[238] Grimmond, C.S.B., and Oke, T.R. (1999) Aerodynamic properties of urban areas derived from analysis of surface form, *J. Appl. Meteor.* **38 (9)**, 1262–1292.

[239] Grimmond, C.S.B., Salmond, J.A., Oke, T.R., Offerle, B., and Lemonsu, A. (2004) Flux and turbulence measurements at a densely built-up site in Marseille: Heat, mass (water and carbon dioxide), and momentum, *J. Geophys Res.* **109, D24101**.

[240] Gross, G. (1987) A numerical study of the air flow within and around a single tree, *Boundary Layer Meteorology* **Vol. 40, No. 4**, 311–327.

[241] Gross, G. (1993) *Numerical Simulation of Canopy Flows*, Berlin – Heidelberg, Springer Verlag.

[242] Guardo, M., and Tomasello, R. (1995) Hydrodynamic simulations of a constructed wetlands in South Florida, *Water Resources Bulletin* **31**, 687–701.

[243] Hall, D.J., Macdonald, R., Walker, S., and Spanton, A.M. (1996) *Measurements of dispersion within simulated urban arrays – a small scale wind tunnel study*. Building Research Establishment, BRE Client Report CR 178/96, November 1996.

[244] Hall, R.C. (Ed.) (1997) *Evaluation of modelling uncertainty – CFD modelling of nearfield atmospheric dispersion*, EU Project EV5V-CT94–0531, Final Report, WS Atkins Consultants Ltd., Woodcote Grove, Ashley Road, Epsom, Surrey KT18 5BW, UK.

[245] Hall, D.J., and Cowan, I.R. (1998) Modelling of atmospheric dispersion near buildings, *NAFEMS International Journal of CFD Case Studies*, April 1998, 7–18.

[246] Hall, D.J., Walker, S., and Spanton, A.M. (1999) Dispersion from courtyards and other enclosed spaces, *Atmospheric Environment* **33**, 1187–1203.

[247] Hall, D.J., Spanton, A.M., Griffiths, I.H., Hargrave, M., Walker, S., and John, C. (2001) The UDM: a puff model for estimating dispersion in urban areas. In *Proceedings of 7th International Conference on Harmonisation within Atmospheric Dispersion Modelling for Regulatory Purposes*, Belgirate, Italy, 256–260.

[248] Hall, D.J., Spanton, A.M., Griffiths, I.H., Hargrave, M., and Walker, S. (2002) *The Urban Dispersion Model (UDM): Version 2.2 Technical Documentation. DSTL/TR04774*, Porton Down, Salisbury SP40JQ UK.

[249] Halsall, P. (1998) *Ancient History Source book: Dio Cassius: Nero and the Great Fire 64 CE*, Internet Ancient History Source book, *http://www.fordham.edu/halsall/*.

[250] Hamdi, M., and Schayes, G. (2005) Validation of the Martilli's Urban Boundary Layer Scheme with measurements from two mid-latitude European cities, *Atmos. Chem. Phys. Discuss.* **5**, 4257–4289.

[251] Hammer, D., and Kadlec, R. (1986) A model for wetland surface water dynamics, *Water Resources Research* **22**, 1951–1958.

[252] Hammerle, A. Haslwanter, A., Schmitt, M., Bahn, M., Cernusca, A., Wohlfahrt, G. (2006) Eddy covariance measurements of carbon dioxide, latent and sensible energy fluxes above a meadow on a mountain slope, *Boundary-Layer Meteorol.* (Submitted)

[253] Hanna, S.R., Briggs, G.A., and Hosker, R.P. (1982) *Handbook on atmospheric diffusion*, DOE/TIC-11223 (DE82–002045), NTIS/USDOC, Springfield, VA.

[254] Hanna, S.R., and Chang, J.C. (2001) Use of the Kit Fox field data to analyze dense gas dispersion modeling issues, *Atmospheric Environment* **35**, 2231–2242.

[255] Hanna, S.R., and Britter, R.E. (2002) *Wind flow and vapor cloud dispersion at industrial and urban sites*, Center for Chemical Process Safety, AIChE, 3 Park Ave., New York, NY 10016–5901.

[256] Hanna, S., Britter, R. and Franzese, P. (2002) Simple screening models for urban dispersion, In *Proceedings of 8th International Conference on Harmonisation within Atmospheric Dispersion Modelling for Regulatory Purposes*, Sofia, Bulgaria, 14–17 October 2002, 269–273.

[257] Hanna, S.R., Britter, R., and Franzese, P. (2003) A baseline urban dispersion model evaluated with Salt Lake City and Los Angeles tracer data, *Atmos. Environ* **37**, 5069–5082.

[258] Hanna, S.R., Chang, J.C., and Strimaitis, D.G. (1993) Hazardous gas model evaluation with field observations, *Atmos. Environ.* **27A**, 2265–2285.

[259] Hanna, S., Fabian, P., Chang, J., Venkatram, A., Britter, R., Neophytou, M., Brook, D. (2004) Use of urban 2000 field data to determine whether there are significant differences between the performance measures of several urban dispersion models, *AMS-2004 Annual Meeting*, paper 7.3.

[260] Hansen, G. (2004) San Francisco, 1906 Earthquake, Virtual Museum of the City of San Francisco, *http://www.sfmuseum.org/1906/06.html* .

[261] Harman, I.N., and Finnigan, J.J. (2006) A unified framework for the flow over a dense canopy, *Boundary-Layer Meteorol*, (Submitted)

[262] Hasager, C.B., Nielsen, N.W., Boegh, E., Jensen, N.O., Christensen, J.H., Dellwik, E., and Soegaard, H. (2003) Effective roughnesses calculated from satellite-derived land cover maps and hedge information and used in a weather forecasting model, *Boundary-Layer Meteorology* **109**, 227–254.

[263] Heskestad, G. (1975) Physical Modeling of Fire, *J. Fire & Flammability*, **Vol. 6, No. 7**, 253–273.

[264] Himoto, K., and Tanaka, T. (2002) Physically-Based Model for Urban Fire Spread, *7th Int. Symposium on Fire Safety Science*, 16–21 June 2002, Worcester Polytechnic Institute, Worcester, MA, pp. 129–140.

[265] Hinch, E.J. (1977) An averaged-equation approach to particle interactions in a fluid suspension, *J. Fluid Mech.* **83**, 695–720.

[266] Hinze, J.O. (1975) Turbulence, McGraw-Hill.

[267] Hirsch, C. (2003) *The QNET-CFD Network Newsletter* V. **2**, *No.* 1, April 2003 (Ed.).

[268] Ho, C.M., and Huerre, P. (1984) Perturbed free shear layers, *Ann. Rev. Fluid. Mech.* **16**, 365–424.

[269] Hoe, S., Sørensen, J.H., and Thykier-Nielsen, S. (1999) The Nuclear Decision Support System ARGOS NT and Early Warning Systems in Some Countries around the Baltic Sea, *Proceedings of the 7th Topical Meeting on Emergency Preparedness and Response*, September 14–17, 1999, Santa Fe, New Mexico, USA.

[270] Hoe, S.C., Muller, H., Gering, F. Thykier-Nielsen, S., and Sørensen, J.H. (2002) ARGOS 2001 a Decision Support System for Nuclear Emergencies, In *Proceedings of the Radiation Protection and Shielding Division Topical Meeting*, April 14–17, 2002, Santa Fe, New Mexico, USA.

[271] Hoel, P., Port, S., and Stone, C. (1972) *Introduction to Stochastic Processes*, Waveland Press, Prospect Heights, Illinois.

[272] Hodur, R. (1997) The Naval Research Laboratory's Coupled Ocean/Atmosphere Mesoscale Prediction System (COAMPS), *Mo. Wea. Rev.***125**, 1414–1430.

[273] Hoerner, S.F. (1965, 1993) *Fluid-Dynamic Drag: practical information on aerodynamic drag and hydrodynamic resistance*, Hoerner Fluid Dynamics, Midland Park, N.J.

[274] Hogstrom, U., and Smedman, A. (1984) The wind regime in coastal areas with special reference to results obtained from the Swedish Wind Energy Program, *Boundary-Layer Meteorol* **33**, 351–373.

[275] Hogstrom, U., Hunt, J.C.R., and Smedman, A.S. (2002) Theory and measurements for turbulence spectra and variances in the near neutral surface layer, *Boundary-Layer Meteorol* **103**, 101–124.

[276] Hort, M., Devenish, B., and Thomson, D. (2002) Building affected dispersion: development and initial performance of a new Lagrangian particle model. In *Proceedings of 15th AMS Symposium on Boundary Layers and Turbulence*.

[277] Hribersek, M., Jesl, R., and Skerget, L. (2002) Fluid flow in channel partially filled with porous material, *Advances in Fluid Mechanics IV* (Rahman,Verhoen, Brebbia – Editors), WIT Press, Ashurst Lodge, Southampton.

[278] Hsi, G., and Nath, J.H. (1970) Wind drag within simulated canopies *J. Appl. Meteorology* **9, 4**, 592–602.

[279] Huettel, M., and Gust, G. (1992) Impact of bioroughness on interfacial solute exchange in permeable sediments, *Mar. Ecol. Prog. Ser.* **89**, 253–267.

[280] Hunt, J.C.R., and Mulhearn, P.J. (1973) Turbulent dispersion from sources near two-dimensional obstacles, *J. Fluid Mech.* **61**, 245–274.

[281] Hunt, J.C.R., Puttock, J.S., and Snyder, W.H. (1979) Turbulent diffusion from a point source in stratified and neutral flows around a three-dimensional hill. Part I. Diffusion equation analysis, *Atmospheric Environment* **13**, 1227–1239.

[282] Hunt, A., and Castro, I.P. (1981) Scalar dispersion in model-building wakes, *J. Wind Engineering and Industrial Aerodynamics* **17**, 89–115.

[283] Hunt, J.C.R., and Simpson, J.E. (1982) Atmospheric Boundary Layers Over Non-Homogeneous Terrain, Chapter 7 from *Engineering Meteorology*, E.J. Plate, ed., Elsevier Scientific Publ. Co., 269–318.

[284] Hunt, J.C.R. (1985) Turbulent diffusion from sources in complex flows. *Ann. Rev. Fluid Mech.* **17**, 447–485.

[285] Hunt, J.C.R., Rottman, J.W., and Britter, R.E. (1985) Some physical processes involved in the dispersion of dense gases. In *Proceedings of IUTAM Symposium on Atmospheric dispersion of heavy gases and small particles* (eds. G. Ooms and H. Tennekes), Springer, 361–395.

[286] Hunt, J.C.R., Holroyd, R.J., and Carruthers, D.J. (1988) *Preparatory studies for a complex dispersion model*, CERC Report HB9/88. This report will also appear on the ADMLC web site, *http://ww.admlc.org.uk.*

[287] Hunt, J.C.R., Leibovich, S., and Richards, K.J. (1988) Turbulent shear flow over low hills, *Q. J. Roy. Meteorol. Soc.* **114**, 1435–1470.

[288] Hunt, J.C.R., Holroyd, R.J., Carruthers, D.J., Robins, A.G., Apsley, D.D., Smith, F.B., and Thomson, D.J. (1991) Developments in modelling air pollution for regulatory uses. In *Proceedings of 18th NATO-CCMS Int. Tech. Mtg. on Air Pollution Modelling and its Applications*, Vancouver, Canada. Ed. H. van Dop, Plenum, New York.

[289] Hunt, J.C.R., Tampieri, F., Weng, W.S., and Carruthers, D.J. (1991) Air flow and turbulence over complex terrain: a colloquium and a computational workshop, *J. Fluid Mech.* **227**, 667–688.

[290] Hunt, J.C.R. (1996) Atmospheric diffusion from a steady source in a turbulent airflow at low mean wind speeds, *Note to UK Atmospheric Dispersion Modelling Working Group (National Radiological Protection Board)*, Report R292, 19–22.

[291] Hunt, J.C.R. (1999) Environmental forecasting and modelling turbulence, *Physica D*, **133**, 270–295.

[292] Hunt, J.C.R., and Durbin, P.A. (1999) Perturbed vortical layers and shear sheltering, *Fluid Dyn Res.* **24**, 375–404.

[293] Hunt, J.C.R., Olafsson, H., and Bougeault, P. (2001) Coriolis effects on orographic and mesoscale flows, *Q. J. R. Met. Soc.***127**, 601–633.

[294] Hunt, J.C.R., and Eames, I. (2002) The disappearance of laminar and turbulent wakes in complex flows, *J. Fluid Mech.* **457**, 111–132.

[295] Hunt, J.C.R., Carruthers, D.J., and Kilbane-Dawe, I. (2002) *Developments in regulatory air pollution modelling*, NRPB report.

[296] Hunt, J.C.R., Carruthers, D., Daish, N., and Britter, R. (2003) *Dispersion from Accidental Releases in Urban Areas*, (to NRPB; ADMLC)

[297] Hunt, J.C.R., Fernando, H.J.S., and Princevac, M. (2003) Unsteady thermally-driven flows on gentle slopes, *Journal of the Atmospheric Sciences*.

[298] Hunt, J.C.R., Orr, A., Rottman, J.W., and Capon, R. (2003) Coriolis effects in mesoscale flows with sharp changes in surface conditions, *Conference on shallow layer flows*, Delft. *Quarterly Journal of the Royal Meteorological Society*.

[299] Hunt, J.C.R. (2004) How can cities mitigate and adapt to climate change? *Building Research & Information* **32(1)**, 55–57.

[300] Hunt, J.C.R., Grinchenko, V.T., and Gayev, Ye.A. (2004) (Eds) Flow and transport processes in complex obstructed geometries, *Abstracts of NATO Advances Study Institute PST.ASI.980064*, Kyiv, Institute of Hydromechanics NASU, May 4–15, 2004.

[301] Hunt, J.C.R., Grinchenko, V.T., and Gayev, Ye.A. (2004) NATO Advanced Study Institute # PST.ASI.980064 Flow and Transport Processes in Complex Obstructed Geometries: from cities and vegetative canopies to industrial problems. Kyiv (Ukraine), May 4–15, 2004. *ERCOFTAC Bulletin*. **63**, 27– 31.

[302] Hunt, J.C.R., Eames, I., and Westerweel, J. (2005) Mechanics of inhomogeneous turbulence and interfacial layers, *Journal of Fluid Mechanics*, in press.

[303] Hurd, C.L. (2000) Water motion, marine macroalgal physiology, and production, *J. Phycol.* **36**, 453–472.

[304] Idelchik, I.E. (1986) *Handbuch of Hydraulic Resistance*, Berlin, Springer-Verlag.

[305] Ikeda, S., and Kanazawa, M. (1996) Three-dimensional organized vortices above flexible water plants, *J. Hydraul. Eng.* **122(11)**, 634- 640.

[306] Inoue, E. (1963) On the Turbulent Structure of Airflow within Crop Canopies, *J. Meteorol. Soc. Japan* **Vol. 41**, 317–326.

[307] Isobe, S. (1972) A spectral analysis of turbulence in a corn canopy, *Bull. Nat. Inst. Agr. Sci. (Japan)* Series A 19, 101–113.

[308] ISO (1997) Wildland/Urban Fire Hazard, ISO Company, *http://www.iso.com* .

[309] Issartel, J.P. (2003) Rebuilding sources of linear tracers after atmospheric concentration measurements, *Atmos. Chem. Phys.***3**, 2111–2125.

[310] Jackson, P.S., and Hunt, J.C.R. (1975) Turbulent wind flow over a low hill, *Q. J. Roy. Meteorol. Soc.***101**, 929–956

[311] Jackson, P.S. (1981) On the displacement height in the logarithmic velocity profile, *Journal of Fluid Mechanics* **111**, 15–25.

[312] Jadhav, R., and Buchberger, S. (1995) Effects of vegetation on flow through free water surface wetlands, *Ecological Engineering* **4**, 481–496.

[313] Jaeger, L. (1985) Estimations of surface roughnesses and displacement heights above a growing pine forest from wind profile measurements over a period of ten years, *The Forest-Atmopshere Interaction*, B.A. Hutchson and B.B. Hicks (eds.), D. Reidel Publishing Company, 71–90.

[314] Jagger, T.A. (1923) The Yokohama-Tokyo Earthquake of September 1, 1923, *Bulletin of the Seismological Society of America* (also see *http://nisee.berkeley.edu/kanto/yokohama.html*)

[315] Jensen, N.O. (1978) Change of surface roughness and the planetary boundary layer, *Quart. J. R. Met. Soc.* **Vol. 104**, 351–356.

[316] Jensen, N.O., and Peterson, E.W. (1978) On the escarpment wind profile, *Quart. J. R. Met. Soc.* **Vol. 104**, 719–728.

[317] Jenter, H., and Duff, M. (1999) Locally-forced wind effects on shallow waters with emergent vegetation, in *Proc. Third International Symposium of Ecohydraulics*, IAHR, Salt Lake City.

[318] Jerram, N., Perkins, R.J., Fung, J.C.H., Davidson, M.J., Belcher, S.E., and Hunt, J.C.R. (1993) Atmospheric flow through groups of buildings and dispersion from localized sources, in *Wind Climate in Cities*, NATO Advanced Study Institute, Karlsruhe, July 1993.

[319] Jerram, N., Belcher, S.E., and Hunt, J.C.R. (1994) Turbulent flow through a distributed force – a model for the wind within and above an urban canopy, in *Flows through Groups of Obstacles, Proc. of the IMA Conf.*, Cambridge, 157–173.

[320] Jerram, N., Perkins, R.J., Fung, J.C.H., Davidson, M.J., Belcer, S.E., and Hunt, J.C.R. (1995) Atmspheric Flow Through Groups of Buildings and Dispersion from Localised Sources, *Wind Climate in Cities*, (J.E. Cermak, et al., eds.), 109–130.

[321] Joffre, S.M. (1982) Momentum and Heat Transfers in the Surface Layer over a Frozen Sea, *Boundary Layer Meteorology* **24**, 211–229.

[322] Kadlec, R. (1990) Overland flow in wetlands: vegetation resistance, *J. Hyd. Eng.* **116**, 691–707.

[323] Kadlec, R., and Knight, R. (1996) *Treatment Wetlands*, Lewis Publishers, New York.

[324] Kaimal, J.C., Finnigan, J.J. (1994) *Atmospheric Boundary Layer Flows: Their Structure and Measurement.*, – N.Y.-Oxford: Oxford University Press.

[325] Karter, M.J., Jr. (2003) *Fire Loss in the United States During 2002*, National Fire Protection Association, Quincy, MA.

[326] Kastner-Klein, P., Rotach, M., and Fedorovich, E. (2000) Experimental study on mean flow and turbulence characteristics in an urban roughness sublayer, in Proceedings of 14th AMS Symposium on Boundary Layers and Turbulence, Aspen, CO, August 7–11, 2000.

[327] Kastner-Klein, P., and Rotach, M.W. (2004) Mean Flow and Turbulence Characteristics in an Urban Roughness Sublayer, *Boundary-Layer Meteorology* **Vol. 111**, 55–84.

[328] Katul, G.G., Albertson, J.D. (1998) An investigation of higher-order closure models for a forested canopy, *Boundary-Layer Meteorol.* **89**, 47–74.

[329] Katul, G., and Chang, W.H. (1999) Principal length scales in second-order closure models for canopy turbulence, *J. Appl. Meteor.***38**, 1631–1643.

[330] Katul, G.G, Finnigan, J.J., Poggi, D., Leuning, R., and Belcher, S.E. (2006) The influence of hilly terrain on canopy-atmosphere carbon dioxide exchange, *Boundary-Layer Meteorol* (In Press).

[331] Kerr, J.W. (1971) Historic Fire Disasters, *Fire Research Abstracts and Reviews* **Vol. 13, No. 1**, 1–16.

[332] Ketzel, M., Louka, P., Sahm, P., Guilloteau, E., Sini, J.F., and Moussiopoulos, N. (2002) Intercomparison of Numerical Urban Dispersion models – Part II. Street Canyon in Hannover, Germany. Water, Air, and Soil Pollution, *Focus 2*, 603–613.

[333] Ketzel, M. (2004) *Dispersion and Transformation of Traffic Exhaust Particles in the Urban Atmosphere*, PhD thesis, Lund University, Department of physics and National Environmental Research Institute.

[334] Kim, S.E., and Boysan, F. (1999) Application of CFD to environmental flows, *Journal of Wind Engineering and Industrial Aerodynamics***81**, 145–158.

[335] Klote, J.H., and Milke, J.A. (2002) Computational Fluid Dynamics, *Chapter 16 of Design of Smoke Management Systems*, ASHRAE, Atlanta, GA, 225–233.

[336] Klote, J.H., and Milke, J.A. (2002) Physical Modeling, *Chapter 15 of Design of Smoke Management Systems*, ASHRAE, Atlanta, GA, 217–224.

[337] Klote, J.H., and Milke, J.A. (2002) *Principles of Smoke Management*, ASHRAE Publications.

[338] Knight, D.W., and Macdonald, J.A. (1979) Hydraulic resistance of artificial strip roughness, *Proc. ASCI, J. Hydraulics Div.* **HY6**, 675–691.

[339] Knutson, P., Brochu, R., Seelig, W., and Inskeep, M. (1982) Wave damping in Spartina alterniflora marshes, *Wetlands* **2**, 87–104.

[340] Koch, D.L., and Brady, J.F. (1985) Dispersion in fixed beds. *J. Fluid Mech.* **154**, 399–427.

[341] Koch, E.W. (1994) Hydrodynamics, diffusion-boundary layers and photosynthesis of the seagrasses Thalassia testudinum and Cymodocea nodosa, *Marine Biology* **118**, 767–776.

[342] Koch, D.L., and Ladd, A.J.C. (1997) Moderate Reynolds number flows through periodic and random arrays of aligned cylinders, *J. Fluid Mech.* **349**, 31–66.

[343] Konstantinow, A.R., and Fedorow, S.F. (1960) Application experience of gradient masts for determining evaporation and heat exchange in forest, *Proc. Main Geophysical Observatory*, **Iss. 81**, 91–105. (in Russian)

[344] Kosorin, K. (1977) Rozdelenie rychlosti a tangencialnych naputi v turbulentnom prude zarasteneho koryta, *Vodohospodarsky Casopis*, **25**, 4, 352–356.

[345] Kothari, K.M., Peterka, J.A., and Meroney, R.N. (1986) Perturbation analysis and measurements of building wakes in a stably-stratified turbulent boundary layer, *Journal of Wind Engineering and Industrial Aerodynamics*, **25**, 49–74.

[346] Koutsourakis, N., Vlachogiannis, D., Sfetsos, A., and Bartzis, J.G. (2003) CFD in atmospheric dispersion problems – state of the art, *QNET-CFD Network Newsletter*, **2(1)**, 10–13.

[347] Kouwen, N., Unny, F.E., and Hill, H.M. (1969) Flow retardance in vegetated channels, *J. of the Irrigation and Drainage Div., Proc. ASCE*, **95(IR2)**, 329–342.

[348] Kouwen, N., and Unny, T. (1973) Flexible roughness in open channels, *J. Hydraul. Div., Am. Soc. Civ. Eng.* **99(HY5)**, 713–727.

[349] Kouwen, N., and Li, R.H. (1980) Biomechanics of vegetative channel linings, *J. Hydr. Eng. Div. ASCE* **106 (6)**, 1085–1106.

[350] Kouwen, N. (1989) Field estimation of the biomechanical properties of grass, *J. Hydraulic Research* **26(5)**, 559–569.

[351] Kouwen, N. (1992) Modern approach to design of grassed channels, *J. Irrig. Drain. E. ASCE* **118, 5**, 733–743.

[352] Kovasznay, L.S.G. (1949) Hot-wire investigation of the wake behind cylinders at low Reynolds numbers, *Proc. R. Soc. Lond.* **A 198**, 174–190.

[353] Kowe, R., Hunt, J.C.R., Hunt, A., Couet, B., and Bradbury, L.J.S. (1988) The effects of bubbles on the volume fluxes and the pressure gradients in unsteady and non-uniform flow of liquids, *Int. J. Multiphase Flow* **14**, 587–606.

[354] Kusaka, H., Kondo, H., Kikegawa, Y., and Kimura, F. (2001) A Simple Single-Layer Urban Canopy Model for Atmospheric Models: Comparison with Multi-Layer and SLAB Models, *Boundary-Layer Meteorol.* **101**, 329–358.

[355] Lagouarde, J.P., Moreau, P., Solliec, F., Groleau, D., Irvine, M., Bonnefond, J.M., and Voogt J. (2002) Etude experimentale et modelisation des effets directionnels dans l'IRT en zone urbaine, *Atelier de Modelisation de l'Atmosphere 2002*, Meteo France, Toulouse, 17–19 Dec. 2002, 111–114.

[356] Landsberg, H.E. (1981) The Urban Climate, *Int. Geophys. Ser.* **v. 28**, Academic Press, N.Y.- London

[357] Launiainen, J. (1995) Derivation of the Relationship between the Obukhov Stability Parameter and the Bulk Richardson Number for Flux-Profile Studies, *Boundary-Layer Meteorol.* **76**, 165–179.

[358] Larue de Tournemine, A., and Roig V. (2004) Mean motion induced by a uniform injection of a swarm of rising bubbles, Submitted to *J. Fluid Mech.*

[359] Lawrence, G. (1995) Natural dispersion in a small lake, *Limnol. Oceanogr.* **40(8)**, 1519–1526.

[360] Lawson, T.V. (1980) *Wind Effects on Buildings, Volume 1: Design Applications*, Applied Science Publishers Ltd.

[361] Lawson, R.E., Jr., Snyder, W.H., and Hunt, J.C.R. (1988) Flow structure of recirculating wake flows downwind of surface-mounted obstacles, *Preprint Volume 8th Symposium on Turbulence and Diffusion*, April 1988, San Diego. Am. Met. Soc., Boston.

[362] Lee, S.L. (1972) Fire Research, *Applied Mechanics Reviews* **Vol. 25, No. 5**, 503–509.

[363] Lee, S.L., and Hellman, J.M. (1974) Heat and Mass Transfer in Fire Research, *Advances in Heat Transfer* **Vol. 10**, 219–284.

[364] Lee, S.L., and Otto, F.W. (1975) Gross Vortex Activities in a Simple Simulated Urban Fire, *15th International Symposium on Combustion, 25–31 August 1974, Plant Engineering*, 157–161.

[365] Lee, J.K, Carter, V., and Rybicki, N.B. (1999) Determining flow-resistance coefficients in the Florida Everglades, *Proc. Third Symposium of Ecohydraulics*, IAHR, Salt Lake City.

[366] Lemon, E.R., and Wright, J.L. (1969) Photosynthesis under field conditions. *Agron. J.* **61**, 405–411.

[367] Leonard, L., and Luther, M. (1995) Flow hydrodynamics in tidal marsh canopies, *Limnol. Oceanogr.* **40**, 1474–1484.

[368] Leonard, L., and Reed, D.J. (2002) Hydrodynamics and sediment transport through tidal marsh canopies, *J. of Coastal Res.* **SI 36**, 459–469.

[369] Lesnik, G.E. (1974) Results of measurement of the turbulent energy balance components in a layer of vegetation, *Atmos. Oceanic Phys.* **10**, 400–401.

[370] Ruh-Ming Li, Shen, H.W. (1973) Effect of tall vegetation on flow and sediment, *Proc. ASCE, J. Hydraulics Div.* **99(HY5)**, 793–814.

[371] Lightbody, A. (2004) *Field and laboratory observations of small-scale dispersion in wetlands*, MS Thesis, Massachusetts Institute of Technology.

[372] Lightbody, A., and Nepf, H. (2006) Prediction of velocity profiles and longitudal dispersion in emergensy salt marsh vegetation, *Limnol. Ocean.* **51 (1)**, 218–228.

[373] Lohmeyer, A., Muller, W.J., and Bachlin, W. (2002) A comparison of street canyon concentration predictions by different modellers. Final results from the Podbiexercise, *Atmospheric Environment* **36**, 157–158.

[374] Long, N., Mestayer, P.G., and Kergomard, C. (2002) Development of a software to describe the city morphology and to compute aerodynamic parameters from an urban data base, *Proceedings of the 4th symposium on Urban Climatology*, American Meteorological Society, 20–24 May 2002, Norfolk, 31–32.

[375] Long, N. (2003) *Analyses morphologiques et aerodynamiques du tissu urbain – Application a la climatologie urbaine de Marseille pendant la campagne ESCOMPTE*, Doctoral Thesis (in French), Universite des Sciences et Techniques de Lille, Dec 2003.

[376] Long, N., Mestayer P.G., and Kergomard, C. (2003) Urban database analysis for mapping morphology and aerodynamic parameters: the case of St Jerome suburban area, in Marseille during ESCOMPTE, *Proceedings of the Fifth International Conference on Urban Climate*, September 1–5 2003, Lodz, Poland.

[377] Lopez, F., and Garcia, M. (1996) *Open-channel flow through simulated vegetation: turbulence modeling and sediment transport*, Technical Report WRP-CP-10; U.S. Army Corps of Engineers, Washington, D.C.

[378] Lopez, F., and Garcia, M. (1998) Open-channel flow through simulated vegetation: suspended sediment transport modeling, *Water Resour. Res.* **34(9)**, 2341–2352.

[379] Louis, J.F. (1979) A parametric model of vertical eddies fluxes in the atmosphere, *Boundary-Layer Meteorol.* **17**, 187–202.

[380] Loytsyanski, L.G. (1973) *Mechanics of fluids and gases*, Moscow: Naucka Publ.

[381] Lumley, J.L. (1967) The structure of inhomogeneous turbulent flows, in A.M. Yaglom and V.I. Tatarsky (eds.), *Atmospheric Turbulence and Radio Wave Propagation*, Nauka, Moscow, 166–178.

[382] Luo, S., Gan, T., and Chew, Y. (1996) Uniform flow past one (or two in tandem) finite length circular cylinder(s), *J. Wind Eng. & Indust. Aerodyn.* **59**, 69–93.

[383] Macdonald, R.W. (1997) *Measurements of Dispersion within Simulated Urban Arrays – A 1:10 Scale Field Experiment*, Report to DSTL on Agreement 2044/014/CBDE, Environmental Technology Centre, UMIST, UK.

[384] Macdonald, R., Griffiths, R.F., and Hall, D.J. (1998) A comparison of results from scaled field and wind tunnel modelling of dispersion in arrays of obstacles, *Atmospheric Environment* **32**, 3845–3862.

[385] Macdonald, R.W., Hall, D.J., Griffiths, R.F. (1998) Scale model study of building effects on dispersion in the urban canopy at intermediate source distances, in *Proceedings of 5th International Conference on Harmonisation within Atmospheric Dispersion Modelling for Regulatory Purposes*, Rhodes, Greece, 18–21 March 1998.

[386] Macdonald R.W. (2000) Modelling the mean velocity profile in the urban canopy layer, *Bound.-Layer Meteorol.* **v. 97**, 25–45.

[387] Macdonald, R.W., Carter-Schofield, S.L., and Slawson, P.R. (2001) Measurements of mean plume dispersion in simple obstacle arrays at 1:200 scale. Presented at *the 5th Annual GMU/DTRA Transport and Dispersion Modelling Workshop*, 18–19 July 2001, George Mason University, Fairfax, VA.

[388] Magnaudet J., Rivero M., Fabre J. (1997) Accelerated flows past a rigid sphere or a spherical bubble. Part 1. Steady straining flow. *J. Fluid Mech.* **284**, 97–135.

[389] Mahura, A., Leroyer, S., Mestayer, P., Calmet, I., Dupont, S., Long, N., Baklanov, A., Petersen, C., Sattler, K., and Nielsen, N.W. (2005) Large Eddy Simulation of Urban Features for Copenhagen Metropolitan Area, *Atmospheric Chemistry and Physics Discuss.* **5**, 11183–11213.

[390] Mahura, A., Sattler, K., Petersen, C., Amstrup, B., Baklanov, A. (2005) DMI-HIRLAM Modelling with High Resolution Setup and Simulations for Areas of Denmark, *DMI Technical Report*, 05–12.

[391] Marchuk, G.I. (1982) *Mathematical modeling in the environmental problems*, Moscow, Nauka. (in Russian)

[392] Marchuk, G.I. (1995) *Adjoint equations and analysis of complex systems*, Kluber Academic Publication.

[393] Martilli, A., Clappier, A., and Rotach, M.W. (2002) An Urban Surface Exchange Parameterisation for Mesoscale Models, *Boundary-Layer Meteorol.***104**, 261–304.

[394] Maruyama, T. (1992) Optimization of roughness parameters for staggered arrayed cubic blocks using experimental data, *J. Wind Engineering***No. 52**, 424–429.

[395] Maruyama, T., and Tanaka, T. (2002) Experimental study on high temperature field behind a flame in a turbulent boundary layer, *Proceedings Euromech, 9th European Turbulence Conference*, 2–5 July 2002, University of Southhampton, UK, 4 pp.

[396] Maryon, R.H., and Buckland, A.T. (1995) Tropospheric dispersion: the first ten days after a puff release, *Q. J. R. Met. Soc.***121**, 1799–1833.

[397] Massman, W. (1987) A comparative study of some mathematical models of the mean wind structure and aerodynamic drag of plant canopies, *Boundary Layer Meteorology*, **Vol. 40**, 179–197.

[398] Masson, V. (2000) A Physically-Based Scheme for the Urban Energy Budget in Atmospheric Models, *Boundary-Layer Meteorol.* **98**, 357–397.

[399] Mastryukov, B.S., and Ivanov, A.V. (2002) Risk assessment of ammonia intoxication caused by plant wreck in town conditions, Moscow State Institute of Steel and Alloys, *PHOENICS Journal* **14, 1**, art. 24: MSISA.

[400] Mayle, R. (1970) *Aerodynamics of the Fire Whirl*, Doctoral Dissertation, Harvard University, Cambridge, MA.

[401] Mazda, Y., Wolanski, E., King, B., Sase, A., Ohtsuka, D. and Magi, M. (1997) Drag force due to vegetation in mangrove swamps, *Mangroves and Salt Marshes* **1**, 193–199.

[402] McBean, G.A. (1968) An investigation of turbulence within the forest, *J. Appl. Meteorol.* **7**, 410–416.

[403] McElroy, J.L., and Pooler, F. (1968) The St. Louis dispersion study – Volume II – analysis, *National Air Pollution Control Admin*, Pub. **No. AP-53**, US DHEW Arlington, VA.

[404] McNaughton, K.G. (1989) Micrometeorology of shelter belts and forest edges, *Phil. Trans. R. Soc. Lond., B* **Vol. 324**, 351–368.

[405] Meinders, E.R. and Hanjalic, K. (1999) Vortex structure and heat transfer in turbulent flow over a wall-mounted matrix of cubes, *Int. J. Heat Fluid Flow* **20**, 255–267.

[406] Mellor, G.L., and Yamada, T. (1974) A hierarchy of turbulence closure models for planetary boundary layers, *J. Atmos. Sci.***31**, 1791–1806.

[407] Menzhulin, G.V. (1970) On the methodology to calculate meteorological regime in vegetative comunity, *Meteorology and Hydrology (Meteorologiya i gidrologiya)* **No. 2**, 92–99.

[408] Menzhulin, G.V. (1972) On aerodynamics parameters of vegetation canopy, *Proc. of Main Geophysical Observatory (GGO)*. **Iss. 282**, 133–143.

[409] Menzhulin, G.V. (1973) On the theory of a stationary meteorological regime of a vegetation canopy, *Proc. Main Geophysical Observatory*. **Iss. 297**, 20–28.

[410] Meroney, R.N. (1968) Characterictics of wind and turbulence in and above model forests, *J. Applied Meteorology***v. 7, 5**, 780–788.

[411] Meroney, R.N. (1970) Wind Tunnel Studies of the Air Flow and Gaseous Plume Diffusion in the Leading Edge and Downstream Regions of a Model Forest, *Atmospheric Environment* Vol. 4, 597–614.

[412] Meroney, R.N. (1978) Studying the Convective Heat Transfer from a Building Model with Infrared Camera Techniques, *1978 ASME Winter Annual Meeting*, December 10–15, 1978, San Francisco, California, 28 p., ASME Paper 78-WA/HT-58, 1978.

[413] Meroney, R.N., and Neff, D.E. (1985) Numerical modelling of water spray barriers for dispersing dense gases, *Boundary-Layer Meteorol.* **31**, 233–247.

[414] Meroney, R.N. (1986) *Wind-Tunnel Modeling of Convective Boundary Layer*, Sonderforchungsbereich 210, University of Karlsruhe, West Germany, July 1986, 37 pp.

[415] Meroney, R.N. (1988) Guidelines for Fluid Modeling of Dense Gas Cloud Dispersion, *Journal of Hazardous Materials* **Vol. 17**, 23–46.

[416] Meroney, R.N. (1990) *Review and Classification of Complex Terrain Models for Use with Integrated Pest Management Program Spray Models*, Colorado State University Civil Engineering Memorandum 89–90-RNM-1, Prepared for Forest Service Technology and Development Program, U.S. Dept. Of Agriculture, Forest Service, Missoula, Montana.

[417] Meroney, R.N. (1992) Dispersion in Non-Flat Obstructed Terrain and Advanced Modeling Techniques, *Plant/Operations Progress* **Vol. 11, No. 1**, 6–11.

[418] Meroney, R.N. (1993) *Wind Tunnel Modelling of Hill and Vegetation Influence on Wind Power Availability, Task1: Literature Review*, CSU Report CER92–93-RNM-1 to Meteorological Services, U.S. Windpower, Inc., Livermore, CA.

[419] Meroney, R.N., McCarthy, E.F., and Neff, D.E. (1993) Elevation and Vegetation Considerations on Wind Power Availability: A Wind Tunnel Study, *23rd Annual American Wind Energy Association Conference (Wind Power '93)*, July 12–16, 1993, San Francisco, CA.

[420] Meroney, R.N., Pavageau, M., Rafailidis, S., and Schatzmann, M. (1996) Study of Line Source Characteristics for 2-d Physical Modelling of Pollutant Dispersion in Street Canyons, *J. Wind Engineering & Industrial Aerodynamics* **Vol. 62**, 37–56.

[421] Meroney, R.N., Banks, D., and Chang, C.H. (2002) CFD Simulation of the Progress of Fires in Building Atria, *Session on Computational Evaluation of Wind Effects on Buildings, Proceedings of ASCE 2002 Structures Congress*, Denver, CO, April 4–6, 2002.

[422] Meroney, R.N. (2003) Fire Whirls and Building Aerodynamics, *Proceedings of 11th Int. Conf. On Wind Engineering*, 2–5 June 2003, Texas Tech University, Lubbock, TX.

[423] Meroney, R.N. (2003) Fire Whirls, Fire Tornadoes and Fire Storms: Physical and Numerical Modeling, *Proceedings of PHYSmod2003: International Workshop on Physical Modeling of Flow and Dispersion Phenomena*, Prato, Italy, 3–5 September 2003.

[424] Meroney, R.N., and Banks, D.B. (2004) Fire and Smoke in Building Atria, *Proceedings of the 1ST International COE Symposium on Wind Effects on Buildings and Urban Environment*, Science Council, Tokyo, 8–9 March 2004.

[425] Mestayer, P.G., and Anquetin, S. (1995) Climatology of cities, In *Diffusion and Transport of Pollutants in Atmospheric Mesoscale Flow Fields*, Kluwer Publishers, 165–189.

[426] Mestayer, P., and Bottema, M. (2002) Parameterisation for roughness parameters in urban areas. In: Rotach M., Fisher B., Piringer M. (Eds.), COST Action *715 Workshop on Urban Boundary Layer Parameterisations* (Zurich, 24–25 May 2001), Office for Official Publications of the European Communities, EUR 20355, 51–61.

[427] Mestayer, P.G., Vachon, G., and Rosant, J.M. (2002) The Nantes '99 data base for model validation of air quality in streets, in *Proceedings of 8th International Conference on Harmonisation within Atmospheric Dispersion Modelling for Regulatory Purposes*, Sofia, Bulgaria, 14–17 October 2002, 297–300.

[428] Mestayer, P., Dupont, S., Calmet, I., Leroyer, S., Mahura, A., Penelon, T. (2004) *SM2-U: Soil Model for Sub-Meso scales Urbanized version. Model Description. Deliverable D4.2 for FUMAPEX WP4*, Project report, Spring 2004, Nantes, ECN, France.

[429] Mestayer, P.G., Durand, P., Augustin, P., Bastin, S., Bonnefond, J.-M., Benech, B., Campistron, B., Coppalle, A., Delbarre, H., Dousset, B., Drobinski, P., Druilhet, A., Frejafon, E., Grimmond, S., Groleau, D., Irvine, M., Kergomard, C., Kermadi, S., Lagouarde, J.-P., Lemonsu, A., Lohou, F., Long, N., Masson, V., Moppert, C., Noilhan, J., Offerle, B., Oke, T., Pigeon, G., Puygrenier, V., Roberts, S., Rosant, J.-M., Said, F., Salmond, J., Talbaut, M., and Voogt, J. (2005) The Urban Boundary Layer Field Experiment over Marseille. UBL/CLU-ESCOMPTE: Experimental Set-up and First Results, *Boundary-Layer Meteorol* **114**, 315–365.

[430] Meyers, T.P., and Paw, U.K.T. (1987) Modelling the plant canopy micrometeorology with higher-order closure principles, *J. Agric. Forest Meteorol.* **41**, 143–163.

[431] Middleton, D.R. (1998) A new box model to forecast urban air quality: BOX-URB, *Environmental Monitoring and Assessment*, **52**, 315–335.

[432] Mikkelsen, T., Larsen, S.E., Thykier-Nielsen, S. (1984) Description of the Riso puff diffusion model, *Nuclear Technology* **67**, 56–65.

[433] Mikkelsen, T., Thykier-Nielsen, S., Astrup, P., Santabarbara, J.M., Sørensen, J.H., Rasmussen, A., Robertson, L., Ullerstig, A., Deme, S., Martens, R., Bartzis, J.G., and Pasler-Sauer, J. (1997) MET-RODOS: A Comprehensive Atmospheric Dispersion Module, *Radiat. Prot. Dosim.* **73**, 45–56.

[434] Miyazaki, T., and Hunt, J.C.R. (2000) Turbulence structure around a columnar vortex: rapid distortion theory and vortex wave excitation, in *Proceedings of the European Turbulence Conference (ETC-7)* (ed. U. Frisch), Kluwer. Also *J. Fluid Mech.***402**, 349–378.

[435] Monin, A.S., and Obukhov, A.M. (1971) *Statistical fluid mechanics*, v. 1, MIT Press, Cambridge, Massachusetts.

[436] Moulinec, C., Hunt, J.C.R., and Nieuwstadt, F. (2003) Disappearing wakes and scalar diffusion in tube bundles, Submitted to *Journal of Flow Turbulence and Combustion*. (See also *ERCOFTAC Bulletin* **No. 56**, 5–9.)

[437] Munich Re (2004) *Trends of Great Natural Catastrophes Since 1950*, TOPICS Geo: Annual Review Natural Catastrophes in 2003. (see *http* : *//www.munichre.com/publications/*302 − −03971_*en.pdf rdm* = 1709)

[438] Murakami, S. (1992) Computational Wind Engineering One, *Proceedings of the 1st International Symposium on Computational Wind Engineering (Cwe92)*, Tokyo, Japan, August 21–23, 1992, Elsevier Science.

[439] Mylne, K.R., and Mason, P.J. (1991) Concentration measurements in a dispersing plume at a range of up to 1000m, *Q. J. R. Met. Soc.***117**, 117–206.

[440] Mylne, K.R. (1992) Concentration fluctuation measurements in a plume dispersing in a stable surface layer, *Boundary-Layer Meteorol.* **60**, 15–48.

[441] Moeng, C.H. (1984) A large-eddy simulation model for the study of planetary boundary-layer turbulence, *J. Atmos. Sci.* **41**, 2052–2062.

[442] Moeng, C.H., and Wyngaard, J.C. (1988) Spectral analysis of large-eddy simulations of the convective boundary layer, *J. Atmos. Sci.* **45**, 3573–3587.

[443] Monteith, J.L. (1963) Gas exchange in plant communities. In: L.T. Evans (Editor), *Environmental Control of Plant Growth*, Academic Press, New York, 95–112.

[444] Moore, D.W. (1963) The velocity of rise of distorted gas bubbles in a liquid of small viscosity. *J. Fluid Mech.* **16**, 659–708.

[445] Morvan, D., and Dupuy, J.L. (2001) Improvement of the Wildland Fire Behavior Model, Fire Star A decision support system for fuel management and fire hazard reduction in Mediterranean wildland – urban interfaces, Contract EVG1-CT-2001–00041, *http://www.eufirestar.org*

[446] Moser, R., and Rogers, M. (1991) Mixing transition and the cascade to small scales in a plane mixing layer, *Phys. Fluids A* **3(5)**, 1128–1134.

[447] Moussiopoulos, N. Mathematisches Modell zur Berechnung von Sprühkühlteichen, Fortschritt-Berichte der VDI Zeitschriften, R. 6, Nr. 105, 190 S.

[448] Moussiopoulos, N. (Editor) (2003) *Air Quality in Cities*, Springer-Verlag, Berlin.

[449] Mozak, N., and Mozak, H. From the Niemen to the Berezina Chronology of the Campaign of 1812 in Russia, Electronic Book downloadable pdf file, 124 pp., *http://www.100megsfree4.com/rusgeneral/1812.htm*

[450] Muraszew, A., Fedele, J.B., and Kuby, W.C. (1979) The Fire Whirl Phenomena, *Combustion and Flame***Vol. 34**, 29–45.

[451] Murgai, M.P., and Emmons, H.V. (1960) Natural convection above fires, *J. Fluid Mech.* **Vol. 8**, 611–624.

[452] Musham, H.A. (1941) The great Chicago Fire, *Papers in Illinois State History and Transactions for the year 1940*, 69–189. *http://www.chicagohs.org/fire/intro/*

[453] Naot, D., Nezu, I., and Nakagawa, H. (1996) Hydrodynamic bahaviour of partly vegetated open channels, *J. of Hydraulic Engineering*, 625–633.

[454] Naot, D., Nezu, I., and Nakagawa, H. (1996) Unstable patterns in partly vegetated channels, *J. of Hydraulic Engineering*, 671–673.

[455] NASA: Earth at Night. *http://antwrp.gsfc.nasa.gov/apod/ap001127.html, 2000.*

[456] *National Commission on Fire Prevention and Control, America Burning* (1973) U.S. Fire Administration.

[457] *National Commission on Fire Rpevention and Control, America Burning Revisited* (1987) U.S. Fire Administration.

[458] Neff, D.E., and Meroney, R.N. (1998) Wind-Tunnel Modeling of Hill and Vegetation Influence on Wind Power Availability, *J. of Wind Engineering and Industrial Aerodynamics* **Vol. 74–76**, 335–343.

[459] Neophytou, M.K., and Britter, R.E. (2004) A simple correlation for pollution dispersion prediction in urban areas, *DAPPLE Cambridge Note 1*, January 2004, *http://www.dapple.org.uk*

[460] Nepf, H.M., Sullivan, J.A., and Zavistoski, R.A. (1997) A model for diffusion within an emergent plant canopy, *Limnol. Oceanogr.* **42(8)**, 85–95.

[461] Nepf, H. (1999) Drag, turbulence and diffusivity in flow through emergent vegetation, *Water Resources Research* **35(2)**, 479–489.

[462] Nepf, H., and Koch, E. (1999) Vertical secondary flows in submersed plant-like arrays, *Limn. & Ocean.* **44(4)**, 1072–1080.

[463] Nepf, H., and Vivoni, E. (2000) Flow structure in depth-limited, vegetated flow, *J. Geophys. Res.* **105(28)**, 547–28, 557.

[464] Nepf, H., White, B., Lightbody, A., Ghisalberti, M., and Tanino, Y. (2004) *Flow and transport processes in complex obstructed geometries, Abstracts of NATO Advances Study Institute PST.ASI.980064*, Kyiv, Institute of Hydromechanics NASU, May 4–15, 2004.

[465] Neunhauserer, L., Fay, B., Baklanov, A., Bjergene, N., Kukkonen, J., Odegaard, V., Palau, J.L., Perez Landa, G., Rantamaki, M., Rasmussen, A., Valkama, I. (2004) Evaluation and comparison of operational NWP and mesoscale meteorological models for forecasting urban air pollution episodes – Helsinki case study. In: Suppan, P. (Ed.), *9th International Conference on Harmonisation within Atmospheric Dispersion Modelling for Regulatory Purposes*, 1–4 June 2004, Garmisch-Partenkirchen, Germany. Vol. 2. pp. 245–249.

[466] Nickitin, I.K. (1980) *Complex turbulent flows and processes of heat and mass exchange*, Kiev, Naukova dumka Publ. (in Russian)

[467] Nielsen, M. (1998) Dense Gas Dispersion in the Atmosphere, Riso-R-1030(EN).

[468] Nigmatullin, R.I. (1978) *Fundamentals of the heterogeneous medium mechanics*, Moscow, Nauka Publishing. (in Russian)

[469] Noilhan, J., and Planton, S. (1989) A Simple Parametrization of Land Surface Processes for Meteorological Models, *Mon. Wea. Rev.* **117**, 536–549.

[470] Nuding, A. (1991) *Fliesswiederstandsverhalten in Gerinnen mit Ufergebusch*, Technische Hochschule Darmstadt, Institut fur Wasserbau **Nr. 35**.

[471] Ohashi, Y., and Kida, H. (2002) Effects of mountains and urban areas on daytime local-circulations in the Osaka and Kyoto regions, *Journal of the Meteorological Society of Japan* **80**, 539–560.

[472] Oke, T.R. (1978) *Boundary layer climates*, London, Methuen & Co Ltd, J. Wiley & Sons, New York.

[473] Oke, T.R. (1988) Street design and urban canopy layer climate, *Energy and Buildings* **Vol. 11**, 103–113.

[474] Oke, T.R., Spronken-Smith, R., Jauregui, E., and Grimmond, C.S.B. (1999) Recent energy balance observations in Mexico City, *Atmos. Environ.* **33**, 3919–3930.

[475] Okubo, A. (1971) Oceanic diffusion diagrams, *Deep-Sea Res.* **18**, 789–802.

[476] Olesen, H.R., Lofstrom, P., Berkowicz, R., and Jensen, A.B. (1992) An improved dispersion model for regulatory use: the OML model, in *Air Pollution Modelling and its Applications IX*, Plenum Press, New York (eds. H. van Dop and G. Kallos).

[477] Owinoh, A., Orr, A., Hunt, J.C.R., and Clark, P. (2005) Numerical modelling of boundary layer flow over a low hill with abrupt surface heat flux change. *To be submitted.*

[478] Palmer, T.Y. (1981) Large Fire Winds, Gases and Smoke, *Atmospheric Environment* **Vol. 15, No. 10/11**, 2079–2090.

[479] Palmer, T.Y. (1990) Nuclear Winter Hysterics, *The Scientist* **Vol. 4, No. 2**, 13 pp., January 20, 1990.

[480] Pardyjak, E.R., Fernando, H.J.S., Hunt, J.C.R., Grachev, A.A. and Anderson, J. (2003) Evolution of nocturnal circulation in complex terrain: Phoenix Air Flow Experiment (PAFEX-1), *Submitted to Boundary Layer Meteorology*. (See also 'Structure of atmospheric boundary layer over the complex terrain of the Phoenix Valley' in *Proceedings of 13th Conference on Boundary Layers and Turbulence*, Am. Met. Soc.)

[481] Park, J., and Schwind, D. (1977) *Wind Power for Farms, Homes and Small Industry*, Nielsen Engineering and Research In., Mountain View, CA, 150 pp

[482] Parker, D.R. (1992) The Oakland-Berkeley Hills Fire, *An Overview, Virtual Museum of the City of San Francisco*, 3 pp. *(http://www.sfmuseum.org/oakfire/overview.html)*

[483] Pasche, E. (1984) Turbulenzmechanismen in naturnahen Fliessgewässern und die Möglichkeiten ihrer mathematischen Erfassung, Institut für Wasserbau und Wasserwirtschaft. Mitteilung 52, *Techn. Hochschule*, Aachen, 1984.

[484] Pasquill, F., and Smith, F.R. (1983) *Atmospheric Diffusion*, 3rd edition, Ellis Horwood Ltd., Chichester.

[485] Pedras, M.H.J., and Lemos, M.J.S. (2001) Macroscopic turbulence modeling for incompressible flow trough undeformable porous media, *Int. J. Heat Mass Trans* **44**, 1081–1093.

[486] Penenko, V.V. (1981) Methods of numerical modeling of the atmospheric processes, Leningrad, Gidrometeoizdat. (in Russian).

[487] Penenko, V., and Baklanov, A. (2001) Methods of sensitivity theory and inverse modeling for estimation of source term and nuclear risk/vulnerability areas, *Lecture Notes in Computer Science* **2074**, 57–66.

[488] Penenko, V., Baklanov A., and Tsvetova, E. (2002) Methods of sensitivity theory and inverse modeling for estimation of source term, *Future Generation Computer Systems* **18**, 661–671.

[489] Penman, H.L., and Long, I.F. (1960) Weather in wheat: an essay in micrometeorology, *Quart. J. Roy. Soc.* **86**, 16–50.

[490] Pernin, the Rev. Peter (1971) The Great Peshtigo Fire: An Eyewitness Account. Madison, Wis.: State Historical Society of Wisconsin, *Reprinted from the Wisconsin Magazine of History* **54**, 246–272 (Summer, 1971).

[491] Persson, C., Rodhe, H., and De Geer, L.E. (1987) The Chernobyl accident: A meteorological analysis of how radionuclides reached and were deposited in Sweden, *Ambio* **16**, 20–31.

[492] Petryk, S., and Bosmajan, G. (1975) Analysis of the flow through vegetation, Proc. ASCI, *J. Hydraulics Div.* **HY7**.

[493] Philip, J.R. (1964) Sources and transfer processes in the air layers occupied by vegetation, *J. Appl. Meteorol.* **3**, 390–395.

[494] Physick, W.L., and Garratt, J.R. (1995), *Boundary-Layer Meteorol.* **74**, 55.

[495] Pielke, R.A. (1984) *Mesoscale meteorological modelling*, Academic Press.

[496] Pigeon, G., Durand, P., Masson, V. (2005) Quantification of anthropogenic heat releases over Toulouse (France) during the CAPITOUL field program, *Short Papers of the 5th International Conference on Urban Air Quality Valencia*, Spain, 29–31 March 2005.

[497] Piringer, M., and Joffre, S. (Eds.) (2005) *The urban surface energy budget and mixing height in European cities: Data, models and challenges for urban meteorology and air quality*/ Baklanov, A., J. Burzynski, A. Christen, M. Deserti, K. De Ridder, S. Emeis, S. Joffre, A. Karppinen, P. Mestayer, D. Middleton, M. Piringer and M. Tombrou. Final Report of WG2 COST-715 Action, Demetra Ltd Publishers, ISBN 954–9526-29–1.

[498] Pitts, W.M. (1991) Wind Effects on Fires, *Prog. Energy Combust. Sci.* **Vol. 17**, 128–134.

[499] Plate, E.J., and Quraishi, A.A. (1965) Modeling of velocity distributions inside and above tall crops, *J. Appl. Meteorol.* **4**, 400–408.

[500] Plate, E.J. (1971) *Aerodynamic Characteristics of Atmospheric Boundary Layers*, U.S. Atomic Energy Commission.

[501] Plate, E.J. (1995) Urban Climaes and Urban Climate Modelling: An Introduction, *Wind Climate in Cities*, (J.E. Cermak et al., eds.), Kluwer Academic Publishers, 23–39.

[502] Poggi, D., Katul, G., and Albertson, J. (2004) A note on the contribution of dispersive fluxes to momentum transfer within canopies, *Boundary-Layer Meteor.* **111**, 615–621.

[503] Poggi, D., Porporato, A., Ridolfi, L., Albertson, J., and Katul, G. (2004) The effect of vegetation density on canopy sub-layer turbulence, *Boundary-Layer Meteor* **111**, 565–587.

[504] Poggi, D., Katul, G.G., and Finnigan, J.J. (2006) Turbulent flows inside dense canopies on gentle hilly terrain. *Q. J. Roy. Meteorol. Soc.* [Submitted]

[505] Poggi, D., Katul, G., and Albertson, J. (2004) Momentum transfer and turbulent kinetic energy budgets within a dense model canopy, *Boundary-Layer Meteor.* **111**, 589–614.

[506] Pope, S.B. (2000) Turbulent flows. Cambridge University Press.

[507] Popov, D.N. (1982) *Non-stationary hydromechanics processes*, Moscow: Mashinostroyenie. (in Russian).

[508] Prahl, J.M., and Tien, J.S. (1973) Preliminary Investigations of Forced Convection on Flame Propagation along Paper and Matchstick Arrays, *Combustion Science and Technology* **Vol. 7**, 271–282,

[509] Prahm, L.P., Conradsen, K., and Nielsen, L.B. (1980) Regional sourse quantification model for sulphur oxides in Europe, *Atmos. Env.* **14**, 1027–1054.

[510] Prandtl, L., Oswatitsch, K., and Wieghard, K. (1984) *Führer durch die Strömungslehre*, Braunschweig, F.Vieweg & Sohn.

[511] Ptasinski, P.K., Boersma, B.J., Nieuwstadt, F.T.M., Hulsen, M.A., Van Den Brule, B.H.A.A., and Hunt, J.C.R. (2003) Turbulent channel flow near maximum drag reduction: simulations, experiments and mechanisms, *Jour. Fluid Mech.* **490**, 251–291.

[512] Pudykiewicz, J.A. (1998) Application of adjiont tracer transport equations for evaluating sourse parameters, *Atmos.Environ.* **32**, 3039–3050.

[513] Puttock, J.S., and Hunt, J.C.R. (1979) Turbulent diffusion from sources near obstacles with separated wakes. Part I. An eddy diffusivity model, *Atmospheric Environment* **13**, 1–13.

[514] Pyne, S.J. (2001) Fire: A Brief History, University of Washington Press, Seattle, WA.

[515] Quintiere, J.G. (1989) Scaling Applications in Fire Research, *Fire Safety Journal*, **Vol. 15**, 3–29.

[516] Quintiere, J.G. (1993) Canadian Mass Fire Experiment, 1989, *J. of Fire Prot. Engr.*, **Vol. 5, No. 2**, 67–78.

[517] Quintela, D.A., and Viegas, D.X. (1995) Convective Heat Losses from Buildings, *Wind Climate in Cities*, (J.E. Cermak et al., eds.), Kluwer Academic Publishers, 503–522.

[518] Quintiere, J.G. (1998) Principles of Fire Behavior, Delmar Publishers, Thompson Learning.

[519] Rappolt, T. (2001) Field test report: measurements of atmospheric dispersion in the Los Angeles urban environment in summer 2001, *Report number 1322, prepared for STI, Bel Air, MD, by Tracer Environ. Sci. and Tech.*, San Marcos, CA 92071. 33 pp. plus data CD.

[520] Rauner, Yu.L. (1972) *Heat balance of vegetating cover*, Leningrad: Hydrometeoizdat. (in Russian)

[521] Raupach, M.R., Thom, A.S., Edwards, I. (1980) A wind-tunnel study of turbulent flow close to regularly arrayed rough surfaces, *Boundary-Layer Meteorology* **18**, 373–397.

[522] Raupach, M.R., Thom, A.S. (1981) Turbulence in and above plant canopies, *Ann. Review Fluid Mech.* **13**, 97–129.

[523] Raupach, M.R., and Shaw, R.H. (1982) Averaging procedures for flow within vegetation canopies, *Boundary-Layer Meteorol.* **22**, 79–90.

[524] Raupach, M.R., Coppin, P.A., and Legg, B.J. (1986) Experiments on Scalar Dispersion Within a Model Plant Canopy. Part I: The Turbulence Structure, *Boundary-Layer Meteorol.* **35**, 21–52.

[525] Raupach, M.R. (1989) Stand Overstorey Processes, *Phil. Trans. R. Soc. Lond.* **B 324**, 175–190.

[526] Raupach, M.R., Finnigan, J.J., and Brunet, Y. (1989) Coherent eddies in vegetation canopies. *Proc. Fourth Australasian Conference on heat and mass transfer, Christchurch, New Zealand*, 9–12 May 1989, 75–90.

[527] Raupach, M., Antonia, R. and Rajagopalan, S. (1991) Rough-wall turbulent boundary layers, *Appl. Mech. Rev.* **44(1)**, 1–25.

[528] Raupach, M.R., Weng, W.S., Carruthers, D.J., and Hunt, J.C.R. (1992) Temperature and humidity fields and fluxes over low hills, *Q. J. Roy. Meteorol. Soc.* **118**, 191–225.

[529] Raupach, M. (1992) Drag and drag partition on rough surfaces, *Boundary-Layer Meteorology* **60**, 375–395.

[530] Raupach, M.R., Finnigan, J.J., and Brunet, Y. (1996) Coherent eddies and turbulence in vegetation canopies: the mixing layer analogy, *Boundary-Layer Meteorol.* **78**, 351–382.

[531] Ree, W.O. (1949) Hydraulic characteristics of vegetation for vegetated waterways, *Agr. Eng.***30**, 184–189.

[532] Rehm, R.G., McGrattan, K.B., and Baum, H.R. (2002) Large eddy simulation of flow over a wooded building complex, *Wind and Structures***Vol. 5, No. 2–4**, 291–300.

[533] Richardson, E.G. (1926) Amplitude of sound waves in pipes, *Proc. Roy. Soc., Ser. A* **112**, 522–541.

[534] Riddle, A., Carruthers, D., Sharpe, A., McHugh, C., and Stocker, J. (2004) Comparisons between FLUENT and ADMS for atmospheric dispersion modelling, *Atmospheric Environment* **38(7)**, 1029–1038.

[535] Risso, F., Ellingse,n K. (2001) Velocity fluctuations in a homogeneous dilute dispersion of high-Reynolds-number rising bubbles, *J. Fluid Mech.* **453**, 395–419.

[536] Risso, F., Legendre, D. (2003) Velocity fluctuations induced by high-Reynolds-number rising bubbles: experiments and numerical simulations. *ERCOFTAC Bulletin*. **56**, 41–45.

[537] Roach, P.J. (1976) *Computational Fluid Dynamics*, Hermosa Publishers, Albuquerque.

[538] Robertson, L., and Lange, J. (1998) Sourse function estimate by means of a variational data data assimilation applied to the ETEX-I tracer experiment, *Atmos.Environ.* **32**, 4219.

[539] Robins, A.G., and Apsley, D.D. (2000) Modelling of building effects in ADMS. ADMS Technical Specification, Paper P16/01N/00. See *http://www.cerc.co.uk/software/pubs/ADMS3–1TechSpec/P16_01.pdf.*

[540] Rodi, W. (1993) *Turbulence Models and Their Applications in Hydraulics*, A State-of-the-Art Review. 3rd edition. – IAHR Monograph Series, A.A.Balkema/Rotterdam/Brookfield.

[541] Rodi, W. (1997) Comparison of LES and RANS calculations of the flow around bluff bodies, J. Wind Eng. and Industrial Aero. **69–71**, 55–75.

[542] Rogers, M., and Moser, R. (1994) Direct simulation of a self-similar turbulent mixing layer, *Phys. Fluids* **A 6**, 903–922.

[543] Roig, V. (1993) *Zones de mélange découlements diphasiques á bulles*, PhD. Dissertation, Institut National Polytechnique de Toulouse, Toulouse, France.

[544] Ross, J. (1981) *The radiation regime and architecture of plant stands*, The Hague: Dr. W.Junk Pub.

[545] Rotach, M.W. (1991) *Turbulence Within and Above an Urban Canopy*, Züricher Geographische Schriften, H. 45, Zürich, Geographisches Institut, Eidgenuossische Technische Hochschule.

[546] Rotach, M.W. (1994) Determination of the zero-plane displacement in an urban area, *Boundary-Layer Metorol.*, 67, 187–193.

[547] Rotach, M.W. (1995) Profiles of turbulence statistics in and above an urban street canyon, *Atmospheric Environment* **29**, 1473–1486.

[548] Rotach, M.W.(1999) On the influence of the urban roughness sublayer on turbulence and dispersion, *Atmospheric Environment* **33**, 4001–4008.

[549] Rotach, M.W., Vogt R., Bernhofer C., Batchvarova E., Christen A., Clappier A., Feddersen B., Gryning S-E., Martucci G., Mayer H., Mitev V., Oke T.R, Parlow E., Richner H., Roth M., Roulet YA., Ruffieux D., Salmond J., Schatzmann M., and Voogt J.(2005) BUBBLE – an Urban Boundary Layer Meteorology Project, *Theoretical and Applied Climatology* **81(3–4)**, 231–261.

[550] Roth, M. (2000) Review of atmospheric turbulence over cities, *Q. J. R. Meteorol. Soc.* **126**, 941–990.

[551] Roulet, Y.-A., Martilli, A., Rotach, M., W., and Clappier, A.(2005) Validation of an Urban Surface Exchange Parameterization for Mesoscale Models – 1D Case in a Street Canyon, *Journal of Applied Meteorology* **Vol. 44, No. 9**,1484–1498.

[552] Routley, J.G. (1991) *The East Bay Hills Fire Oakland-Berkeley, California (October 19–22, 1991)*, Report TR-060, Major Fires Investigation Project, Federal Emergency Management Agency, U.S. Fire Administration, National Fire Data Center.

[553] Rouve, G., Pasche, E., and Bertram, H.U. (1987) *Hydraulische Probleme beim naturnahen Gewässerbau*, Forschungbericht: DFG, Weincheim; New York: VCH

[554] Sabetta, F., Piva, R., Di Giacinto, M. (1976) Navier Stokes flows with suspended particles: mathematical modelling and numerical simulation, *Theoretical and applied mechanics. Proc. XIY IUTAM Congress*, Delft, The Netherlands, 30 Aug.–4 Sept.

[555] Saffman, P.G. (1992) *Vortex dynamics*. Cambridge University Press.

[556] Sangani, A.S., and Acrivos, A. (1982) Slow flow past periodic arrays of cylinders with application to heat transfer, *Int. J. Multiphase Flow* **8(3)**, 193–206.

[557] Sass, B., Nielsen, N.W., Jorgensen, J.U., Amstrup, B., Kmit, M., and Mogensen, K.S. (2002) *The operational DMI-HIRLAM system – 2002-version*, DMI Technical Report 02–05.

[558] Satoh, K., and Yang, K.T. (1996) Experimental Observations of Swirling Fires, HTD **Vol. 335**, *Proceedings of the ASME Heat Transfer Division* **Vol. 4**, 393–400.

[559] Satoh, K., and Yang, K.T. (1997) Simulations of Swirling Fires Controlled by Channeled Self-generated Entrainment Flame, *Fire Safety Science, 5th International Symposium*, 201–212.

[560] Satoh, K., and Yang, K.T. (2000) A Horizontal Fire-Whirl Design Scenario for Engineering Performance-Based Fire-Code Applications, *Int. Journal on Engineering Performance-Based Fire Codes*. **Vol. 2, No. 2**,48–57.

[561] Schatzmann, M., and Leitl, B. (2002) Validation and application of obstacle resolving urban dispersion models, *Atmospheric Environment* **36**, 4811–4821.

[562] Schatzmann, M., (2005) Quality assurance and improvement of micro-scale meteorological models, *Short Papers of the 5th International Conference on Urban Air Quality Valencia*, Spain, 29–31 March 2005, Plenary, 14–17.

[563] Schayes, G., Thunis, P., and Bornstein, R. (1996) Topographic Vorticity-Mode Mesoscale-K (TVM) Model. Part1: Formulation, *Journal of Applied Meteorology* **Vol. 35**, 1815–1824.

[564] Schiller, L. (1932) *Strömungen in Rohren. Handbuch der Experimentalphysik*, B. IY, Teil 4. Leipzig.

[565] Schlichting, H. (1960) *Boundary Layer Theory*, McGraw-Hill Book Co., New York.

[566] Schlichting, H. (1966) *Grenzschicht-Theorie*, Karlsruhe, Verlag G. Braun.

[567] Scire, J.S. Strimaitis, D.S., and Yamartino, R.J. (1999) *A user's guide for CALPUFF dispersion model (Version 5)*, Earth Tech Inc., Concord, MA. See also *http://www.src.com/calpuff/calpuff1.htm.*

[568] Seginer, I., Mulhearn, P., Bradley, E., and Finnigan, J. (1976) Turbulent flow in a model plant canopy, *Boundary-Layer Met.* **10**, 423–453

[569] Seibert, P. (2001) Inverse modelling with a Lagrangian particle dispersion model: application to point releases over limited time intervals. In:*Gryning and Schiermeier (eds.): Air pollution modeling and its application XIV, Plenum*, NY, 381–389.

[570] Serra, T., Fernando, H.J.S, and Rodriquez, R. (2004) Effects of emergent vegetation on lateral diffusion in wetlands, *Water Research*, **38**, 139–147.

[571] Shaw, R.H., Silversides, R.H., and Thurtell, G.W. (1974) Some observations of turbulence and turbulent transport within and above plant canopies, *Boundary-Layer Meteorol.* **5**, 429–449.

[572] Shaw, R.H. (1977) Secondary wind speed maxima inside plant canopy, *J. Applied Meteorology*, **16**, 514–521.

[573] Shaw, R.H., Tavanger, J., and Ward, D.P. (1983) Structure of the Reynolds stress in a canopy layer., *J. Climate and Applied Meteorol.* **22**, 1922–1931.

[574] Shaw, R.H,. and Seginer, I. (1985) The Dissipation of Turbulence in Plant canopies, Extended Abstract: *American Meteorol. Soc.* 7^{th} *Symposium on Turbulence and Diffusion abstracts*, 200–203.

[575] Shaw, R.H., Paw, U.K.T., and Gao, W. (1989) Detection of temperature ramps and flow structures at a deciduous forest site, *Agric. For. Meteorol.* **47**, 123–138.

[576] Shaw, R.H., and Schumann, U. (1992) Large eddy simulation of turbulent flow above and within a forest, *Boundary Layer Meteorol.* **Vol. 61**, 47–64.

[577] Shaw R.H., Brunet Y., Finnigan J.J., and Raupach M.R. (1995) A wind-tunnel study of air flow in waving wheat: two-point velocity statistics, *Boundary-Layer Meteorology*, **76**, 349–376.

[578] Shaw, R.H., and Patton, E.G. (2003) Canopy element influences on resolved- and Subgrid-scale energy within a large-eddy simulation, *Agric. Forest Meteorol.* **115**, 5–17.

[579] Sherenkov, I.A. (1978) *Applied problems of plane calm hydraulics flows*, Moscow, Energy Publ.

[580] Shi, Z., Pethick, J., and Pye, K. (1995) Flow structure in and above the various heights of a saltmarsh canopy: A laboratory flume study, *Journal of Coastal Research*, **11**, 1204–1209.

[581] Shimizu, Y., and Tsujimoto, T. (1994) Numerical analysis of turbulent open-channel flow over a vegetation layer using a k-ϵ turbulence model, *J. Hydroscience and Hydraulic Engineering*, **11(2)**, 57–67.

[582] Snyder, W.H. (1972) Similarity Criteria for the Application of Fluid Models to the Study of Air Pollution Meteorology, *Boundary Layer Meteorol.* **Vol. 3**, 113–134.

[583] Sohier, A., and Hardeman, F. (2005). Radiological Dispersion Devices: Are we prepared? *(NKS Conference on Radioactive Contamination in Urban Areas*, May 7–9, 2003, Riso, Roskilde, Denmark), *J. Envir. Radioact.* (In press.)

[584] Sokhi1, R., Baklanov, A., Clark, P., Joffre, S., Millan, M.M., and Schlunzen, K.H. (2005) Enhancing meso-scale meteorological modelling capabilities for air pollution and dispersion applications (COST 728), *Short Papers of the 5th International Conference on Urban Air Quality Valencia*, Spain, 29–31 March 2005, Plenary,10–13.

[585] Sokolov, Yu.Yu. (1984) Equations of flexible vegetation inclination in connection with flood-land resistance calculation, *Dynamics and thermal regime of rivers and ponds*, Moscow: Nauka Publ., 72–85.

[586] Soma, S., and Saito, K. (1991) Reconstruction of Fire Whirls Using Scale Models, *Combustion and Flame* **Vol. 86**, 269–284.

[587] Sørensen, J.H. (2003) *Modelling the Atmospheric Spread of Foot-and-Mouth Disease*,. DMI Sci. Rep. 03–17, *http://www.dmi.dk/dmi/sr03–17.pdf*

[588] Sørensen, J.H. (2005) Preparedness for Biological Emergencies, *WMO Workshop on Development of Scope and Capabilities of Emergency Response Activities*, 7–9 December 2004, Geneva, CBS-DPFS/Wshop/ERA-DSC/INF.1

[589] Sorbjan, Z., and Uliasz, M. (1982) Some numerical urban boundary-layer studies, *Boundary-Layer Meteorology* **22**, 481–502.

[590] Soulhac, L., Weber, B., and Perkins, R.J. (1998) A practical model for dispersion in a network of streets, In *Proceedings of International Conference on Air Pollution Modelling and Simulation (APMS '98)*, Champ-sur-Marne, France, 253–262.

[591] Soulhac, L. (2000) *Modelisation de la dispersion atmospherique a l'interieur de la canopee urbaine*, Ph.D. thesis, Ecole Centrale de Lyon.

[592] Soulhac, L., Mejean, P., and Perkins, R.J. (2001) Modelling vehicle-generated atmospheric pollution in a quartier of Lyon using the model SIRANE, In *Proceedings of 7th International Conference on Harmonisation within Atmospheric Dispersion Modelling for Regulatory Purposes*, Belgirate, Italy.

[593] Soulhac, L., Preadelle, F., Perkins, R.J. (2004) An evaluation of the urban dispersion models SIRANE and ADMS Urban, using field data from Lyon, 9th conference on *Harmonisation within Atmospheric Dispersion Modelling for Regulatory Purposes*, June 1–4, 2004 in Garmisch-Partenkirchen, Germany.

[594] Soulhac, L., and Perkins, R.J. (2005) An operational modelling system for urban air quality, *CAPAC*, 22–25 June 2005, METU, Ankara, Turkey.

[595] Stacey, G.R., Belcher, R.E., Wood, C.J., and Gardiner, B.A. (1994) Wind flows and forces in a model spruce forest, *Boundary-Layer Meteorology* **69**, 311–334.

[596] Stoesser, T., Mathey, F., Fröchlich, J., and Rodi, W. (2003) LES of flow over multiple cubes, *ERCOFTAC Bulletin* **32**, 15–19.

[597] Stone, B.M., and Shen, H.T. (2002) Hydraulic resistance of flow in channels with cylindrical roughness, *J. Hydraul. Eng. ASCE***128(5)**, 500, doi: 10.1061/0733–9429.

[598] Straatman, A.G., Khayat, R.E., and Haj-Qasem, E. (2002) On the hydrodynamic stability of pulsatile flow in a plane channel, *Phys. of Fluids* **14, No. 6**, 1938–1944.

[599] Stull, R.B. (1984) Transilient turbulence theory. Part 1: The concept of eddy mixing across finite distances, *J. Atmospheric Science* **41**, 3351–3367.

[600] Tachie, M.F., James, D.F., and Gurrie, I.G. (2004) Slow flow through a brush, *Phys. Fluids*. **16, No. 2**, 445–451.

[601] Tardu, F.S., and Binder, G. (1993) Wall shear stres modulation in unsteady turbulent channel flow with high imposed frequencies, *Phys. of Fluids* **8**.

[602] Tarrel, A. (1997) A field investigation of diffusion within a submerged plant canopy, *MS Thesis. Woods Hole Oceanographic Institution and MIT*.

[603] Taylor, G.I. (1928) The energy of a body moving in an infinite fluid with application to airships, *Proc. R. Soc. Lond. A*. **70**, 13–21.

[604] Taylor, G.I. (1954) The dispersion of matter in turbulent flow through a pipe, *Proc. Royal Soc. London Ser.* **A, 223**, 446–468.

[605] Taylor, T.D., and Ndefo, D.E. (1971) Performance of the viscous fluid flow in the duct by means of a splintering method. In: *Proc. 2nd Int. Conference on numerical methods in fluid dynamics*, Sept. 15–19, 1970, California, Berkeley. Berlin N.Y.: Springer-Verlag.

[606] Tennekes, H., and Lumley, J.L. (1990) *A First Course in Turbulence*, MIT Press, Cambridge, Ma.

[607] Teshukov, V.M., and Gavrilyuk, S.L. (2002) Kinetic model for the motion of compressible bubbles in a perfect fluid, *Eur. J. Mech. B/Fluids* **21**, 469–491.

[608] Theurer, W., Baechlin, W., and Plate, E.J. (1992) Model Study of the Development of Boundary Layers Above Urban Areas, *Journal of Wind Engineering and Industrial Aerodynamics*. Vol. 41–44, 437–448.

[609] Theurer, W. (1995) Point sources in urban areas: modelling of neutral gas clouds with semi-empirical models, *Wind Climates in Cities*, 485–501. Eds. J.E. Cermak, A.G. Davenport, E.J. Plate and D.X. Viegas. Kluwer Academic Publisher, Dordrecht.

[610] Thom, A.S. (1968) The exchange of momentum, mass and heat between an artificial leaf and airflow in a wind tunnel, *Q.J.R. Meteorol. Soc.* **94**, 44–55.

[611] Thom, A.S. (1971) Momentum absorption by vegetation, *Q. J. R. Meteorol. Soc.* **97**, 414–428.

[612] Thomson, D.J. (2000) Concentration fluctuations in ADMS 3, including fluctuations from anisotropic and multiple sources, *ADMS Technical Specification*. **Paper P13/07D/00**. See *http://www.cerc.co.uk/software/pubs/ADMS3–1TechSpec/P13_07.pdf.*

[613] Thykier-Nielsen, S., Deme, S., and Mikkelsen, T. (1999) *Description of the Atmospheric Dispersion Module RIMPUFF*, Report RODOS(WG2)-TN(98)-02. Riso National Laboratory. See also *http://www.rodos.fzk.de/RodosHomePage/RodosHomePage/ Documents/ Public/Handbook/Volume3/4_2_6_RIMPUFF.pdf*

[614] Thykier-Nielsen, S., and Griffiths, I.H. (2003) Dispersion as a consequence of detonation of a dirty bomb in an urban area. *NKS Conference on Radioactive Contamination in Urban Areas*, May 7–9, 2003, Riso, Roskilde, Denmark.

[615] Trevitt, C. (1995) The January 1994 fires in Sydney, N.S.W., *FSTY3002 Fire Science and Management course*, School of Resource and Environmental Management, Department of Forestry, Australian National University, *http://sres.anu.edu.au/associated/fire/firecourse.html*

[616] Tritton, D.J. (1988) Physical Fluid Dynamics, 2nd ed., Oxford University Press, Oxford, England.

[617] Tsujimoto, T., Shimizu, Y., Kitamura, T., and Okada, T. (1992) Turbulent open-channel flow over bed covered by rigid vegetation, *J. Hydroscience and Hydraulic Engineering* **10(2)**, 13–25.

[618] Tsujimoto, T., and Kitamura, T. (1995) Lateral bed-load transport and sand-rigde formation near vegetation zone in an open-channel, *J. Hydroscience and Hydraulic Engineering* **13(1)**, 35–45.

[619] Tsujimoto, T., Kitamura, T., Fujii, Y., and Nakagawa, H. (1996) Hydraulic resistance of flow with flexible vegetation in open-channel, *J. Hydroscience and Hydraulic Engineering*. **14, N 1**, 47–56.

[620] Turco, R., Toon, O., Ackerman,T., Pollack, J., and Sagan, C. (1983) Nuclear winter: Global consequences of multiple nuclear explosions, *Science*, 1293–1302.

[621] Turfus, C. (1986) Diffusion from a continuous source near a surface in steady reversing shear flow, *J. Fluid Mech.* **172**, 183–209.

[622] Turfus, C. (1988) Calculating mean concentrations for steady sources in recirculating wakes by a particle trajectory method, *Atmospheric Environment*, **22**, 1271–1290.

[623] Uchijima, Z. (1962) Studies on the microclimate within the plant communities. 1. On the turbulent transfer coefficient within plant layers, *J. Agric. Meteor.* (Tokyo). **18**, 1–10.

[624] Uijttewaal, W.S.J., and Tukker, J. (1998) Development of quasi two-dimensional structures in a shallow free-surface mixing layer, *Exp. in Fluids* **24**, 192–200.

[625] Uijttewaal, W.S.J., and Booij, R. (2000) Effects of shallowness on the development of free-surface mixing layers, *Phys. Fluids*, **12(2)**, 392–402.

[626] USGS (1996) Vegetation affects water movement in the Florida Everglades, Fact Sheet 147–96, *United States Geological Survey*, Reston, VA.

[627] Valiela, I., Teal, J.M., and Deuser, W.G. (1978) The nature of growth forms in the salt marsh grass Spartina alterniflora, *American Naturalist* **112**, 461–470.

[628] Van Prooijen, B., and Uijttewaal, W.S.J. (2002) A linear approach for the evolution of coherent structures in shallow mixing layers, *Phys. Fluids*, **14(12)**, 4105–4114.

[629] Van Dyke, M.D. (1975) *Perturbation Methods in Fluid Mechanics*, Stanford, CA: *Parabolic Press*, Annot. Ed.

[630] Vardoulakis, S., Fisher, B.E. A., Pericleous, K., and Gonzalez-Flesca, N. (2003) Modelling air quality in street canyons: a review, *Atmos. Environ.* **37**, 155–182.

[631] *Vegetation and the Atmosphere* (1976) Academic Press, in two volumes edited by J.L. Monteith.

[632] Venkatram, A., Upadhyay, J., Heumann, J., and Klewicki, J. (2002) The development and evaluation of a dispersion model for urban areas, *4th AMS Symposium on the Urban Environment*, Norfolk, VA, May 2002.

[633] Venkatram, A., Isakov, V., Pankratz, D., Heumann, J., and Yuan, J. (2004) The analysis of data from an urban dispersion experiment, *Atmos. Environ.* **38**, 3647–3659.

[634] Virtual Information Center, Urban Fires Primer. (2000) (see *http://www.vic-info.org/*)

[635] Viegas, D.X. (1998) Convective Processes in Forest Fires, *Phil. Trans. Of the Royal Society*, **A, Vol. 356**, 2907–2928.

[636] Vincent, J.H. (1977) Model experiments on the nature of air pollution transport near buildings, *Atmospheric Environment* **11**, 765–774.

[637] Vivoni, E. (1998) *Flow through flexible vegetation*, M.S. Thesis, MIT, Cambridge, MA, USA.

[638] Vogel, M. and Williams, F.A. (1970) Flame Propagation Along Matchstick Arrays, *Combustion Science and Technology*, **Vol. 1**, 429–436.

[639] Vosper, S.B., and Mobbs, S.D. (1996) Lee waves over the English Lake District, *Q. J. R. Met. Soc.* **122**, 1283–1305.

[640] Walton, A., Cheng, A.Y.S., and Yeung, W.C. (2002) Large-eddy simulation of pollution dispersion in an urban street canyon, Part I: comparison with field data, *Atmos. Environ.* **36**, 3601–3613.

[641] Wallis, G.B. (1969) *One-dimensional 2-Phase Flow.* McGraw-Hill.

[642] Watanabe, T. (2004) Large-eddy simulation of coherent turbulence structures associated with scalar ramps over plant canopies, *Boundary-Layer Meteor.* **112**, 307–341.

[643] White, B.L., and Nepf, H.M. (2003) Scalar transport in random cylinder arrays at moderate Reynolds number, *J. Fluid Mech.* **487**, 43–79.

[644] Williams, F.A. (1969) Scaling Mass Fires, *Fire Research and Abstract Reviews* **Vol. 11, No. 1**, 1–23.

[645] Williams, D.W., Adams, J.S., Batten, J.J., Whitty, G.F., and Richardson, G.T. (1970) *Operation Euroka: An Australian Mass Fire Experiment*, Report 386, Maribyrnor, Victoria, Australia, Defense Standards Laboratory.

[646] Williams, F.A. (1992) Urban and Wildland Fire Phenomenology, *Progress Energy Combustion Science*, **Vol. 8**, pp. 317–354.

[647] Wilson, N.R., and Shaw, R.H. (1977) A higher-order closure model for canopy flow, *J. Appl. Meteorol. 16*, 1197–1205.

[648] Wilson, J.D. (1988) A second-order model for flow through vegetation, *Boundary-Layer Meteorol.* **42**, 371–392.

[649] Winant, C.D., Browand, F.K. (1974) Vortex pairing, the mechanism of turbulent mixing-layer growth, at moderate Reynolds number, *J. Fluid Mech.* **63**, 237–255.

[650] Wippermann, F. (1984) Air flow over and in broad valleys: channeling and counter-current, *Beitr. Phys. Atmos.* **57**, 92–105.

[651] Wood, N., Mason, P.(1991) The Influence of Static Stability on the Effective Roughness Lengths for Momentum and Heat Transfer, *Q.J.R. Meteorological Society*, **Vol 117**, 1025–1056.

[652] Wood, C.J. (1995) Understanding wind forces on trees, In *Wind and Trees* (Edited by Coutts M.P. and Grace J), Cambridge University Press, 133–164.

[653] Worcester, S.(1995) Effects of eelgrass beds on advection and turbulent mixing in low current and low shoot density environments, *Mar. Ecol. Prog. Ser.*, **126**, 223–232.

[654] Wright, J.L., and Lemon E.R. (1966) Photosynthesis under field conditions, VIII. Analysis of wind speed fluctuation data to evaluate turbulent exchange within a corn crop, *Agron. J.* **58**, 255–261.

[655] Wu, J. (1973) Spray in the atmospheric surface layer: laboratoty study, *J. Geophysical Research*, v. 78, No. 3, 511–518.

[656] Wu, G., and Meroney, R.N. (1995) Impact of changes of surface roughness on surface layer winds, turbulence, and plume dispersion, *Proceedings of 9th Int. Conf. on Wind Engineering*, New Delhi, India

[657] Wu, F.C., Shen, H.W., and Chou, Y.J. (1999) Variation of roughness coefficients for unsubmerged and submerged vegetation, *J. Hydraul. Eng. -ASCE*, **125(9)**, 934- 942.

[658] Wu, W., and Wang, S.Y. (2004) Depth-averaged numerical modeling of flow and sediment transport in open channels with vegetation, Riparian Vegetation and Fluvial Geomorphology (S.J. Bennett and A. Simon eds.), *American Geophysics Union*, USA, 253–265.

[659] Wygnanski, I., and Fiedler, H. (1970) The two-dimensional mixing region, *J. Fluid Mech.* **41**, 327–361.

[660] Xue, M., K.K. Droegemeier, and Wong, V. (2000) The Advanced Regional Prediction System (ARPS) – A multiscale nonhydrostatic atmospheric simulation and prediction tool. Part I: Model dynamics and verification, *Meteor. Atmos. Physics.* **75**, 161–193.

[661] Xue, M., Droegemeier, K.K.,Wong, V., Shapiro, A., Brewster, K., Carr, F., Weber, D., Liu, Y., and Wang, D.H. (2001): The Advanced Regional Prediction System (ARPS) – A multiscale nonhydrostatic atmospheric simulation and prediction tool. Part II: Model physics and applications, *Meteor. Atmos. Physics.* **76**, 134–165.

[662] Yamada, T. (1982) A numerical model study of turbulent airflow in and above a forest canopy, *J. of Meteorological Society of Japan* **Vol. 60, No. 1**, 439–454.

[663] Yano, M. (1966)*The Turbulent Diffusion in a Simulated Vegetative Cover*, Thesis, Civil Engineering Department, Colorado State University.

[664] Zavistoski, R.A. (1994) *Hydrodynamic effects of surface piercing plants*, MS thesis, MIT, Cambridge, MA, USA.

[665] Zhang, D.Z., Prosperetti, A. (1994) Averaged equation for inviscid disperse two-phase flow, *J. Fluid Mech.* **267**, 185–219.

[666] Zhang, H.J., and Zhou, Y. (2001) Effect of unequal cylinder spacing on vortex streets behind three side-by-side cylinders, *Physics of Fluids*, **13(12)**, 3675–3686.

[667] Zhou, Y., So, R.M.C., Liu, M.H., and Zhang, H.J. (2000) Complex turbulent wakes generated by two and three side-by-side cylinders, *Int. J. of Heat and Fluid Flow***21**, 125–133.

[668] Zilitinkevich, S.S. (1970) *Dynamics of the Atmospheric Boundary Layer*, Leningrad: Gydrometizdat. (in Russian).

[669] Zilitinkevich, S., Grachev, A., and Hunt, J.C.R. (1998) Surface frictional processes and non-local heat/mass transfer in the shear-free convective boundary layer, in *Buoyant Convection in Geophysical Flows* (eds. E.J. Plate and E. Fedorovich), Kluwer, Dordrecht.

[670] Zilitinkevich, S.S., Hunt, J.C.R., Grachev, A.A., Esau, I.N., Lalas, D.P., Akylas, E., Tombrou, M., Fairall, C.W., Fernando, H.J.S., Baklanov, A., Joffre, S.M. (2005) The effect of large eddies on the convective heat/mass transfer over complex terrain: advanced theory and its validation against experimental and LES data, *Croatian Meteorological Journal*, **40**, 20–26.

[671] Zilitinkevich, S., Baklanov, A.(2005) An analytical model of the mean-wind and the momentum flux profiles in the urban roughness layer. Ch. 3 in *DMI Scientific Report #04–08, ISBN: 87–7478-510–9*. (To be submitted to Boundary-Layer Meteorol.).

[672] Zilitinkevich, S., Baklanov, A., Mammarella, I., Joffre, S. (2006) The effect of stratification on the surface resistance for very rough vegetated and urban surfaces. In: *6th International Conference on Urban Climate*, June 12–16, 2006, Göteborg, Sweden, ISBN-10:91–613-9000–1, 415–418. (to be submitted to *Boundary Layer Meteorology*.)

[673] Zukauskas, A. (1987) Heat transfer from tubes in cross-flow, *Adv. Heat Trans.* **18**, 87–159.

Index

accident release, 29, 30, 34, 45, 65, 75, 77, 79, 85, 271, 312, 314, 318, 343, 344, 347, 348, 350–352, 354, 356
ambient (external) flow, 25, 106, 251, 254, 263, 270
annihilation, 252, 259, 264–266, 269
aquatic vegetation, 9, 12, 221
artificial canopy, 182
atmospheric boundary layer, ABL, 48, 51, 67, 72, 188, 281
averaging, 46, 70, 191, 198, 200, 202, 229, 233, 234, 236, 240

backward facing step problem, 114
bed stress (drag), 226, 242, 243
blocking, 252, 259, 263–269
boundary layer, 8, 15, 29, 30, 32, 34–36, 38, 42, 43, 45, 47, 49–52, 54, 72, 75–78, 85, 102, 104, 105, 107, 121, 126, 127, 131, 137, 139, 141, 147, 152, 156, 157, 161, 164, 165, 173, 176, 180, 189, 199, 201, 203, 206, 211, 213, 218, 221, 223, 243, 246, 283, 287, 307
boundary layer approach, 108, 109, 122, 129
boundary layer turbulence, 200, 201, 222
bubble, 24, 251, 261, 264–268
buoyancy, 31–34, 42–45, 85, 86

canopy, 2–5, 7, 8, 11, 14, 17, 22, 24, 25, 256
canopy (EPR) density, 166, 224, 227, 228, 233
canopy (EPR) flow regions, 32, 105, 118, 139
canopy (internal) flow, 25, 269
canopy flow categorisation, 15, 32, 37, 39, 40
Canopy-shear-Layer parameter, CSL, 246–248
channel flow, 261, 265
characteristic eddy, 195
coherent/organized structures, 176, 179, 183, 184, 191–193, 195, 197, 201, 202, 221, 243, 250
complex topography, 34, 35, 199, 204, 215, 217, 311, 344
computational model, 90, 95, 100, 108, 116, 122, 138, 140, 145, 251, 252, 264, 270
conditional sampling, 190, 201
convection (Reynolds number, 277
convection column, 275, 276, 297, 299
Coriolis force, 5, 7, 31, 281
counter-gradient flux, 186, 201, 202
counter-rotating vortices, 193, 195, 198

diffusion boundary layer, 222
dimensionless quantity, 92, 96, 103, 118, 127, 128, 134, 167, 254, 266, 269
dispersion, 29–31, 38, 40, 44–52, 60, 61, 63, 67, 72–75, 77–79, 230, 236, 237
dispersion coefficient, 232, 233, 235, 236, 238, 239
distributed roughness, 298
drag, 252
drag (force) parameterization, 6, 21, 91, 188
drag (force) partition, 6, 225, 245
drag discontinuity, 92, 104, 221, 223, 241, 242, 245, 250
drag force, 5, 6, 21, 201, 202, 204, 206, 207, 217, 218
droplet, 18, 25, 251
droplet canopy (droplet EPR), 22

easily penetrable roughness, PR, EPR, 122, 126, 131, 140
eddy cascade, 188, 191, 199, 203, 218

eddy diffusivity, 46, 53, 54, 65, 74, 77, 80, 85, 185, 200, 201
eddy viscosity, 43, 46
emergency modelling (Nuclear, biological, chemical), 30, 54, 78, 311, 312, 314, 316, 318, 343–347, 351, 354, 356
emergent canopy, 224, 226, 227, 229
Empirical Orthogonal Function Analysis, EOF, 194–198
entrance region length problem, 108, 109, 111
EPR made up of immobile elements (model of a forest), 89, 94, 99
EPR made up of mobile elements (Droplet EPR), 89
equivalent size problem, 143
Euler, Eulerian, 54, 260–263, 267
Eulerian framework (approach), 21, 27, 146, 150
experiment, 47, 54, 68, 78, 79, 82

Fick, 151, 232, 235, 238
field experiment, 6, 8, 19, 20, 30, 44, 51, 66, 68, 78, 152, 165, 197, 202, 274, 296, 314, 321, 334, 338, 351
fires, 271
firestorm, 275
flexible canopy/obstacles, 8, 10, 11, 14, 29, 36, 121, 248
flow deceleration, 4, 13, 18, 25, 26
flow displacement, 35, 36, 38, 51, 61, 68, 76, 82, 86, 129
forced convection, 19
forest fires, 271–273, 296, 300, 303, 308
forest model, 298, 300
Fourier, 41
free (natural) convection, 19, 20, 42, 168, 172
free-surface flow, 9, 226
friction velocity, 3, 47, 180, 205, 229, 230, 240, 282, 293
Froude number, Fr, 32, 216, 217, 219, 278, 307
FUMAPEX, European research project, 314, 315

Gauss's Theorem, 262
Gaussian profile, 54, 58, 60, 62, 64, 75, 78, 79, 85, 86, 231, 233, 253, 255, 258, 300, 301, 350, 351

heat (mass) flux parameterization, 21, 116, 117
heat exchange, 7
heat exchange coefficient, 150, 151
heat exchanger, 17, 24, 116
higher-order closure, 177, 186, 187, 189, 202, 203
horizontal-plane hydraulic problem, 12–14

inertial force, 252
inflection point, 181, 203, 218
initial region of EPR flow, 104, 105, 107, 118–120, 126, 129, 136, 166, 167, 169
instability, 199, 221, 223, 243, 250

Kelvin-Helmholtz (K-H) instability, 221, 223, 243, 250
Kelvin-Helmholtz (K-H) vortices, 222, 244, 247, 249
Kolmogorov, ix, 230, 231, 279, 282
Kolmogorov lengthscale, 199, 203

laboratory experiment, 9–12, 14, 17, 23–25, 28, 30, 92, 152–154, 159, 162, 172, 173, 197, 202, 209, 211, 236, 238, 247–249, 264, 265, 268, 282, 297, 303, 308, 351
Lagrange, Lagrangian, 21, 22, 48, 54, 74, 78, 146
Lagrangian framework (approach), 202, 203
Laplace, 95, 101, 261, 262
large-eddy simulation, LES, 7, 43, 184, 187–192, 194, 195, 197, 198, 203, 295, 299, 301, 302, 304–306, 308, 341, 346, 350, 354, 356
Leaf Area Index, (*LAI*), 215
linear force (drag) law, 6, 27, 91, 103, 104, 108–112, 114, 123, 127, 146, 150, 228
LNF, 'localized near field' model, 202
logarithmic law, logarithmic profile, 2, 3, 13, 15, 16, 23, 86, 159, 162, 163, 168, 180, 181, 204, 205, 212, 227, 239, 241, 272, 282, 288, 324

main region of EPR flow, 5, 104, 105, 107, 118, 119, 129, 136, 157, 162, 166
Manning, 242
mass exchange, 7

mass exchange coefficient, 150, 151
mixing layer, 197, 199, 203, 218, 360
mixing length model, 160, 200, 205, 207, 211, 217
mixing-layer hypothesis, 195, 207
morphology of canopy/homogeneous canopy (EPR), 10, 92, 106, 224, 225
morphology of canopy/inhomogeneous canopy (EPR), 4, 20, 92, 93, 107, 154, 157, 227, 236
MOST, Monin-Obukhov similarity theory, 322, 324, 326, 332
MOST, Monin-Obukhov similarity theory, 335
multibody flows, 252, 254, 259, 264, 269, 270

Navier—Stokes equations, 13, 90, 100, 101, 108, 109, 111, 192, 225, 350
neutral stratification, 37, 163, 289
nonlocal phenomenon, 186
Nuclear Winter, 272, 274, 275
Nusselt number Nu, 151
NWP, numerical weather prediction model, 312, 313, 318, 322, 331

obstruction, isolated roughness elements, 2, 5, 8, 9, 11, 12, 14–16, 20, 22, 24, 26, 27, 30, 31, 33, 35, 38, 40, 44, 49, 52, 89, 92, 93, 100, 101, 103, 116, 118–121, 132, 150, 152, 158, 173, 174, 176, 182, 226, 228, 229, 234, 289, 291
Obukhov (Monin-Obuknov) length, 180, 282

paradox, 202
pattern of obstructions, 30, 35, 37, 40, 49, 52
PE, population exposure model, 314
penetrable canopy, 16
penetrable roughness, PR, EPR, 2, 23–26, 89, 95, 99, 102, 104, 108, 109, 116, 121, 150, 152, 165, 170, 176, 279, 360
pipe/duct flow, 89–92, 94, 95, 97, 100, 105, 108, 112, 115, 121, 124, 130, 142, 158, 251, 282
plant canopy, 251, 252, 269
Poiseuille flow, 90, 98, 114
porous medium, 22
Prandtl, 1–3, 102, 108, 119, 151, 160, 279
Prandtl number Pr, 134

quadrant analysis, 183, 201
quadratic force (drag) law, 7, 10, 27, 104, 108, 109, 111, 113, 114, 123, 150, 163, 226, 228

ramp pattern, 183, 190, 191, 197
recirculating flow, 38, 46–50, 60–63, 68, 71, 114, 234, 236
resistance, 242, 250
resistance (drag), 4, 7, 32, 37, 94, 99, 157, 181, 227, 229, 232, 242, 243, 245, 246
resistance (drag) coefficients, 6, 182, 188, 227, 228, 247
resistance (drag), 10, 45, 113, 123, 142, 150, 228
resistance (drag) coefficients, 93, 227, 248
resistance coefficients, 9, 93, 103, 110, 114, 226, 227
resolved scale, 187–191
reversed flow, 217
Reynolds number (global) Re, 102, 158
Reynolds number of turbulent wake, 259
Reynolds number, local Re' (stem Reynolds number Re_d), 158, 227, 228
Reynolds number, local Re' (stem Reynolds number Re_d), 171
Reynolds number, local (stem Reynolds number), Re', 102
Richardson, 203
Richardson number Ri, 168, 216, 282, 298
Richardson's "annular effect, 98
Rossby length number, 307
Rossby length scale, 31, 35
Rossby number, 87, 307
roughness, 1, 2, 23, 218, 230, 239, 242, 280
roughness change, 30, 31, 45, 47, 77, 285, 288
roughness length, roughness height, 3, 15, 23, 37, 42, 46, 86, 159, 162, 180, 281, 293, 322, 325, 326, 328, 332, 333, 335, 342, 347, 350
roughness sublayer, 16, 47, 181, 183, 199, 203, 241, 243
roughness sublayer, RSL, 205

sand roughness, 1, 23
Schmidt number Sc, 119, 134
secondary maximum (bulge, or zero-wind gradient) phenomenon, 4, 126,

131, 172, 181, 186, 202, 227, 281
shallow-water shear-layer, SSL, 243
sheltering effect, 36, 171, 228
skewness, 183
spatial range, 29
spatial structure of the turbulent field, 184, 195
spectra, 172, 174, 175, 177, 196
spraying cooling system (SCS), 1, 17, 18, 20, 22, 25, 26, 120, 122, 131, 135, 140, 143, 146, 148, 165, 167, 170, 171
stability, 34, 35, 180, 185, 203, 303, 326, 329, 334, 345, 354
stability parameter, 180
stable stratification, 216, 279, 344
stable stratification, 163, 311
stagnation, 252, 263
stagnation zone, 40, 52, 59, 67, 68, 87, 104–106, 131, 137
street canyon effects, 31, 41, 50, 71, 74, 75, 80, 85, 86
subgrid-scale, SGS, 187–189
submerged canopy, 222, 239, 241, 243
surface roughness, 31, 180, 280, 281
sweeps/ejections, 179, 183, 191–193, 195, 197, 198, 201
swirling wake, 36, 39, 50, 70

Taylor, x, 202, 237, 262
Taylor's hypothesis, 191, 265
technical roughness, 23, 24
thermal boundary layer, 120, 142
thermal stratification, 283, 326
transilient theory, 172
transport Reynolds number, Re_t, 235
turbulent boundary layer, 301
turbulent kinetic energy, 43, 85, 179, 187
turbulent kinetic energy, TKE, 46, 182, 189, 190, 203, 229, 244, 316, 332, 335
turbulent wake, 259

UAP, urban air pollution model, 311, 314, 315
unstable stratification, 163, 168
urban boundary layer, 289
urban canopy, 15–17
urban roughness, 16, 290
urban weather, 314, 318

vegetation canopy, 27, 201
vertical-plane hydraulic problem, 9–11
von Karman's constant, 3, 37, 86, 160, 168, 180, 205, 282
vortices shedding, 158
vorticity cancellation, 38, 68

wake intermingling, 252, 256, 266, 269
wind mill, 17

zero-plane displacement, 3, 37, 55, 159, 162, 180, 181, 205, 281–283, 289, 290, 293, 321–323, 326, 336